Behaviour and Analysis of Steel and Macro-Synthetic Fibre Reinforced Concrete Subjected to Reversed Cyclic Loading: A Pilot Investigation

by

David Joseph Carnovale

A thesis submitted in conformity with the requirements
for the degree of Master's of Applied Science

Graduate Department of Civil Engineering

University of Toronto

Behaviour and Analysis of Steel and Macro-Synthetic Fibre Reinforced Concrete Subjected to Reversed Cyclic Loading: A Pilot Investigation

David Joseph Carnovale

Master's of Applied Science

Graduate Department of Civil Engineering
University of Toronto

2013

Abstract

The benefits of fibre reinforced concrete (FRC) have been thoroughly investigated. Much of this work has focussed on steel FRC subjected to monotonic loads. Data on the structural behaviour of macro-synthetic FRC or FRC under cyclic loads is scarce.

A pilot investigation on the shear behaviour of macro-synthetic FRC and on the behaviour of FRC under reversed cyclic in-plane shear loading was carried out. Five in-plane shear panel tests were performed. The parameters under study were the fibre material type (steel or macro-synthetic) and loading protocol. Additionally, a number of compression, direct tension, and flexural tests were performed to determine the material properties of the concretes for comparison. The material response of 2.0% by volume of macro-synthetic FRC matched closely with 1.0% steel FRC.

Finally, building upon an existing steel FRC model, a model for macro-synthetic FRC in tension was proposed and a short verification study was undertaken.

Acknowledgments

First of all, I would like to express my deepest gratitude to my supervisor, Professor F.J. Vecchio. Without the expertise and guidance provided I would not have been able to complete this study. I would also like to thank Professor D.P. Gauvreau for his insight, expertise and valuable comments while reviewing this thesis.

I would like to acknowledge the generous financial support that I received from the Government of Canada (Natural Sciences and Engineering Research Council Engage Research Grant and Alexander Graham Bell Canada Graduate Scholarship), the Government of Ontario (Ontario Graduate Scholarship), the Department of Civil Engineering at the University of Toronto, and Professor Vecchio. The material donations provided by N.V. Bekaert S.A., BASF, Holcim Canada Inc., Dufferin Aggregates and BASF Canada are also gratefully acknowledged. Without such financial support, I could not have completed this work.

I would also like to express my appreciation to the staff of the University of Toronto Structural Testing Facility for their advice and technical support throughout my experimental program: Renzo Bassett, John MacDonald, Xiaoming Sun, Giovanni Buzzeo, Alan McClenaghan, Bryant Cook, and Michel Fiss.

In addition, I would like to express my deepest appreciation to my friends and colleagues who have helped me throughout the completion of this work, both physically in the lab, technically with my analytical work, and emotionally throughout the whole process: Dr. Seong-Cheol Lee, Dr. Trevor Hyrnyk, Dr. Jimmy Susetyo, Fady El Mohandes, Ivan Chak, Vahid Sadeghian, William Luo, Heather Trommels, Paolo Calvi, David Ruggiero, Giorgio Proestos, Brad Hunt, Loreto Caprara, Robert Netopilik, Arjang Tavassoli, Doug Getzlaf, David Johnson, Lisa Vint, David Wang and Ardavan Amirchoupani. I would also like to thank the undergraduate students who helped me with my experimental work: Alessandro Baselli, Raymond Ma, Momo Sun, Charlie Guan, Allan Kuan, Edvard Bruun, Max Ho and Kanwar Johal.

Finally, I would like to give my heartfelt thanks to my wonderful fiancée, Elisa, and my family for their constant support and encouragement.

Table of Contents

List of Tables

List of Figures

List of Notations

Latin Upper Case Symbols

AR_f	aspect ratio of fibre [l_f/d_f]
A_b	area of steel reinforcing bar [mm^2]
A_c	cross-sectional area of the failure crack, bh [mm^2]
A_f	cross-sectional area of the fibres [mm^2]
$A_{j,comp}$	area of the compression jacks of the panel tester [mm^2]
$A_{j,tens}$	area of the tension jacks of the panel tester [mm^2]
A_{panel}	cross-sectional area of the panel [mm^2]
A_s	cross-sectional area of steel reinforcing bar [mm^2]
CV	coefficient of variation [%]
D	diameter of concrete compression cylinder [mm]
E_{cs}	secant modulus of elasticity for concrete in compression [MPa]
E_{ct}	secant modulus of elasticity for concrete in tension [MPa]
E_f	Young's Modulus of fibre [MPa]
E_s	Young's Modulus of steel reinforcing bar [MPa]
G_F	fracture energy of concrete [N/m]
G_{abs}	absorbed energy for reversed cyclic tests [kN·mm]
G_{fe}	engagement energy of FRC [N/m]
$K_{def,i}$	K_{def} at a crack width of l_{sp}
K_{def}	factor to represent average pull-out stress in fibre due to mechanical anchorage of deformations
$K_{eh,i}$	K_{eh} at a crack width of l_{eh}
K_{eh}	factor to represent average pull-out stress in fibre due to mechanical anchorage of end-hook
K_f	frictional bond modulus [MPa]
K_{st}	factor to represent average pull-out stress in fibre due to frictional bond
L	span length of concrete specimen [mm]
N_f	number of fibres crossing the failure crack

P_1	first cracking load of concrete in bending for MOR tests [kN]
P_{XXX}^D	residual load at a midspan displacement of L/XXX for MOR tests [kN]
P_{cr}	first diagonal cracking load [kN]
$P_{def,avg,i}$	average mechanical anchorage force at l_{sp} for deformed fibre [N]
$P_{def,avg}$	average mechanical anchorage force for deformed fibre [N]
$P_{def,max}$	maximum mechanical anchorage force for aligned deformed fibre [N]
$P_{eh,avg,i}$	average mechanical anchorage force at l_{eh} for end-hooked fibre [N]
$P_{eh,avg}$	average mechanical anchorage force for end-hooked fibre [N]
$P_{eh,max}$	maximum mechanical anchorage force for aligned end-hooked fibre [N]
$P_{f,0}$	maximum pull-out force for aligned fibre [N]
$P_{f,tot}$	total pull-out force for aligned fibre (frictional and mechanical anchorage components included) [N]
$P_{f,\theta}$	maximum pull-out force for fibre inclined at angle θ [N]
$P_{j,comp}$	recorded hydraulic pressure in the compression jacks of the panel tester [MPa]
$P_{j,tens}$	recorded hydraulic pressure in the tension jacks of the panel tester [MPa]
P_{norm}	normalized pull-out load of inclined fibre [N]
P_p	peak load of concrete in bending for MOR tests [kN]
P_u	ultimate load [kN]
PSR	ratio between polypropylene and steel fibre bond strength
$R_{T,XXX}^D$	equivalent flexural strength ratio of concrete specimen for MOR tests [%]
SA	surface area [mm^2]
T_{XXX}^D	toughness of concrete specimen for MOR tests (area under the load versus displacement curve up until a midspan displacement of L/XXX) [J]
V_f	fibre volume fraction (ratio of the volume of fibres to the volume of concrete) [%]

Latin Lower Case Symbols

a	shear span for beams [mm]
a/d	shear span-to-depth ratio for beams
a_{max}	maximum aggregate diameter (VecTor2) [mm]
b	width of concrete specimen, beam, or failure crack [mm]

c	attenuation factor for exponential concrete tension softening (VEM; Voo and Foster, 2003)
d	depth of concrete specimen [mm]
d_a	maximum aggregate diameter (Bazant, 2002) [mm]
d_b	diameter of steel reinforcing bar [mm]
d_f	diameter of fibre [mm]
d_v	effective shear depth for beams [mm]
f	snubbing coefficient
f_1	first cracking stress of concrete in bending for MOR tests [MPa]
f_{XXX}^D	residual stress at a midspan displacement of L/XXX for MOR tests [MPa]
$f_{c,Test}$	peak compressive stress in the concrete on panel test day [MPa]
f_c'	28-day compressive strength of concrete [MPa]
$f_{c1,cr}$	principal tensile stress of concrete at cracking [MPa]
$f_{c1,max}$	maximum principal tensile stress of concrete [MPa]
$f_{c1,u}$	principal tensile stress of concrete at ultimate [MPa]
f_{c1}	principal tensile stress of concrete [MPa]
$f_{c2,u}$	principal compressive stress of concrete at ultimate [MPa]
f_{c2}	principal compressive stress of concrete [MPa]
f_{ct}	residual tensile stress in concrete [MPa]
f_{cu}	cube compressive strength of concrete [MPa]
f_{cx}	stress in the concrete in the x-direction for concrete panel [MPa]
f_{cy}	stress in the concrete in the y-direction for concrete panel [MPa]
f_{def}	mechanical anchorage component (due to deformations) of overall fibre tension contribution [MPa]
f_{eh}	mechanical anchorage component (due to end-hook) of overall fibre tension contribution [MPa]
f_f	total fibre tensile srress [MPa]
f_p	peak stress of concrete in bending for MOR tests [MPa]
f_r	modulus of rupture of concrete [MPa]
f_{st}	frictional component of overall fibre tension contribution [MPa]

$f_{sx,max}$ maximum stress in the reinforcement in the x-direction for concrete panel [MPa]

f_{sx} stress in the reinforcement in the x-direction for concrete panel [MPa]

$f_{sy,max}$ maximum stress in the reinforcement in the x-direction for concrete panel [MPa]

f_{sy} stress in the reinforcement in the y-direction for concrete panel [MPa]

$f_{t,FRC}$ total residual tensile stress in FRC member, according to DEM and SDEM [MPa]

$f_{t,max}$ maximum tensile stress in concrete during strain hardening (dogbones) [MPa]

f_t' first cracking strength of concrete [MPa]

f_{te} minimum tensile stress in concrete immediately after cracking (dogbones) [MPa]

f_{tu} ultimate tensile stress attained by dogbone specimen after first cracking [MPa]

f_u ultimate strength of steel reinforcing bar [MPa]

f_{uf} ultimate tensile strength of fibre [MPa]

f_y yield strength of steel reinforcing bar [MPa]

h height of concrete specimen [mm]

k factor to account for fibre type (Stroeven, 2009)

l length of concrete specimen [mm]

l_n clear span of concrete beam [mm]

l_a embedded length of short part of fibre [mm]

l_{def} crack width at the end of mechanical anchorage for macro-synthetic fibre [mm]

l_{eh} length of end-hook for an end-hooked steel fibre [mm]

l_f length of fibre [mm]

$l_{po,0}$ pull-out length for aligned fibre [mm]

$l_{po,\theta}$ pull-out length for fibre inclined at angle θ [mm]

s_1 slip at the end of the first cycle for deformed fibre pull-out tests [mm]

$s_{cr,avg}$ average crack spacing [mm]

s_{def} slip at maximum mechanical anchorage for aligned deformed fibre [mm]

s_{eh} slip at maximum mechanical anchorage for aligned end-hooked fibre [mm]

$s_{f,\theta}$ inclination angle dependant slip at maximum bond strength for straight fibre [mm]

s_f slip at maximum frictional bond strength for aligned straight fibre [mm]

s_{long} slip of long part of fibre [mm]

s_m average crack spacing (panel tests) [mm]

s_{mx} VecTor2 input for maximum crack spacing in the x-direction [mm]

s_{my} VecTor2 input for maximum crack spacing in the y-direction [mm]

s_{short} slip of short part of fibre [mm]

t thickness of concrete specimen [mm]

v_{cr} cracking shear stress (panel tests) [MPa]

v_u ultimate shear stress (panel tests) [MPa]

v_{xy} shear stress [MPa]

w/c water-to-cement ratio

$w_{cr,avg}$ average crack width [mm]

$w_{cr,e}$ width of the crack at fibre engagement [mm]

$w_{cr,max}$ maximum crack width [mm]

w_{cr} crack width [mm]

w_e fibre engagement length [mm] (VEM; Voo and Foster, 2003)

w_m average crack width (panel tests) [mm]

$w_{p\theta,eh}$ inclination angle dependant crack width at maximum mechanical anchorage force [mm]

$w_{p\theta,f}$ inclination angle dependant crack width at maximum bond strength for straight fibre [mm]

Greek Symbols

Δ_{max} maximum vertical displacement in direct shear test (Khaloo and Kim, 1997) [mm]

α material parameter representing resistance to slip (VEM; Voo and Foster, 2003)

α_f fibre orientation factor

α_o parameter to account for aggregate shape (Bazant, 2002)

β_{def} factor to account for the ignored slip on the longer embedded part of the fibre

β_{eh} factor to account for the ignored slip on the longer embedded part of the fibre

β_f factor to account for the ignored slip on the longer embedded part of the fibre

γ_{cr} cracking shear strain (panel tests) [x10^{-3}]

γ_u ultimate shear strain (panel tests) [x10^{-3}]

γ_{xy} shear strain [x10^{-3}]

δ_{max} deflection at maximum applied load [mm]

δ_u	deflection at failure [mm]
$\varepsilon_{1,cr}$	principal tensile strain at cracking [x10^{-3}]
$\varepsilon_{1,max}$	principal tensile strain at $f_{c1,max}$ [x10^{-3}]
$\varepsilon_{1,u}$	principal tensile strain at ultimate [x10^{-3}]
ε_1	principal tensile strain [x10^{-3}]
$\varepsilon_{2,u}$	principal compressive strain at ultimate [x10^{-3}]
ε_2	principal compressive strain [x10^{-3}]
ε_h or ε_{45°	horizontal direction strain for concrete panel [x10^{-3}]
$\varepsilon_{c,Test}$	peak compressive strain of concrete on panel test day [x10^{-3}]
ε_c'	concrete strain at peak compressive stress [x10^{-3}]
ε_{c1}	principal tensile strain of concrete [x10^{-3}]
ε_{c2}	principal compressive strain of concrete [x10^{-3}]
ε_f	fibre elongation/strain [%]
ε_{sx}	x-direction reinforcement strain for concrete panel [x10^{-3}]
ε_{sy}	y-direction reinforcement strain for concrete panel [x10^{-3}]
$\varepsilon_{t,max}$	strain of concrete dogbone specimen at $f_{t,max}$ [x10^{-3}]
ε_t'	concrete strain at cracking stress [x10^{-3}]
ε_u	ultimate strain of steel reinforcing bar [x10^{-3}]
ε_v or ε_{135°	vertical direction strain for concrete panel [x10^{-3}]
ε_x	x-direction strain for concrete panel [x10^{-3}]
ε_y	yield strain of steel reinforcing bar [x10^{-3}]
ε_y	y-direction strain for concrete panel [x10^{-3}]
θ	fibre inclination angle, measured to the normal to the crack surface [°]
$\theta_{crit,eh}$	the critical fibre inclination angle at which the force due to mechanical anchorage begins to decline for a given crack width [°]
$\theta_{crit,f}$	the critical fibre inclination angle at which plastic frictional bond behaviour will commence for a given crack width [°]
θ_ε	angle of inclination of the principal tensile strain (counter clockwise to the x-axis) [°]
θ_σ	angle of inclination of the principal tensile stress (counter clockwise to the x-axis) [°]

μ_δ	ductility of flexure critical beams subjected to reversed cyclic loading (Daniel and Loukili, 2002)
ρ_l	longitudinal reinforcement ratio in concrete beams [%]
ρ_w	web shear reinforcement ratio [%]
ρ_x	reinforcement ratio in the longitudinal (or x-) direction [%]
ρ_y	reinforcement ratio in the transverse (or y-) direction [%]
$\sigma_{f,cr,avg}$	average stress in aligned fibre at the crack [MPa]
$\sigma_{f,cr,eh}$	average tensile stress due to mechanical anchorage in fibre [MPa]
$\sigma_{f,cr,st}$	average tensile stress due to frictional bond in straight fibre [MPa]
τ_b	fibre bond strength [MPa]
$\tau_{def,max}$	maximum mechanical anchorage stress for aligned deformed fibre [MPa]
$\tau_{eh,max}$	maximum mechanical anchorage stress for aligned end-hooked fibre [MPa]
$\tau_{f,avg}$	average frictional bond stress for straight fibre [MPa]
$\tau_{f,max,\theta}$	maximum frictional bond strength for fibre inclined at angle θ [MPa]
$\tau_{f,max}$	maximum frictional bond strength for aligned straight fibre [MPa]
$\tau_{f,tot,poly}$	total bond strength for aligned straight polypropylene fibre [MPa]
$\tau_{f,tot,steel}$	total bond strength for aligned straight steel fibre [MPa]
$\tau_{f,tot}$	total bond strength for aligned straight fibre [MPa]
τ_{long}	bond stress in longer embedded portion of fibre [MPa]
τ_{max}	maximum shear stress attained in direct shear test (Khaloo and Kim, 1997) [MPa]
τ_{short}	bond stress in shorter embedded portion of fibre [MPa]
ω_2	degree of planar fibre orientation (Stroeven, 2009)

List of Equations

Chapter 1
Introduction

1 Introduction

1.1 Fibre Reinforced Concrete

American Concrete Institute (ACI) Committee 544 (2008) defines fibre reinforced concrete as "concrete made primarily of hydraulic cements, aggregates, and discrete reinforcing fibres". For many centuries, the idea of reinforcing brittle materials with discrete fibres has been employed in construction practices. The Ancient Egyptians, for example, used straw to improve the post-cracked behaviour of sun-dried mud bricks for huts (Mansour et al., 2007). However, the modern era of research and development for discrete fibre reinforcement technologies did not begin until the 1960s, with groundbreaking reports from Romualdi and Baston in 1963 followed by Romualdi and Mandel in 1964. In these papers, the feasibility of using fibres to improve the tensile ductility of concrete was demonstrated.

In the decades that followed, extensive research was undertaken to expand on this finding. Investigations into the types of fibres that may be used in concrete applications have been performed. These were carried out to determine the properties that fibres, and fibre materials, must possess to be effective in improving the brittle tensile behaviour of concrete. Vast ranges of materials have been tested such as steel, carbon, glass, plastic, polypropylene, nylon, and natural materials such as cotton. From this research, ACI Committee 544 (2008) has categorized fibre reinforced concrete into four groups based on the fibre materials: steel fibre reinforced concrete (SFRC), glass fibre reinforced concrete (GFRC), synthetic fibre reinforced concrete (SNFRC), and natural fibre reinforced concrete (NFRC). Synthetic fibres are further subdivided into micro-synthetic fibres (with a diameter less than 0.30 mm) and macro-synthetic fibres (with a diameter greater than 0.30 mm) and may be composed of materials such as polyester, acrylic, polyethylene and polypropylene (Richardson and Landless, 2009). Glass and natural fibres show susceptibility to environmental conditions, leaving steel and synthetic fibres as the most viable concrete reinforcement options (ACI Committee 544, 2008).

In general, the introduction of fibres into the concrete matrix was found to significantly alter the brittle tension response of the concrete material. Before cracking, and under compressive loads, the addition of fibres has little effect (ACI Committee 544, 2008; Nataraja et al., 1999). However, even small amounts of fibre addition leads to significant increases in the post-cracked toughness and ductility of concrete (Shah and Rangan, 1971; Batson, 1976; Thomas and Ramaswamy, 2007). Also, significant improvements in crack control can be achieved, with a reduction in crack width and crack spacing in the concrete (Banthia et al., 1993; Grzybowski and Shah, 1990; Susetyo et al., 2011). The smaller crack widths and increased abrasion resistance promotes an improvement in the long-term serviceability of the structure by preventing the ingress of chemicals and water that can have deleterious effects (Johnston, 2001). This is of particular importance during a time of deteriorating infrastructure, when a great deal of the built environment is proving unable to sustain the service lives originally planned (Wang et al., 1987). A tragic example of this is the collapse of the de la Concorde overpass in Laval, Québec on September 30, 2006 (Figure 1.1), which claimed five lives. An inquiry into the collapse revealed that the 40-year-old bridge should have been able to withstand a longer service life. The inquiry also revealed that 46.7% of primary road network bridges that fall under the Ministère des Transports du Québec are structurally deficient (Johnson et al., 2007). The beneficial properties of fibre reinforced concrete can be taken advantage of to prevent these issues in future structures.

Figure 1.1: Collapse of the de la Concorde overpass (adapted from Johnson et al., 2007)

In addition to these serviceability improvements, it has been found that steel fibres can be used in place of minimum temperature and shrinkage reinforcement to control cracking in slabs (Susetyo, 2009). As well, past tests on fibre reinforced concrete shear panel elements and beams have shown that steel fibres can be used to reduce the need for transverse shear reinforcing bars while improving the overall ductility and controlling crack growth (Casanova et al., 1997; Meda et al., 2005; Susetyo et al., 2011). Thus, these bars may be replaced and the code requirement to provide adequate cover to such bars would no longer apply. Concrete sections can be made much thinner, generating savings on material usage, labour costs and greenhouse gas emissions generated by the cement production process.

FRC has been used for numerous applications throughout the construction industry, such as in highways and airport runways, in shotcrete tunnel wall linings, as minimum shear and transverse reinforcement in precast bridge sections and decks, and in slabs-on-grade (Wang et al., 1987; Meda et al., 2005; Minelli, 2005). Steel fibres have also seen limited use in framed slabs and in other flexure-critical structural members (Meda et al., 2005). However, FRC has not been substantially utilized in more critical structural elements (Richarson and Landless, 2009). This is likely attributable to the limited development of rational design codes and standards needed to build the confidence of practitioners in the benefits and application of the material (Lee et al., 2013; Noghabai, 2000).

Also, despite the fact that there has been a focus on steel fibre reinforced concrete in the research over the past four decades, very little research has been conducted on macro-synthetic polypropylene fibre reinforced concrete (PPFRC). This type of fibre should be of particular interest due to its corrosion resistance relative to steel (Zheng and Feldman, 1995), its resistance to alkali attack (Wang et al., 1987), its relatively low cost (Richadson, 2005), and its durability under a long service life (Mu et al., 2002). Polypropylene fibres can also be made into a variety of cross-sectional shapes and can be designed with different surface finishes, allowing for further improvement in bond properties (Wang et al., 1987). In addition, recent developments in synthetic fibre microstructure technologies have led to the production of a new generation of high modulus polypropylene fibres with improved matrix bond properties. Much of the research regarding these developments is carried out by individual manufacturers and is not adequately peer reviewed (Richardson and Landless, 2009). Thus, focus on evaluation of the behaviour of

PPFRC in the research is required to improve understanding and build confidence in the viability of such fibres for critical structural applications. More details on past investigations of SFRC and PPFRC behaviour are provided in Chapter 2.

1.2 Scope of the Thesis

The main objectives of this thesis are threefold:

1. To investigate the compressive, tensile, flexural, and shear behaviour of macro-synthetic structural fibres as reinforcement for concrete elements, in comparison to the behaviour exhibited by steel fibres.

2. To perform a pilot investigation into the effects of reversed cyclic shear loading conditions on the behaviour of SFRC and PPFRC, so as to determine the suitability of these types of reinforcement for shear-critical cyclically loaded elements such as beam-column joint regions.

3. To study the bond behaviour of macro-synthetic fibres and subsequently propose modifications to a simplified robust constitutive model for the tensile behaviour of steel fibre reinforced concrete, such that this model can be used for the tensile behaviour of macro-synthetic polypropylene fibre reinforced concrete.

In order to fulfill these objectives, an experimental program was developed and completed in the structural laboratories at the University of Toronto. Three material tests were utilized to investigate the behaviour of steel and macro-synthetic FRC in compression (cylinder compression tests), tension (uniaxial direct tension tests), and flexure (modulus of rupture tests). In addition, larger scale panel tests were performed using the Panel Element Test Facility at the University of Toronto to investigate the behaviour in pure shear. Three of the five panel tests (one for plain concrete, one for SFRC and one for PPFRC) were carried out under a reversed cyclic pure shear loading condition; the other two (one for SFRC and one for PPFRC) were carried out under monotonic pure shear. This provided a preliminary indication of the effects of loading protocol on the structural response of these concretes, as groundwork for a more extensive research investigation.

Subsequently, using the results of the uniaxial direct tension tests and substantial literature study, some logical modifications to an existing constitutive law were proposed, such that the model could be expanded to represent the tensile response of PPFRC. After completion of this proposal, the modifications were implemented into the nonlinear finite element analysis software program, VecTor2 (Vecchio, 1990). A short verification study was undertaken, involving the performance of finite element analyses on the panel tests and on a few large-scale PPFRC shear-critical beams tested by Altoubat, Yazdanbakhsh and Reider (2009). From the result of this study, some deficiencies in the proposed modifications and areas of future work were revealed.

1.3 Organization of the Thesis

In this thesis, experimental and analytical investigations into the behaviour of steel and macro-synthetic fibre reinforced concrete were undertaken. This was done in an attempt to contribute to the overall understanding of the materials, with the eventual end goal of more widespread use and codification of fibre reinforced concrete. The background of fibre reinforced concrete usage was discussed in Chapter 1.

Chapter 2 provides a review of the available research on the behaviour of steel fibre reinforced concrete and macro-synthetic fibre reinforced concrete, including the developments of macro-synthetic fibre technologies. In addition, a summary of past experimental programs into the shear (monotonic and reversed cyclic) behaviour of steel and macro-synthetic fibre reinforced concrete is presented. Lastly, the details of some constitutive models for FRC tension are briefly outlined.

In Chapter 3, the experimental program undertaken as a part of this work is discussed. The experimental program employed was based on past research of steel fibre reinforced concrete behaviour completed at the University of Toronto (Susetyo, 2009). Two main parameters were studied: the fibre material type and the loading protocol. To achieve this, five main sets of specimens were constructed, along with two sets of preliminary specimens. For each of the main sets, cylinder compression tests, uniaxial direct tension tests, modulus of rupture tests and panel tests were performed; for the preliminary sets, cylinder compression tests and uniaxial direct tension tests were carried out. Details of the specimen dimensions, material properties, casting procedures, workability observations, test setups, and test instrumentation are given.

In Chapter 4, the results of the experiments are presented. Details of the data analysis employed for each type of specimen are outlined, and the results of the data analysis are presented. Comparisons of the responses are shown and the influence of fibre type and loading protocol on the behaviour are discussed. From this, some preliminary conclusions about steel and macro-synthetic FRC behaviour are drawn.

Chapter 5 discusses the analytical investigation of the properties of macro-synthetic fibres with surface indentations. This begins with a discussion of the Diverse Embedment Model and Simplified Diverse Embedment Model for FRC in tension (Lee et al., 2011a; Lee et al., 2011b; Lee et al., 2013). The applicability of the simplified model for PPFRC is discussed, and modifications for the bond parameters of macro-synthetic polypropylene fibres are proposed. A short verification study using simple spreadsheet calculations is employed to outline the effectiveness of the model.

Building from this verification study, Chapter 6 presents details of finite element analyses undertaken. The mesh generation, material properties and constitutive models used in the finite element models are outlined, and the results of the analysis are discussed. This is done to highlight the successes and deficiencies of structure-level modelling using the proposed tension softening model for polypropylene fibre reinforced concrete in combination with the existing FRC implementation in VecTor2.

Finally, the conclusions drawn from this work are summarized in Chapter 7. Some recommendations for further work are given.

Chapter 2
Literature Review

2 Literature Review

2.1 Introduction

The goal of this literature review is to build an understanding of the developments in the field of fibre reinforced concrete and to reveal the areas where knowledge about FRC behaviour is lacking. At first, the parameters that are known to affect the behaviour of SFRC will be discussed, as a lead-in to the discussion about the development of PPFRC. Next, some experimental investigations into the shear behaviour of SFRC and PPFRC will be discussed in brief, with a focus on monotonic and reversed cyclic applied shear loads. Finally, a summary of some of the available constitutive models for FRC in tension will be provided. In this way, the contributions of this thesis can be placed within the framework of FRC development.

2.2 Properties of Steel Fibre Reinforced Concrete

The primary benefits of fibre addition are improved tensile response after cracking and improved crack control (Shah and Rangan, 1971). In this section, macro-fibre technologies and properties that affect SFRC behaviour are discussed. Extensive work on such topics has been performed for steel fibres.

There are a number of variables affecting the behaviour of fibre reinforced concrete in tension. One such variable is the fibre volume content, V_f. Uniaxial direct tension tests, flexural tests and direct shear tests have shown that any addition of fibres, regardless of fibre material and properties, improves the tensile toughness of the concrete (Figure 2.1; Shah and Rangan, 1971). This results in a marginal increase in strength and a substantial increase in ductility (Minelli, 2005; Mirsayah and Banthia, 2002; Khaloo and Kim, 1997). Fibre volume contents of 0.5% to 1.0% are able to effectively control crack widths and yield post-cracked behaviour similar to that of minimum conventional steel reinforcement (Meda et al, 2005; Noghabai, 2000). In addition, concretes containing high fibre volume contents (1.0 to 1.5%) have shown the potential to exhibit tensile or flexural strain hardening behaviour and multiple cracking (Deluce, 2011; Susetyo, 2009). These benefits come at the expense of workability of the fresh concrete. Special mixing and placing methods are required for high fibre percentages to ensure even distribution of fibres and coarse aggregate (Zollo, 1997). Despite this, ACI Committee 544 (1993) suggests an acceptable fibre volume ratio from 0.25% to 2.0%, to ensure an adequate balance between structural benefit and workability. It is important to note that there may exist a “fibre saturation point”, above which any increase in fibre volume content only marginally improves the behaviour; past experimental findings showed this limit to be around 1.0% (Susetyo, 2009; Mirsayah and Banthia, 2002).

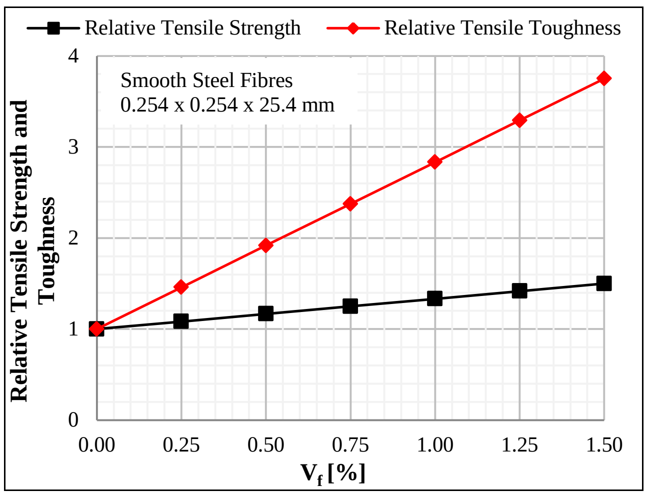

Figure 2.1: Influence of fibre content on tensile behaviour of SFRC (Shah and Rangan, 1971)

The aspect ratio, $AR_f = l_f/d_f$, of the fibre has a great effect on the tensile behaviour of SFRC. A higher aspect ratio (longer length per unit diameter) means the fibre has a large surface area to engage a small volume of steel through bond action with the concrete. This leads to a stiffer fibre with improved composite action (Johnston, 2001). Thus, it is clear that the higher the aspect ratio, the greater the ability of steel fibres to transmit tensile stresses across a crack (Shah and Rangan, 1971). This was exhibited by the direct shear tests carried out by Khaloo and Kim (1997). Specimens reinforced with fibres having an aspect ratio of 58 exhibited higher shear strength and sustained a larger displacement at ultimate in comparison to those reinforced with fibres having an aspect ratio of 29. This is shown in Table 2.1. In most cases, the concrete containing the fibre with AR_f = 58 achieved a normalized shear strength greater than that of the concrete with the AR_f = 29 fibre in a higher volume content.

Table 2.1: Effect of Fibre Content and Aspect Ratio on Direct Shear Response (Khaloo and Kim, 1997)

Test Set	AR_f	V_f [%]	f'_c [MPa]	τ_{max} [MPa]	$\tau_{max}/\sqrt{f'_c}$	Δ_{max} [mm]
NC	-	-	44.0	4.21	0.635	0.13
NC-0.5-16	29	0.5	45.3	4.49	0.667	0.29
NC-0.5-32	58	0.5	45.2	5.53	0.823	0.30
NC-1.0-16	29	1.0	45.3	5.62	0.835	0.30
NC-1.0-32	58	1.0	47.8	6.43	0.930	0.38
NC-1.5-16	29	1.5	48.7	6.18	0.886	0.35
NC-1.5-32	58	1.5	41.5	7.00	1.087	0.41

The geometry of the fibre also affects behaviour. In the early days of steel fibre reinforcement, most of the fibres used were straight and smooth. More recently, tests have shown that fibres with deformations providing some mechanical anchorage are more effective than straight fibres as stress transfer across the crack is improved (Naaman and Najm, 1991; Banthia and Trottier, 1994). Images of typical fibres with mechanical anchorages are shown in Figure 2.2. Much of the focus on constitutive model development has revolved around straight and end-hooked fibres, as these are relatively inexpensive to produce and provide adequate structural benefits (Voo and Foster, 2003; Lee et al., 2011a).

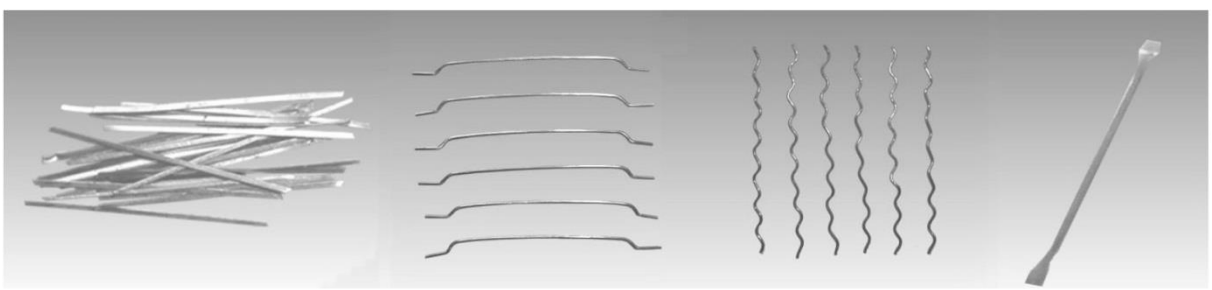

Figure 2.2: Steel fibres with various mechanical anchorages - From left to right: straight, end-hooked, crimped, flattened-end (adapted from Susetyo, 2009)

Next, the length of the fibre, l_f, is another significant factor. A shorter fibre length leads to an improvement in the overall response of SFRC (Deluce, 2011; Susetyo, 2009). This is because for two fibres with the same aspect ratio, the shorter fibre has a smaller volume. Therefore, in order for two concrete mixes using a long and short fibre of identical aspect ratio to have the same fibre volume content, the concrete with the shorter fibre will need to have a greater number of fibres in the matrix. This is demonstrated for two Dramix® steel fibres in Table 2.2 (N.V.

Bekaert S.A., 2003). The RC80/30BP mix contains nearly four times as many fibres; there are many more fibres available within the matrix to facilitate crack control and to transmit tensile stresses across the cracks (Susetyo, 2009).

Table 2.2: Number of Fibres in Concrete Mix

Fibre Type	AR_f	V_f [%]	l_f [mm]	d_f [mm]	N_f in 1 m^3 of Concrete
RC80/60BP	80	1.0	60	0.75	377,000
RC80/30BP	80	1.0	30	0.38	1,470,000

Fibre orientation has an effect on the response of SFRC. As can be expected, the fibre reinforcement is most efficient if all fibres are perfectly aligned in the direction of the tensile stresses (Shah and Rangan, 1971). However, this is an impractical scenario, as the discrete fibres randomly distribute throughout the matrix in three dimensions, giving random orientations to the principal loading direction. The fibres that are oriented at more acute angles to the crack have a reduced effective embedment length. Consequentially, the inclined fibre cannot transmit appreciable tensile stresses across the crack and pulls out at a reduced applied load (Shah and Rangan, 1971; Lee and Foster, 2007). Some constitutive models incorporate efficiency factors to account for this uncertainty in orientation (Stroeven, 1977; Voo and Foster, 2003; Lee et al., 2011a). These fibre orientation factors, α_f, are based on probabilistic evaluation of fibre inclination angle as affected by member dimensions and fibre length (Lee et al., 2011).

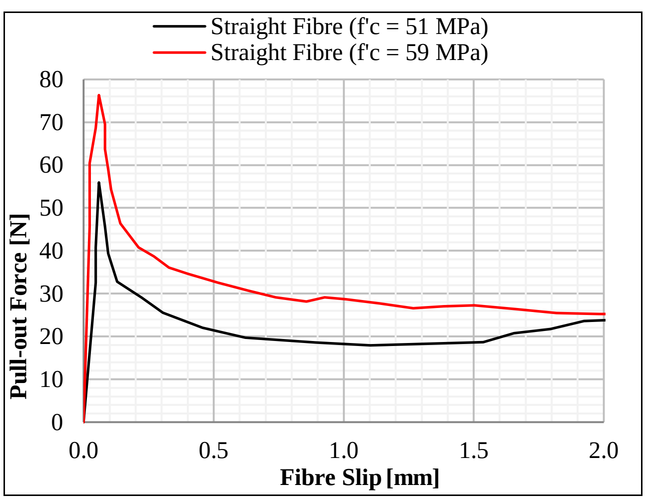

Figure 2.3: Influence of concrete strength on fibre pull-out (Naaman and Najm, 1991)

Finally, the strength of the materials (fibre and matrix) affects the structural behaviour, albeit to a lesser extent. The concrete strength has the effect of increasing the bond strength of the steel fibres as shown in Figure 2.3 (Naaman and Najm, 1991). This in turn increases the effectiveness of crack control, since sufficient tensile stresses can be attained across a wider crack without fibre pull-out (Vandewalle, 1999). Also, a high tensile strength of the fibre prevents failure by brittle fibre fracture, allowing for improved ductility (Susetyo, 2009). Fibre pull-out is the desired mode of failure, as the action of pulling out the fibres dissipates energy (Minelli, 2005). This phenomenon is promising for fatigue loading, seismic conditions, or for structures under blast and impact (Otter and Naaman, 1988; Chalioris, 2013).

2.3 Synthetic Fibres

Synthetic fibres may be made of a number of different polymer materials as shown in Table 2.3. These include relatively low modulus fibres such as polypropylene and polyethylene, and high modulus fibres such as carbon and Kevlar. Polypropylene fibres have seen the most extensive use even though it has been noted in the literature that fibres with a modulus of elasticity greater than concrete are required to increase the strength of the concrete (Bentur, 2007). In addition, bond strength between polypropylene fibres and the concrete is relatively low, meaning that the ability to transmit stresses across a matrix crack through interfacial bond is limited (Bentur, 2007). However, many of the readily available synthetic fibre materials also exhibit these issues and polypropylene offers many other advantageous properties.

Polypropylene can be easily cold worked to produce a fibre with a higher modulus of elasticity and tensile strength (Gregor-Svetec and Sluga, 2005). The consequence of this is a reduction in elongation at rupture (5 to 10% after cold working (Chatterjee and Deopura, 2006; Gregor-Svetec and Sluga, 2005), compared to 15 to 25% beforehand (Balaguru, 1992; Daniel, 1991)). This is of limited concern for fibre reinforced concrete as a pull-out failure mechanism is desired and is most often exhibited (Minelli, 2005). Also, polypropylene fibres can be easily formed into a variety of shapes and sizes with different surface finishes (Wang et al., 1987). This improves bond properties (Choi et al., 2012) and can be done at a low cost, since polypropylene fibres are roughly ten times less expensive by weight than glass fibres (Richardson, 2005; Mu et al., 2002). Additionally, these fibres exhibit resistance to alkalis and corrosion, and remain stable in a cementitious environment over a substantial service life (Wang et al., 1987). Conversely, polypropylene exhibits susceptibility to fire and sensitivity to sunlight and oxygen, but for a fibre encased in concrete cover this is of little concern (Bentur, 2007).

Table 2.3: Typical Synthetic Fibre Properties (Daniel, 1991; Bentur, 2007)

Fibre Type	Diameter [mm]	Tensile Strength [MPa]	Elastic Modulus [MPa]	Ultimate Elongation [%]
Acrylic	0.020-0.350	200-1,000	14,000-19,000	10-50
Carbon	0.008-0.019	500-4,000	30,000-480,000	0.5-2.4
Kevlar	0.010-0.012	2,300-3,500	63,000-120,000	2-4.5
Nylon	0.023-0.400	750-1,000	4,100-5,200	16-20
Polyester	0.010-0.200	230-1,200	10,000-18,000	10-50
Polyethylene	0.025-1.000	80-600	5,000	3-100
Polyolefin	0.150-0.640	275	2,700	15
Polypropylene				
-Monofilament	0.100-0.200	450-500	3,500-5,000	15-25
-Fibrillated	0.300-1.000	550-760	3,500-9,000	8
PVA	0.014-0.650	800-1,500	29,000-36,000	5.7
Steel	0.100-1.000	500-2600	210,000	0.5-3.5
Concrete	-	3-7	10,000-45,000	0.02

Much of the pioneering work regarding the improvement of synthetic FRC is described in detail in the works of Zonsveld (1975) and later by Krenchel and Shah (1986). These works were focused on the need to overcome the poor bonding to concrete, as early research showed that polypropylene exhibited hydrophobic behaviour in concrete. This behaviour led to reduced cement paste coverage, low bond capacity, and poor fibre dispersion (Bentur, 2007). However, subsequent developments on surface treatments and other advances in polymer technologies have relaxed these concerns (Bentur, 2007). These developments are ongoing and are mostly proprietary with little available information in the literature (Richardson and Landless, 2009). Thus, a brief overview of some known advances is provided in the subsequent sections.

2.3.1 Micro-Synthetic Fibres

Micro-synthetic fibres have a diameter of less than 0.3 mm (Richarson, 2005). Micro-synthetic polypropylene fibres may be further divided into two subcategories based on fabrication methods. These are monofilament fibres and fibrillated fibres as shown in Figure 2.4 (Synthetic Resources, 2003; Richardson, 2005). As can be seen from the photograph, the monofilament fibres are individual extruded thin polymers that are cut to appropriate lengths (Bentur, 2007). Fibrillated fibres are stretched into thin sheets, slit into individual filaments and then held together by cross-linking along the length. This forms a “tape” that can then be twisted into bundles and cut to appropriate lengths (Zheng and Feldman, 1995; Bentur, 2007). The benefit of collated fibrillated fibres is improved bond strength with the concrete (Soroushian et al., 1992).

Despite the aforementioned extensive research into the effects of various fibre properties on the behaviour of steel fibres, similar research has not been carried out for micro-synthetic fibres. This is because micro-synthetic fibres have seen limited use in structural applications; they have been more typically used to control shrinkage micro-cracking (Buratti et al., 2011; Soroushian et al., 1992). In some cases, these fibres are mixed together with steel fibres such that one component can act as structural shear reinforcement and the other as temperature/shrinkage reinforcement (Banthia and Sappakittipakorn, 2007). This has proven to be a useful FRC application, yet does not merit the need for extensive research into the effects of fibre length, fibre aspect ratio, fibre tensile strength and fibre geometry. Further discussion on micro-synthetic fibre technologies is outside the scope of this thesis.

(a) Monofilament synthetic fibres (b) Fibrillated synthetic fibres

Figure 2.4: Micro-synthetic fibre types magnified (adapted from Synthetic Resources, 2013)

2.3.2 Development of Macro-Synthetic Fibres

More recently, the desire to use polypropylene fibres as structural reinforcement has grown. To this end, macro-synthetic polypropylene fibres have been developed (Altoubat et al., 2009). An example of one such fibre is the MasterFiber™ MAC Matrix macro-synthetic fibre developed by BASF (2012). This fibre, depicted in Figure 2.5, was utilized in the experimental program discussed in this thesis; the product data sheet is provided in Appendix A.5.2. Similar to other macro-synthetic fibres, the MAC Matrix fibre has a relatively high elastic modulus for polypropylene (10,000 MPa). The fibre is "stick-like" and consists of two filaments cross-linked along the fibre length. In addition, the surface of the fibre is embossed to create deformations that provide mechanical anchorage between the fibre and the concrete. Thus, the benefits of a high modulus of elasticity, cross-linking (similar to fibrillating for micro-synthetic fibres), and mechanical anchorage are utilized. These changes lead to bond improvements.

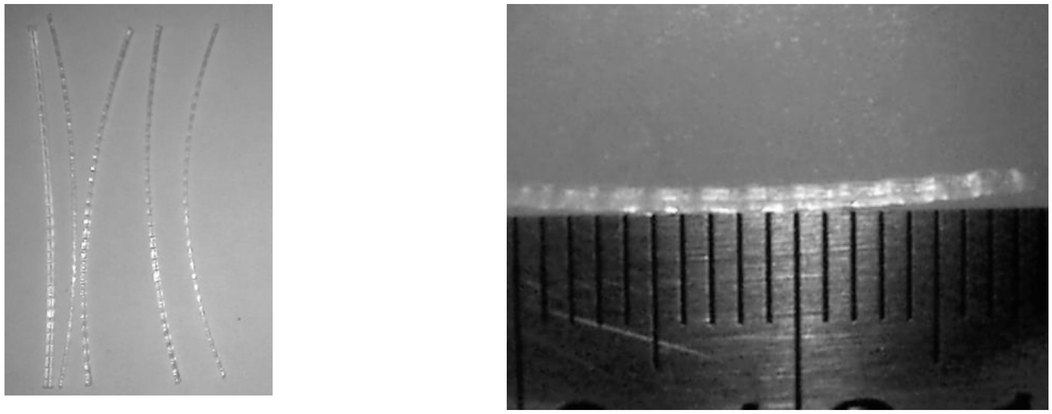

(a) Collection of full length fibres (b) 10 times magnified; ruler divisions in mm

Figure 2.5: MAC Matrix macro-synthetic polypropylene fibre

Table 2.4: Bond Strengths of Macro-Synthetic Fibres with Mechanical Anchorages (Won et al., 2006)

Mechanical Anchorage Type	τ_b **[MPa]**	$\tau_b / \tau_{b,sraight}$
Straight	0.28	1.00
Crimped	1.82	6.50
Twisted	0.56	2.00
Enlarged Ends	0.71	2.54
Sinusoidal Ends	0.72	2.57
End-Hooked	0.40	1.43
Double Duoform	1.10	3.93

Table 2.5: Bond Strengths of Macro-Synthetic Fibres with Varying Cross Sections (Choi et al., 2012)

Cross Section	$SA^* / SA_{circular\ fibre}$	$\tau_{b,straight}$ **[MPa]**	$\tau_{b,crimped}$ **[MPa]**
Clover	1.11	0.37	3.38
Cross	1.48	0.49	3.23
Star	1.51	0.43	2.69
Hexagram	1.73	0.48	4.13

* SA is the fibre surface area

Won et al. (2006) performed a series of pull-out tests on monofilament macro-synthetic fibres with varying types of mechanical anchorages. Bond strengths were greatly improved in relation to a straight, smooth macro-synthetic polypropylene fibre, as shown in Table 2.4. Subsequently, Choi et al. (2012) performed an investigation on the effects of fibre surface area on the bond properties of the fibre. This paper showed that significant increases in surface area can be achieved by changing the cross-sectional shape, which in turn leads to an increase in bond strength as shown in Table 2.5. Fibre crimping further increases the bond strength. More importantly, Choi et al. (2012) found that crimped macro-synthetic fibres with modified cross sections (cross, star, etc.) can attain a bond stress versus bond slip relationship similar to that of steel fibres, characterized by a steep and linear elastic frictional bond component, followed by a "bend-over point" and a subsequent parabolic increase to the maximum bond stress (Choi et al., 2012; Banthia and Trottier, 1994). Thus, these improvements in macro-synthetic bond behaviour should lead to improved performance as structural reinforcement in future tests. Macro-synthetic fibre bond properties are investigated in more detail in Chapter 5 of this thesis as a part of the constitutive model development.

2.3.3 Properties of Polypropylene Fibre Reinforced Concrete

The effects of adding fibres to the brittle concrete matrix are similar, regardless of the fibre type; they include improved post-cracked response of the concrete in terms of ductility, toughness and cracking behaviour (Shah and Rangan, 1971). These effects are directly proportional to the fibre volume content (Bentur, 2007). In turn, the control of crack widths promotes improved aggregate interlock of the concrete (Altoubat et al., 2009). To improve the understanding of the structural benefits of macro-synthetic fibres, uniaxial direct tension tests, flexural tests, cylinder compression tests and shear panel tests were undertaken as a part of the experimental program in this work.

Since research on the structural response of synthetic FRC with differing fibre geometries is not available, data on the effect of fibre aspect ratio, length, geometry and orientation on structural response are also not available as the state-of-the-art technology is continually changing. However, the mechanics of fibre reinforcement are the same, regardless of fibre material type. The fibre pull-out tests presented in the previous section show that a higher surface area improves the bond of macro-synthetic fibres (Choi et al., 2012). Also, adding mechanical anchorages such as end-hooks or crimps further increases the bond strength (Won et al., 2006). Thus, tensile ductility and toughness should be improved through increasing the aspect ratio and mechanical anchorage of macro-synthetic fibres. The effects of fibre orientation on the response is also the same as that of steel fibres, however, in theory the long length of a typical macro-synthetic fibre (~50 mm) would lead to increased fibre alignment for a finite member (Lee et al., 2011b). This is not always the case, though, as the flexibility of the fibres improves fibre dispersion (Buratti et al., 2011).

As with steel fibres, the concrete strength affects the bond of the polypropylene fibre to the matrix (Richardson, 2005). But, due to the low modulus and infrequency of fibre rupture, fibre tensile strength is of less importance (Valle and Buyukozturk, 1993).

The addition of polypropylene fibres does not have a significant effect on the direct tensile cracking strength (Bentur, 2007). However, in moderate volume replacements (0.33-0.5%) the addition of macro-synthetic polypropylene fibres showed a 10 to 15% increase in splitting tensile strength (Hasan et al., 2011). In flexure, Roesler et al. (2006) performed tests on large-scale PPFRC slabs-on-grade and found that a substantial increase in flexural cracking load (32%), flexural strength (34%) and deformability can be achieved with 0.5% by volume macro-synthetic fibres. In compression, high volume fractions have been shown to affect the compressive strength due to poor compaction, but in most cases the effect of fibre addition on compressive strength is negligible (Bentur, 2007). Conversely, the peak strain and post-peak ductility in compression are improved through the addition of macro-synthetic fibres (Hasan et al., 2011).

In terms of shear strength, Valle and Buyukozturk (1993) performed direct shear tests on SFRC and micro-synthetic PPFRC in comparison with plain concrete. They found that the direct shear strengths of the SFRC specimens were greatly increased relative to the plain concrete, whereas the micro-synthetic PPFRC specimens achieved a marginal increase in shear strength (Table 2.6). Conversely, Hasan et al. (2011) showed a 65% increase in shear strength using new generation macro-synthetic fibres. More importantly, the addition of fibres changed the failure mode (Hasan et al., 2011; Valle and Buyukozturk, 1993). Where the plain concrete specimens failed suddenly and without warning, the addition of both fibre types led to the development of numerous diagonal cracks and gradual failure through fibre pull-out (Valle and Buyukozturk, 1993). It is worth noting that the high strength concrete specimens with steel fibres failed by fibre rupture, but the polypropylene fibres still exhibited pull-out failure due to the relatively low modulus of elasticity. In terms of deformability, the PPFRC specimens exhibited a 1400% increase in ductility relative to plain concrete, compared to merely 500% for SFRC (Valle and Buyukozturk, 1993). The polypropylene fibres have a beneficial effect on the shear ductility of concrete, holding the concrete together after development of shear cracks (Hasan et al., 2011; Valle and Buyukozturk, 1993).

Table 2.6: Results of Direct Shear Tests (adapted from Valle and Buyukozturk, 1993)

Concrete Type	Concrete Strength	$\tau_{max}/\sqrt{f'_c}$	% increase over plain concrete
Plain	Normal	11.3	-
SFRC	Normal	15.4	36.0
PPFRC	Normal	12.4	9.76
Plain	High	8.95	-
SFRC	High	14.2	58.6
PPFRC	High	10.5	17.2

For PPFRC under dynamic loads, low fibre volume fractions of micro-synthetic polypropylene fibres can greatly improve the impact resistance of concrete. A 153 mm diameter FRC cylinder reinforced with 0.1% by volume micro-synthetic fibrillated polypropylene fibres withstood three times as many impacts from a 64 mm diameter steel ball as plain concrete (Soroushian et al., 1992). In addition, polypropylene fibres in low volume fractions are shown to increase the energy absorbed during the fracture process (Cifuentes and Medina, 2012; Elser et al., 1996a). This benefit in terms of energy absorption was a main motivation for the reversed cyclic shear panel tests in this work.

Flexural toughness and residual flexural strength are improved with the addition of polypropylene fibres. This is supported by the findings of Richardson et al. (2010) which show that similar residual strength and toughness may be achieved from steel and macro-synthetic FRC flexural tests, if the mix design is balanced according to bond strength. In this paper, the authors increased the number of synthetic fibres added to the matrix by the ratio of the experimentally determined pull-out strengths. Richardson (2010) determined that the bond strength of the smooth macro-synthetic fibre used (90% polypropylene, 10% polyethylene with a modulus of elasticity of 9,500 MPa, a tensile strength of 620 MPa, a fibre length of 40 mm, and a rectangular fibre cross section of 1.67 x 0.095 mm) had a bond strength that was roughly nine times less than that of a typical end-hooked steel fibre. Thus, in subsequently prepared flexural specimens, the macro-synthetic FRC mix was proportioned so as to have nine times more synthetic fibres than the steel fibre mix. This worked out to a fibre volume fraction of 0.5% for the steel fibres and 0.75% for the polypropylene fibres. The mean results of the test sets are presented in Figure 2.6. Clearly, it can be seen that after the beam displacement increases above 2.0 mm, the macro-synthetic FRC has a greater residual load-carrying capacity and toughness. However, in initial post-cracked stages, the steel fibres exhibit an improved ability to arrest the sudden load decay. The macro-synthetic FRC exhibits a much larger drop in load prior to the arrest of crack growth. This is supported by the findings of many researchers regarding the properties of macro-synthetic fibres; a large strain (and, thus, crack width) is needed to mobilize the strength of the polypropylene fibres in tension (Buratti et al., 2011; Bentur, 2007; Won et al., 2006; Oh et al., 2002). After this initial drop, the PPFRC specimens can sustain some increase in residual load-carrying capacity to high crack widths as the relatively low modulus allows for utilization of full fibre anchorage without rupture (Won et al., 2006; Oh et al., 2002). To further investigate this behaviour, modulus of rupture bending tests (in accordance with ASTM C1609/C1609M (2010)) and uniaxial direct tension tests (details in Chapter 3) were carried out.

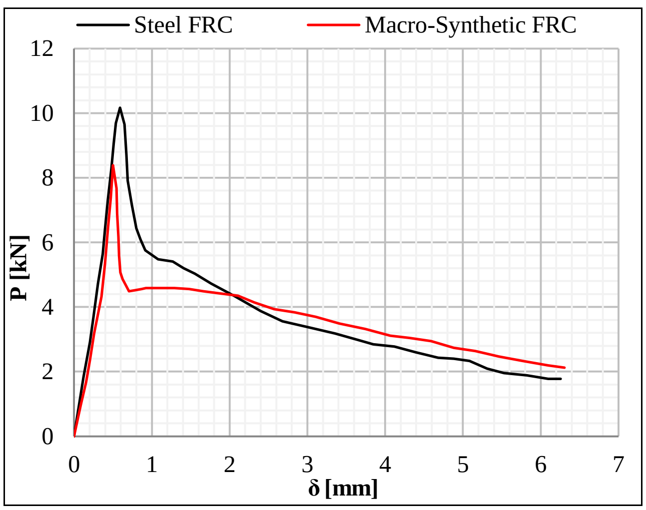

Figure 2.6: Mean results of flexural tests (Richardson et al., 2010)

Lastly, strain hardening and multiple cracking were not observed for the fibre volume fraction used by Richardson et al. (2010). Thus, some higher percentage of macro-synthetic fibre replacement is required before development of multiple cracks. This is consistent with the comments by Bentur (2007), who reported that researchers have found the critical volume fraction required to develop multiple cracking is 3.0% for micro-synthetic fibres. This is mostly a consequence of the bond properties of the fibres (Bentur, 2007); a macro-synthetic fibre with an improved bond mechanism can possibly be used in a lesser volume fraction to achieve strain hardening.

2.4 Experimental Investigations

A brief summary of some pertinent experimental investigations into the structural properties of FRC in shear are presented in this section. This is done to highlight the state-of-the-art of FRC structural knowledge and to determine how this work may contribute to the knowledge base.

2.4.1 Shear Behaviour - Monotonic Loading

As a result of decades of research into the shear behaviour of steel fibre reinforced concrete, ACI Committee 318 (2008) now lists SFRC beams in Section 11.4.6.1 among elements exempt from minimum structural shear reinforcement. This is the first time that SFRC has been permitted for structural use in the ACI building code (Altoubat et al., 2009), and is a result of extensive experimental investigation into the benefits of fibre addition on shear behaviour. Conversely, macro-synthetic fibre use has not been codified, as limited research exists.

2.4.1.1 Steel Fibre Reinforced Concrete

The extensive database of the shear strength of 147 SFRC beams compiled by Parra-Montesinos (2006) shows that the addition of deformed steel fibers increases the shear resistance of concrete (Parra-Montesinos, 2006; Minelli, 2005; Adebar et al. 1997). All of the FRC beams reported in the Parra-Montesinos (2006) database with at least 0.75% by volume of steel fibres exhibit a shear strength greater than $0.30\sqrt{f_c'}$. The suggested value for concrete contribution to shear strength of sections containing at least minimum shear reinforcement is $0.18\sqrt{f_c'}$ (CAN/CSA Standard A23.3-04, 2004). Thus, concrete shear strengths well above that required by the Canadian Standard for the Design of Concrete Structures can be attained with such fibre replacement. Results of select beam tests are presented in Table 2.7.

Fibres also prevent localization of excessive diagonal crack damage in the web. This increases the beam stiffness after diagonal cracking occurs, decreasing beam deflection and promoting multiple web cracking (Choi et al., 2007; Alshour et al., 1992). Shear ductility is also improved, as the control of diagonal crack widths promotes aggregate interlock and, thus, allows stress to be transmitted across the crack at higher applied displacements (Aoude et al., 2012; Parra-Montesinos, 2006). Energy absorption is improved in comparison to plain reinforced concrete beams (Sharma, 1986). The benefit of fibre addition on shear ductility is more pronounced for high-strength concrete, due to the more brittle nature of such concretes (Khuntia et al., 1999). Also, fibre effectiveness increases as the shear span-to-depth ratio, a/d, of the beam increases (Li et al., 1992).

Table 2.7: Select SFRC Shear Beam Test Results (adapted from Parra-Montesinos, 2006)

Ref	Specimen ID	d [mm]	a/d	ρ_l [%]	f'_c [MPa]	l_f [mm]	AR_f	V_f [%]	v_u [MPa]	$v_u/\sqrt{f'_c}$	δ_u [mm]
Adebar et al. (1997)	FC1	558	1.6	2.12	60.0	-	-	-	1.75	0.23	3.2
	FC2	558	1.6	2.12	54.1	30	60	0.75	3.24	0.44	5.2
	FC3	558	1.6	2.12	49.9	30	60	1.5	3.81	0.54	≥ 10
	FC7	558	1.6	2.12	57.0	-	-	-	1.43	0.19	0.6
	FC8	558	1.6	2.12	54.8	30	60	0.4	2.40	0.32	2.8
	FC9	558	1.6	2.12	56.5	30	60	0.6	2.73	0.36	1.2
	FC10	558	1.6	2.12	46.9	50	100	0.4	2.90	0.42	8.8
	FC11	558	1.6	2.12	40.8	50	100	0.6	2.79	0.44	≥ 10
Minelli (2005)	NSC1-PC	435	2.5	1.04	24.8	-	-	-	1.46	0.29	9.1
	NSC1-FRC1	435	2.5	1.04	24.8	30	50	0.38	2.97	0.60	19.6
	NSC2-PC	435	2.5	1.04	33.5	-	-	-	1.80	0.32	11.5
	NSC2-FRC1	435	2.5	1.04	33.5	50	50	0.38	2.63	0.45	18.8
	NSC3-PC	435	2.5	1.04	38.6	-	-	-	1.79	0.29	9.5
	NSC3-FRC1	435	2.5	1.04	38.6	30	50	0.38	3.13	0.50	20.1
	HSC-PC	435	2.5	1.04	60.5	-	-	-	2.48	0.32	12.8
	HSC-FRC1	435	2.5	1.04	61.1	30	45	0.64	4.28	0.55	26.4
	HSC-FRC2*	435	2.5	1.04	58.3	30	80	0.64	5.00	0.64	78.0
Swamy et al. (1993)	3TL-1	265	2.0	1.55	37.4	-	-	-	2.15	0.35	-
	3TLF-1	265	2.0	1.55	35.7	50	100	1.0	4.63	0.77	-
	3TL-2	265	3.4	1.55	32.8	-	-	-	1.02	0.18	-
	3TLF-2*	265	3.4	1.55	34.5	50	100	1.0	2.83	0.48	-
	3TL-3	265	4.9	1.55	33.8	-	-	-	1.03	0.18	-
	3TLF-3*	265	4.9	1.55	32.5	50	100	1.0	2.01	0.35	-
Cucchiara et al. (2004)	A00	219	2.79	1.92	41.2	-	-	-	1.23	0.19	10.0
	A10	219	2.79	1.92	40.9	30	60	1.0	2.93	0.46	23.0
	A20*	219	2.79	1.92	43.2	30	60	2.0	3.14	0.48	30.0
	B00	219	2.0	1.92	41.2	-	-	-	1.51	0.24	4.5
	B10	219	2.0	1.92	40.9	30	60	1.0	3.50	0.55	14.5
	B20	219	2.0	1.92	43.2	30	60	2.0	3.52	0.54	28.0

* Beam failed in flexure

In some cases, depending on the shear span-to-depth ratio of the beam, the longitudinal reinforcement ratio ρ_l, and the fibre volume content, the failure mode can be altered from brittle shear to shear-flexure or even flexural failure (Aoude et al., 2012; Khuntia et al., 1999). This is displayed by the findings from the lightweight crimped steel FRC I-beams tested by Swamy et al.

(1993). The plain concrete beams all failed in brittle shear, with tension splitting along the longitudinal bars and crushing in the compression flange. However, the steel fibres held the compression flange intact and reduced the bond splitting. The failure occurred through the rotation and merger of several shear cracks, as opposed to one dominant crack. Additionally, beams with $a/d \geq 3.43$, ρ_l = 1.55%, and V_f = 1.0% exhibited longitudinal steel yielding and flexural failure (Swamy, 1993).

Aoude et al. (2012) showed that the addition of fibres to beams with sufficient conventional transverse reinforcement so as to create a flexural failure experienced a marginal increase in strength. However, substantial improvements in ductility and deformability were achieved; 0.5% fibre addition was shown to increase the ultimate deflection by 50%, and 1.0% fibre addition increased the ultimate deflection by 90% relative to plain reinforced concrete (Aoude et al., 2012). In addition, the fibres improved the cracking behaviour, limiting flexural crack widths to 0.5 mm prior to failure whereas the cracks in the plain reinforced concrete beam rapidly increased after the yielding of the longitudinal steel (Aoude et al., 2012). These findings have also been extended to full-scale prestressed beams with stirrups. Tests by Meda et al. (2005) on both the transfer zone and diffused zone of the beams showed that the correct amount of steel fibre reinforcement performed at least as well as minimum shear reinforcement in terms of shear strength. If the fibres were added in addition to stirrups, the shear strength was increased by up to 30%; a more stable, ductile post-cracked behaviour was promoted (Meda et al., 2005). Crack widths were reduced and spread throughout the zone of interest, and the merging of the cracks into the main shear failure plane was delayed (Meda et al., 2005). Thus, steel fibres can be used to eliminate conventional stirrups in high performance structures, reducing bar congestion, relaxing cover requirements, and leading to thinner more efficient cross sections (Susetyo et al., 2011).

Despite this research into SFRC shear critical beams, Susetyo et al. (2011) noted that general constitutive models that characterize the fibre contribution to the concrete in shear are not available. To this end, Susetyo (2009) performed a research investigation on a series of 890 x 890 x 70 mm shear panels with varying types of steel fibres in comparison to low amounts of transverse steel reinforcement. These were tested under pure monotonic in-plane shear loads using the Panel Element Tester at the University of Toronto (Vecchio, 1979). The tests were carried out to isolate and determine the various aspects of SFRC behaviour (tension stiffening, tension softening, compression softening) such that SFRC in shear could be represented using the Modified Compression Field Theory (MCFT; Vecchio and Collins, 1986) or the Disturbed Stress Field Model (DSFM; Vecchio, 2000). The results (summarized in Table 2.8) show that, for fibre volume contents of 1.0% and above, reasonably similar shear strength and ductility was attained by SFRC without conventional transverse steel. For all of the panels reinforced with 1.0% steel fibres, shear strength of at least 87% of the conventionally reinforced concrete (RC) control specimen was attained; a shear ductility of at least 62% of the control panel was attained. Further improvements at V_f = 1.5% were limited. More importantly, the post-cracked principal tensile behaviour was greatly improved, exhibiting a response similar to RC with as little as 0.5% by volume of steel fibres. Also, the failure mode of the SFRC panels was different than that of RC characterized by crack shear slip after the breakdown of fibre bridging and aggregate interlock. This work also showed that short fibres with a high aspect-ratio are the most effective in crack control and improving structural behaviour, as seen from the result for C1F2V3.

Table 2.8: Results of Shear Panel Tests (adapted from Susetyo et al., 2011)

Specimen ID	l_f [mm]	AR_f	V_f [%]	f'_c [MPa]	v_u [MPa]	γ_u [x10^{-3}]	$f_{c1,max}$ [MPa]	$f_{c1,u}$ [MPa]	w_m [mm]	s_m [mm]
C1C	-	-	-	65.7	5.77	6.01	2.87	1.43	0.55	57
C1F1V1	50	81	0.5	51.4	3.53	2.77	2.83	1.85	0.55	114
C1F1V2	50	81	1.0	53.4	5.17	5.27	3.04	2.82	0.45	55
C1F1V3	50	81	1.5	49.7	5.37	5.10	3.13	2.97	0.45	57
C1F2V3	30	79	1.5	59.7	6.68	6.20	3.89	3.69	0.45	38
C1F3V3	35	64	1.5	45.5	5.59	4.27	3.85	3.08	0.50	57
C2C	-	-	-	90.5	6.40	7.00	2.55	1.23	0.50	66
C2F1V3	50	81	1.5	79.0	6.90	5.25	3.66	3.44	0.70	36
C2F2V3	30	79	1.5	76.5	6.31	4.35	3.75	3.62	0.65	47
C2F3V3	35	64	1.5	62.0	5.57	4.97	2.93	2.89	0.60	41

2.4.1.2 Macro-Synthetic Fibre Reinforced Concrete

As with steel fibres, it was found that synthetic polyethylene fibres can promote improved shear strength and resistance by controlling cracking and allowing tensile stresses to be transmitted across the main diagonal crack (Noghabai, 2000; Altoubat et al., 2009). This was shown by Altoubat et al. (2009), who performed an extensive study on large-scale PPFRC beams without stirrups using the new generation macro-synthetic fibres (Table 2.9). Both the slender ($a/d \geq$ 2.5) and short ($a/d \leq 2.5$) beams showed improvements in shear strength (Altoubat et al., 2009). Majdzadeh et al. (2006) carried out an investigation on small-scale specimens containing micro-synthetic polypropylene fibres, macro-synthetic polypropylene fibres, and steel fibres in varying reinforcement ratios. The results presented in Table 2.10 show that the macro-synthetic FRC can achieve an increase in shear strength greater than micro-synthetic FRC, yet still less than that of steel FRC. Both of these test sets showed that the shear strength lower limit for SFRC beams of $0.3\sqrt{f_c'}$ (according to ACI 318-08 (ACI Committee 318, 2008)) can be achieved using 0.75% PPFRC (Table 2.9 and 2.10). Since this requirement must be met to allow fibres to be used as minimum shear reinforcement (Parra-Montesinos, 2006), it can be seen from the experimental results that macro-synthetic polypropylene fibres may also potentially be used as minimum shear reinforcement if further studies continue to show this trend.

Table 2.9: Macro-Synthetic Polypropylene FRC Shear Beam Test Results (Altoubat et al., 2009)

Specimen ID	d [mm]	a/d	ρ_l [%]	f_c' [MPa]	l_f [mm]	AR_f	V_f [%]	v_u [MPa]	$v_u/\sqrt{f_c'}$	δ_{max} [mm]
L1-0.0	400	3.5	2.15	40.9	-	-	-	1.53	0.24	5.3
L1-0.50	400	3.5	2.15	41.9	40	90	0.50	1.73	0.27	7.4
L1-0.75	400	3.5	2.15	41.9	40	90	0.75	1.91	0.30	9.6
L2-0.0	330	3.5	3.18	40.9	-	-	-	1.54	0.24	3.7
L2-0.50	330	3.5	3.18	41.9	40	90	0.50	1.75	0.27	6.0
L2-0.75	330	3.5	3.18	41.9	40	90	0.75	1.73	0.27	7.1
L2-1.0	330	3.5	3.18	35.6	40	90	1.00	1.87	0.31	7.3
Sh1-0.0	400	2.3	2.15	40.9	-	-	-	1.75	0.27	2.6
Sh1-0.50	400	2.3	2.15	41.9	40	90	0.50	1.96	0.30	4.0
Sh2-0.0	330	2.3	3.18	40.9	-	-	-	1.78	0.28	1.7
Sh2-0.50	330	2.3	3.18	41.9	40	90	0.50	2.09	0.32	3.5
Sh2-0.75	330	2.3	3.18	41.9	40	90	0.75	2.24	0.35	4.1

The addition of the macro-synthetic fibres led to an increase in the first diagonal cracking load (Altoubat et al., 2009). After this crack, the PPFRC beams exhibited a drop in load, and increase in midspan displacement, before the crack width opening was arrested and the load-carrying capacity increased (Altoubat et al., 2009). This observation is consistent with the findings of research into PPFRC flexural behaviour as noted earlier (Buratti et al., 2011; Bentur, 2007; Won et al., 2006; Oh et al., 2002). Also, the fibres slowed the widening and propagation of the diagonal crack in relation to plain concrete, increasing the load at which the crack fully developed (Altoubat et al., 2009). Post-cracked stiffness in beams was improved, leading to reduced deflections under service loads (Li et al., 1992; Madjzadeh et al., 2006). Multiple shear cracking was developed in the beam webs. These crack widths were well controlled, promoting shear ductility, deformability and toughness (Altoubat et al., 2009). Both slender and short beams exhibited improved deformation capacity, with a 93% increase in deflection at ultimate for the 0.75% by volume PPFRC slender beams and a 138% increase for the short beams (Altoubat et al., 2009).

Table 2.10: Micro- and Macro-Synthetic Polypropylene FRC Beam Test Results, Compared to Steel FRC and Stirrups (Madjzadeh et al., 2006)

Specimen ID	d [mm]	a/d	ρ_l [%]	f'_c [MPa]	l_f [mm]	AR_f	V_f [%]	v_u [MPa]	$v_u/\sqrt{f'_c}$	δ_{max} [mm]
No Stirrup	120	3.0	3.3	47.1	-	-	-	2.11	0.31	1.4
0.5% Steel	120	3.0	3.3	45.5	60	80	0.5	2.84	0.42	3.2
1.0% Steel	120	3.0	3.3	44.6	60	80	1.0	3.47	0.52	4.1
1.5% Steel	120	3.0	3.3	40.9	60	80	1.5	3.31	0.52	3.6
0.5% Synthetic 1	120	3.0	3.3	43.4	54	360	0.5	2.28	0.35	3.0
1.0% Synthetic 1	120	3.0	3.3	44.8	54	360	1.0	2.78	0.42	3.0
1.5% Synthetic 1	120	3.0	3.3	42.0	54	360	1.5	2.75	0.42	3.4
0.5% Synthetic 2	120	3.0	3.3	43.9	50	85	0.5	2.39	0.36	4.9
1.0% Synthetic 2	120	3.0	3.3	44.2	50	85	1.0	3.14	0.47	4.0
1.5% Synthetic 2	120	3.0	3.3	43.1	50	85	1.5	2.89	0.44	3.7
Stirrups*	120	3.0	3.3	45.3	-	-	-	3.11	0.46	3.3
0.5% Steel + Stirrups*	120	3.0	3.3	41.3	60	80	0.5	4.14	0.64	4.8
0.5% Synthetic 1 + Stirrups*	120	3.0	3.3	44.1	54	360	0.5	3.20	0.48	4.2
0.5% Synthetic 2 + Stirrups*	120	3.0	3.3	37.8	50	85	0.5	3.78	0.61	4.7

* Reinforced with ρ_w = 0.28% stirrups

After reaching peak loads, high modulus synthetic fibres (Kevlar, carbon, etc.) showed a sudden decrease in load-carrying capacity. Lower modulus fibres like polypropylene and polyethylene exhibited a gradual and controlled decrease in load-carrying capacity, as desired for structural reinforcement (Noghabai et al., 2000; Li et al., 1992). Despite this, Altoubat et al. (2009) note that further investigation into shear ductility must be carried out to determine if such fibres may be used in place of minimum stirrups. This is because, converse to SFRC, flexural yielding was not exhibited if polypropylene fibres are used (Altoubat et al., 2009; Noghabai et al., 2000). However, the PPFRC beams did exhibit distributed flexural cracking before the propagation of the first diagonal shear crack. In addition, the synthetic fibres helped to prevent splitting cracks along the longitudinal reinforcement, due to the increased confining ability of the fibres around the steel bars (Altoubat et al., 2009; Majdzadeh et al., 2006). Overall, polypropylene fibres are less effective as shear reinforcement than steel fibres, yet the failure is still retarded due to the increase in energy required to cause fibre pull-out (Furlan and De Hanai, 1997).

For PPFRC beams with stirrups, the strength, ductility and cracking characteristics were improved. However, the effect of steel fibres on the response of conventionally reinforced beams was more pronounced (Madjzadeh et al., 2006). Good synergy between the macro-synthetic reinforcement and stirrups was exhibited, resulting from controlled crack growth and crack bridging. This caused a confining effect on the concrete, allowing for continued effectiveness of the stirrups up to high deformations. For the Madjzadeh et al. (2006) beams, at around 15 mm of midspan displacement, the beams reinforced with stirrups and macro-synthetic PPFRC exhibited a higher residual load-carrying capacity than those with just stirrups or with stirrups and SFRC, supporting the notion of improved synergy using macro-synthetic polypropylene under large displacements.

No tests on shear panels or similar specimens that can isolate the response of an element to in-plane shear stresses have previously been carried out on PPFRC. Thus, one monotonic shear panel test on PPFRC was carried out in this work as a pilot investigation into the comparative behaviour to SFRC panels previously tested.

2.4.2 Shear Behaviour - Reversed Cyclic Loading

Numerous researchers have reported the positive effect on energy dissipation when using fibre reinforcement in concrete (Minelli, 2005; Bentur, 2007; Soroushian, 1992; Otter and Naaman, 1988; Chalioris, 2013). However, research on this behaviour for structural elements subjected to reversed cyclic shear loading is limited.

2.4.2.1 Steel Fibre Reinforced Concrete

A number of studies have been carried out on the behaviour of SFRC shear-critical beam-column joint regions (Gencoglu and Eren, 2002; Filiatraut et al., 1995; Filiatraut et al., 1994; Jiuru et al., 1992). This is worth mentioning as large shearing forces are obtained in beam-column joints due to the termination of longitudinal beam steel in the joint core (Jiuru et al., 1992). The inclusion of a high percentage of tightly spaced transverse reinforcement resists this shear force, but causes steel congestion in joint regions (Jiuru et al., 1992). Steel fibres have been shown to generally improve shear resistance, toughness and energy absorption in joint regions (Namaan et al., 1987). Specifically, the addition of steel fibres provides a confining effect to the joint region, which leads to increases in shear strength. Also, the resulting tightly spaced cracks (due to structural crack bridging) allow for increased stiffness and reduction in shear deformation (Jiuru et al., 1992). Energy dissipation through the cycling is improved with addition of fibres (Gencoglu and Eren, 2002) and, if SFRC usage extends into the plastic hinge region, diagonal cracking in the joint is reduced; a vertical flexural crack is formed instead at the column face (Jiuru et al., 1992).

Interestingly, Filiatraut et al. (1994 and 1995) note that beam reinforcement yielding did not occur during negative half-cycles of SFRC exterior and interior joint tests. The Canadian Design Code (CAN/CSA Standard A23.3-04, 2004) requires double the positive flexural steel on the negative flexural side for seismic joint detailing. In this case of high longitudinal reinforcement ratios, SFRC effectiveness is greatly reduced. Shear failure is exhibited, as successive stretching and buckling of the fibres causes fibre bridging failure before yielding the longitudinal steel. Also, the stiffness and strength of SFRC joint specimens degrade more rapidly than those reinforced with stirrups. The joint response is dependent on fibre type used. Filiatrault et al. (1994) found that 1.6% by volume of a straight fibre with an aspect ratio of 100 promoted plastic hinge formation; 1.0% by volume straight fibres with an aspect ratio of 60 did not. Also, energy dissipation with stirrups is still greater than SFRC alone (Gencoglu and Eren, 2002). Thus, SFRC may possibly be used in place of some transverse steel in the joint regions, but full replacement or even replacement of a high percentage of stirrups is not feasible (Gencoglu and Eren, 2002).

In terms of beams subjected to cyclic loads, similar improvements in cracking behaviour and stiffness are achieved (Chalioris, 2013; Daniel and Loukili, 2002). However, for high strength flexural-critical beams under reversed cyclic loads, the steel fibres reduced the ductility (taken by Daniel and Loukili (2002) as the ratio of ultimate deflection to deflection at maximum load, $\mu_\delta = \delta_u/\delta_{max}$). This is shown in Table 2.11, and points to fibre inefficiency after peak loads are attained, due to repetitive stretching and buckling of the fibres (Filiatraut et al., 1995). In terms of absorbed energy, G_{abs}, at low longitudinal reinforcement ratios this was improved using both short and long fibres. The short fibres were ineffective at high values of ρ_l as the energy dissipation was decreased throughout the post-peak regime (Daniel and Loukili, 2002).

Table 2.11: Ductility of SFRC Flexure-Critical Beams under Reversed Cyclic Loads (Daniel and Loukili, 2002)

Specimen ID	d [mm]	a/d	ρ_l [%]	f'_c [MPa]	l_f [mm]	AR_f	V_f [%]	μ_δ	G_{abs} [kN·mm]
L-ref	270	4.1	0.55	97.0	-	-	-	1.52	1030
L-30	270	4.1	0.55	110.0	30	79	1.0	1.31	1150
L-60	270	4.1	0.55	116.0	60	80	1.0	1.28	1500
M-ref	270	4.1	0.97	95.0	-	-	-	1.40	1570
M-30	270	4.1	0.97	112.0	30	79	1.0	1.22	1200
M-60	270	4.1	0.97	117.0	60	80	1.0	1.20	2220
H-ref	270	4.1	1.52	94.0	-	-	-	1.20	1760
H-30	270	4.1	1.52	114.0	30	79	1.0	1.20	1350
H-60	270	4.1	1.52	117.0	60	80	1.0	1.18	2280

Chalioris (2013) noted that, for shear-critical beams, steel fibre hysteretic loops showed greater pinching and residual deformation in comparison to plain concrete, meaning the presence of steel fibres prevents crack closing. Overall, as shown in Table 2.12, SFRC increased the shear strength, but not to the same degree as beams with stirrups. Also, the stirrups created flexural failure, but fibres did not; 0.75% by volume of fibres created a shear-flexure failure with longitudinal bars yielding just before formation of a diagonal shear failure plane. This is contrary to the observed behaviour of monotonically loaded shear-critical beams as noted previously (Khuntia et al., 1999). In addition, the SFRC was unable to withstand an extended number of cycles, leading to less energy absorbed in comparison to stirrups. Lastly, the degradation of the ultimate load attained for the 0.5% by volume SFRC beam was 14% in comparison to the monotonic test, representing only a slight improvement compared to the 20% degradation exhibited for plain concrete without stirrups (Chalioris, 2013).

Table 2.12: Investigation of SFRC Beams under Reversed Cyclic Shear (Chalioris, 2013)

Specimen ID	d [mm]	a/d	ρ_l [%]	f'_c [MPa]	l_f [mm]	AR_f	V_f [%]	v_u [MPa]	$v_u/\sqrt{f'_c}$	G_{abs} [kN·mm]
MP^	275	2.0	0.55	27.0	-	-	-	0.98	0.19	-
MP50^	275	2.0	0.55	27.0	60	75	0.5	1.56	0.30	-
CP	275	2.0	0.55	27.0	-	-	-	0.78	0.15	30
CP50	275	2.0	0.55	27.0	60	75	0.5	1.34	0.26	50
CP75	275	2.0	0.55	27.0	60	75	0.75	1.44	0.28	70
CP-S*+	275	2.0	0.55	27.0	-	-	-	1.48	0.28	80
CP50-S*+	275	2.0	0.55	27.0	60	75	0.5	1.63	0.31	100

* Reinforced with ρ_w = 0.50% stirrups
+ Flexural failure
^ Subjected to monotonic shear loads, as opposed to reversed cyclic

All of this supports the hypothesis that full replacement of transverse reinforcement with fibres in the panel test carried out in this work will not produce a result similar to conventional reinforced concrete under reversed cyclic loading. However, one such panel test (reversed cyclic in-plane shear on SFRC with no transverse reinforcement) was carried out as a pilot investigation of this response.

2.4.2.2 Macro-Synthetic Fibre Reinforced Concrete

For PPFRC, no comparable test programs have been carried out. However, Ma et al. (2012) have provided an investigation into the seismic performance of macro-synthetic FRC ductile columns as a baseline for future work. They found that a rapid decline in stiffness was exhibited immediately following the formation of cracks, pointing to the relatively large initial crack widths observed in other PPFRC tests discussed earlier (Bentur, 2007). After this, significant reductions in load were experienced upon excursion to higher displacements, but the total deformation capacity of the PPFRC columns was increased by two to three times above that of plain reinforced concrete. Lastly, the concrete held together after longitudinal steel yielding, delaying rapid stiffness decline and allowing for energy absorption.

Thus, to further investigate this finding, one pilot panel test on PPFRC under reversed cyclic in-plane shear loading was undertaken in this work.

2.5 Constitutive Models

The primary benefits of adding discrete fibres to concrete are improved tensile ductility, increased residual tensile load-carrying capacity, and improved crack control. In shear-critical structures where the failure is often through diagonal tension splitting and aggregate interlock failure along the main shear crack (Li et al., 1992), the effects of FRC on the post-peak tensile response is of utmost importance for numerical representation (Noghabai, 2000; Khuntia et al., 1999). The effect on cracking behaviour and tension stiffening are also of importance for structure-level modelling (Deluce, 2011), yet the details of these developments are outside the scope of this thesis.

Table 2.13: Models of SFRC Members in Tension (adapted from Lee et al., 2013)

Paper	Model
Marti et al. (1999)	$$f_f = \frac{V_f l_f \tau_b}{2d_f}\left(1 - \frac{2w_{cr}}{l_f}\right)^2$$ where: τ_b is the constant bond stress in the fiber.
Voo and Foster (VEM) (2003)	$$f_f = \frac{V_f l_f \tau_b}{d_f}\frac{tan^{-1}(w_{cr}/\alpha)}{\pi}\left(1 - \frac{2w_{cr}}{l_f}\right)^2$$ where: $\alpha = d_f/3.5$.
Stroeven (2009)	$$f_f(x) = \frac{1}{3}\frac{l_f}{d_f}V_f\tau_b\left(1 + \frac{1}{2}\omega_2\right)\left(1 - k\frac{w_{cr}}{l_f}\right)$$ $$f_f(z) = \frac{1}{3}\frac{l_f}{d_f}V_f\tau_b(1 - \omega_2)\left(1 - k\frac{w_{cr}}{l_f}\right)$$ where: ω_2 is the degrees of planar fibre orientation, k is 8 or 4 for straight or end-hooked fibres, respectively.
Lee et al. (DEM) (2011)	$$f_f = \frac{1}{A_c}\int_{A_c} \alpha_{f,3D}(y,z)\, V_f \sigma_{f,cr,avg}(y,z) dA_c$$ where: $$\sigma_{f,cr,avg} = \frac{2}{l_f}\int_0^{l_f/2}\int_0^{\pi/2} \sigma_{f,cr}(l_a,\theta) sin\theta d\theta dl_a,$$ $\sigma_{f,cr}$ is the fiber tensile stress at the crack, l_a is the embedded length of the shorter side of the fibre, θ is the fibre inclination angle, measured to the perpendicular to the crack surface.
Lee et al. (SDEM) (2013)	$$f_f = f_{st} + f_{eh}$$ where: $$f_{st} = \alpha_f V_f \sigma_{f,cr,st},$$ $$\sigma_{f,cr,st} = \tau_{f,avg}\frac{l_f}{d_f}\left(1 - \frac{2 \cdot w_{cr}}{l_f}\right)^2,$$ $\tau_{f,avg}$ is the average frictional bond strength of the fibre at the crack, and; $$f_{eh} = \alpha_f V_f \sigma_{f,cr,eh},$$ $$\sigma_{f,cr,eh} = \frac{4P_{eh,avg}}{\pi d_f^2}\left(\frac{(l_f - 2l_{eh}) - 2w_{cr}}{l_f}\right)^2,$$ $P_{eh,avg}$ is the average mechanical anchorage force due to end-hooks, l_{eh} is the length of the end-hook.

2.5.1 Constitutive Models for FRC in Tension

The goal of a constitutive model for FRC in tension is to represent the post-cracked tensile stress versus crack width, $f_{c1} - w_{cr}$, or tensile stress versus tensile strain, $f_{c1} - \varepsilon_1$, relationships. Two types of modelling approaches are used to achieve this goal. This first involves separately considering the contribution of the concrete (tension softening after cracking) and the fibres (tensile load-carrying capacity). Thus, the fibres are considered as reinforcement to the concrete, providing a tension stiffening effect to the brittle concrete matrix (Lee et al., 2011a). Models of this sort are often robust and provide a direct evaluation of the tensile response based on independent parameters such as fibre aspect ratio, fibre volume content, and fibre bond strength. Conversely, the alternative approach employs fracture mechanics to develop the governing tension softening curve of the material. This procedure involves performing an inverse analysis using the measured response from fracture tests such as wedge splitting tests (Lofgren et al., 2005). A unique set of empirical parameters are obtained for each set of tests, with limited universal applicability. However, successful structure-level modelling in finite element analyses can be achieved if such fracture tests are performed and the empirical tension softening curve is used in the analysis (RILEM Final Recommendation TC-162-TDF, 2003; Minelli, 2005). Despite this, the goal of this research program was to develop a robust approach for PPFRC tension modelling. Thus, the focus was on models of the first type. A brief summary of some available models in the literature for SFRC in tension is presented; the pertinent equations of the models are presented in Table 2.13.

2.5.1.1 Marti et al. (1999)

In this model, a simple equation for the overall fibre tensile behaviour was presented. Based on the investigations by Aveston and Kelly (1973), this model used a simplified assumption that once a crack forms in the concrete, the effective reinforcement ratio of fibres across the crack is half of the total reinforcement ratio. This has been proven accurate for an infinite member, yet is not true when member boundary conditions are considered (Stroeven, 1977; Gettu, Gardner, Saldívar and Barragán, 2005; Lee et al., 2011b). Marti et al. (2009) also suggested that as the crack width increases, the number of fibres bonded to the matrix decreases linearly. This leads to the parabolic decay function, $\left(1 - 2w_{cr}/l_f\right)^2$, for the relationship between fibre tension and crack width. As the crack width approaches half the fibre length the decay function and, thus, the fibre stress approach zero. This relationship is frequently utilized in other FRC models (Voo and Foster, 2003; Leutbecher and Fehling, 2008).

2.5.1.2 Variable Engagement Model (Voo and Foster, 2003)

This model was developed with consideration of randomly oriented fibres under uniaxial tensile stress and was derived by integrating the behaviour of a single fibre over a three-dimensional matrix space. Similar to Marti et al. (1999), the effects of the member boundary on fibre orientation were ignored. However, this model introduced a number of factors that have been subsequently used in further model development.

First, the assumption was made that the embedded fibre is pulled out from the side of the crack with the shorter embedded fibre length, while the longer embedded end of the fibre remains rigid. As will be discussed further in Chapter 5, this assumption allows for a much easier solution process, yet also leads to an overestimation of the fibre tension at small crack widths (Lee et al., 2013). The axial elastic deformation of the fibres was also ignored, as it has been shown to have little effect on the overall response of the fibre tension at large crack widths (Sujivorakul et al., 2000).

Also, Voo and Foster (2003) proposed that the total tensile response of an SFRC member should be comprised of the concrete tension softening curve and the fibre contribution. An exponential tension softening relationship was provided as:

$$f_{ct} = f_t' \cdot \exp(-c * w_{cr}) \tag{2.1}$$

where:

c = an attenuation factor for the matrix tension decay after cracking, taken as 15 for concrete and 30 for mortar.

Next, the concept of fibre engagement was introduced. This concept states that in order for a fibre possessing mechanical anchorage to become effective in carrying tensile forces, some slip must first occur between the fibre and the matrix. Thus, the tensile contribution provided by the mechanical anchorage of the fibre would be delayed until a certain crack width is attained at which the fibres become engaged, w_e. This engagement length is given by:

$$w_e = \alpha \cdot \tan(\theta) \tag{2.2}$$

where:

α = a material parameter to represent the resistance to slip, taken as $d_f/3.5$ for end-hooked and straight steel fibres.

This delayed engagement also results in energy absorption as a crack propagates through the concrete. This manifests itself in a softening of the post-cracked decay for a uniaxial direct tension test. Where the drop for plain concrete would be very steep, the drop for FRC is less so due to this absorption of energy. The selection of the attenuation factor is meant to capture the increased energy. This concept as it applies to PPFRC is further discussed in Chapter 5.

2.5.1.3 Stroeven (2009)

This approach applied the stereological principles of spatial modelling to the problem of randomly oriented fibres in the matrix, with consideration for the effects of member boundaries and compaction procedures on the fibre alignment within the structural element. The statistical probability that a fibre in the area of a crack crosses that crack was considered. In addition, and more significantly, a probabilistic distribution of fibre inclination angle according to spatial constraints was developed. This led to the development of an efficiency factor for fibre tensile capacity, based on the effect of fibre inclination angle. This concept was employed in the development of future models (Lee et al., 2011a).

2.5.1.4 Diverse Embedment Model and Simplified Diverse Embedment Model (Lee et al., 2011a; Lee et al., 2011b; Lee et al., 2013)

More recently, a more robust Diverse Embedment Model (DEM) has been developed. Building upon the VEM, the DEM considers the pull-out behaviour of a single fibre and sums the contribution of all fibres crossing a crack with explicit consideration for the probability distribution of fibre orientation angle and fibre embedded length. The DEM considers member boundary effects on fibre orientation, as fibres will tend to align parallel to the axis of the member when at a member edge. Thus, a full three-dimensional derivation of the fibre orientation factor, α_f, is included in the model. This model also provides an improved representation of mechanical anchorage on the pull-out behaviour of end-hooked steel fibres, by assuming that once the fibre slip is greater than the length of the end-hook the concrete or fibre have deteriorated enough that the mechanical anchorage is no longer present. Lastly, the DEM also considers the crack width to be the sum of the slip from both the short and long ends of the fibre crossing a crack (Lee et al., 2011a). This assumption leads to a complex formulation, with the need to perform an iterative double numerical integration to find the fibre stress for a given crack width. This is not desirable, since the end goal is to develop models for FRC that may be easily implemented into finite element analysis procedures and in design codes (Lee et al., 2013).

Thus, the Simplified Diverse Embedment Model (SDEM) was proposed. This model ignores the slip on the longer embedded side of the fibre, eliminating the need for an iterative solution. In addition, to reduce the double numerical integration to a single analytical integration, simple relationships for fibre orientation factor in two dimensions are three dimensions were proposed as shown below (Oh, 2011):

$$\alpha_{f,3D} = \frac{0.13}{(bh/l_f^2)^{1.12}} + 0.087\left(\left(\frac{l_f}{b}\right)^{1.12} + \left(\frac{l_f}{h}\right)^{1.12}\right) + 0.5 \tag{2.3}$$

$$\alpha_{f,2D} = \begin{matrix} -0.05 * \left(\dfrac{h}{l_f}\right)^{2.8} + 0.64 & for\ \ \dfrac{h}{l_f} \leq 1 \\ 0.087 * \left(\dfrac{l_f}{h}\right)^{1.12} + 0.5 & for\ \ \dfrac{h}{l_f} > 1 \end{matrix} \tag{2.4}$$

where *b* and *h* are the member thickness and height respectively.

As a result, a direct relationship for fibre tension, with separate consideration of frictional bond and mechanical anchorage, was derived (Lee et al., 2013). This model is selected as the baseline for PPFRC modelling, and is covered in more detail in Chapter 5.

2.5.1.5 Models for PPFRC

Limited work on tensile modelling of PPFRC has been performed. In addition, much of the work that has been carried out utilizes the empirical fracture mechanics approach (Li et al., 1991; Elser et al., 1996b; Cifuentes and Medina, 2012), which is not in line with the goal of this work. Wang et al. (1989) developed a statistical tensile model for PPFRC that considers the probability distribution of randomly oriented fibres with varying embedded lengths, much the same as the DEM and SDEM. This model also included the effect of fibre stretching on the response of the composite, which led to a complicated, multi-tiered computational procedure with separate equations for different fibre conditions (ie. pulled out, stretched with end slip, stretched with no end slip, fractured). The authors note that the model provided a reasonable overall shape of the tensile curve but an overprediction was consistently obtained (Wang et al., 1989). Thus, models of this type were consulted in the development of modifications to the SDEM, yet were not the focus of the thesis.

It is also worth noting that the cracking and tension stiffening behaviour of conventionally reinforced concrete with polypropylene fibres is of particular importance for structure-level shear modelling. However, in order to modify the formulations for SFRC provided in VecTor2, an extensive research program similar to that carried out by Deluce (2011) involving tension tests on PPFRC prisms reinforced with a conventional steel bar must be carried out. In the absence of such results, these effects were not investigated in this work.

Chapter 3
Experimental Program

3 Experimental Program

3.1 Introduction

This chapter provides a description of the laboratory study performed in this work. Table 3.1 gives a brief summary of the types of experiments performed, as well as the data sought through the performance of these tests. All of the tests were performed over a span of approximately 12 months, starting with trial concrete batches in November and December of 2011, followed by a preliminary investigation on PPFRC from February to April of 2012, concluding with the main experimental program from May to October of 2012. All work was performed in the Structural Laboratories at the University of Toronto.

Section 3.2 of this chapter touches on the variables investigated in the study, as well as the reasoning for the choices made. Sections 3.3 and 3.4 include a discussion on material properties and casting procedures/findings. Finally, Sections 3.5 to 3.8 provides details on the various types of experiments performed including details on the specimen preparation, test setup and instrumentation. Results of the experiments are covered in Chapter 4.

Table 3.1: Experimental Tests Performed

Name of Experiment	Purpose of Experiment
Cylinder Compression Test	• to test the compressive strength of the concrete to verify the adequacy of the concrete mix. • to investigate the compressive behaviour of SFRC and PPFRC.
Uniaxial Direct Tension (Dogbone) Test	• to investigate the direct tension strength and behaviour of the SFRC and PPFRC specimens without notches.
Modulus of Rupture Test	• to investigate the bending strength as well as the residual flexural strength and toughness of SFRC and PPFRC.
Panel Test	• to investigate the shear behaviour of uni-axially reinforced PPFRC as it compares to some previously tested SFRC panels of similar design. • to perform an initial investigation into the response of SFRC and PPFRC under reversed cyclic shear loading.

3.2 Experimental Parameters

At the outset of this work, it was determined that a number of parameters that are known to affect the behaviour of SFRC were adequately investigated in another work previously performed at the University of Toronto (Susetyo, 2009). The study performed by Susetyo (2009) contained five parameters that were deemed to have an influence on fibre behaviour. These were the concrete compressive strength, fibre volume content, fibre length, fibre aspect ratio and fibre ultimate strength (Susetyo, 2009). The focus of ongoing experimental work shifted to studying the influence of the fibre type used (steel vs. macro-synthetic), since the developments on macro-synthetic fibres warrant further research (Altoubat et al., 2009). In addition, the effects of loading condition (monotonic vs. reversed cyclic shear) were investigated. It was also determined that a number of specimens prepared by Susetyo (2009) could be used included in the discussion.

For this investigation, the lower of the two concrete strengths used by Susetyo (2009) (50 MPa) was chosen due to the high degree of variability observed in the high strength (80 MPa) concrete mix (Deluce 2011; Susetyo, 2009).

The types of fibres used, and the properties thereof, were governed by the findings of the literature study. For the experiments performed herein, Dramix® end-hooked steel fibres RC80/30BP (N.V. Bekaert, 2003) were used, in a fibre volume fraction of 1.0%. These fibres were chosen due to their short length and high aspect ratio, as the past experimental findings discussed in Section 2.2 showed that such a fibre yields the greatest improvements in structural behaviour (Susetyo, 2009; Johnston, 2001; Khaloo and Kim, 1997). In addition, this relatively short fibre provided for a reasonably realistic fibre orientation considering the thin cross sections of the specimens tested (Lee et al., 2011a). $V_f = 1.0\%$ was chosen due to the finding that the behaviour of SFRC is not drastically changed when a fibre volume fraction of greater than 1.0% is used (Susetyo, 2009). The specimens prepared by Susetyo (2009) that will be discussed for comparative purposes used Dramix® end-hooked steel fibres RC80/50BN (also supplied by Bekaert).

For the macro-synthetic fibres, the MasterFiber™ MAC Matrix macro-synthetic fibre (BASF, 2012) was used in a fibre volume fraction of 2.0%. This seemingly high fibre volume fraction was deemed acceptable as both a literature study and trial concrete batches showed that good finishing and fibre distribution was still reasonably achievable at this fibre volume ratio given the flexibility of the polypropylene fibres (Buratti et al., 2011; Johnston, 2011; ASTM Committee 544, 2008). In addition, literature study and preliminary direct tension tests (the results of which will be discussed in Chapter 4) showed that a high fibre volume fraction was required to achieve strain hardening and multiple cracking (Bentur, 2007). This was used as criteria to ensure a reasonable structural shear response of the main panel tests.

Table 3.2: Test Matrix

Series Name	f'_c [MPa]	Fibre Type	V_f [%]	Loading Protocol
Tests Performed by Carnovale				
DC-P1	50	-	-	Reversed Cyclic
DC-P2	50	RC80/30BP	1.0	Monotonic
DC-P3	50	MAC Matrix	2.0	Monotonic
DC-P4	50	RC80/30BP	1.0	Reversed Cyclic
DC-P5	50	MAC Matrix	2.0	Reversed Cyclic
Tests Performed by Susetyo (2009)				
C1C	50	-	-	Monotonic
C1F1V1	50	RC80/50BN	0.5	Monotonic
C1F1V2	50	RC80/50BN	1.0	Monotonic
C1F1V3	50	RC80/50BN	1.5	Monotonic

3.3 Material Properties

3.3.1 Concrete

In this research program two separate mix designs were used, one for the plain concrete specimens and one for the FRC specimens. The specified compressive strength for both mixes was 50 MPa, but since the presence of fibres changes the composition of the matrix, some differences in the mix design were required to achieve this goal. This is consistent with findings by Susetyo (2009). In addition, some slight differences were necessary within the mixes for the SFRC and PPFRC specimens to allow for reasonably good workability. This amounted to merely observing the consistency of the concrete during the mixing process and adding small volumes of water and super-plasticizer (typically 1000 mL and 50 mL at a time respectively) until the workability was deemed acceptable.

Overall, the details of the mix design followed those of Susetyo (2009) to try to ensure consistency of the concrete between the related research programs. The only slight difference was in the admixtures used, as the original mix called for a water-reducer (Polyheed® 997 by BASF) and a super-plasticizer (Rheobuild® 1000 by BASF). In discussion with the supplier, it was determined that these materials were obsolete and an updated mix was developed using the high-range water-reducer Glenium® 7700 (Hoxby, 2011). The water-to-cementitious materials ratio used to achieve the specified strength was 0.37 for plain concrete and 0.40 for FRC. Table 3.3 contains the details of each mix design.

Table 3.3: Concrete Mix Designs (per m^3 of concrete)

Material	Unit	PC*	SFRC	PPFRC
Type 10 Cement	kg	375	500	500
Water	kg	139	200	200
Sand	kg	847	1114	1114
10mm Limestone Coarse Aggregate	kg	1080	792	792
High-Range Water-Reducer (Glenium® 7700)	mL	3300	3670	4000
Steel Fibres	kg	-	78.5	-
Macro-synthetic Fibres	kg	-	-	18.2

* PC refers to the non-fibre reinforced concrete

The Type 10 cement used in this experimental program was obtained from the Holcim Canada Inc. plant in Mississauga, ON. The sand and limestone aggregate were obtained from Dufferin Construction. The coarse aggregate came with a maximum size of 5/8”, but was sieved down to the desired size of 10 mm using the facilities at the University of Toronto. As mentioned before, the admixtures used were products of BASF.

A number of trial batches were performed to verify the achievability of the specified strength and workability using these mix designs. Workability data for the trials and the main batches is presented in Section 3.4. Details of the hardened concrete properties for the preliminary PPFRC trial batches (as these batches were used for the preliminary PPFRC dogbone specimens) as well as the main DC-P1 through DC-P5 batches is presented in Chapter 4.

3.3.2 Reinforcing Steel

Steel reinforcement was utilized only in the shear panel specimens. All other specimens tested contained no conventional steel reinforcement. For the plain concrete panels, two different types of reinforcing steel were used: D8 deformed wire for the longitudinal (or x-) direction reinforcement, and D4 deformed wire for the transverse (or y-) direction. The FRC panels contained only the longitudinal direction reinforcement (D8 bars), as the desire was to compare the behaviour and failure obtained using low amounts of transverse conventional steel reinforcement to that of SFRC and PPFRC.

In order to determine the properties of the shipments of steel received, a number of steel coupon tests were performed in accordance with *ASTM A370 Standard Test Methods and Definitions for Mechanical Testing of Steel Products* (ASTM A370, 2012). The tests were performed on specimens with a free length of 100 or 150 mm and in both cases, an MTS clip gauge with a gauge length of 50mm was used to record strains. Table 3.4 contains the experimentally determined mechanical properties of the steel; the complete stress vs. strain relationships are presented in Appendix A.4. The exact values of pertinent properties of these steel bars differ from those used in the panel tests performed previously. For details on those reinforcing bars, please refer to Table 4.5 in Susetyo (2009).

Table 3.4: Reinforcing Steel Mechanical Properties

Bar Type	d_b [mm]	A_b [mm^2]	E_s [MPa]	f_y [MPa]	ε_y [x10^{-3}]	f_u [MPa]	ε_u [x10^{-3}]
D4	5.72	25.81	183850	484.3	2.67	624.4	22.7
D8	8.10	51.61	192515	466.4	2.43	605.4	37.1

* the yield strength and strain are taken at the limit of proportionality

Table 3.5: Mechanical Properties of Fibres

Designation	l_f [mm]	d_f [mm]	AR_f	f_{uf} [MPa]	E_f [MPa]
RC80/30BP	30	0.38	79	2300	200,000
RC80/50BN	50	0.62	81	1050	200,000
MAC Matrix	54	0.81	67	520	10,000

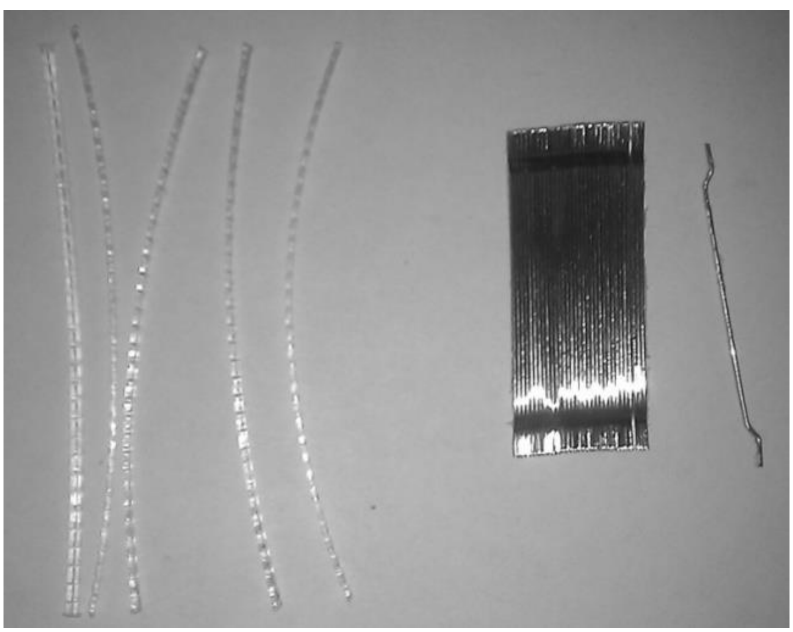

Figure 3.1: Fibres used in this program

3.3.3 Fibres

As mentioned previously, two different types of fibres were used in this experimental study: the Dramix® end-hooked steel fibres RC80/30BP supplied directly by Bekaert (2007) and the MasterFiber™ MAC Matrix macro-synthetic fibre supplied by BASF (2011). In addition, the specimens from the C1F1 series of tests performed by Susetyo (2009) used Dramix® end-hooked steel fibres RC80/50BN, also from Bekaert (2007). The fibres used in this program are shown in Figure 3.1, and the properties of all the fibres (including those used by Susetyo (2009)) are summarized in Table 3.5.

3.4 Concrete Casting

Different mixing procedures were used for the two types of concrete (plain and FRC), although the differences in general were small. Each cast consisted of one panel specimen, three dogbones, two modulus of rupture prisms and nine cylinders. This required a total of about 145 L of concrete; the mixer used in the University of Toronto laboratories had a capacity of 150 L. Thus, a 150 L batch size was used for all casts, so that all specimens within the cast would be comprised of the same concrete. On occasion, eight cylinders were cast instead of nine due to concrete lost during the casting procedure. This was not a major concern.

3.4.1 Mixing Procedures

The mixing of the non-fibre reinforced concrete followed a ten-step procedure:

1. The concrete mixer drum, rotor and chute were rinsed with water. Excess water from this process was drained out of the drum.
2. The coarse aggregate was added to the mixer and the mixer was run for 30 seconds.
3. All of the sand and cementitious materials were added to the mixer. The mixing process continued for 3 minutes.
4. One-third of the required high-range water-reducer (150 mL) and half of the required water were added to the mix. The mixing process continued for three minutes. At this stage the large volume of the relatively stiff contents inside the mixer occasionally led to issues with the mixer overheating and shutting down. To avoid this issue, the rotor and drum were instead jogged for one minute.
5. The mixing process was stopped for a two-minute rest.

6. One-third of the required high-range water-reducer (150 mL) and one-quarter of the required water were added and the mixing process continued for another two minutes.
7. The remaining super-plasticizer (150 mL) and water were added and the mixing process continued for another two minutes.
8. The consistency of the concrete was then inspected and, if required, small amounts of high-range water-reducer (50 mL) and water (1.0 L) were added. The concrete was mixed for two minutes after each addition.
9. The concrete mix was then loaded into a buggy and the specimens were cast.
10. The mixer and all tools were then cleaned.

Similarly, the mixing of the fibre reinforced concrete followed this twelve-step procedure:

1. The concrete mixer drum, rotor and chute were rinsed with water. Excess water from this process was drained out of the drum.
2. The coarse aggregate was added to the mixer and the mixer was run for 30 seconds.
3. All of the sand and cementitious materials were added to the mix. The mixing process continued for 3 minutes.
4. Two-fifths of the required high-range water-reducer (200 mL) and half of the required water were added to the mix. The mixing process continued for another minute. At this stage the large volume of the relatively stiff contents inside the mixer occasionally led to issues with the mixer overheating and shutting down. To avoid this issue, the rotor and drum were jogged for one minute.
5. One-quarter of the required water was added and the mixing process continued for another minute.
6. The mixing process was stopped for a one-minute rest.
7. One-eighth of the required water was added and the mixing process continued for another minute.
8. The remaining high-range water-reducer (300 mL) and one-eighth of the water were added to the mix, and the drum was run for another minute.
9. The consistency of the concrete was then inspected and, if required, small amounts of high-range water-reducer (50 mL) and water (1.0 L) were added. After each addition, the concrete was mixed for one minute.

10. The fibres were then gradually sprinkled into the concrete mix as the drum rotated. The mixing process continued until it was observed that all fibres had been uniformly dispersed in the concrete mix (typically two minutes).
11. The concrete mix was then loaded into a buggy and the specimens were cast.
12. The mixer and all tools were then cleaned.

3.4.2 Workability Observations

As previously mentioned, the addition of fibres to the concrete mix can have detrimental effects on the workability of the concrete (Johnston, 2001). This was a serious concern in this research project, compounded by the relatively tight reinforcement cage used in the panel specimens (see Figure 3.16 and Figure 3.17). As a result, a number of trial batches were performed prior to the five main batches to investigate the workability of the concrete. Four trial batches with $V_f = 1.0\%$ of steel fibres and two trial batches, one each with $V_f = 2.0\%$ and $V_f = 3.0\%$, of macro-synthetic fibres were cast. Details on the slump values are presented in Table 3.6.

Table 3.6: Workability Data for Trial Batches

Set ID	Concrete Type	Volume [L]	w/c ratio	HRWR* [mL/m^3]	Slump [mm]	f'_c [MPa]
TB1	1.0% SFRC	35	0.325	2286	75	68.5
TB2	1.0% SFRC	50	0.325	3900	63	62.8
TB3	1.0% SFRC	75	0.4	3900	200	58.9
TB4	1.0% SFRC	150	0.4	3100	113	63.1
DC-DB1	2.0% PPFRC	60	0.4	3900	200	58.0
DC-DB2	3.0% PPFRC	40	0.4	3900	45	56.1

* High-Range Water-Reducer in mL per m^3 of concrete

Table 3.7: Workability Data for Main Test Set

Set ID	Concrete Type	Volume [L]	w/c ratio	HRWR* [mL/m^3]	Slump [mm]	f'_c [MPa]
DC-P1	Non-FRC	150	0.37	3300	70	71.7
DC-P2	1.0% SFRC	150	0.4	3900	200	62.1
DC-P3	2.0% PPFRC	150	0.4	3200	60	50.9
DC-P4	1.0% SFRC	150	0.4	3670	136	64.0
DC-P5	2.0% PPFRC	150	0.4	4000	162	54.3

* High-Range Water-Reducer in mL per m^3 of concrete (including additions based on observed consistency)

From the results of the six trial batches, the mix designs summarized in Table 3.3 were formulated. Please note that the similarity in size and the subsequent results of TB3 and DC-DB1 led to the conclusion that at the full 150 L batch size, the 2% by volume PPFRC batch should yield similar workability results to TB4. This workability result, along with the structural response of the dogbones made using DC-DB1 and DC-DB2, led to the choice of 2.0% by volume of PPFRC for the main experimental study.

The main concrete batches were executed using this knowledge. The workability results of these are given in Table 3.7, where it can be seen that DC-P4 and DC-P5 were the most successful. Compaction and finishing for these specimens were much easier than for the rest of the batches. Figure 3.2 presents some photographs of the slump and workability of each primary batch.

DC-P1 DC-P2 DC-P3

DC-P4 DC-P5

Figure 3.2: Slump cone tests for the main test set

3.4.3 Curing

Once the specimens were cast and finished, they were allowed to sit for about two to three hours in open air to commence the setting process. After this time, one final pass with trowels was performed to try and remove any slight imperfections and, in the case of FRC, remove any fibres protruding out from the finished surface of the specimens. The specimens were covered with one or two layers of wet burlap and a sheet of polytarp plastic and left overnight. On the next day, the dogbone, modulus of rupture prisms and panel specimens were removed from their moulds and again wrapped in wet burlap and plastic for the next six days. Cylinders were also demoulded and placed in a curing chamber located in the Concrete Materials Lab at the University of Toronto at 100% relative humidity for the next six days. On the seventh day after casting, all of the specimens were uncovered and left to cure to maturity in ambient conditions.

3.4.4 Fibre Distribution

Another measure of the success of the batching process is the apparent fibre distribution within the specimens. This is impossible to ascertain until after the specimens have been failed and, even then, it can only be done if a complete split is made at the failure surface. Fortunately, the nature of the failure for dogbone tests and panel tests allowed for the number of fibres crossing the crack to be counted. From this, the following relationships were used to determine the actual volume fraction within the specimens:

$$\frac{N_f}{A_c} = \alpha_f \frac{V_f}{A_f} \tag{3.1}$$

with

$$\alpha_f = \frac{0.13}{(bt/l_f^2)^{1.12}} + 0.087\left(\left(\frac{l_f}{b}\right)^{1.12} + \left(\frac{l_f}{t}\right)^{1.12}\right) + 0.5 \tag{2.3}$$

where

A_c = cross-sectional area of the failure crack [mm^2]

A_f = cross-sectional area of the fibres [mm^2]

N_f = number of fibres crossing the failure crack

V_f = fibre volume fraction (ratio of the volume of fibres to the volume of concrete) [%]

b = length of failure crack [mm]

t = width of failure crack [mm]

l_f = length of fibre [mm]

α_f = fibre orientation factor (as discussed in the Chapter 2).

This relationship for the fibre orientation factor is for three-dimensional members, and is calibrated to the values obtained from the double integration method employed in the DEM (Lee et al., 2011b; Lee, 2012a; Oh, 2011).

Table 3.8: Fibre Distribution across Panel Failure Surface

Panel	$N_{f,TOP}$	$N_{f,BOT}$	% on Top*	t^+ [mm]	b^+ [mm]	α_f	$V_{f,Design}$ [%]	$V_{f,Actual}$ [%]
DC-P2	1409	594	70.3	46.8	987	0.5571	1.00	0.88
DC-P3	1041	145	87.8	53.8	890	0.5991	2.00	2.13
DC-P4	1125	691	61.9	54.8	890	0.5487	1.00	0.77
DC-P5	663	252	72.6	53.8	890	0.5991	2.00	1.64

* % of total fibres on the top half of the panel (as cast)
+ as measured, minus the diameter of reinforcing bars running parallel to the crack

Table 3.9: Fibre Distribution across Dogbone Failure Surface

Specimen ID	$N_{f,TOTAL}$	t* [mm]	b^* [mm]	α_f	$V_{f,Design}$ [%]	$V_{f,Actual}$ [%]
DC-DB1-1	157	70.0	105.0	0.6579	2.00	1.67
DC-DB1-2	165	70.0	105.0	0.6579	2.00	1.76
DC-DB1-3	142	70.0	105.0	0.6579	2.00	1.51
DC-DB1-4	168	70.0	105.0	0.6579	2.00	1.79
DC-DB2-1	218	70.0	105.0	0.6579	3.00	2.32
DC-DB2-2	208	70.0	105.0	0.6579	3.00	2.22
DC-DB2-3	247	70.0	105.0	0.6579	3.00	2.63
DC-P2-1	418	71.2	114.1	0.5669	1.00	1.03
DC-P2-2	409	70.5	109.4	0.5690	1.00	1.06
DC-P2-3	395	70.5	116.1	0.5668	1.00	0.97
DC-P3-1	172	70.9	107.5	0.6541	2.00	1.78
DC-P3-2	147	72.5	107.0	0.6519	2.00	1.50
DC-P3-3	179	72.0	106.8	0.6529	2.00	1.84
DC-P4-1	337	71.3	110.3	0.5682	1.00	0.86
DC-P4-2	278	72.0	106.0	0.5691	1.00	0.73
DC-P4-3	235	72.3	104.8	0.5694	1.00	0.62
DC-P5-1	164	71.8	102.8	0.6570	2.00	1.74
DC-P5-2	119	71.8	106.0	0.6540	2.00	1.23
DC-P5-3	127	71.5	103.8	0.6565	2.00	1.34

* as measured for DC-P series, since crack locations varied

As can be seen from Table 3.8 and Table 3.9, and as one would expect, fibre distribution within a specimen was quite variable. It is likely that the response would be quite different depending on the location of the failure crack and the number of fibres crossing this crack. This was inherently obvious when observing the structural responses of each dogbone (Section 4.3). Also, for the panels, it became clear from Table 3.8 and Figure 3.3 to Figure 3.6 that the fibres had a difficult time moving down through the relatively tightly spaced reinforcing cage of the panels (see Figure 3.17 for reinforcement drawing). There was a higher concentration of the fibres in the top half of the panel (as cast) which may be used as an explanation for certain aspects of the structural response that will be discussed in the next chapter.

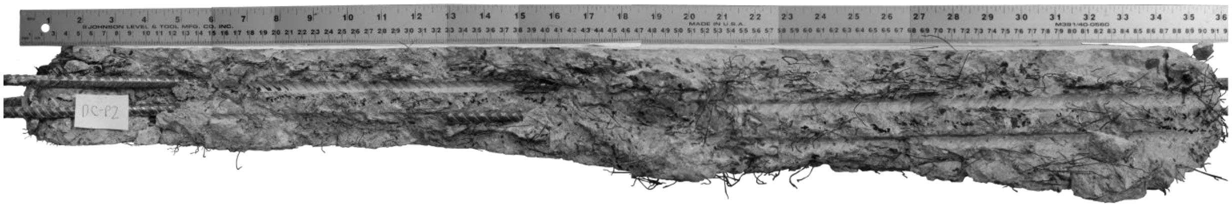

Figure 3.3: Fibre distribution for failed panel cross section DC-P2
(Finished face on top)

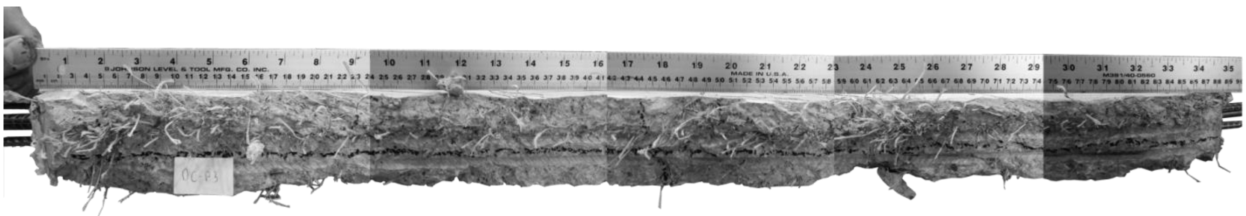

Figure 3.4: Fibre distribution for failed panel cross section DC-P3
(Finished face on top)

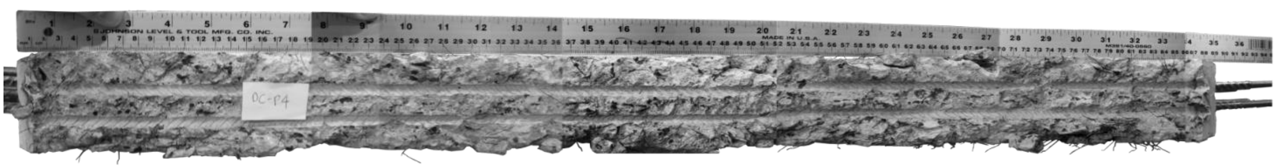

Figure 3.5: Fibre distribution for failed panel cross section DC-P4
(Finished Face on Bottom)

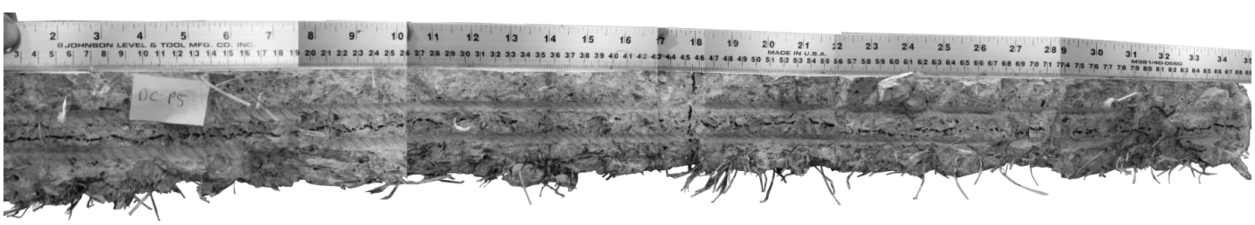

Figure 3.6: Fibre distribution for failed panel cross section DC-P5
(Finished Face on Bottom)

It also appeared that the restricted ability of the fibres to move to the lower half of the panel was worse for the macro-synthetic fibres, likely due to the longer length of the fibres but also due to the fibres floating to the top surface of these specimens when using a form vibrator. Figure 3.7 presents images of panels DC-P3, DC-P4 and DC-P5 (from left to right) to show a contrast of the appearance of the top surface of each panel just after vibratory compaction and before finishing.

It was clear that a large percentage of macro-synthetic fibres remained at the concrete surface, whereas this same phenomenon was not observed in the SFRC specimen.

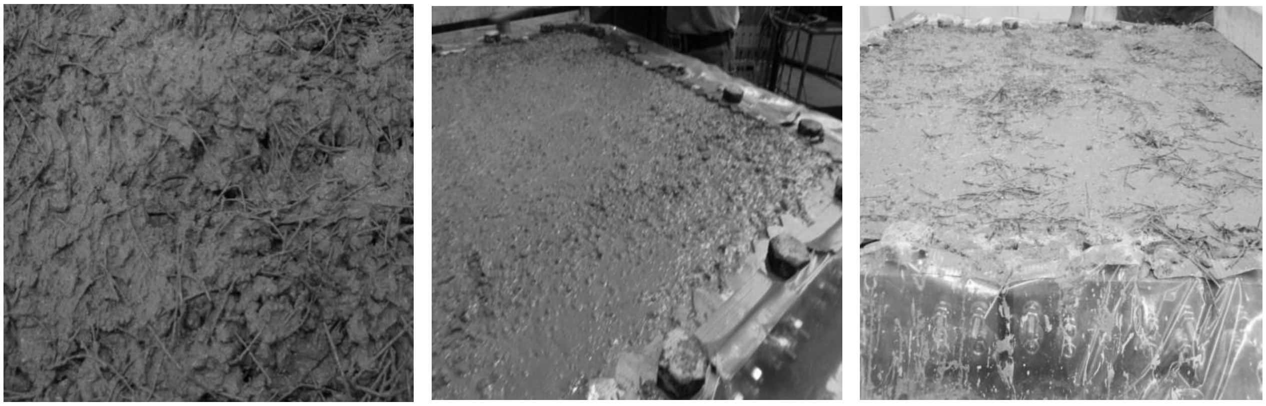

DC-P3 DC-P4 DC-P5

Figure 3.7: Floating fibres after compaction

3.5 Cylinder Compression Tests

Cylinder tests were performed to evaluate the compressive behaviour of the concrete, including the peak strength, peak strain and the Young's Modulus in compression.

A total of eight or nine specimens were cast with each test set. Each cylinder was 152 mm (6") in diameter. The concrete was placed into the moulds in three lifts and the moulds were subjected to vibration using a form vibrator between each lift. The top of the cylinder was then finished with a trowel and an attempt was made to remove fibres that were protruding out of the finished face. In many cases this was not 100% achievable.

The day after casting, the cylinders were demoulded and placed in a curing room at 100% relative humidity for the following six days. On the seventh day after casting, the cylinders were removed and left to cure in ambient conditions with the corresponding specimens.

Before testing, it was necessary to clean the ends of the cylinders in order to remove the weak paste layer and to prevent edge failures. To do this, plain concrete cylinders were ground flat using a cylinder grinding machine and FRC cylinders were saw cut. In both cases, approximately 10 to 12 mm of concrete were removed from each end of the cylinder. Then, to ensure a smooth and level contact surface for the saw cut ends, a sulfur capping compound was used. The cap typically had a thickness of around 5 to 7 mm.

Figure 3.8: Cylinder compression test

Cylinders were tested at seven days, 28 days, and on the panel test day (if not sufficiently close to 28 days). Seven day cylinders were tested using a Forney testing machine, merely to ensure that the compressive strength of the concrete was as expected. No strain data were recorded.

For the 28-day and test day cylinders, an MTS stiff frame testing machine was used to apply the load. A full stress-strain curve was required for these. This was done using a 250 mm gauge length LVDT mounting rig that was centered on the specimen with the help of a ruler. The Linear Variable Differential Transducers (LVDTs) were then attached to the specimen. The LVDTs had a stroke of ±5 mm, but were initially positioned at 3 mm so as to be able to carry the test to a maximum displacement of 8 mm. Once mounted, the test commenced using a loading rate of 0.005 mm/s. The test continued until the maximum stroke of the LVDTs was reached. Some images were taken periodically throughout the course of the test to document the failure. Figure 3.8 shows the configuration of the capped cylinder after attaching the mounting rig and loading into the testing machine.

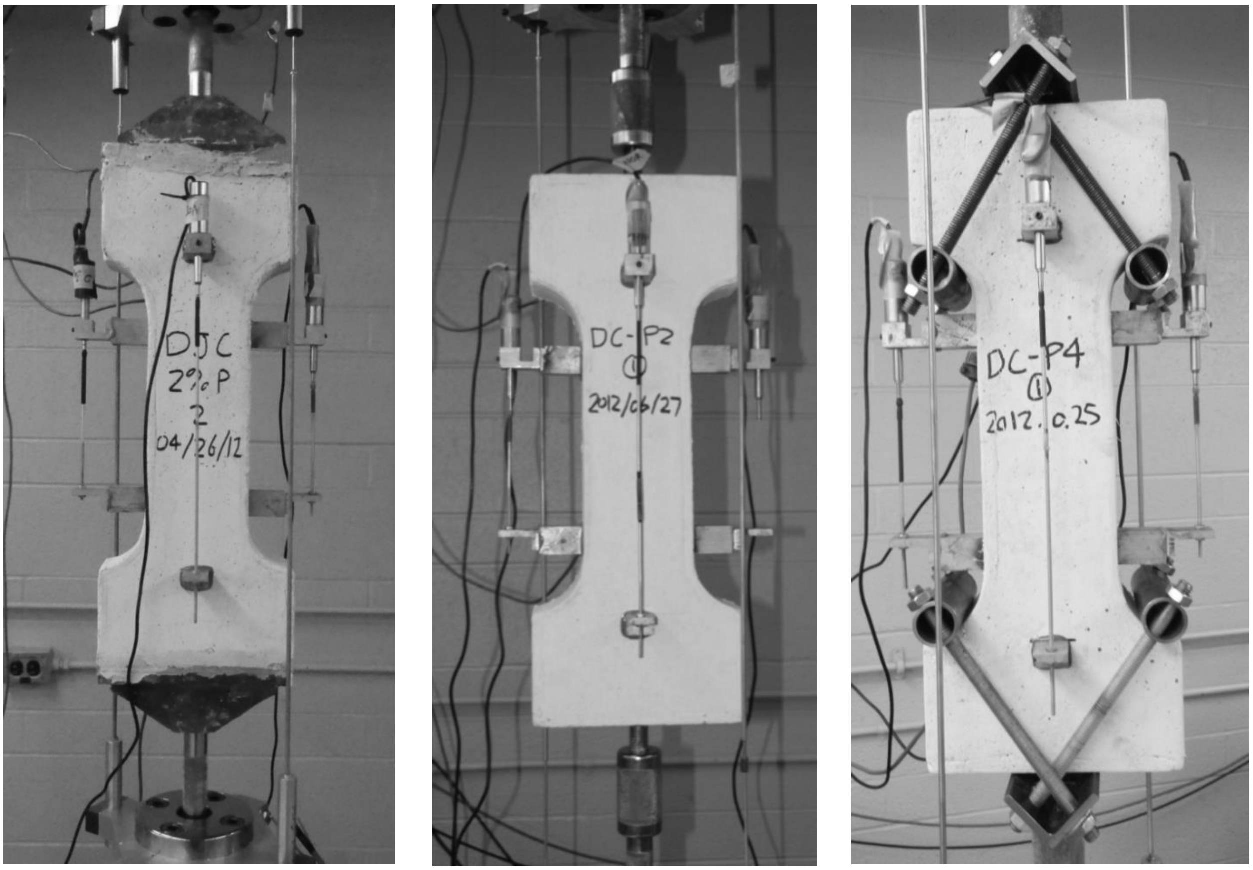

(a) (b) (c)

Figure 3.9: Uniaxial direct tension (Dogbone) tests

3.6 Uniaxial Direct Tension Tests

In order to characterize the behaviour of the concrete in tension, a number of different standard test methods are used. In many cases, uniaxial tension tests are not performed due to the great deal of care and difficulty associated with performing the test successfully. A number of other test methods, such as the modulus of rupture bending tests (ASTM C1609/C1609M, 2010) have been proposed to avoid this problem. Yet, for FRC specimens, it is important to be able to investigate the contribution of the fibres in a direct tension case, so as to be able to observe the improvements in post-cracked behaviour, ductility and toughness. Also, the experimental results obtained from uniaxial tests allowed for direct evaluation of the quality of the predictions provided by the SDEM that represents the direct tension response of FRC. In addition, these responses were used to make adjustments to the SDEM for the modelling of PPFRC specimens, an option that was not present in VecTor2 when this work was commenced. As a consequence of this objective, uniaxial direct tension (or “dogbone”) tests were attempted. Figure 3.9 shows the variable configurations used throughout the testing program.

3.6.1 Specimen Description

As can be expected, it is difficult to perform a uniaxial direct tension test with proper instrumentation due to uncertainty regarding the location of the crack. Also, it has been deemed undesirable to use a notched specimen as the crack will be forced to propagate from that location at a lower load due to the presence of the stress concentration. The formation of cracks will thus not be natural (Benson and Karihaloo, 2005). Much of this problem was solved through the development of a test method at the University of Toronto in the past, yet still the cracking location remains highly variable (Susetyo,2009).

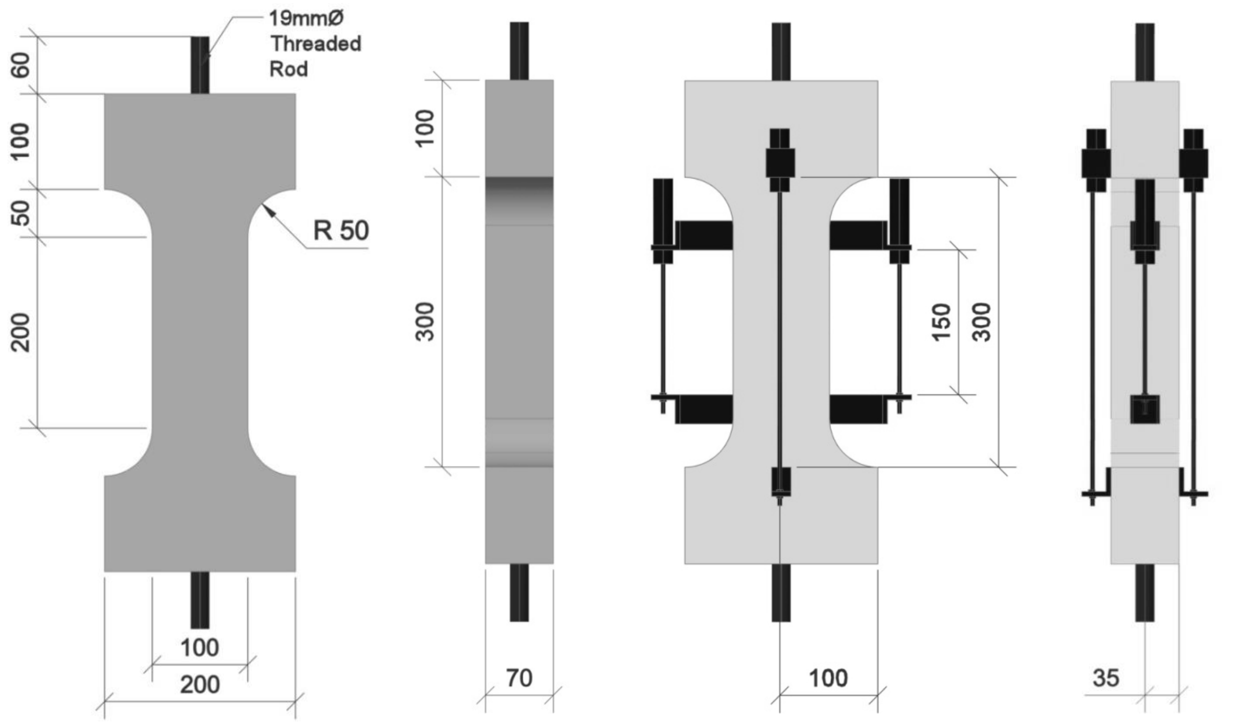

(a) (b)

Note: All dimensions in mm

Figure 3.10: Uniaxial tension test: (a) Specimen dimensions (b) LVDT configuration

A total of six dogbones from the DC-DB1 and DC-DB2 series were tested using the method of bonding large steel end blocks to the dogbones as shown in Figure 3.9(a). The casting of these dogbones was performed in two phases, using a form vibrator to consolidate the concrete at each phase. Also, between the two phases, a small piece of welded wire mesh (previously cut to fit directly into the ends of the dogbones) was inserted on top of the compacted first phase. The next phase was completed and the concrete was finished using a trowel. As mentioned before, the concrete was covered in wet burlap and plastic for seven days after casting. To prepare these dogbones for the bonding of the end plates, the ends of dogbones were smoothed using a milling machine. Then an angle grinder with a diamond blade was used to make inclined cuts spaced at about one inch in the ends of the specimens. The dogbones were then set up on saw horses and the milled/cut surface was made level. Next, using Sikadur® 30 structural epoxy, the steel end blocks were merged onto the dogbone. The epoxy was given a day to set, and then the dogbones were flipped and blocks were merged to the other end (Deluce, 2011). Thus, it is clear that this process is time consuming and labour intensive, while also making it very difficult to ensure that the lines of action of the two end blocks are concentric with each other and with the centreline of the dogbone. Therefore, part of the goal of this work was to find a way to modify this testing procedure.

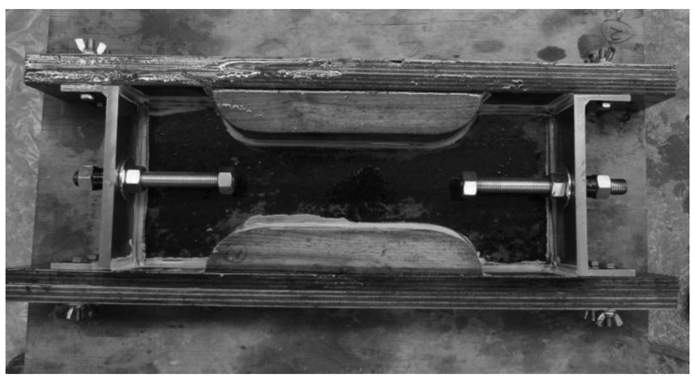

Figure 3.11: Dogbone forms with steel end plates and ¾" threaded rods locked in place

One possible solution to this problem was to follow the procedure used at Seoul National University in South Korea. These tests used a reinforcing bar cast into the widened portion of the specimen and protruding out of the ends of the specimen. A small welded wire mesh was inserted into the end regions to provide some reinforcement (Lee, 2012b). This bar was then directly attached to the testing machine. The 55 kips (245 kN) MTS Universal Testing Machine at the University of Toronto used for these tests came already equipped with two sets of universal joints. These joints also had a mechanical coupler with ¾"-10 threads. Thus it was decided to cast a ¾" threaded rod into the specimen, similar to what is done in Korea. The connection to the testing machine could then be made without having to mill and cut the ends of the dogbones and without the need for bonding steel blocks. To achieve this, steel form end plates were fabricated with the location of the threaded hole for the bars carefully measured. Then, when preparing the form for casting, the level and alignment of the threaded rods were checked from the inside of the form and then locked into place using a nut (see Figure 3.11). Casting of these specimens was done in three phases instead, placing two welded wire mesh pieces into the concrete after each of the first two phases (one underneath the threaded rod and one above the rod). Figure 3.12 depicts the appearance of the specimen after each phase.

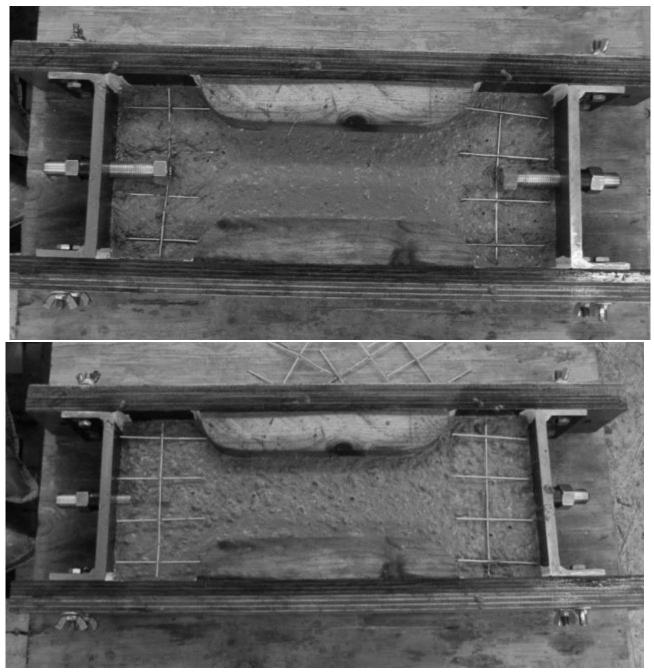

Figure 3.12: Casting of the modified dogbones (phase 1 and phase 2)

This procedure is in development. The first attempt was to extend the rod 120 mm into the specimen from each end. A nut was placed on the end of the rod to help with stress transfer. This was done for specimens from the DC-P1 and DC-P2 series (Figure 3.9(b)). The results of the test indicated that this bar length was too long, and the end of the rod may have caused the propagation of the failure crack due to the stress concentration present at this location. After these results, it was decided to reduce the length of the threaded rod inside the specimen to 60 mm. This was used for DC-P3, DC-P4 and DC-P5. Upon testing these specimens, a splitting crack was observed at the edges of the specimen. To counteract this, the clamping rig depicted in Figure 3.9(c) was fabricated. After the first test that developed the splitting crack, the tests performed with the clamping rig were successful and crack propagation was not affected. It is also believed that if the specimens are constructed without the relatively large nut on the end of the threaded rod (1-1/8”, leaving only 20 mm of cover), then this splitting crack will not form. However, this has not been attempted as of yet. Also, a finer welded wire mesh would likely improve this condition.

3.6.1 Test Instrumentation

The dimensions of the dogbone specimens and the instrumentation locations for each of the three configurations used are depicted in Figure 3.10. The instrumentation location was based on that which has been done in the past at the University of Toronto (Deluce, 2011; Susetyo, 2009). The desire remained to have the crack form within the gauge length of the shorter LVDTs, yet the cracking location in concrete is highly variable. Thus, the longer LVDTs were used as well; even though these LVDTs encompassed the change in cross section, this was deemed insignificant in the analysis procedure employed.

To prepare the dogbones for testing, instrumentation mount locations were marked off using a ruler and a set square. These lines were drawn such that the instrumentation mounts could be installed in the direct centre of each face of the specimen, with a gauge length of 300 mm or 150 mm as required. The specimens were then painted using a mixture of 1 part white paint to 1 part water. Instrumentation mounts were then epoxied on to the dogbones using Fastweld 10 epoxy and a rig designed to ensure that the correct gauge length was maintained.

3.6.2 Test Procedure

The specimens were loaded into the aforementioned 55 kips (245 kN) MTS Universal Testing Machine at the University of Toronto. LVDTs with a stroke of ±5 mm were then attached to the mounts and set to -3 mm (so as to allow 8 mm of stroke over the course of the test). The LVDTs were then zeroed. External displacement control was used at an initial loading rate of 0.001 mm/s. The test was run without changes until first cracking and then subsequently until the maximum load after cracking was achieved. Photographs were taken periodically. When the peak load was reached and a significant amount of degradation in load-carrying capacity had subsequently occurred, the loading rate was gradually increased to a maximum of 0.01 mm/s. If the LVDTs approached saturation, they were reset to -3 mm; this was accounted for in the data analysis. At around 20% of the maximum residual load, instrumentation was removed and the machine cross-head was then lifted to split the dogbones into two pieces. Since two distinct pieces were obtained, it was possible to count and catalogue the number of fibres crossing the main failure crack. Cross-sectional dimensions adjacent to the failure crack were measured and recorded as well.

3.7 Modulus of Rupture Tests

Modulus of rupture bending tests were performed as another means of comparison between the behaviour of the macro-synthetic and steel fibre reinforced concretes. These tests were deemed important as they allow for the evaluation of the response of the concrete when subjected to bending moments. In this way, residual flexural strength values and toughness characteristics of the materials could be calculated and compared. To perform these tests, the ASTM C1608/C1608M Test Standard was followed.

3.7.1 Specimen Description

The specimen dimensions used were those required by the governing standard. The beam specimens had a shape of 152x152x533 mm (6”x6”x21”). Specimens were cast at the same time as their corresponding panel, using two lifts with vibratory compaction between each lift to ensure good consolidation. The top was then finished using a trowel and excess fibres protruding out of the edges of the top surface were removed. As with all other specimens, these were covered with wet burlap and plastic and left cure for one day in the form, and then six more days outside of the form.

The dimensions, loading arrangement and instrumentation setup used can be seen through the drawing in Figure 3.13 and pictorially in Figure 3.14. As required in the standard, the clear span between supports was 457 mm (18”) and the locations of the four point loading were 152 mm (6”) from each support (quarter-point loading).

3.7.2 Test Instrumentation

In order to obtain mid-span deflection data, two LVDTs with a total stroke of ±8 mm were used to measure the mid-span displacement on each vertical face of the beam. A rectangular mounting rig previously fabricated at the University of Toronto that exactly follows the requirements of Section 6.2 of the testing standard was used to arrange these LVDTs (ASTM C1609/C1609M, 2010). The use of this rig, which was mounted directly onto the specimen at the mid-depth, removed the need to measure the displacement at the supports, a method that has been known to produce extraneous results (Susetyo, 2009). The instrumentation orientation is also presented in Figure 3.13.

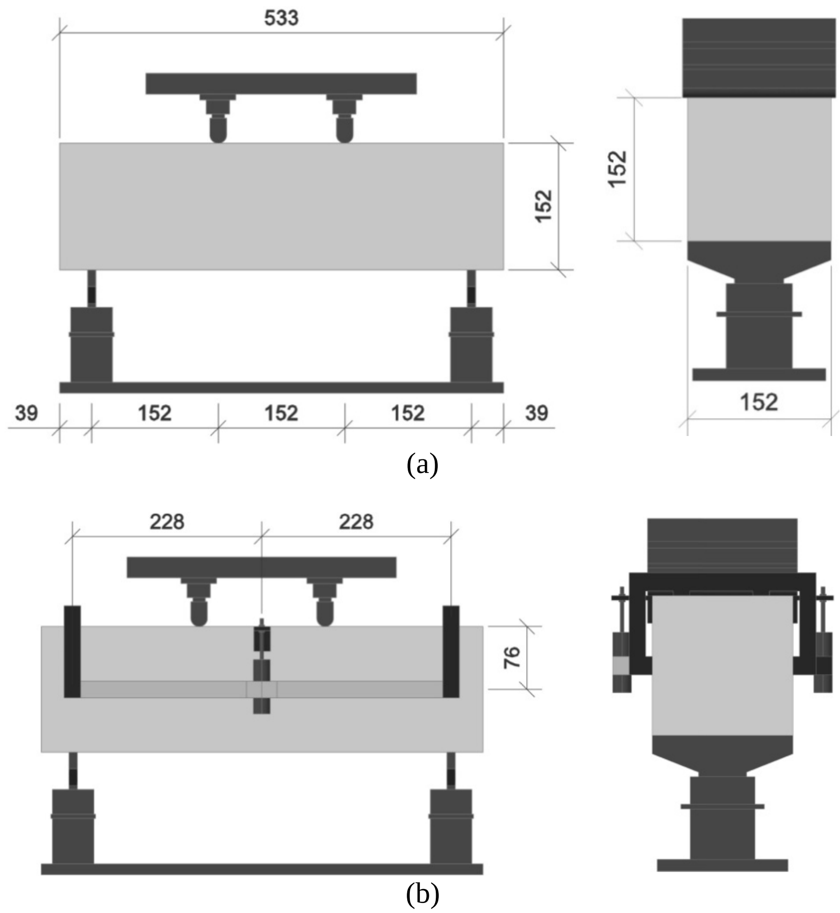

Note: All dimensions in mm

Figure 3.13: The ASTM C1609/C1609M Specimen: (a) Dimension (b) Instrumentation

In order to prepare the specimen for testing, the following procedure was employed. First, the specimens as cast were rotated by 90 degrees for testing, such that the finished face was the back face of the tested specimen. Then, the locations of the 4-point loading were marked on all four sides of the specimen. This was done by finding the average centre of the specimens using a ruler and then marking off the supports 229 mm (9”) each way from the centre and the loading points 76 mm (3”) each way from the centre. The mid-depth was also found and marked so that the rectangular rig could be more easily attached. The prisms were then painted with one part white paint to one part water. After the paint had dried two instrumentation reaction plates (one in the front and one in the back) were epoxied to the specimen using Fastweld 10 epoxy. The surface over which these mounts were attached to the concrete was made as small as possible so that the plates would move with the mid-span of the beam.

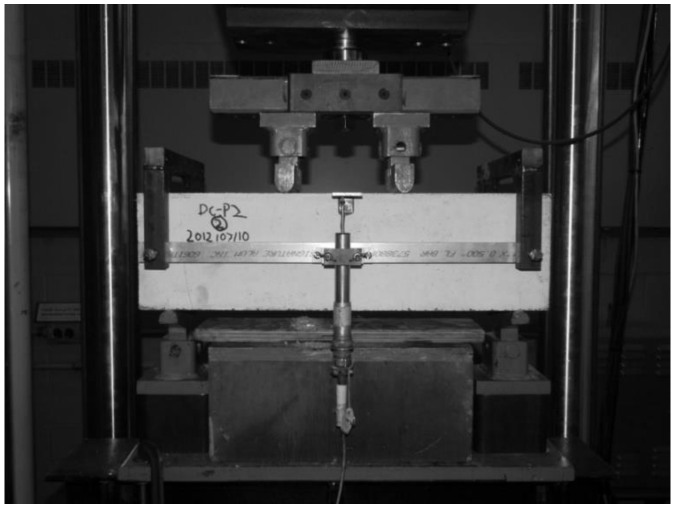

Figure 3.14: The Modulus of Rupture test

3.7.3 Testing Procedure

The specimen was loaded into the 1000 kN MTS Four Post Test Machine that is frequently used to perform such tests at the University of Toronto. At this point, the rectangular rig was carefully attached to the prism. A level and a ruler were used to make adjustments and to ensure the rig was centred and level. Next, the LVDTs were mounted onto the rig and set to a value of 4 mm, so as to allow for a total of 12 mm of stroke for the test (the specification requires that the test be terminated after a deflection of L/60 is achieved, corresponding to 7.5 mm for these specimens) (ASTM C1609/C1609M, 2010). The cross-head was then lowered to ensure that the prism was in the correct location (centred in the machine and on the supports). After this was completed, loading commenced at a rate of 0.006 mm/s. The test continued at this rate until a peak load was obtained, at which point the loading rate was increased gradually up to a maximum of 0.02 mm/s. The test was continued until at least 7.5 mm of midspan deflection was achieved; pictures were taken periodically throughout the duration. After completion, the specimen was removed from the machine, and the cross-sectional dimensions adjacent to the failure fracture were measured.

3.8 Panel Tests

The goal of the panel tests was to investigate the structural response of SFRC and PPFRC to in-plane pure shear and to compare the results against each other and against conventional reinforced concrete (RC) members. These comparisons were needed to determine the viability of the fibre products in structural applications and, more specifically, in situations where the concrete was reinforced with both conventional steel and fibres. In addition, these results could then be used to investigate the capabilities of available models to predict the behaviour of FRC when also reinforced with conventional steel. The presence of a reinforcement cage allowed for an observation of the practical challenges surrounding FRC compaction in a more realistic situation, as already discussed in Section 3.4.

The panel tests were performed using the Panel Element Test Facility at the University of Toronto (Figure 3.15). This machine was designed to subject square panel elements of fixed geometry (890x890x70 mm) to any combination of in-plane stresses (Vecchio, 1979). The test panel is constructed with twenty shear keys around the perimeter, which act both as the form during casting but also as a means of connecting the specimen into the testing machine. The machine consists of 37 hydraulic cylinders and three rigid links. These 40 links are oriented horizontally and vertically, and the panel is installed with the edges inclined 45° such that at each of the twenty shear keys a horizontal and vertical force can be applied (see Figure 3.15 (a) and (b)). Two of the three rigid links connect at one key, creating a pin connection, while the other rigid link acts as a vertical roller. To restrain the specimen from out-of-plane movements, tension links are used to attach the keys to the back frame. These can be adjusted to ensure the panel is directly centred on the line of action of the jacks.

Each hydraulic jack has a capacity of 218.2 kN (49.1 kips) in compression and 95.6 kN (21.5 kips) in tension. The jacks on each opposing side of the panel apply the same force through four distinct pressure lines that are controlled through the use of a load maintainer, thus resulting in a self-equilibrating system. Proper configuration of these four load controlled pressure lines in conjunction with the use of four-way valves allows the loading direction to be reversed so that reversed cyclic tests can be performed.

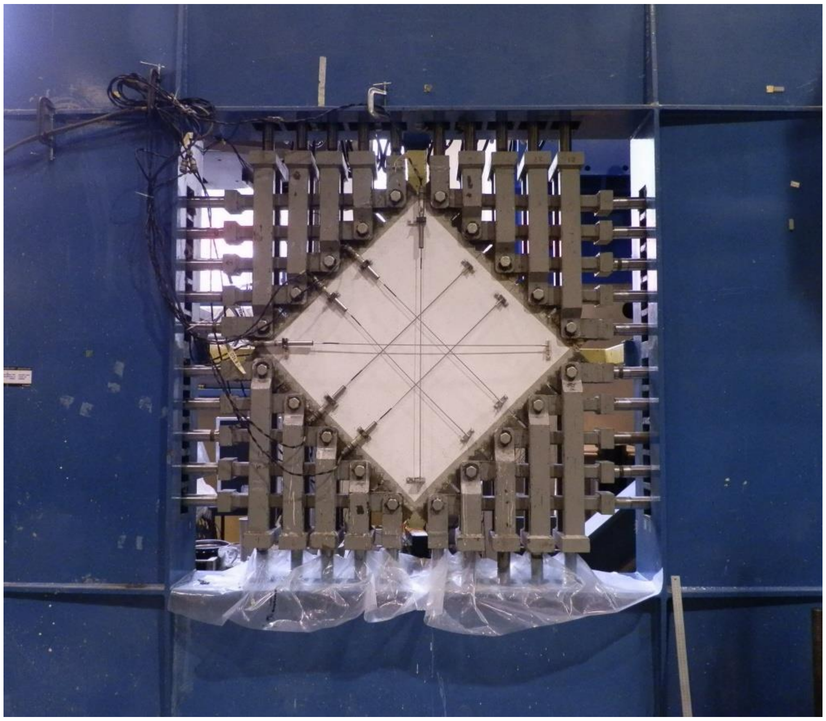

(a)

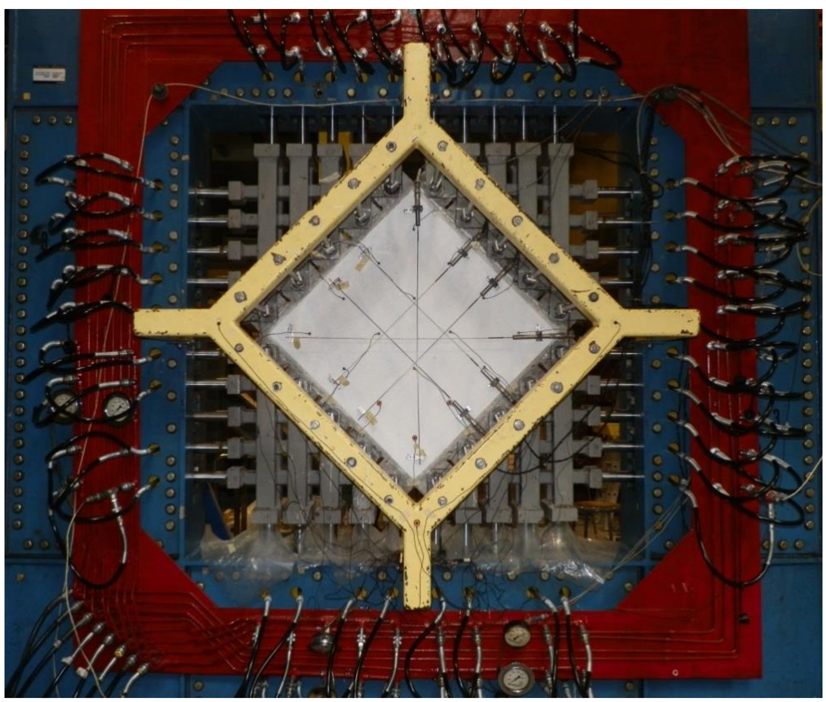

(b)

Figure 3.15: Panel Element Test Facility: (a) Front (b) Back

3.8.1 Specimen Description

In this program, and in the program executed by Susetyo (2009), two types of panel reinforcement configurations were used. The first configuration was used for the control panel DC-P1 which was constructed with plain concrete and had reinforcement in the x- and y-direction. The second reinforcement layout consisted of reinforcement only in the x-direction and was used for each of the fibre reinforced concrete panels.

The design of the control panels is represented in Figure 3.16, with the design of the FRC panels represented in Figure 3.17. This shows the heavy reinforcement in the x-direction for both panels; 40 D8 deformed wires were used yielding a total area of 2064 mm^2 and a reinforcement ratio of 3.31% (since the panel cross section is 62,300 mm^2 or 890x70 mm). In the y-direction for the control panel, 10 D4 deformed wires were provided to yield a total reinforcement area of 258 mm^2 and a reinforcement ratio of 0.42%. For both directions, the bars were extended through the shear keys and the ends of the bars were threaded so that a nut could be attached to hold the reinforcement cage in place. In addition to the D4 wires, 20 5/16" threaded rods were also provided to improve the connection of the shear keys to the panel concrete and to aid in stress transfer from the keys to the specimen. For the FRC panels, no wires were provided in the y-direction, but 40 5/16" threaded rods were provided here as well. In both cases, a nut and a washer were placed on the end of each threaded rod to improve the stress transfer to the concrete. Also, as can be seen in the drawing in Figure 3.17, the y-direction threaded rods in the FRC panels were staggered to avoid creating a distinct plane of weakness (Susetyo, 2009).

The x-direction reinforcement ratio was chosen by Susetyo (2009) in such a way that yielding of the x-direction steel could be avoided, while still preventing the panel from failing shortly after cracking, so that the post-cracked behaviour of FRC could be adequately investigated. The reinforcement ratio of 3.31% proved successful in the past and, thus, was used again in this study (Susetyo, 2009). The steel reinforcement in the y-direction of the control panels was meant to represent near the minimum steel reinforcement requirements of CAN/CSA Standard A23.3-04 (2004) Clause 7.8, which calls for a reinforcement ratio of 0.2% of the gross cross section. Also, the Canadian Highway Bridge Design Code (CHBDC) (CAN/CSA Standard S6-06, 2006) states in Clause 8.12.6 "minimum area of shrinkage and temperature reinforcement in each face and in each direction shall be 500 mm^2/m and the spacing of the bars shall not exceed 300 mm." If one takes a typical concrete deck thickness of 250 mm, this works out to a reinforcement ratio of 0.4%. Thus, the reinforcement ratio of 0.42% was used (Susetyo, 2009).

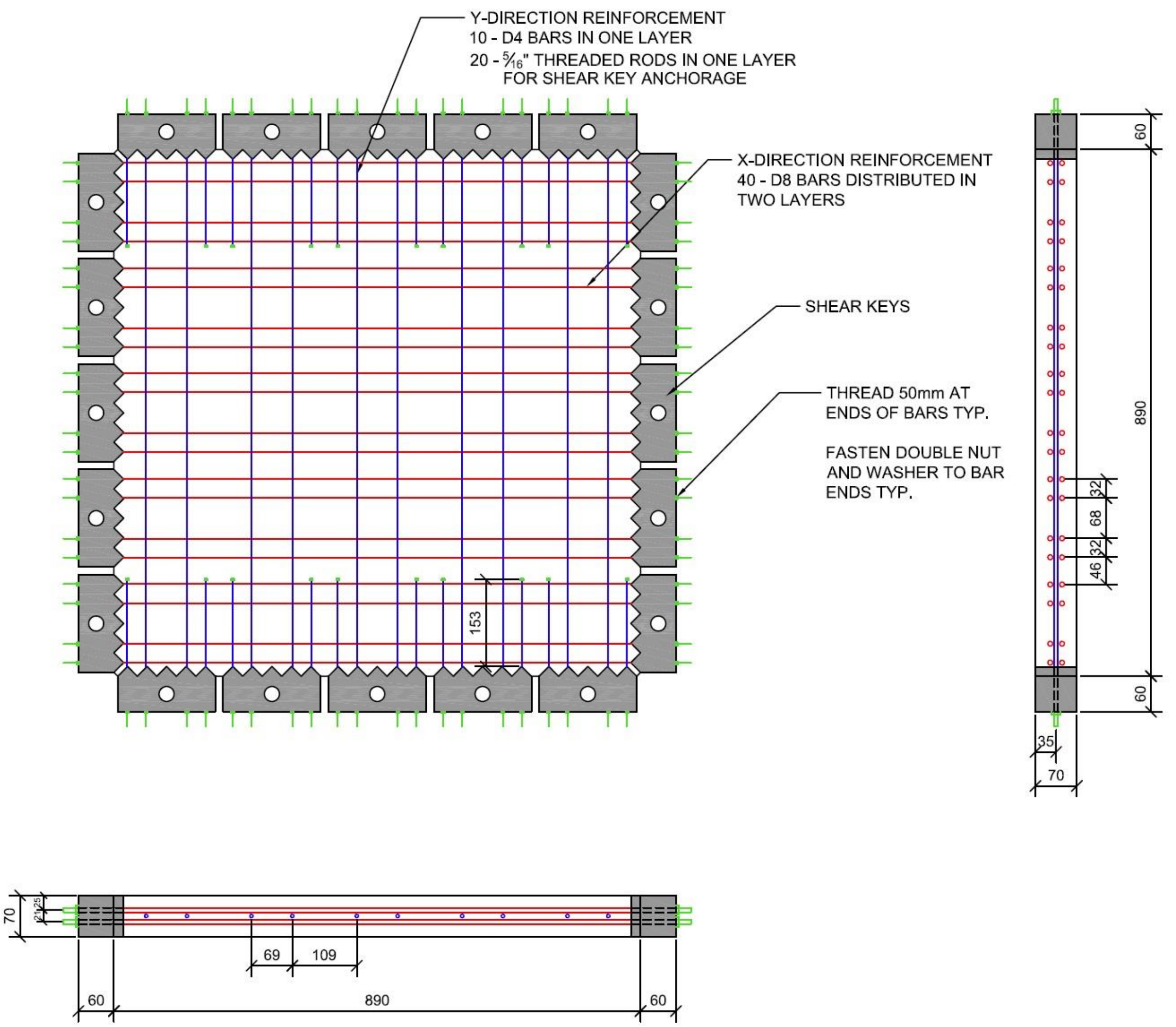

(a)

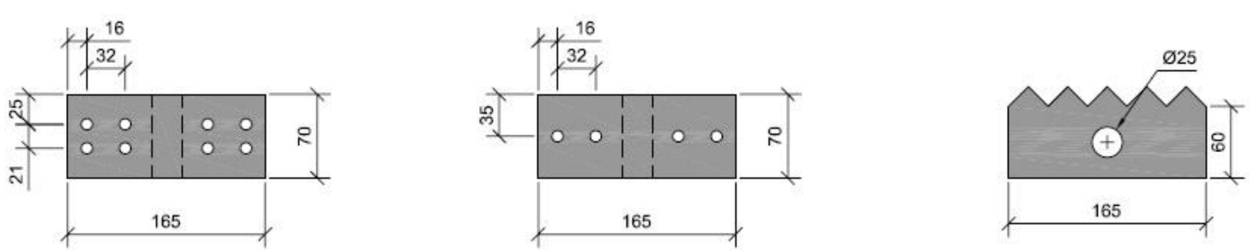

(b)

Note: All dimensions in mm

Figure 3.16: Control panel drawing: (a) Reinforcement layout (b) Shear key details

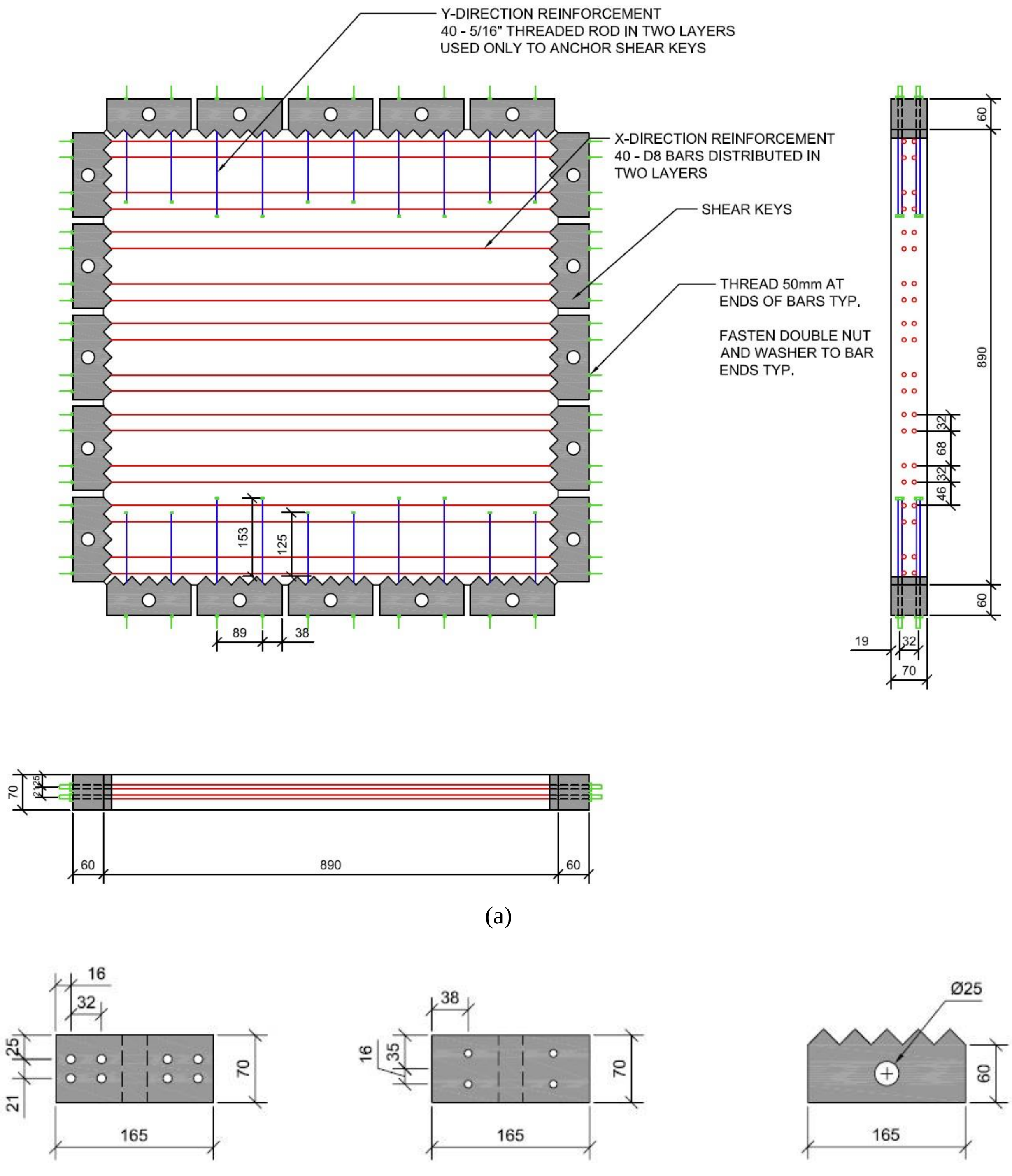

Note: All Dimensions in mm

Figure 3.17: FRC panel drawing: (a) Reinforcement layout (b) Shear key details

3.8.2 Specimen Construction

First, the reinforcing bars were cut to the appropriate lengths (1050 mm for full reinforcing bars (D8 or D4) and alternating 225 or 255 mm for long and short dowels respectively). The ends of all bars were ground and polished to remove sharp edges. Then, approximately 50 mm on each end of each deformed wire bar was threaded using either an M8 dye (D8 bars) or M6 dye (D4 bars). The bars were then wiped with acetone to remove any oil or dirt.

The twenty shear keys were then placed on the casting table and aligned, and construction of the cage commenced one layer at a time. Each bar was fastened to the end of the shear keys using a double nut connection. Finally, unused holes within the shear keys and gaps between the shear keys were filled with plasticine to complete the form.

For casting, the concrete was placed in two lifts, vibrating each lift with the form vibrators attached to the casting table each time. In extreme circumstances, tamping rods or immersion vibrators were used to aid in concrete consolidation, particularly around the teeth of the shear keys. The top surface was then screeded and finished. After being allowed to set for about two hours, the panel was covered with wet burlap and plastic and left to cure for three days on the table. Afterwards, the panel was removed from the table and placed on a wooden pallet, still wrapped in burlap and plastic until the seventh day after casting. After this, the burlap and plastic were removed and the specimen was left to cure in ambient conditions.

3.8.3 Test Instrumentation

3.8.3.1 Linear Variable Differential Transducers (LVDTs)

LVDTs measure the displacements between two fixed points with the gauge lengths being the distance between the instrument mount and the reaction plate. Thus, LVDTs give an average strain value over the given gauge length and will harmonize any localized strain readings (which can be much higher or lower based on the cracking distribution through a localized region). These data were acquired throughout the duration of the test.

Figure 3.18 depicts the LVDT arrangement used in this testing program. A total of 12 instruments were used (some had a stroke of ±15 mm while others had a stroke of ±24 mm based on instrumentation availability in the laboratory). On each face, two were used to measure the strains in the x-direction, two in the y-direction, one in the 45° direction and one in the 135° direction.

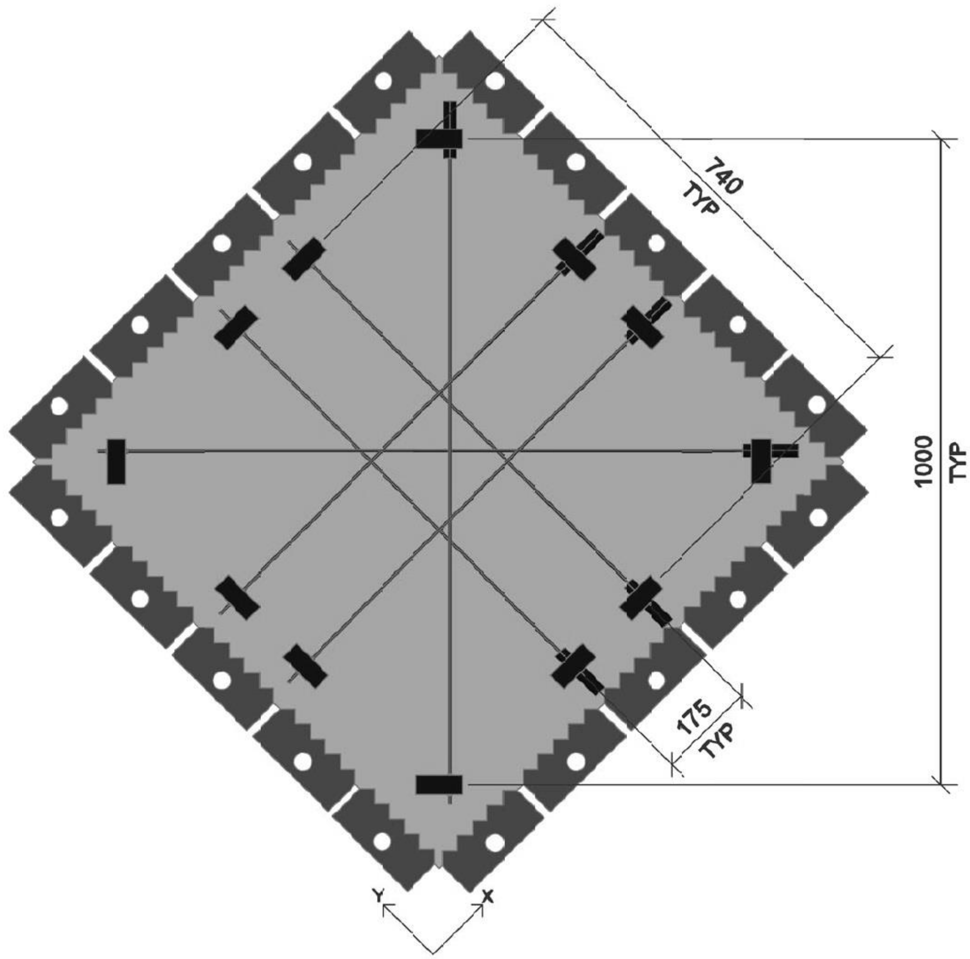

Figure 3.18: Panel LVDT configuration (panel front and back)

3.8.3.2 LED Targets

Another deviation from the work of Susetyo (2009) was in the decision to move away from Zurich gauges as a means of measuring localized strains and to instead use the Metris K610 3D camera and LED targets for this purpose. This system recorded position data to the nearest 20 μm. Through post-processing, the position data were converted into strain data.

A 200x200 mm subgrid consisting of a total of 16 nodes was utilized to record localized strain data over the middle 600x600 mm of the panel. The configuration of the targets can be seen in Figure 3.19. The targets were attached to the back face of the panel with hot glue and then the

3D camera was activated to ensure that each of the targets were in view. Figure 3.20 shows a photograph of the 3D camera with the mounting configuration used during the test. In addition, the use of this system necessitates a fixed reference plane so that the subsequent test readings can be rotated into a single xy-plane for strain calculations. For this testing program, the reference system consisted of three LED targets mounted on the corners of the yellow back frame of the Panel Element Test Machine as depicted in Figure 3.15(b).

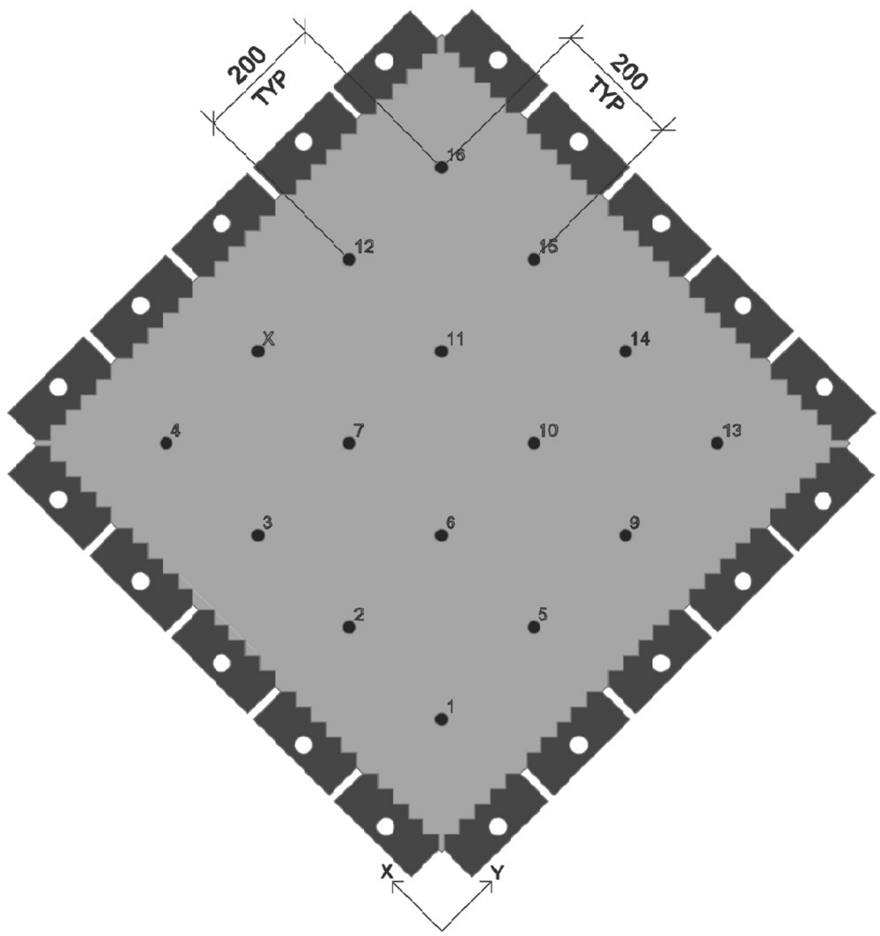

Figure 3.19: Panel LED configuration (panel back face only)

This system was set to run during the loading process, but was then switched off during the taking of a load stage to avoid flooding the results files with unnecessary data (as the performance of crack measurements often obstructs the camera's view of the targets). As will be discussed further in Chapter 4, this led to complications in the data analysis.

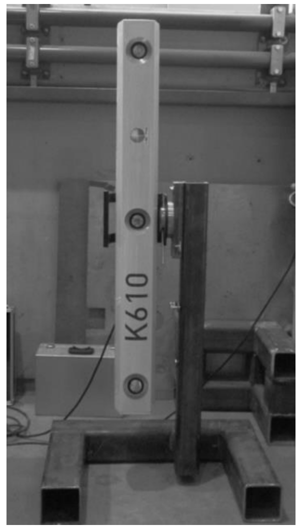

Figure 3.20: Metris K610 3D LED camera on mount

3.8.3.3 Load Cells and Pressure Transducers

The three aforementioned rigid links were each connected to a load cell within the frame of the test machine. These load cells record the reaction data at the supports, which should match the forces applied through each of the hydraulic jacks so as to preserve the equilibrium of the system.

In addition, four pressure transducers were used to record pressure data at four points within the system. Typically, one of these were used on each of the two input pressure lines to verify the ratios of applied pressure were correct. The other two transducers were periodically moved around the various hydraulic jack intakes to try to verify that the pressure applied through the load maintainer was also being correctly applied in the necessary jacks.

3.8.4 Test Preparation

First, on the back face (finished face), the LED grid and LVDT mounting points were marked out with pencil. More prominent marks were then bolded using a marker. Then, a masonry drill bit was used to pilot drill holes into the specimen at the locations of the LVDT mounts. After this, the panel was painted using one part white paint and one part water. Then, using Fastweld 10 epoxy, 10-32 threaded rods were then fastened into the holes; these rods were later used to attach the LVDT mounts. Being careful not to damage the rods, the panel was then flipped over so that the front face (formed face) was now facing up. The drilling, painting and epoxying of rods was done on this face as well.

Next, the panel was lifted into the test machine with the help of a crane. The rigid links were first extended and bolted onto the panel to ensure correct positioning of the specimen, at which point the specimen was taken off of the crane. Next, using a hydraulic pump and a series of valves and hoses, the hydraulic jacks were extended two at a time (the horizontal and vertical jack that meet at the same shear key) and bolted to the panel.

With the installation complete, the instrumentation was then applied to the panel. LVDT mounts were screwed into place on the previously epoxied rods and the LVDTs were mounted. These were set as close to zero as possible. Next, the LED targets were hot-glued to the back face of the specimen and hooked up to the acquisition computer. Both of the systems were checked.

At this point, the load maintainer was used to apply 0.54 MPa of biaxial tension to the specimen in the machine. This was meant to remove any out-of-straightness in the system. The out-of-plane tension links were then attached to the specimen by first being tightened to the end of the bolts used to attach the panel to the machine and then being loosely attached to the yellow back frame. Some symmetrical arrangement of three of the tension rods were then tightened. The others were left relatively loose. Finally, the specimen was checked and deemed ready for testing.

3.8.5 Test Procedure

The test was started by turning on all necessary systems and ensuring proper function. Please note that the LED system was set to acquire data at a rate of 1 to 2 Hz. The LVDT system was set to acquire data every time the shear stress changed by ±0.033 MPa, or if the horizontal/vertical LVDT readings changed by ±0.1 mm. A manual reading could be taken at any time by pressing F8, which was used frequently at critical stages of the test. Loading was then commenced using a load maintainer, with the help of a testing technician.

The load maintainer was operated until the target shear stress was reached. Photographs were taken throughout the course of loading. When the target stress was reached, a load stage was taken; this involved stopping and saving the corresponding LED system file, marking and measuring cracks, and taking photos. Crack measurements for reversed cyclic tests were not taken at every load stage in the interest of time. The process was repeated until failure with the caveat that if the tests were monotonic, the tests continued exactly like this until failure but if the test was reversed cyclic, the load was reduced to zero, the four-way valves were reversed, and the panel was reloaded in the opposite shear condition.

After failure, the panel was removed from the machine, and the fibres crossing the failure plane were counted and catalogued. The cross-sectional dimensions of the failure plane were measured as well.

Chapter 4
Experimental Results

4 Experimental Results

4.1 Introduction

Test results for each of the four types of specimens are presented in this chapter. Comparisons will be made to explore the advantages and disadvantages of the different fibre types. The effects of the reversed cyclic loading protocol on the response of the panels will be discussed. In addition, the calculation procedures used to process the raw data will be outlined. This chapter will commence with a discussion on cylinder compression tests, followed by uniaxial direct tension dogbone tests, then modulus of rupture prisms and, lastly, the panel element tests. Summary charts and comparisons will be presented, with a more complete set of plots and tabulated results presented in Appendix A for the material tests and Appendix B for panel tests.

4.2 Cylinder Compression Tests

In this section, the results of the cylinder compression tests are discussed. As mentioned in the previous chapter, two to three cylinder tests were performed at an age of seven days for each batch; peak strength data only were obtained for these tests. Next, three more cylinders were tested on the 28^{th} day after casting; a full stress-strain curve was obtained for these tests. Lastly, if required, three more cylinders were tested on the day of the panel test, so as to obtain a measure of the concrete properties at the age of testing. Full cylinder test data are presented in Appendix A.1, with the data for the 28-day tests summarized in this section.

4.2.1 Data Analysis

Cylinder data analysis was performed in accordance with ASTM C469 (2002) using the following procedure. First, the LVDT readings were averaged and converted to strain data by dividing by 250 mm, the gauge length of the LVDT mounting rig used in testing (see Figure 3.8). Then, load cell data were converted to stress by dividing by the area of the cylinder. The intent was to use six-inch diameter cylinders. In measuring the diameter of the moulds available for use in the structural laboratories, they were found to be approximately 152 mm and, in nearly every case, the cylinder moulds were not of uniform shape throughout the depth. Every attempt was made to use consistent cylinder moulds yet this may not have been the case. Regardless, the area of the specimens was taken as: $A = \frac{\pi}{4}D^2 = \frac{\pi}{4}(152.4\ mm)^2 = 18{,}241\ mm^2$. From this resulting stress and strain data, the secant modulus of elasticity for the concrete in compression was determined as:

$$E_{cs} = \frac{(S_2 - S_1)}{(\varepsilon_2 - \varepsilon_1)} \tag{4.1}$$

where:

S_1 = stress corresponding to a longitudinal strain of $50\text{x}10^{-6}$ [MPa];

S_2 = stress corresponding to 40% of the ultimate load attained by the cylinder [MPa];

ε_1 = $50\text{x}10^{-6}$;

ε_2 = longitudinal strain corresponding to S_2.

Table 4.1: Cylinder Compression Tests Results Summarized

Specimen ID	V_f **[%]**	**Fibre Type**	E_{cs} **(CV) [MPa]**	f'_c **(CV) [MPa]**	ε'_c **(CV) [x 10^{-3}]**	$E_{cs}/\sqrt{f'_c}$
DC-DB1	2.00	MAC Matrix	29,900 (6.04)	58.0 (1.19)	2.994 (6.85)	3930
DC-DB2	3.00	MAC Matrix	34,000 (2.99)	56.1 (0.60)	2.680 (2.25)	4590
DC-P1	-	-	40,200 (1.65)	71.7 (0.55)	2.555 (1.06)	4750
DC-P2	1.00	RC80/30BP	36,000 (3.35)	62.1 (1.46)	3.169 (5.66)	4570
DC-P3*	2.00	MAC Matrix	32,700 (9.45)	50.9 (1.89)	2.655 (6.25)	4580
DC-P4	1.00	RC80/30BP	36,000 (3.98)	64.0 (1.23)	3.160 (5.43)	4500
DC-P5	2.00	MAC Matrix	34,300 (5.75)	54.3 (2.88)	2.877 (4.72)	4650
C1C	-	-	33,500 (3.70)	65.7 (0.30)	2.409 (3.90)	4130
C1F1V1	0.50	RC80/50BN	32,400 (22.7)	51.4 (1.90)	2.147 (22.8)	4520
C1F1V2	1.00	RC80/50BN	32,200 (26.0)	53.4 (5.40)	2.671 (15.9)	4400
C1F1V3	1.50	RC80/50BN	36,200 (29.5)	49.7 (3.40)	2.504 (14.0)	5130

* The average result of this set is based on two cylinders

Table 4.1 presents the calculated data from the 28-day cylinder tests performed. The average values of secant modulus (E_{cs}), 28-day compressive strength (f_c') and compressive strain at peak stress (ε_c') are presented along with the coefficient of variation (CV in %) resulting from the three tests. Figure 4.1 shows representative photographs of the cylinders at failure for most of the sets tested in this work.

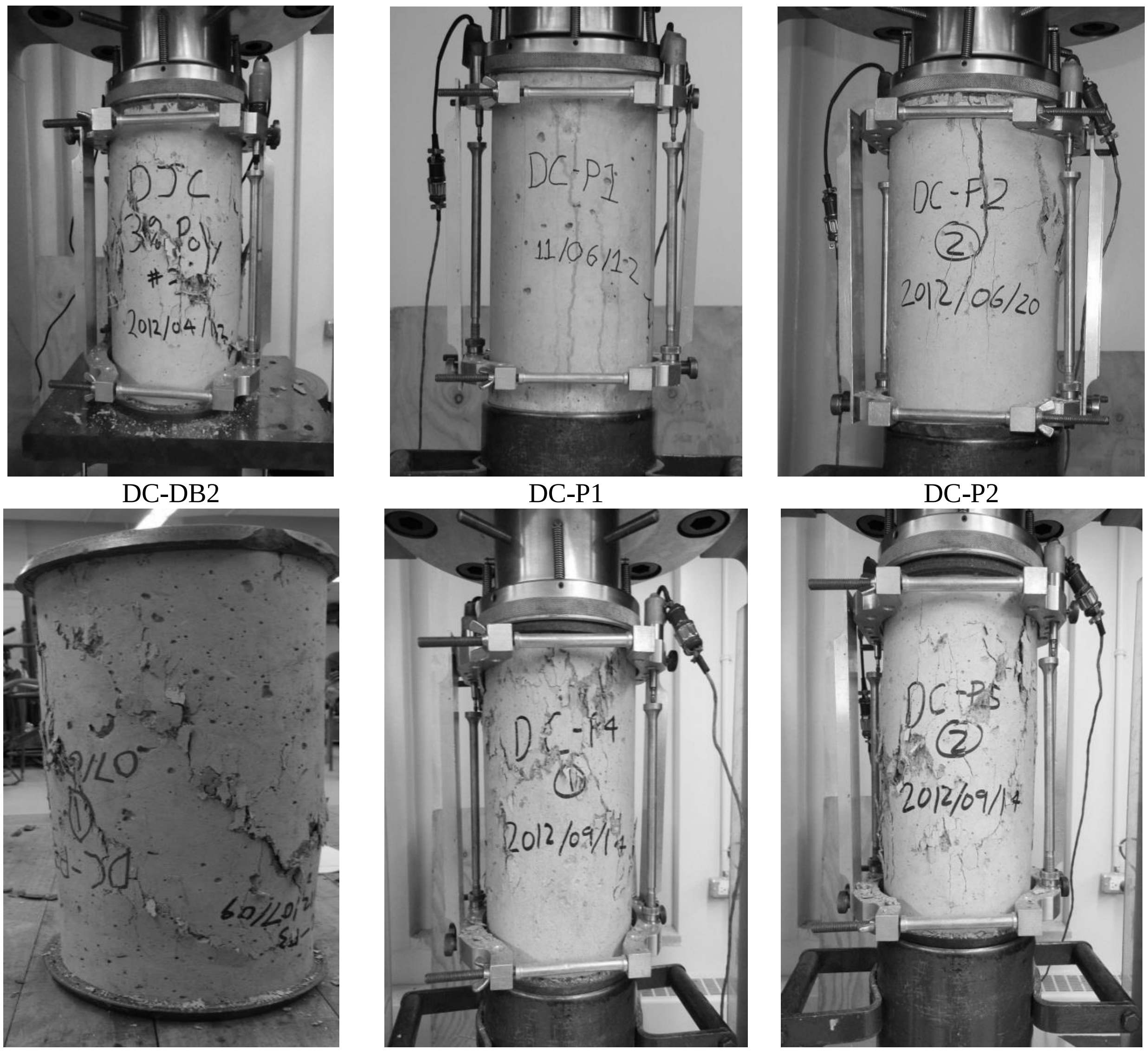

DC-DB2 DC-P1 DC-P2

DC-P3 DC-P4 DC-P5

Figure 4.1: Representative cylinder compression specimens

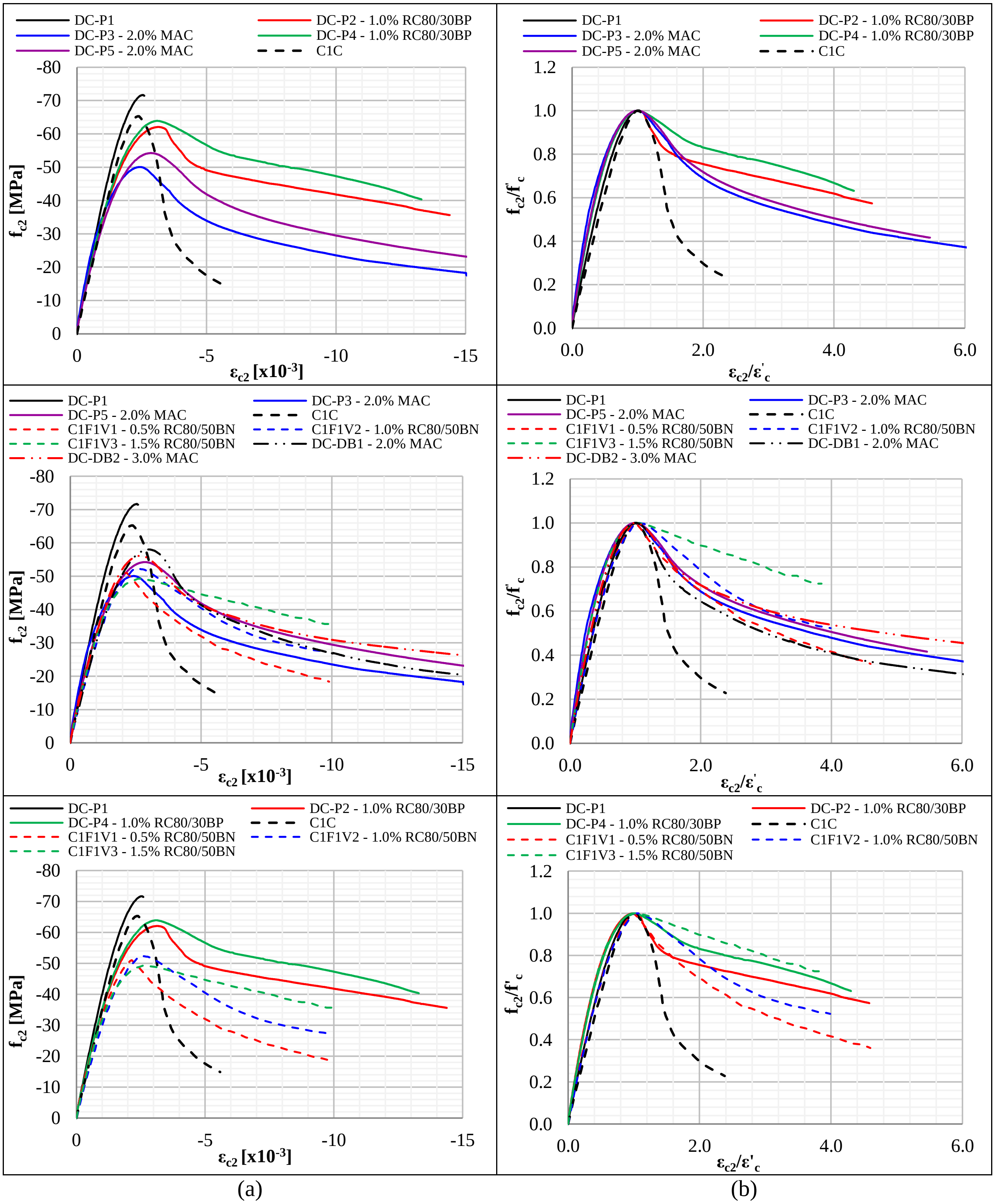

Figure 4.2: Comparison of the compressive stress-strain curves obtained from cylinder tests: (a) Non-normalized (b) Normalized

4.2.2 Results of Data Analysis

As shown in Table 4.1, the mix design of the plain concrete yielded a higher strength when compared to the FRC. Within the FRC mixes, the strength of the concretes with the shorter steel fibres was greater. The length, aspect ratio and volume fraction of fibres have not been shown to have an effect on the peak compressive strength of the concrete (Nataraja et al., 1999; Ou et al., 2012).

The compressive secant stiffness of the concrete was not drastically affected by the addition of the fibres. In most cases, the secant stiffness as measured was similar to that calculated using $E_{cs} = 4500\sqrt{f_c'}$, as suggested in the Canadian Concrete Design Handbook (CAN/CSA Standard A23.3-04, 2004). No systematic differences between the secant modulus of elasticity were observed when comparing concrete batches of different fibre type or volume so as to draw a definitive conclusion about the effects of fibre addition on this parameter. All of the batches exhibited similar slopes up to approximately $0.4f_c'$ (see Figure 4.2). This is consistent with findings in the literature that fibre addition does not have a significant effect on the pre-peak response of concrete in compression (Ou et al., 2012).

Conversely, the compressive strain at the peak stress was increased for the FRC batches relative to the plain concrete batches (as shown in Table 4.1). This is more evident when considering the graphs in Figure 4.2. The FRC specimens exhibited a departure from linearity at an earlier stage as the load continued to increase. The normalized responses in Figure 4.2 show that the pre-peak portion of the response for FRC is much more nonlinear than that of plain concrete. This is due to the peak stress occurring at a higher strain. The increase in the strain at peak stress was consistent for fibres of the same length and independent of the fibre material type. The shorter steel fibres enhanced this effect, consistent with the findings of other experimental programs into the compressive behaviour of FRC (Nataraga et al., 1999; Thomas and Ramaswamy, 2007).

Lastly, as expected, the behaviour of the FRC specimens in the post-peak region was significantly better than that of plain concrete (Nataraga et al., 1999). The load-carrying capacity of plain concrete in compression dropped suddenly after the peak, yet for FRC the stress reduction was controlled. This led to improved ductility and toughness as the concrete reached strains of at least 300% of ε_c'. Also, from the second set of curves in Figure 4.2, it was seen that the PPFRC specimens performed reasonably well in this post-peak region. Immediately after crushing, the load for PPFRC specimens dropped in a fashion similar to that of C1F1V1, which contained 0.5% by volume steel fibres. Yet, as the strain increased further, the PPFRC specimens exhibited an improved residual strength capacity, somewhat close to that of C1F1V2 (1.0% by volume steel fibres). Thus, the overall compressive response for macro-synthetic fibre reinforced concrete was similar to that of SFRC containing end-hooked steel fibres of similar length. Post-peak ductility and toughness were similar to those of 0.5% to 1.0% by volume of steel fibres. Also, the response was further improved when the PPFRC fibre volume was increased to 3.0% (exhibited through the response of DC-DB2).

4.3 Uniaxial Direct Tension Tests

In this section, the dogbone test results are covered in detail. For most batches, three dogbones were constructed and tested, with the only exception being DC-DB1, for which four dogbones were tested. The specimens were tested at various ages from 35 to 112 days, based on the required preparation lead time and availability of laboratory machinery. Full test data are presented in Appendix A.2, with average results and discussion in this section.

4.3.1 Test Observations

As has been shown in the past, the dogbone tests performed in this work exhibited some variability in the results. There are a number of reasons for the inconsistent behaviour. First, the location of the crack along the height of the specimen had an effect on the cracking load. A crack will typically form at the weakest location along the height of the specimen and the degree of imperfection at this location has a large effect on the load attained (Susetyo, 2009). In addition, fibre orientation is a critical factor affecting the results obtained for uniaxial tests performed on FRC (Shah and Rangan, 1971). Longer fibres tend to orient in the direction of the length of these specimens, since the width and thickness dimensions are small. This yields a higher fibre orientation factor for the longer fibres, as this direction also happens to be the loading direction (Gettu et al., 2005). In addition, the number of fibres crossing the failure crack for specimens constructed from the same batch of concrete was variable. Table 3.9 presents both the fibre orientation and number of fibres. In combination, these factors led to varied levels of post-cracked load-carrying capacity and ductility. Also, as will be covered in more detail, the dogbones from batch DC-P1 and DC-P2 contained a cast-in threaded rod that proved to be too long, and likely resulted in the propagation of the first crack at a reduced load. Crack patterns for selected tests are shown in Figure 4.3.

It is also worth noting that for some tests, the north (or formed) face LVDT (see Figure 3.10 (b)) gave anomalous results at pre-cracked stages. This may have been due to out-of-plane movements towards the south face of the specimen as a result of the difficulty encountered in centring the end-block or cast-in rods (as mentioned in Section 3.6), or due to the fact that the formed face contained a higher amount of coarse aggregate and fibres, as observed from the failed specimens (Figure 4.4). This made the formed face stiffer. The error may also be attributed to the LVDT plunger not moving freely at the low displacements being considered. Before cracking, LVDT readings were used to determine the modulus of elasticity of the concrete in tension (E_{ct}) and the cracking strain (ε_t'). Grossly erroneous results were excluded from the data analysis at pre-cracked stages; however, results that were not ignored may have led to the high coefficient of variation on the values of E_{ct} and ε_t' that have been calculated.

After cracking, in some instances, out-of-plane bending was exhibited in the specimen, likely due to uneven distribution of fibres. The average responses of the LVDTs measuring the crack tended to show a reasonable behaviour despite the bending, and so the crack width calculation was done individually for all LVDT readings and then averaged.

The plain concrete dogbone specimens tested (DC-P1) showed brittle behaviour, with a sudden and complete drop in load-carrying capacity immediately following the first crack. This is consistent with the findings from test set C1C (Susetyo, 2009). In addition, each of the three dogbones tested cracked near the cast-in threaded rod, meaning the cracking load was possibly affected by the stress concentration present at the end of the rod. All LVDTs on the three specimens tested were used in calculation of the pre-cracked response. The average response of these specimens is depicted in Figure 4.5.

The response of DC-P1 was different from those observed for all FRC specimens. The latter exhibited a ductile post-cracked response, with the ability to carry residual tensile stresses to large crack widths.

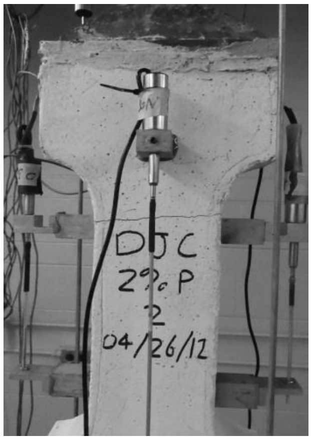

DC-DB1
2.0% PPFRC

DC-DB2
3.0% PPFRC

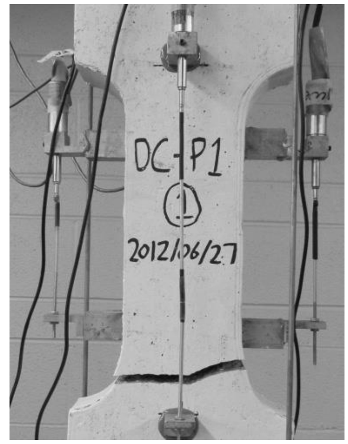

DC-P1
Plain

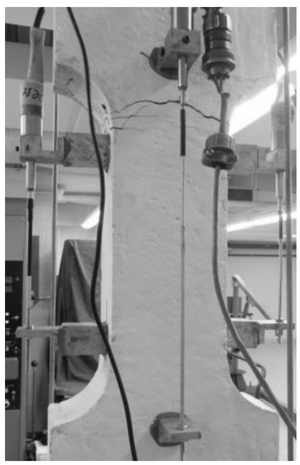

DC-P2
1.0% SFRC

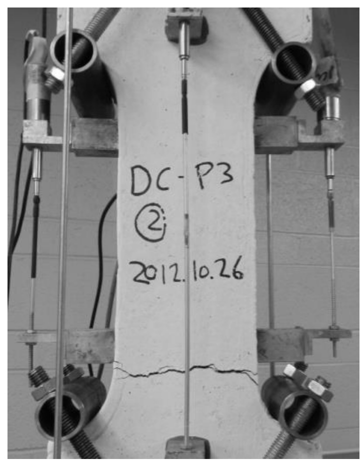

DC-P3
2.0% PPFRC

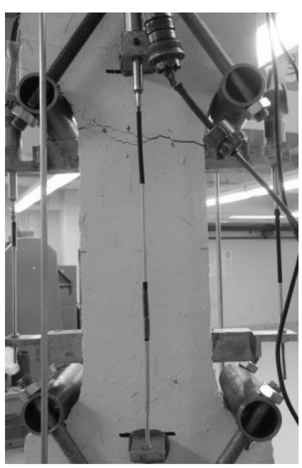

DC-P4
1.0% SFRC

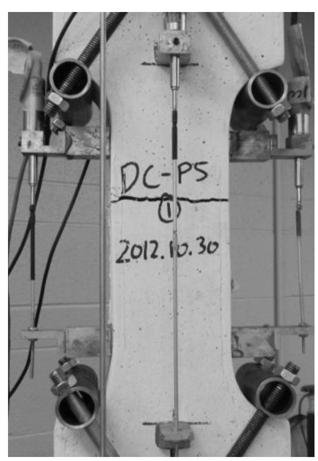

DC-P5
2.0% PPFRC

Figure 4.3: Representative dogbone crack patterns

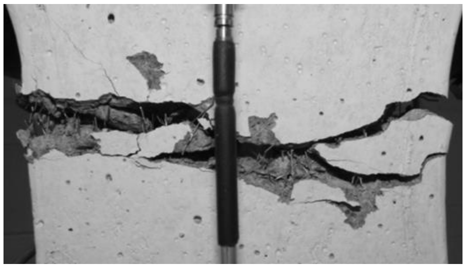

Formed Face (DC-P4)

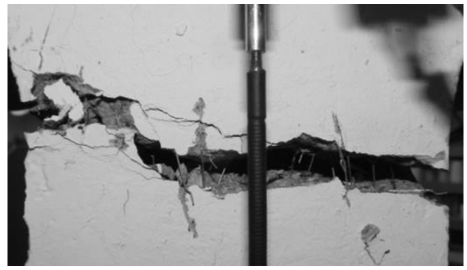

Finished Face (DC-P4)

Figure 4.4: SFRC dogbone depicting high percentage of fibres and aggregate on formed face

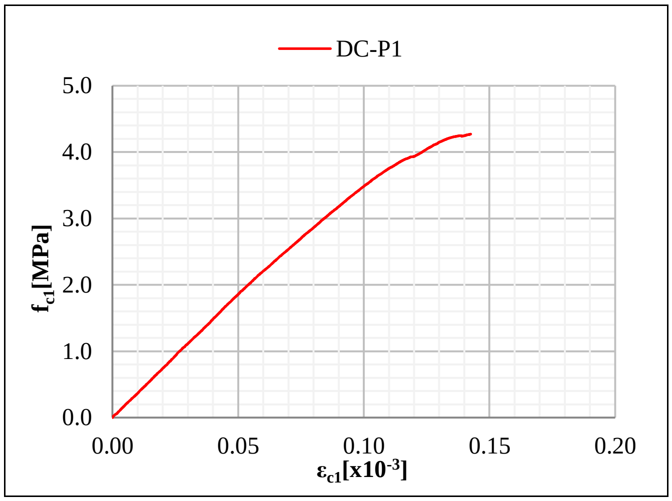

Figure 4.5: Uniaxial tension test result for set DC-P1 (pre-cracked tensile stress vs. strain)

For the FRC specimens tested in this research program, strain hardening behaviour was not observed; however some specimens tested at higher volume ratios of SFRC have shown that strain hardening and multiple cracking can be attained (Deluce, 2011; Susetyo, 2009). Overall, the fibres of both types greatly improved the tensile behaviour of the concrete.

Test set DC-DB1 contained 2.0% by volume MAC Matrix fibres. As mentioned earlier, this set, along with set DC-DB2, was tested to determine a suitable fibre volume ratio to be used for the shear panel tests. This was done to ensure that a reasonably ductile structural response without a sudden and brittle failure could be expected for the panels. For DC-DB1, a significant degradation in the load-carrying capacity immediately after cracking was observed (the average cracking stress, f_t', was 4.76 MPa with a minimum stress after cracking, f_{te}, of 1.58 MPa occurring at a crack width, w_{cr}, of 0.38 mm). This was consistent for all the PPFRC dogbones tested. However, after the initial drop, the load-carrying capacity increased as the fibres became aligned and engaged, reaching a maximum residual tensile stress, f_{tu}, of 2.36 MPa at a crack width of 2.3 mm. From here, the load-carrying capacity decayed gradually and continued until failure at a crack width of around 13 mm. The average residual tensile stress at a crack width of 3 mm was 2.25 MPa. For each of the specimens in this set, the failure crack occurred outside of the shorter LVDT gauge length. Two of the dogbones tested exhibited out-of-plane bending after cracking and were dealt with in the post-cracked analysis as discussed in Section 4.3.2. Also, the north LVDT readings from the second and third test were left out of the pre-cracked analysis, due to erroneous results. The average response of this set is depicted in Figure 4.6.

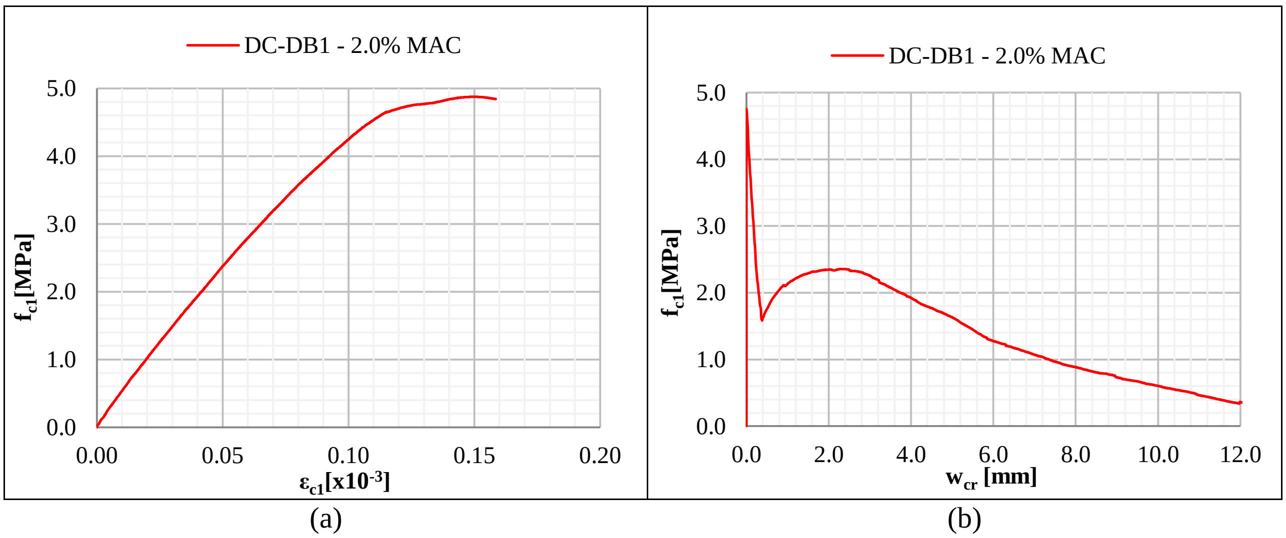

Figure 4.6: Uniaxial tension test result for set DC-DB1: (a) Pre-cracked tensile stress vs. strain (b) Post-cracked tensile stress vs. crack width

Test set DC-DB2 contained 3.0% by volume MAC Matrix fibres. For these, the degradation in the load-carrying capacity after cracking was reduced due to the higher percentage of fibres present in the mix (the average cracking stress was 4.806 MPa with f_{te}= 1.97 MPa at w_{cr} = 0.29 mm). The slope of the post-cracked drop in load matched that of DC-DB1, but fibre engagement occurred at a smaller crack width and higher stress (see Figure 4.12). The maximum residual tensile stress attained was 2.95 MPa at a crack width of 2.1 mm. The average residual tensile stress at a crack width of 3 mm was 2.45 MPa, higher than that of C1F1V3 (2.32 MPa). Also, some localized multiple cracking was observed, as depicted in Figure 4.3. For each of the specimens, the failure crack occurred outside of the shorter LVDT gauge length, and no out-of-plane movements were observed after cracking. All LVDT readings were used in the pre-cracked analysis, except for the north LVDT on specimen one of three. Figure 4.7 shows the pre- and post-cracked curves.

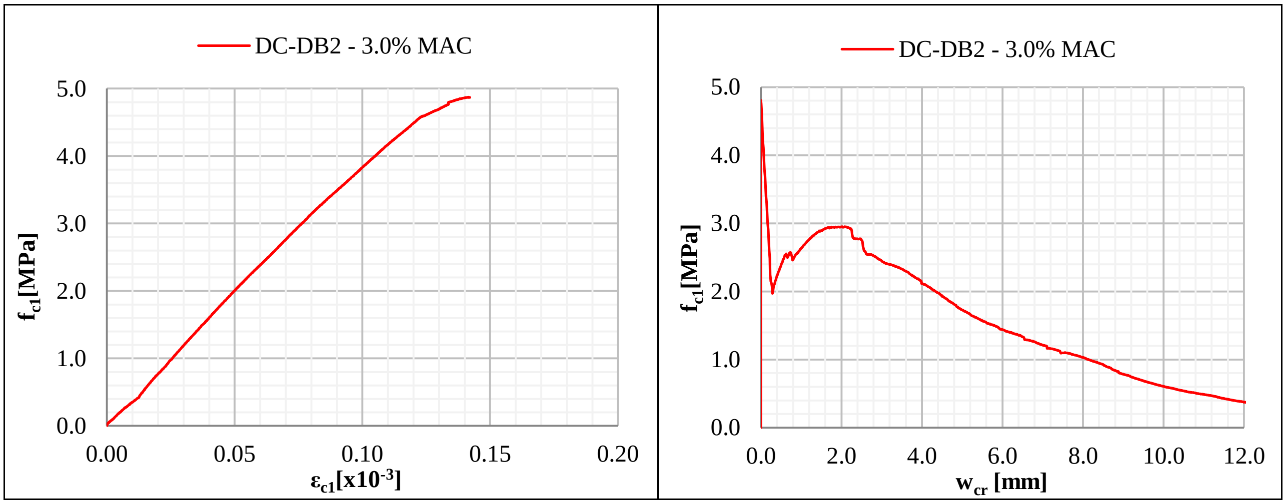

(a) (b)

Figure 4.7: Uniaxial tension test result for set DC-DB2: (a) Pre-cracked tensile stress vs. strain (b) Post-cracked tensile stress vs. crack width

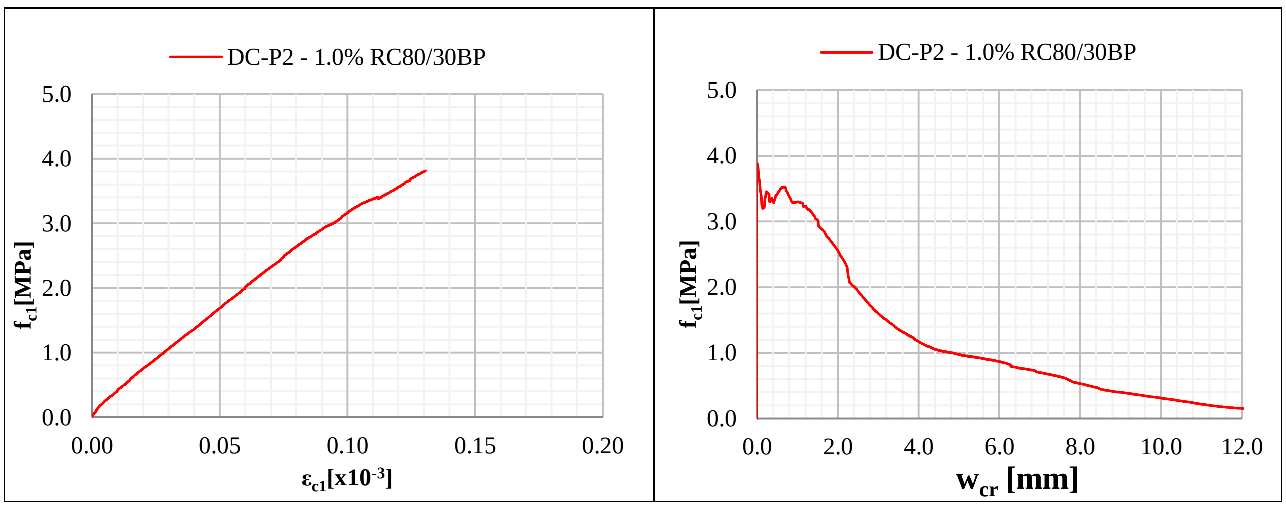

(a) (b)

Figure 4.8: Uniaxial tension test result for set DC-P2: (a) Pre-cracked tensile stress vs. strain (b) Post-cracked tensile stress vs. crack width

Test set DC-P2 was constructed with 1.0% by volume RC80/30BP end-hooked steel fibres. This set of dogbones exhibited the most out-of-plane movements of the dogbones tested. This was dealt with in the post-cracked analysis as discussed in the next section. The first cracking load attained (f_t'=3.90 MPa) was low when compared to the other specimens tested both in this series and in the past ($f_t' = 0.495\sqrt{f_c'}$, as compared to higher cracking stresses for the other test sets shown in Table 4.2). The early cracking was likely due to the propagation of the first crack at the end of the embedded threaded rod. Fibre engagement was seen to occur at a small crack width for these; the average engagement stress was 3.20 MPa occurring at a crack width of 0.14 mm. In general, the end-hooked steel fibres limited the drop in load at cracking. The specimens subsequently reached a maximum residual stress of 3.52 MPa at a crack width of 0.65 mm; this peak is at a smaller crack width than for PPFRC. The load remained consistent up to a crack width of about 1.2 mm, at which point a rapid decline in load was observed. Finally, at 2.3 mm, the load reduction became more stable and gradual. The residual stress at a crack width of 3 mm was 1.60 MPa. For each of these, the failure crack occurred outside the gauge length of the short LVDT, and the north LVDT reading for all three specimens was left out of the pre-cracked analysis. Figure 4.8 contains the average response of these specimens.

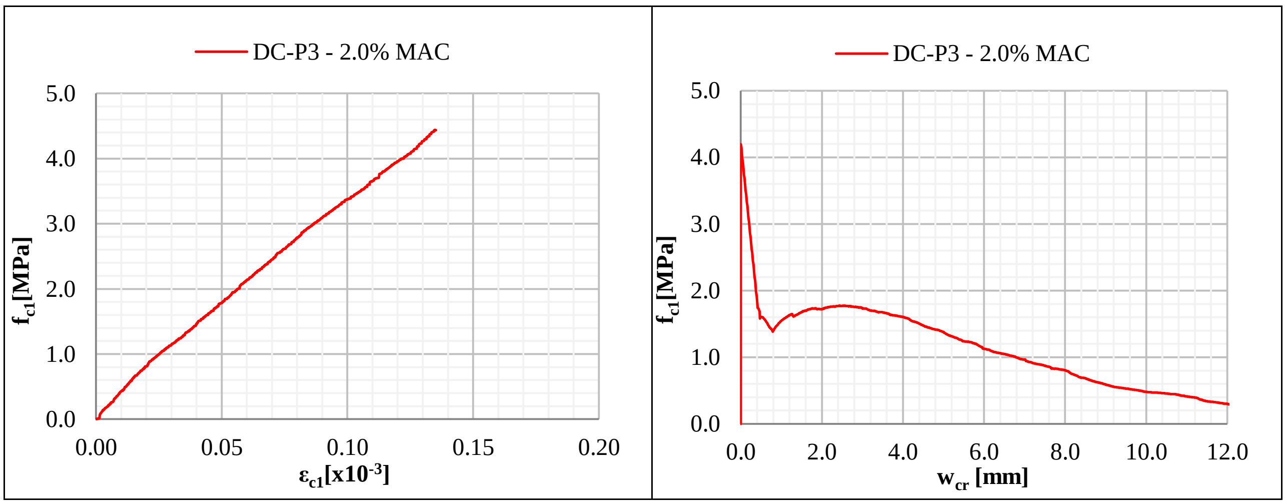

(a) (b)

Figure 4.9: Uniaxial tension test result for set DC-P3: (a) Pre-cracked tensile stress vs. strain (b) Post-cracked tensile stress vs. crack width

Test set DC-P3 contained 2.0% by volume MAC Matrix fibres. These specimens were constructed with a shorter cast-in threaded rod. The first of these specimens exhibited a splitting crack at the top of the dogbone when tested. As a result, the clamping rig depicted in Figure 3.9 (c) was developed and used successfully in subsequent tests for this set, set DC-P4 and set DC-P5. The pre-cracked response for this dogbone was ignored in the analysis due to the splitting crack; however, the post-cracked response was deemed to be unaffected and was used. The average cracking stress was 4.49 MPa with an engagement stress of 1.58 MPa at 0.47 mm. After a slight increase in stress, it subsequently dropped to a minimum of 1.39 MPa at a crack width of 0.79 mm. The maximum residual tensile stress attained was 1.78 MPa at a crack width of 2.51 mm, meaning the residual capacity of this set was the lowest amongst all the PPFRC tests. This may have been due to poor fibre distribution and a poor coating of cement paste on the fibres in the mix; the photographs in Figure 3.7 show that the fibres in this batch were less evenly coated than those in DC-P5. The average residual tensile stress at a crack width of 3 mm was 1.73 MPa. For each of the specimens in this set, the failure crack occurred outside of the shorter LVDT gauge length. All LVDT readings were used in the pre-cracked analysis. Figure 4.9 shows the analysis results on average for these tests.

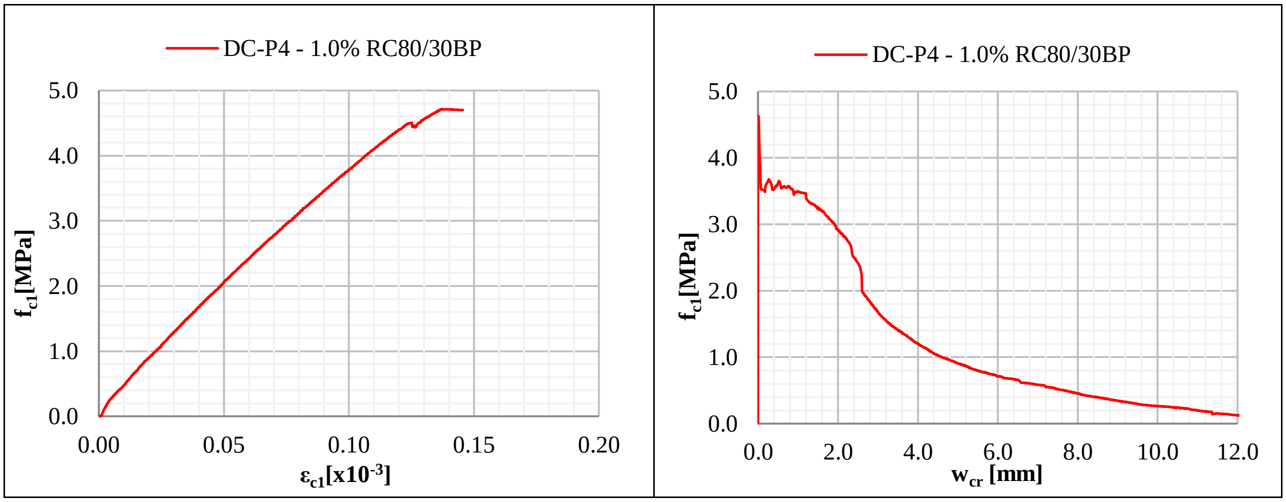

(a) (b)

Figure 4.10: Uniaxial tension test result for set DC-P4: (a) Pre-cracked tensile stress vs. strain (b) Post-cracked tensile stress vs. crack width

Test set DC-P4 was also constructed with 1.0% RC80/30BP end-hooked steel fibres. Interestingly, this set, like DC-P2, exhibited some out-of-plane bending after cracking, yet in general the PPFRC dogbones exhibited little to no uneven tension. Since the bending was towards the formed face, this behaviour was likely a result of having a higher percentage of the fibres at the bottom of the form as cast, due to the downward settlement of steel fibres that typically occurs (Ferrara et al., 2008). This was confirmed when the distribution of fibres crossing the failure plane was observed after the completion of the tests (Figure 4.4). The high stiffness and bond strength of the end-hooked steel fibres would then increase this out-of-plane effect much more than the relatively soft polypropylene fibres. Overall, the behaviour of this set was nearly identical to DC-P2, with slightly better residual stress performance. As can be seen in Figure 4.12, the stress versus crack width relationships were consistent for the two sets. Cracking occurred at a stress of 4.64 MPa, and was followed by a drop to a minimum stress of 3.49 MPa at a crack width of 0.17 mm. The maximum residual stress was 3.68 MPa at a crack width of 0.27 mm. The same sudden drop seen in DC-P2 occurred here as well, with a steadying of the decay at a crack width of 2.6 mm. At 3 mm, the average residual stress was 1.68 MPa. It is worth noting that the post-cracked response for this set was determined from two tests, since one of the three dogbones was tested under a cyclic tension loading regime (discussed separately in Section 4.3.3). For all of these dogbones, the failure crack occurred outside the gauge length of the short LVDT; the north LVDT reading for one of the specimens was omitted from the pre-cracked analysis (as it yielded a secant modulus of more than double the rest of the LVDTs). The average of the monotonic tests is presented in Figure 4.10.

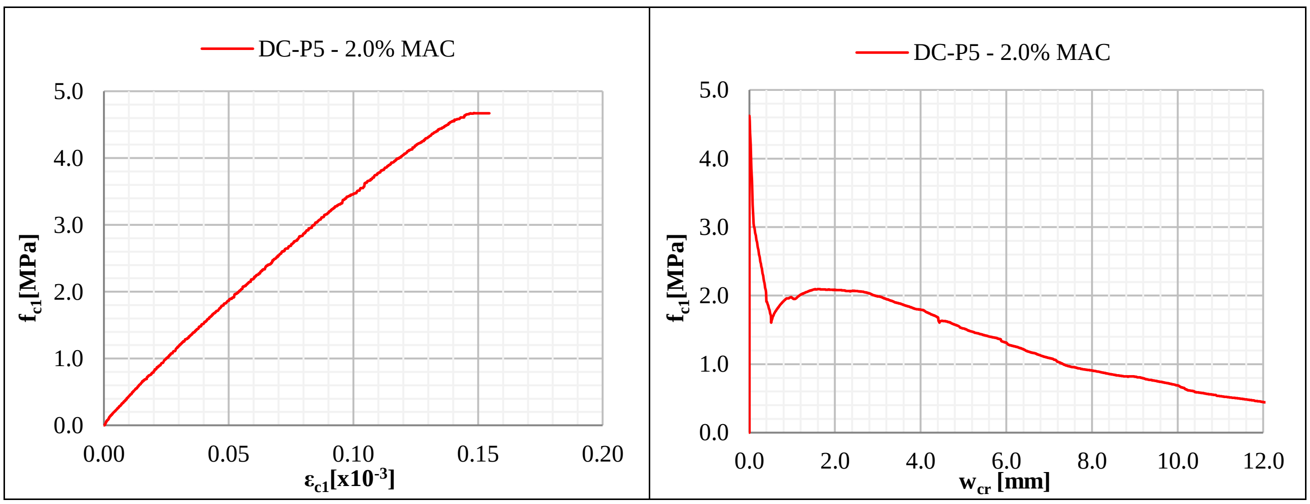

(a) (b)

Figure 4.11: Uniaxial tension test result for set DC-P5: (a) Pre-cracked tensile stress vs. strain (b) Post-cracked tensile stress vs. crack width

Test set DC-P5 contained 2.0% by volume MAC Matrix fibres. The monotonic response was composed of the average of two tests; the third dogbone was tested under a cyclic tension loading regime and is discussed separately. The average cracking stress was 4.63 MPa with an engagement stress of 1.61 MPa at a crack width of 0.51 mm. As with the preliminary dogbone tests, DC-P3 and DC-P5 both followed a similar unloading path until the point of engagement was reached. The maximum residual tensile stress attained was 2.10 MPa at a crack width of 1.59 mm. This crack width at f_{tu} was smaller than DC-P3, yet the DC-P5 response held steady at this residual stress to a crack width of about 2.3 mm. The average residual tensile stress at a crack width of 3 mm was 1.99 MPa, slightly better than DC-P3. For two of the specimens in this set, the failure crack occurred outside of the shorter LVDT gauge length, yet the crack occurred at a favourable location (within the middle third of the dogbone height) for DC-P5 #1. All

LVDT readings were used in the pre-cracked analysis. The monotonic response is presented in Figure 4.11. A comparison of the cyclic tension response of DC-P4 and DC-P5 is presented in Section 4.3.3.

The specimens tested in this research program are compared to test sets C1C, C1F1V1, C1F1V2 and C1F1V3 performed by Susetyo (2009). Table 4.2 (pre-cracked behaviour) and Table 4.3 (post-cracked behaviour) provide a summary of the parameters discussed in this section.

4.3.2 Dogbone Data Analysis

The data analysis was performed independently for the pre- and post-cracked regimes. In the pre-cracked region, the desire was to obtain the tensile stress versus tensile strain ($f_{c1} - \varepsilon_{c1}$) relationship up to the point of cracking. Using this, the typical tensile properties of concrete could be examined and compared. In the post-cracked region, the desire was to determine the residual strength capacity and the ability of the FRC to carry load up to large crack widths.

In the data analysis, the following assumptions were made:

1. The elastic tensile strains were distributed evenly across the height of the zone of interest, ignoring the change in cross-sectional area in the shoulders of the dogbones.
2. Any possible stress concentrations were ignored.
3. In the post-cracked region, it was assumed that the total deformation was equal to the sum of the elastic portion of the deformation at a given stress and the crack width.
4. It followed from number 3 that the uncracked zones of the concrete experienced elastic unloading while the crack opened and the stress dropped.

To accomplish this, first the raw LVDT data for each of the LVDTs were divided by their gauge lengths to obtain a strain value (300 mm for the longer LVDTs on the north and south faces of the specimen, and 150 mm for the shorter LVDTs on the east and west). The LVDT mounts were installed onto the specimens with the help of a fixed length mounting rig to ensure these gauge lengths were accurate. Next, the applied stress was obtained by dividing the testing machine load by the area of the concrete specimen. The area was taken as $A = bt$, where b and t were the width and thickness of the specimen at the location of the failure crack (as measured after completion of the test). Then, the full tensile stress versus strain response before cracking was found by averaging the strain readings obtained from each LVDT. Using the stress and strain values, the secant elastic modulus was determined from:

$$E_{ct,i} = \frac{\left(S_{t2} - S_{t1,i}\right)}{\left(\varepsilon_{t2} - \varepsilon_{t1}\right)} \tag{4.2}$$

where:

$S_{t1,i}$ = stress corresponding to a longitudinal strain of $1.0\text{x}10^{-6}$ for LVDT i [MPa];

S_{t2} = stress corresponding to 50% of the cracking load attained by the specimen [MPa];

ε_{t1} = $1.0\text{x}10^{-6}$;

$\varepsilon_{t2,i}$ = longitudinal strain corresponding to S_{t2} for LVDT i.

This was done separately for each LVDT and then averaged to determine E_{ct}. Also, f_t' was determined as the maximum stress just before a significant drop in load; ε_t' was taken as the average of the strains on each face at f_t'. As mentioned previously, in some cases, the LVDT readings from the north face were excluded.

After cracking, the goal was to convert the LVDT readings to crack widths. Thus, if the crack occurred outside the gauge length of the shorter LVDTs they were left out of this portion of the analysis. For each LVDT individually, the crack width was found from:

$$w_{cr,i} = \Delta_i - \frac{S}{E_{ct,i}} * Length_{LVDT,i} \tag{4.3}$$

where:

$w_{cr,i}$ = crack width from LVDT i [mm];

Δ_i = reading of LVDT i [mm];

S = stress [MPa];

$E_{ct,i}$ = secant modulus of elasticity as calculated using the readings from LVDT i [MPa];

$Length_{LVDT,i}$ = gauge length of LVDT i [mm].

In this way, the elastic portion of the deformation was removed from the overall LVDT reading and, since there was no multiple cracking observed, the rest of the deformation was taken as the crack width. Also, if the result of Equation 4.3 was negative, then the crack width was taken as zero. It was observed from the tests that in all cases the crack formed simultaneously on all faces, but the occasional out-of-plane bending caused some "compressive readings" on the LVDT. This did not mean that the face of the specimen was necessarily in compression, though, as the LVDTs were located on a plane offset from the face of the dogbone. Thus, it was reasonable to take the crack width as zero until Equation 4.3 yielded a positive value. Once the above procedure was completed for each LVDT, the crack width values were averaged to obtain the tensile stress versus crack width relationship.

Lastly, linear interpolation was used to determine the tensile stress at regular intervals of crack width (or tensile strain) for each specimen, so that the average response of the specimens tested in each set could be found. These average responses are used for discussion.

4.3.3 Results of the Data Analysis

The results of the uniaxial tension tests are presented in Table 4.2 (pre-cracked response) and Table 4.3 (post-cracked response). The specimens tested in this work did not exhibit strain hardening behaviour as the fibre volume fraction used was too low to promote such behaviour (Bentur, 2007). This regime was left out of the analysis for all specimens. Of the tests performed by Susetyo (2009), C1F1V3 (1.5% by volume RC80/50BN) was the only specimen to exhibit strain hardening behaviour. In the analysis for this test set, the tensile stress versus tensile strain relationship was presented up until the maximum stress, with the assumption that until this point the deformation was uniformly distributed over the gauge length of the LVDT despite the multiple cracking (Susetyo, 2009). Then, for the post-cracked response, it was assumed that deformations were localized at the main crack. Figure 4.12 and Figure 4.14 present comparisons of the results for the specimens considered in the pre- and post-cracked regimes.

The effects of fibre addition on the properties of the concrete prior to cracking were negligible (Table 4.2). The modulus of elasticity measured for each of the FRC mixes was not significantly different than that of plain concrete. In all cases, the modulus of elasticity was reasonably similar to that suggested in the Canadian Concrete Design Handbook, which states that the secant modulus of elasticity for concrete may be taken as $E_{cs} = 4500\sqrt{f_c'}$ (CAN/CSA Standard A23.3-04, 2004). In addition, the cracking stresses for all concretes were reasonably similar, ranging from $0.5\sqrt{f_c'}$ to $0.63\sqrt{f_c'}$. The cracking strain was similarly unaffected. After cracking, however, the results were different than for plain concrete. The plain concrete exhibited a brittle failure, whereas the FRC specimens exhibited a ductile and gradual reduction in load.

Table 4.2: Dogbone Pre-Cracked Tests Results Summarized

Specimen ID	V_f [%]	Fibre Type	E_{ct} (CV) [MPa]	f_t' (CV) [MPa]	ε_t' (CV) [x 10^-3]	$f_t'/\sqrt{f_c'}$	$E_{ct}/\sqrt{f_c'}$
DC-DB1	2.00	MAC Matrix	39,400 (12.1)	4.77 (7.35)	0.171 (16.4)	0.626	5170
DC-DB2	3.00	MAC Matrix	41,200 (5.26)	4.80 (4.18)	0.140 (15.8)	0.641	5500
DC-P1	-	-	38,600 (9.31)	4.35 (4.52)	0.148 (9.70)	0.514	4560
DC-P2	1.00	RC80/30BP	29,000 (15.2)	3.90 (11.5)	0.184 (26.0)	0.495	3680
DC-P3	2.00	MAC Matrix	35,700 (20.8)	4.49 (4.59)	0.132 (9.02)	0.629	5000
DC-P4	1.00	RC80/30BP	37,900 (9.87)	4.76 (4.33)	0.151 (9.86)	0.595	4740
DC-P5	2.00	MAC Matrix	38,100 (4.79)	4.67 (0.24)	0.147 (2.75)	0.634	5170
C1C	-	-	40,700 (12.3)	4.07 (11.5)	0.101 (12.6)	0.502	5020
C1F1V1	0.50	RC80/50BN	30,900 (1.65)	3.75 (13.1)	0.123 (16.4)	0.529	4160
C1F1V2	1.00	RC80/50BN	27,500 (11.8)	3.46 (16.7)	0.127 (20.4)	0.473	3760
C1F1V3*	1.50	RC80/50BN	32,900 (45.5)	4.34 (7.30)	0.147 (28.4)	0.616	4670

* C1F1V3 exhibited strain hardening, reaching $f_{t,max}$ = 4.36MPa (CV of 8.5%) at $\varepsilon_{t,max}$= 1.670x10^{-3} (CV of 67.6%)

Table 4.3: Dogbone Post-Cracked Tests Results Summarized

Specimen ID	V_f [%]	Fibre Type	f_{te} [MPa]	w_{cr} at f_{te} [mm]	f_{tu} [MPa]	w_{cr} at f_{tu} [mm]	f_{c1} at w_{cr} of 3mm [MPa]
DC-DB1	2.00	MAC Matrix	1.58	0.38	2.36	2.33	2.25
DC-DB2	3.00	MAC Matrix	1.97	0.29	2.95	2.08	2.45
DC-P2	1.00	RC80/30BP	3.20	0.14	3.52	0.65	1.60
DC-P3	2.00	MAC Matrix	1.58	0.47	1.78	2.51	1.73
DC-P4	1.00	RC80/30BP	3.49	0.17	3.68	0.27	1.68
DC-P5	2.00	MAC Matrix	1.61	0.51	2.10	1.59	1.99
C1F1V1	0.50	RC80/50BN	1.67	0.16	1.69	0.19	0.60
C1F1V2	1.00	RC80/50BN	2.70	0.17	2.87	0.26	1.79
C1F1V3	1.50	RC80/50BN	3.85	0.17	3.93	0.29	2.32

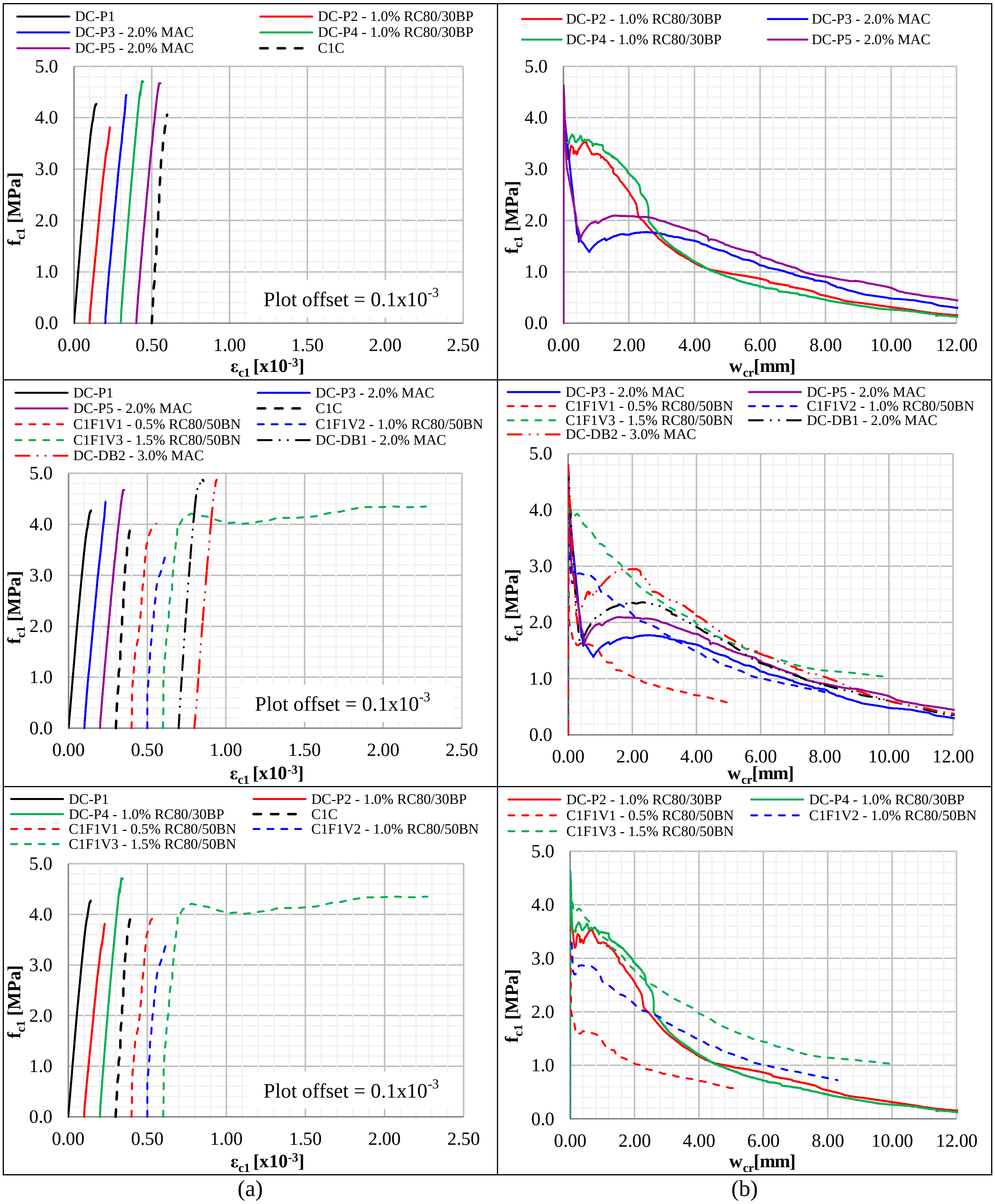

Figure 4.12: Influence of fibre type on uniaxial tension test results: (a) Pre-cracked tensile stress vs. strain (b) Post-cracked tensile stress vs. crack width

4.3.3.1 Influence of Fibre Type

A graphical comparison of the influence of the fibre type is presented in Figure 4.12. Three sets of graphs are presented, with each set comprised of pre- and post-cracked responses. The first set shows the main batches tested in this work plus the plain concrete set (C1C) tested by Susetyo (2009). The middle set of graphs depicts a comparison of concretes constructed with 50 mm long fibres for the two material types investigated (steel and macro-synthetic). The volume ratio of SFRC was 0.5%, 1.0% and 1.5%; the ratio of PPFRC was 2.0% and 3.0%. Finally, the last set of curves depicts a comparison of all SFRC dogbones.

All duplicate test sets (i.e. sets with the same volume fraction and fibre type) yielded a relatively consistent response. Also, it can be seen that increasing the volume content of fibres improved the post-crack response in general. For the SFRC dogbones, the shorter steel fibres were more effective than the longer steel fibres at a volume fraction of 1.0%. This is consistent with past findings and is attributable to the fact that there is a larger number of individual fibres in the mix for shorter steel fibres, at a given volume fraction. This has been shown to be a governing factor influencing the load-carrying capacity of SFRC (Susetyo, 2009). At a significantly large crack width, though, the SFRC with shorter fibres began to rapidly lose load-carrying capacity and the residual stress dropped below that of the longer steel fibres. This is also consistent with findings reported in the literature, since the shorter fibres will completely pull-out at a smaller crack width, dependent on the embedded length (Lee et al., 2011a; Filiatraut et al., 1994). Also, the crack width at engagement for the steel fibres was consistent regardless of the fibre length (Table 4.3), suggesting that engagement was instead dependent on bond properties and fibre stiffness. The magnitude of the drop in load to the point of engagement was inversely proportional to the fibre volume content.

The response was different for the PPFRC specimens. The drop after cracking was larger than SFRC regardless of the volume fraction. Also, a large crack width was required before the macro-synthetic fibres began to engage (Buratti et al., 2011). However, despite this initial drop, the PPFRC response regained some strength. In some cases, the maximum residual tensile stress was as much as 150% of the stress at engagement. This maximum residual tensile stress occurred at a much greater crack width than with the SFRC specimens (Table 4.3). This was true for all volume ratios, with the only difference being the 3.0% by volume PPFRC dogbones strengthened sooner. Above a crack width of 1.0 mm, DC-DB2 exhibited a greater residual load-carrying capacity than the 1.0% by volume SFRC dogbones (C1F1V2). Beyond a crack width of 2.4 mm to 2.8 mm, the steel fibres began to lose bond strength due to the straightening of the end-hook; the macro-synthetic fibres performed more favourably at this level of cracking. DC-DB2 (3.0% MAC) was reasonably similar to C1F1V3 (1.5% RC80/50BN) at a crack width of 1.8 mm and above, whereas the sets with 2.0% macro-synthetic fibres were similar to C1F1V2 (1.0% RC80/50BN) from approximately 2.1 mm and above. However, in service, such crack widths are not desirable so within practical regions it would appear that macro-synthetic fibres are in need of some improvement.

The engagement properties of the macro-synthetic fibres were affected by the flexibility of the fibres. At first cracking, some fibres were likely oriented in non-orthogonal directions to the crack. These fibres had to become bent around the matrix entrance points at both sides of the crack and become aligned with the direction of load before becoming effective. This is typical of flexible fibres (Leung and Ybanez, 1997). Since these fibres have some finite stiffness, this does not happen instantly and some crack opening is required to allow this alignment to occur. This explains the need for a relatively large crack opening before fibre engagement in relation to SFRC. In addition, this process requires more energy than the engagement process of SFRC, increasing the amount of work done by macro-synthetic fibres during the initial crack opening. This energy softens the slope of the descending portion of the stress versus crack width curve immediately after cracking. Therefore, at small crack widths, only fibres aligned perfectly perpendicular to the crack can be expected to transmit significant tensile stresses across the crack. Instead, the effect of the macro-synthetic fibres at low crack widths was on the energy required to create the crack opening. At larger crack widths these unaligned fibres became straightened so as to line up orthogonally to the crack and, thus, became more effective (Figure 4.13). In a few isolated cases, macro-synthetic fibre rupture was observed. The behaviour observed for SFRC was a result of the improved bond strength provided by the end-hooks (Lee et al., 2011a). Thus, some form of increased mechanical anchorage beyond the surface indentations would allow the macro-synthetic fibres to develop substantial tensile stresses at smaller crack widths. However, this increase in bond strength may lead to fibre rupture or pull-out at a smaller crack width, reducing ductility. Increased fibre strength could counteract the fibre rupture (Susetyo, 2009).

Figure 4.13: Alignment of macro-synthetic fibres

4.3.3.2 Influence of Loading Protocol

Comparisons for the two dogbones that were tested under a cyclic tension loading protocol are presented in this section. These specimens were brought to the cracking load as would be done for any other dogbone. After the first crack, the loading rate was increased to 0.002 mm/s and the loading continued to a machine displacement of 1 mm. Here, the first cycle was performed by reversing the direction of machine displacement until the load was fully released. Then the displacement was increased to 1 mm at a loading rate of 0.01 mm/s. Then, the loading rate was set back to 0.002 mm/s and the test carried on. Further cycles (following the same procedure) were taken at 2 mm, 4 mm, 6 mm, etc. until the load dropped below 2 kN. The data analysis procedure was identical as for all other dogbones. Figure 4.14 presents these results, again in three sets; set one contains the SFRC comparison (cyclic and monotonic), set two contains the PPFRC comparison (cyclic and monotonic), and set three compares the response of each cyclic dogbone.

The responses of the PPFRC and SFRC cyclic dogbones exhibited similar engagement characteristics to those of the monotonic specimens. The SFRC cyclic dogbone, however, underwent a significant reduction in load-carrying capacity when compared to the monotonic specimens. The cycles taken at 2 mm and 4 mm specifically show the inability of the dogbone to return to the load carried before the cycle was taken. Also, the loading and reloading branches followed a similar slope, with little or no hysteretic loops. This is attributed to the breakdown of fibre crack-bridging as a result of the repetitive stretching and buckling of the fibres (Filiatraut et al., 1994).

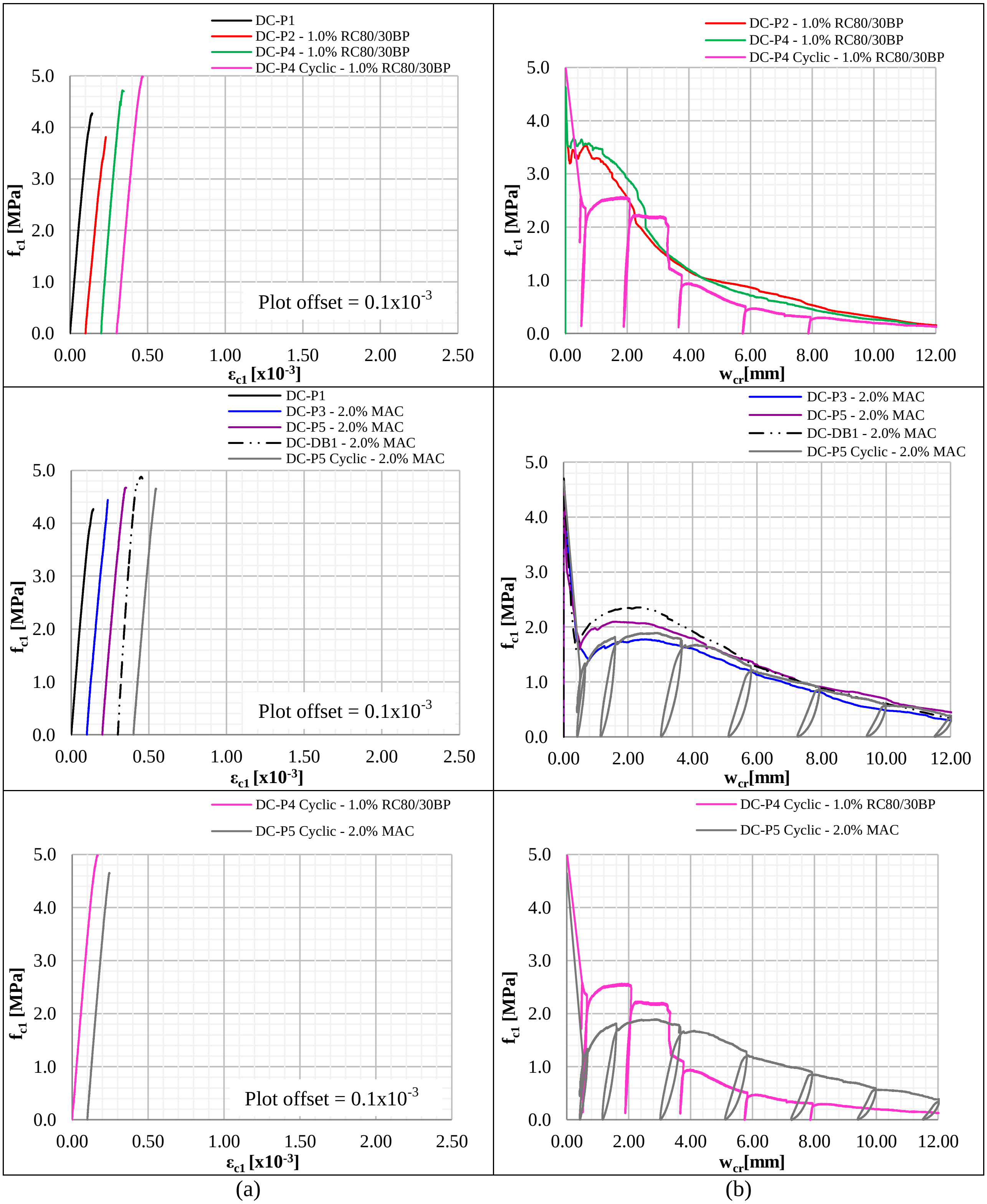

Figure 4.14: Influence of loading protocol on uniaxial tension test results: (a) Pre-cracked tensile stress vs. strain (b) Post-cracked tensile stress vs. crack width

The PPFRC cyclic dogbone exhibited a different response. There was little to no difference in residual load-carrying capacity when compared against the monotonically loaded dogbones. In addition, the unloading and reloading branches exhibited a ductile hysteretic behaviour allowing for improved energy dissipation. Upon reloading, the specimen achieved a load reasonably similar to what the specimen had experienced before the cycle. Thus, under cyclic loads, the PPFRC specimen showed more ductility and less degradation of the load-carrying capacity when compared to SFRC. This was further displayed by the response of the shear panels (see Section 4.5.3.3).

4.4 Modulus of Rupture Tests

In this section, the results of the modulus of rupture (MOR) tests performed in accordance with ASTM C1609/C1609M (2010) are discussed. For each main batch, two specimens were constructed and tested. These were tested at various ages from 48 to 99 days, based on the availability of laboratory machinery. Full test data are presented in Appendix A.3, with average results and discussion in this section.

4.4.1 Test Observations

In general, a high degree of variability was exhibited by the specimens tested. The location of the crack had a large effect on the cracking load and the post-cracked peak load. The closer the crack was to the mid-span of the specimen, the higher the cracking and peak loads in the four-point bending condition. Representative crack patterns for the specimens tested are presented in Figure 4.15.

As expected, the plain concrete test set DC-P1 exhibited brittle behaviour, failing immediately after the prism cracked. As with the dogbones, the addition of fibres to the mix controlled the abrupt opening of the failure crack. In all cases, the FRC specimens exhibited an ability to carry residual flexural loads after first cracking and the load-carrying capacity decreased steadily and gradually as the crack continued to open. The load-deflection curves for the test sets are presented in Figure 4.16.

For the SFRC batches tested (DC-P2 and DC-P4 at 1.0% by volume RC80/30BP), strain hardening in flexure was observed. A slight drop in load after cracking was accompanied by a slight change in stiffness as the load continued to increase. Multiple cracks or crack extensions formed until the peak load was reached. From this point it was observed that further deformations were localized at one of the cracks and the load-carrying capacity began to drop in a rapid yet controlled fashion. Unfortunately, after testing both modulus of rupture prisms from set DC-P2 it was discovered that the midspan LVDTs were mistakenly not switched to collect data. As a result, post-cracked parameters and response were not available for this set.

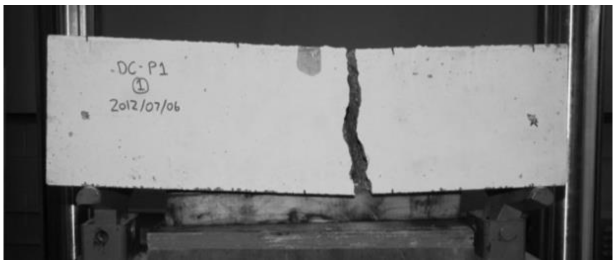

DC-P1
Plain

DC-P2
1.0% SFRC

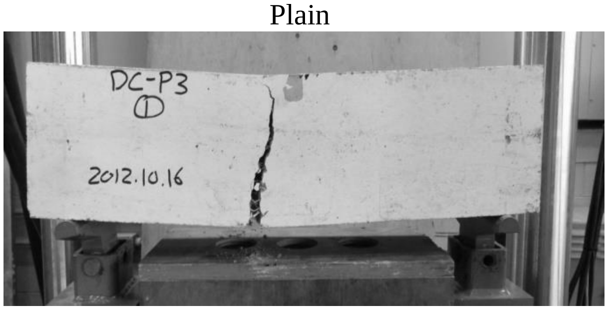

DC-P3
2.0% PPFRC

DC-P4
1.0% SFRC

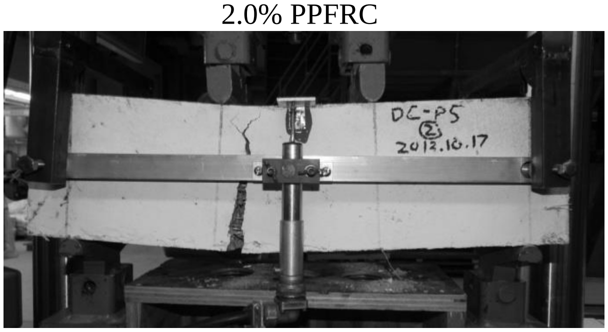

DC-P5
2.0% PPFRC (No strain hardening)

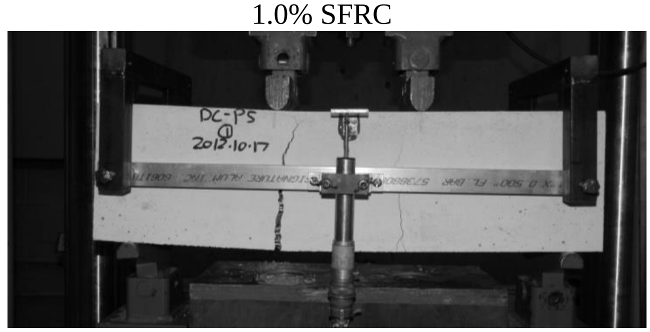

DC-P5
2.0% PPFRC (Strain hardening)

Figure 4.15: Representative modulus of rupture test crack patterns

For the macro-synthetic FRC test sets (DC-P3 and DC-P5 at 2.0% by volume MAC Matrix fibres), most of the specimens exhibited a sudden drop in load at the onset of cracking similar to that of the PPFRC dogbones. This drop continued to the point at which the fibres became sufficiently engaged. From here the response softened, yet load increased until the post-cracked peak was attained. After reaching this secondary peak, the load-carrying capacity dropped gradually as the crack mouth continued to open. One of these specimens (DC-P5 #1) exhibited strain hardening behaviour. After the first crack opened, a relatively small 12% drop in load was observed. Then, the specimen began to take on more load (at a reduced stiffness) reaching a peak greater than the first cracking load. A second crack opened followed by a larger 48% drop in load. Thus, while some strain hardening in flexure is possible with these fibres, the need to open a relatively large crack prior to fibre engagement was still observed.

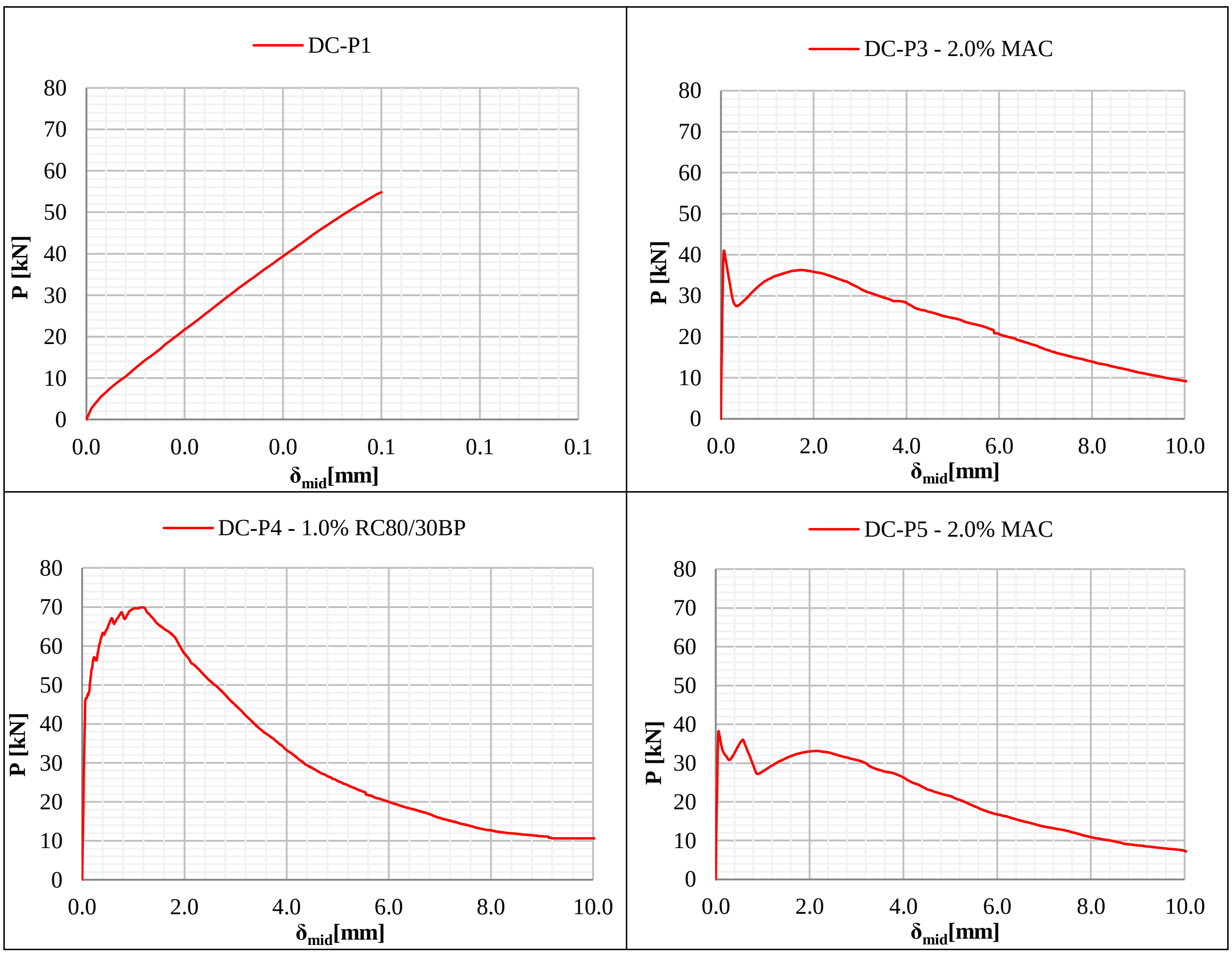

Figure 4.16: Load vs. deflection responses for MOR tests

This observed behaviour is consistent with the findings of ASTM C1018 (1997) tests performed in the past. C1F1V1 and C1F1V2 (0.5% and 1.0% by volume of RC80/50BN fibres) did not exhibit strain hardening behaviour, yet a gradual release of load occurred as the crack width opened. C1F1V3, at 1.5% by volume of RC80/50BN fibres, exhibited strain hardening behaviour, followed by a rapid drop in load-carrying capacity, much like DC-P4 (Susetyo, 2009). These specimens will be included in the graphs and tables of this section for comparison.

4.4.2 Data Analysis

Data analysis was performed in accordance with the requirements of ASTM C1609/C1609M (2010). Mid-span displacement data were obtained by taking an average of the readings recorded by the two LVDTs (see Figure 3.13 (b)). Load data were taken directly from the MTS machine readings. The following procedure was used to determine the values presented in Table 4.4:

1. From the first peak (or cracking) load in kN, P_1, the first peak stress in MPa, f_1, was determined from:

$$f_1 = \frac{P_1 L}{bd^2} \tag{4.4}$$

   where:

   L = span length of the specimen [mm] (457 mm for all cases);

   b = average width of the specimen adjacent to the fracture as measured [mm];

   d = average depth of the specimen adjacent to the fracture as measured [mm].

2. Equation 4.4 was used to find the peak stress in MPa, f_p, corresponding to the peak load in kN, P_p. In this formula, it is assumed that the neutral axis is located at the mid-depth of the specimen. After cracking, it was clear that the neutral axis was not located at the mid-depth, yet this formula was still used in accordance with the governing test standard.
3. The residual load values, $P_{600}^D$and P_{150}^D in kN, corresponding to net deflection values of $L/600$ and $L/150$ were found from the response.
4. Again, using Equation 4.4, the residual strength values in MPa, f_{600}^D and f_{150}^D, were determined.
5. Next, the toughness of the specimen up to a deflection of $L/150$ in Joules, T_{150}^D, was found by taking the area under the load-deflection curve from $\delta = 0$ to $\delta = L/150$. This was accomplished using the trapezoidal rule:

$$T_{150}^D = \sum_{i=1}^{n} \frac{1}{2}(\delta_{i+1} - \delta_i)(P_{i+1} + P_i) \tag{4.5}$$

   where:

δ = midspan displacement [mm].

6. Finally, the equivalent flexural strength ratio, $R_{T,150}^{D}$, was found from:

$$R_{T,150}^{D} = \frac{150 \cdot T_{150}^{D}}{f_1 b d^2} \cdot 100\% \tag{4.6}$$

Even though C1F1V1, C1F1V2 and C1F1V3 were tested in accordance with ASTM C1018 (1997), digitizer software (WinDIG 2.5 (Lovy, 1996)) was used to extract the average MOR test data from the curves provided in the thesis written by Susetyo (2009). The above calculation procedure was performed, allowing for a comparison of toughness and residual strength values.

Table 4.4: Modulus of Rupture Test Results

Specimen ID	V_f [%]	Fibre Type	f_1 (CV) [MPa]	f_p (CV) [MPa]	f_{600}^{D} (CV) [MPa]	f_{150}^{D} (CV) [MPa]	T_{150}^{D} (CV) [J]	$R_{T,150}^{D}$ (CV) [%]	$f_1 / \sqrt{f'_c}$
DC-P1	-	-	7.22 (4.91)	7.22 (4.91)	-	-	-	-	0.850
DC-P2	1.00	RC80/30BP	6.78 (13.0)	7.40 (0.96)	-	-	-	-	0.860
DC-P3	2.00	MAC Matrix	5.31 (13.9)	5.31 (13.9)	4.05 (10.5)	4.01 (15.9)	102.4 (14.5)	80.6 (0.00)	0.747
DC-P4	1.00	RC80/30BP	6.77 (11.5)	8.95 (7.11)	8.71 (5.69)	5.61 (14.5)	179.3 (9.85)	110.5 (3.20)	0.844
DC-P5	2.00	MAC Matrix	4.88 (7.98)	5.45*	3.41 (20.8)	3.89 (10.0)	96.3 (5.89)	81.9 (0.00)	0.662
C1C	-	-	3.83 (10.1)	3.83 (10.1)	-	-	-	-	0.473
C1F1V1	0.50	RC80/50BN	7.70 (13.4)	7.70 (13.4)	4.54	2.65	92.2	51.8	1.074
C1F1V2	1.00	RC80/50BN	6.23 (9.70)	6.23 (9.70)	5.06	3.43	103.0	74.2	0.853
C1F1V3	1.50	RC80/50BN	9.26 (21.2)	10.29 (25.7)	10.08	6.55	278.2	160.7	1.314

* From DC-P5 #1, which exhibited strain hardening behaviour

4.4.3 Results of the Data Analysis

The results of the MOR tests are summarized in Table 4.4, and the load versus deflection responses are depicted in Figure 4.17. This figure presents three sets of graphs to be used to compare the load-deflection curve for the different fibre types. The first set shows the non-normalized and normalized responses of the prisms tested in this series; the second set shows a comparison of the C1F1 series (0.5%, 1.0% and 1.5% by volume RC 80/50BN fibres) with DC-

P3 and DC-P5 (2.0% by volume MAC Matrix fibres); the third set shows the responses of all the SFRC specimens.

The comparisons that can be made in flexural tension are similar to those for direct tension as discussed in Section 4.3. The short steel fibres were more effective in residual load-carrying capacity, due to that fact that more individual fibres were present to transmit load across the crack (Susetyo, 2009). From the normalized response, it was clear that concretes with as little as 1.0% by volume of the short fibres experienced elevated amounts of strain hardening, and attained the greatest peak load (relative to cracking strength) at all mid-span displacements.

However, the toughness values for the specimens containing 1.5% by volume steel fibres showed that the energy absorption of the SFRC with longer steel fibres was better (278.2 J compared to 179.3 J for DC-P4). As before, the short steel fibres were the most effective in residual load-carrying capacity, yet the longer fibres exhibited more ductility.

From the PPFRC responses, it was clear that at low crack widths, the macro-synthetic fibres did not become sufficiently engaged. This is attributed to the low stiffness of the fibres (meaning fibres oriented not roughly perpendicular to the crack had little effect until they became significantly aligned (Leung and Ybanez, 1997)). However, as with the dogbones, at a high mid-span displacement these fibres proved to be effective in sustaining a gradual release of load. At a midspan displacement of over 4 mm, specimens containing PPFRC showed the greatest residual flexural load-carrying capacity. More specifically, the normalized residual load-carrying capacity of DC-P5 surpassed that of C1F1V2 (1.0% by volume RC80/50BN end-hooked steel fibres) at a midspan displacement of 1.25 mm; it surpassed that of C1F1V3 (1.5% by volume RC80/50BN end-hooked steel fibres) at 1.95 mm. In addition, the values of toughness and equivalent flexural strength ratio were similar to those of C1F1V2. These were 99.4 J and 81.3% respectively, compared against 103 J and 74.2% for C1F1V2. Thus, it was evident that the macro-synthetic fibres, despite a more sudden drop in load immediately after cracking, provided significant improvements in residual load-carrying capacity, toughness and ductility over plain concrete. This improvement was similar to that of 1.0% by volume of end-hooked steel fibres with the same length; consistent with the experimental findings of Richardson et al. (2010).

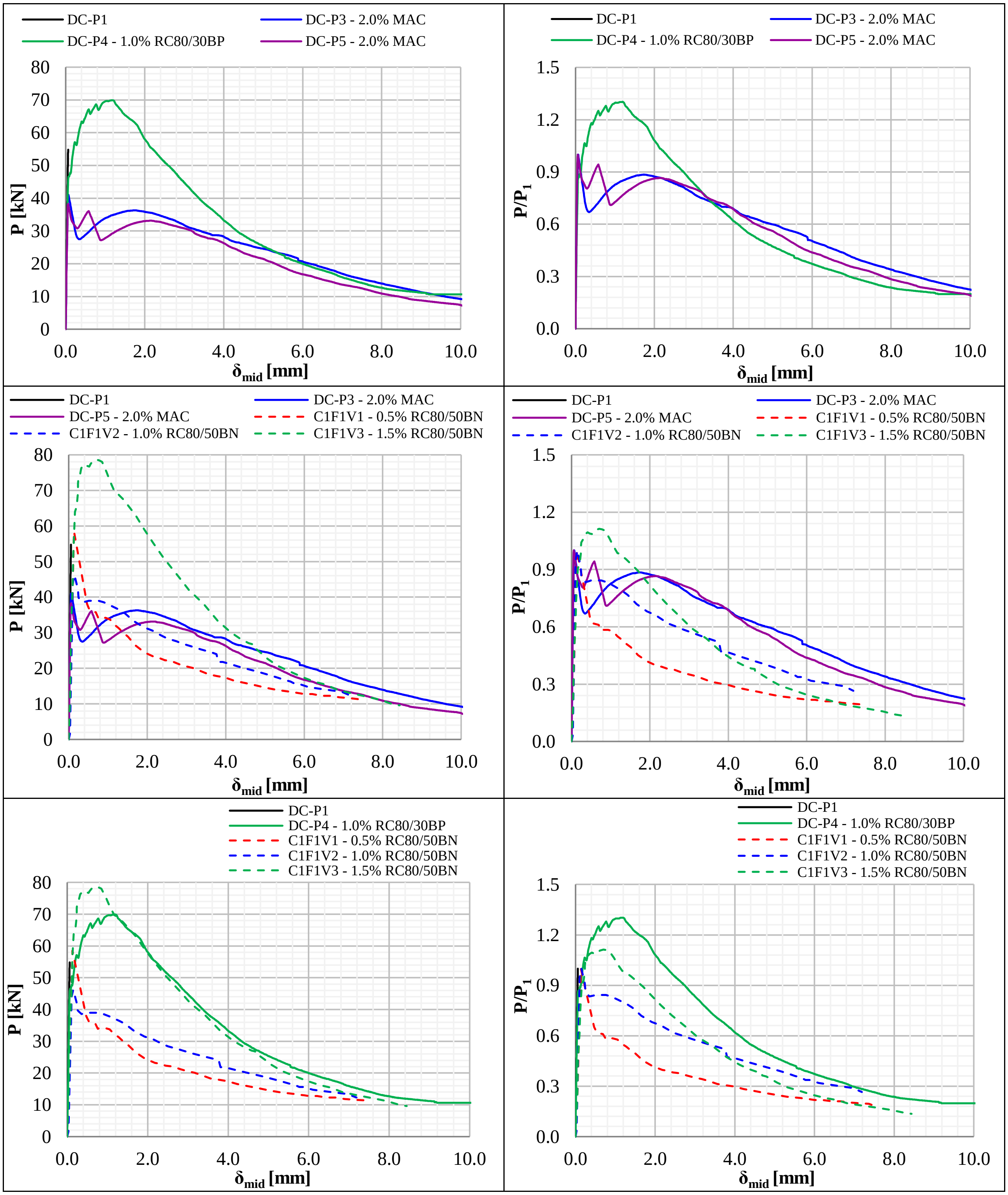

(a) (b)

Figure 4.17: Influence of fibre type on load vs. deflection curve for modulus of rupture tests: (a) Non-normalized (b) Normalized

4.5 Panel Tests

In this section, the results of the five shear panel experiments are discussed. Comparisons are made with the results obtained from four panels tested by Susetyo (2009). For each concrete batch, one panel was constructed and tested. The specimens were tested at various ages, as summarized in Table 4.5. For specimens tested at an age significantly older than 28 days, additional panel test day compressive cylinder tests were performed; these data are also presented in Table 4.5. Section 4.5.1 provides an account of observations made during the course of the experiments. Section 4.5.2 outlines the data analysis procedure employed and verification of the data from the two acquisition systems used. Finally, in Section 4.5.3, response comparisons are made. Full panel test data are presented in Appendix B; a summary of the results for each test are presented in this chapter. Table 4.6 provides a brief overview of pertinent test results.

Table 4.5: Panel Test Age and Strength

Specimen ID	V_f [%]	Fibre Type	Age at Testing [Days]	Test Day Cylinder Results		
				E_{cs} (CV) [MPa]	$f_{c,Test}$ (CV) [MPa]	$\varepsilon_{c,Test}$ (CV) [x 10^{-3}]
DC-P1	-	-	28-31	40,200*(1.65)	71.7*(0.55)	2.555*(1.06)
DC-P2	1.00	RC80/30BP	30	36,000*(3.35)	62.1*(1.46)	3.169*(5.66)
DC-P3	2.00	MAC Matrix	35	32,100 (1.87)	54.2 (3.97)	2.848 (9.68)
DC-P4	1.00	RC80/30BP	42-48	34,700 (12.9)	66.0 (1.27)	3.386 (10.2)
DC-P5	2.00	MAC Matrix	40-41	33,400 (1.47)	55.5 (5.47)	2.698 (18.9)

* From 28-day cylinder compressive tests

Table 4.6: Panel Test Results Summarized

Specimen ID	v_{cr} [MPa]	γ_{cr} [x10^{-3}]	v_u [MPa]	γ_u [x10^{-3}]	w_m [mm]	s_m [mm]	Failure Mode
DC-P1	1.43	0.116	5.79*	7.98	0.57	55.6	y-reinf. rupture
DC-P2	2.60	0.136	5.97	5.94	0.21	43.0	interlock failure
DC-P3	2.20	0.153	3.87	7.96	0.57	72.0	interlock failure
DC-P4	2.60	0.136	4.47*	2.87	0.22	71.0	interlock failure
DC-P5	2.23	0.104	3.43*	5.15	0.59	59.0	interlock failure
C1C	2.01	0.086	5.77	6.01	0.55	57.2	y-reinf. yielding
C1F1V1	2.09	0.197	3.53	2.77	0.55	114.4	interlock failure
C1F1V2	2.65	0.139	5.17	5.27	0.45	54.7	interlock failure
C1F1V3	1.83	0.055	5.37	5.10	0.45	57.2	interlock failure

* Maximum stress attained during the course of the test (failure at subsequent cycles may have occurred at a lower stress but higher strain)

A goal of this research program was to examine the suitability of macro-synthetic fibres at replacing low levels of conventional transverse shear reinforcement and to draw comparisons with end-hooked steel fibres. In addition, a pilot investigation into the effects of reversed cyclic loading conditions on the shear response of SFRC and PPFRC was performed. Thus, two of the panels (DC-P2 and DC-P3) were tested under a monotonic shear condition, and three of the panels (DC-P1, DC-P4 and DC-P5) were tested under a reversed cyclic shear condition. These five, along with panel C1C (plain concrete monotonic), form the basis for comparison of the cyclic degradation exhibited by reinforced concrete with light reinforcement in the transverse direction (C1C and DC-P1), steel fibre reinforced concrete (DC-P2 and DC-P4) and macro-synthetic fibre reinforced concrete (DC-P3 and DC-P5).

A pure shear load condition was used, comprised of tangential forces acting along each of the edges of the specimen with no normal component. This condition is depicted in Figure 4.18 (a). Also, the application of positive pure shear using the Panel Tester in is shown in Figure 4.18 (b).

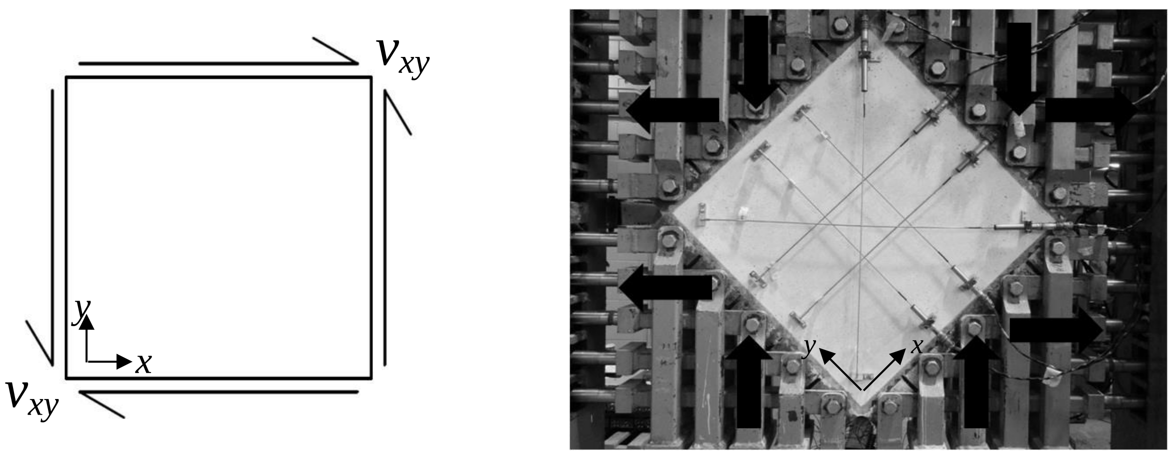

(a) (b)

Figure 4.18: Definition of positive pure shear loading condition

4.5.1 Panel Test Observations

4.5.1.1 Panel DC-P1

This specimen was constructed with plain reinforced concrete and acted as a control panel for specimens subjected to reversed cyclic loading. It was constructed to match the monotonic counterpart (C1C) tested by Susetyo (2009). It had a longitudinal reinforcement ratio, ρ_x, of

3.31% and a transverse reinforcement ratio, ρ_y, of 0.42%. From the material tests, it was found that the panel had a 28-day compressive strength of 71.7 MPa and a tensile strength of 4.35 MPa.

This panel was the first of those tested in the reversed cyclic condition and, thus, was also used as a learning experience. An initial trial cycle was taken to a maximum shear stress of 0.5 MPa to ensure that the instrumentation was recording correctly and that the hydraulic pressures were applied to the panel in the correct ratios. The test began on the following day. Two cycles were taken at each loading level. A load stage was taken after the target stress for the cycle was reached; after reaching this peak, 10% of the load was removed for safety purposes. Crack measurements were performed at the positive and negative target stresses for the second of the two cycles and at other pertinent points in time. A schematic of the loading protocol used in this test is presented in Figure 4.19.

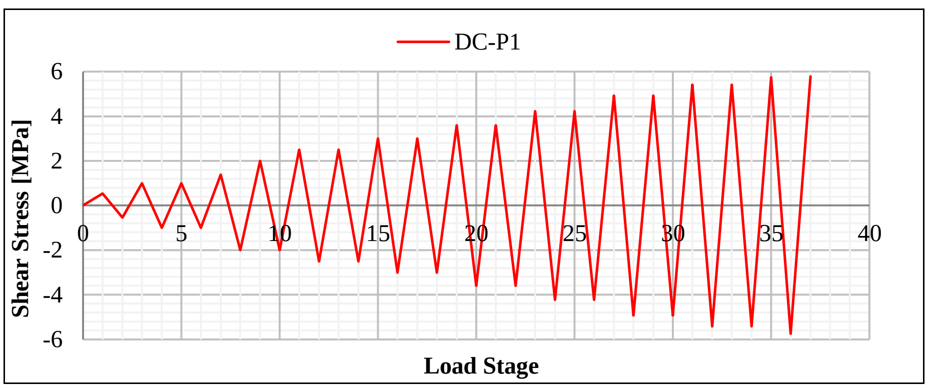

Figure 4.19: Loading protocol for DC-P1

At early stages, the goal was to increase the target stress of the double cycles in shear stress increments of 1.0 MPa. After significant softening, the target stress for these double cycles was the stress at which the shear strain had increased by 0.5x10^{-3} over the maximum shear strain previously attained. For a load-controlled test, this was somewhat difficult to accurately perform and, towards the end of the test, a significant increase in shear strain was observed when returning to the same target stress on subsequent cycles. However, the loading protocol was successful and was consistent throughout the experimental program.

For DC-P1, some problems were encountered at low load levels. A first cracking load was observed in the positive direction at a stress, v_{cr}, of 1.43 MPa and a strain, γ_{cr}, of 0.166x10^{-3}. This was premature, so the half cycle was terminated and loading proceeded in the negative direction. Here, the target stress of 2.0 MPa was attained without any cracking, as expected. Additionally, this first crack was only visible on the front face of the panel. As a result, an extra two cycles at a load level of 2.5 MPa were added to further investigate this situation. After the first full cycle at 2.5 MPa, it was decided to shorten the out-of-plane tension links provided around the back of the panel (see Figure 3.15 (b)) to try and improve this out-of-plane condition. When loading to 2.5 MPa on the second cycle, cracking was observed on both faces. The tightening of the tension links was used in all subsequent tests. This vastly improved out-of-plane issues; however, some were still observed in other tests as discussed in Section 4.5.2.2. Then, after resuming the normal loading protocol, one further stress-governed double cycle was taken at 3.0 MPa, followed by strain-governed double cycles at 3.59, 4.23, 4.93, 5.42 and 5.74 MPa of target shear stress. As the test progressed beyond the cracking point, no out-of-plane movements were observed. Transverse direction reinforcement yielding was observed on the 13th cycle during the excursion to a target positive shear stress of 4.93 MPa. Finally, the specimen failed at an applied shear stress, v_u, of 5.79 MPa and a shear strain, γ_u, of 7.98x10^{-3}. The full shear stress versus shear strain response is shown in Figure 4.20.

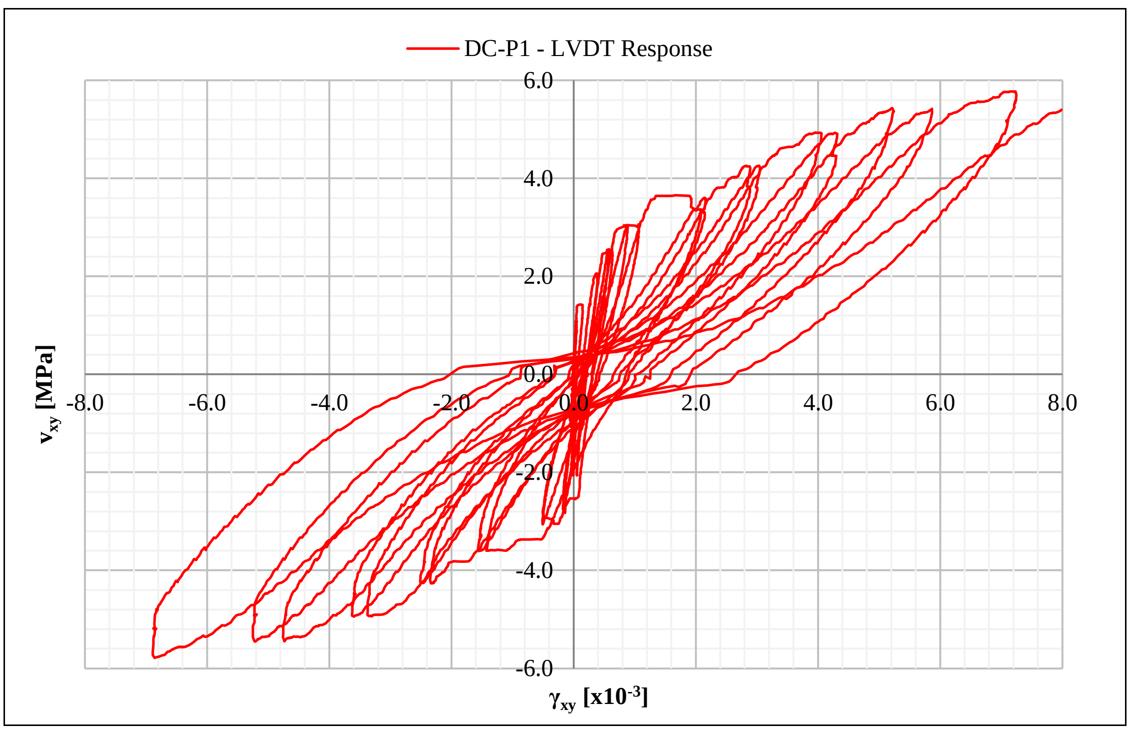

Figure 4.20: DC-P1 shear stress vs. shear strain response

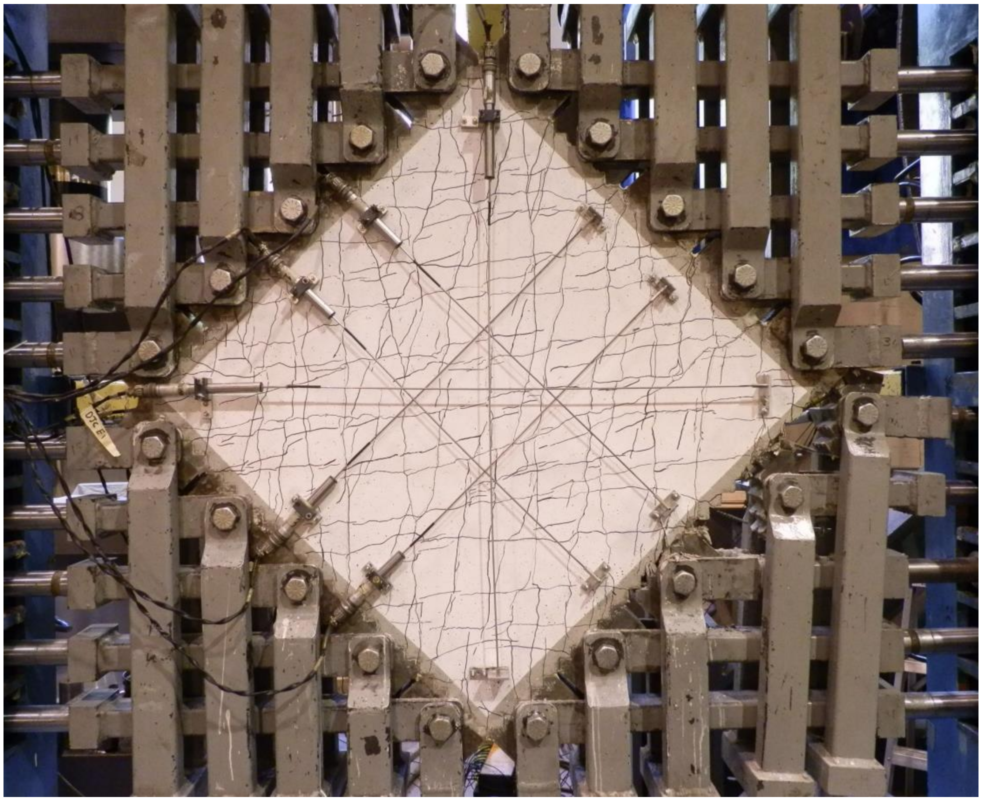

Figure 4.21: DC-P1 failure crack pattern

4.5.1.2 Panel DC-P2

Panel DC-P2 was constructed with normal strength steel fibre reinforced concrete, using 1.0% by volume end-hooked RC80/30BP Dramix® fibres with l_f = 30 mm, d_f = 0.38 mm a f_{uf} = 2300 MPa and E_f = 200,000 MPa. The longitudinal reinforcement ratio for this and all other FRC panels was also 3.31%; no transverse direction steel was provided. The material tests performed revealed that this panel had a 28-day compressive strength of 62.1 MPa and a tensile strength of 3.90 MPa. This panel was tested under monotonic pure shear. For the monotonic tests, the shear stress was increased until first cracking was observed, at which point a load stage was taken. Subsequent, load stages were taken at increments of 0.27 MPa of shear stress.

Out-of-plane issues were not as prevalent in this test, although the first crack was observed only on the front face of the panel at v_{cr} = 2.60 MPa and γ_{cr} = 0.136x10^{-3}. Subsequently, while taking a load stage at a shear stress of around 3.40 MPa, cracks began to open on the back face of the panel. Figure 4.22 shows the shear stress versus shear strain response of this test. The opening of cracks was accompanied by a substantial increase in strain at 3.40 MPa. Gradual softening of the response was observed after cracking until failure occurred at v_u = 5.97 MPa and γ_u = 5.94x10^{-3}. Failure was gradual and with sufficient warning as the maximum crack widths grew steadily larger. Eventually, aggregate interlock broke down and fibres pulled out as the load steadily dropped to zero. Just before failure, the average crack width was measured to be 0.21 mm and the average crack spacing was 43.0 mm. Thus, this panel exhibited significantly improved crack control over plain concrete. Figure 4.23 depicts the panel at failure.

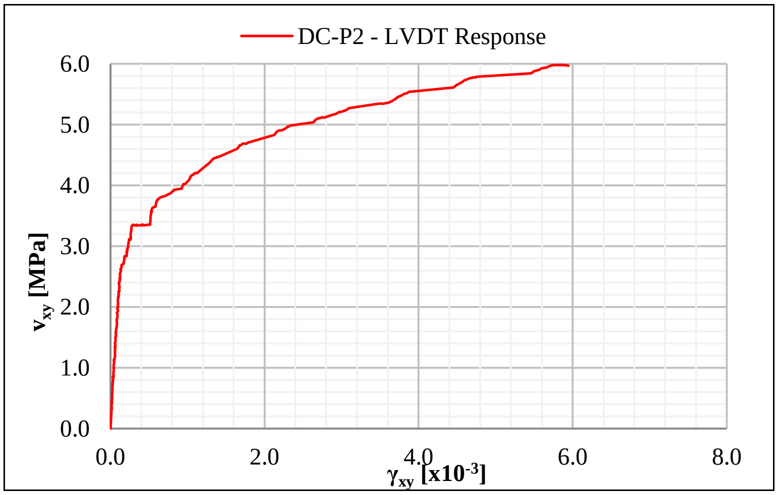

Figure 4.22: DC-P2 shear stress vs. shear strain response

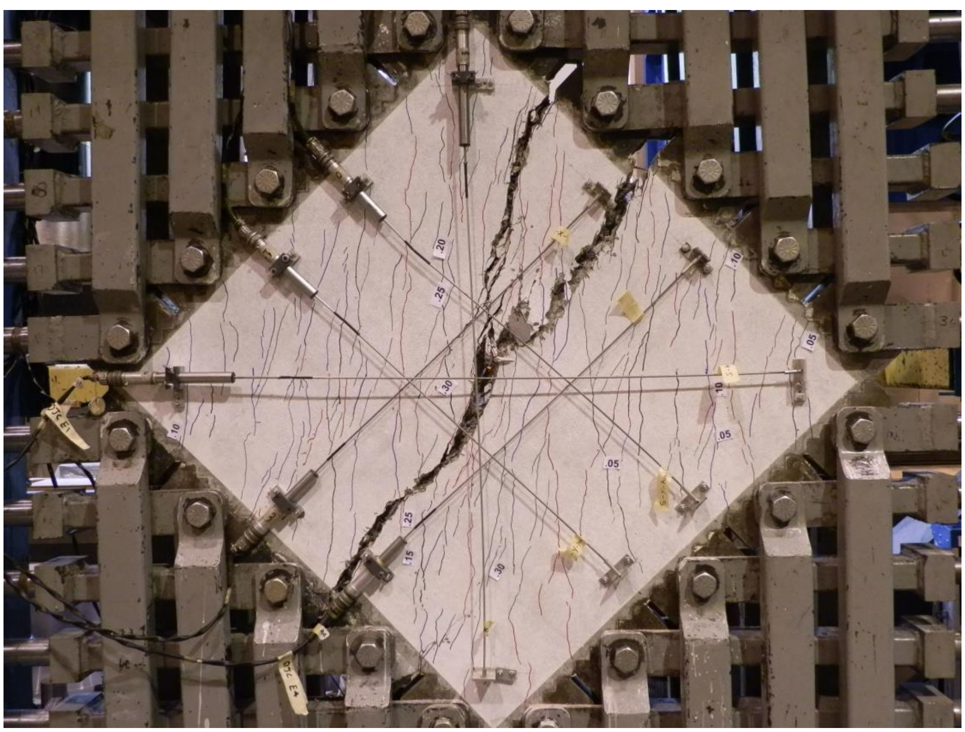

Figure 4.23: DC-P2 failure crack pattern

4.5.1.3 Panel DC-P3

Panel DC-P3 was made with normal strength macro-synthetic fibre reinforced concrete, using 2.0% by volume MasterFiber™ MAC Matrix fibres with l_f = 54 mm, d_f = 0.81 mm, f_{uf} = 520 MPa and E_f = 10,000 MPa. The 28-day cylinder compressive strength was 50.9 MPa and the tensile strength was 4.49 MPa. This panel was tested under monotonic pure shear. After cracking, load stages were taken at increments of 0.27 MPa of shear stress, until a significant softening was observed. The stress increments were reduced to 0.11 MPa as a result of this softening.

In this test, a premature first crack was visually observed at 1.50 MPa of shear stress; however, there was no softening of the response. Subsequently, at v_{cr} = 2.17 MPa and γ_{cr} = 0.148x10^{-3}, a more definite softening was observed. This is taken as the cracking point in the discussion. During the 8th load stage, an hydraulic pump malfunction occurred as an electrical box adjacent to the pump overheated and shut down. This resulted in a quick drop in the hydraulic pressure of one of the two input lines used, while the other lingered and slowly released oil pressure. This was equivalent to a biaxial tension plus shear loading condition. The pump problem was corrected and the test continued to failure at v_u = 3.87 MPa and γ_u = 7.96x10^{-3}. It is believed that the pump failure only altered the location of the failure crack, but did not compromise the shear stress versus shear strain response depicted in Figure 4.24.

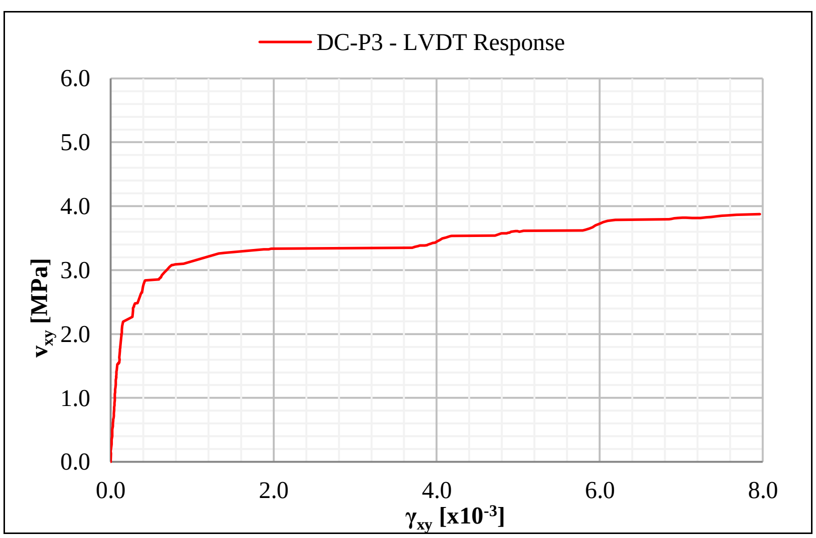

Figure 4.24: DC-P3 shear stress vs. shear strain response

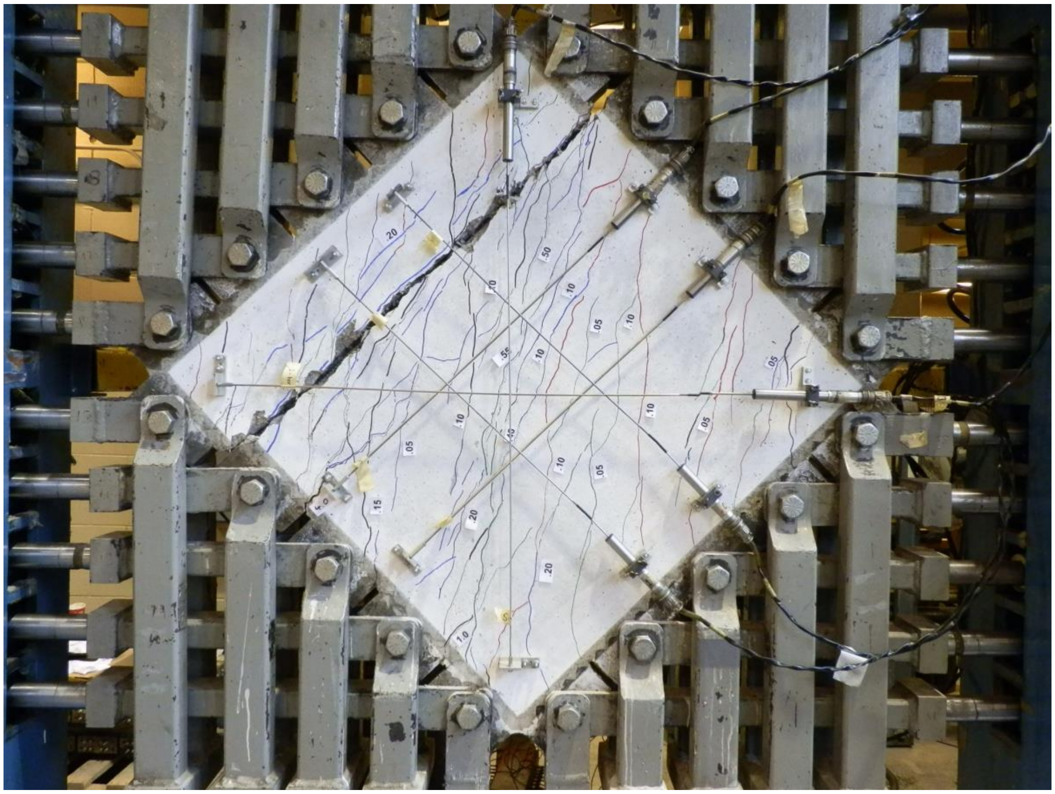

Figure 4.25: DC-P3 failure crack pattern

This failure mechanism still involved the breakdown of aggregate interlock, but the failure plane for this panel was oriented parallel to the longitudinal bars; the failure of DC-P2 was slightly more inclined. Nevertheless, the failure was gradual and well controlled; large crack widths appeared on the specimen well before the failure. The specimen, overall, exhibited a low ultimate stress capacity but a high ductility. Just before failure, the average crack width was measured to be 0.57 mm and the average crack spacing was 72.0 mm, both significantly higher than those of DC-P2. Figure 4.25 depicts the panel at failure.

4.5.1.4 Panel DC-P4

Panel DC-P4 was constructed to be identical to DC-P2. Material tests results show that this panel had a 28-day compressive strength of 64.0 MPa and a tensile strength of 4.76 MPa. This panel was tested under reversed cyclic pure shear with the loading protocol presented in Figure 4.29. The stress-controlled regime continued to one load level beyond cracking (double cycles at 1.0, 2.0, 2.6 and 3.57 MPa), before the strain-controlled regime began (double cycles at 4.12 and 4.47 MPa).

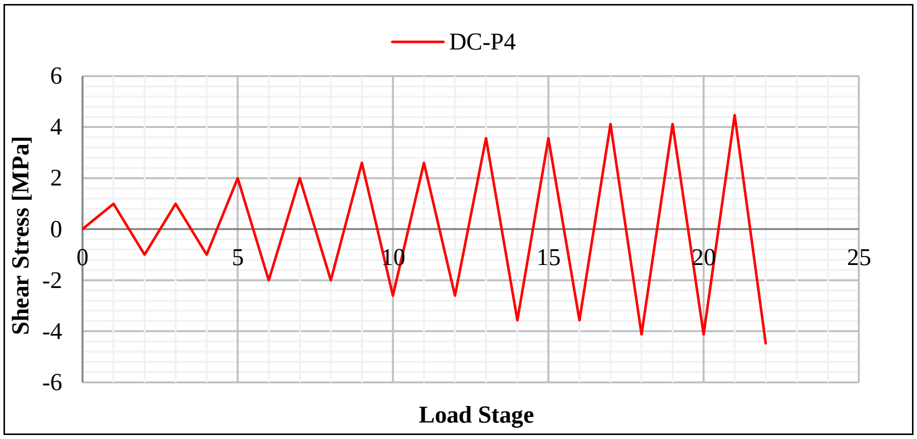

Figure 4.26: Loading protocol for DC-P4

In this test, some out-of-plane issues were observed at early stages, yet premature cracking was not exhibited. It is worth noting, however, that on the first positive half-cycle at the cracking load, the vertical crack was only found on the front face; on the corresponding negative half cycle, the horizontal crack was only found on the back face. This cracking occurred at v_{cr} = 2.60 MPa and γ_{cr} = 0.136x10^{-3}, identical to the monotonic test. The test continued until the positive half-cycle of the 8th cycle was completed. At this point, it could be seen from the pressure transducers that the two hydraulic pressure lines were not increasing in the required ratio. After some investigation it was determined that one of the hydraulic cylinders inside the Panel Tester had failed and hydraulic oil was bypassing through the cylinder piston seal. The test was stopped for six days while repairs were performed on the machine. Fortunately, no detrimental effects of this repair were seen in the panel response. When the test resumed, some softening was observed, as a significant strain increase was seen when returning to previously attained load levels. Finally, on the negative half-cycle of the 11th cycle performed, the panel failed abruptly at γ_u = 2.87x10^{-3}. The previously attained maximum shear stress was v_u = 4.47 MPa. This represented a substantial strength degradation when compared to the response of DC-P2. The shear stress versus shear strain response for DC-P4 is presented in Figure 4.30.

Failure was not as gradual, yet some large crack widths were observed during the final load stages. The failure was through aggregate interlock sliding. As the failure was occurring, significant "popping" sounds could be heard, attributable to fibre pull-out. At the load stage taken just before failure, the average crack width was found to be 0.22 mm at a crack spacing of 71.0 mm; a photograph of the failure is given in Figure 4.31.

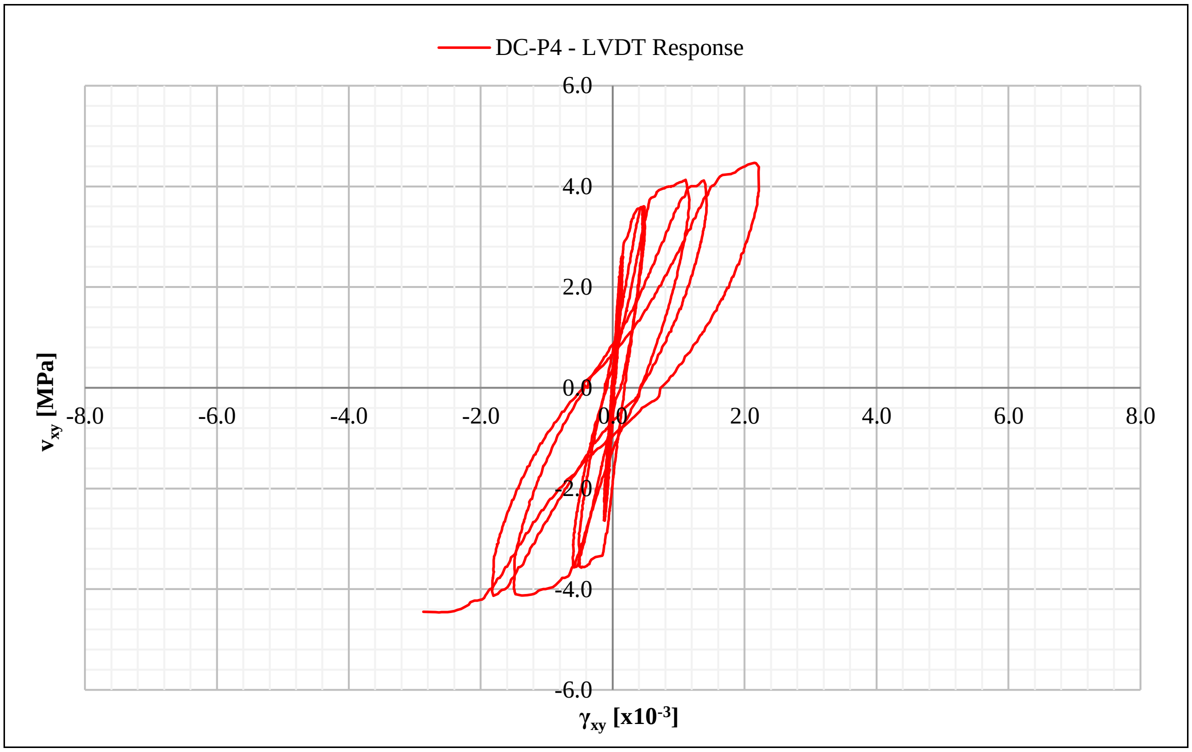

Figure 4.27: DC-P4 shear stress vs. shear strain response

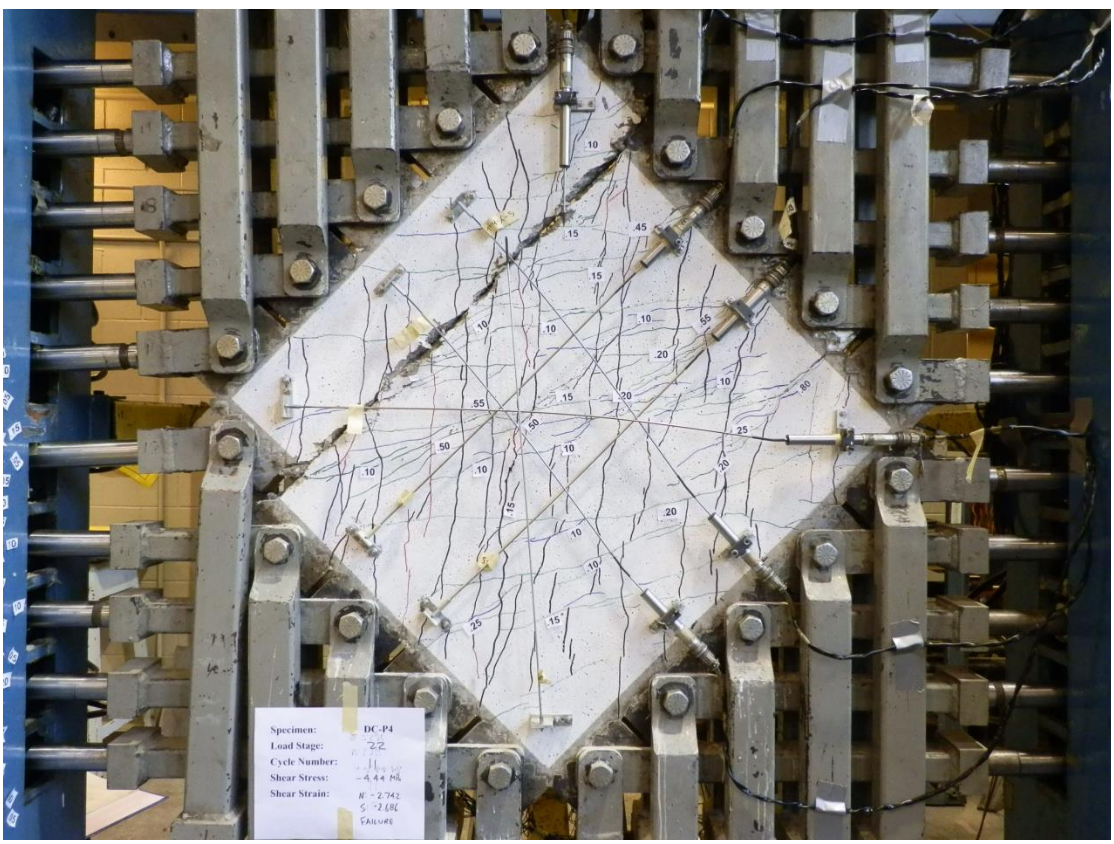

Figure 4.28: DC-P4 failure crack pattern

4.5.1.5 Panel DC-P5

Panel DC-P5 was constructed to be identical to DC-P3. The 28-day compressive strength was 54.3 MPa, and the tensile strength determined from uniaxial direct tension tests was 4.67 MPa. This panel was tested under reversed cyclic pure shear with the loading protocol presented in Figure 4.29. The stress-controlled regime continued up to cracking (double cycles at 1.0, 2.0 and 2.23 MPa), before the strain-controlled regime began (double cycles at 2.71, 3.14 and 3.43 MPa).

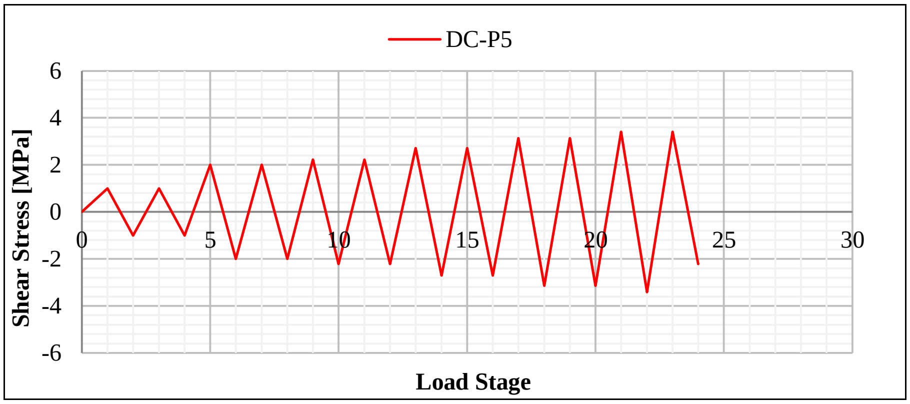

Figure 4.29: Loading protocol for DC-P5

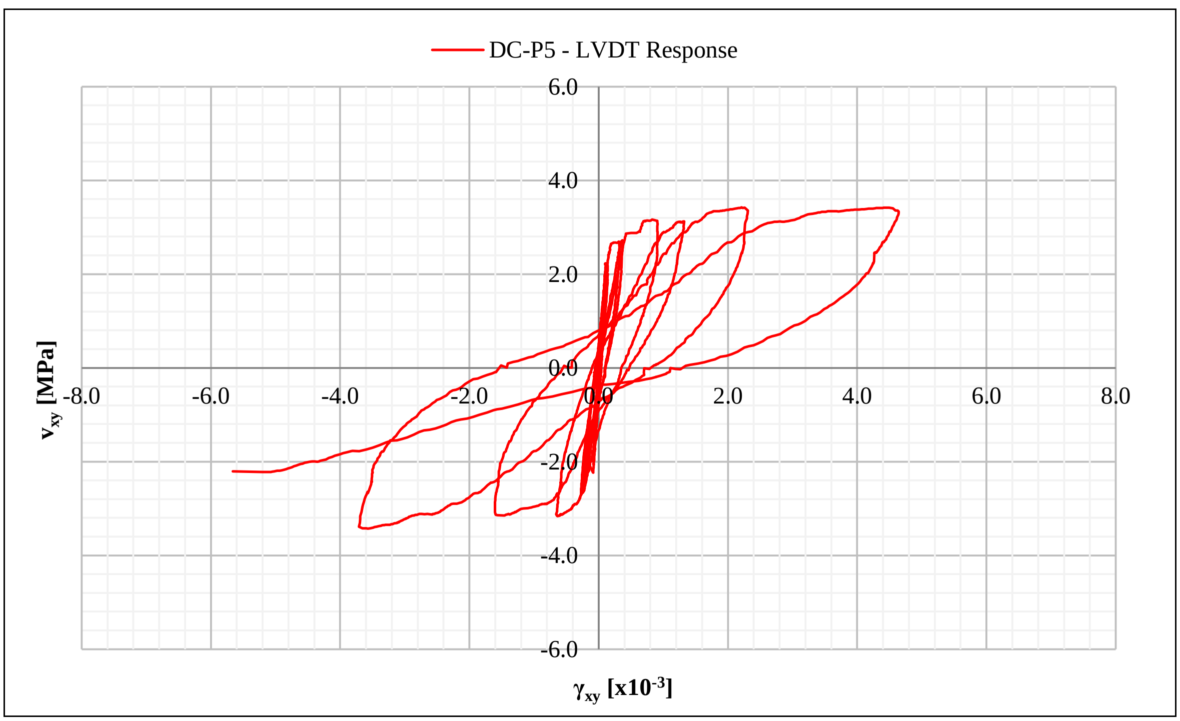

Figure 4.30: DC-P5 shear stress vs. shear strain response

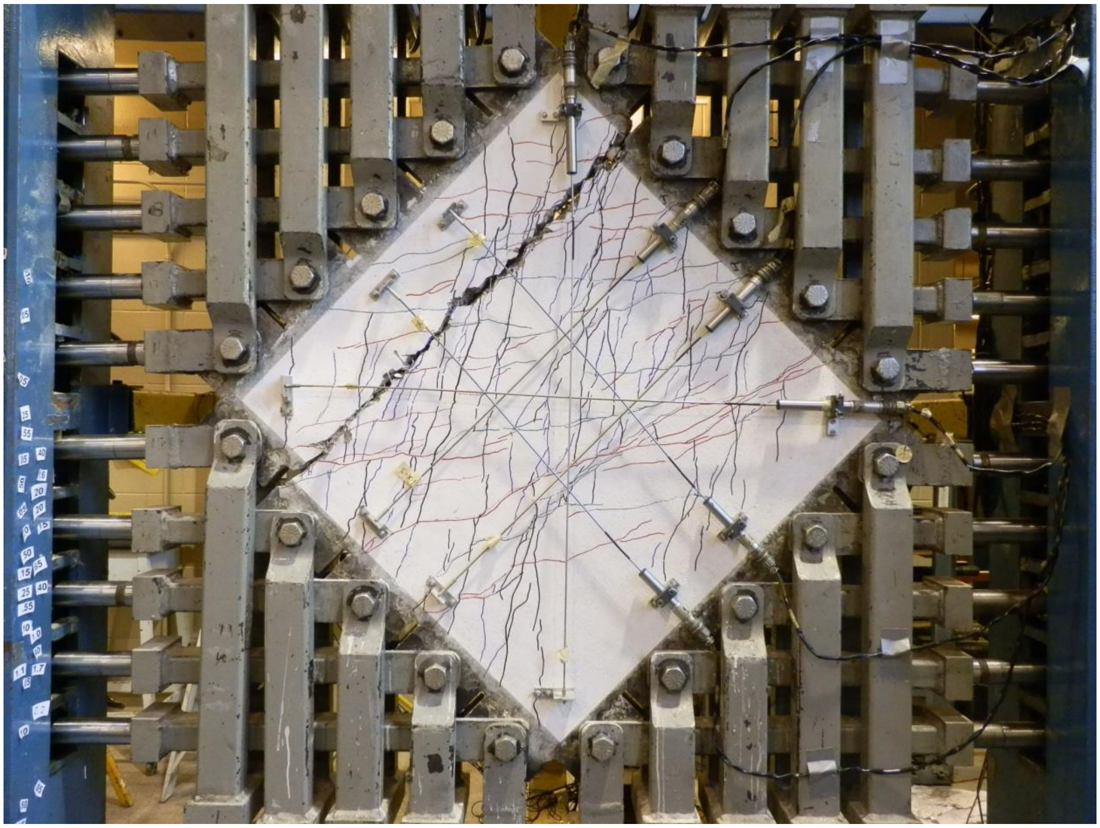

Figure 4.31: DC-P5 failure crack pattern

In this test, the out-of-plane issues observed were similar to those of DC-P4; premature cracking was not exhibited. Cracking occurred at v_{cr} = 2.23 MPa and γ_{cr} = 0.104x10^{-3}. This represents a nearly identical cracking stress, yet a substantially lower cracking strain than that of DC-P3 (cracking in DC-P5 occurred at roughly 70% of the cracking strain for DC-P3). This was likely due to the small premature crack observed on panel DC-P3 as mentioned in Section 4.5.1.3. After cracking, the test continued without issues. Consistent with what was found for the monotonic panels, DC-P5 exhibited significantly more softening than DC-P4, as crack widths grew significantly larger before failure. Finally, a gradual failure occurred on the negative half-cycle of the 12th cycle at γ_u = 5.15x10^{-3}. The previously attained maximum shear stress was v_u = 3.43 MPa. Again, some degradation was evident when compared to the monotonically loaded DC-P3, yet this degradation was not as significant as that of the SFRC specimen. The full stress-strain response is presented in Figure 4.30.

Failure was gradual and with some forewarning. At the load stage taken just prior to the failure, the average crack width was 0.59 mm at a crack spacing of 59.0 mm. This again showed the relatively large crack widths and crack spacings that were sustained by the PPFRC specimens. Also, these measurements were similar to those of the monotonic panel (DC-P3), whereas the SFRC specimen (DC-P4) exhibited a reduction in crack control when compared against the monotonic counterpart (DC-P2). A photograph of the failure is given in Figure 4.31.

4.5.2 Panel Data Analysis

In this experimental program, two data acquisition systems were used to continuously record data. The first, comprised of LVDTs, recorded continuously without any pauses, including during the taking of crack width measurements at the load stages. The data acquisition system used to acquire the LVDT readings was also used to acquire the load cell and pressure transducer data. Therefore, whenever a datum point was acquired by the system, both LVDT and stress data were recorded at the same time. Thus, a stress versus strain relationship could be directly found without a need for time synchronization. The LVDT system provides average strain data over the gauge length of 740 mm (for the x- and y-direction instruments) and 1000 mm (for the horizontal and vertical instruments) as shown in Figure 3.18. This system recorded data for both the front and back face of the panel. Thus, a comparison was made between the two faces to check for out-of-plane bending. The overall response was found by averaging the two faces.

The other data acquisition system, for the LED targets, was paused during the performance of the load stage crack width measurements. Past experimental programs performed using this system suffered a loss of data when the system crashed and dumped data from RAM after running for the full duration of a one-day test without pauses. As a result, a separate data file was saved for each loading phase. In addition, this system was not directly linked to the pressure transducers, so the pressure recordings had to be synchronized with the LED data based on the real time of the acquired recordings. To further complicate this matter, it was found that the two computers used to run the data acquisition systems did not keep time at the same rate; if synchronization was performed at the start of the test, this synchronization was only accurate for about one hour, at which point the synchronization would be off by approximately 0.64 s. Since the LED system acquired data at 1 to 2 Hz, this represented a substantial error. This problem was not found until the full experimental program has been executed. Thus, substantial work was required to correct this issue. A program written at the University of Toronto, Timeline.exe (Ruggerio, 2011), was used to stitch together the LED data and convert the data to linear strains within the LED subgrid. Then, the data were output to a spreadsheet where the pressure readings could be synchronized using linear interpolation based on the time of the recordings. This system was used to calculate local strain conditions within the 200x200 mm subgrids. These could then be averaged over the 600x600 mm total gauge length and compared to the LVDT response. This system recorded data for the back face of the panel only, as the laboratory at the University of Toronto possesses only one LED camera.

4.5.2.1 Analysis Procedure

The data calculation started with the development of a Mohr's circle relationship for the strains. Since strain data were collected in four directions (x-, y-, 45° to the x-axis and 135° to the x-axis) the Mohr's circle could be constructed and verified. Then, using this Mohr's circle and the four strain parameters (ε_x, ε_y, $\varepsilon_h = \varepsilon_{45^\circ}$, $\varepsilon_v = \varepsilon_{135^\circ}$), the principal tensile strain ε_1, principal compressive strain ε_2, shear strain γ_{xy}, reinforcement strains ε_{sx} and ε_{sy} (as applicable), and angle of orientation of the principal tensile strain direction θ_ε were found. From the strain condition, the stress parameters, such as the reinforcement stresses f_{sx} and f_{sy} (as applicable), concrete normal stresses f_{cx} and f_{cy}, concrete principal tensile stress f_{c1}, concrete principal compressive stress f_{c2}, and the orientation of the principal tensile stress direction θ_σ could also be ascertained. The step-by-step procedure used is as follows:

1. The strain readings in the x-, y-, horizontal and vertical directions were determined as the average of the *n* number of instruments providing data.

$$\varepsilon_x = \frac{1}{n}\sum_{i=1}^{n}\varepsilon_{x,i} \;\; ; \;\; \varepsilon_y = \frac{1}{n}\sum_{i=1}^{n}\varepsilon_{y,i} \;\; ; \;\; \varepsilon_h = \frac{1}{n}\sum_{i=1}^{n}\varepsilon_{h,i} \;\; ; \;\; \varepsilon_v = \frac{1}{n}\sum_{i=1}^{n}\varepsilon_{v,i} \qquad (4.7)$$

2. The shear strains in three independent directions were calculated and averaged.

$$\gamma_{xy(x,y,v)} = 2\varepsilon_v - \left(\varepsilon_x + \varepsilon_y\right) \qquad (4.8a)$$

$$\gamma_{xy(x,v,h)} = \varepsilon_v - \varepsilon_h \qquad (4.8b)$$

$$\gamma_{xy(y,v,h)} = \varepsilon_v - \varepsilon_h \qquad (4.8c)$$

$$\gamma_{xy} = \frac{\gamma_{xy(x,y,v)} + \gamma_{xy(x,v,h)} + \gamma_{xy(y,v,h)}}{3} \qquad (4.9)$$

3. The principal tensile and principal compressive strains were calculated.

$$\varepsilon_{1,2} = \frac{\varepsilon_x + \varepsilon_y}{2} \pm \sqrt{\left(\frac{\varepsilon_x - \varepsilon_y}{2}\right)^2 + \left(\frac{\gamma_{xy}}{2}\right)^2} \tag{4.10}$$

4. The orientation of the principal tensile strain was calculated.

$$\theta_\varepsilon = \frac{1}{2}\tan^{-1}\left(\frac{\gamma_{xy}}{\varepsilon_x - \varepsilon_y}\right) \tag{4.11}$$

5. The average reinforcement stresses were found using the experimentally determined stress-strain relationship of the reinforcement (presented in Appendix A.4).

$$\varepsilon_{sx} = \varepsilon_x \;\; ; \;\; f_{sx} = f(\varepsilon_{sx}) \tag{4.12a}$$

$$\varepsilon_{sy} = \varepsilon_y \;\; ; \;\; f_{sy} = f(\varepsilon_{sy}) \tag{4.12b}$$

   For panel DC-P1, the y-direction steel yielded. To find f_{sy} at a strain of ε_{sy} beyond the yielding strain, an elastic-plastic relationship was used, with linear unloading and reloading following the initial stiffness of the steel (as shown in Appendix B.2).

6. The concrete stresses in the normal directions were calculated.

$$f_{cx} = -\rho_x f_{sx} \tag{4.13a}$$

$$f_{cy} = -\rho_y f_{sy} \tag{4.13b}$$

7. The applied shear stress was determined.

$$v_{xy} = \frac{\left(P_{j,comp} \cdot A_{j,comp} + P_{j,tens} \cdot A_{j,tens}\right) \cdot \sin(45^\circ) \cdot 5}{A_{panel}} \tag{4.14}$$

   where:

   $P_{j,comp}$ = recorded pressure in the compression jacks of the Panel Tester [MPa];

   $P_{j,tens}$ = recorded pressure in the tension jacks [MPa];

   $A_{j,comp}$ = area of the compression jacks [mm^2];

   $A_{j,tens}$ = area of the tension jacks [mm^2];

   A_{panel} = cross-sectional area of the panel [mm^2].

8. The principal tensile and principal compressive stresses were calculated.

$$f_{c1,2} = \frac{f_{cx} + f_{cy}}{2} \pm \sqrt{\left(\frac{f_{cx} - f_{cy}}{2}\right)^2 + \left(v_{xy}\right)^2} \tag{4.15}$$

9. The orientation of the principal tensile stress direction was found.

$$\theta_\sigma = \frac{1}{2}\tan^{-1}\left(\frac{2v_{xy}}{f_{cx} - f_{cy}}\right) \tag{4.16}$$

Detailed results of the panel tests are presented in Appendix B.1 to B.6. This includes plots showing some of measured strains obtained from the LVDTs and LEDs, as well as the calculated shear stress versus shear strain response. Principal tensile stress versus principal tensile strain, principal compressive stress versus principal tensile strain, and the principal stress and strain angles of inclination as calculated from the LVDTs are presented. Photographs of the load stages and the measured crack widths and spacings are also shown.

4.5.2.2 Data Verification

The data obtained from the two data acquisition systems (LVDT and LED) and from the front and back of the panels (using the LVDT readings) were compared and checked. Plots of these comparisons and discussion are presented in Appendix B.

From the comparison of the LVDT and LED data sets, it was determined that the overall shear stress versus shear strain relationship calculated from the LVDT back face and the LED system were similar. However, there appeared to be a consistent discrepancy, with the LED responses showing a higher shear strain reading at a given shear stress level. This was particularly clear when looking at DC-P2 and DC-P3. The discrepancy was due to the fact that the overall gauge length of the LEDs was shorter than that of the LVDTs. The displacement reading recorded by the two systems was nearly the same, as most of the cracking occurred within the 600 mm gauge length of the LEDs. Taking a nearly identical displacement and dividing by this shorter gauge length yields a higher strain. In addition, the high frequency of readings for the LED system led to some noise. In post-processing the data, it was seen that certain LED targets would register as invisible for a few seconds, even though this was not displayed by the data acquisition computer during the experiments. If invisible, the LED system does not record position data. This uncertainty in the response obtained using the LED system, coupled with the desire to leave out local effects, led to the decision to focus the analysis and discussion on the LVDT response.

The comparison of the LVDT data between the front and back face of the specimen reveals some inconsistencies between the readings. This suggests some out-of-plane bending occurred during the experiments. The out-of-plane bending seemed to be worse when performing loading in the positive shear direction. Both the monotonic tests as well as the positive half cycles of the reversed cyclic tests exhibited discrepancies between the two faces. This discrepancy was not as large during the negative half cycle of the reversed cyclic tests. In all the tests the first crack was only visible on the front face of the panel, leading to a higher cracking stress on the panel back face. This is consistent with findings of past experimental programs performed using the Panel Tester (Susetyo, 2009).

The source of the out-of-plane bending is unknown, yet there are a number of possible causes. Firstly, the improper alignment of the panel during installation into the test machine could be a source of the error. The in-plane alignment of panel specimens was controlled by adjusting the length of the links that are oriented around the back of the test machine (see Figure 3.15 (b)). The technique used to arrange these links was to apply a biaxial tension stress of 0.54 MPa to the specimen (so as to straighten the hydraulic cylinders within the machine and to also pull the panel into plane with the line of action of the cylinders). With the load applied, a few of the adjustable links were tightened to hold the panel at this theoretically correct location. This may not have been sufficient. A slightly higher biaxial stress (or another method altogether) may be needed to perform a proper alignment.

Another possible cause of the out-of-plane bending was the overtightening of the bolts that connect the jacks to the shear keys. The connection between the jacks and the shear keys is meant to freely rotate while transmitting the applied axial load from the jack to the panel. Although care was taken to only tighten the nuts by one-quarter turn past hand tight, perhaps this was not done uniformly for all twenty connections. This would cause an uneven restraint of the movement of the shear keys, leading to out-of-plane bending as the panel deforms to overcome this restraint (Susetyo, 2009).

Concerning the construction of the panel specimen itself, another possible cause was the thicker cover of the back face than that of the front face. The front face was the formed face as cast, meaning this face was flush with the shear keys. Due to the difficulty in finishing a level surface with high volumes of FRC, this was much harder to achieve on the back (or finished) face. It was also noted during casting that, due to the sieve effectively formed by the fibres and the tightly spaced reinforcement, there was a larger concentration of coarse aggregate near the top face of the panels (particularly for DC-P2, DC-P3 and DC-P5). A larger concentration of course aggregate led to the higher cracking strength observed for the back face.

These hypotheses are further supported by the findings of DC-P1. The installation issues of DC-P1 were covered in Section 4.5.1.1. From the comparison of the two faces of DC-P1 it was seen that once cracking occurred on the back face of the plain reinforced concrete panel, the out-of-plane bending did not worsen as the test continued. The shear stress versus shear strain responses show a consistent strain offset between the back and front face that does not increase. Thus, the non-uniform distribution of the fibres across the cracks (as discussed in Section 3.4.4) was a factor for the FRC panels. In all cases, there was a higher concentration of fibres located on the back face of the panel as tested (or top face as cast). As expected, this led to a stiffer response for the back face of the panel after cracking; more fibres were present to control cracking and increase stress transfer across the cracks. This is consistent with the observation of many small cracks on the back face of the panels during the experiments.

All of these factors were present in each test to generate the observed out-of-plane bending; however, the behavioural results of all of the panels were consistent. Thus, the average LVDT response was used in the discussions and in finite element analyses.

4.5.3 Comparisons of Panel Behaviour

In this section, the structural response of the panels is discussed. The shear stress versus shear strain, principal tensile stress versus principal tensile strain, principal compressive stress versus principal compressive strain. angles of inclination of the principal tensile directions, crack control characteristics, and failure mode of each of the panels are presented and discussed. The effects of fibre type and loading protocol on each of these responses are presented and some preliminary conclusions are drawn. Pertinent stress data are presented in Table 4.7 with the corresponding ductility and cracking information summarized in Table 4.8. As before, this discussion includes panels C1C, C1F1V1, C1F1V2 and C1F1V3 tested by Susetyo (2009), to compare the response of the 2.0% by volume macro-synthetic FRC (DC-P3) to that of the end-hooked steel FRC panels containing fibres of similar lengths.

Table 4.7: Panel Stress Results

Specimen ID	v_{cr} [MPa]	v_u [MPa]	$f_{c1,cr}$ [MPa]	$f_{c1,max}$ [MPa]	$f_{c1,u}$ [MPa]	$f_{c2,u}$ [MPa]	$f_{sx,max}$ [MPa]	$f_{sy,max}$ [MPa]
DC-P1	1.43	5.79	1.43	2.82	0.65	-11.63	267	611
DC-P2	2.60	5.97	2.49	3.37	2.95	-12.05	275	-
DC-P3	2.17	3.87	2.13	2.42	1.73	-8.69	210	-
DC-P4	2.60	4.47	2.60	3.54	2.59	-7.66	153	-
DC-P5	2.23	3.43	2.12	2.56	1.27	-3.83	204	-
C1C	2.01	5.77	2.05	2.87	1.43	-11.70	250	501
C1F1V1	2.09	3.53	2.21	2.83	1.85	-6.73	148	-
C1F1V2	2.65	5.17	2.59	3.04	2.82	-9.46	201	-
C1F1V3	1.83	5.37	1.85	3.13	2.97	-9.70	204	-

Table 4.8: Panel Ductility Results

Specimen ID	γ_{cr} [x10^{-3}]	γ_u [x10^{-3}]	$\varepsilon_{1,cr}$ [x10^{-3}]	$\varepsilon_{1,max}$ [x10^{-3}]	$\varepsilon_{1,u}$ [x10^{-3}]	$\varepsilon_{2,u}$ [x10^{-3}]	w_m [mm]	s_m [mm]
DC-P1	0.116	7.98	0.048	0.967	10.60	-0.445	0.57	55.6
DC-P2	0.136	5.94	0.075	1.466	8.58	0.141	0.21	43.0
DC-P3	0.148	7.96	0.075	0.717	11.82	-0.434	0.57	72.0
DC-P4	0.136	2.87	0.071	0.402	6.75	0.399	0.22	71.0
DC-P5	0.104	5.15	0.071	1.615	10.94	-0.399	0.59	59.0
C1C	0.086	6.01	0.034	0.360	6.29	-0.618	0.55	57.2
C1F1V1	0.197	2.77	0.089	0.724	5.66	0.286	0.55	114.4
C1F1V2	0.139	5.27	0.080	0.266	5.61	-0.572	0.45	54.7
C1F1V3	0.055	5.10	0.017	0.447	5.39	-0.540	0.45	57.2

4.5.3.1 Inclination of Stress and Strain Fields

4.5.3.1.1 Comparisons of θ_σ and θ_ε

Figure 4.32 compares the angle of inclination of the principal tensile stress direction and the angle of inclination of the principal tensile strain direction (both measured as the counter clockwise angle from the positive x-axis) for each of the panels tested. At early load stages, the principal stress and principal strain angles coincided relatively well, centred at approximately 45° (or 135°) to the x-axis. At the onset of cracking, the inclination angles became more steeply inclined. This corresponded to the rotation of the cracks observed when performing crack marking during the tests. In most cases, the principal strain angle was more steeply inclined than the principal stress angle at a given applied stress, except for panel DC-P2 and the early stages of panel DC-P3. This observation was magnified at negative shear stresses for cyclic tests.

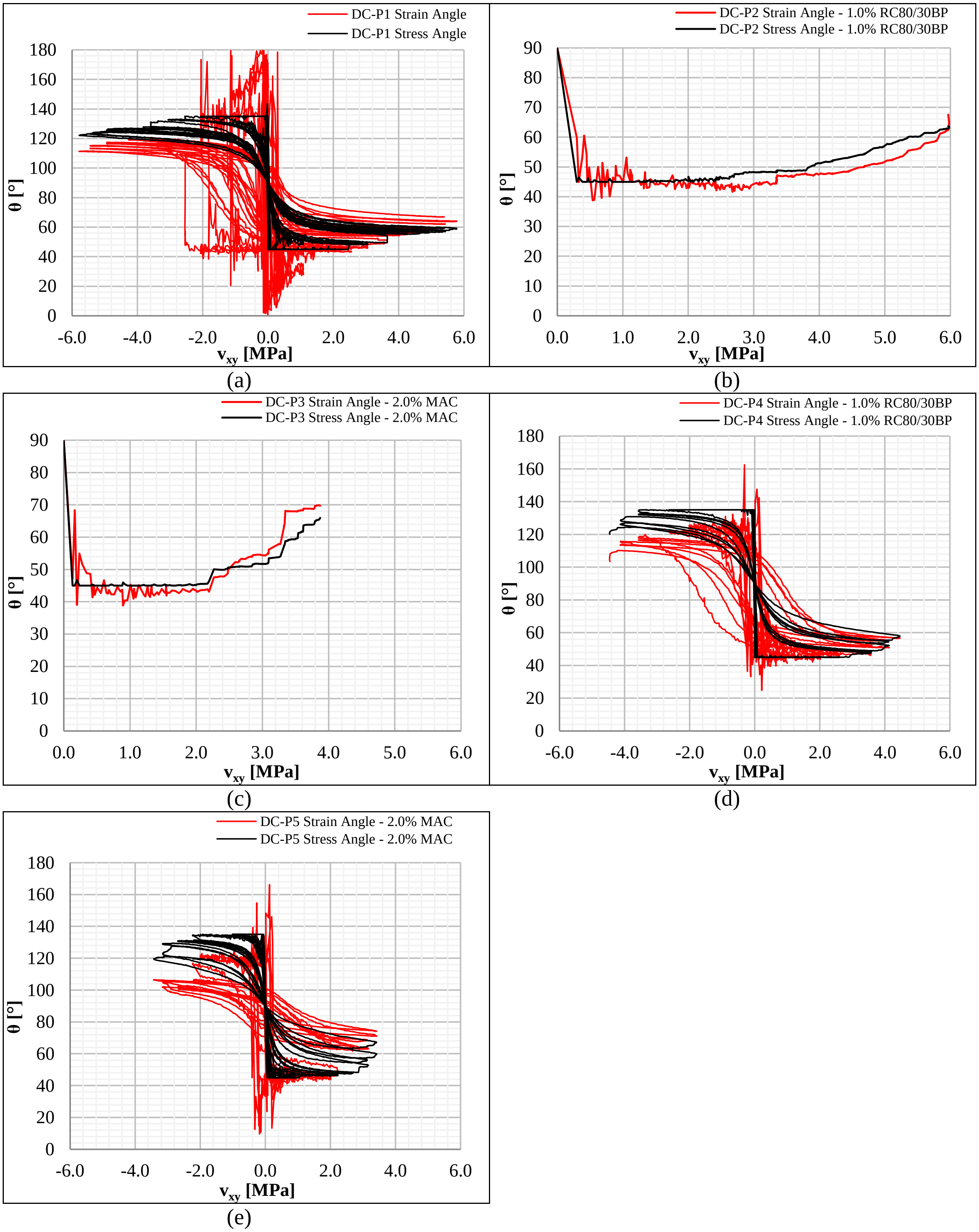

Figure 4.32: Inclination of the stress field for all panels tested

Also, the principal stress angle increased at a more gradual and uniform rate and, during the cyclic tests, consistently returned to 90° at zero stress. The principal strain angle, on the other hand, contains noise (particularly for the reversed cyclic tests), and the overall trend suggests that the angle of inclination did not return to 90° at zero load; some offset was observed. The discrepancy between the principal stress and principal strain angles signified lag in the rotation of the principal tensile strain direction as a result of shear slip along crack surfaces (Vecchio, 2000). Also, a high inclination to the x-axis suggested principal tensile stresses and strains oriented nearly perpendicular to the conventional steel reinforcement that was provided in the x-direction. Thus, the FRC panels which exhibited a more gradual rotation of the cracks (DC-P2, C1F1V2 and C1F1V3) performed better, achieving a higher maximum stress in the x-direction reinforcement (275 MPa for DC-P2 compared to 210 MPa for DC-P3). Lastly, the steep inclination of the principal tensile strain directions for panels DC-P3, DC-P4 and DC-P5 was consistent with the failure plane that was oriented parallel to the x-direction reinforcement.

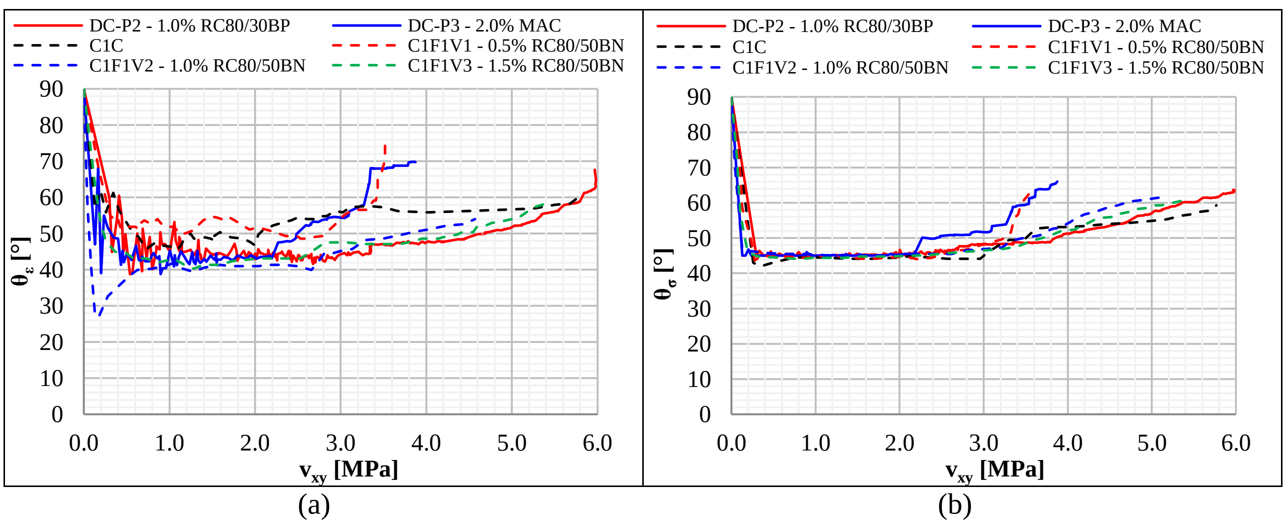

Figure 4.33: Comparison of inclination angles for panels tested under monotonic shear: (a) $\theta_\varepsilon - v_{xy}$; (b) $\theta_\sigma - v_{xy}$

4.5.3.1.2 Comparisons of θ_σ and θ_ε for Panel Tested in Monotonic Shear

Figure 4.33 compares the angles of inclination for each of the panels tested under a monotonic loading regime. These are all reasonably similar. The control panel and most of the SFRC panels exhibited a gradual increase in the stress angles. This is not true for the PPFRC specimen, DC-P3, and the 0.5% by volume SFRC specimen, C1F1V1. These two specimens exhibited a steeper increase in principal tensile stress direction, which was consistent with the failure planes.

These observations were mirrored for the principal tensile strain directions as well, with the exception being that the principal strain angle for the control panel increased rapidly at the onset of cracking, before stabilizing at higher load levels.

4.5.3.1.3 Comparisons of θ_σ and θ_ε for Panel Tested in Reversed Cyclic Shear

Lastly, Figure 4.34 presents a comparison of the angles of inclination of the principal tensile stress and principal tensile strain directions for the panels tested in reversed cyclic shear against their respective monotonic counterparts. Similar to the comparison discussed in Section 4.5.3.1.2, the principal stress angles corresponded well. The only exception was for panel DC-P4, where the inclination of the stress field was steeper than it was for DC-P2 at an applied shear stress above 4.0 MPa. This signified a diminished ability of the steel fibres to transmit tensile stresses across the cracks (as will be discussed further in Section 4.5.3.3.2). The differences in the behaviours of the monotonic and reversed cyclic specimens were clearer when examining the principal strain angles. These exhibited a larger discrepancy, particularly under negative shear loading. The crack rotation occurred at a much lower applied stress for the cyclically loaded panels, particularly for the FRC specimens. As mentioned before, this steep inclination was undesirable as there was only conventional reinforcement in the x-direction.

4.5.3.2 Influence of Fibre Type

Figure 4.35 depicts the responses of six of the panels tested under monotonic shear loading. Included in this figure are graphs of the shear stress versus shear strain, principal tensile stress versus principal tensile strain, shear stress versus mean crack width and shear stress versus mean crack spacing. The structural responses and cracking characteristics of the various FRC types can be investigated. The six panels presented are: DC-P2 (containing 1.0% by volume RC80/30BP end-hooked steel fibres); DC-P3 (containing 2.0% by volume MAC Matrix macro-synthetic fibres); C1C (plain reinforced concrete); and C1F1V1, C1F1V2 and C1F1V3 (containing 0.5%, 1.0% and 1.5% by volume RC80/50BN end-hooked steel fibres). Thus, comparisons may be drawn between the short steel fibres and long steel fibres, as well as between the fibre material types for a constant fibre length of 50 mm (see Table 3.5 for complete fibre properties).

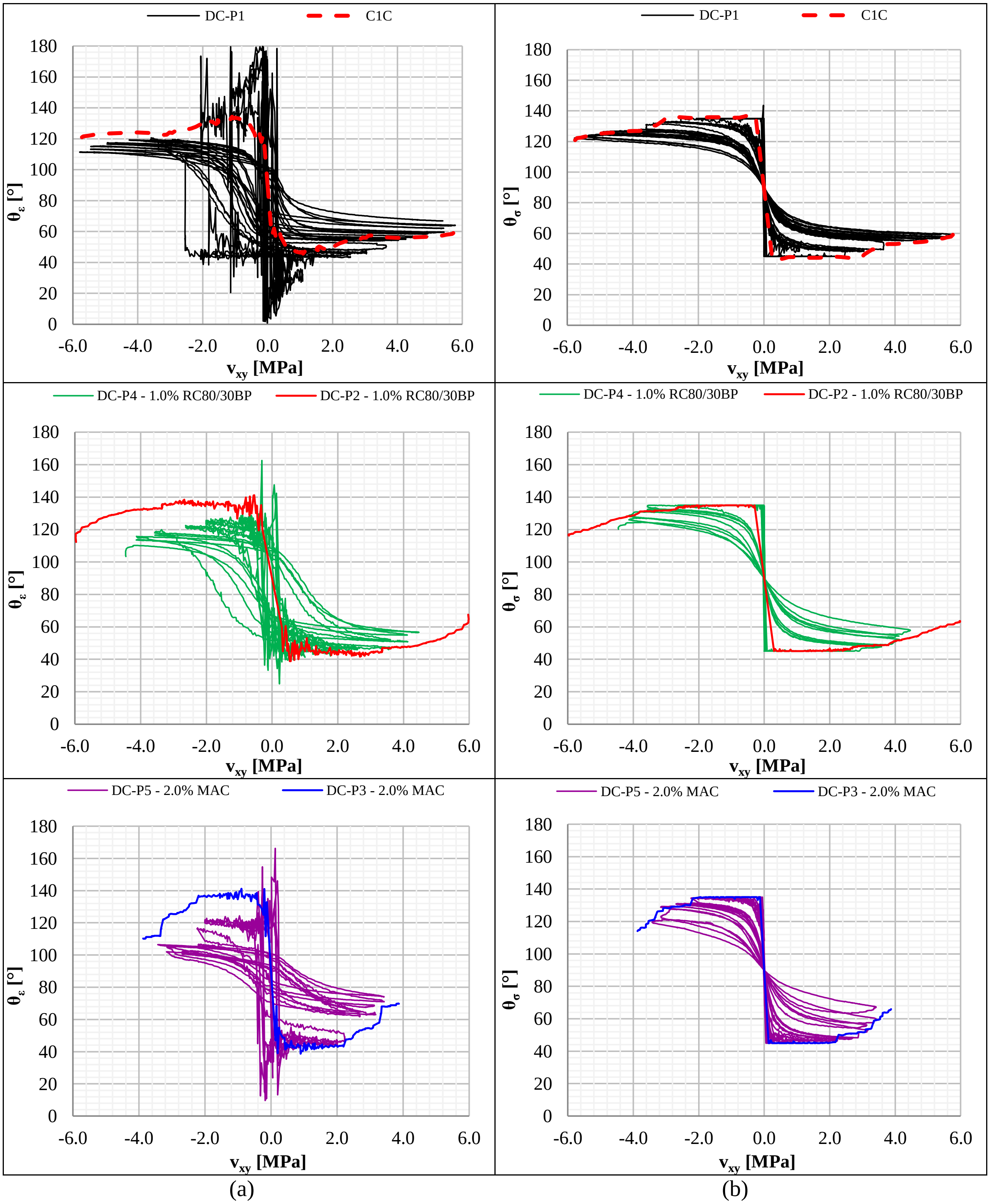

Figure 4.34: Comparison of inclination angles for panels tested under reversed cyclic shear: (a) $\theta_\varepsilon - v_{xy}$; (b) $\theta_\sigma - v_{xy}$

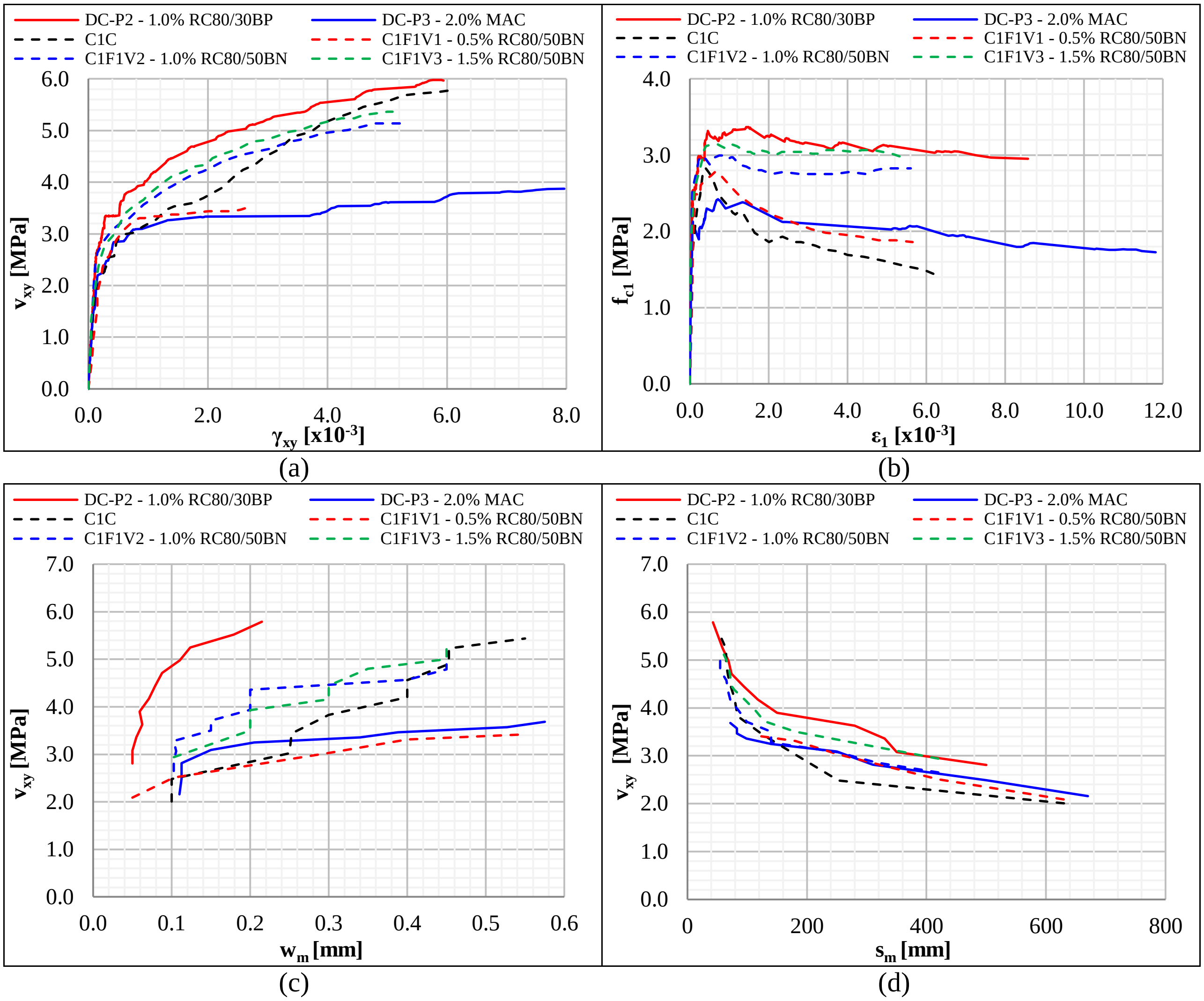

Figure 4.35: Influence of fibre type on panel test responses: (a) $v_{xy} - \gamma_{xy}$; (b) $f_{c1} - \varepsilon_1$; (c) $v_{xy} - w_m$; (d) $v_{xy} - s_m$

4.5.3.2.1 Shear Resistance and Ductility

Beginning with the shear stress versus shear strain response (Figure 4.35 (a)), it was clear that the SFRC specimens, with the exception of C1F1V1, achieved similar shear strengths and ductilities to those of the control panel C1C. The addition of 1.0% by volume of end-hooked steel fibres is a viable option for replacing this amount of conventional steel. DC-P2 achieved a 3.5% increase in shear strength with only a 1.2% reduction in ductility when compared to those of plain reinforced concrete. Panels C1F1V2 and C1F1V3 performed slightly worse. C1F1V3, for example, saw a 6.9% reduction in strength and 15% reduction in ductility relative to the control panel. The shorter steel fibres in the lower volume fraction performed better than longer fibres of the same aspect ratio. The light volume fraction of steel fibres in C1F1V1 was insufficient in retaining an adequate strength and ductility.

The PPFRC specimen, DC-P3, was unable to achieve an equivalent shear strength (3.87 MPa, a 32.9% reduction compared to C1C), yet the shear strain at ultimate was increased by 32.4%. This panel achieved a ductility significantly greater than any of the others presented in this comparison, achieving an ultimate shear strain that was 287% that of C1F1V1, and 151% that of C1F1V2 (representing the worst and best ductilities achieved by the specimens reinforced with 50 mm end-hooked steel fibres). Thus, these fibres exhibited an ability to deform elastically and bridge large cracks without significant fibre pull-out or rupture, improving toughness and ductility (Won et al., 2006; Oh et al., 2002). The strength achieved by DC-P3 was 11% greater than that of C1F1V1, meaning that the shear strength capacity of this specimen was similar to that of 0.5% by volume SFRC. It is clear that these improvements are not significant enough to warrant the full replacement of conventional steel with macro-synthetic fibres.

4.5.3.2.2 Principal Stress and Strain Responses

The observations for shear strength and ductility were repeated in the principal tensile behaviour (Figure 4.35 (b)). The cracking loads of all the panels were relatively consistent, as was found through the performance of the uniaxial tension tests. After cracking, all of the SFRC specimens exhibited similar maximum tensile strengths to that of the control specimen (between 2.83 MPa and 3.37 MPa). The PPFRC specimen reached 2.42 MPa at maximum (16% less than the stress attained by the control panel 23% less than the 1.5% SFRC panel). This supports the finding of the relatively low engagement of these fibres at low crack widths, as a result of the low fibre stiffness and lack of mechanical anchorage (Buratti et al., 2011). However, the residual load-carrying capacity of the PPFRC specimen showed improvement over that of plain reinforced concrete and was similar to that of C1F1V1 (as with the shear response). Tensile ductility, on the other hand, was improved through the use of macro-synthetic fibres. The ultimate tensile strain achieved by each of the panels containing 50 mm end-hooked steel fibres was similar, suggesting that the cracking sustained at this level of principal tensile strain was the maximum attainable for these types of fibres. However, the macro-synthetic FRC withstood at least 1.75 MPa of residual tensile stress to a much higher ultimate tensile strain of 11.82×10^{-3}. The ultimate tensile strain of PPFRC was 188% that of the control panel and 211% that of C1F1V2.

The graph presented in Figure 4.39 (a) shows, as expected, that there was not a significant difference in the pre-peak compression behaviour of the specimens. Fibres have not been found to cause an appreciable difference in this behaviour (Ou et al., 2012). Also, C1F1V1 and DC-P2 showed a shift to the positive strain region at the end of the test. This suggests large crack slips (Susetyo, 2009).

4.5.3.2.3 Crack Control Characteristics

Figure 4.35 (c) and (d) present the relationship of shear stress to average crack widths and average crack spacings respectively. First, it was evident that panels reinforced with conventional transverse steel or high percentages of steel fibres achieved an appreciable amount of stress above the cracking stress. First cracking for these panels occurred at around 40% of the ultimate attained stress, whereas for DC-P3 cracking occurred at 56% of ultimate. Also, crack widths in DC-P3 increased without a substantial increase in applied stress. At nearly all levels of applied stress, the crack widths in the PPFRC panel were similar to those of panel C1F1V1 and greater than those of the high volume SFRC specimens. This was also true of crack spacings, as the PPFRC panel exhibited larger crack spacing (synonymous with fewer individual cracks) at most levels of applied stress. This observation signified the inability of these fibres to transmit enough stress across a crack to form subsequent cracks at the fibre volume fraction used (Bentur, 2007). However, the fact that these large cracks were sustained without failure suggests that macro-synthetic FRC can sustain significant damage, as the fibres remain anchored to the concrete up to large crack widths (Won et al., 2006; Oh et al., 2002). DC-P2, with short steel fibres, exhibited the smallest crack widths and tightest crack spacings.

4.5.3.3 Influence of Loading Protocol

Figure 4.36, Figure 4.37 and Figure 4.38 present graphs of the shear stress versus shear strain, principal tensile stress versus principal tensile strain, shear stress versus mean crack width and shear stress versus mean crack spacing for the three pairs of panel tests performed. Figure 4.36 presents the relationships for the plain reinforced concrete specimens (C1C monotonic and DC-P1 reversed cyclic); Figure 4.37 presents the SFRC responses (DC-P2 monotonic and DC-P4 reversed cyclic) and Figure 4.38 presents the PPFRC responses (DC-P3 monotonic and DC-P5 reversed cyclic).

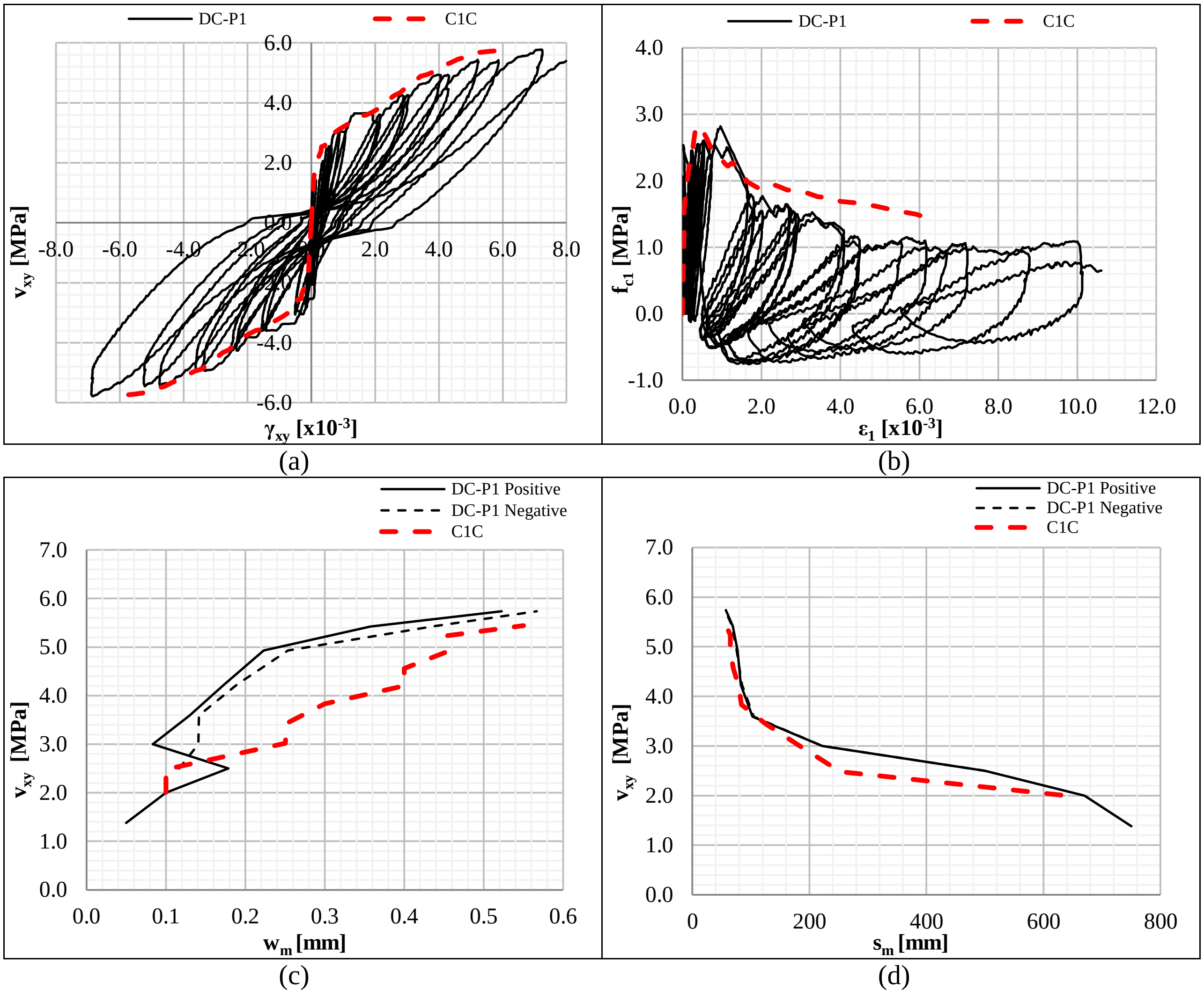

Figure 4.36: Influence of reversed cyclic loading on plain concrete panel test responses: (a) $v_{xy} - \gamma_{xy}$; (b) $f_{c1} - \varepsilon_1$; (c) $v_{xy} - w_m$; (d) $v_{xy} - s_m$

4.5.3.3.1 Plain Reinforced Concrete

The plain concrete specimen, DC-P1, did not experience any stress degradation and, in fact, achieved a 33% increase in shear ductility compared to the monotonically loaded C1C. This was not expected, and is likely attributed to the difference in steel properties of the D4 wires used in the two panels tested five years apart. The D4 wires used in DC-P1 exhibited a higher ultimate strength (624 MPa) when compared to the steel used by Susetyo in performing test C1C in 2007 (549 MPa) (Susetyo, 2009). The higher ultimate capacity delayed the failure by bar rupture for the test executed under load control. Conversely, the residual principal tensile stress capacity was negatively affected as expected. The tensile stress attained at a given tensile strain was lower than the monotonic test from a relatively early point in the loading protocol (cycle nine of

17). DC-P1 exhibited greater crack control (smaller average crack widths at a given stress). In addition, crack openings and crack slip were well controlled (suggested from the small positive principal compressive strains compared to those of other cyclic panels shown in Figure 4.39). It is worth noting that crack width measurements are subjective. Since the crack measurements for these two panels were performed by different groups of people, there may be some interpretation error inherent in these results. Overall, though, it would appear that the cycling of load had an expected detrimental effect on the response of the reinforced concrete specimens with light transverse reinforcement. This would have been more pronounced if the properties of the D4 wires were the same for the two tests.

4.5.3.3.2 Steel Fibre Reinforced Concrete

The shear resistance and ductility of the SFRC specimen was greatly affected by the loading protocol. The maximum shear stress attained by DC-P4 was reduced by 25% compared to DC-P2; the ultimate shear strain was reduced by 52% as a result of the cycling of load. This is consistent with the result of past experimental findings of SFRC beams tested under reversed cyclic shear loads (Chalioris, 2013).

The maximum principal tensile stress achieved by DC-P4 was similar to that of DC-P2; however, as further cycles progressed, the residual tensile load-carrying capacity began to degrade. Simultaneously, it was found that the principal compressive strain had become positive (Figure 4.39 (c)), suggesting cracks were slipping and not fully closing. The average crack spacing for DC-P4 at a given shear stress was larger than that of DC-P2, meaning that the ability of the fibres to transmit enough stress across existing cracks and generate further cracking had diminished. The tensile strain continued to increase to a maximum of 6.75×10^{-3}, a 21% reduction when compared to the monotonic test; other parameters were shown to be more drastically affected. At this point, the average crack widths were identical to those of the monotonic test near failure meaning that, across the failure plane, the ability of these fibres to control the crack widths and promote adequate aggregate interlock had diminished. Thus, the reversed cyclic loading protocol was substantially detrimental to the behaviour of the SFRC specimens containing these short fibres. In addition, the eventual failure plane of DC-P4 was steeply inclined, suggesting an increased rotation of the principal tensile direction as a result of cyclic loading. This is supported by the discussion in Section 4.5.3.1.3.

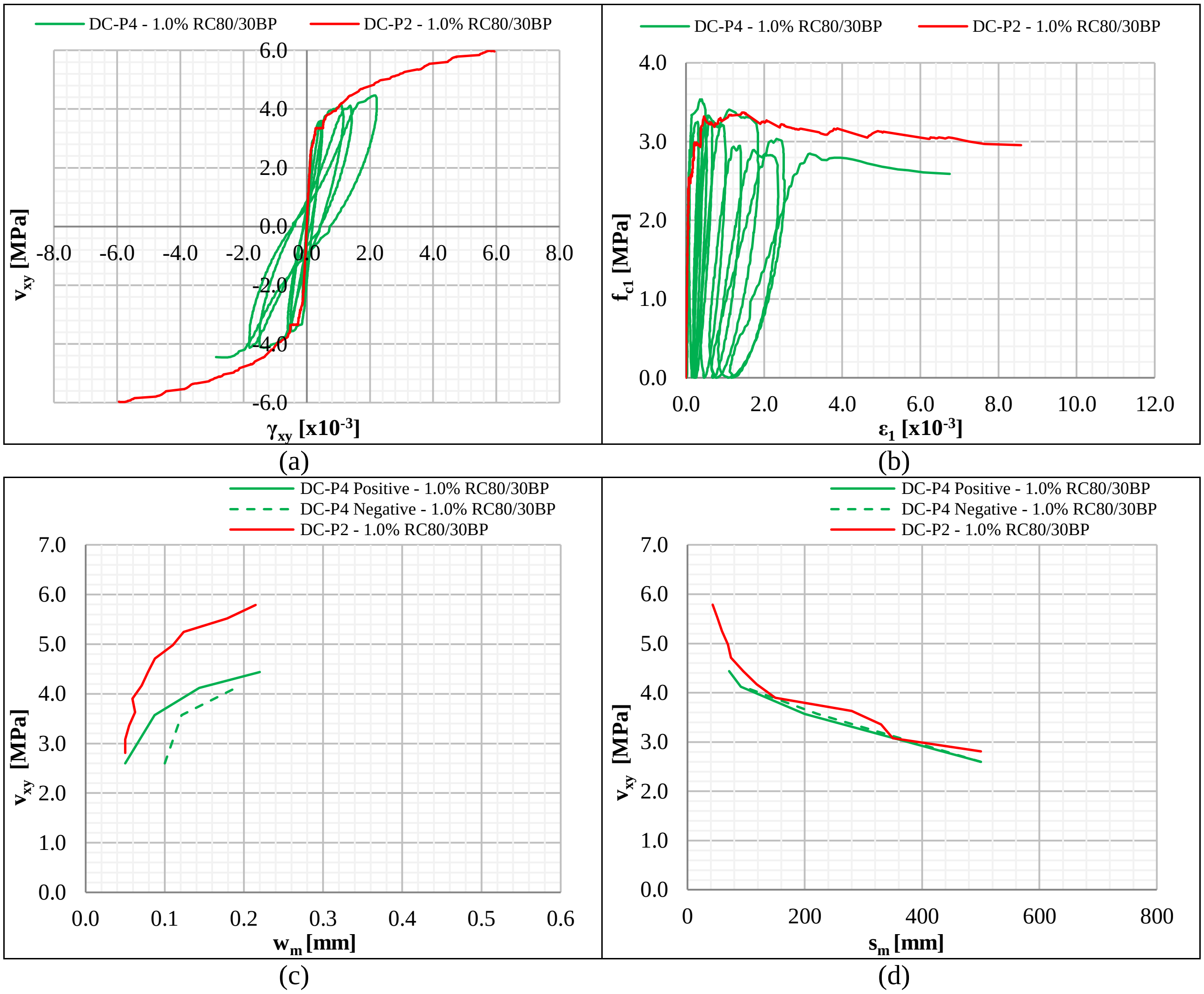

Figure 4.37: Influence of reversed cyclic loading on SFRC panel test responses: (a) $v_{xy} - \gamma_{xy}$; (b) $f_{c1} - \varepsilon_1$; (c) $v_{xy} - w_m$; (d) $v_{xy} - s_m$

4.5.3.3.3 Macro-Synthetic Fibre Reinforced Concrete

The responses of DC-P3 and DC-P5 are presented in Figure 4.38. Again, the shear response was detrimentally affected by the reversed cyclic loading protocol. The maximum shear stress attained was reduced by 11% and the ultimate shear strain was reduced by 35%. However, when compared to the degradation experienced by the SFRC panel, the degree of degradation was not as severe. This is further supported by observing the responses presented in Figure 4.38.

Up until the last cycle of the twelve performed, the principal tensile stress versus principal tensile strain response did not undergo significant degradation. The maximum tensile stress and strain attained for most of the cycles matched closely with that of the monotonically loaded DC-P3.

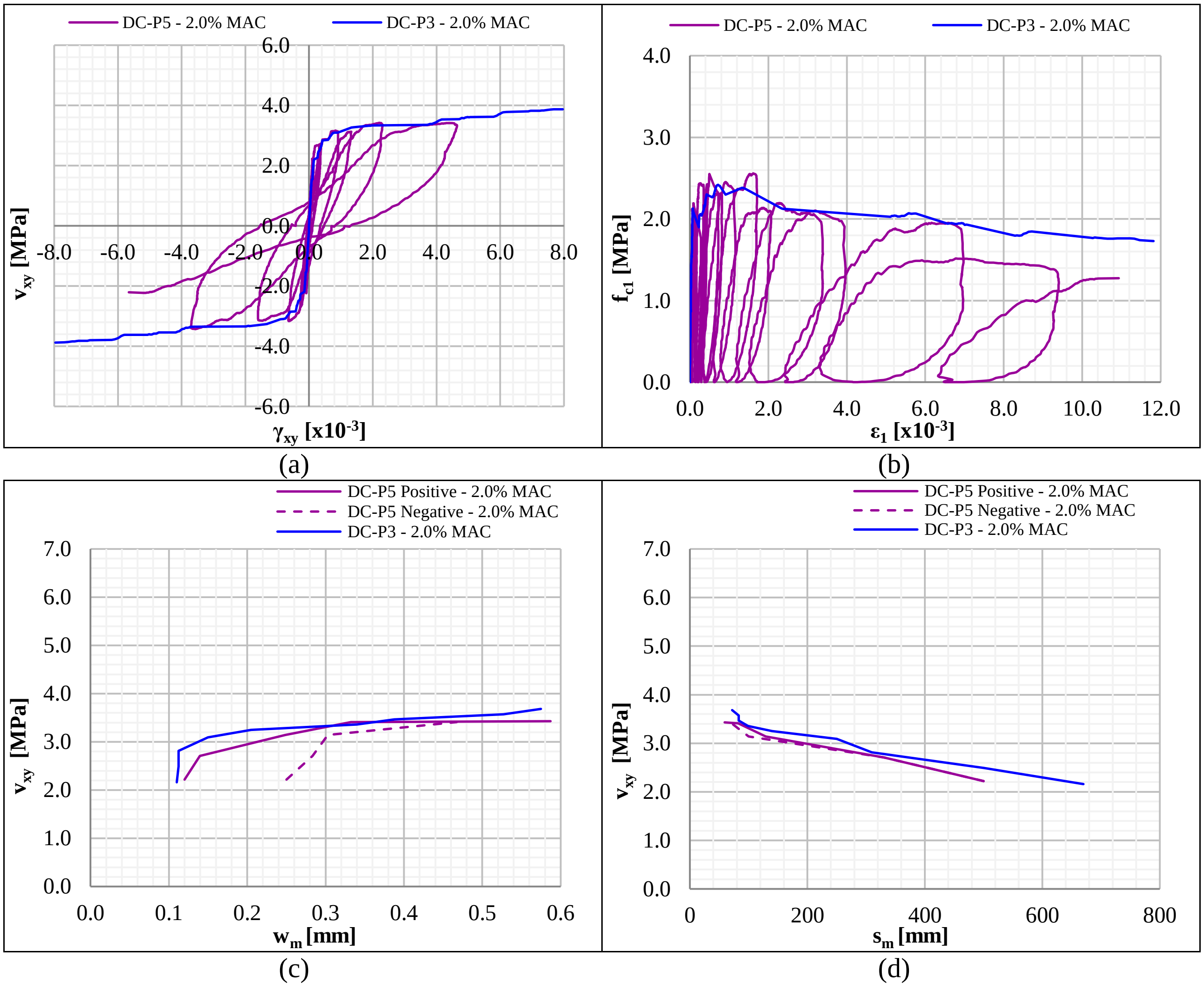

Figure 4.38: Influence of reversed cyclic loading on PPFRC panel test responses: (a) $v_{xy} - \gamma_{xy}$; (b) $f_{c1} - \varepsilon_1$; (c) $v_{xy} - w_m$; (d) $v_{xy} - s_m$

Also, even though cracks did not fully close and large crack slips occurred (evident from the positive principal compressive strains exhibited in Figure 4.39 (d)), the maximum principal compressive stress attained during the test was similar to that of DC-P3. Converse to SFRC, the average crack spacing and average crack widths were similar throughout the duration of the cyclic test, meaning that the ability of these fibres to transmit tensile stresses across the cracks and generate further cracking was not significantly affected by the crack slip and lack of crack closing caused by the reversed cyclic loading protocol. The crack spacing and crack width at failure, and the failure plane, were nearly identical between the monotonic and reversed cyclic test. Lastly, at failure, the principal tensile strain attained was 10.94x10^{-3}, which represented a relatively small reduction of 7.4% as compared to the monotonic test. This ultimate tensile strain was also larger than that of any of the SFRC specimens tested, whether under reversed cyclic or monotonic loading protocols.

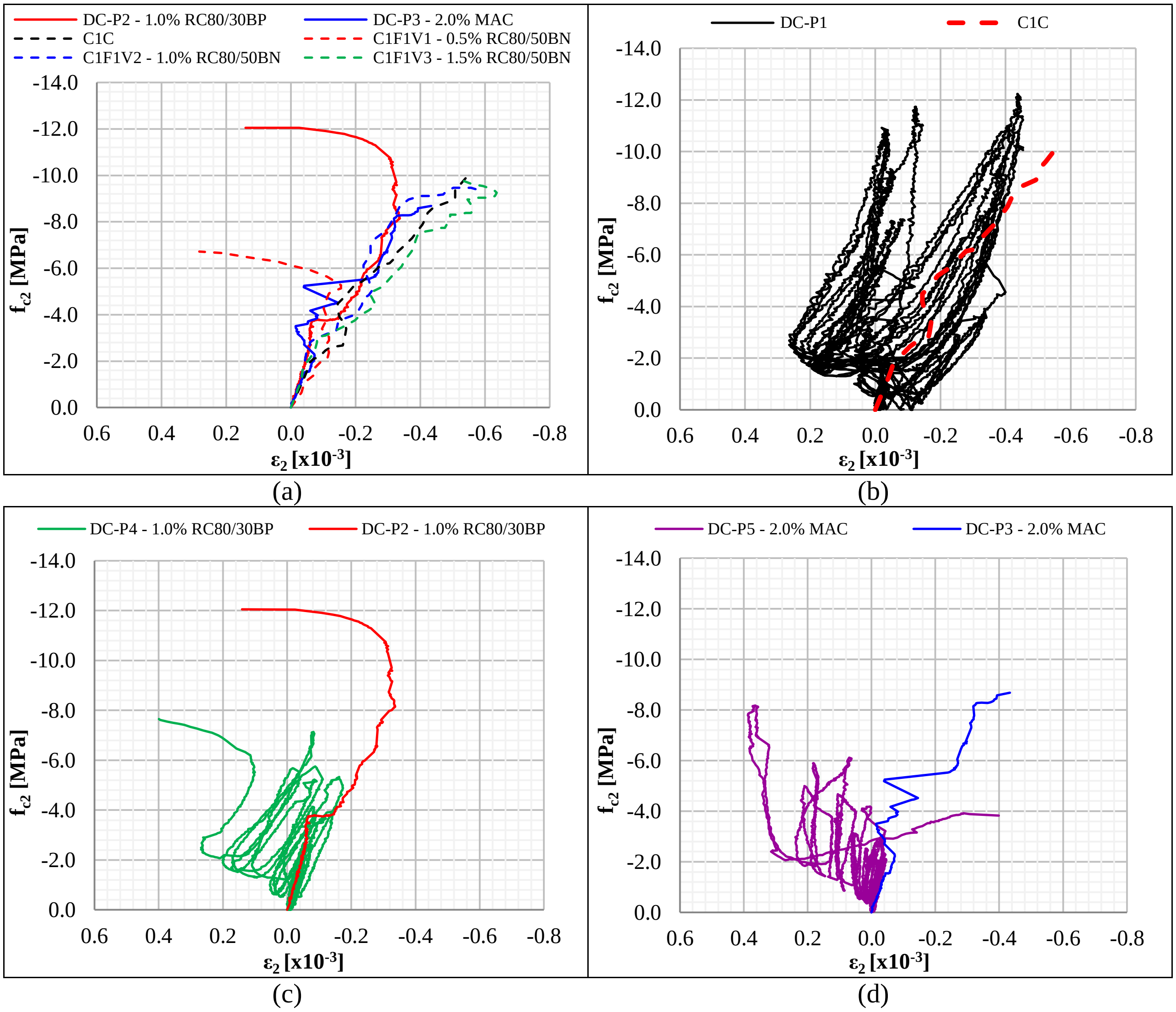

Figure 4.39: Comparison of $f_{c2} - \varepsilon_2$ relationships: (a) Comparison of panels tested under monotonic shear; (b)(c)(d) Comparison of panels tested under reversed cyclic shear

4.5.3.3.4 Comparison

The load-carrying and crack-bridging tendencies of short, stiff, end-hooked steel fibres were reduced when a cyclic loading regime was considered. The fibres exhibited bond degradation and a straightening of the end-hooks. After completion of the tests, the steel fibres subjected to cyclic loading exhibited a wavy shape, evidence of plastic fibre deformation due to repetitive stretching and buckling of the fibres (Filiatraut et al., 1994). This was also consistent with the findings of the uniaxial tension tests. Conversely, the crack control characteristics and principal tensile stress-strain response of the PPFRC specimen showed that long, flexible macro-synthetic fibres did not suffer the same degree of degradation. The low stiffness of the fibres allowed for flexibility as cracks began to slip, preventing the breakdown of fibre-concrete bond. Overall, the energy absorption was better where the PPFRC fibres were used. However, it is clear that full stirrup replacement using fibres for shear-critical structures subjected to reversed cyclic loads is not possible (Gencoglu and Eren, 2002).

4.6 Summary of Experimental Findings

In summary, the following preliminary conclusions can be drawn using the results of this experimental work:

1. The pre-peak compressive behaviour was not affected by the presence of fibres. The modulus of elasticity and 28-day compressive strengths exhibited no systematic differences as a result of fibre addition.
2. The post-peak compressive behaviour of concrete was improved; the strain at peak stress was increased for all FRC specimens, and greater ductility and toughness in compression was achieved. Short steel fibres exhibited the greatest improvement in toughness.
3. The compressive response of 2.0% by volume PPFRC was similar to that of 1.0% by volume end-hooked steel FRC.
4. Similarly, the pre-cracked direct tension response was not affected by the addition of fibres.
5. After cracking, under direct tension all FRC specimens exhibited a gradual and ductile release of load as the fibres pulled out or ruptured.
6. PPFRC specimens in direct tension exhibited an abrupt drop in load immediately after cracking, before strengthening. Steel fibres engaged at a smaller crack width and achieved a post-cracked peak at a lower crack width. However, the residual load-carrying capacity of SFRC dropped more suddenly than that of PPFRC.
7. 2.0% by volume PPFRC dogbones attained residual tensile strengths similar to those of 1.0% by volume SFRC above a crack width of about 2 mm. Below this crack width, the macro-synthetic fibres did not transmit significant tensile stresses. Increased fibre bond

strength (through mechanical anchorage) and higher fibre stiffness may improve the response.

8. A few of the macro-synthetic fibres ruptured, suggesting that a higher ultimate strength of these fibres would be needed if stiffness and anchorage are improved. This would help preserve the ductility exhibited by PPFRC specimens.
9. In cyclic direct tension, SFRC experienced a reduction in post-cracked load-carrying capacity. This same reduction was not exhibited by the PPFRC specimen.
10. In flexural tension, the same findings were made. The SFRC four-point bending prisms exhibited strain hardening followed by a ductile and controlled release of load. The equivalent flexural strength ratio of these was higher than that of PPFRC.
11. The PPFRC exhibited the same sudden drop in load in flexural tension as seen in direct tension. However, one of the four PPFRC prisms tested exhibited strain hardening. The flexural load-deflection curve of 2.0% by volume PPFRC was similar to that of 1.0% by volume end-hooked SFRC. As with direct tension, improvement is needed at low mid-span displacements.
12. The in-plane shear panel tests showed that the response attained by panels reinforced with 1.0% by volume steel fibres was reasonably similar to that of low amounts of conventional transverse steel reinforcement. The strength capacity of PPFRC was not sufficient.
13. PPFRC shear panel specimens exhibited large improvements in ductility over conventionally reinforced concrete and SFRC.
14. The short, end-hooked steel fibres exhibited the best crack control characteristics. In general, the PPFRC panels saw fewer and larger cracks at all stages.
15. The monotonic response of PPFRC in pure shear was similar to that of 0.5% end-hooked SFRC, with significant improvements in ductility.
16. In reversed cyclic-shear, the SFRC panel exhibited significant degradation when compared to the monotonic counterpart. Failure occurred at a much lower shear stress, shear strain and principal tensile strain. Crack control characteristics were negatively affected as the fibres showed evidence of plastic deformation.

17. The PPFRC panel did not exhibit the same level of degradation. Shear stress, peak tensile strain and crack control at failure were not as severely affected. Plastic deformation of the fibres was not observed and, thus, the ability of the fibres to transmit stresses across the cracks was not negatively affected.

In general, the SFRC specimens performed better in terms of post-cracked strength. PPFRC specimens performed better in terms of ductility and residual strength capacity at significant levels of cracking. Also, the overall effect of reversed cyclic loading on the response of FRC was negative; full replacement of conventional transverse steel reinforcement in reversed cyclically loaded structural elements is not yet advisable from the results of this work.

Chapter 5
Constitutive Model Development

5 Constitutive Model Development

5.1 Introduction

In this chapter, the details of a rational modification to the Simplified Diverse Embedment Model (SDEM) for the prediction of the tensile behaviour of polypropylene fibre reinforced concrete will be discussed. Currently, the SDEM is used for the prediction of the tensile behaviour of SFRC using either straight or end-hooked steel fibres (Lee et al., 2013). At first, the full (DEM) and simplified (SDEM) Diverse Embedment Models will be presented in more detail. Next, the proposed modifications and rationale for modelling decisions will be discussed. Finally, the model will be used to predict the behaviour of dogbones DC-DB1, DC-DB2, DC-P3 and DC-P5 using simple spreadsheet calculations.

After completion of the model development, the modifications were implemented into the finite element analysis software VecTor2, again building upon the finite element analysis implementation of the SDEM for steel fibres already included in the program source code. In Chapter 6, the details of a few finite element models of PPFRC specimens will be presented. The successes of the proposed modification and possible areas for future work will be mentioned.

5.2 Models for Steel Fibre Tension

The SDEM is a rational method of evaluation of the contribution of steel fibres to the plain concrete tension softening response. This model is a simplification to the full Diverse Embedment Model (DEM), such that implementation into finite element analysis software, design codes and standards could be more straightforward (Lee et al., 2011a; Lee et al., 2013).

5.2.1 The Diverse Embedment Model

In the DEM, the problem of fibre pull-out from a concrete matrix is solved analytically with consideration given to the slip of the fibre on both sides of the crack. That is to say that the width of the crack is the sum of the slips of the longer embedded part of the fibre, l_f - l_a, and the shorter embedded part of the fibre, l_a, as shown in Figure 5.1. The elastic deformation of the fibre is not considered as it has been shown to be negligible (Nammur and Naaman,1989; Voo and Foster, 2003). This represents the compatibility relation for the model. The equilibrium requirement is that the axial force in each segment of the fibre at the crack must be equal, which reduces to the relationship shown in Equation 5.2. Finally, a constitutive relation is used to relate the bond stress to the bond slip between a straight fibre and the concrete matrix. This is shown in Figure 5.2 and is adapted from the work of Lim et al. (1987) and subsequently Nammur and Naaman (1989). These compatibility, equilibrium and constitutive relations are used to derive the average stress in a fibre aligned perpendicular to the crack at the crack location, $\sigma_{f,cr,avg}$. If the fibre is hooked, then the constitutive relation for force due to mechanical anchorage versus bond slip in Figure 5.3 is incorporated into the solutions as well.

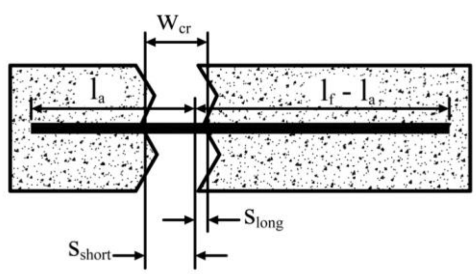

Figure 5.1: Compatibility relation of fibre embedded on both sides

$$\pi d_f(l_a - s_{short})\tau_{f,short} = \pi d_f\left(l_f - l_a - s_{long}\right)\tau_{f,long} \tag{5.1}$$

This equilibrium and compatibility condition cannot be directly solved, and an iterative procedure must be used to ensure equilibrium is satisfied. Further complications arise, due to the random orientation of fibres. Across the crack, the length of the shorter embedded part of the fibre will vary from $0 \leq l_a \leq l_f/2$, and the angle of orientation of the fibre to the perpendicular to the crack surface, θ, will vary from $0 \leq \theta \leq \pi/2$ for all fibres in the matrix. Thus, the probability of any given fibre having a certain embedded length and fibre orientation angle is also considered in the model, creating a complex relationship. In addition, the theoretical solution for the fibre orientation factor for three-dimensional members, $\alpha_{f,3D}$, is derived based on the probability density function of the fibre orientation angle, $sin\,\theta$. This is used to represent the effectiveness of the fibres to carry axial loads across the crack, based on their orientation to the crack. This factor is combined with $\sigma_{f,cr,avg}$ to determine the total tensile stress provided by the fibres averaged over the concrete cross section, f_f:

$$f_f = \frac{1}{A_c} \int_{A_c} \alpha_{f,3D}(y,z)\, V_f \sigma_{f,cr,avg}(y,z) dA_c \tag{5.2}$$

where:

y, z = location of a point on the crack surface on an axis system parallel to the crack surface.

This formula for the determination of f_f has shown good agreement with dogbone tests (Lee et al., 2011b), yet the solution of the equation involves an iterative procedure using a double numerical integration, as a result of the need to consider the variation in fibre embedment length and angle. The implementation of such a procedure into finite element analysis software is complex and, thus, a simplification to the model has been developed (Lee et al., 2013).

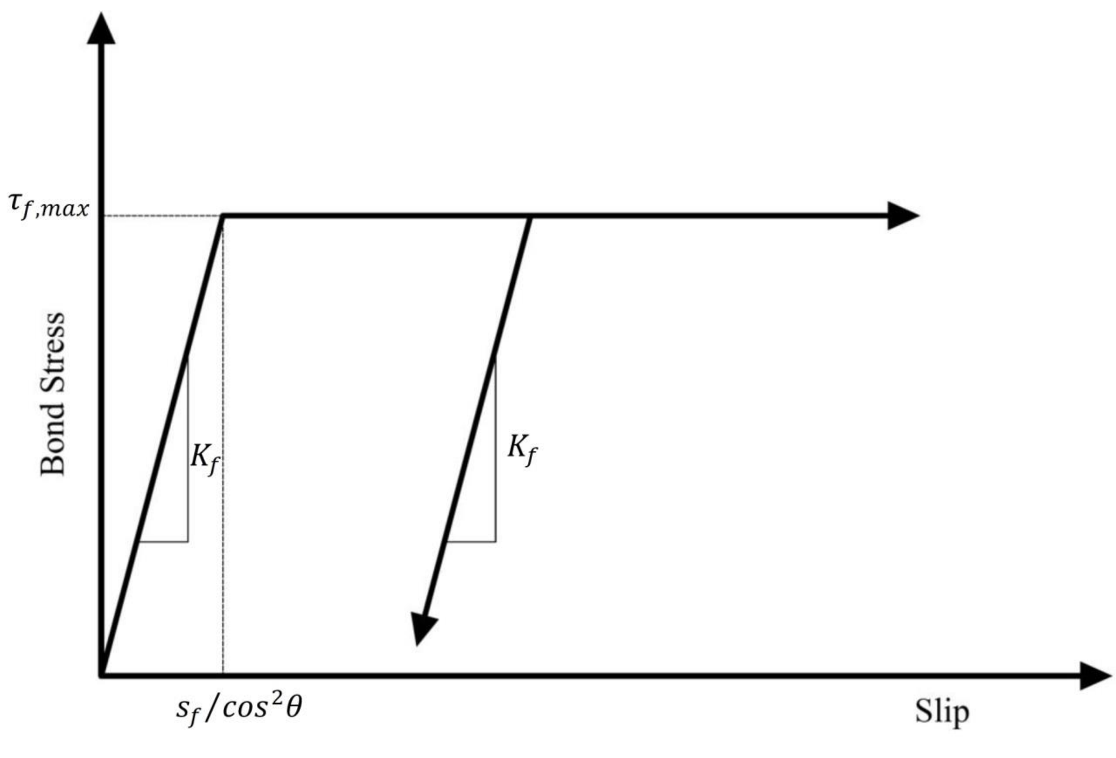

Figure 5.2: Bond stress-slip relationship due to friction (Lee et al., 2011; Nammur et al., 1989)

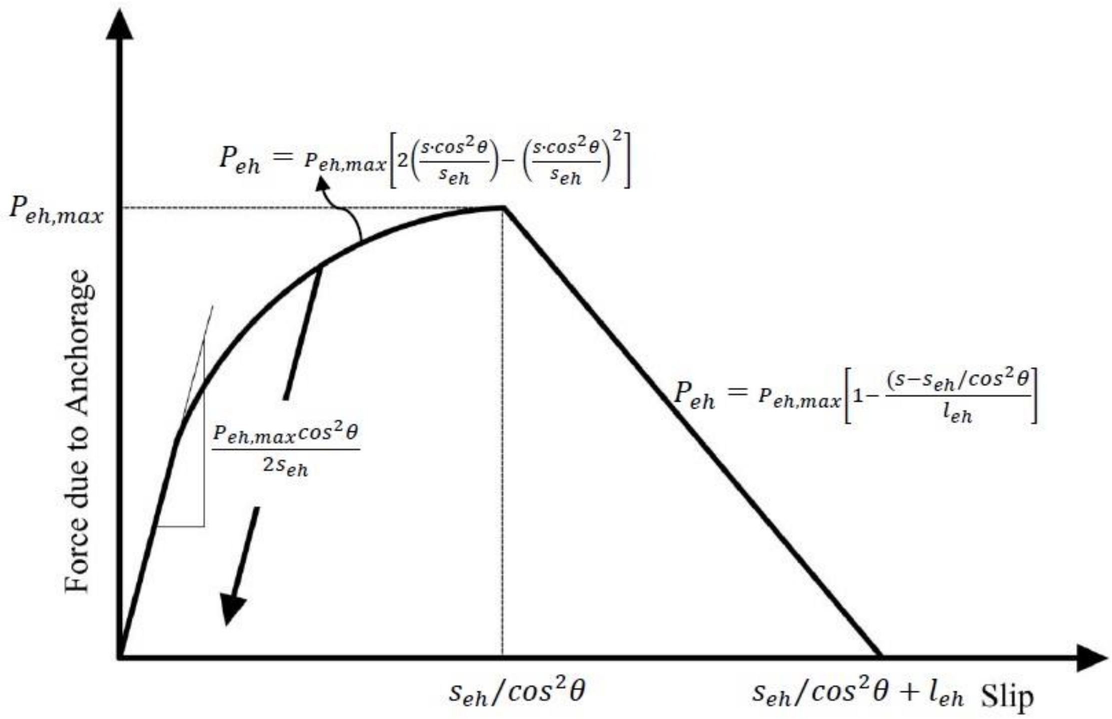

Figure 5.3: Mechanical force-slip relationship used in the DEM and SDEM (Lee et al., 2011)

5.2.2 The Simplified Diverse Embedment Model

5.2.2.1 Model Assumptions

A number of simplifying assumptions are made to reduce the Diverse Embedment Model to a direct relationship between the crack width and the average tensile stress in the fibres.

First, the assumption is made to ignore the slip of the longer embedded part of the fibre. This makes the compatibility relationship much simpler and eliminates the need for the iterative double numerical integration. However, Lee (2013) notes that at small crack widths the effect of fibre slip on the longer embedded side can be significant. This can be expected because, at crack widths below s_f or s_{eh}, full debonding of the shorter side has not yet occurred, meaning that the slip of the longer side could be large, depending on the ratio of the embedded lengths of the two sides of the fibre. In this case, if the fibre slip of the longer embedded part is neglected, then the fibre tension would be greatly overestimated. Thus, some coefficients are developed to prevent this overestimation at low crack widths. For the frictional bond component, the factor is set at $\beta_f = 0.67$; for the mechanical anchorage component the factor is set at $\beta_{eh} = 0.76$, as these show good correlation with the DEM (Lee et al., 2013). At crack widths above s_f or s_{eh}, the shorter embedded length will have fully debonded. To maintain equilibrium, the longer embedded portion of the fibre experiences unloading and, thus, recovers some of the slip on this side of the fibre (Wang et al., 1988). Thus, this assumption will hold with the inclusion of the β factors at low crack widths.

In addition, two simplified equations for the fibre orientation factor, one for 2D applications and one for 3D applications, are derived to fit the theoretical equation for fibre orientation factor presented in the DEM. This has been shown to correspond well with the theoretical solution (Oh, 2011) and is thus employed in the SDEM. The relationship for three-dimensions (as presented in Equation 2.3) is:

$$\alpha_f = \frac{0.13}{(bh/l_f^2)^{1.12}} + 0.087\left(\left(\frac{l_f}{b}\right)^{1.12} + \left(\frac{l_f}{h}\right)^{1.12}\right) + 0.5 \qquad (2.3)$$

and the two-dimensional relationship (Equation 2.4) is:

$$\alpha_f = \begin{matrix} -0.05 * \left(\frac{h}{l_f}\right)^{2.8} + 0.64 & for \ \frac{h}{l_f} \leq 1 \\ 0.087 * \left(\frac{l_f}{h}\right)^{1.12} + 0.5 & for \ \frac{h}{l_f} > 1 \end{matrix} \qquad (2.4)$$

From these assumptions, the relationships for the SDEM can be derived.

5.2.2.2 Bond Relationships Used in the SDEM

Consistent with the DEM, the constitutive relationships used in the SDEM are those presented in Figure 5.2 and Figure 5.3.

The relationship for frictional bond behaviour used by Lee (2011a) is adapted from that proposed by Lim et al. (1987) and Nammur and Naaman (1989). The original relationship, however, did not consider the effects of the fibre angle of inclination on the bond strength, $\tau_{f,max}$, or the fibre slip at which the maximum bond strength is achieved, s_f. However, pull-out tests on deformed steel fibres by Banthia and Trottier (1994) revealed that the slip at maximum bond stress increased as the fibre inclination angle increased. This has been attributed to local crushing of the concrete where the fibre enters the matrix, resulting in a straightening of the inclined fibre and leading to an increased slip (Banthia and Trottier, 1994). Thus, Lee (2011a) considers this by relating the slip at maximum stress to the fibre inclination angle through:

$$s_{f,\theta} = \frac{s_f}{cos^2\theta} \tag{5.5}$$

This idealized relationship matches well with the results of the end-hooked fibre pull-out tests performed by Banthia and Trottier (1994) (Figure 2.1(a)).

For the bond strength, the findings of the same end-hooked fibre pull-out tests are used (Figure 2.1(b)). These tests showed that no correlation exists between the fibre inclination angle and the bond strength. There is some contradiction in the literature on this topic. Other tests performed by Banthia and Trottier (1994) using crimped fibres, as well as the pull-out tests executed by Ouyang et al. (1994), showed an increase in pull-out strength for fibre inclintation angles above 30°. However, tests performed by Lee and Foster (2007) showed a decrease in the bond strength of a straight fibre with an increase in fibre inclination angle. As a result of this uncertainty, the bond strength is treated as constant and independent of the fibre alignment.

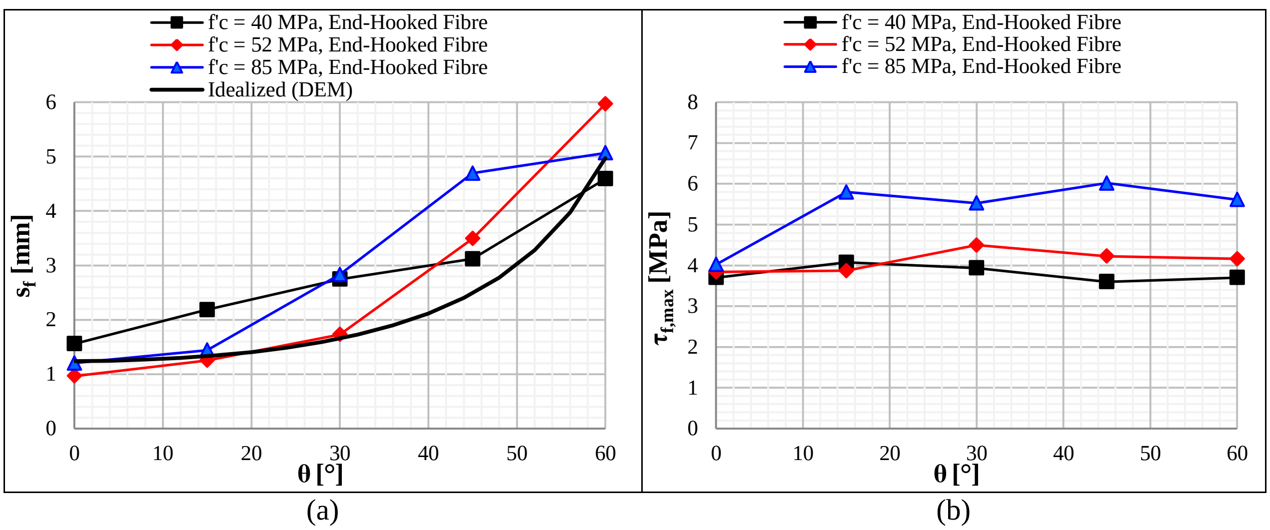

Figure 5.4: Effect of fibre inclination angle on: (a) slip at pull-out strength, (b) pull-out strength (Banthia and Trottier, 1994; Lee et al., 2011a)

Figure 5.3 presents the constitutive relationship for the contribution of mechanical anchorage to the overall bond response. According to the pull-out tests performed by Sujivorakul et al. (2000) on straight steel fibres with end anchorage, significantly higher pull-out forces are achievable with mechanical deformations. This tensile force is idealized with a parabolic pre-peak and a linear post-peak relationship. The slip at the peak mechanical anchorage force is dependent on the fibre inclination angle, but the peak mechanical anchorage force is taken as constant.

In order to employ these constitutive relationships in the SDEM, some reasonable values for the unknown parameters are required. Voo and Foster (2003) present values for the bond strengths of individual straight and end-hooked fibres as part of the Variable Engagement Model. These values are shown in Table 5.1, and are used in the DEM and SDEM as well. It is worth noting that the maximum force due to mechanical anchorage in the constitutive law can be related to the mechanical anchorage strength through:

$$\tau_{eh,max} = \frac{2 \cdot P_{eh,max}}{\pi d_f l_f} \tag{5.6}$$

with the assumption that the maximum force is obtained if the fibre embedded length is half of the total fibre length (Lee et al., 2013). These bond strength values have been shown to match well with experimental results when used with the DEM (Lee et al., 2011b).

Table 5.1: Pull-out Strength of Steel Fibers (Voo and Foster, 2003)

Fibre Type	Matrix Type	Pull-out Strength
End-Hooked	Concrete	$\tau_{f,tot} = 2.5 * f_t' = 0.825\sqrt{f_c'}$ $[MPa]$ so $\tau_{eh,max} = 0.429\sqrt{f_c'}$ $[MPa]$
	Mortar	$\tau_{f,tot} = 2.0 * f_t' = 0.660\sqrt{f_c'}$ $[MPa]$ so $\tau_{eh,max} = 0.330\sqrt{f_c'}$ $[MPa]$
Straight	Concrete	$\tau_{f,tot} = \tau_{f,max} = 1.2 * f_t' = 0.396\sqrt{f_c'}$ $[MPa]$
	Mortar	$\tau_{f,tot} = \tau_{f,max} = 1.0 * f_t' = 0.330\sqrt{f_c'}$ $[MPa]$

For the values of s_f and s_{eh}, the pull-out tests performed by Naaman and Najm (1991) were used. In this paper, the full experimental load-slip curves were presented for straight, deformed and end-hooked steel fibres. Selected results of these tests are presented in Section 5.3.2.2. The experimental test setup did not measure the elastic deformation of the fibres but, for the straight fibres, the values of slip at peak load were presented after subtracting the theoretical elastic component. From this, s_f was found to be consistently around 0.01 mm. For the end-hooked fibres, the elastic deformation was also not considered, yet it was clear from the experimental results that the peak loads occurred at much higher slips. Also, it has been noted in the literature that at high slips, the typical pull-out test method used may be measuring other effects, such as machine softening (Wang et al., 1988). Using this knowledge, and the response of the dogbone tests performed by Susetyo (2009), an s_{eh} of 0.1 mm was selected. These values for s_f and s_{eh} yield a good estimation of the response of the Susetyo (2009) dogbone tests, as demonstrated in Figure 4.32 (c), (d) and (e) (Lee et al., 2011b). Lastly, the value of l_{eh}, used to represent the termination of mechanical anchorage, was selected as 4 mm, as this is the length of the end-hook for the RC80/30BP fibres and is consistent with past research (Sujivorakul et al., 2000).

5.2.2.3 Relationship for Frictional Bond Behaviour

In order to complete the derivation of the SDEM, these relationships for bond stress versus bond slip must then be utilized to determine the average bond stress in the fibres at the crack, $\tau_{f,avg}$. This is done by summing the bond stress of all the fibres for all possible fibre inclination angles (using a probability density function of $sin\,\theta$) and taking the average (Lee et al., 2011a). Since the constitutive relation for frictional bond behaviour is bi-linear, the solution must be undertaken in two parts. The first phase is for small crack widths ($w_{cr} < s_f$), such that all fibres are experiencing elastic bond behaviour. The second phase occurs when the crack width is sufficiently large ($w_{cr} \geq s_f$) such that some fibres have entered the plastic portion of the constitutive law depending on the fibre inclination angle. Thus, the solution for average bond stress is piecewise. In addition, due to the assumption that the crack width is equal to the slip on the shorter embedded side of the fibre, the relationship between bond stress and crack width is identical to that for bond stress and slip. As mentioned before, the β_f factor is used to account for the overestimation of bond stress for those fibres in the elastic portion of the curve. Thus, in phase one, the solution for average bond stress is:

$$\tau_{f,avg} = \begin{matrix} \beta_f \dfrac{2\pi \cdot \int_0^{\pi/2} \dfrac{w_{cr}}{w_{p\theta,f}} \tau_{f,max} sin\theta d\theta}{2\pi} \\ \dfrac{\beta_f}{3} \dfrac{w_{cr}}{s_f} \tau_{f,max} \end{matrix} \qquad for\; w_{cr} < s_f \qquad (5.7)$$

where:

$w_{p\theta,f}$ $= s_f / cos^2\theta$.

Similarly, in phase two:

$$\tau_{f,avg} = \begin{cases} \dfrac{2\pi \cdot \int_0^{\theta_{crit,f}} \tau_{f,max} sin\theta d\theta}{2\pi} + \beta_f \dfrac{2\pi \cdot \int_{\theta_{crit,f}}^{\pi/2} \dfrac{w_{cr}}{w_{p\theta,f}} \tau_{f,max} sin\theta d\theta}{2\pi} \\ \left(1 - \sqrt{\dfrac{s_f}{w_{cr}}} + \dfrac{\beta_f}{3}\sqrt{\dfrac{s_f}{w_{cr}}}\right)\tau_{f,max} \end{cases} \quad for\ w_{cr} \geq s_f \quad (5.8)$$

where:

$\theta_{crit,f}$ = the critical fibre inclination angle at which frictional bond behaviour will commence for a given crack width; $\theta_{crit,f} = cos^{-1}\left(\sqrt{s_f/w_{cr}}\right) \quad for\ w_{cr} \geq s_f$.

Finally, this average frictional bond stress can be converted into the average fibre tensile stress at the crack, $\sigma_{f,cr,st}$, by integrating the average frictional bond stress over the embedded length according to the relationships of the DEM. This is done by utilizing a uniform probability density function for the length of the shorter embedded side of the fibre; the resulting relationship is shown in Equation 5.9.

$$\sigma_{f,cr,st} = \tau_{f,avg} \frac{l_f}{d_f}\left(1 - \frac{2 \cdot w_{cr}}{l_f}\right)^2 \quad (5.9)$$

Next, utilizing Equation 3.1 for the number of fibres per unit area of concrete cross section, the full relationship for the frictional bond component of the overall fibre tensile behaviour is found to be:

$$f_{st} = \alpha_f V_f K_{st} \tau_{f,max} \frac{l_f}{d_f}\left(1 - \frac{2w_{cr}}{l_f}\right)^2 \quad (5.10)$$

where:

$$K_{st} = \begin{cases} \dfrac{\beta_f}{3}\dfrac{w_{cr}}{s_f} & for\ w_{cr} < s_f \\ 1 - \sqrt{\dfrac{s_f}{w_{cr}}} + \dfrac{\beta_f}{3}\sqrt{\dfrac{s_f}{w_{cr}}} & for\ w_{cr} \geq s_f \end{cases}$$

This relationship has been shown to match well with the prediction of the DEM, and is much simpler for implementation into design codes/standards, as well as in structural analysis software (Lee et al., 2013).

5.2.2.4 Relationship for Mechanical Anchorage

For mechanical anchorage, an analogous derivation to that of frictional bond behaviour must be undertaken (Lee et al., 2013). According to the constitutive law for mechanical anchorage shown in Figure 5.3, there are three phases to consider; the parabolic ascending branch for $w_{cr} < s_{eh}$, the linear descending branch for $s_{eh} \leq w_{cr} < l_{eh}$, and the failure of mechanical anchorage at large crack widths. The β_{eh} factor is used here as well for the ascending branch of the curve. Thus, in phase one, the solution for the average mechanical force is:

$$P_{eh,avg} = \begin{array}{c} \beta_{eh} \dfrac{2\pi \cdot \int_0^{\pi/2} P_{eh,max} \left[2\left(\dfrac{w_{cr}}{w_{p\theta,eh}}\right) - \left(\dfrac{w_{cr}}{w_{p\theta,eh}}\right)^2\right] sin\theta d\theta}{2\pi} \\ \beta_{eh}\left[\dfrac{2}{3}\dfrac{w_{cr}}{s_{eh}} - \dfrac{1}{5}\left(\dfrac{w_{cr}}{s_{eh}}\right)^2\right] P_{eh,max} \end{array} \quad for\ w_{cr} < s_{eh} \quad (5.11)$$

where:

$w_{p\theta,eh}$ $= s_{eh}/cos^2\theta.$

Similarly, in phase two:

$$\begin{aligned} P_{eh,avg} &= \frac{2\pi \cdot \int_0^{\theta_{crit,eh}} P_{eh,max} \left[1 - \left(\dfrac{w_{cr} - w_{p\theta,eh}}{l_{eh}}\right)\right] sin\theta d\theta}{2\pi} \\ &+\beta_{eh} \frac{2\pi \cdot \int_{\theta_{crit,eh}}^{\pi/2} P_{eh,max} \left[2\left(\dfrac{w_{cr}}{w_{p\theta,eh}}\right) - \left(\dfrac{w_{cr}}{w_{p\theta,eh}}\right)^2\right] sin\theta d\theta}{2\pi} \quad for\ s_{eh} \leq w_{cr} < l_{eh} \quad (5.12) \\ P_{eh,avg} &= \left[1 + \left(\frac{7\beta_{eh}}{15} - 1\right)\sqrt{\frac{s_{eh}}{w_{cr}}} - \frac{\left(\sqrt{w_{cr}} - \sqrt{s_{eh}}\right)^2}{l_{eh}}\right] P_{eh,max} \end{aligned}$$

where:

$\theta_{crit,eh}$ = the critical fibre inclination angle at which the force due to mechanical anchorage will begin to decline for a given crack width; $\theta_{crit,eh} = cos^{-1}\left(\sqrt{s_{eh}/w_{cr}}\right) \quad for\ w_{cr} \geq s_{eh}$.

In phase three, the mechanical anchorage is no longer effective as either the hook in the fibre has straightened or fractured or the concrete tunnel around the fibre has deteriorated. The derivation in this phase is complex, so a simpler parabolic decay was introduced:

$$P_{eh,avg} = \left(\frac{\left(l_f - 2l_{eh}\right) - 2w_{cr}}{l_f - 4l_{eh}}\right)^2 P_{eh,avg,i} \quad for\ l_{eh} \leq w_{cr} < \frac{\left(l_f - 2l_{eh}\right)}{2} \quad (5.13)$$

where:

$P_{eh,avg,i}$ = average tensile force in the fibre due to mechanical anchorage at $w_{cr} = l_{eh}$.

Above $\left(l_f - 2l_{eh}\right)/2$, all mechanical anchorages are assumed to have failed. Finally, similar to frictional bond, the average tensile stress at the crack due to mechanical anchorage can be found, with consideration for a diverse distribution of embedment lengths. This is taken as:

$$\sigma_{f,cr,eh} = \frac{4P_{eh,avg}}{\pi d_f^2}\left(\frac{\left(l_f - 2l_{eh}\right) - 2w_{cr}}{l_f}\right)^2 \tag{5.14}$$

Utilizing Equations 3.1 and 5.6, the full relationship for the mechanical anchorage component of the overall fibre tensile behaviour is found to be:

$$f_{eh} = \alpha_f V_f K_{eh} \tau_{eh,max} \frac{2\left(\left(l_f - 2l_{eh}\right) - 2w_{cr}\right)}{d_f} \tag{5.15}$$

where:

$$K_{eh} = \begin{cases} \beta_{eh}\left[\frac{2}{3}\frac{w_{cr}}{s_{eh}} - \frac{1}{5}\left(\frac{w_{cr}}{s_{eh}}\right)^2\right] & for\ w_{cr} < s_{eh} \\ 1 + \left(\frac{7\beta_{eh}}{15} - 1\right)\sqrt{\frac{s_{eh}}{w_{cr}}} - \frac{\left(\sqrt{w_{cr}} - \sqrt{s_{eh}}\right)^2}{l_{eh}} & for\ s_{eh} \le w_{cr} < l_{eh} \\ K_{eh,i}\left(\frac{\left(l_f - 2l_{eh}\right) - 2w_{cr}}{l_f - 4l_{eh}}\right)^2 & for\ l_{eh} \le w_{cr} < \frac{\left(l_f - 2l_{eh}\right)}{2} \end{cases}$$

and $K_{eh,i}$ is K_{eh} at $w_{cr} = l_{eh}$.

This relation is then added to the frictional bond component and the concrete tension softening curve to determine the total tensile stress in the FRC member:

$$f_{t,FRC} = f_{ct} + f_{st} + f_{eh} = f_{ct} + f_f. \tag{5.16}$$

For the SDEM, the concrete tension softening relationship presented in the VEM is recommended (Voo and Foster, 2003). This relation was given in Equation 2.1:

$$f_{ct} = f_t' \cdot \exp(-15 * w_{cr}) \tag{2.1}$$

These relationships for the SDEM provide a nearly identical prediction to that of the DEM for end-hooked steel fibres. This is shown in Figure 5.5, where the properties of test set C1F1V2 (1.0% by volume RC80/50BN fibres with f_c' = 53.4 MPa) are used with the assumption of an infinite cross section (so α_f = 0.5). As can be seen, the SDEM slightly underpredicts at all crack widths in relation to the DEM but, overall, the estimated response is similar. Thus, considering the direct relationships for fibre tension that have been derived, the benefits of ignoring slip on the longer part of the fibre are favourable (Lee et al., 2013).

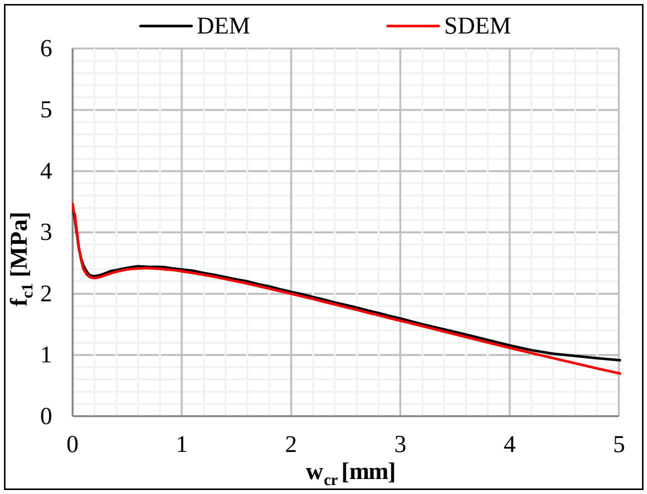

Figure 5.5: Comparison of DEM and SDEM predictions

5.2.2.5 SFRC Dogbone Response Simulations Using SDEM

Figure 4.32 presents the simulations of the responses of select SFRC dogbones using this model. Test sets DC-P2, DC-P4, C1F1V1, C1F1V2 and C1F1V3 are displayed. As can be seen, the response is predicted well with the relationships of the SDEM. However, for the short RC80/30BP fibres, the model underpredicts the fibre tensile response at low crack widths, up to approximately 2.5 mm. This is likely due to the fact that the SDEM considers the total tension force in the fibres to be directly proportional to the volume fraction. However, it has been shown in past studies that a fibre saturation point exists for SFRC members. Above this point, increasing the fibre volume content does not drastically increase the maximum attainable tensile stress (Susetyo, 2009). For the C1F1 series of dogbones, the responses are well predicted in terms of post-cracked stress decay, peak residual tensile stress, and crack width at peak residual tensile stress. The prediction becomes less accurate as the fibre volume content increases, again suggesting that the effect of fibre volume fraction on the response of SFRC members should be further investigated. In addition, the coefficient of variation for fibre orientation factor has been found to be as high as 20%; the fibre tensile stress may be frequently over or underpredicted by this amount (Oh, 2011). With this factor in mind, the predictions are reasonable, which is why the decision was made to use the SDEM as the baseline for the modelling of PPFRC.

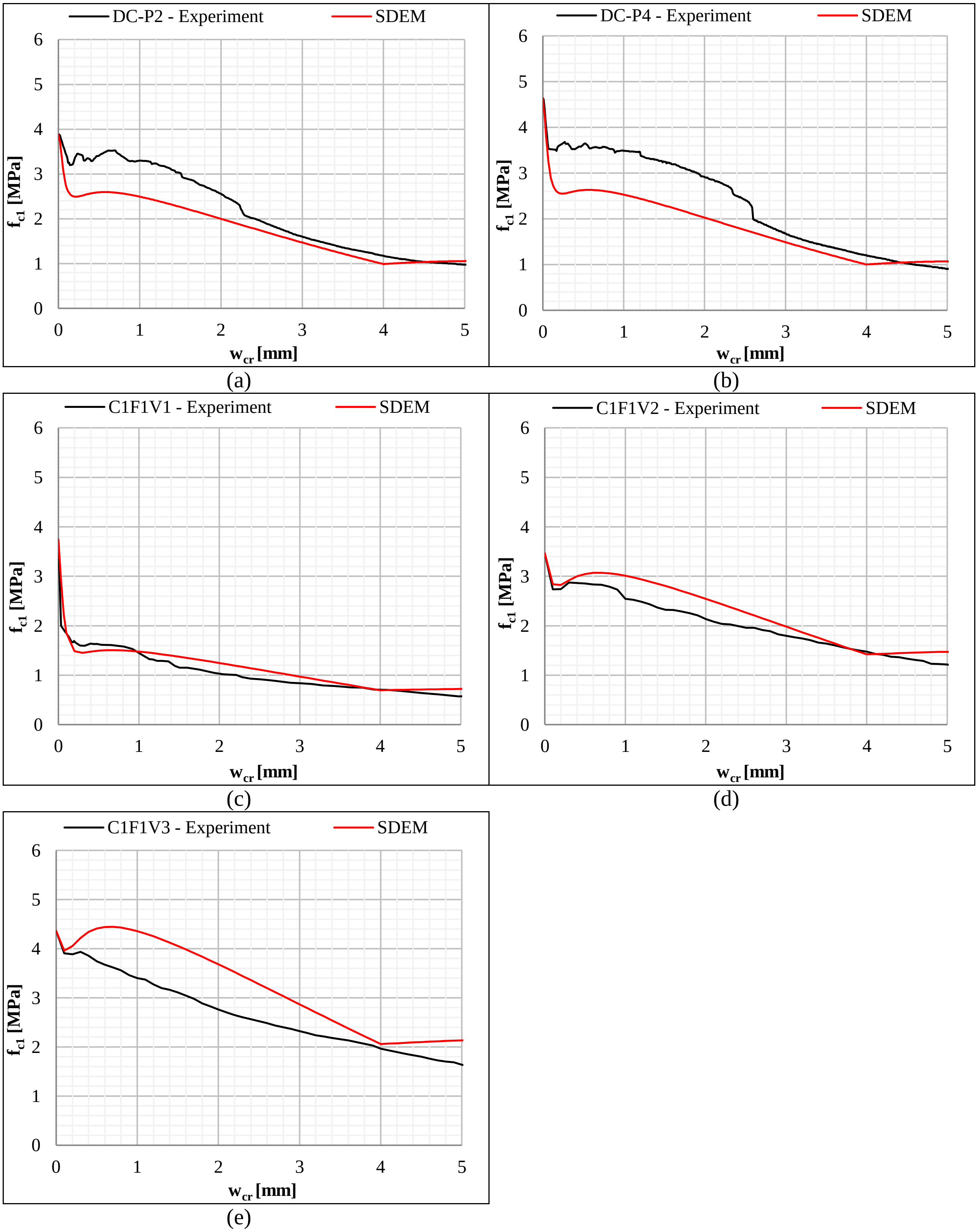

Figure 5.6: Experimental versus SDEM estimation for SFRC dogbones

5.3 Modelling of Macro-Synthetic Fibre Reinforced Concrete

In order to adjust the existing SDEM model so that it may be used for macro-synthetic fibres, the assumptions of the model must be verified for this new material. It must be determined if the relationships of the model are suitable. In addition, the bond parameters used for steel fibre reinforced concrete must be investigated and adjusted to represent the behaviour of macro-synthetic fibre reinforced concrete. To do this, a literature review was undertaken to determine if assumptions inherent in the model are applicable to the behaviour of synthetic fibres. Then, some rational bond parameters were selected, using both the findings in the literature and the results of the uniaxial direct tension dogbone specimens. This procedure is used in lieu of reliable pull-out tests of macro-synthetic fibres, as such test programs have not been performed yet, both in general and specifically for the MAC Matrix fibres used herein.

5.3.1 Assumptions of the SDEM

The assumptions used in the SDEM for steel FRC must be investigated and applicability for macro-synthetic FRC must be verified. First, the fundamental problem of fibre pull-out remains the same regardless of material type (Naaman et al., 1991a). Thus, the equilibrium and compatibility relationships presented in Equation 5.2 and Figure 5.1 are unaffected.

Next, the fundamental assumption of the SDEM contends that the crack width is equal to the slip of the shorter embedded part of the fibre. With the inclusion of the β_f and β_{eh} factors, the relationships of the SDEM are shown to match the estimation of the DEM when slip of the longer embedded part of the fibre is neglected (Figure 5.5). The material type will have no effect on this aspect. Also inherent in this condition is the assumption that the elastic deformation of the fibre can be neglected. For polypropylene fibres, this has not been investigated in detail. However, at large slip displacements, axial fibre deformations have been shown to have little effect on the overall response (Sujivorakul et al., 2000; Naaman et al., 1991b). At low values of slip, overestimation of fibre contribution as a result of the assumption to ignore the slip of the longer embedded side of the fibre has already led to the introduction of the β_f and β_{eh} factors in the model. Thus, in a sense, ignoring elastic deformation at low crack widths has already been handled, as overestimation of bond stress at low crack widths has already been controlled. More specifically, as mentioned in Chapter 4, at small crack widths flexible polypropylene fibres are not engaged and do not become effective until they bend around the fibre-matrix entrance points and align in the direction of load (Leung and Ybanez, 1997). As shown in the experiments, this happened at relatively large crack widths. This is because the fibres are not perfectly flexible and instead have some finite stiffness, so some load and energy must be used during the cracking process to cause these fibres to bend (Leung and Ybanez, 1997). Thus, at small crack widths, only a few aligned fibres have become engaged and begin to transmit stresses, while the non-aligned fibres absorb the energy required to become bent into the loading direction. At larger crack widths, all fibres become engaged and frictional/mechanical anchorage bond stresses begin to develop, lending to the increase in residual tensile stresses after engagement (Won, Lim and Park, 2006). This is consistent with the observation of a few fibre ruptures during dogbone tests as shown in Figure 5.7. It is postulated that the ruptured fibres are those that are sufficiently embedded in the matrix (so as to not pull out) and are roughly perpendicular to the crack without need for alignment; the few fibres meeting these conditions must undergo elastic deformation immediately after cracking while other fibres bend. However, on average, axial elastic deformations do not occur in most fibres until alignment. Since the complete fibre alignment and engagement was observed to occur at large crack widths the elastic deformations of these fibres can be ignored, based on the findings of Sujivorakul (2000). To further support this, it has been shown that high modulus (and, thus, cold drawn) collated, fibrillated polypropylene fibres exhibit a roughly linear-to-rupture tensile behaviour, and with an elongation of 5 to 10% at rupture (Daniel, 1991; Gregor-Svetec and Sluga, 2005; Chatterjee and Deopura, 2006; Li et al., 1991). Thus, taking the maximum residual tensile stresses obtained by the dogbones tested in the experimental program, the average elongation of a straight aligned fibre at this peak stress can be found using this linear-to-rupture axial behaviour (Table 2.1). For test set DC-P5, the post-cracked peak stress was 2.10 MPa (Table 4.3), the mean total number of fibres counted was 137 (Table 3.9), and the average concrete cross-sectional area was 7471 mm^2 (Table 3.9). Thus, using:

$$\varepsilon_f = \frac{\sigma_{f,cr,avg}}{E_f} = \frac{f_f}{\alpha_f V_f E_f} = \frac{f_f A_c}{N_f A_f E_f} = \frac{(2.10\ MPa)(7471\ mm^2)}{(137)(0.515\ mm^2)(10{,}000\ MPa)} \tag{5.17}$$

the average elongation of the fibres is 2.22% under this condition. The fibre elongation accounts for only about 2 to 10% of the crack width on average. Thus, it was concluded that elastic fibre elongation may be neglected in the model for polypropylene fibres as well.

Table 5.2: Average Elongation of Fibres in Dogbone Tests

Test Set	$f_{f,max}$ [MPa]	$N_{f,avg}$	$A_{c,avg}$* [mm^2]	$\sigma_{f,cr,avg}$ [MPa]	ε_f [%]
DC-DB1	2.36	158	7350	213.1	2.13
DC-DB2	2.95	224	7350	187.8	1.88
DC-P3	1.78	166	7690	160.0	1.60
DC-P5	2.10	137	7471	222.2	2.22

Figure 5.7: Fibres approaching rupture during dogbone test

Next, the assumption that the bond strength of the fibres is independent of the fibre inclination angle must be considered. It had been shown in past pull-out tests on polypropylene fibres that the pull-out load increased with the fibre inclination angle. In addition, the fibre inclination angle caused a decrease in fibre pull-out length, due to concrete spalling at the point where the fibre entered the matrix. These two results combined led to an observed increase in fibre bond strength as the fibre inclination angle increased (Li et al., 1990). This is shown in Figure 5.8(a), where the normalized pull-out load, $P_{norm} = P_{f,\theta} l_{po,\theta} / P_{f,0} l_{po,0}$, is plotted against the fibre inclination angle for the tests performed. This increase in pull-out load is a result of the additional frictional snubbing force that is present for flexible fibres, due to the bending of the fibre at the point of entrance to the matrix.

However, as can be seen from Figure 5.8(a), there was a great deal of scatter in the experimental results, particularly at high fibre inclination angles. Also, for fibres inclined at angles less than 45° the normalized pull-out loads were nearly constant and fibre bending was of much greater concern than fibre snubbing (Bentur, 2007). This snubbing effect has not been thoroughly investigated, as no inclined pull-out tests have been performed on macro-synthetic fibres like the ones used in the experimental program. As a result, the decision was made to stay consistent with the original derivation of the SDEM and assume that bond strength is constant and independent of the fibre inclination angle.

Li et al. (1990) used their experimental investigations and proposed a snubbing model to represent the relationship between the fibre inclination angle and bond strength as follows:

$$\tau_{f,max,\theta} = \tau_{f,max} e^{f\theta} \tag{5.18}$$

where:

f = snubbing coefficient = 0.7 for polypropylene fibres.

The experimental results obtained by Li et al. (1990) are consistent with subsequent pull-out investigations performed on synthetic fibres (Leung and Ybanez, 1997). This second paper, though, discredited the snubbing model by stating that it ignores the effects of matrix spalling at high angles. The claim is made that the snubbing would increase as spalling occurs (Bentur, 2007). This leads to an underprediction of the bond strength at high inclination angles (Leung and Ybanez, 1997). In addition to this, inputting the snubbing model into the equations of the SDEM for average bond stress (Equations 5.7, 5.8, 5.11 and 5.12) would lead to complex relationships that are inconvenient for implementation into finite element analysis procedures. Thus, the following relationship is proposed, in keeping with the relationship used for slip (Equation 5.5):

$$\tau_{f,max,\theta} = \frac{\tau_{f,max}}{cos\theta}. \tag{5.19}$$

This relationship, together with the snubbing model and the average normalized pull-out load from Li et al. (1990), is presented in Figure 5.8(b). It is clear that the proposed relationship performs at least as well as the snubbing model at low inclination angles and is better suited to represent the high bond strengths that are attainable at large inclination angles. In addition, this relation can be more easily implemented in the equations of the SDEM. Thus, if further investigations into the snubbing effect are undertaken and the dependence of bond strength on inclination angle is proven, then the relationship proposed in Equation 5.19 can be implemented into the SDEM.

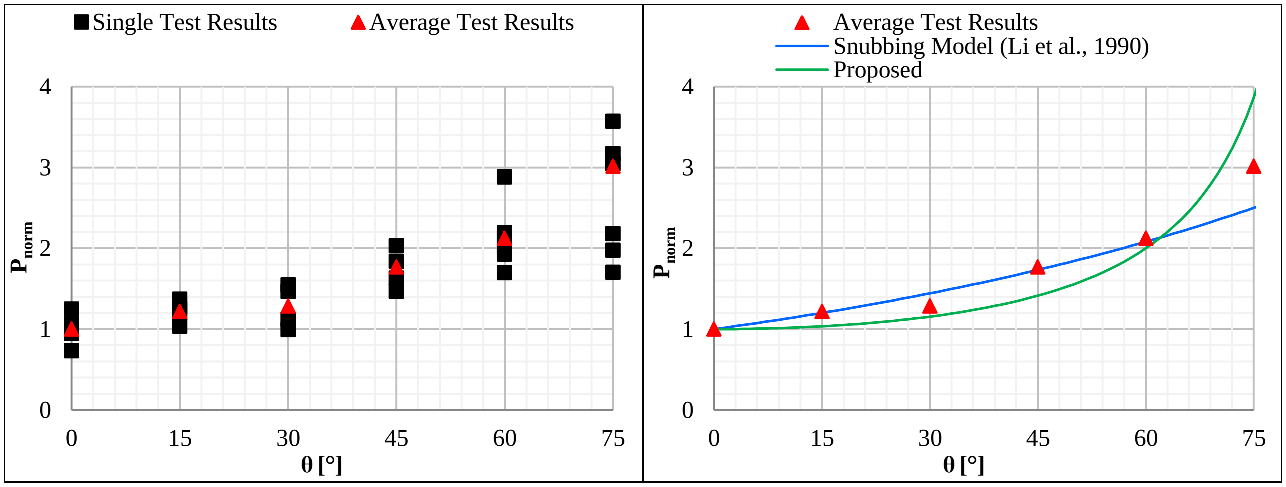

(a) (b)

Figure 5.8: Effect of fibre inclination angle on synthetic fibre pull-out: (a) Experimental results; (b) Analytical representations

5.3.2 Bond Stress-Slip Relationships

From this point, the assumption has been made to treat macro-synthetic polypropylene fibres in an identical way to steel fibres in the SDEM. That is to say, the overall fibre tension is considered to be constituted of the frictional bond behaviour and the mechanical anchorage provided by the surface indentations on the MAC Matrix fibres. In this way, the bond stress versus slip relationship for frictional bond behaviour is the same as that presented in Figure 5.2; the force due to mechanical anchorage versus slip relationship is the same as that shown in Figure 5.3, with the exception that the subscript "eh" can be replaced with the subscript "def" for "deformations". This updated constitutive law is shown in Figure 5.9. The decision to use the same relationships is reasonable as it has been shown that the response of steel and polypropylene fibres with different forms of mechanical anchorages all follow a similar characteristic curve, regardless of the type of mechanical anchorage provided (Naaman and Najm, 1991, Banthia and Trottier, 1994; Sujivorakul et al., 2000; Choi et al., 2012). A linear response is exhibited at low slips up to a "bend-over point," followed by a softened, parabolic response up to the peak. This bend-over point is taken as the end of elastic frictional bond and occurs at approximately the same slip for different steel fibres (Banthia and Trottier, 1994). Thus, the only difference between deformed, crimped and end-hooked fibres steel fibres is in the peak mechanical anchorage force, and the slip at peak force. As a result of the foregoing discussion, the problem of modelling polypropylene fibres can be reduced to determining suitable values for the bond parameters, s_f, $\tau_{f,max}$, s_{def}, $\tau_{def,max}$ and l_{def}. This is in accordance with the suggested procedure for determination of fibre bond relationships from experimental pull-out curves; only a select few factors (such as the ones listed) need to be adjusted (Naaman et al., 1991a). In order to do this, further literature study was undertaken.

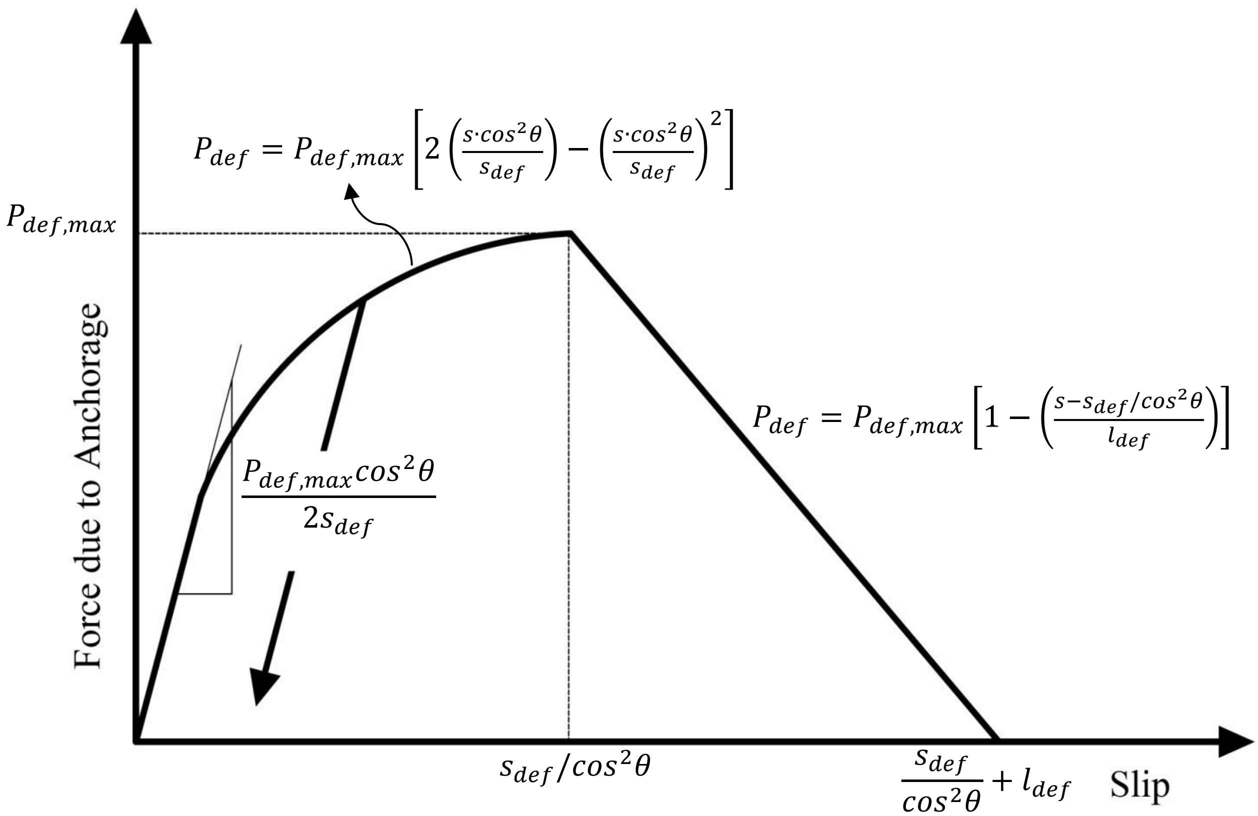

Figure 5.9: Mechanical anchorage due to polypropylene fibre surface deformations

5.3.2.1 Frictional Bond Behaviour

As mentioned in Section 5.2.2.2, the results of the pull-out tests performed by Naaman and Najm (1991) on straight steel fibres were used to calibrate the DEM and SDEM. Lee et al. (2011b) note that the elastic deformation of the fibre was not measured during the pull-out test. Thus, after subtracting the elastic deformation from the test result, the average value of s_f = 0.01 mm was found. Won et al. (2006) performed pull-out tests on smooth polypropylene fibres as part of an experimental program on the nature of synthetic fibre pull-out from a mortar matrix. These tests showed the slip at peak load was much higher than that of steel, approximately 2.5 mm, but there was no consideration of the elastic fibre deformation of the free portion of the fibre.

Also the fibres used in the test were circular monofilaments, whereas most structural macro-synthetic fibres in practical use, including the MAC Matrix fibres used in the experimental program, are made of two circular filaments that are cross-linked into one stick-like fibre. Synthetic fibres of this type have been shown to provide improved mechanical bonding to concrete (Soroushian et al., 1992; Zheng and Feldman, 1995; Choi et al., 2012). Thus, the result by Won et al. (2006) is not applicable, as a fundamentally different frictional bond behaviour can be expected for this type of fibre. In addition, the elastic deformation of the free portion of the polypropylene fibre during a pull-out test can be expected to be much greater than that of steel fibres, due to the relatively low Yonge's Modulus (1/20th that of steel). Also, machine softening and other effects may have influenced the measurements for typical pull-out tests (Wang et al., 1988). Thus, a value for s_f that is similar to steel fibres is deemed reasonable.

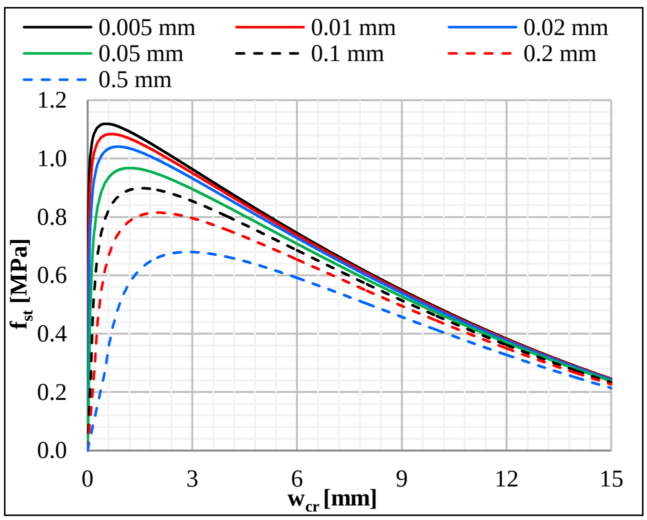

Figure 5.10: Sensitivity study on the effect of s_f on frictional bond behaviour

To investigate this further, a sensitivity study was performed using the properties of test set DC-P5 to determine a feasible value for s_f (as shown in Figure 5.10). The value of s_f was varied and the effect on the overall shape of the f_{st} versus w_{cr} response was monitored. It can be seen that as s_f is increased, the peak tensile stress due to frictional bond is reduced and shifted to higher crack widths. In addition, the slope of the descending branch at high crack widths and the magnitude of residual tensile stresses are reduced. Thus, it is logical to use a lower value of s_f, since the typical dogbone curves for PPFRC specimens exhibit a relatively steep but controlled drop in load after reaching the peak residual stress, while continuing to carry load to large crack widths. Also, the arrest of the initial crack opening occurs when the fibres become engaged (Voo and Foster, 2003). As noted earlier, this crack width was seen to be large in the tests, yet this was because of the fibre alignment process that was occurring for the flexible fibres. It is reasonable to assume that once the fibres were aligned, the peak frictional bond was quickly achieved to arrest further drop in load. Thus, a lower value of s_f was found to provide a good agreement with the fibre engagement point in the dogbones tested. As a result of this sensitivity study, the value of 0.01 mm was selected.

In terms of the frictional bond strength, it was difficult to separate out the effects of frictional bond and mechanical anchorage, so these discussions are combined in Section 5.3.2.3.

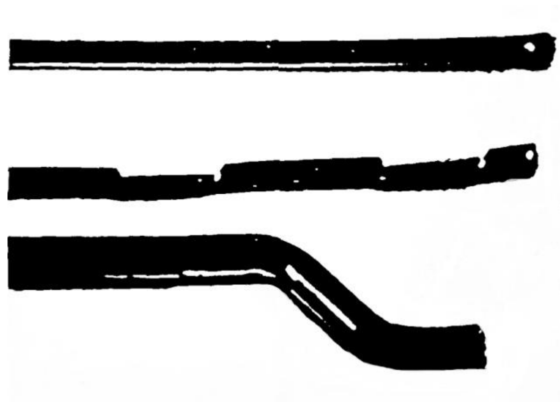

Figure 5.11: Straight, deformed and hooked fibres tested by Naaman et al. (1989) (adapted from Naaman et al., 1989)

5.3.2.2 Mechanical Anchorage Behaviour of Deformed Fibres

A similar approach was taken for mechanical anchorage. Naaman et al. (1989) performed an extensive investigation into the pull-out behaviour of straight, deformed and end-hooked steel fibres. An image of the fibres used is presented in Figure 5.11. In this paper two types of tests are used, pull-out and pull-through; for the pull-through tests the fibres extend through the concrete slab and out the bottom. That is to say that once the test commenced, the embedded length of the fibre remained unchanged as the slip progressed. For deformed fibres, this means that the number of deformations that were bonded to the concrete matrix remained constant until the lower part of the fibre began to pull-through the concrete tunnel. This is useful for the characterisation of the deformed fibre response as it allows for separate investigation of the frictional bond and the mechanical anchorage bond. In addition, tests on greased deformed fibres were performed to separate the frictional and mechanical anchorage component. These are presented in Figure 5.19 of Section 5.3.2.3.

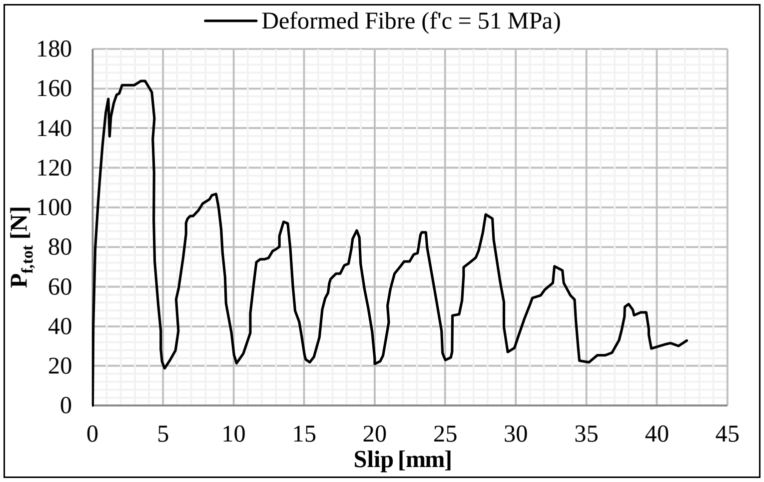

Figure 5.12: Typical deformed steel fibre pull-through/pull-out curve (Naaman et al., 1989)

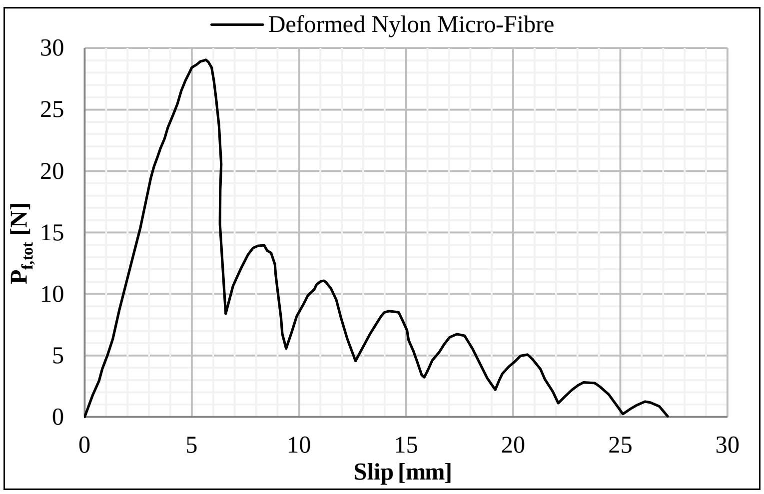

Figure 5.13: Deformed nylon micro-synthetic fibre pull-out curve (Li et al., 1990)

A typical pull-through/pull-out curve for a deformed steel fibre is shown in Figure 5.12. A cyclic response was observed, attributable to the behaviour of the indentations as they progress through the concrete tunnel. On the first cycle, the frictional bond and mechanical anchorage both contribute. Then, the mechanical deformations cause local matrix crushing within the concrete tunnel (Nammur and Naaman, 1989). This caused the sudden drop in load observed in the pull-out curve. As the fibre pull-out progressed, the deformations engaged at a new location in the concrete tunnel. This phenomenon occurred about every 5 mm, which was the same as the length of the surface indentation on the fibres used (Naaman and Najm, 1991). It can be seen that, for the pull-through portion of the test, the maximum load attained on subsequent cycles was nearly constant, since the same number of deformations remained active in the tunnel. Then, when the pull-out regime began at a slip of roughly 30 mm, subsequent cycles attained a reduced maximum load. Pull-out tests on micro-synthetic nylon fibres with surface indentations exhibited similar overall behaviour, as shown in Figure 5.13 (Li et al., 1990). From the shape of the individual cycles, the representation of the mechanical anchorage using the parabolic ascending branch and a linear descending branch is reasonable for deformed fibres. Figure 5.14 shows this first cycle with typical end-hooked and straight steel fibre pull-out curves for comparison. The overall shape of the first cycle is similar to that of end-hooked fibres, with the exception that the peak stress is reached at a higher slip. However, the slip at which the mechanical anchorage contribution becomes zero should be substantially higher than that of end-hooked steel due to the cyclic nature of the response. Theoretically, these mechanical anchorages due to surface deformations remain active until the fibre is completely pulled out as at least one deformation is bonded to the matrix. However, the fibres in the tests performed on the dogbones and panels showed significant fraying after the tests were completed (Figure 5.15).

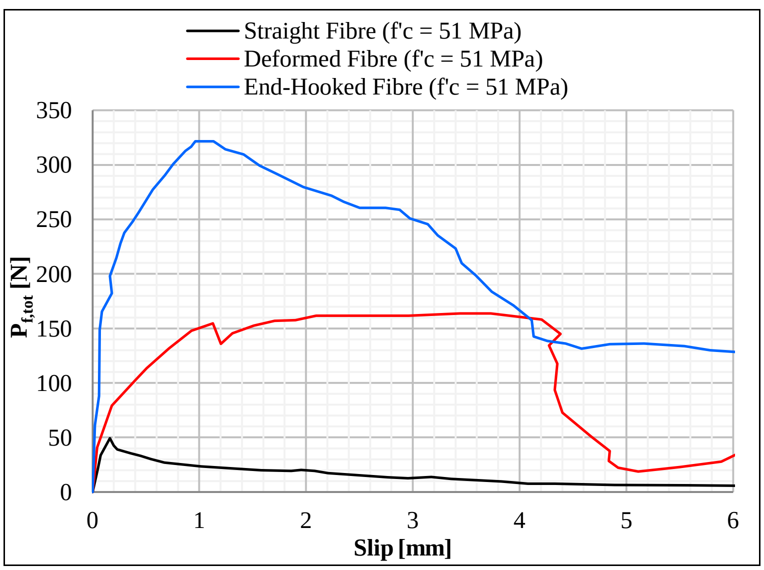

Figure 5.14: Influence of mechanical anchorage on fibre pull-out (Naaman et al., 1989)

This is consistent with the findings of many researchers (Won et al., 2006; Leung and Ybanez, 1997; Elser et al., 1996a; Wang et al., 1987), and with the scanning electron microscope (SEM) image shown in Figure 5.16 of a synthetic fibre after completion of a pull-out test. Thus, it is reasonable to assume that, due to the low stiffness of the macro-synthetic fibres, significant damage is done to the fibre deformations by the concrete tunnel as the pull-out progresses. As a result, the slip at termination of mechanical anchorage was taken to be much less than the theoretically achievable $l_f/2$. This shows good agreement with the dogbone tests.

Figure 5.15: Frayed fibres after completion of a panel test

Figure 5.16: SEM image of synthetic fibre surface after pull-out test (adapted from Won et al., 2006)

For the value of s_{def}, the responses of the straight, deformed and end-hooked fibres in an average strength matrix with no admixtures were considered (Naaman et al., 1989). In addition, the results of crimped steel and macro-synthetic fibre tests were investigated (Banthia and Trottier, 1994; Won et al., 2006). A summary of the fibre properties, peak loads and slip at peak loads are presented in Table 5.3. Also, photos of the synthetic fibres tested by Won et al. (2006) are presented in Figure 5.17 for reference. The short and tall crimped fibres were used in this discussion as, from the images, it appears that the short crimped fibres used are similar to the MAC-Matrix fibres (with the exception of the bundling discussed earlier) and to the deformed steel fibres tested by Naaman et al. (1989). The tall crimped fibres used are similar to the crimped steel fibres tested by Banthia and Trottier (1994). The end-hooked fibres were considered as well, although it would appear from the image that the hooks on the macro-synthetic fibres are much smaller than those on the steel fibres shown in Figure 5.11. Thus, much lower bond strength may be expected for these, due to the low stiffness and relative ease with which the hooks are deformed during pull-out.

Table 5.3: Results of Various Macro Fibre Pull-out Tests

Paper	Matrix Type	f'_c [MPa]	Fibre Material	Fibre Type	d_f [mm]	l_f [mm]	$P_{f,tot}$ [N]	$\tau_{f,tot}$ [MPa]	$\tau_{f,tot}/\sqrt{f'_c}$	s_{peak} [mm]
Naaman et al. (1991)	Concrete	51	Steel	Straight	0.483	50.8	56.0	1.45	0.203	0.018
	Concrete	51	Steel	End-Hooked	0.762	50.8	357.2	5.87	0.823	0.90
	Concrete	51	Steel	Deformed	0.457	50.8	157.4	4.32	0.605	1.30
Banthia and Trottier (1994)	Concrete	40	Steel	End-Hooked	0.8	60	272.9	3.62	0.572	1.55
	Concrete	40	Steel	Crimped	1.0	40	676.5	10.77	1.703	2.56
	Concrete	52	Steel	End-Hooked	0.8	60	287.2	3.81	0.528	0.98
	Concrete	52	Steel	Crimped	1.0	40	680.0	10.82	1.500	2.44
	Concrete	85	Steel	End-Hooked	0.8	60	296.5	3.93	0.426	1.19
	Concrete	85	Steel	Crimped	1.0	40	670.9	10.68	1.158	2.09
Won, Lim and Park (2006)	Mortar	20	Synthetic	Straight	1.4x0.7	30	17.4	0.33*	0.074	2.77
	Mortar	20	Synthetic	End-Hooked	1.4x0.7	30	24.9	0.47*	0.105	1.28
	Mortar	20	Synthetic	Tall Crimped	1.4x0.7	30	153.4	2.92*	0.653	8.73
	Mortar	20	Synthetic	Short Crimped	1.4x0.7	30	115.8	2.21*	0.494	3.40
	Mortar	32	Synthetic	Straight	1.4x0.7	30	17.7	0.34*	0.060	2.34
	Mortar	32	Synthetic	End-Hooked	1.4x0.7	30	41.6	0.79*	0.140	1.85
	Mortar	32	Synthetic	Tall Crimped	1.4x0.7	30	168.0	3.20*	0.566	9.96
	Mortar	32	Synthetic	Short Crimped	1.4x0.7	30	169.0	3.22*	0.569	4.03

* Pull-out load multiplied by 1.2 for mortar matrix for comparison to concrete, according to relationships for bond strength given in the VEM (Voo and Foster, 2003).

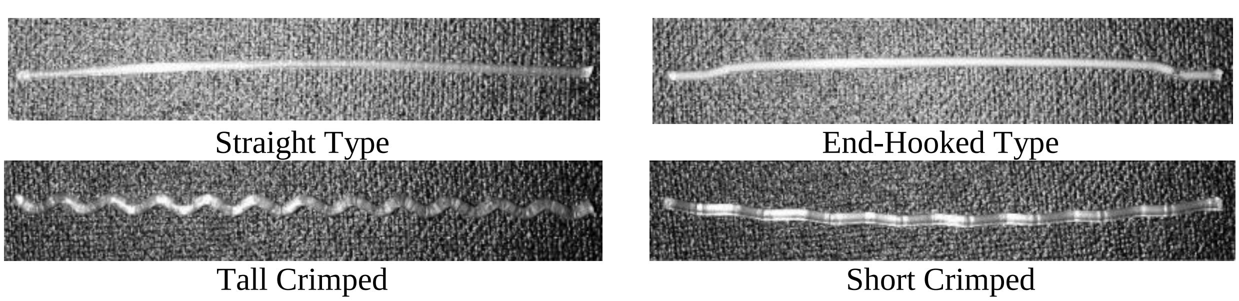

Figure 5.17: Images of synthetic fibres tested (adapted from Won et al., 2006)

It is clear from the results summarized in Table 5.3 that the slip at peak load for deformed or crimped fibres is much greater than that of end-hooked fibres. In addition, the slip at peak for synthetic fibres with mechanical anchorage is greater in all cases than the slip at peak for steel fibres. It is worth noting that details of the tests in terms of free length of the fibre outside the concrete matrix and fibre elastic deformation were not presented in the papers consulted. Regardless, it can be discerned that the value of s_{def} to be used in conjunction with the SDEM needs to be approximately 2 to 5 times that of s_{eh}. To complete this discussion, a sensitivity analysis was performed on the values of s_{def} and l_{def} to determine the most suitable relationship. This is shown in Figure 5.18.

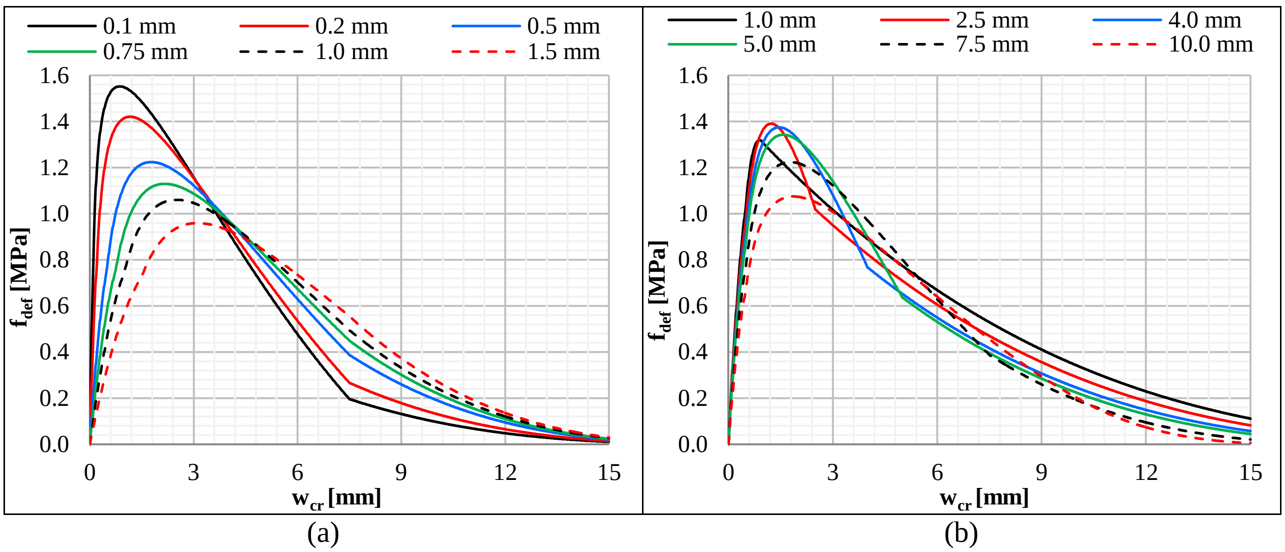

Figure 5.18: Sensitivity study on the effect of s_{def} and l_{def} on mechanical anchorage behaviour: (a) s_{def}, with l_{def} = 7.5 mm; (b) l_{def}, with s_{def} = 0.5 mm

It is clear from the result of this sensitivity study that, for the range of values of s_{def} that shows good agreement with the literature, the highest value of s_{def} must be used. This is because of the effect of s_{def} on the location of the peak f_{def} value. From the dogbone tests, the peak residual tensile stresses occurred at crack widths of 1.6 to 2.5 mm. The peak stress for s_{def} < 0.5 mm occurs at crack widths that are much too low. As a result, a value of s_{def} = 0.5 mm was chosen, as this gave a crack width at a peak stress of 1.77 mm for 2.0% by volume PPFRC. This value of s_{def} works well with l_{def} = 7.5 mm to yield a smooth degradation of the residual tensile response, consistent with the dogbone tests. Other values of l_{def} produce a significant and undesirable kink in the response. Also, this value of l_{def} is nearly double that of l_{eh} used for end-hooked steel fibres and is, thus, consistent with the findings of the typical deformed fibre pull-out response discussed earlier (Figure 5.12 to Figure 5.14).

5.3.2.3 Bond Strength of Deformed Polypropylene Fibres

Lastly, some reasonable values for the overall bond strength of polypropylene fibres are required. With the absence of pull-out tests, this can be challenging. As a result, the parameter of total bond strength of these deformed fibres is left somewhat open-ended in the finite element analysis implementation. However, an attempt is made to determine a logical default parameter. The details follow.

First, as before, the pull-out tests of deformed or crimped steel fibres were examined. From the test summary presented in Table 5.3, the crimped fibres exhibit much higher bond strengths than that of the end-hooked or deformed steel fibres. This can be attributed to the nature of the debonding pull-out for crimped fibres. One of two things may happen with these fibres. First, the fibre may remain in its original shape, and the matrix around the crimps may fail. Second, the tunnel in the matrix can remain unaffected, while the fibre is deformed through plastification and pulled out of its initial print. If the strain induced by this deformation demand is too great, the crimped fibres will rupture (Chanvillard and Aïtcin, 1996). These two failure modes are similar to the expected failure modes of deformed fibres discussed in the previous section, yet it can be expected that significantly more concrete will be activated by the crimps than the relatively small deformations. Thus, the high fibre pull-out stresses attained by crimped fibres are not applicable to the case of fibres with smaller surface indentations and were used only as a means of determining the relative bond strength of polypropylene fibres when compared to steel.

Instead, in the paper by Naaman et al. (1989), two pull-out tests were performed on deformed steel fibres with greased surfaces. The resulting pull-out responses are shown, with their ungreased counterparts, in Figure 5.19. These tests were done to investigate the pure behaviour of the mechanical anchorage, without the frictional bond. In addition, the cyclic nature of the deformed fibre pull-out can be used as an indication of the mechanical anchorage component after the frictional bond was mostly overcome. If the residual frictional bond force (taken as the force at the minimum between the cycles of the pull-out response) is subtracted, then the load due to mechanical anchorage can be isolated. The results of these tests were used to determine the default ratio of mechanical anchorage stress due to deformations to total bond stress, shown in Table 5.4. From the result of this analysis, it was determined that the deformations account for 55% of the overall bond strength. Thus, using the relationships of the VEM presented in Table 5.1, if $\tau_{f,max} = 1.2 * f_t'$ and $\tau_{def,max}/\tau_{f,tot} = 0.55$ then this would yield $\tau_{def,max} = 1.47 * f_t'$ and $\tau_{f,tot} = 2.67 * f_t'$ for deformed fibres. This is slightly greater than the VEM relationship for end-hooked fibres and, thus, is conservative and reasonable as the tests by Banthia and Trottier (1994) show an average normalized bond strength for end-hooked steel fibres that is slightly lower than that of the deformed steel fibres tested by Naaman et al. (1989).

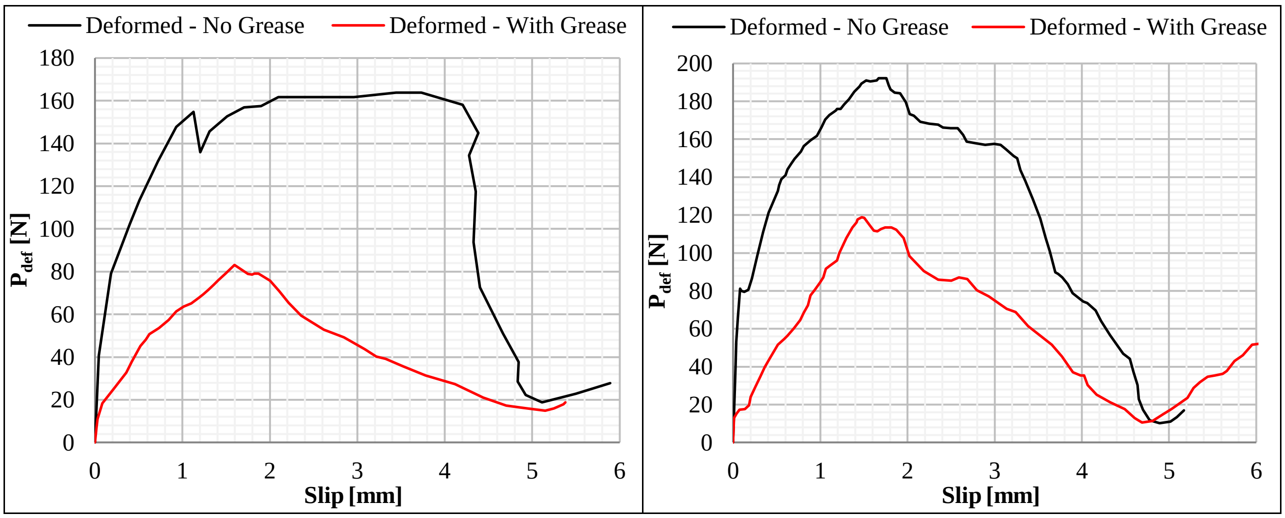

Figure 5.19: Deformed fibre behaviour with and without grease

The final step is to determine the ratio between total bond of steel fibres and total bond of polypropylene fibres. This parameter, called PSR for polypropylene-to-steel ratio, is used to relate steel fibre bond to polypropylene fibre bond through:

$$\tau_{f,tot,poly} = PSR \cdot \tau_{f,tot,steel} \tag{5.20}$$

where:

$\tau_{f,tot,poly}$ = total bond strength of polypropylene fibres;

$\tau_{f,tot,steel}$ = total bond strength of steel fibres.

Table 5.4: Deformed Anchorage Compared to Frictional Bond

Paper	Fibre Material	Test Type	d_f [mm]	l_f [mm]	s_1 [mm]	$P_{f,tot}$ [N]	$P_{def,max}$ [N]	$\tau_{f,tot}$ [MPa]	$\tau_{def,max}$ [MPa]	$\tau_{def,max}/\tau_{f,tot}$
Naaman et al. (1991)	Steel	Greased	0.457	50.8	-	192.1	108.3	5.27	2.97	0.564
	Steel	Greased	0.457	50.8	-	163.8	65.3	4.49	1.79	0.508
	Steel	Pull-through	0.457	50.8	-	163.8	73.2	4.49	2.01*	0.448
	Steel	Pull-out	0.457	50.8	4.79	150.0	81.7	4.11	2.76*	0.672
	Steel	Pull-out	0.457	50.8	4.76	192.3	87.1	5.27	2.94*	0.558
									Average:	0.550
									CV (%):	17.4

* For the deformed fibre pull-through test, the average mechanical anchorage peak force was taken as the average of peaks 2 to 5 of the cyclic response, minus the residual frictional bond force component. The fibre embedded length is constant so the embedded length remains $l_f/2$ in subsequent cycles. For pull-out tests, the peak of the second cycle is taken, again minus the average residual frictional bond component, and the embedded length is taken as $(l_f/2 - s_1)$; where s_1 is the slip at the end of the first cycle.

In the absence of reliable pull-out tests using macro-synthetic fibres, the fibre bond strength is left as an open parameter in the VecTor2 implementation of these modifications. If a user inputs an experimentally determined value for the maximum bond strength of the deformed polypropylene fibres, it is partitioned, with 55% of the input being allocated to mechanical anchorage and 45% allocated to frictional bond, in keeping with the findings detailed in Table 5.4. A default value for PSR is also included with the model. This is determined by comparing the steel and macro-synthetic pull-out tests presented in Table 5.3, to come up with a reasonable range of values for PSR (see Table 5.5). The value of PSR is highly variable. However, as noted in the discussion, the cross section of the straight fibres tested by Won et al (2006) are different from that of the MAC Matrix fibres. A straight, undeformed MAC Matrix fibre would achieve a higher bond strength, due to the multiple filament cross section (Li et al., 1987; Soroushian et al., 1992). In addition, the end-hooks of the polypropylene fibres are small in relation to the steel fibres tested by Naaman et al. (1989) (see Figure 5.11 and Figure 5.17). Thus, the default PSR value should be greater than the PSR calculated from these two fibre types. Conversely, it should be lower than that of the deformed fibre comparison, as the polypropylene fibres tested by Won et al. (2006) were slightly crimped. Thus, a reasonable range of values for PSR would be 0.4 to 0.7. This range of values was then plotted against the direct tension result of test-set DC-P5, so that the most reasonable default value could be selected.

Table 5.5: Comparison of Steel and Polypropylene Bond Strengths

Fibre Type	Steel Fibres			Polypropylene Fibres			PSR*
	f'_c [MPa]	$\tau_{f,tot}$ [MPa]	$\tau_{f,tot}/\sqrt{f'_c}$	f'_c [MPa]	$\tau_{f,tot}$ [MPa]	$\tau_{f,tot}/\sqrt{f'_c}$	
Straight	51	1.45	0.203	20	0.33	0.074	0.330
	-	-	-	32	0.34	0.060	
End-Hooked	51	5.87	0.823	20	0.47	0.105	0.209
	40	3.62	0.572	32	0.79	0.140	
	52	3.81	0.528	-	-	-	
	85	3.93	0.426	-	-	-	
Deformed/Short Crimped	51	4.32	0.605	20	2.21	0.494	0.879
	-	-	-	32	3.22	0.569	
Tall Crimped	40	10.77	1.703	20	2.92	0.653	0.419
	52	10.82	1.500	32	3.20	0.566	
	85	10.68	1.158	-	-	-	

* Average value of $\tau_{f,tot}/\sqrt{f'_c}$ for the given fibre type is used to calculate PSR.

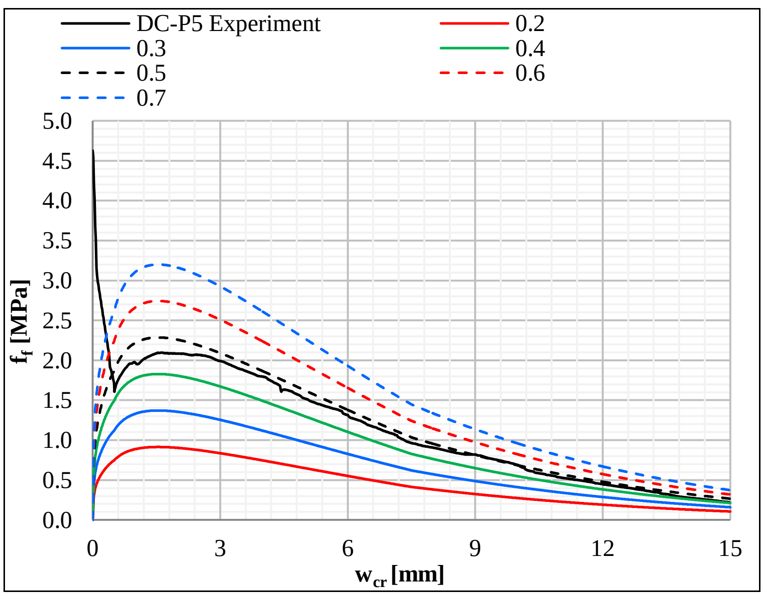

Figure 5.20: Sensitivity study on the effect of PSR on the SDEM prediction

Thus, from this final sensitivity study, the default PSR value chosen was 0.5, well within the determined acceptable range. This yields the default values of $\tau_{f,tot} = \tau_{f,max} = PSR * 1.2 * f'_t = 0.198\sqrt{f'_c}$ for the frictional bond component of polypropylene fibres and $\tau_{f,tot} = PSR * 2.67 * f'_t = 0.441\sqrt{f'_c}$ for deformed polypropylene fibres, with $\tau_{def,max} = 0.243\sqrt{f'_c}$. These default values are summarized in Table 2.13. This is in good agreement with the suggestion given by Richardson (2005). In this paper, Richardson (2005) performed a series of tests on the pull-out of macro-synthetic structural polypropylene fibres, with varying levels of surface indentation, from mortar cubes. The test was performed by hanging the mortar cubes such that the fibre is facing down, attaching a clamp to the end of the fibre and incrementally hanging weights from the end of the clamp. From the result, Richardson (2005) proposed that the bond strength of these fibres can be predicted using $\tau_{f,tot} = 0.288\sqrt{f_{cu}}$, where f_{cu} is the cube compressive strength of the mortar. Adjusting for cylinder compressive strength ($f_c' = 1.2 * f_{cu}$ (Wong et al., 2012)), this becomes roughly $0.315\sqrt{f_c'}$, 14% lower than the value proposed herein for deformed polypropylene fibres in mortar (Table 2.13). However, it can be expected that the test method employed by Richardson (2005) would yield lower pull-out loads relative to a condition with monotonically increasing applied displacements. This is because the clamp would create a nipping of the fibre, reducing the cross-sectional area, and the application of the weights would create a sudden dynamic increase in load. Nevertheless, it can be confirmed using this result that the bond strength proposed herein is reasonable. With this final parameter, the initial proposed adjustments to the SDEM for the modelling of the direct tension response of polypropylene fibre reinforced concrete are complete.

Table 5.6: Default Pull-out Strengths of Polypropylene Fibers

Fibre Type	Matrix Type	Pull-out Strength
Deformed	Concrete	$\tau_{f,tot} = PSR * 2.67 * f_t' = 0.441\sqrt{f_c'}$ $[MPa]$ so $\tau_{def,max} = 0.243\sqrt{f_c'}$ $[MPa]$
	Mortar	$\tau_{f,tot} = PSR * 2.22 * f_t' = 0.366\sqrt{f_c'}$ $[MPa]$ so $\tau_{def,max} = 0.201\sqrt{f_c'}$ $[MPa]$
Straight	Concrete	$\tau_{f,tot} = \tau_{f,max} = PSR * 1.2 * f_t' = 0.198\sqrt{f_c'}$ $[MPa]$
	Mortar	$\tau_{f,tot} = \tau_{f,max} = PSR * 1.0 * f_t' = 0.165\sqrt{f_c'}$ $[MPa]$

5.3.3 Summary of the Proposed SDEM Modifications

The following is a summary of the SDEM modifications for the modelling of polypropylene fibres:

1. In keeping with the existing relationships of the SDEM for steel fibres, the elastic deformation of the fibres was neglected. This effect accounts for about 2 to 10% of the

crack width after sufficient engagement occurs. However, engagement occurs at large crack widths for flexible fibres, and it has been shown in the literature that the elastic deformation can be conservatively ignored at large crack widths (Sujivorakul et al., 2000). In addition, the slip on the longer embedded side of the fibre is neglected.

2. Despite some pull-out tests indicating a relationship between fibre bond strength and fibre inclination angle (Li et al., 1990; Leung and Ybanez, 1997), this effect was ignored in the model so as to be consistent with the model for steel fibres. For steel fibres, this effect has been neglected by many researchers (Voo and Foster, 2003; Lee et al., 2011a). This was similarly ignored by Wang et al. (1989) in the development of their statistical tensile model for synthetic FRC.

3. Should further studies indicate that this snubbing effect mentioned in item 2 is valid for macro-synthetic fibres, the following relationship was proposed in lieu of the snubbing model.

$$\tau_{f,max,\theta} = \frac{\tau_{f,max}}{cos\theta} \tag{5.19}$$

   This relationship can be easily incorporated into the equations of the SDEM.

4. The overall bond stress-slip relationships used for end-hooked steel fibres were also used for macro-synthetic fibres with surface deformations, as the bond relationships of all fibres tested with mechanical anchorages follow similar characteristic curves. The frictional bond behaviour is shown in Figure 5.2; the relationship for mechanical anchorage is shown in Figure 5.9.

5. The problem of modelling polypropylene fibres was reduced to determining suitable values for the bond parameters, s_f, $\tau_{f,max}$, s_{def}, $\tau_{def,max}$ and l_{def}. In order to do this, a literature study was undertaken.

6. From the literature study on the properties of frictional bond, the proposed relationship for frictional bond behaviour of macro-synthetic fibres is:

$$f_{st} = \alpha_f V_f K_{st} \tau_{f,max} \frac{l_f}{d_f}\left(1 - \frac{2w_{cr}}{l_f}\right)^2 \tag{5.10}$$

   where:

$$K_{st} = \begin{cases} \dfrac{\beta_f}{3}\dfrac{w_{cr}}{s_f} & for\ w_{cr} < s_f \\ 1 - \sqrt{\dfrac{s_f}{w_{cr}}} + \dfrac{\beta_f}{3}\sqrt{\dfrac{s_f}{w_{cr}}} & for\ w_{cr} \geq s_f \end{cases}$$

$$\tau_{f,max} = PSR * 1.2 * f_t' = 0.198\sqrt{f_c'} \quad [MPa]$$

$$s_f = 0.01\ mm$$

$$\beta_f = 0.67$$

$$PSR = 0.5.$$

7. From the literature study on the properties of surface deformations on mechanical anchorage, the relationship for mechanical anchorage due to deformations is:

$$f_{def} = \alpha_f V_f K_{def} \tau_{def,max} \frac{2\left(\left(l_f - 2l_{def}\right) - 2w_{cr}\right)}{d_f} \tag{5.21}$$

where:

$$K_{def} = \begin{cases} \beta_{def}\left[\dfrac{2}{3}\dfrac{w_{cr}}{s_{def}} - \dfrac{1}{5}\left(\dfrac{w_{cr}}{s_{def}}\right)^2\right] & for\ w_{cr} < s_{def} \\ 1 + \left(\dfrac{7\beta_{def}}{15} - 1\right)\sqrt{\dfrac{s_{def}}{w_{cr}}} - \dfrac{\left(\sqrt{w_{cr}} - \sqrt{s_{def}}\right)^2}{l_{def}} & for\ s_{def} \leq w_{cr} < l_{def} \\ K_{def,i}\left(\dfrac{\left(l_f - 2l_{def}\right) - 2w_{cr}}{l_f - 4l_{def}}\right)^2 & for\ l_{def} \leq w_{cr} < \dfrac{\left(l_f - 2l_{def}\right)}{2} \end{cases}$$

$K_{def,i}$ is K_{def} at $w_{cr} = l_{def}$.

$$\tau_{def,max} = PSR * 1.47 * f_t' = 0.243\sqrt{f_c'} \quad [MPa]$$

$$s_{def} = 0.5\ mm$$

$$l_{def} = 7.5\ mm$$

$$\beta_{def} = 0.76$$

$$PSR = 0.5.$$

8. The values of $\tau_{f,max}$ and $\tau_{def,max}$ given in items 6 and 7 are default values implemented into VecTor2. However, the maximum bond strength of the fibre $\tau_{f,tot}$ was left as an open parameter and may be input by the user based on experimental results. If this is

done, the input bond strength will be broken down such that $\tau_{def,max}/\tau_{f,tot} = 0.55$ and $\tau_{f,max}/\tau_{f,tot} = 0.45$, in keeping with the findings of the literature study.

9. Overall, the assumptions made in this model should be verified through the execution of an extensive experimental program. This program should investigate the effect of fibre inclination angle on ultimate bond strength, the adequacy of the parameters selected for the bond constitutive laws (i.e. s_f, $\tau_{f,max}$, s_{def}, $\tau_{def,max}$ and l_{def}), the energy required to pull-out a polypropylene fibre from a concrete matrix and the value of the polypropylene-to-steel fibre bond ratio.

5.3.4 Verification Study

Utilizing the proposed relationship, the responses of dogbone tests DC-DB1, DC-DB2, DC-P3 and DC-P5 can be estimated to verify the applicability of the model. This is shown in Figure 5.21. In addition, after the model was implemented into VecTor2, the program was used to model these dogbones, the macro-synthetic FRC panels (DC-P3 and DC-P5), and a short set of large-scale macro-synthetic FRC beams. Details of this study are presented in Chapter 6.

Overall, the model well predicts the experimental response for each of the four dogbones. The tensile stress at fibre engagement is well predicted and the degradation of the fibre tension after reaching the peak residual stress is well represented. The prediction is sufficiently smooth and follows a shape similar to that of the experiment. Also, the crack width at the peak load is well predicted in most cases, with the exception of DC-P3, which experimentally exhibited an unexpectedly large crack width at the peak residual stress.

Conversely, the post-cracked peak load, and the response in general from crack widths of 0.5 to 3.0 mm, is overestimated in most cases. This is attributable to the three-dimensional fibre orientation factor, which will be large when the small cross section of the dogbones and the long length of the macro-synthetic fibres are considered. It has been shown that the fibre orientation factor has a 20% coefficient of variation, making it difficult to accurately predict (Oh, 2011). In addition, as shown in Table 3.9, the actual fibre volume fraction calculated by counting the number of fibres crossing the failure plane was less than the fibre volume fraction added to the concrete in all cases. This also causes an overprediction of the experimental result. This is consistent with the drastic overprediction for DC-DB2 (Figure 5.21(b)), as the actual fibre volume fraction was merely 2.39%, compared to the design volume fraction of 3.0%.

Lastly, the crack width at the point of engagement is underpredicted in all cases. This is also shown by the steep slope of the model response immediately after cracking and before fibre engagement, contrary to the experimental findings. This is not related to the model for fibre tension and is instead a result of the tension softening response of the concrete selected.

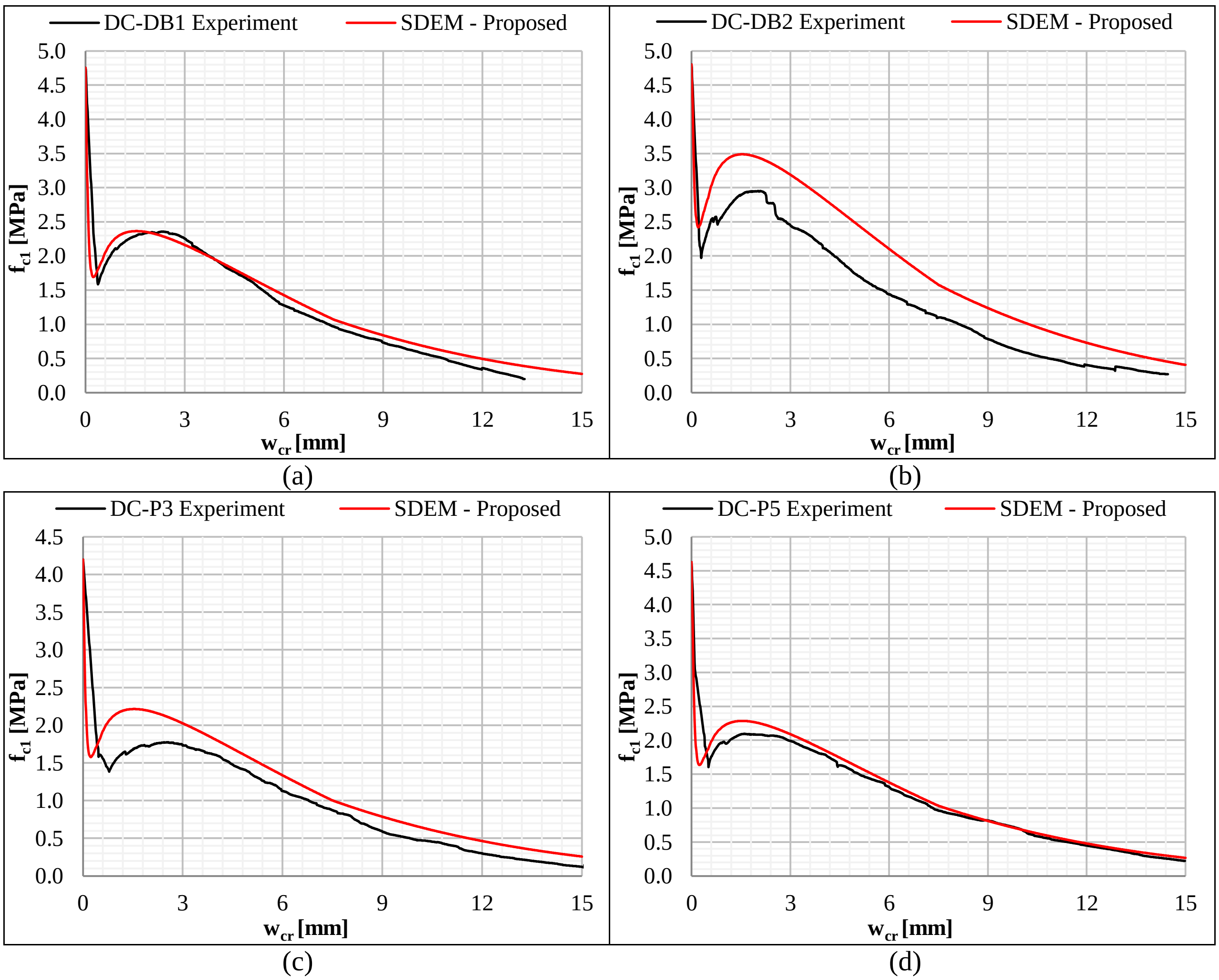

Figure 5.21: Experimental versus modified SDEM estimation for PPFRC dogbones

5.3.4.1 Engagement Energy

To improve the prediction of fibre engagement, a better understanding of FRC modelling is required. As touched upon in Chapter 2, two methods of representing the response of fibre reinforced concrete are employed. The first involves the superposition of the fibre and concrete contributions to the overall response. In this way, the fibres act as reinforcement, providing tension stiffening effects to the brittle concrete. The VEM, DEM and SDEM are all examples of this type of modelling approach. The second is related to fracture mechanics where experiments, such as wedge splitting tests or three-point bending tests on notched specimens, are used to determine the stress versus crack opening relationship of the FRC. Using these results, an inverse analysis is performed to determine reasonable values of selected parameters such as bond strength, total fracture toughness, etc. (Lofgren et al., 2005). It has been noted in the literature that proper representation of the slope of the initial descending branch of the stress versus crack width relationship immediately after cracking is paramount to a successful inverse analysis (Lofgren et al., 2005). However, with models of the first type, the representation of the response at this point of engagement should only consider the concrete with no contribution of the fibres (as the fibre contribution to strength correctly begins at zero for zero crack width). Thus, this initial descending portion is treated as plain concrete, and an overly steep slope is incorrectly predicted.

As mentioned earlier, the recommended plain concrete tension softening response for SFRC, according to the VEM, is: $f_{ct} = f_t' \cdot \exp(-15 * w_{cr})$, as shown in Equation 2.1 (Voo and Foster, 2003). This is a simplification of the full exponential tension softening model, which is:

$$f_{ct} = f_t' \cdot \exp(-f_t'/G_F * w_{cr}) \tag{5.22}$$

where:

G_F = fracture energy of the concrete (the energy required to completely open a crack over a unit area of concrete) [N/m].

Clearly, this presents a problem, as fracture energy is the energy required to open a full and complete crack. This is not accurate for FRC, as this would represent the area under the entire load-displacement curve for a uniaxial tension test until the last fibre is pulled out. This value is not applicable to the situation of modelling the tension softening response of the concrete component of FRC. Essentially, what is needed instead is the engagement energy, or the energy required to cause full fibre engagement. This would involve consideration of the slight pull-out and slip of the stiff steel fibre, or the bending of the flexible polypropylene fibre, that occurs before fibre engagement.

In VecTor2, the relationship for fracture energy is that given by Bazant (2002). This is based on the fracture mechanics of plain reinforced concrete and is as follows:

$$G_F = 2.5 \cdot \alpha_o \left(\frac{f_c'}{0.051}\right)^{0.46} \left(1 + \frac{d_a}{11.27}\right)^{0.22} \left(\frac{w}{c}\right)^{-0.3} \tag{5.23}$$

where:

d_a = maximum diameter of the aggregate [mm];

w/c = water-to-cement ratio;

α_o = factor to account for the aggregate shape, taken as 1.44 for crushed aggregate.

Using the properties of test set DC-P5, the calculated fracture energy from Bazant (2002) is 134 N/m. The suggested relationship given in the VEM is used to represent an increase in fracture energy to account for the effect of the steel fibre engagement energy by introduction the attenuation factor, c, which is taken as 15 for a concrete matrix and 30 for a mortar matrix (Voo and Foster, 2003). Using this relationship for DC-P5, the calculated fracture energy is 308 N/m. From the predictions shown in Figure 5.21, it is clear that this engagement energy is too low for macro-synthetic fibres. This is consistent with the findings of Oh et al. (2007). The authors of this paper present the total pull-out energy of crimped or sinusoidal macro-synthetic fibres, compared to that of steel. The macro-synthetic fibre pull-out energy to a slip of 10 mm is roughly 1.5 to 2.0 times that of steel. In addition, as discussed earlier in this chapter, the nature of engagement for flexible fibres is fundamentally different when compared to that of steel fibres. The stiff steel fibres all engage somewhat instantaneously, regardless of fibre inclination angle. For polypropylene fibres, many of the unaligned fibres must first undergo fibre bending to align perpendicular to the crack before becoming effectively engaged. If the fibres were perfectly flexible, this could occur instantly and would require no energy. However, these fibres do have some finite stiffness and, thus, energy is required to complete this engagement process (Leung and Ybanez, 1997). This absorbed energy is what causes the reduced slope of the descending portion of the experimental dogbone curves after cracking. Thus, significantly higher engagement energy can be expected for PPFRC in relation to SFRC. This is supported by the findings of Shao and Wang (2012), who reported that polypropylene fibres exhibit the greatest energy absorption throughout the debonding process. However, this phenomenon has not been thoroughly investigated in the literature, and should be the focus of an extensive research program if the representation of PPFRC is to be improved. Also, since the SDEM is formulated to consider the fibre and concrete contributions independently, then some further adjustments are required to improve the representation of the descending branch of the response immediately after cracking. In the interim, the predictions provided by the modified SDEM are presented again in Figure 5.22 using instead $f_{ct} = f_t' \cdot \exp(-7.5 * w_{cr})$. This rough estimate of the attenuation factor was determined by calculating the engagement energy, G_{fe}, as the area under the experimental stress versus crack width curve up to engagement from:

$$G_{fe} = \frac{f_t' - f_{te}}{2} w_{cr,e} \tag{5.23}$$

where:

$w_{cr,e}$ = width of the crack at engagement [mm].

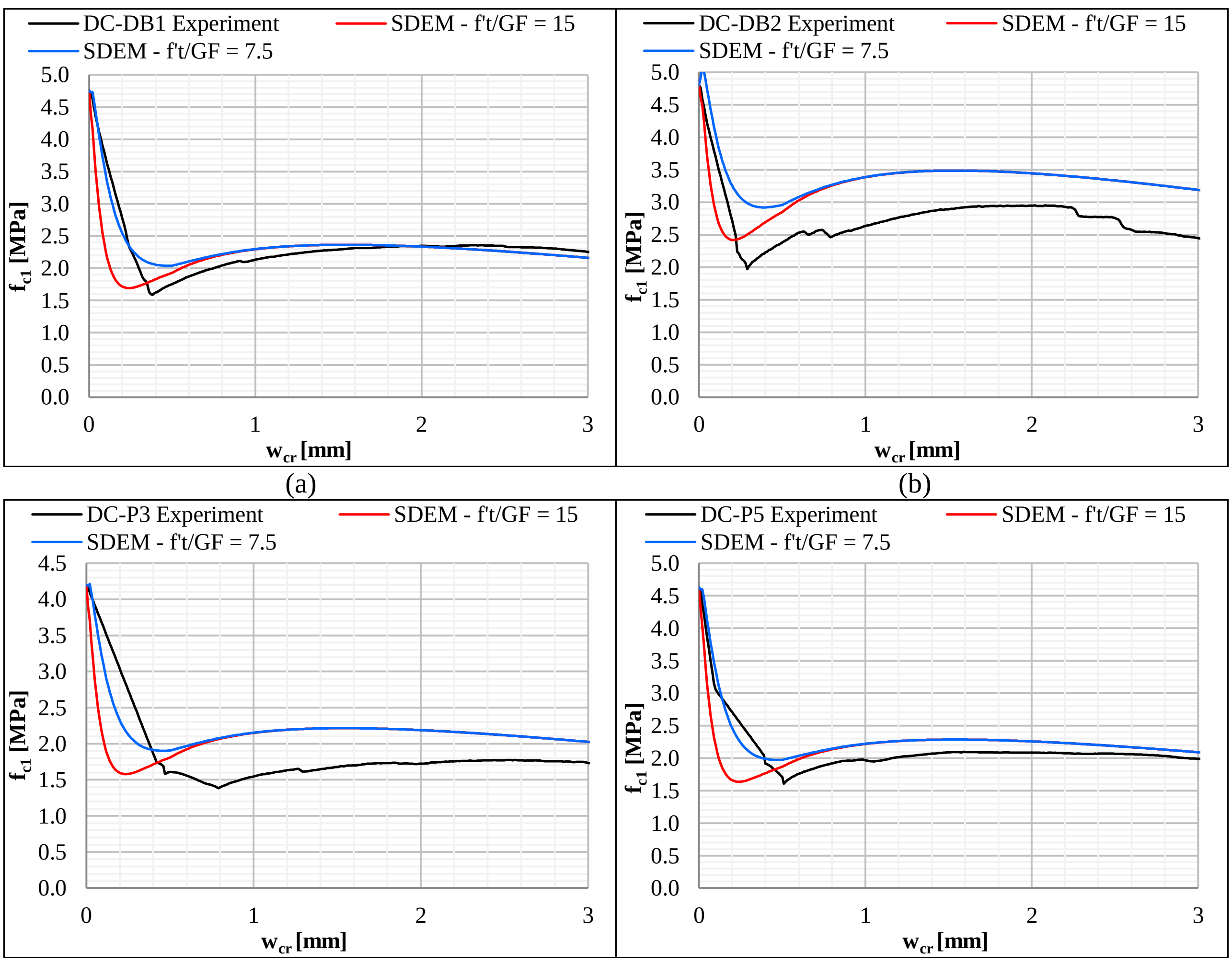

(a) (b) (c) (d)

Figure 5.22: Effect of fracture energy on modified SDEM estimation

Table 5.7: Engagement Energy of Macro-Synthetic FRC Specimens

Specimen ID	f_t' [MPa]	f_{te} [MPa]	$w_{cr,e}$ [mm]	G_{fe} [N/m]	f_t'/G_{fe}
DC-DB1	4.77	1.58	0.38	606	7.87
DC-DB2	4.80	1.97	0.29	410	11.71
DC-P3	4.49	1.58	0.47	684	6.56
DC-P5	4.67	1.61	0.51	780	5.99

The calculations for all of the PPFRC dogbones tested are shown in Table 5.7. It is worth noting that the value of G_{fe} may be dependent on the fibre volume fraction, as it is lower for DC-DB2. However, as mentioned before, a more thorough investigation of this behaviour is required and is outside the scope of this work.

Using $f_t'/G_F = 7.5$ for DC-P5, the fracture energy is calculated as 617 N/m. As can be seen from the updated model predictions, the slope of the decay immediately after cracking and the crack width at engagement are much more accurately represented using this estimation. This effect of engagement energy on the fracture energy and the predicted response of PPFRC was further investigated using the finite element models discussed in Chapter 6.

Chapter 6
Finite Element Modelling

6 Finite Element Modelling

6.1 Introduction

In this chapter, the implementation of polypropylene FRC into the finite element (FE) analysis program VecTor2 (Vecchio, 1990) will be outlined. Following this, numerical models of the in-plane shear panels tested in this work will be presented and the results will be discussed. The newly introduced fibre reinforcement types for macro-synthetic polypropylene fibres will be demonstrated through numerical models for panels DC-P3 and DC-P5. Finally, one series of the Altoubat et al. (2009) PPFRC shear-critical beams will also be presented to investigate the adequacy of available constitutive models for structure-level modelling of PPFRC. All of the models were made using the pre-processor software FormWorks-Plus (Sadeghian, 2012). Also, the post-processor, Augustus, was used to read the results and generate charts (Bentz, 2010).

6.2 Finite Element Implementation

In order to provide the user the option to model PPFRC structures and to accommodate the formulations for polypropylene fibres as discussed in Chapter 5, two new smeared fibre reinforcement types were added to the FE analysis program VecTor2. These were "Polypropylene – Deformed" (smeared Reinforcement Type 14 in the structure input file, *.S2R) and "Polypropylene – Smooth" (smeared Reinforcement Type 15). The user inputs for these fibres are identical to those for the previously implemented "Steel – End-Hooked" and "Steel – Straight" (smeared Reinforcement Types 6 and 7 respectively). These inputs (in the order they appear in FormWorks-Plus and in the structure input file) are: fibre volume fraction (V_f in %), fibre length (l_f in mm), fibre diameter (d_f in mm), fibre tensile strength (f_{fu} in MPa) and fibre bond strength ($\tau_{f,tot}$ in MPa). Many of these properties are readily available on fibre product data sheets. For the fibre bond strength, if experimentally determined values are available, then these may be input by the user. In the case of Polypropylene – Deformed fibres, this input bond strength is sub-divided into the frictional bond strength (45%) and mechanical anchorage strength (55%), based on the findings summarized in Chapter 5. If Polypropylene – Smooth fibres are used, then the input bond strength is assigned entirely to the frictional bond component, as no mechanical anchorage is assumed. If the user does not input a value for bond strength, then the default bond parameters are used.

$$\begin{aligned} \tau_{f,tot} &= 0.441\sqrt{f_c'} \text{ for Polypropylene} - \text{Deformed fibres} \\ \tau_{f,tot} &= 0.198\sqrt{f_c'} \text{ for Polypropylene} - \text{Smooth fibres} \end{aligned} \tag{6.1}$$

Beyond the addition of the new reinforcement types, the implementation of the formulations developed in Chapter 5 was straightforward. In the calculation for fibre tension according to the SDEM, the formulas for both the monotonic and cyclic models were updated to include the adjusted values of slip at peak frictional bond strength ($s_f = 0.01\,mm$), slip at peak mechanical anchorage strength ($s_{def} = 0.5\,mm$), and the crack width at the termination of mechanical anchorage effects ($l_{def} = 7.5\,mm$). These apply only if polypropylene fibres are selected.

Also, the source code was merely updated to include material types 14 and 15 for all statements related to FRC. In this way, the existing relationships for steel fibres in terms of cracking, contributions to tension stiffening with conventional steel bars, stiffness matrix derivation, etc. were utilized for polypropylene fibre types as well. Details of such implementations for steel fibres can be found in the Updated FormWorks and VecTor2 User's Manual in Sections 2.2.6, 2.4.1, 4.4.2, 4.6.2, 4.6.3, 4.6.4 and 4.11 (Wong et al., 2012). It is worth noting that the VecTor2 program also offers the user the option to model materials such as Concrete-SFRC Laminates or Masonry-SFRC Laminates (Wong et al., 2012). These have not been updated to include PPFRC Laminates as such experimental investigations have not been performed.

Finally, poor secant stiffness convergence was found in initial analyses using polypropylene fibres. Upon investigation this was found to be caused by the calculation of slip at the maximum crack width. For SFRC members, Equation 6.2 is used in VecTor2 to relate the average crack width to the maximum crack width for an element size of 1000 mm (Wong et al., 2012).

$$w_{cr,max} = \left(1.7 + 3.4\frac{V_f l_f}{d_f}\right) w_{cr,avg} \tag{6.2}$$

For an element size less than 1000 mm the maximum crack width is interpolated as shown in Figure 6.1. Since structural panels are customarily modelled as a single 890 x 890 mm element (as discussed in Section 6.3), and since the fibre volume fraction used for the polypropylene specimens was high, this gives a maximum crack width five to six times greater than the average crack width. As a result of this, even though the slip of FRC members is typically low (Susetyo, 2009), an exaggerated slip was calculated at the maximum crack width, leading to instability in the numerical model. As a result, it was deemed prudent to turn off the slip calculation at the maximum crack width for PPFRC members until further investigation into the relationship between average and maximum crack width is completed. This greatly improved the convergence of the panel models.

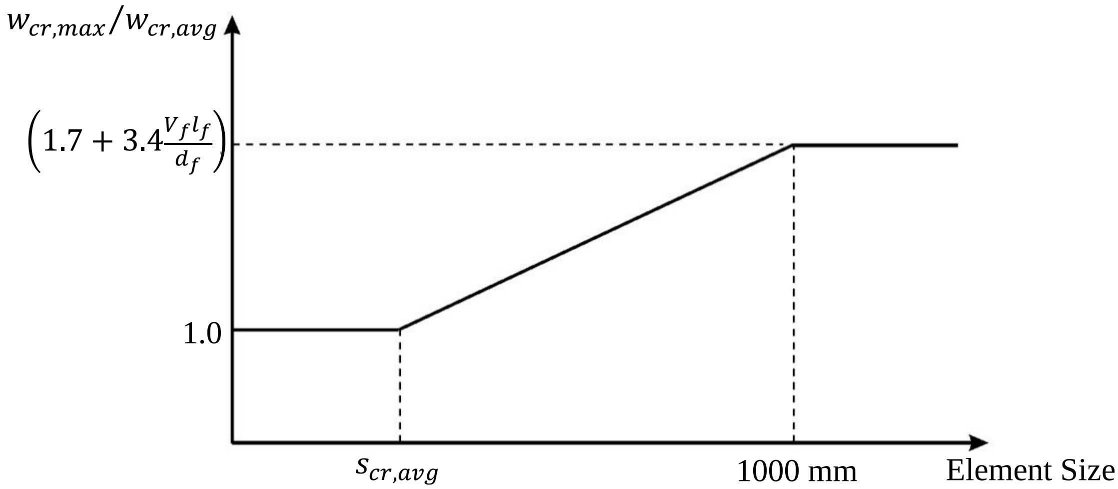

Figure 6.1: Effect of element size on maximum crack width used for SFRC in VecTor2

6.3 Modelling of the Panel Specimens

In VecTor2, the panel specimens were modelled as a single in-plane rectangular finite element with dimensions of 890 x 890 mm, and a thickness of 70 mm (Susetyo, 2009). The restraints were assigned as a pin connection in the lower left corner and a vertical roller in the lower right corner, as depicted in Figure 6.2.

The numerical models were constructed for load-controlled analyses, to be consistent with the force-controlled experiments. For the monotonic panels, the numerical loading (also depicted in Figure 6.2) was monotonically increased by 0.5 kN (or 0.016 MPa) at each analysis step until failure. For the panels experimentally tested under reversed cyclic loading, it was deemed sufficient to increase the maximum shear stress at each cycle by 0.5 MPa. This represented an average increase in shear stress consistent with the loading protocols used in the experimental program. Thus, the reversed cyclic numerical models were subjected to two repetitions of cycles that increased by 0.5 MPa until failure. A load step of 0.5 kN (or 0.016 MPa) was used for these models as well.

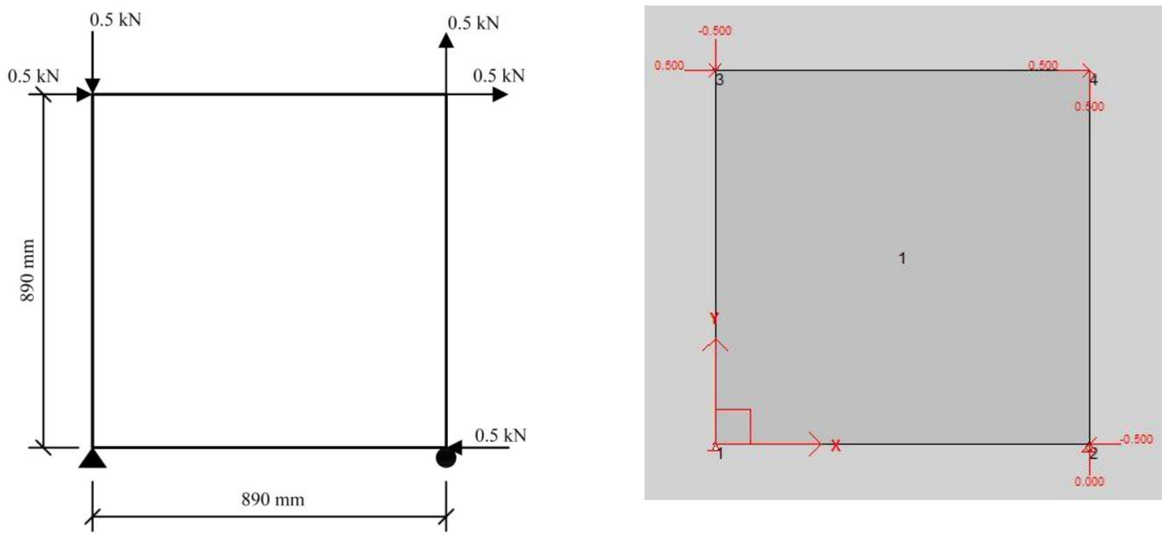

(a) (b)

Figure 6.2: Panel element subjected to positive pure shear for numerical modelling: (a) Idealized panel sketch; (b) FormWorks-Plus model

The experimentally determined properties of the concrete, such as the secant modulus of elasticity or peak strain, were not input into the analysis program, with the exception of the concrete compressive strength and maximum aggregate size. In this way, default concrete parameters included in the software were used. The fibre reinforcement was modelled as smeared reinforcement by selecting Reinforcement Type 6 for end-hooked steel or Type 14 for deformed polypropylene. The properties of these fibres were input to the model, with the exception of the bond strengths as the program default values were used. It is worth noting that in order to investigate the benefits of the modelling strategy developed in Chapter 5, the PPFRC panels DC-P3 and DC-P5 were also analysed using Reinforcement Type 7 (Steel – Straight), as this was the best method available for PPFRC fibre modelling in the previous version of VecTor2. Details of the concrete and fibre inputs are presented in Table 3.5.

In addition, the x- and y-direction conventional reinforcements were modelled as smeared reinforcement embedded in the concrete. The reinforcement properties presented in Table 6.2 were input to the model. The FRC panels contained only the x-direction reinforcement.

Finally, the constitutive models used in the FE analysis were the default models included in VecTor2. The motivation for this choice was the desire to investigate the ability to achieve a reasonable numerical result without tweaking a number of available relationships. Thus, a user with limited knowledge of advanced constitutive models for concrete may still achieve a reasonable result. There were exceptions to this decision. The first was the pre-peak compression model for concrete, for which the Popovics High Strength Concrete model (Compression Pre-Peak Model 3) was selected due to the high strength concrete used ($f_c' \geq 41$ MPa). Second, the exponential tension softening model (Tension Softening Model 5) was selected as this is the concrete tension softening model recommended for use with the SDEM. The constitutive and analysis models used are presented in Table 6.3 and Table 6.4.

Table 6.1: Concrete and Fibre Properties for Panel Models

Panel	f_c' [MPa]	a_{max} [mm]	Fibre Type	V_f [%]	l_f [mm]	d_f [mm]	f_{uf} [MPa]
DC-P1	71.7	10	-	-	-	-	-
DC-P2	62.2	10	Steel – End-Hooked	1.0	30	0.38	2300
DC-P3	50.9	10	Polypropylene - Deformed	2.0	54	0.81	520
DC-P4	64.0	10	Steel – End-Hooked	1.0	30	0.38	2300
DC-P5	54.3	10	Polypropylene - Deformed	2.0	54	0.81	520
C1C	65.7	10	-	-	-	-	-
C1F1V1	51.4	10	Steel – End-Hooked	0.5	50	0.62	1050
C1F1V2	53.4	10	Steel – End-Hooked	1.0	50	0.62	1050
C1F1V3	49.7	10	Steel – End-Hooked	1.5	50	0.62	1050

Table 6.2: Reinforcement Properties for Panel Models

Panel	ρ [%]	d_b [mm]	f_y [MPa]	f_u [MPa]	E_s [MPa]	ε_{sh} [x10^{-3}]	ε_u [x10^{-3}]
DC-P1 (X-Direction)	3.31	8.10	446.4	605.4	192,515	3.15	39.6
DC-P1 (Y-Direction)	0.42	5.72	484.3	624.4	183,850	3.30	22.7
DC-P2 (X-Direction)	3.31	8.10	446.4	605.4	192,515	3.15	39.6
DC-P3 (X-Direction)	3.31	8.10	446.4	605.4	192,515	3.15	39.6
DC-P4 (X-Direction)	3.31	8.10	446.4	605.4	192,515	3.15	39.6
DC-P5 (X-Direction)	3.31	8.10	446.4	605.4	192,515	3.15	39.6
C1C (X-Direction)	3.31	8.10	552.0	647.0	224,700	2.58	45.4
C1C (Y-Direction)	0.42	5.72	447.0	549.0	187,200	2.41	57.6
C1F1V1 (X-Direction)	3.31	8.10	552.0	647.0	224,700	2.58	45.4
C1F1V2 (X-Direction)	3.31	8.10	552.0	647.0	224,700	2.58	45.4
C1F1V3 (X-Direction)	3.31	8.10	552.0	647.0	224,700	2.58	45.4

Table 6.3: Constitutive Models used in Panel Analysis

Concrete Constitutive Models			
Compression Pre-Peak	Popovics (HSC)	**Dilation**	Variable - Kupfer
Compression Post-Peak	Modified Park-Kent	**Cracking Criterion**	Mohr-Coulomb (Stress)
Compression Softening	Vecchio 1992-A	**Crack Stress Calc**	Basic (DSFM/MCFT)
Tension Stiffening	Modified Bentz 2003	**Crack Width Check**	Agg/5.0 Max Crack Width
Tension Softening	Exponential	**Crack Slip Calc**	Walraven (Monotonic)
FRC Tension	SDEM - Monotonic	**Hysteretic Response**	Nonlinear w/ Plastic Offsets
Confined Strength	Kupfer/Richart		
Reinforcement Constitutive Models			
Hysteretic Response	Bauschinger Effect (Seckin)	**Buckling**	Refined Dhakal-Maekawa
Dowel Action	Tassios (Crack Slip)	**Concrete Bond**	Eligehausen

Table 6.4: Analysis Options used in Panel Analysis

Maximum Number of Iterations	60	**Strain History**	Previous Loading Considered
Averaging Factor	0.6	**Strain Rate Effects**	Not Considered
Convergence Limit	1.0001	**Structural Damping**	Not Considered
Convergence Criteria	Displacements – Weighted Average	**Geometric Nonlinearity**	Considered
Analysis Mode	Static Nonlinear – Load Step	**Crack Process**	Uniform

For each of the panels, a number of the experimental and numerical responses are presented for comparison. These are the shear stress versus shear strain, principal tensile stress versus principal tensile strain, principal compressive stress versus principal compressive strain, shear stress versus inclination of the principal stress field, and shear stress versus inclination of the principal strain field. In addition, tables of pertinent analytical and numerical values are shown.

6.3.1 Conventionally Reinforced Concrete Panels

For the purpose of this study, both Panel C1C (monotonic pure shear tested by Susetyo (2009)) and Panel DC-P1 (reversed cyclic pure shear tested in this work) were modelled to investigate the quality of the prediction attained for conventionally reinforced panels under monotonic or reversed cyclic loads. The experimental and numerical responses of Panel C1C and Panel DC-P1 are presented in Figure 6.3 and Figure 4.32 respectively, with summary values in Table 6.5.

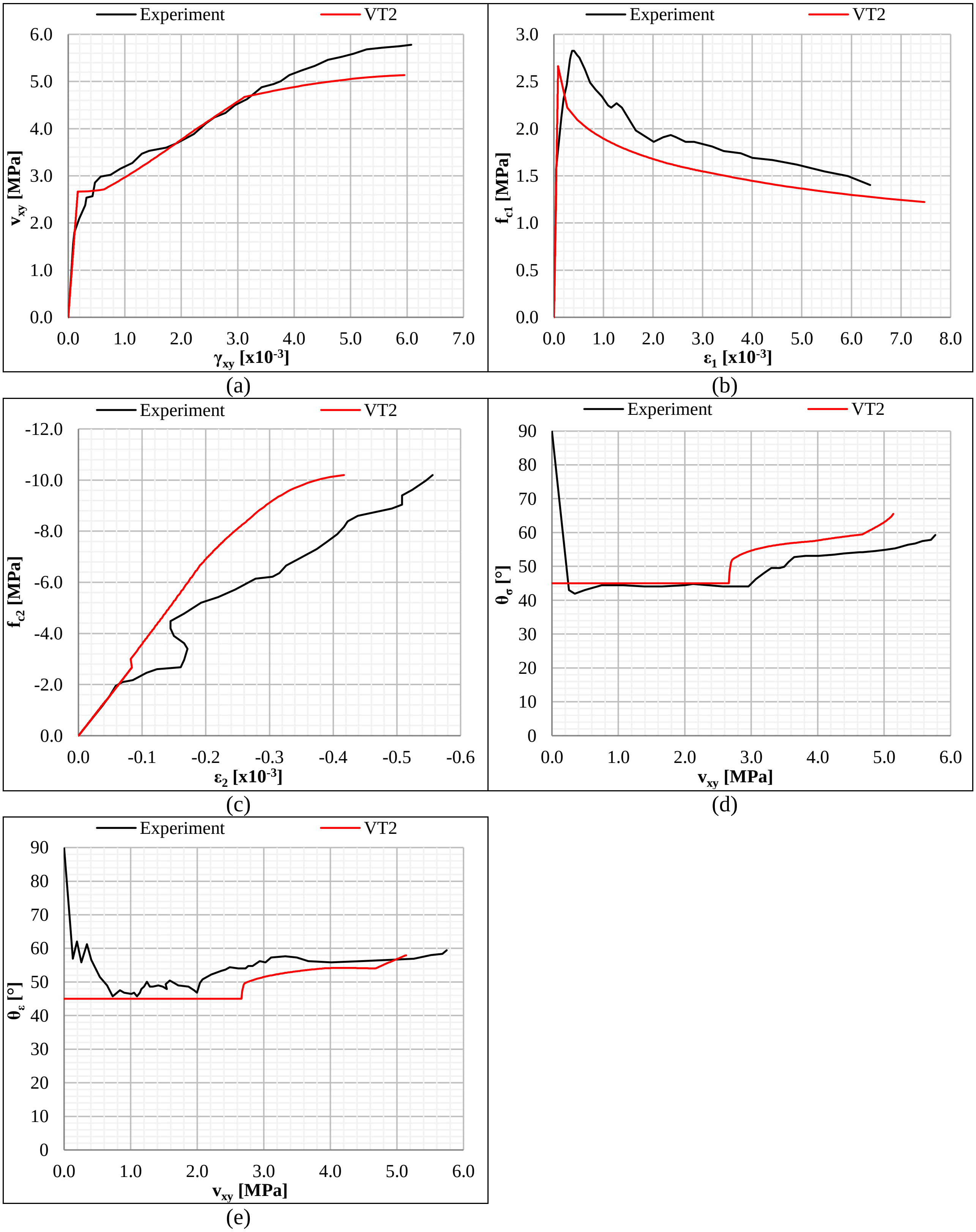

Figure 6.3: Comparison of experimental and numerical responses for Panel C1C: (a) $v_{xy} - \gamma_{xy}$; (b) $f_{c1} - \varepsilon_1$; (c) $f_{c2} - \varepsilon_2$; (d) $\theta_\sigma - v_{xy}$; (e) $\theta_\varepsilon - v_{xy}$

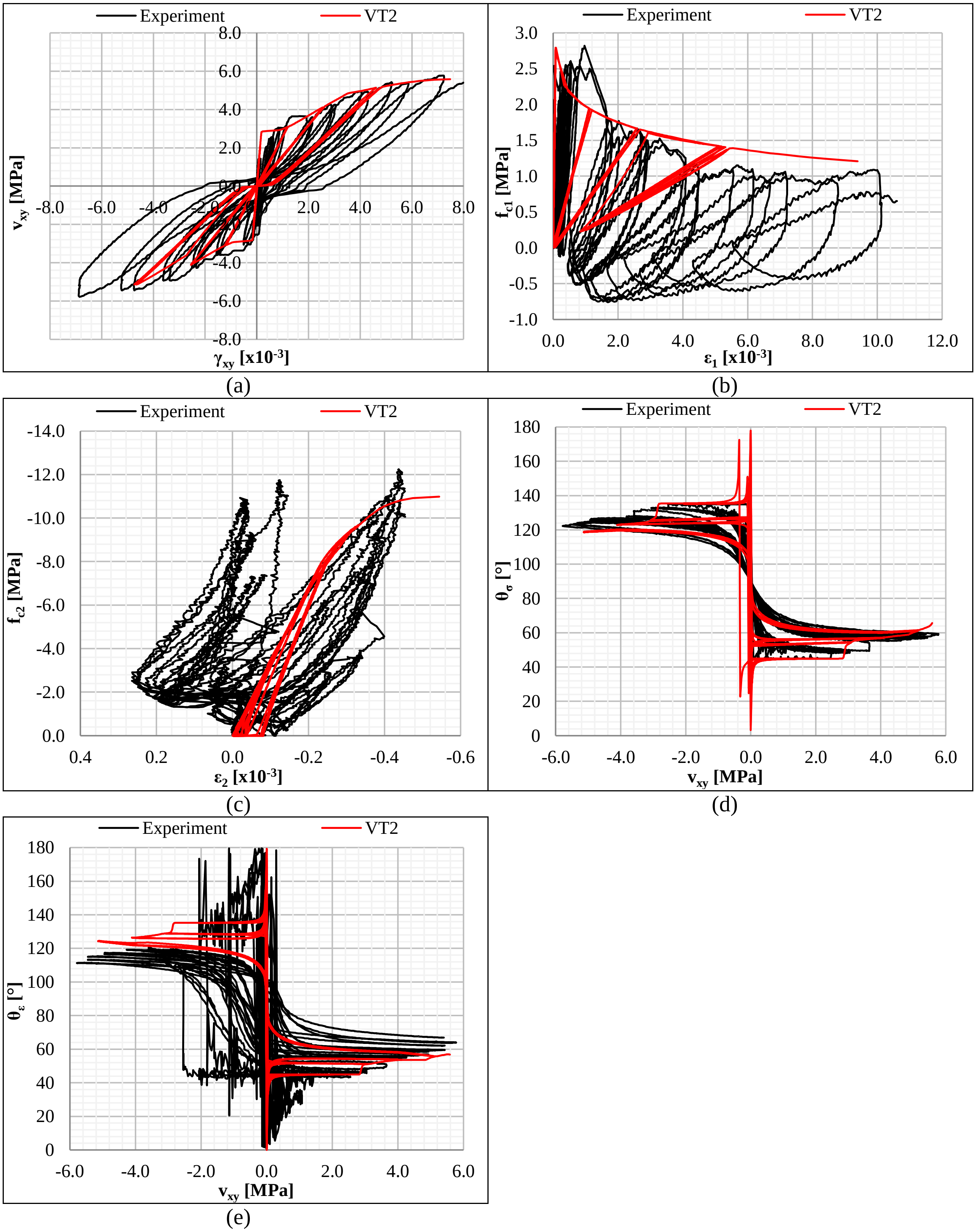

Figure 6.4: Comparison of experimental and numerical responses for Panel DC-P1: (a) $v_{xy} - \gamma_{xy}$; (b) $f_{c1} - \varepsilon_1$; (c) $f_{c2} - \varepsilon_2$; (d) $\theta_\sigma - v_{xy}$; (e) $\theta_\varepsilon - v_{xy}$

Table 6.5: Summary of Numerical and Experimental Results for Conventionally Reinforced Concrete Panels

Panel	v_u [MPa]	$f_{c1,max}$ [MPa]	$f_{c1,u}$ [MPa]	$f_{c2,u}$ [MPa]	$\theta_{\sigma,u}$ [°]	$f_{sx,max}$ [MPa]	$f_{sy,max}$ [MPa]	$v_{ci,u}$ [MPa]	$\frac{v_{u,VT2}}{v_{u,exp}}$
C1C	5.14 (5.77)	2.66 (2.87)	1.22 (1.43)	-10.20 (-11.70)	65.5 (59.5)	211 (250)	472 (501)	1.86	0.89
DC-P1	5.58 (5.79)	2.79 (2.82)	1.21 (0.65)	-10.98 (-11.63)	65.6 (59.2)	222 (267)	574 (611)	1.74	0.96

Panel	γ_u [x10^{-3}]	$\varepsilon_{1,max}$ [x10^{-3}]	$\varepsilon_{1,u}$ [x10^{-3}]	$\varepsilon_{2,u}$ [x10^{-3}]	$\theta_{\varepsilon,u}$ [°]	w_m [mm]	s_m [mm]	$\delta_{s,u}$ [mm]	$d\theta_u$ [°]	$\frac{\gamma_{u,VT2}}{\gamma_{u,exp}}$
C1C	5.95 (6.01)	0.084 (0.360)	7.47 (6.29)	-0.417 (-0.618)	58.0 (59.9)	0.86 (0.55)	107 (57.2)	0.26	4.72 (-0.43)	0.99
DC-P1	7.46 (7.98)	0.084 (0.967)	9.39 (10.60)	-0.544 (-0.445)	56.8 (66.9)	0.95 (0.57)	105 (55.6)	0.31	5.0 (-7.7)	0.93

Note: values in brackets are experimentally determined

Overall, the experimental responses for both of the panels were well represented with the numerical model. The predicted ultimate shear strength and shear strain were well within acceptable limits of 20%. Other stress and strain parameters were similarly well predicted, with the exception of the principal tensile strain at maximum principal tensile stress. This was because the experimentally observed strain hardening was not exhibited in the numerical result for both panels. In addition, the crack width and crack spacing at the end of the test were overpredicted for both panels.

In terms of the reversed cyclic DC-P1, the softness of the unloading branch of the shear stress versus shear strain response was well captured, matching closely with that determined from the experiments. The same cannot be said for the principal tensile stress versus principal tensile strain response, although the overall degradation in principal tensile stress through the progression of the test was adequately represented. The amount of plastic offset in the shear strain and principal tensile strain were also underestimated. For both panels, the inclination of the principal tensile stress direction was consistently steeper and the inclination of the principal tensile strain direction was consistently shallower for the numerical models.

Lastly, the failure through yielding of the y-direction reinforcement was correctly captured, as the numerical model predicted y-direction reinforcement stresses at failure to be greater than the input yield strength. This yielding correctly occurred before the maximum concrete stress was reached, consistent with the absence of concrete crushing in the experiments. The slight underprediction of all stress parameters was due to the premature failure of the models since an idealized steel stress-strain response with a small yield plateau was input for simplicity. The steel coupons tests exhibited no yield plateau.

6.3.2 Steel Fibre Reinforced Concrete Panels

Panels C1F1V1, C1F1V2, C1F1V3, DC-P2 and DC-P4 were similarly modelled to determine the adequacy of available constitutive models for SFRC representation under monotonic and reversed cyclic shear loads. The responses are plotted in Figure 6.5 to Figure 6.9, and pertinent values are summarized in Table 6.6.

Contrary to the findings of Susetyo (2009), the response of SFRC was well represented with the use of the SDEM and the Disturbed Stress Field Model (Vecchio, 2000) in VecTor2. Susetyo (2009) obtained significant overpredictions of shear strength and ductility when modelling the experimental panels. Susetyo (2009) noted that this was due to the lack of calculated slip at the crack for FRC members. Without this local effect, the analysis continued until either the concrete crushed or the x-direction steel yielded, inconsistent with the experimental result (Susetyo, 2009). This has subsequently been corrected in the VecTor2 source code, as each of the SFRC models exhibited some slip stresses and displacements. In all cases neither the maximum concrete strength nor the x-direction reinforcement yield strength were achieved, suggesting the failure mode was correctly predicted as aggregate interlock failure due to the termination of fibre crack bridging abilities across the maximum crack width.

The shear strength was well represented, with a mean predicted-to-experimental shear strength of 1.00 (CV = 16.7%). Interestingly, the prediction of all strength parameters for DC-P2 were consistently low (predicted-to-experimental shear strength ratio of 0.78). This was consistent with the underprediction obtained when using the SDEM to model the response of the DC-P2 dogbones as shown in Figure 5.6. This is attributed to the significant coefficient of variation in fibre orientation, and in the number of fibres crossing the crack, which has been reported as 20% (Oh, 2011). The overprediction attained for C1F1V3 (predicted-to-experimental shear strength ratio of 1.23) is likely also attributable to this phenomenon, but may also be attributed to the underprediction of crack width for this specimen (0.26 mm numerically compared to 0.45 mm experimentally). This inaccurately small crack width would lead to a higher tensile contribution of the fibres when using the SDEM. In most other cases, the mean crack widths at failure were accurately represented, albeit consistently low for long fibres and high for short fibres.

The shear strain at ultimate was also within an acceptable range on average (1.16 with a CV of 30.5%), but in some cases the prediction was poor. For DC-P2, all ultimate strains were underestimated, likely suggesting that crack bridging for short fibres was not adequately represented in the analysis. This is consistent with the overestimated crack widths.

In general, the responses of the monotonic panels were well captured with the use of VecTor2. The most notable exceptions to this were for C1F1V1 and DC-P2, as both the shear stress and principal tensile stress were underpredicted at low strains. The degree of strain hardening was underestimated for each of these specimens.

The reversed cyclic Panel DC-P4 was also poorly represented. Due to the absence of yielded steel reinforcement, plastic offsets were incorrectly not exhibited. The unloading portions of the responses were peculiar and curvilinear, while always returning to zero. Also, the principal compressive strain remained negative throughout the duration of the analysis, converse to the experiment which exhibited positive compressive straining as a result of cracks not fully closing. Similar to DC-P2, both the shear stress and principal tensile stress were substantially underestimated at low strains, suggesting that the relatively good prediction for the ultimate shear stress and principal tensile stress was coincidental. It is clear that the degradation in crack bridging tendencies of the fibres and in aggregate interlock exhibited in the reversed cyclic experiment were not well captured in the analysis. This delayed the crack slip failure in the analysis and allowed for improvements of the load-carrying capacity at high strains, giving the seemingly accurate predictions of shear strength and principal tensile stress at failure, but also leading to a poor estimation of shear strain (predicted-to-experimental ratio of 1.59). Overall, the degradation of SFRC as a result of successive stretching and buckling of the steel fibres was not well represented. This tendency was similarly exhibited for Panel DC-P5, as will be shown in Section 6.3.3. Improvements to the available models are required to capture the effects of fibres on crack closing and crack slip. This may improve the prediction of response degradation and plastic offset in FRC.

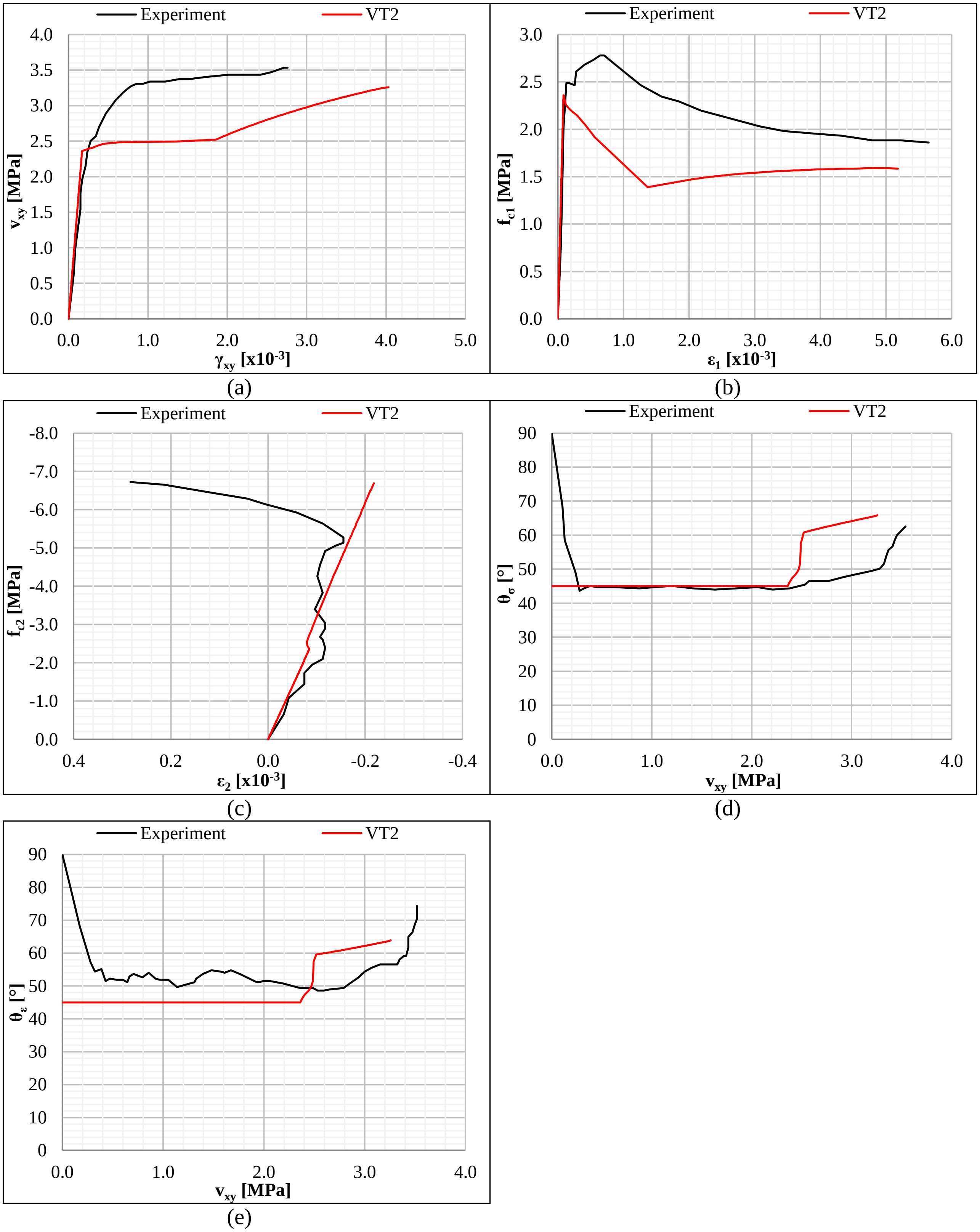

Figure 6.5: Comparison of experimental and numerical responses for Panel C1F1V1: (a) $v_{xy} - \gamma_{xy}$; (b) $f_{c1} - \varepsilon_1$; (c) $f_{c2} - \varepsilon_2$; (d) $\theta_\sigma - v_{xy}$; (e) $\theta_\varepsilon - v_{xy}$

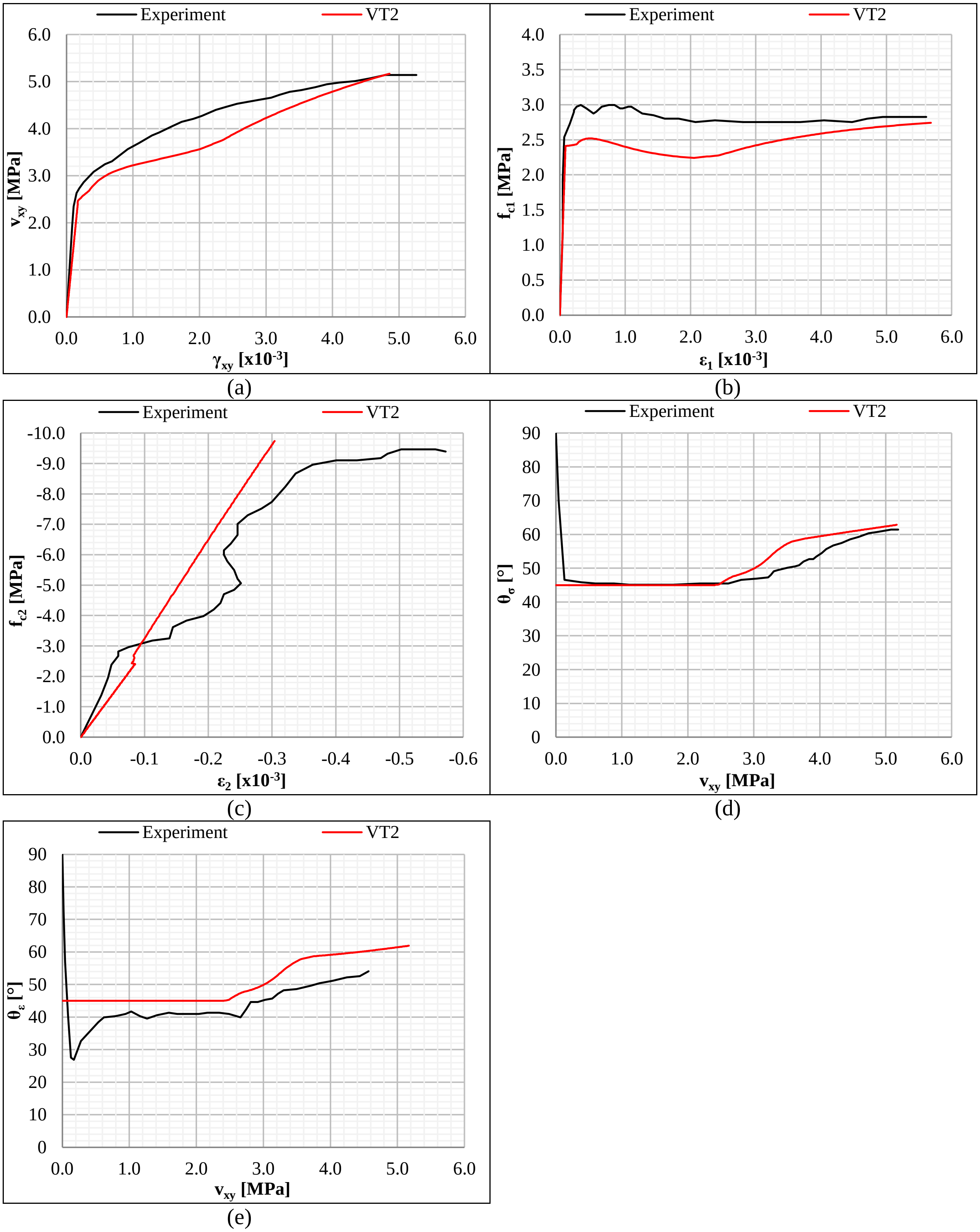

Figure 6.6: Comparison of experimental and numerical responses for Panel C1F1V2: (a) $v_{xy} - \gamma_{xy}$; (b) $f_{c1} - \varepsilon_1$; (c) $f_{c2} - \varepsilon_2$; (d) $\theta_\sigma - v_{xy}$; (e) $\theta_\varepsilon - v_{xy}$

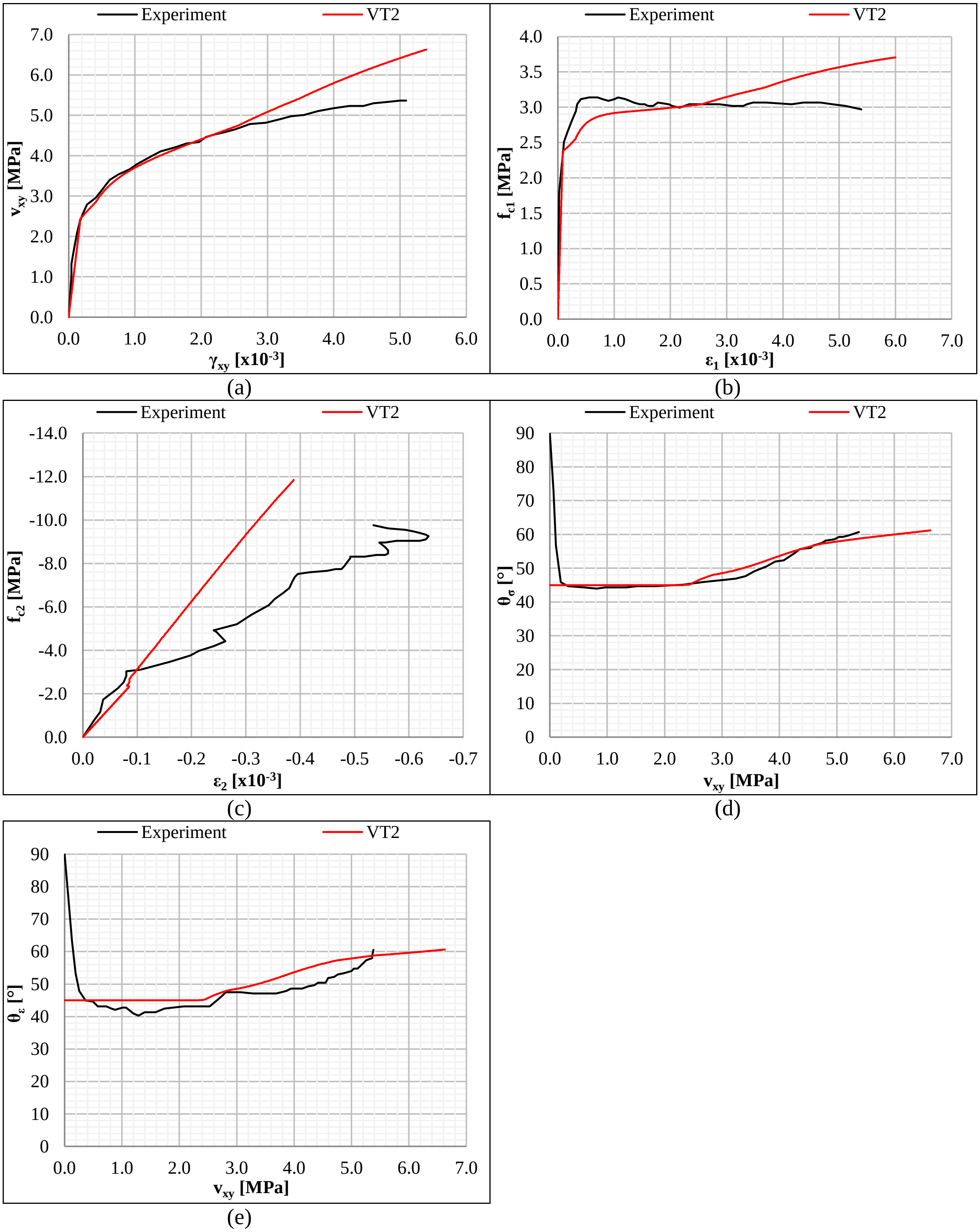

Figure 6.7: Comparison of experimental and numerical responses for Panel C1F1V3: (a) $v_{xy} - \gamma_{xy}$; (b) $f_{c1} - \varepsilon_1$; (c) $f_{c2} - \varepsilon_2$; (d) $\theta_\sigma - v_{xy}$; (e) $\theta_\varepsilon - v_{xy}$

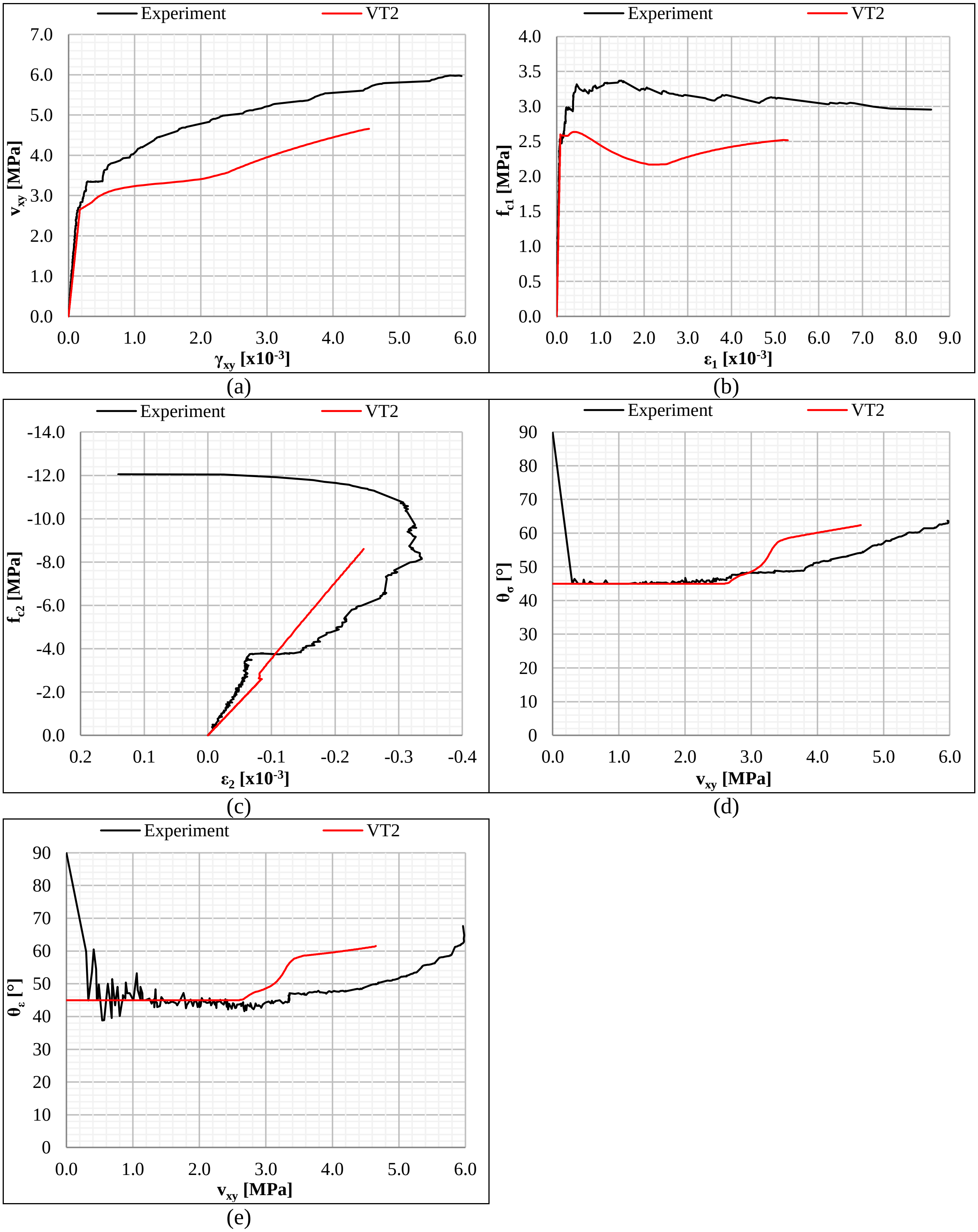

Figure 6.8: Comparison of experimental and numerical responses for Panel DC-P2: (a) $v_{xy} - \gamma_{xy}$; (b) $f_{c1} - \varepsilon_1$; (c) $f_{c2} - \varepsilon_2$; (d) $\theta_\sigma - v_{xy}$; (e) $\theta_\varepsilon - v_{xy}$

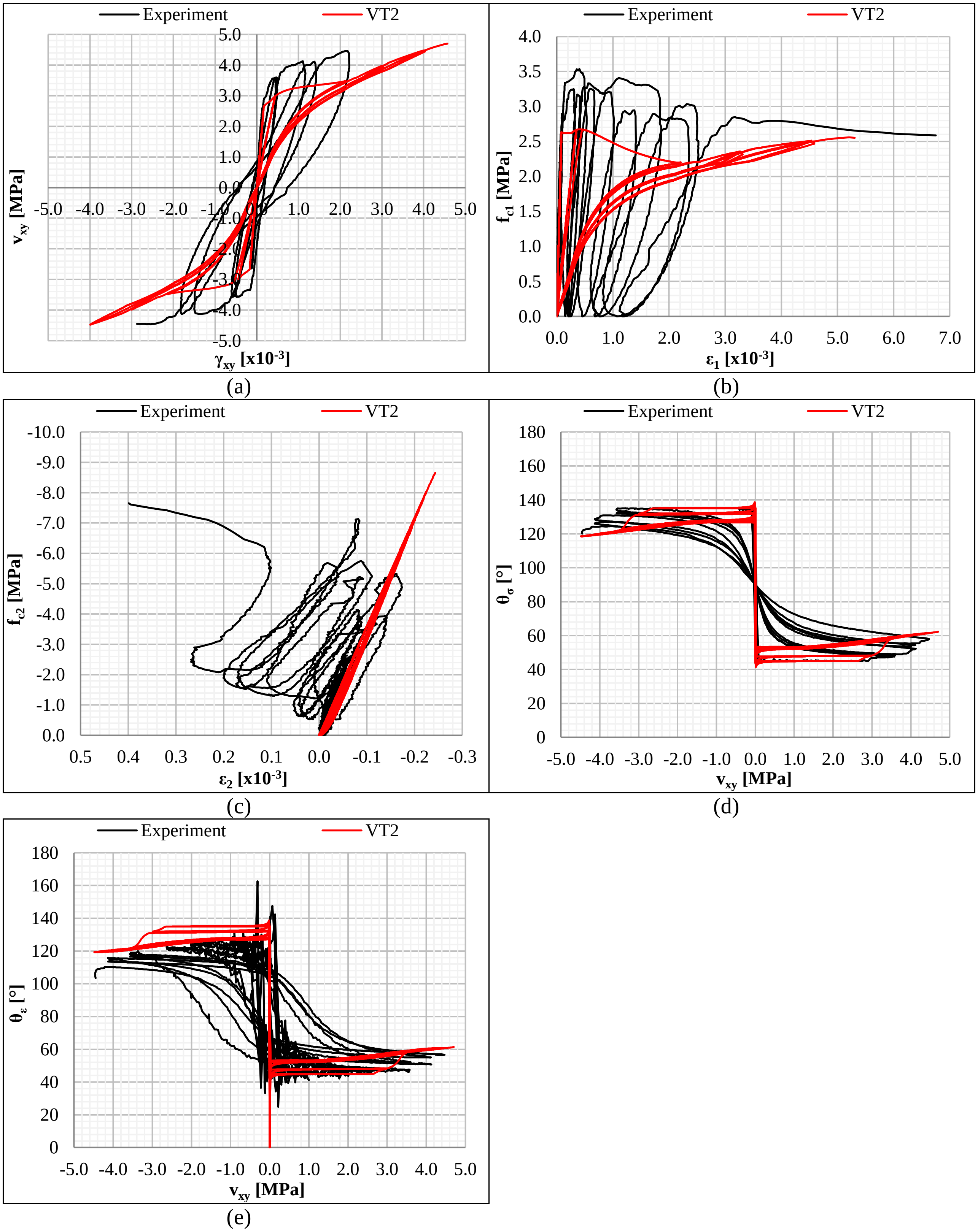

Figure 6.9: Comparison of experimental and numerical responses for Panel DC-P4: (a) $v_{xy} - \gamma_{xy}$; (b) $f_{c1} - \varepsilon_1$; (c) $f_{c2} - \varepsilon_2$; (d) $\theta_\sigma - v_{xy}$; (e) $\theta_\varepsilon - v_{xy}$

Table 6.6: Summary of Numerical and Experimental Results for SFRC Panels

Panel	v_u [MPa]	$f_{c1,max}$ [MPa]	$f_{c1,u}$ [MPa]	$f_{c2,u}$ [MPa]	$\theta_{\sigma,u}$ [°]	$f_{sx,max}$ [MPa]	$f_{sy,max}$ [MPa]	$v_{ci,u}$ [MPa]	$\frac{v_{u,VT2}}{v_{u,exp}}$
DC-P2	4.66 (5.97)	2.64 (3.37)	2.52 (2.95)	-8.60 (-12.05)	62.4 (63.7)	184 (275)	-	0.31	0.78
DC-P4	4.70 (4.47)	2.67 (3.54)	2.55 (2.59)	-8.66 (-7.66)	62.3 (-59.8)	184 (153)	-	0.31	1.05
C1F1V1	3.26 (3.53)	2.36 (2.83)	1.59 (1.85)	-6.69 (-6.73)	65.9 (62.3)	154 (148)	-	0.56	0.92
C1F1V2	5.17 (5.17)	2.74 (3.04)	2.74 (2.82)	-9.74 (-9.46)	62.9 (61.4)	211 (201)	-	0.29	1.00
C1F1V3	6.63 (5.37)	3.71 (3.13)	3.71 (2.97)	-11.85 (-9.70)	61.2 (61.0)	246 (204)	-	0.16	1.23

Panel	γ_u [x10^{-3}]	$\varepsilon_{1,max}$ [x10^{-3}]	$\varepsilon_{1,u}$ [x10^{-3}]	$\varepsilon_{2,u}$ [x10^{-3}]	$\theta_{\varepsilon,u}$ [°]	w_m [mm]	s_m [mm]	$\delta_{s,u}$ [mm]	$d\theta_u$ [°]	$\frac{\gamma_{u,VT2}}{\gamma_{u,exp}}$
DC-P2	4.54 (5.94)	0.408 (1.466)	5.29 (8.58)	-0.245 (0.141)	61.5 (67.6)	0.28 (0.21)	53 (43.0)	0.01	0.52 (-3.9)	0.76
DC-P4	4.57 (2.87)	0.410 (0.402)	5.31 (6.75)	-0.243 (0.399)	61.4 (-76.6)	0.28 (0.22)	53 (71.0)	0.01	0.51 (16.8)	1.59
C1F1V1	4.03 (2.77)	0.085 (0.724)	5.18 (5.66)	-0.218 (0.286)	63.9 (74.5)	0.38 (0.55)	74 (114.4)	0.03	1.15 (-12.2)	1.45
C1F1V2	4.86 (5.27)	5.68 (0.266)	5.68 (5.61)	-0.304 (-0.572)	61.9 (60.9)	0.31 (0.45)	55 (54.7)	0.01	0.54 (0.55)	0.92
C1F1V3	5.40 (5.10)	6.00 (0.447)	6.00 (5.39)	-0.388 (-0.540)	60.7 (60.3)	0.26 (0.45)	43 (57.2)	0.00	0.32 (0.68)	1.06

Note: values in brackets are experimentally determined
Mean $v_{u,VT2}/v_{u,exp}$ = 1.00 with a CV of 16.7%; Mean $\gamma_{u,VT2}/\gamma_{u,exp}$ = 1.16 with a CV of 30.5%

6.3.3 Macro-Synthetic Fibre Reinforced Concrete Panels

In this section the analysis results for Panels DC-P3 and DC-P5 are presented. Three separate analyses were performed for these panels, so as to evaluate the benefits of the polypropylene fibre implementation developed in this work. The first analyses were run using the Reinforcement Type 7 (Steel – Straight fibres), representing the best representation of PPFRC response that could be attained using VecTor2 prior to this thesis. This is termed VT2 – Original in the figures provided. The second set of analyses, termed VT2 – PPFRC, used Reinforcement Type 14 (Polypropylene – Deformed) after the implementation detailed in Section 6.2 was completed. Finally, the third set of analyses utilized an attenuation factor of $c = 7.5$ to determine the fracture energy, in accordance with Section 5.3.4.1 of this work. This analysis is termed VT2 – PPFRC – f_t'/G_F = 7.5.

As discussed in Section 5.3.4.1, the attenuation factor $c = 15$ was proposed as part of the VEM to represent the tension softening behaviour of the concrete when steel fibres are used (Voo and Foster, 2003). Thus, the full exponential tension softening model:

$$f_{ct} = f_t' \cdot \exp(-f_t'/G_F * w_{cr}) \tag{5.22}$$

is replaced with:

$$f_{ct} = f_t' \cdot \exp(-c * w_{cr}) \tag{2.1}$$

such that the fracture energy becomes:

$$G_F = \frac{0.33\sqrt{f_c'}}{c} = \frac{0.33\sqrt{f_c'}}{7.5} \tag{6.3}$$

using the attenuation factor of $c = 7.5$ selected herein.

It is worth noting here that the attenuation factor of 7.5 was purposely left out of the program implementation. Thus, in order to use this attenuation factor, the fracture energy must be calculated from Equation 6.3 and input into the VT2.AUX file, or into the "Define Job → Auxiliary" dialog box in FormWorks-Plus (as shown in Figure 6.10). The value in the numerator of Equation 6.3 is the default value of cracking strength, f_t', used in VecTor2. If the user has input an experimentally determined value for cracking strength of concrete, then this input value should instead be used in the numerator of Equation 6.3. For DC-P3, the input fracture energy for this third set of analyses was 0.31 kN/m; a value of 0.32 kN/m was used for DC-P5.

The experimental and numerical results from the VT2 – Original and VT2 – PPFRC sets of analyses are presented for each panel in Figure 6.11 and Figure 6.12 and discussed in the next section. Subsequently, the experimental and numerical results from VT2 – PPFRC and VT2 – PPFRC – f_t'/G_F = 7.5 are presented for comparison in Figure 6.13 and Figure 6.14. Also, pertinent values for each of the analyses are summarized in Table 6.7, Table 6.8 and Table 6.9 respectively.

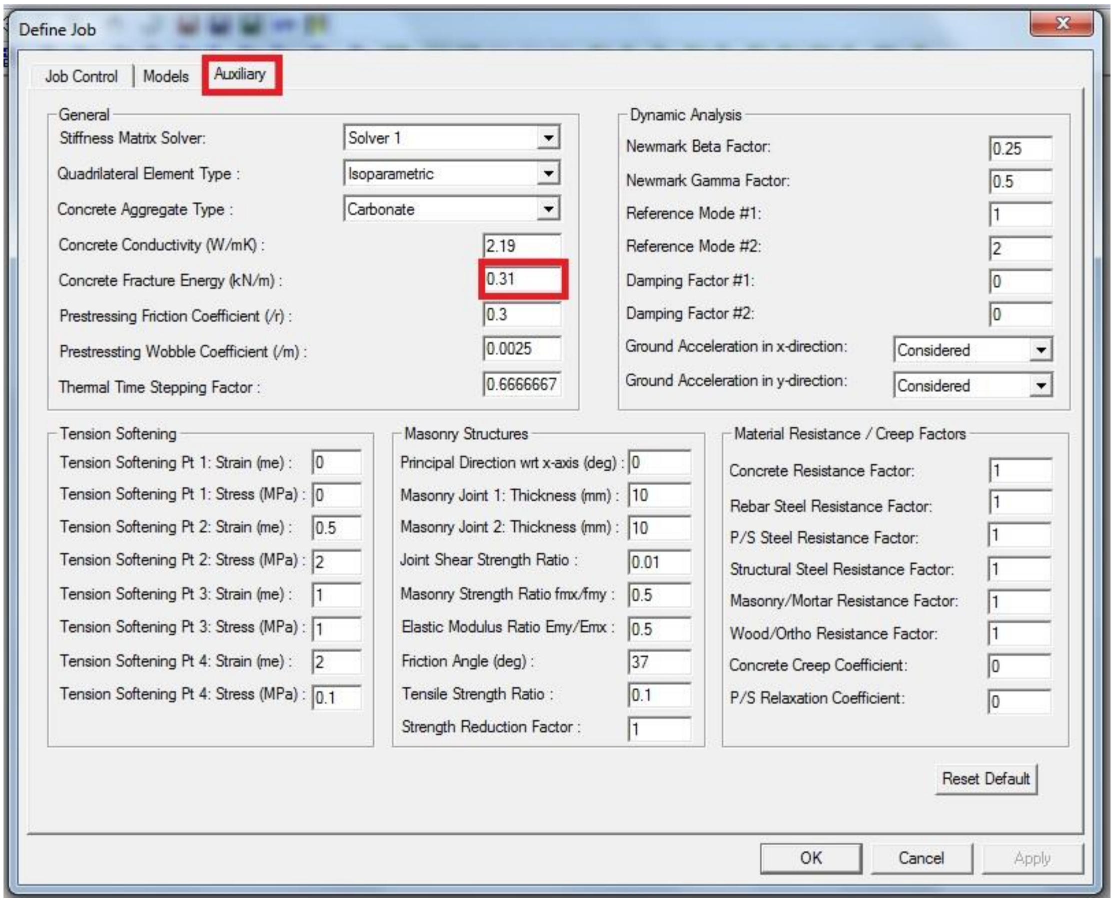

Figure 6.10: Fracture energy input field in FormWorks-Plus "Define Job" dialog box

6.3.3.1 Analysis Result using Newly Implemented Polypropylene Fibres

As can be seen from Figure 6.11 and Figure 6.12, the response of DC-P3 and DC-P5 were poorly represented using the previous version of VecTor2. Although strength values were reasonably well captured ($v_{u,VT2}/v_{u,exp}$ = 0.97 and 1.12 respectively), the ductility was poorly estimated ($\gamma_{u,VT2}/\gamma_{u,exp}$ = 0.48 and 0.75). Table 6.7 shows that the strains at ultimate were greatly underpredicted in all cases, likely due to the small calculated crack widths and slips at failure. Clearly, since the experimental program showed that PPFRC was able to transmit tensile stresses across large cracks, the analysis must be able to accommodate the corresponding large crack widths and strains at failure. The implementation of smooth and deformed polypropylene fibres corrected this deficiency in the VecTor2 prediction. As shown in Table 6.8, the numerical shear strain values at ultimate were substantially improved (predicted-to-experimental ratio of 0.90 for DC-P3, compared to 0.48). The crack widths at failure were much more accurately estimated meaning that the accommodation of large crack widths with polypropylene fibres was captured.

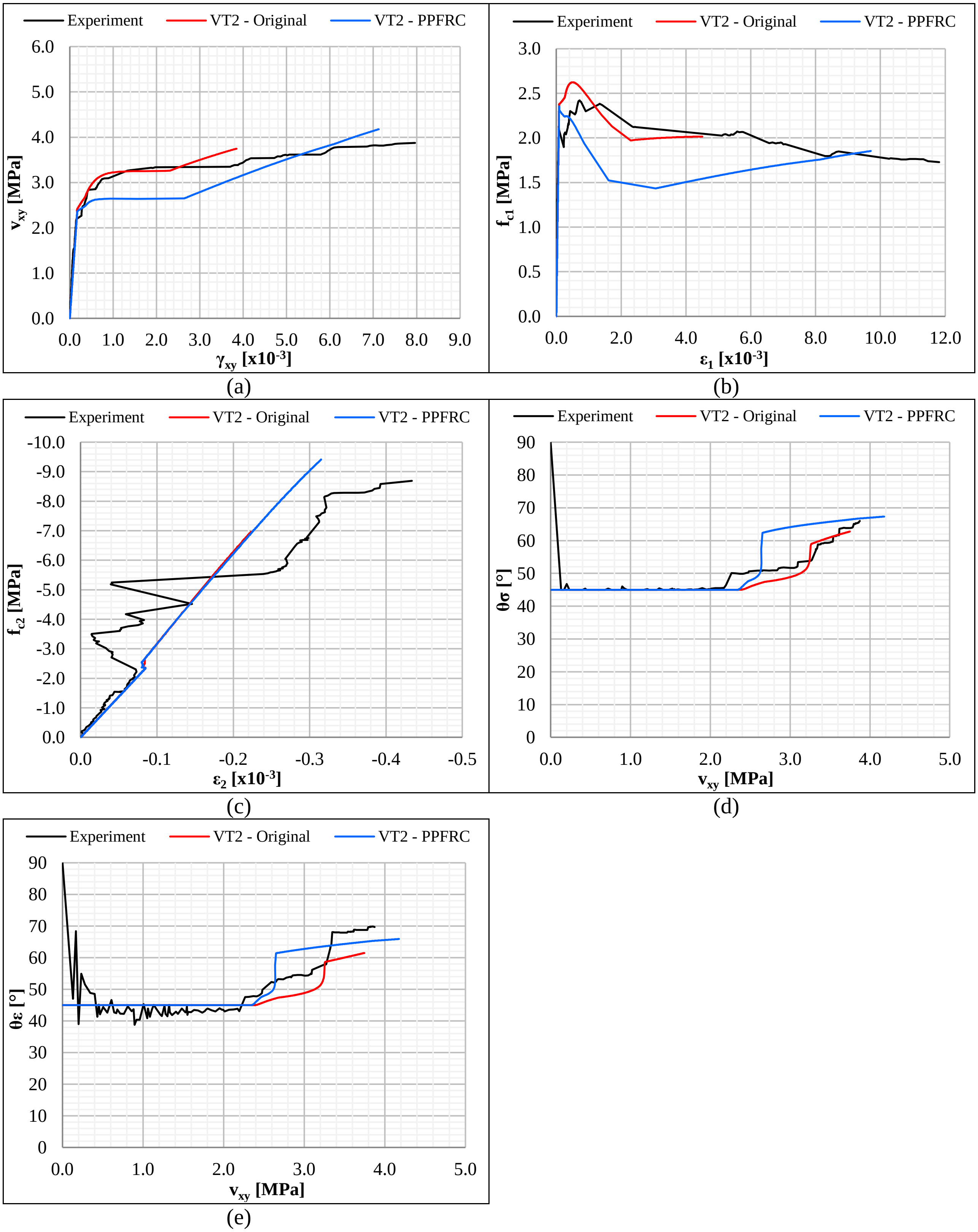

Figure 6.11: Comparison of experimental and numerical responses for Panel DC-P3: (a) $v_{xy}-\gamma_{xy}$; (b) $f_{c1}-\varepsilon_1$; (c) $f_{c2}-\varepsilon_2$; (d) $\theta_\sigma-v_{xy}$; (e) $\theta_\varepsilon-v_{xy}$

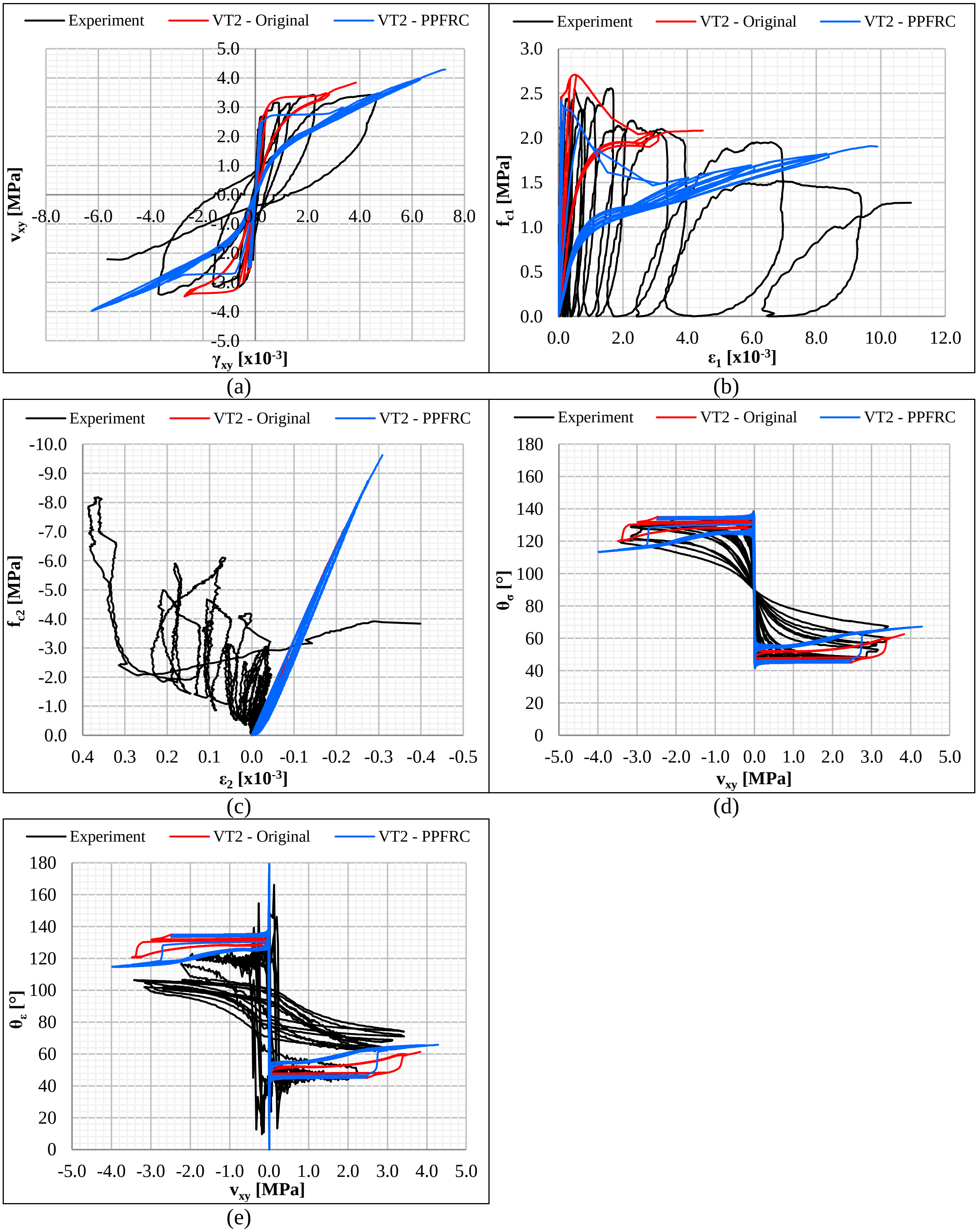

Figure 6.12: Comparison of experimental and numerical responses for Panel DC-P5: (a) $v_{xy} - \gamma_{xy}$; (b) $f_{c1} - \varepsilon_1$; (c) $f_{c2} - \varepsilon_2$; (d) $\theta_\sigma - v_{xy}$; (e) $\theta_\varepsilon - v_{xy}$

Table 6.7: Summary of Numerical and Experimental Results for PPFRC Panels using VT2 – Original

Panel	v_u [MPa]	$f_{c1,max}$ [MPa]	$f_{c1,u}$ [MPa]	$f_{c2,u}$ [MPa]	$\theta_{\sigma,u}$ [°]	$f_{sx,max}$ [MPa]	$f_{sy,max}$ [MPa]	$v_{ci,u}$ [MPa]	$\frac{v_{u,VT2}}{v_{u,exp}}$
DC-P3	3.75 (3.87)	2.62 (2.42)	2.02 (1.73)	-6.97 (-8.69)	62.8 (66.0)	149 (210)	-	0.36	0.97
DC-P5	3.84 (3.43)	2.71 (2.56)	2.08 (1.27)	-7.07 (-3.83)	62.5 (-60.0)	151 (204)	-	0.37	1.12

Panel	γ_u [x10^{-3}]	$\varepsilon_{1,max}$ [x10^{-3}]	$\varepsilon_{1,u}$ [x10^{-3}]	$\varepsilon_{2,u}$ [x10^{-3}]	$\theta_{\varepsilon,u}$ [°]	w_m [mm]	s_m [mm]	$\delta_{s,u}$ [mm]	$d\theta_u$ [°]	$\frac{\gamma_{u,VT2}}{\gamma_{u,exp}}$
DC-P3	3.85 (7.96)	0.494 (0.717)	4.50 (11.82)	-0.223 (-0.434)	61.5 (69.7)	0.24 (0.57)	54 (72.0)	0.01	0.71 (-3.7)	0.48
DC-P5	3.85 (5.15)	0.363 (1.615)	4.48 (10.94)	-0.218 (-0.399)	61.3 (-75.0)	0.24 (0.59)	53 (59.0)	0.01	0.69 (15.0)	0.75

Note: values in brackets are experimentally determined

Table 6.8: Summary of Numerical and Experimental Results for PPFRC Panels using VT2 – PPFRC

Panel	v_u [MPa]	$f_{c1,max}$ [MPa]	$f_{c1,u}$ [MPa]	$f_{c2,u}$ [MPa]	$\theta_{\sigma,u}$ [°]	$f_{sx,max}$ [MPa]	$f_{sy,max}$ [MPa]	$v_{ci,u}$ [MPa]	$\frac{v_{u,VT2}}{v_{u,exp}}$
DC-P3	4.18 (3.87)	2.35 (2.42)	1.85 (1.73)	-9.42 (-8.69)	67.3 (66.0)	229 (210)	-	0.34	1.08
DC-P5	4.29 (3.43)	2.42 (2.56)	1.90 (1.27)	-9.63 (-3.83)	67.3 (-60.0)	233 (204)	-	0.35	1.25

Panel	γ_u [x10^{-3}]	$\varepsilon_{1,max}$ [x10^{-3}]	$\varepsilon_{1,u}$ [x10^{-3}]	$\varepsilon_{2,u}$ [x10^{-3}]	$\theta_{\varepsilon,u}$ [°]	w_m [mm]	s_m [mm]	$\delta_{s,u}$ [mm]	$d\theta_u$ [°]	$\frac{\gamma_{u,VT2}}{\gamma_{u,exp}}$
DC-P3	7.13 (7.96)	0.085 (0.717)	9.70 (11.82)	-0.315 (-0.434)	65.9 (69.7)	0.61 (0.57)	63 (72.0)	0.03	0.83 (-3.7)	0.90
DC-P5	7.27 (5.15)	0.085 (1.615)	9.90 (10.94)	-0.309 (-0.399)	65.9 (-75.0)	0.62 (0.59)	63 (59.0)	0.03	0.81 (15.0)	1.42

Note: values in brackets are experimentally determined

In addition, the slip achieved before the breakdown of fibre crack bridging and aggregate interlock failure was tripled. This all led to an increase in the shear strength values, yet these still remained within an acceptable range of 20%.

Additionally, the mean predicted-to-experimental ratios were drastically skewed by the numerical result of Panel DC-P5. As previously noted, the ability of the analysis models to capture the degradation of FRC subjected to reversed cyclic loading was lacking. The peculiar curvilinear unloading branches and lack of plastic offsets were similar to Panel DC-P4. The adequacy of FRC modelling under cyclic loading is, overall, still deficient.

If only the prediction of DC-P3 is examined, the stress and strain values at failure were substantially improved in comparison to the VT2 – Original analysis. The angles of inclination of the principal tensile directions were also more accurately calculated, as higher values were obtained for the VT2 – PPFRC analysis in comparison to the original model. Unfortunately, these ductility benefits came at the expense of the numerical strain hardening behaviour. In the experiment for DC-P3, the first cracking occurred at a tensile stress of 2.17 MPa. This was followed by a drop in tensile stress before subsequent strain hardening to a maximum of 2.42 MPa (an increase of 12% above the cracking stress). The original VecTor2 analysis exhibited a cracking stress of 2.35 MPa, followed by an 11% increase to 2.62 MPa. The implementation of the new model, despite the ductility benefits, did not capture the strain hardening behaviour. The numerical analysis showed a rapid growth in crack width, similar to the experiment, yet this incorrectly occurred without an increase in the applied shear stress. This is likely attributable to the inaccuracy of the implemented tension stiffening and cracking behaviour for SFRC in representing PPFRC behaviour. Further work on the cracking behaviour and the response of PPFRC with steel reinforcement is required to improve the structural response after cracking.

6.3.3.2 Influence of Fracture Energy

It was postulated that the tensile behaviour prediction could be improved if the attenuation factor of 7.5 was used to determine the fracture energy for the PPFRC specimens due to the energy and force required to align and engage the flexible fibres. Thus, Equation 6.3 was used to calculate the fracture energy and this value was input to the analysis. This analysis was compared to the VT2 – PPFRC analysis, which used the default fracture energy values that were calculated using the Bazant (2002) relationship (Equation 5.23). It is worth noting that the default value for fracture energy for DC-P3 was 0.14 kN/m compared to the user input 0.31 kN/m; for DC-P5 the default was 0.14 kN/m compared to the user input 0.32 kN/m.

As shown in Figure 6.13 and Figure 6.14, and in Table 6.9, the two analyses provide very similar failure predictions. The major effect of the user input fracture energy was on the shear and principal tensile behaviour at low strains. Some strain hardening was exhibited; for DC-P3 a maximum tensile stress of 2.54 MPa was attained (representing an increase of 8% above the cracking stress). The shear stress versus shear strain response was stiffened and matched remarkably well with the experimentally determined curve, as higher values of shear stress were achieved at low shear strains. At higher shear strains, the numerical responses for both analyses were identical, and matched well with the experimental stiffness.

This benefit was realized because of the effect of engagement energy on the response of PPFRC. The attenuation factor represents the increased energy required to form a crack in PPFRC in comparison to plain concrete. This energy increase is due to the fibre bending required before engagement of the fibres (that is, the energy expended before the polypropylene fibres align across the crack such that they can become effective in carrying tensile stresses). The effect of the attenuation factor on the direct tensile response of PPFRC was demonstrated in Section 5.3.4.1. With the default fracture energy value, the numerical crack propagation occurs suddenly with a low release of energy. This manifests itself in a large increase in shear strain, without substantial increase in shear stress. The attenuation factor corrects this, by accounting for the load and energy required to generate this large crack opening. Thus, some strain hardening and related increases in shear stress were achieved using the attenuation factor. However, this is not a permanent solution.

The applicability of the attenuation factor has not been adequately investigated, neither in small- nor large-scale tests. In addition, a great deal of research would be required to determine when such a factor should be used; that is to say, the relationship between the fibre volume ratio and attenuation factor would have to be investigated. A great deal of uncertainty surrounds this factor and, thus, it was left out of the FE implementation. Despite the success of the analysis model using the attenuation factor, this should not replace further investigations into the cracking and tension stiffening behaviour of PPFRC. It is postulated that the numerical response at low strains can be substantially improved if applicable behavioural models for PPFRC cracking and for the tensile response of PPFRC elements with conventional reinforcement are developed and implemented. This should be the main focus of future research programs.

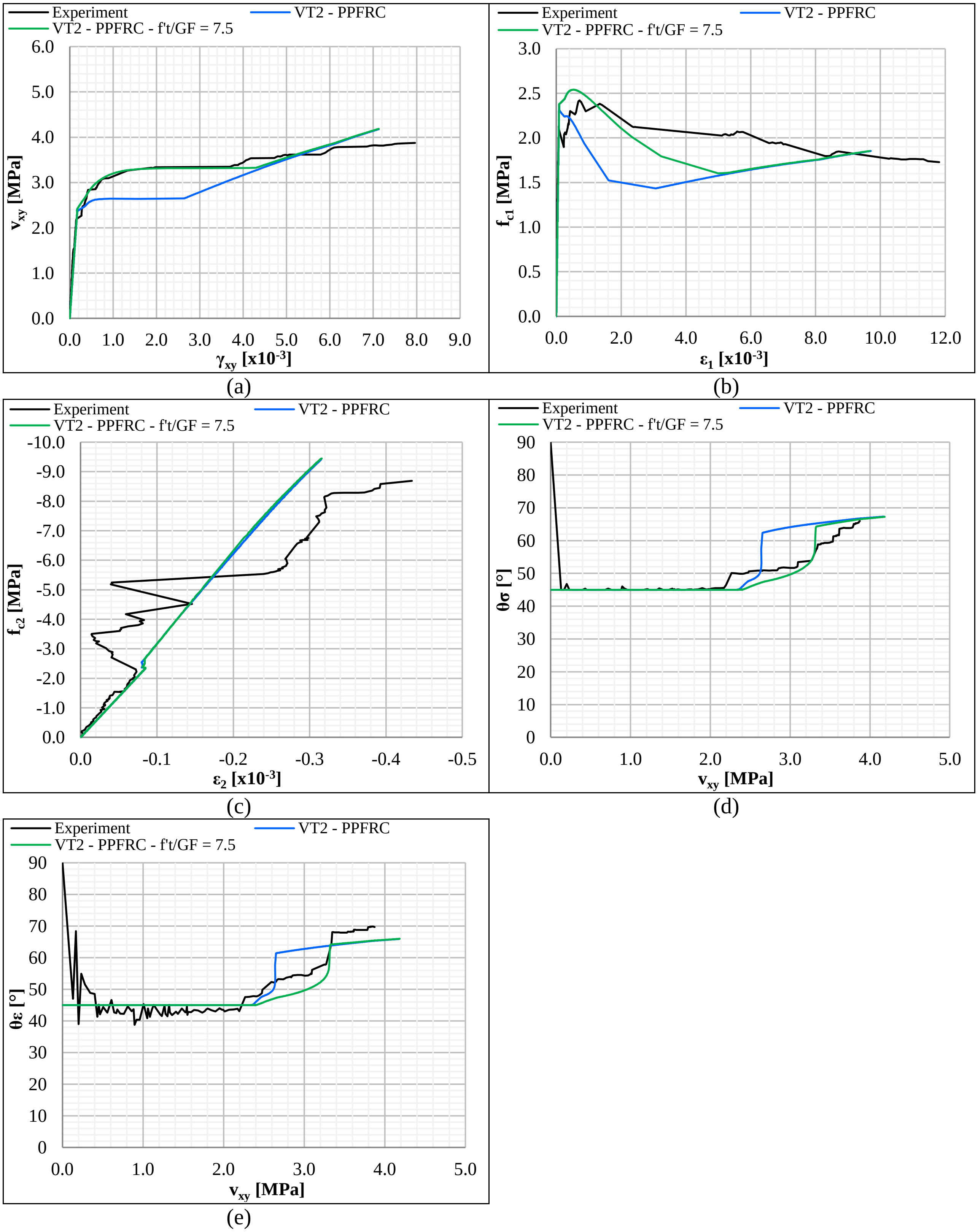

Figure 6.13: Influence of fracture energy on numerical responses for Panel DC-P3: (a) $v_{xy} - \gamma_{xy}$; (b) $f_{c1} - \varepsilon_1$; (c) $f_{c2} - \varepsilon_2$; (d) $\theta_\sigma - v_{xy}$; (e) $\theta_\varepsilon - v_{xy}$

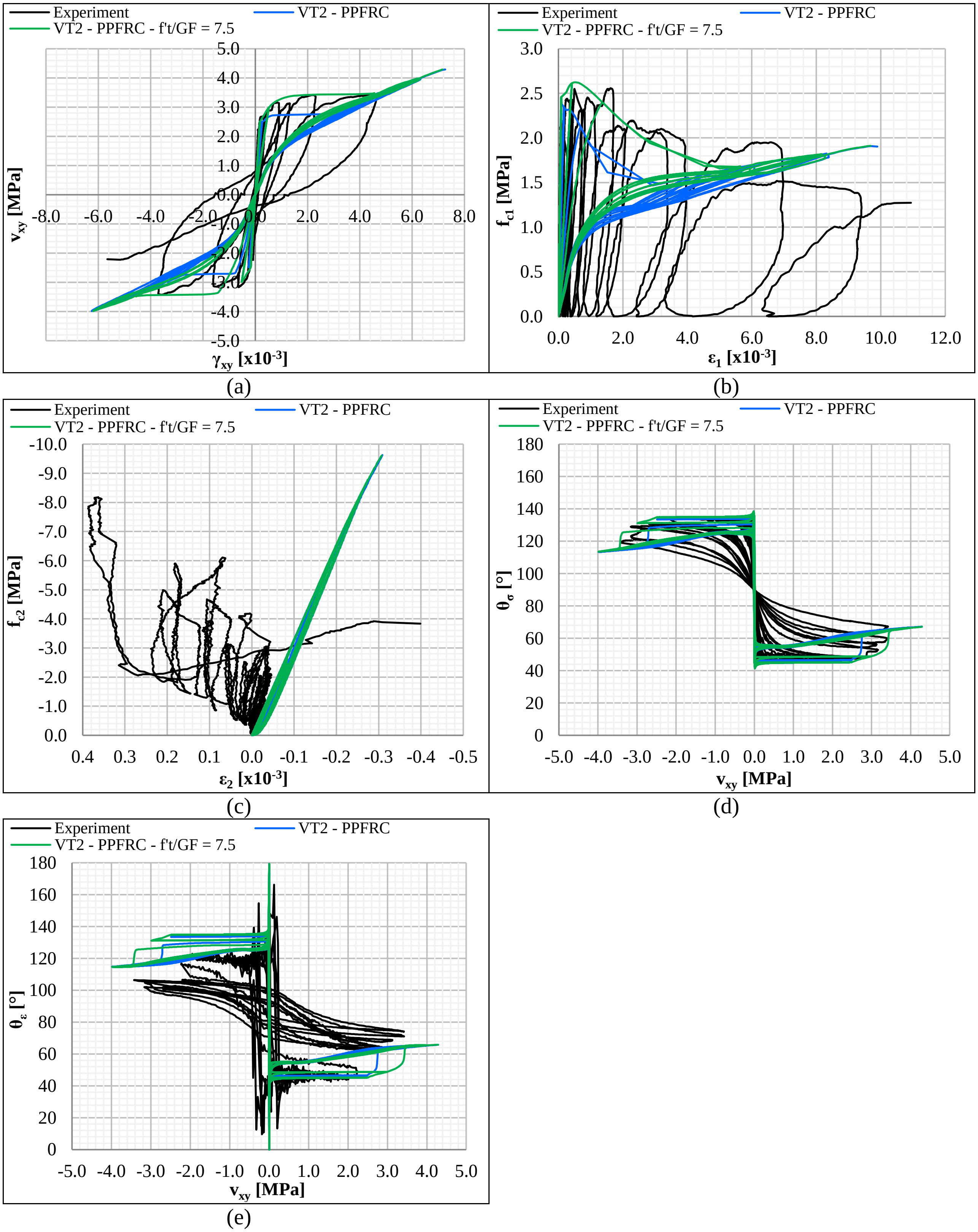

Figure 6.14: Influence of fracture energy on numerical responses for Panel DC-P5: (a) $v_{xy} - \gamma_{xy}$; (b) $f_{c1} - \varepsilon_1$; (c) $f_{c2} - \varepsilon_2$; (d) $\theta_\sigma - v_{xy}$; (e) $\theta_\varepsilon - v_{xy}$

Table 6.9: Summary of Numerical and Experimental Results for PPFRC Panels using VT2 – PPFRC (with User Input Fracture Energy)

Panel	v_u [MPa]	$f_{c1,max}$ [MPa]	$f_{c1,u}$ [MPa]	$f_{c2,u}$ [MPa]	$\theta_{\sigma,u}$ [°]	$f_{sx,max}$ [MPa]	$f_{sy,max}$ [MPa]	$v_{ci,u}$ [MPa]	$\frac{v_{u,VT2}}{v_{u,exp}}$
DC-P3	4.19 (3.87)	2.54 (2.42)	1.85 (1.73)	-9.45 (-8.69)	67.3 (66.0)	230 (210)	-	0.30	1.08
DC-P5	4.29 (3.43)	2.62 (2.56)	1.91 (1.27)	-9.61 (-3.83)	67.1 (-60.0)	233 (204)	-	0.31	1.25

Panel	γ_u [x10^{-3}]	$\varepsilon_{1,max}$ [x10^{-3}]	$\varepsilon_{1,u}$ [x10^{-3}]	$\varepsilon_{2,u}$ [x10^{-3}]	$\theta_{\varepsilon,u}$ [°]	w_m [mm]	s_m [mm]	$\delta_{s,u}$ [mm]	$d\theta_u$ [°]	$\frac{\gamma_{u,VT2}}{\gamma_{u,exp}}$
DC-P3	7.13 (7.96)	0.505 (0.717)	9.67 (11.82)	-0.316 (-0.434)	66.0 (69.7)	0.61 (0.57)	64 (72.0)	0.03	0.72 (-3.7)	0.90
DC-P5	7.17 (5.15)	0.500 (1.615)	9.68 (10.94)	-0.307 (-0.399)	65.8 (-75.0)	0.61 (0.59)	63 (59.0)	0.03	0.70 (15.0)	1.39

Note: values in brackets are experimentally determined

6.4 Modelling of Large-Scale PPFRC Beams

To investigate the adequacy of the polypropylene fibre implementation for structure-level modelling, some large-scale shear-critical PPFRC beams were also modelled with VecTor2. These beams, tested by Altoubat et al. (2009), were constructed with no stirrups and smooth polypropylene macro-synthetic fibres. The experimental variables included longitudinal reinforcement ratio, effective depth and shear span-to-depth ratio. The findings of these tests showed that shear strength sufficiently close to the FRC minimum limit of $0.3\sqrt{f_c'}$ could be attained using at least 0.75% by volume PPFRC. Multiple diagonal shear cracks were exhibited in the web of the beams and the crack widths were well controlled, leading to improvements in deformation capacity over plain concrete (Altoubat et al., 2009). Further details regarding the test results can be found in Section 2.4.1.2 and in Table 2.9.

The experimental configurations and dimensions for a selection of beam tests executed by Altoubat et al. (2009) are presented in Figure 6.15 and Table 6.10. The beams are named according to the shear span-to-depth ratio ("Sh" for short beams with $a/d = 2.3$ and "L" for slender beams with $a/d = 3.5$), the experimental series ("2" for the second series with d = 330 mm and ρ_l = 3.18%), and the fibre volume fraction ("0.0", "0.5", "0.75" and "1.0"). In addition, each beam test was duplicated, denoted as "a" for the first beam and "b" for the second. For the purpose of this study, the second series of beams were modelled using the fibre Reinforcement

Type 7 (Steel – Straight fibres) and subsequently with Reinforcement Type 15 (Polypropylene – Smooth fibres). In this way, the numerical result obtained using the original version of VecTor2 (VT2 – Original) was compared against the result from the updated version (VT2 – PPFRC).

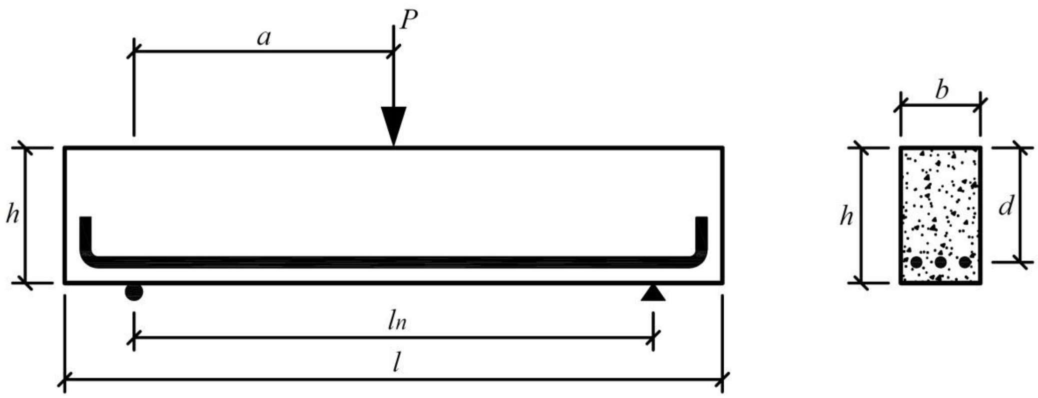

Figure 6.15: Schematic outline of experimental beam configuration (Altoubat et al., 2009)

Table 6.10: Altoubat et al. (2009) Beam Dimensions

Beam	l [mm]	l_n [mm]	a [mm]	h [mm]	d [mm]	b [mm]	a/d	ρ_l [%]
Sh2-0.0	1,900	1,500	750	390	330	230	2.3	3.18
Sh2-0.5	1,900	1,500	750	390	330	230	2.3	3.18
Sh2-0.75	1,900	1,500	750	390	330	230	2.3	3.18
L2-0.0	2,700	2,300	1,150	390	330	230	3.5	3.18
L2-0.5	2,700	2,300	1,150	390	330	230	3.5	3.18
L2-0.75	2,700	2,300	1,150	390	330	230	3.5	3.18
L2-1.0	2,700	2,300	1,150	390	330	230	3.5	3.18

6.4.1 Structure Inputs and Mesh Development

Images of the FormWorks-Plus models for these beams are presented in Figure 6.16 and Figure 6.17. Taking advantage of symmetry, half-beams were modelled, with an overall outside dimension of 390 mm x 950 mm for the short beams or 390 mm x 1,350 mm for the slender beams. The thickness of both beams was 230 mm and these were modelled with in-plane rectangular elements. The mesh depicted was deemed to be the most efficient; a finer mesh yielded similar predictions with undesired increases in run-time. Thus, 19 elements were used through the depth of the beams, with an average element size of 20 mm in the y-direction and 25 mm in the x-direction. The longitudinal reinforcing bars were modelled as truss bars centred at 330 mm below the top of the beam.

The support conditions were represented with a vertical roller located at 200 mm from the bottom-left corner of the beam and horizontal rollers throughout the depth along the right edge. For these models, displacement control was used, with a monotonically increasing vertical displacement applied directly to the top right corner of the specimen (representing centre point loading). This was increased in load steps of 0.1 mm until the shear failure was reached. It is customary to use steel loading plates to avoid local failures at the vertical roller and under the applied displacement. This was also investigated during a preliminary study and was found to provide unstable numerical results. Since the experimental setup did not include loading plates, these were not included in the final models.

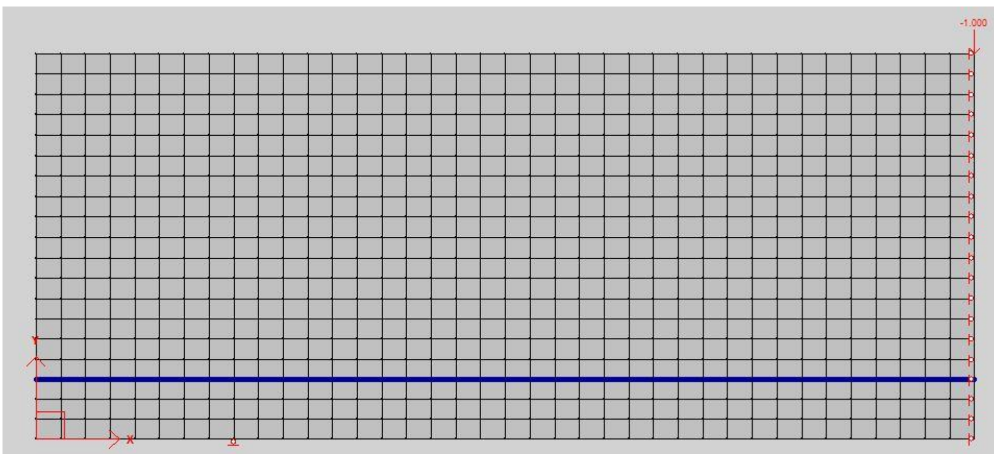

Figure 6.16: FormWorks-Plus model for short beams
(Element size: ~25 x 20 mm; 19 elements through the depth of the beam)

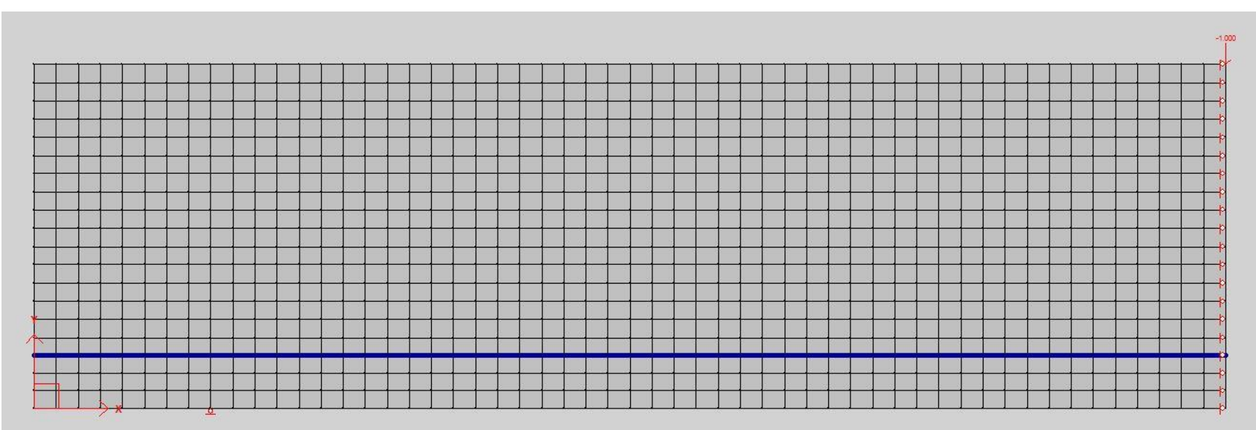

Figure 6.17: FormWorks-Plus model for slender beams
(Element size: ~25 x 20 mm; 19 elements through the depth of the beam)

Table 6.11: Altoubat et al. (2009) Concrete and Fibre Properties

Beam	f'_c [MPa]	a_{max} [mm]	s_{mx} [mm]	s_{my} [mm]	Fibre Type	V_f [%]	l_f [mm]	d_f [mm]	f_{uf} [MPa]
Sh2-0.0	40.9	20	297	297	-	-	-	-	-
Sh2-0.5	41.9	20	297	297	Polypropylene - Smooth	0.5	40	0.433	620
Sh2-0.75	41.9	20	297	297	Polypropylene - Smooth	0.75	40	0.433	620
L2-0.0	40.9	20	297	297	-	-	-	-	-
L2-0.5	41.9	20	297	297	Polypropylene - Smooth	0.5	40	0.433	620
L2-0.75	41.9	20	297	297	Polypropylene - Smooth	0.75	40	0.433	620
L2-1.0	35.6	20	297	297	Polypropylene - Smooth	1.0	40	0.433	620

Table 6.12: Altoubat et al. (2009) Reinforcement Properties

Beam	Bars	A_s [mm^2]	d_b [mm]	f_y [MPa]	f_u [MPa]	E_s [MPa]	ε_{sh} [x10^{-3}]	ε_u [x10^{-3}]
Sh2-0.0	3 - 32 mm	2413	32.0	400	600	200,000	10	100
Sh2-0.5	3 - 32 mm	2413	32.0	400	600	200,000	10	100
Sh2-0.75	3 - 32 mm	2413	32.0	400	600	200,000	10	100
L2-0.0	3 - 32 mm	2413	32.0	400	600	200,000	10	100
L2-0.5	3 - 32 mm	2413	32.0	400	600	200,000	10	100
L2-0.75	3 - 32 mm	2413	32.0	400	600	200,000	10	100
L2-1.0	3 - 32 mm	2413	32.0	400	600	200,000	10	100

The concrete input properties were as shown in Table 6.11. As with the panels, the concrete strength and aggregate size were provided. In addition, it was deemed necessary to set the maximum crack spacing in the x- and y- directions, s_{mx} and s_{my}, to d_v (where d_v is the effective shear depth, taken as $0.9d$ in accordance with the shear provisions of the Canadian Concrete Design Code (CAN/CSA Standard A23.3-04, 2004)). This was used in lieu of the default maximum crack spacing of 1000 mm included in VecTor2. The default maximum crack spacing was unrealistic (a crack spacing of roughly three times the depth of the beam is not attainable) and led to large crack widths and premature analytical failure. Default parameters were used for all other concrete properties. In addition, the fibre input properties used are also shown in Table 6.11. As before, the fibre bond strength was not input so that the default parameter from Equation 6.1 could be used. Also, the reinforcing steel material properties were not provided in the paper, so typical steel properties were selected as shown in Table 6.12.

Finally, the constitutive and analytical models used were identical to those used for the panel analyses (Table 6.3 and Table 6.4), again with the desire to investigate the prediction attained with default models.

6.4.2 Results of Numerical Analyses

The experimental and numerical load versus deflection responses are presented in Figure 6.18 for the short beams and in Figure 6.19 for the slender beams. The duplicate beams were individually plotted in keeping with the article by Altoubat et al. (2009). In addition, the numerical result from the VT2 – Original and VT2 – PPFRC analyses are presented in Table 6.13 and Table 6.14 respectively. Failure crack patterns are also presented in Figure 6.20 and Figure 6.21.

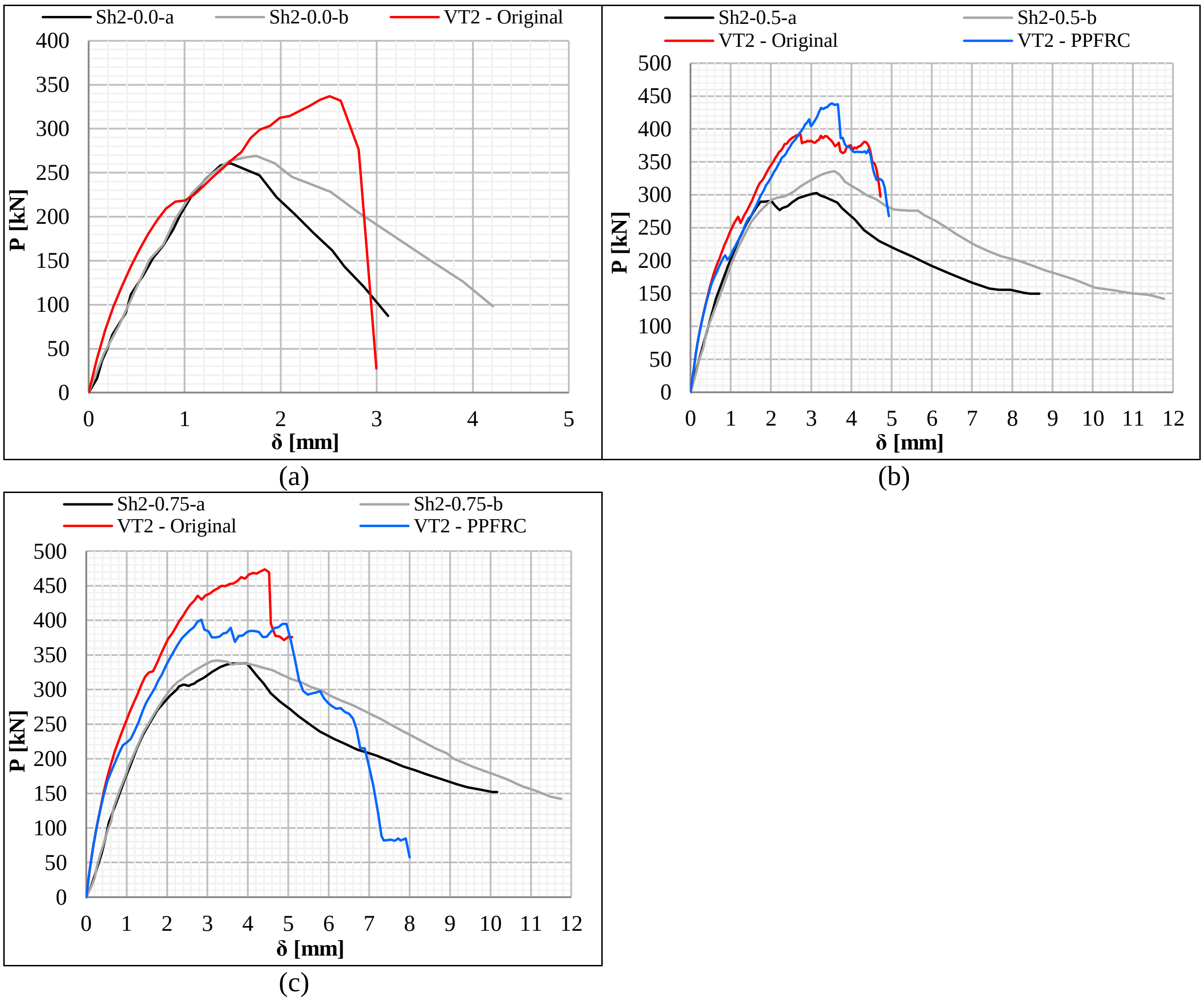

Figure 6.18: Comparison of experimental and numerical responses for short beams: (a) Sh2-0.0; (b) Sh2-0.5; (c) Sh2-0.75

For the short fibre reinforced concrete beams, the predictions provided by VecTor2 were somewhat inaccurate. Even though the failure mode was correctly captured as diagonal tension splitting in the web of the members followed by longitudinal bond splitting along the reinforcement bars, the short beams experienced some arching action after the first diagonal cracking and prior to reaching this failure. Using the original VecTor2, the cracking load was well represented, but the increase in load-carrying capacity from cracking to failure was grossly overestimated. This phenomenon was also exhibited in the analyses using the updated version of VecTor2. Interestingly, the analysis of Sh2-0.75 using the updated program exhibited a reduced ultimate load in comparison to Sh2-0.5, despite the higher fibre volume fraction. This is explained by the distributed web cracking exhibited in the analysis of Sh2-0.75 (Figure 6.20); an effective compression strut could not form in the analysis. This suggests that further investigation into the distribution of cracking in PPFRC specimens may improve the prediction.

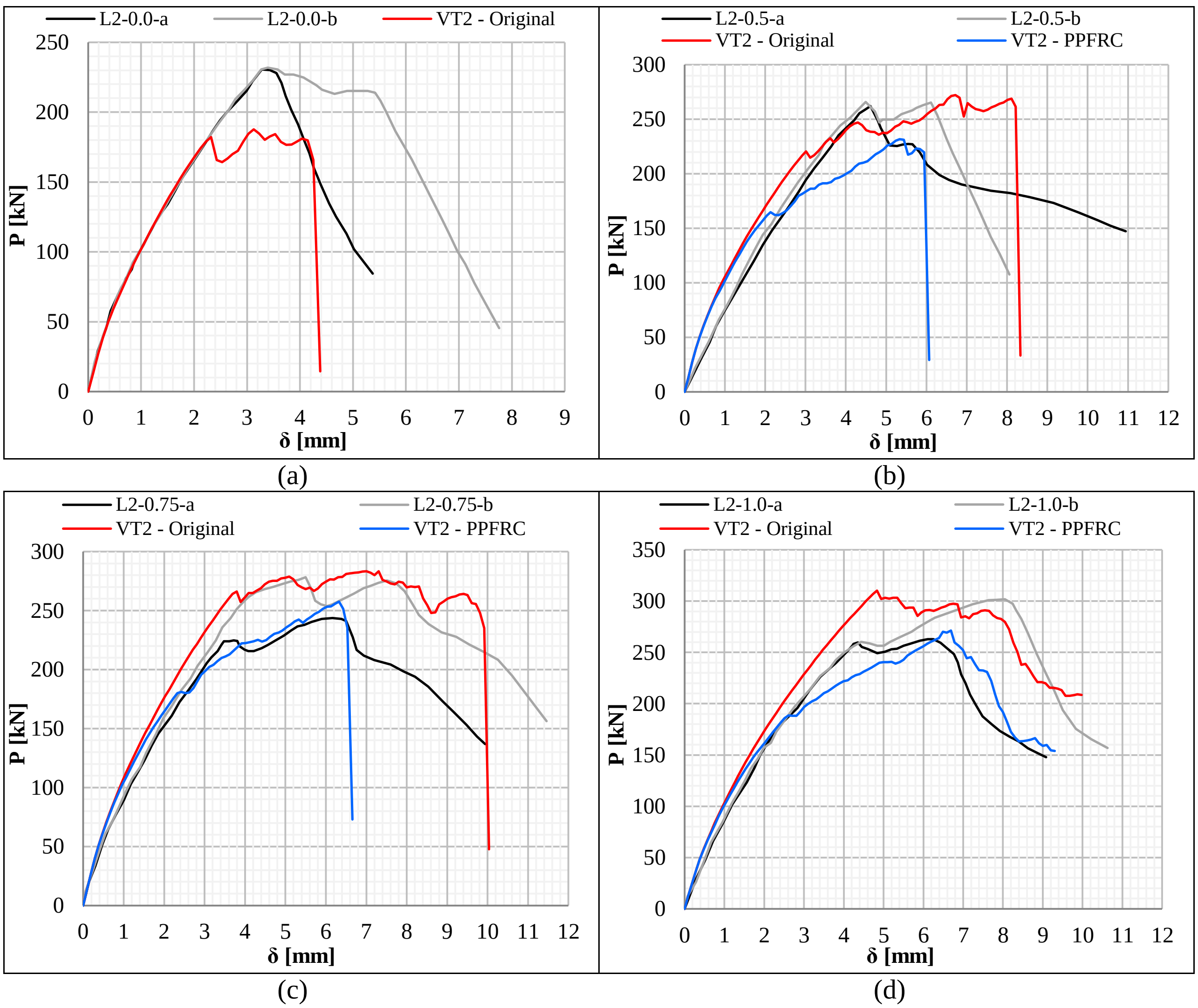

Figure 6.19: Comparison of experimental and numerical responses for slender beams: (a) L2-0.0; (b) L2-0.5; (c) L2-0.75; (d) L2-1.0

Table 6.13: Altoubat et al. (2009) Numerical and Experimental Results (Using VT2 - Original)

Beam	P_{cr}* [kN]	P_u [kN]	δ_u [mm]	Failure Mode	$\frac{P_{cr,VT2}}{P_{cr,exp}}$	$\frac{P_{u,VT2}}{P_{u,exp}}$	$\frac{\delta_{u,VT2}}{\delta_{u,exp}}$
Sh2-0.0	218.4 (270)	336.8 (270)	2.51 (1.7)	Shear	0.81	1.25	1.48
Sh2-0.5	266.8 (285)	392.2 (318)	2.73 (3.5)	Shear	0.94	1.23	0.78
Sh2-0.75	326.6 (308)	473.8 (339)	4.42 (4.1)	Shear	1.06	1.40	1.08
L2-0.0	182.2 (233)	187.6 (233)	3.13 (3.7)	Shear	0.78	0.81	0.85
L2-0.5	220.4 (262)	272.0 (265)	6.72 (6.0)	Shear	0.84	1.03	1.12
L2-0.75	266.2 (247)	283.4 (262)	7.31 (7.1)	Shear	1.08	1.08	1.03
L2-1.0	310.2 (260)	310.2 (284)	4.84 (7.3)	Shear	1.19	1.09	0.66
				Mean+	1.02	1.17	0.93
				COV (%)+	13.21	12.90	21.67

* First diagonal cracking load
+ Excluding plain reinforced concrete beams (Sh2-0.0 and L2-0.0)
Note: values in brackets are experimentally determined

Table 6.14: Altoubat et al. (2009) Numerical and Experimental Results (Using VT2 - PPFRC)

Beam	P_{cr}* [kN]	P_u [kN]	δ_u [mm]	Failure Mode	$\frac{P_{cr,VT2}}{P_{cr,exp}}$	$\frac{P_{u,VT2}}{P_{u,exp}}$	$\frac{\delta_{u,VT2}}{\delta_{u,exp}}$
Sh2-0.0	218.4 (270)	336.8 (270)	2.51 (1.7)	Shear	0.81	1.25	1.48
Sh2-0.5	208.2 (285)	439.0 (318)	3.53 (3.5)	Shear	0.73	1.38	1.01
Sh2-0.75	219.4 (308)	401.0 (339)	2.85 (4.1)	Shear	0.71	1.18	0.70
L2-0.0	182.2 (233)	187.6 (233)	3.13 (3.7)	Shear	0.78	0.81	0.85
L2-0.5	162.2 (262)	231.8 (265)	5.34 (6.0)	Shear	0.62	0.87	0.89
L2-0.75	180.0 (247)	257.6 (262)	6.33 (7.1)	Shear	0.73	0.98	0.89
L2-1.0	192.2 (260)	271.4 (284)	6.69 (7.3)	Shear	0.74	0.96	0.92
				Mean+	0.71	1.07	0.88
				COV (%)+	6.98	19.10	12.81

* First diagonal cracking load
+ Excluding plain reinforced concrete beams (Sh2-0.0 and L2-0.0)
Note: values in brackets are experimentally determined

The plain reinforced concrete slender beam, L-2-0.0, failed prematurely just after first diagonal cracking, yet the stiffness of the response until this point matched closely with the experiment. Thus, a higher diagonal cracking load would have likely led to a near perfect estimation. This low first diagonal cracking load was consistently the most notable discrepancy using the updated version of the program. The diagonal cracking load was underpredicted in all cases (mean predicted-to-experimental ratio of 0.71, whereas the mean predicted-to-experimental ratio for diagonal cracking load was 1.02 using the original VecTor2). For the plain concrete beams, this may be attributed to the use of the default value for cracking strength of the concrete, $f_t' = 0.33\sqrt{f_c'}$, as this represents a lower bound estimation of the cracking strength for reinforced concrete. In lieu of cracking data for the concrete used, this default value must be employed.

The low cracking load of the PPFRC beams was likely due to the representation of cracking distribution in such members. As per usual, the cracking patterns at initial stages of the analysis were flexural at the midspan with shear-flexural cracks closer to the supports. However, these shear-flexural cracks rapidly opened and propagated into dominant shear cracks at reduced loads. From here, a sudden change in stiffness and increase in midspan deflection were correctly exhibited in the analytical responses, in keeping with the experimental finding regarding large initial cracks in PPFRC specimens. The load-carrying capacity increased after first diagonal cracking, but the ability of the fibres to transmit significant tensile stresses across the shear crack was underestimated. The numerical load-carrying capacities of the slender beams after diagonal cracking were consistently less than the experiment. In terms of the slender beam crack patterns, the slope of the shear crack was correctly reduced with increasing fibre addition, but the analyses did not exhibit multiple web cracking before the longitudinal bond splitting propagated to failure (as shown by the failure crack patterns in Figure 6.21). It is postulated that improved understanding of the crack spacing of PPFRC may improve the prediction of crack widths in the web of the beams. These improved crack predictions would in turn promote increased tensile capacity of the fibres across the diagonal crack, creating multiple web cracking, stiffening the response, and improving the prediction of load-carrying capacity after diagonal cracking. In addition, the underestimation of fibre tensile stress across the shear crack may be attributed to the default smooth polypropylene fibre bond strength. This default value may not be accurate for the fibres used in the experiments, yet no such bond data were available for input.

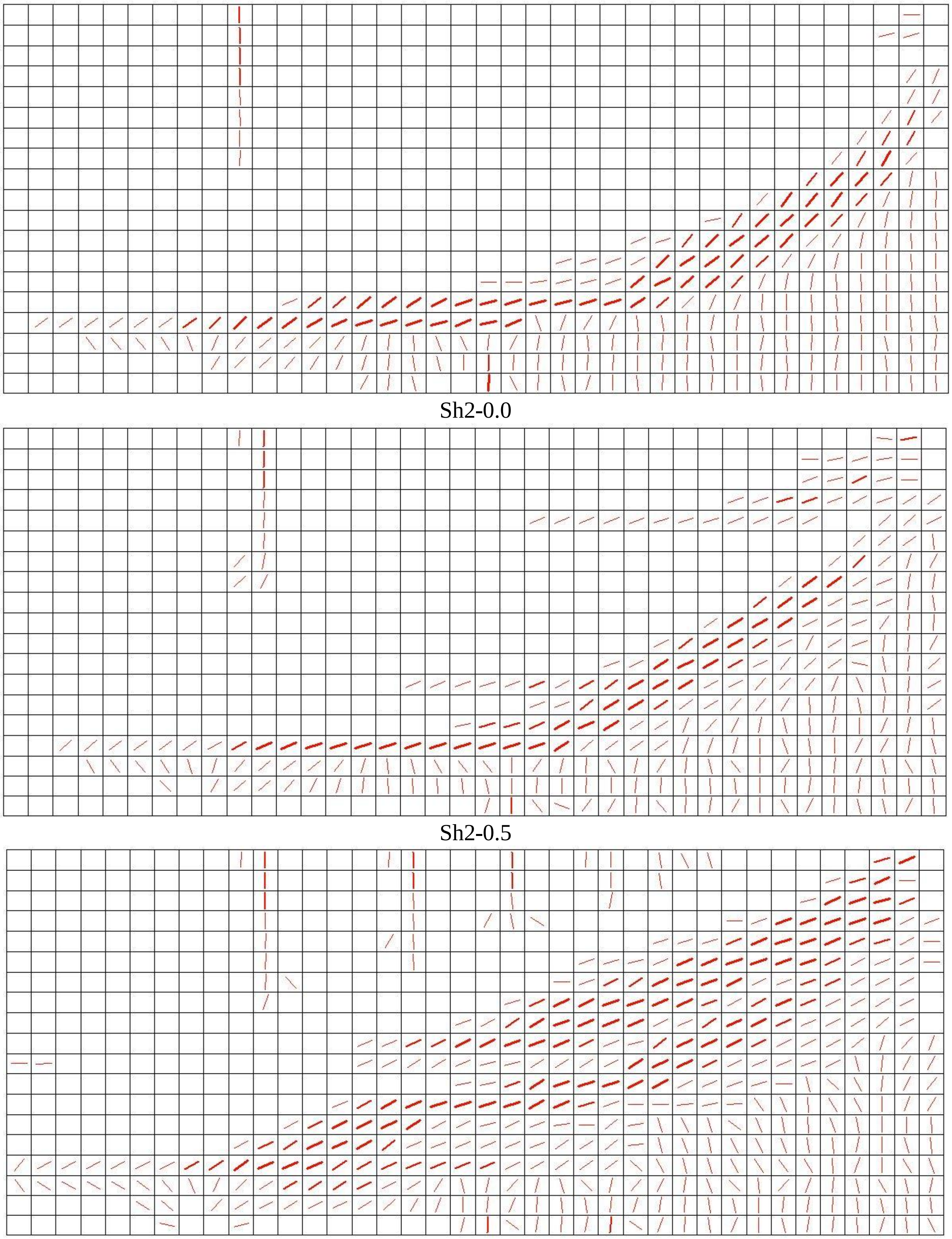

Sh2-0.0

Sh2-0.5

Sh2-0.75

Figure 6.20: Crack patterns at failure for short beams

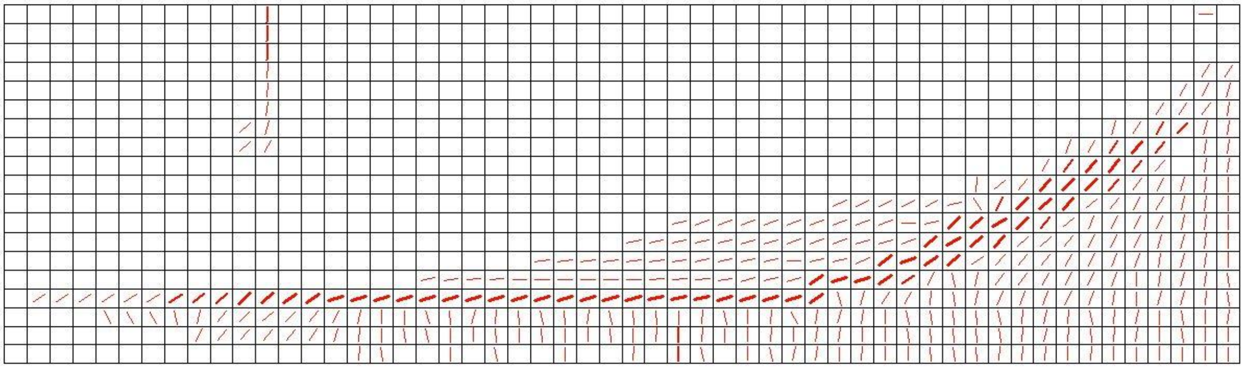

L2-0.0

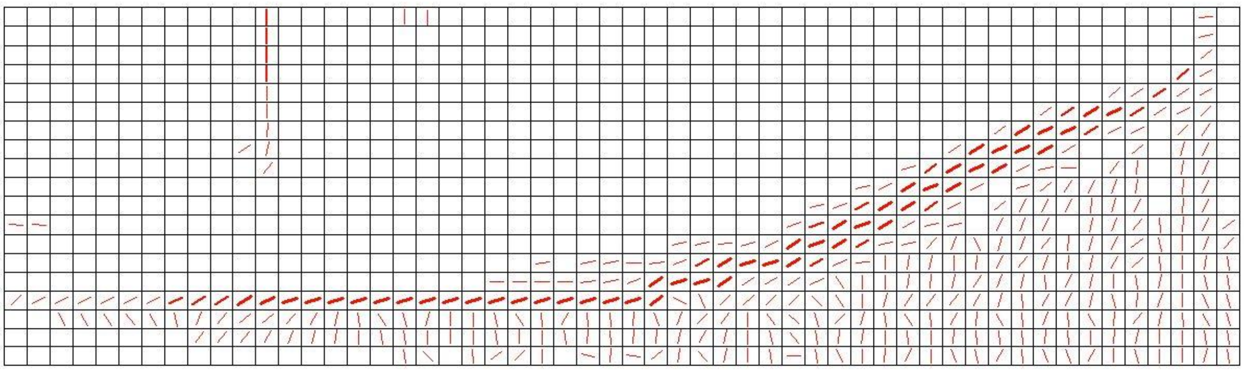

L2-0.5

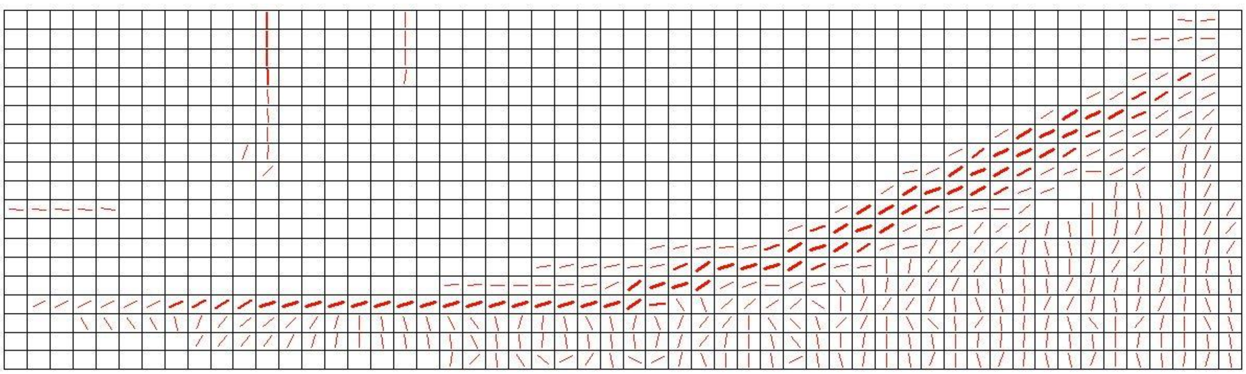

L2-0.75

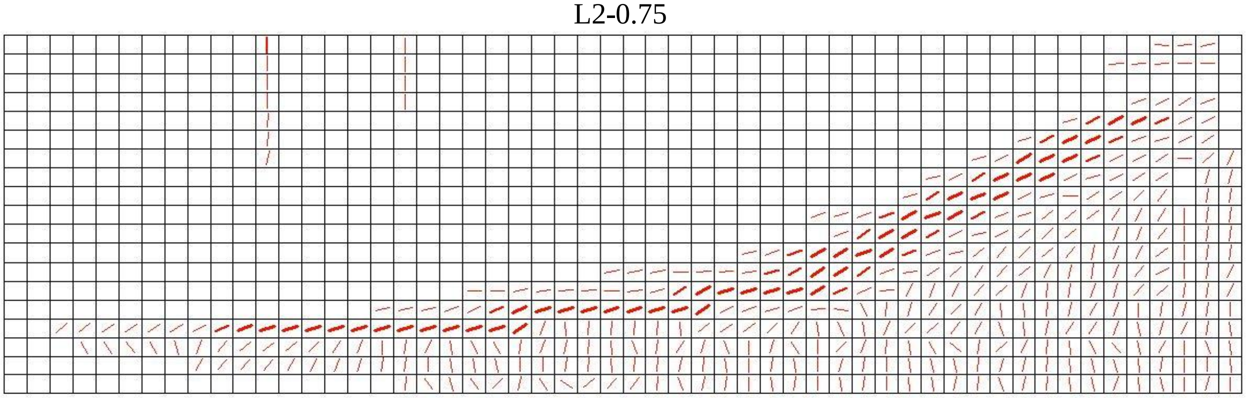

L2-1.0

Figure 6.21: Crack patterns at failure for slender beams

Despite the difficulties in cracking load predictions, the overall predictions of the PPFRC beams were improved using the new polypropylene fibre model. The stiffness of the experimental response, both before and after diagonal cracking, was more accurately represented by the updated analysis for each of the PPFRC beams. Also, the numerical responses were more stable, exhibiting less erroneous scatter after diagonal cracking. As seen from the predicted-to-experimental ratios shown in Table 6.13 and Table 6.14, the prediction of ultimate load and deflection were improved and were well within an acceptable range of ±20% (with the exception of the short PPFRC beams as noted previously). The mean predicted-to-experimental ratio of ultimate load was improved from 1.17 (CV = 12.90%) to 1.07 (CV = 19.10%) after implementation of the new polypropylene fibre reinforcement type. The mean predicted-to-experimental ratio of deflection at ultimate was 0.93 with a CV of 21.67% using the original VecTor2 and was changed to 0.88 with a coefficient of variation of 12.81%. Even though the ratio was negatively affected, the estimation of ultimate deflection for each beam was improved and was much more consistent. Indeed if Sh2-0.75 is ignored, the predicted-to-experimental ratio of ultimate deflection becomes 0.93 with a relatively small coefficient of variation of 6.12% using the updated VecTor2. Thus, the implementation of the new polypropylene fibre types in VecTor2 was generally successful, yet much work is still required to improve PPFRC representation.

It is worth noting that an additional set of analyses was executed using the user input fracture energy according to Equation 6.3. The applicability of such a factor is limited for large-scale structures with multiple cracks (numerical panel models effectively exhibit one crack due to the use of a single element). As expected, the input fracture energy had the effect of marginally increasing the first diagonal cracking load (on the order of 5%), but had little effect on the slope of the response, cracking distribution, and failure condition.

6.5 Adequacy of Available Models

To summarize the findings of the FE analyses, the improvement in numerical ductility, stiffness and load-carrying capacity of the PPFRC models represented a step in the right direction. The predictions of the strains at failure for the PPFRC panels were substantially improved, and the shear strength predictions remained within an acceptable range. These predictions were at least as successful as those for SFRC or plain reinforced concrete panel elements. The stiffness, load, and deformability of the large-scale beams were similarly improved.

However, the new formulations were not completely satisfactory and a number of discrepancies still remain. The first diagonal cracking loads of the beams were underestimated, which led to an underestimation of the load-carrying capacity from cracking to failure (even though the slope attained from cracking to failure was similar to the experiments). This was also exhibited in the response of the panel specimens, as the shear stress at low strains was similarly underestimated. For the panel specimens, increasing the fracture energy markedly improved the prediction, yet this does not represent a permanent solution. Instead, it is believed that the numerical response at low strains (and after first diagonal cracking for structure-level models) can be substantially improved if behavioural models for PPFRC crack spacing and for the tensile response of PPFRC elements with conventional reinforcement are developed and implemented into FE analysis procedures. These models would better capture the crack widths and spacings that were sustained in the early stages of PPFRC panel tests without a reduction in load or a reduction in the ability to develop subsequent cracking. This improved prediction of crack widths for PPFRC members would promote improved predictions in fibre tensile stresses, leading to accurate multiple cracking and effective estimation of structure-level behaviour.

Finally, substantial research into the modelling of cyclically loaded FRC elements is required. The unloading and reloading paths of the numerical models did not match the experimental curves, and no plastic offsets were numerically estimated. This is inaccurate and, thus, investigation into the effects of fibre addition on crack closing and crack slip for cyclically loaded elements is required to improve such analyses.

Chapter 7
Conclusions

7 Conclusions

7.1 Objectives

The goal of the experimental portion of this thesis was to perform a pilot investigation on the compressive, tensile, flexural, and shear behaviour of concrete elements reinforced with macro-synthetic structural fibres, and to compare their performance to that of steel fibres. An experimental program was undertaken at the University of Toronto involving experimental tests on small-scale material specimens (compression cylinder tests, uniaxial direct tension dogbone tests, and modulus of rupture bending tests), as well as on larger scale in-plane shear panel specimens. In addition, a pilot investigation into the effects of reversed cyclic shear loading on the behaviour of SFRC and PPFRC was performed, so as to determine the suitability of fibre reinforcement for shear-critical cyclically loaded elements. Three of the five panel specimens were tested under a reversed cyclic pure shear loading regime to investigate such effects. Comparisons were drawn between the two types of fibre reinforced concretes and to concrete with low percentages of conventional transverse steel reinforcement.

In the analytical portion of this work, the primary goal was to study the bond behaviour of macro-synthetic fibres and propose a strategy for modelling the direct tensile behaviour of PPFRC. The robust Simplified Diverse Embedment Model for the tensile behaviour of steel fibre reinforced concrete was chosen as the baseline for adjustments, due to its simple relationships, accurate representation of fibre mechanical anchorage, and ease of implementation into finite element analysis software or design codes. A literature review was undertaken to determine reasonable bond constitutive laws for macro-synthetic fibres. Then, a sensitivity study was carried out to calibrate these laws to the results of the direct tension tests executed in this work. Lastly, the PPFRC model was implemented into the finite element analysis program VecTor2 and a short verification study was undertaken to investigate the accuracy of currently available constitutive models for PPFRC, and for FRC under reversed cyclic loads.

7.2 Summary

7.2.1 Material Tests

7.2.1.1 Cylinder Compression Tests

The pre-peak compressive behaviour of the concrete was not affected by the addition of fibres. No discernible influence on the secant stiffness or 28-day compressive strength was discovered. However, the specimens with long steel or polypropylene fibres did exhibit consistently lower strengths than those with short steel or no fibres. This suggested the presence of larger pore spaces in the concretes with longer fibres. The post-peak behaviour, on the other hand, was altered through the use of fibres. The strain at peak stress was increased for all FRC specimens, resulting from the confining effects of the fibres. Also, fibre addition improved ductility and toughness in compression.

7.2.1.2 Uniaxial Direct Tension Tests

The pre-cracked tension behaviour was unaffected by fibre addition. None of the dogbone specimens tested exhibited strain hardening behaviour or multiple cracking. After cracking, ductility and residual tensile load-carrying capacity were greatly improved. The steel fibres engaged quickly and arrested crack growth. The PPFRC specimens showed a large drop in load coupled with a large crack width before fibre engagement. After this initial drop in load, the PPFRC specimens stiffened and recovered load-carrying capacity. SFRC, on the other hand, sustained elevated levels of residual tensile stress followed by a sudden decrease in load-carrying capacity upon failure of the fibre mechanical anchorage. At these high crack widths above 3.0 mm, the PPFRC specimens exhibited more stable and gradual reductions in load.

The crack bridging tendencies of the steel fibres were severely impacted by cyclic loading; significant degradation was exhibited. The same was not found with the PPFRC specimens, as the monotonic and cyclically tested dogbones attained comparable responses.

7.2.1.3 Modulus of Rupture Tests

The observations of flexural behaviour were similar to those from the direct tensile behaviour. PPFRC exhibited a large drop in load and the opening of a large crack width immediately upon first cracking. Flexural strain hardening was exhibited by the steel and, on occasion, the macro-synthetic FRC test sets.

7.2.2 Panel Tests

The monotonic in-plane shear panel tests showed that shear strength similar to that of low percentages of conventional transverse reinforcement (ρ_y = 0.42%) could be attained using 1.0% by volume steel fibre reinforcement. The same was not found for 2.0% by volume of polypropylene fibres. The shear strength attained by PPFRC was only 67% of the shear strength for low percentages of conventional steel, while 1.0% by volume SFRC attained shear strength of at least 90% of the shear strength for low percentages of conventional steel.

Substantial ductility improvements were achieved through the use of PPFRC. The ultimate shear strain was 32% greater than conventional steel reinforcement and 51% greater than 1.0% by volume of steel fibres. The average and maximum crack widths of the PPFRC panel were substantially greater than the SFRC. The crack spacings were also larger, suggesting that the degree of multiple cracking was greater for the end-hooked steel fibres. In addition, the overall principal tensile response of the PPFRC panel was markedly similar to that of 1.0% SFRC, while sustaining a 211% increase in tensile strain at failure. Thus, the benefits in ductility through the use of polypropylene fibres cannot be denied, yet greater bond strength would be beneficial in improving shear strength and promoting distributed cracking. To maintain the ductility of the response, this improved bond strength must be coupled with higher fibre tensile strength to prevent brittle fibre fracture.

The degradation of the SFRC in-plane shear response under reversed cyclic loading was substantial. Ductility, toughness and strength were severely affected, as the ultimate shear stress and shear strain were reduced by 25% and 52% respectively compared to the monotonic panel. The same degree of degradation did not occur for the PPFRC specimens; the shear strength was reduced by 11% and the shear strain was reduced by 35%. Neither of the cyclically loaded FRC panels achieved shear strength or ductility comparable to the specimen reinforced with conventional transverse steel.

7.2.3 Analytical Modelling

The SDEM was shown to reasonably predict the behaviour of SFRC. Thus, it was adapted to also model PPFRC tensile response. Fibre snubbing was ignored, as it was determined that such effects have not been adequately investigated for new generation macro-synthetic fibres. If further studies prove the need to consider fibre snubbing, a strategy was proposed to easily incorporate this effect into the relationships of the SDEM, while maintaining the simplicity of the model. In addition, despite the observation of a few fibre ruptures during PPFRC dogbone tests, elastic fibre deformation was also ignored. It was postulated that these ruptures occurred in fibres that were aligned in the loading direction immediately upon cracking. Thus, these fibres carried exaggerated tensile loads before other fibres became aligned and effective. Additionally, new generation macro-synthetic fibres possess an elongation at rupture of around 5 to 10%, so this was deemed insignificant.

From a literature study on the bond properties of synthetic fibres, it was observed that the behaviour of such fibres could be represented in a manner similar to steel fibres. That is to say, the frictional bond component and mechanical anchorage component could be separately represented. The frictional component was shown to behave similarly regardless of material type. Thus, the value of slip at maximum frictional bond strength was chosen to be 0.01 mm, in keeping with the value used for steel fibres. For the slip at peak mechanical anchorage strength, 0.5 mm was chosen as experiments showed that peak fibre bond strength for polypropylene fibres occurred at larger crack widths than end-hooked steel fibres. It was found from past bond tests on deformed steel fibres that 55% of the total bond strength was attributed to mechanical anchorage, with the remaining 45% attributed to frictional bond. This was used for deformed polypropylene fibres. Also, default bond strengths were postulated for polypropylene fibres. These were found to be roughly 50% of those for steel fibres.

Using this new model, the slope of the degradation in direct tension after cracking was overpredicted. To counteract this, an attenuation factor that considers the effect of fibre engagement on the energy released during cracking was proposed. This factor improved the response prediction but substantial research is required to verify the accuracy of this attenuation factor, specifically, and the effect of fibre addition on fracture energy in general. A relationship between fibre volume fraction and cracking attenuation or fracture energy is required.

7.2.4 Finite Element Modelling

The panel specimens and a series of large-scale shear critical beams were modelled using VecTor2 to inspect the adequacy of the existing FRC implementation for PPFRC, and for cyclic modelling of FRC. It was observed that the ductility, stiffness and failure load predictions for PPFRC members were improved using the new polypropylene fibre tension model. The predictions attained were consistently within an acceptable range, and were at least as successful as those attained for SFRC or plain RC members. However, a number of discrepancies exist, mostly surrounding the predicted load-carrying capacity and degree of strain hardening immediately after cracking. At last, it was observed that the modelling of cyclically loaded FRC elements was poor. The unloading and reloading paths were poorly represented and no plastic offsets were predicted. This was inaccurate in comparison to the experiments.

7.3 Conclusions

The following conclusions are made:

1. The characteristic benefits of steel fibre addition (in terms of post-cracked residual strength, tensile ductility and control of crack widths) can be achieved with polypropylene fibres.
2. A relatively high macro-synthetic fibre volume fraction (~2.0%) is required to ensure strain hardening and multiple cracking.
3. This percentage of fibres leads to significant challenges in workability of the concrete; and in fibre distribution amongst tight reinforcement cages. Shorter fibre lengths may improve distribution.
4. Short steel fibres provide the greatest structural improvements in terms of strength.
5. These fibres, as well as high percentages of long steel fibres, may be used in place of low percentages of conventional transverse steel reinforcement.
6. Replacement of minimum transverse steel with polypropylene fibres is not advisable, at least until bond technologies can be improved and sufficient PPFRC shear strength can be assured.
7. First cracking of PPFRC is accompanied by a sharp drop in load and a large increase in crack width. This is required for the fibres to bend and become aligned and engaged across the crack.

8. Substantial ductility improvements can be attained using polypropylene fibres, as these fibres can transmit relatively high amounts of tensile stresses across large crack widths (2.0 mm and greater).
9. For fibres of similar length (~50 mm in this work), concrete with 2.0% by volume of polypropylene fibres exhibits a structural response similar to that of 1.0% by volume of steel fibres.
10. The degradation of SFRC response due to reversed cyclic loading is significant, and crack bridging abilities are negatively affected.
11. The degradation of PPFRC response due to reversed cyclic loading is not as significant, meaning that polypropylene fibres may be better suited to sustain such loading conditions.
12. Complete replacement of minimum transverse conventional steel reinforcement with fibres, for cyclic load applications, is not yet advisable. Some fibre replacement remains possible, suggesting that congested beam-column joint regions and similar elements can benefit from the energy dissipation of fibre reinforcement.
13. Polypropylene fibres with surface deformations may be accurately represented with the proposed adjustments to the SDEM, with the exception of the behaviour immediately after cracking.
14. This poor prediction immediately upon cracking is due to the lack of understanding regarding fibre engagement. A large energy is required to engage polypropylene fibres before these fibres begin to carry tensile loads.
15. Fibre snubbing, if applicable, can be easily and cleanly incorporated into the SDEM relationships.
16. Despite the success of the modified SDEM for PPFRC representation, a number of discrepancies exist in numerical modelling of PPFRC specimens, and in the modelling of FRC under cyclic loads.
17. Improved relationships for PPFRC crack spacing, for direct tension behaviour of PPFRC with conventional steel reinforcement, and for the effects of fibres on crack closing and crack slip may lead to improved numerical representation.

7.4 Recommendations

As a result of this thesis, a number of areas for future work have been revealed. The following recommendations for future work are made:

1. Continued work on developing macro-synthetic fibre technologies is required. Such developments should focus on improvements in bond properties of the fibre (through the use of various cross-sectional shapes or fibre crimping) and on increases in fibre stiffness and fibre tensile strength.
2. The effects of such newly developed fibres on the hardened concrete properties should be subsequently investigated through an extensive research program similar to the one described in this thesis.
3. In general, more extensive research programs on the properties of PPFRC are needed to improve numerical representations of the material.
4. Reliable pull-out tests on new generation polypropylene fibres are required to determine the bond strength and to verify the presence of fibre snubbing.
5. An assessment of the engagement energy of FRC is required to improve the prediction of the direct tensile response immediately after cracking.
6. Using the results from the previous three recommendations, the SDEM model for polypropylene fibres could be further updated and verified.
7. An assessment of the effects of polypropylene fibres on the tension stiffening behaviour of conventionally reinforced concrete is needed. An improved relationship for PPFRC tension stiffening in FE analysis is required.
8. An assessment of the cracking behaviour of PPFRC should be performed and the findings should be incorporated into FE analysis software.
9. More substantial research on the effects of cyclic loading on FRC is required.
10. A model for the effects of fibre reinforcement on crack closing, crack slip and plastic offset in cyclically loaded FRC elements is required.
11. After the above research is performed, the predictions attained using FE analysis of PPFRC structures, and FRC structures subjected to reversed cyclic loading, should be further investigated to determine the adequacy of newly formulated models.

References

ACI Committee 318, (2008). *Building code requirements for structural concrete (ACI 318-08) and commentary*. Farmington Hills, MI.: American Concrete Institute, 436 p.

ACI Committee 544, (1993). Guide for specifying, mixing, placing, and finishing steel fiber reinforced concrete. *ACI Materials Journal, 90*(1), January-February, 1993, pp. 94-101.

ACI Committee 544, (2008). State-of-the-art report on fiber reinforced concrete – ACI 544.1R-96 (reapproved 2002). *ACI Manual of Concrete Practice, Part 6*, pp. ACI544.1R-7-ACI544.1R-24.

Adebar, P., Mindess, S., St.-Pierre, D., and Olund, B., (1997). Shear tests of fibre concrete beams without stirrups. *ACI Structural Journal, 94*(1), January-February 1997, pp. 68-76.

Alhozaimy, A. M., Soroushian, P., and Mirza, F., (1996). Mechanical properties of polypropylene fiber reinforced concrete and the effects of pozzolanic materials. *Cement and Concrete Composites*, *18*(2), 1996, pp. 85-92.

Altoubat, S., Yazdanbakhsh, A., and Rieder, K. A., (2009). Shear behavior of macro-synthetic fiber-reinforced concrete beams without stirrups. *ACI Materials Journal, 106*(4), July-August 2009, pp. 381-389.

Aoude, H., Belghiti, M., William, D. C., and Mitchell, D., (2012). Response of steel fiber-reinforced concrete beams with and without stirrups. *ACI Structural Journal*, *109*(3), March-April 2012, pp. 359-367.

Ashour, S. A., Hasanain, G. S., and Wafa, F. F., (1992). Shear behavior of high-strength fiber reinforced concrete beams. *ACI Structural Journal*, *89*(2), March-April 1992, pp. 176-184.

ASTM A370, (2012). ASTM A370 standard test methods and definitions for mechanical testing of steel products. *ASTM International, West Conshohocken, PA.,* 10 p.

ASTM C1018, (1997). ASTM standard C1018 standard test methods for flexural toughness and first-crack strength of fiber-reinforced concrete (using beam with third-point loading). *ASTM International, West Conshohocken, PA.*, 6 p.

ASTM C1609/C1609M, (2010). ASTM C1609/C1609M standard test methods for flexural performance of fiber-reinforced concrete (using beam with third-point loading). *ASTM International, West Conshohocken, PA.*, 9 p.

ASTM Standard C469, (2002). Standard test method for static modulus of elasticity and poisson's ratio of concrete in compression. *ASTM International, West Conshohocken, PA*, 5 p.

Aveston, J., and Kelly, A., (1973). Theory of multiple fracture of fibrous composites. *Journal of Materials Science, 8*, 1973, pp. 352-362.

Balaguru, P. N., (1992). Shah, S. P., (Ed.), *Fiber-reinforced cement composites*. New York: McGraw-Hill.

Banthia, N., Azabi, M., and Pigeon, M., (1993). Restrained shrinkage cracking in fibre-reinforced cementitious composites. *Materials and Structures, 26*(7), August 1993, pp. 405-413.

Banthia, N., and Trottier, J. F., (1994). Concrete reinforced with deformed steel fibers, part I: Bond-slip mechanisms. *ACI Materials Journal, 91*(5), September-October 1994, pp. 435-446.

Banthia, N., and Sappakittipakorn, M., (2007). Toughness enhancement in steel fiber reinforced concrete through fiber hybridization. *Cement and Concrete Research, 37*(9), September 2007, pp. 1366-1372.

BASF - The Chemical Company, (2012). *MasterFiber™ MAC Matrix Macrosynthetic Fiber – Product Data Sheet.* Retrieved February 28, 2013, from http://www.basf-admixtures.com/SiteCollectionDocuments/Data%20Sheets/Specialty/OTH-DAT-0715%20MasterFiber%20MAC%20Matrix%20050212_WEB.pdf

Batson, G., (1976). Steel fiber reinforced concrete. *Materials Science and Engineering, 25*, 1976, pp. 53- 58.

Bazant, Z. P., (2002). Concrete fracture models: Testing and practice. *Engineering Fracture Mechanics, 69*, 2002, pp. 165-205.

Benson, S. D. P., and Karihaloo, B. L., (2005). CARDIFRC - development and mechanical properties. Part III: Uniaxial tensile response and other mechanical properties. *Magazine of Concrete Research, 57*(8), October 2005, pp. 433-443.

Bentur, A., (2007). Mindess, S., (Ed.), *Fibre reinforced cementitious composites* (2nd Edition). New York: Taylor & Francis.

Bentz, E., (2010). *Augustus: Post Processor for VecTor2 - Version 5.6.5.* Copyright 1996-2010 E. Bentz.

Buratti, N., Mazzotti, C., and Savoia, M., (2011). Post-cracking behaviour of steel and macro-synthetic fibre-reinforced concretes. *Construction and Building Materials, 25*(5), January 2011, pp. 2713-2722.

CAN/CSA Standard A23.3-04, (2004). *Design of concrete structures* (Third Edition). Ottawa, Ontario, Canada: Cement Association of Canada, 214 p.

CAN/CSA Standard S6-06, (2006). *Canadian highway bridge design code*. Ottawa, Ontario, Canada: Canadian Standards Association, pp. 301-379.

Casanova, P., Rossi, P., and Schaller, I., (1997). Can steel fibers replace transverse reinforcements in reinforced concrete beams? *ACI Materials Journal, 94*(5), September-October 1997, pp. 341-354.

Chalioris, C. E., (2013). Steel fibrous RC beams subjected to cyclic deformations under predominant shear. *Engineering Structures, 49*, April 2013, pp. 104-118.

Chanvillard, G., and Aïtcin, P.C., (1996). Pull-out behavior of corrugated steel fibres. *Advanced Cement Based Materials, 4*(1), July 1996, pp. 28-41.

Chatterjee, A., and Deopura, B., (2006). High modulus and high strength PP nanocomposite filament. *Composites Part A: Applied Science and Manufacturing, 37*(5), May 2006, pp. 813-817.

Choi, K. K., Park, H. G., and Wight, J. K., (2007). Shear strength of steel fiber-reinforced concrete beams without web reinforcement. *ACI Structural Journal, 104*(1), January-February 2007, pp. 12-21.

Choi, S. Y., Park, Y. H., and Jung, W. T., (2012). A study on the bond performance improvement of polypropylene macro fibers according to the change of surface area. *Advanced Materials Research, 557-559,* 2012, pp. 1440-1446.

Cifuentes, H., and Medina, F., (2012). Experimental fracture behavior of polypropylene fiber reinforced concrete specimens with variable width. *Key Engineering Materials, 488-489*, 2012, pp. 642-645.

Cucchiara, C., Mendola, L. L., and Papia, M., (2004). Effectiveness of stirrups and steel fibres as shear reinforcement. *Cement and Concrete Composites*, *26*(7), October 2004, pp. 777-786.

Daniel, J. I., (1991). *Fiber reinforced concrete*. Illinois, USA: Portland Cement Association, 48 p.

Daniel, L., and Loukili, A., (2002). Behavior of high-strength fiber-reinforced concrete beams under cyclic loading. *ACI Structural Journal, 99*(3), March-April 2002, pp. 248-256.

Deluce, J. R., (2011). *Cracking behaviour of steel fibre reinforced concrete containing conventional steel reinforcement.* M.ASc. Dissertation, University of Toronto: Department of Civil Engineering, 507 p.

Elser, M., Tschegg, E. K., and Stanzl-Tschegg, S. E., (1996a). Fracture behaviour of polypropylene-fibre-reinforced concrete under biaxial loading: An experimental investigation. *Composites Science and Technology, 56*(8), March 1996, pp. 933-945.

Elser, M., Tschegg, E. K., Finger, N., and Stanzl-Tschegg, S. E., (1996b). Fracture behaviour of polypropylene-fibre-reinforced concrete: Modelling and computer simulation. *Composites Science and Technology, 56*(8), March 1996, pp. 947-956.

Ferrara, L., Park, Y. D., and Shah, S. P., (2008). Correlation among fresh state behavior, fiber dispersion, and toughness properties of SFRCs. *Journal of Materials in Civil Engineering, 20*(7), July 2008, pp. 493-501.

Filiatrault, A., Ladicani, K., and Massicotte, B., (1994). Seismic performance of code-designed fiber reinforced concrete joints. *ACI Materials Journal, 91*(5), September-October 1994, pp. 564-571.

Filiatrault, A., Pineau, S., and Houde, J., (1995). Seismic behavior of steel-fiber reinforced concrete interior beam-column joints. *ACI Materials Journal, 92*(5), September-October 1995, pp. 543-552.

Furlan Jr., S., and De Hanai, J. B., (1997). Shear behaviour of fiber reinforced concrete beams. *Cement and Concrete Composites, 19*(4), May 1997, pp. 359-366.

Gencoglu, M., and Eren, I., (2002). An experimental study on the effect of steel fiber reinforced concrete on the behavior of the exterior beam-column joints subjected to reversal cyclic loading. *Turkish Journal of Engineering and Environmental Sciences, 26*(6), February 2002, pp. 493-502.

Gettu, R., Gardner, D. R., Saldívar, H., and Barragán, B. E., (2005). Study of the distribution and orientation of fibers in SFRC specimens. *Materials and Structures, 38*, January-February 2005, pp. 31-37.

Gregor-Svetec, D., and Sluga, F., (2005). High modulus polypropylene fibers. I. mechanical properties. *Journal of Applied Polymer Science, 98*(1), January 2005, pp. 1-8.

Grzybowski, M., and Shah, S. P., (1990). Shrinkage cracking on fiber reinforced concrete. *ACI Materials Journal, 87*(2), March-April 1990, pp. 138-148.

Hasan, M. J., Afroz, M., and Mahmud, H. M. I., (2011). An experimental investigation on mechanical behavior of macro synthetic fiber reinforced concrete. *International Journal of Civil and Environmental Engineering, 11*(3), June 2011, pp. 18-23.

Hoxby, C., (2011). *Personal communication*. Mississauga, Ontario, Canada: BASF Canada - Construction Chemicals.

Hsu, L. S., and Hsu, C. T., (1994). Stress-strain behavior of steel-fiber high-strength concrete under compression. *ACI Structural Journal, 91*(4), July-August 1994, pp. 448-457.

Jiuru, T., Chaobin, H., Kaijian, Y., and Yongcheng, Y., (1992). Seismic behavior and shear strength of framed joint using steel-fiber reinforced concrete. *Journal of Structural Engineering, 118*(2), 1992, pp. 341-358.

Johnson, P. M., Couture, A., and Nicolet, R., (2007). *Commission of inquiry into the collapse of a portion of the de la concorde overpass: Report*. Transcontinental Métrolitho, Montréal, Québec: Gouvernement du Québec, 222 p.

Johnston, C. D., (2001). *Fibre-reinforced cements and concretes*. Ottawa, Ontario, Canada: Gordon and Breach Science Publishers, 372 p.

Khaloo, A. R., and Kim, N., (1997). Influence of concrete and fiber characteristics on behavior of steel fiber reinforced concrete under direct shear. *ACI Materials Journal, 94*(6), November-December 1997, pp. 592-601.

Khuntia, M., Stojadinovic, B., and Goel, S. C., (1999). Shear strength of normal and high-strength fiber reinforced concrete beams without stirrups. *ACI Structural Journal, 96*(2), March-April 1999, pp. 282-289.

Krenchel, H., and Shah, S., (1986). Swamy, R.N., Wagstaffe, R.L., and Oakley, D.R., (Eds.), *Synthetic fibres for tough and durable concrete.* Developments in Fiber Reinforced Cement and Concrete, Proc. RILEM Symposium, Sheffield, RILEM Technical Committee 49-FTR, 1986, Paper 4.7, pp. 333-338.

Lee, G. G., and Foster, S. J., (2007). Behavior of steel fibre reinforced mortar in shear III: Variable engagement model II. *Uniciv Report no. R-448, School of Civil and Environmental Engineering, The University of New South Wales, Sydney, Australia*, 86 p.

Lee, S. C. (2012a). *Personal communication*. KEPCO International Nuclear Graduate School (KINGS), Ulsan, South Korea: Department of NPP Engineering.

Lee, S. C. (2012b). *Personal communication*. University of Toronto, Toronto, Ontario, Canada: Department of Civil Engineering.

Lee, S. C., Cho, J. Y., and Vecchio, F. J., (2013). Simplified diverse embedment model for SFRC elements in tension. *American Concrete Institute Materials Journal, 110*(3), [NOT YET PUBLISHED].

Lee, S. C., Cho, J. Y., and Vecchio, F. J., (2011a). Diverse embedment model for steel fiber-reinforced concrete in tension: Model development. *ACI Materials Journal, 108*(5), September-October 2011, pp. 516-525.

Lee, S. C., Cho, J. Y., and Vecchio, F. J., (2011b). Diverse embedment model for steel fiber-reinforced concrete in tension: Model verification. *ACI Materials Journal, 108*(5), September-October 2011, pp. 526-535.

Leung, C. K. Y., and Ybanez, N., (1997). Pullout of inclined flexible fiber in cementitious composite. *Journal of Engineering Mechanics, 123*(3), March 1997, pp. 239-246.

Leutbecher, T., and Fehling, E., (2008). Crack width control for combined reinforcement of rebars and fibers exemplified by ultra-high-performance concrete. *Fib Task Group 8.6, Ultra High Performance Fiber Reinforced Concrete - UHPFRC,* September, 2008, pp. 1-28.

Li, V. C., Wang, Y., and Backer, S., (1990). Effect of inclining angle, bundling and surface treatment on synthetic fibre pull-out from a cement matrix. *Composites, 21*(2), March 1990, pp. 132-140.

Li, V. C., Wang, Y., and Backer, S., (1991). A micromechanical model of tension-softening and bridging toughening of short random fiber reinforced brittle matrix composites. *Journal of the Mechanics and Physics of Solids, 39*(5), 1991, pp. 607-625.

Li, V. C., Ward, R., and Hamza, A. M., (1992). Steel and synthetic fibers as shear reinforcement. *ACI Materials Journal, 89*(5), September-October 1992, pp. 499-508.

Lim, T. Y., Paramasivam, P., and Lee, S. L., (1987). Analytical model for tensile behavior of steel-fiber concrete. *ACI Materials Journal, 84*(4), July-August 1987, pp. 286-298.

Löfgren, I., Stang, H., and Olesen, J. F., (2005). Fracture properties of FRC determined through inverse analysis of wedge splitting and three-point bending tests. *Journal of Advanced Concrete Technology*, *3*(3), October 2005, pp. 423-434.

Lovy, D., (1996). *WinDIG 2.5: Free digitizer software*. Copyright 1996-1998 D.Lovy.

Ma, H., Wang, H. H., Li, Z. B., Sun, X. Y., and Zhang, X. W., (2012). Experimental study on the seismic performance of macro-synthetic fiber-reinforced concrete ductile columns. *Advanced Materials Research, 446*, January 2012, pp. 2345-2350.

Majdzadeh, F., Soleimani, S. M., and Banthia, N., (2006). Shear strength of reinforced concrete beams with a fiber concrete matrix. *Canadian Journal of Civil Engineering, 33*(6), August 2006, pp. 726-734.

Mansour, A., Srebric, J., and Burley, B. J., (2007). Development of straw-cement composite sustainable building material for low-cost housing in Egypt. *Journal of Applied Sciences Research, 3*(11), 2007, pp. 1571-1580.

Marti, P., Pfyl, T., Sigrist, V., and Ulaga, T., (1999). Harmonized test procedures for steel fiber-reinforced concrete. *ACI Materials Journal, 96*(6), November-December 1999, pp. 676-686.

Meda, A., Minelli, F., Plizzari, G. A., and Riva, P., (2005). Shear behaviour of steel fibre reinforced concrete beams. *Materials and Structures, 38*, April 2005, pp. 343-351.

Minelli, F., (2005). *Plain and fiber reinforced concrete beams under shear loading: Structural behaviour and design aspects.* Ph.D Dissertation, University of Brescia: Department of Civil Engineering, 429 p.

Mirsayah, A. A., and Banthia, N., (2002). Shear strength of steel fiber-reinforced concrete. *ACI Materials Journal*, *99*(5), September-October 2002, pp. 473-479.

Mu, B., Meyer, C., and Shimanovich, S., (2002). Improving the interface bond between fiber mesh and cementitious matrix. *Cement and Concrete Research, 32*, May 2002, pp. 783-787.

N.V. Bekaert S.A., (2003). *Product data sheet for dramix fibers*. Retrieved February 28, 2013 from: http://www.bekaert.com/building.

Naaman, A.E., Nammur, G., Najm, H., and Alwan, J., (1989). *Bond Mechanisms in Fiber Reinforced Cement-Based Composites.* Report No. UMCE 89-9, Department of Civil Engineering, University of Michigan Ann Arbor, August 1989, 254 p.

Naaman, A. E., Wight, J. K., and Abdou, H., (1987). SIFCON connections for seismic resistant frames. *Concrete International*, *9*(11), November 1987, pp. 34-39.

Naaman, A. E., and Najm, H., (1991). Bond-slip mechanisms of steel fibers in concrete. *ACI Materials Journal*, *88*(2), March-April 1991, pp. 135-145.

Naaman, A. E., Namur, G. G., Alwan, J. M., and Najm, H. S,. (1991a). Fiber pullout and bond slip. I. Analytical study. *Journal of Structural Engineering*, *117*(9), September 1991, pp. 2769-2790.

Naaman, A. E., Namur, G. G., Alwan, J. M., and Najm, H. S., (1991b). Fiber pullout and bond slip. II. Experimental validation. *Journal of Structural Engineering, 117*(9), September 1991, pp. 2791-2800.

Nammur Jr., G., and Naaman, A. E., (1989). Bond stress model for fiber reinforced concrete based on bond stress-slip relationship. *ACI Materials Journal*, *86*(1), January-February 1989, pp. 45-57.

Nataraja, M. C., Dhang, N., and Gupta, A. P., (1999). Stress-strain curves for steel-fiber reinforced concrete under compression. *Cement and Concrete Composites, 21*(5-6), May 1999, pp. 383-390.

Noghabai, K. (2000). Beams of fibrous concrete in shear and bending: Experiment and model. *Journal of Structural Engineering, 126*(2), February 2000, pp. 243-251.

Oh, J.H., (2011). *Uniaxial behaviour of steel fiber reinforced concrete.* Master's Thesis, Seoul National University, South Korea, 122 p. (Korean).

Oh, B. H., Kim, J. C., and Choi, Y. C., (2007). Fracture behavior of concrete members reinforced with structural synthetic fibers. *Engineering Fracture Mechanics, 74*(1-2), January 2007, pp. 243-257.

Oh, B. H., Park, D. G., Kim, J. C., and Won, J. P., (2002). Realistic prediction of post-cracking behavior in synthetic fiber reinforced concrete beam. *Korea Concrete Institute Journal, 14*(6), 2002, pp. 900-909.

Otter, D. E., and Naaman, A. E., (1988). Properties of steel fiber reinforced concrete under cyclic loading. *ACI Materials Journal, 85*(4), July-August 1988, pp. 254-261.

Ou, Y. C., Tsai, M. S., Liu, K. Y., and Chang, K. C., (2012). Compressive behavior of steel-fiber-reinforced concrete with a high reinforcing index. *Journal of Materials in Civil Engineering, 24*(2), February 2012, pp. 207-215.

Ouyang, C., Pacios, A., and Shah, S. P., (1994). Pullout of inclined fibers from cementitious matrix. *Journal of Engineering Mechanics, 120*(12), December 1994, pp. 2641-2659.

Parra-Montesinos, G. J., (2006). Shear strength of beams with deformed steel fibers. *Concrete International 28*(11), November 2006, pp. 57-66.

Richardson, A.E., and Landless, S., (2009). Synthetic fibres and steel fibres in concrete with regard to bond strength and toughness. *Northumbria Working Paper Series: Interdisciplinary Studies in the Built and Virtual Environment,* December 2009, pp. 128-140.

Richardson, A. E., (2005). Bond characteristics of structural polypropylene fibres in concrete with regard to post-crack strength and durable design. *Structural Survey, 23*(3), 2005, pp. 210-230.

Richardson, A. E., Coventry, K., and Landless, S., (2010). Synthetic and steel fibres in concrete with regard to equal toughness. *Structural Survey, 28*(5), November 2010, pp. 355-369.

RILEM Final Recommendation TC-162-TDF. (2003). Recommendations of RILEM TC 162-TDF: σ-ε design method. *Materials and Structures, 36*, 2003, pp. 560-567.

Roesler, J. R., Altoubat, S. A., Lange, D. A., Rieder, K., and Ulreich, G. R., (2006). Effect of synthetic fibers on structural behavior of concrete slabs-on-ground. *ACI Materials Journal-American Concrete Institute, 103*(1), January-February 2006, pp. 3-10.

Romualdi, J. P., and Batson, G. B., (1963). The mechanics of crack arrest in concrete. *Journal, ASCE, 89* (EM3, Paper 3558), June 1963, pp. 147-168.

Romualdi, J. P., and Mandel, J. A., (1964). Tensile strength of concrete affected by uniformly distributed closely spaced short lengths of wire reinforcements. *ACI Journal, Proceedings, 61*(6), June 1964, pp. 657-671.

Ruggerio, D., (2011). *Timeline version 1.0.* Copyright 2011 D.Ruggerio.

Sadeghian, V., (2012). *FormWorks-Plus: Improved pre-processor for VecTor analysis software.* M.A.Sc. Dissertation, Department of Civil Engineering, University of Toronto, 164p.

Shah, S. P., and Rangan, B. V., (1971). Fiber reinforced concrete properties. *ACI Journal, 68*(2), February 1971, pp. 126-137.

Shao, Y., and Wang, W., (2012). Experimental study on fracture properties of hybrid fiber reinforced concrete, *Advanced Materials Research, 450-451*, 2012, pp. 518-522.

Sharma, A. K., (1986). Shear strength of steel fiber reinforced concrete beams. *ACI Journal, 83*(4), July-August 1986, pp. 624-628.

Soroushian, P., Khan, A., and Hsu, J., (1992). Mechanical properties of concrete materials reinforced with polypropylene or polyethylene fibers. *ACI Materials Journal, 89*(6), November-December 1992, pp. 535-540.

Stroeven, P., (1977). The analysis of fibre distributions in fibre reinforced materials. *Journal of Microscopy, 111*, December 1977, pp 283-295.

Stroeven, P., (2009). Stereological principals of spatial modeling applied to steel fiber reinforced concrete in tension. *ACI Materials Journal, 106*(3), May-June 2009, pp. 213-222.

Sujivorakul, C., Waas, A., and Naaman, A.E., (2000). Pullout response of a smooth fiber with an end anchorage. *Journal of Engineering Mechanics, 126*(9), September 2000, pp. 986-993.

Susetyo, J., Gauvreau, P., and Vecchio, F. J., (2011). Effectiveness of steel fiber as minimum shear reinforcement. *ACI Structural Journal, 108*(4), July-August 2011, pp. 488-496.

Susetyo, J., (2009). *Fibre reinforcement for shrinkage crack control in prestressed, precast segmental bridges.* Ph.D. Dissertation, University of Toronto: Department of Civil Engineering, 532 p.

Swamy, R. N., Jones, R., and Chiam, A. T. P., (1993). Influence of steel fibers on the shear resistance of lightweight concrete I- beams. *ACI Structural Journal, 90*(1), January-February 1993, pp. 103-114.

Synthetic Resources, (2013). Fibrillated fiber vs. monfilament fiber. Retrieved February 28, 2013, from http://www.syntheticresources.com/fibernet08/fibrillated_vs_monofilament.asp

Thomas, J., and Ramaswamy, A., (2007). Mechanical properties of steel fiber-reinforced concrete. *Journal of Materials in Civil Engineering, 19*(5), May 2007, pp. 385-392.

Valle, M., and Buyukozturk, O., (1993). Behavior of fiber reinforced high-strength concrete under direct shear. *ACI Materials Journal, 90*(2), March-April 1993, pp. 122-133.

Vandewalle, L., (1999). Reinhardt, H. W., and Naaman, A.E., (Eds.), *Influence of tensile strength of steel fibre on toughness of high strength concrete.* Proceedings of Third International Workshop on High-Performance Cement Composites (Mainz, Germany), RILEM Publications, Bagneux, France, pp. 331- 337.

Vecchio, F. J., (1990). *VecTor2 nonlinear finite element analysis*. Copyright 1990-2013 F.J. Vecchio.

Vecchio, F. J., (1979). *Shear rig design.* M.Eng. Dissertation, University of Toronto: Department of Civil Engineering, 246 p.

Vecchio, F. J., (2000). Disturbed stress field model for reinforced concrete: Formulation. *ASCE Journal of Structural Engineering, 126*(9), September 2000, pp. 1071-1077.

Vecchio, F. J., and Collins, M. P., (1986). The modified compression field theory for reinforced concrete elements subject to shear. *ACI Journal*, *83*(2), March-April 1986, pp. 219-231.

Voo, J. Y. L., and Foster, D. S. J., (2003). Variable engagement model for fibre reinforced concrete in tension. *University of New South Wales, School of Civil and Environmental Engineering.* 87 p.

Wang, Y., Backer, S., and Li, V. C., (1987). An experimental study of synthetic fibre reinforced cementitious composites. *Journal of Materials Science, 22*(12), December 1987, pp. 4281 - 4291.

Wang, Y., Backer, S., and Li, V. C., (1989). A statistical tensile model of fibre reinforced cementitious composites. *Composites, 20*(3), May 1989, pp. 265-274.

Wang, Y., Li, V. C., and Backer, S., (1988). Modelling of fibre pull-out from a cement matrix. *International Journal of Cement Composites and Lightweight Concrete, 10*(3), April 1988, pp. 143-149.

Won, J. P., Lim, D. H., and Park, C. G., (2006). Bond behaviour and flexural performance of structural synthetic fibre-reinforced concrete. *Magazine of Concrete Research, 58*(6), April 2006, pp. 401-410.

Wong, P. S., Vecchio, F. J., and Trommels, H., (2012). Updated FormWorks and VecTor2 user's manual. *University of Toronto,* 339 p.

Zheng, Z., and Feldman, D., (1995). Synthetic fibre-reinforced concrete. *Progress in Polymer Science*, *20*(2), 1995, pp. 185-210.

Zollo, R. F., (1997). Fiber-reinforced concrete: An overview after 30 years of development. *Cement and Concrete Composites*, *19*, 1997, pp. 107-122.

Zonsveld, J. J., (1975). Neville, A., (Ed.), *Properties and testing of concrete containing fibers other than steel.* Fibre Reinforced Cement and Concrete, Proc. RILEM Symp., The Construction Press, U.K., 1975, pp. 217-226.

APPENDIX A

Material Test Results

A.1 Cylinder Test Data

A.1.1 Test Set DC-DB1

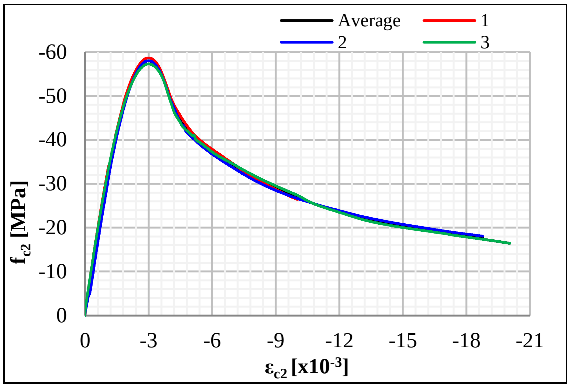

DC-DB1 – 28-Day Cylinder Tests

Cylinder	7-Day f'_c [MPa]	28-Day f'_c [MPa]	28-Day ε'_c [x10^{-3}]	28-Day E_{cs} [MPa]
1	49.3	58.7	2.974	31296
2	49.8	58.1	3.015	27856
3	49.5	57.3	2.993	30533
Average	49.5	58.0	2.994	29895

A.1.2 Test Set DC-DB2

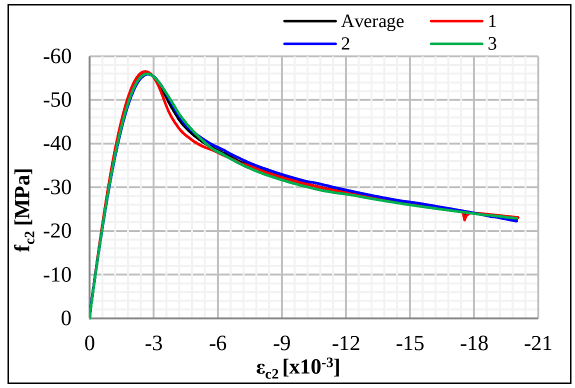

DC-DB2 – 28-Day Cylinder Tests

Cylinder	7-Day f'_c [MPa]	28-Day f'_c [MPa]	28-Day ε'_c [x10^{-3}]	28-Day E_{cs} [MPa]
1	-	56.5	2.974	31296
2	-	55.9	3.015	27856
3	-	56.0	2.993	30533
Average	-	56.1	2.994	29895

A.1.3 Test Set DC-P1

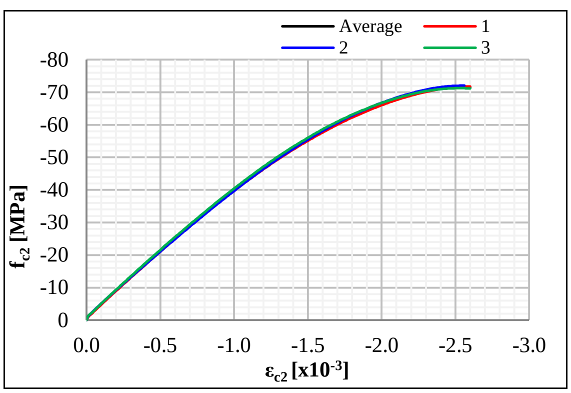

DC-P1 – 28-Day Cylinder Tests

Cylinder	8 Day f'_c [MPa]	28-Day f'_c [MPa]	28-Day ε'_c [x10^{-3}]	28-Day E_{cs} [MPa]
1	60.7	71.8	2.974	31296
2	59.5	72.0	3.015	27856
3	-	71.3	2.993	30533
Average	60.1	71.7	2.994	29895

A.1.4 Test Set DC-P2

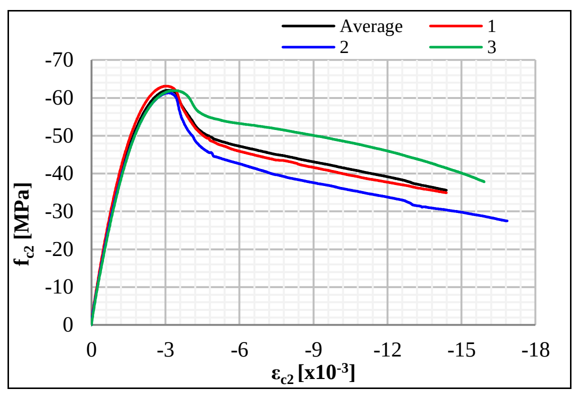

DC-P2 – 28-Day Cylinder Tests

Cylinder	7-Day f'_c [MPa]	28-Day f'_c [MPa]	28-Day ε'_c [x10^{-3}]	28-Day E_{cs} [MPa]
1	57.5	63.1	2.974	31296
2	55.1	61.3	3.015	27856
3	-	62.0	2.993	30533
Average	56.3	62.1	2.994	29895

A.1.5 Test Set DC-P3

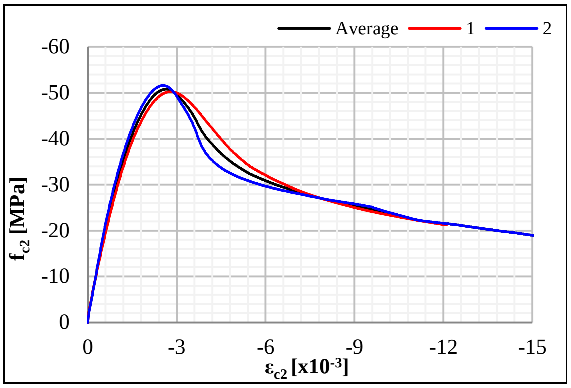

DC-P3 – 29-Day Cylinder Tests

Cylinder	7-Day f'_c [MPa]	29-Day f'_c [MPa]	ε'_c [x10^{-3}]	E_{cs} [MPa]
1	46.1	50.2	2.974	31296
2	45.5	51.6	3.015	27856
Average	45.8	50.9	2.994	29895

A.1.6 Test Set DC-P3

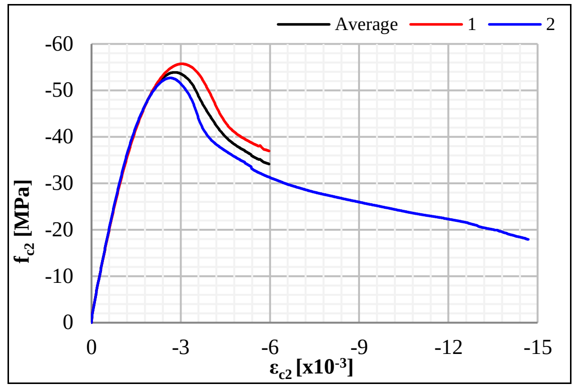

DC-P3 – Test Day Cylinder Tests

Cylinder	Test Day f'_c [MPa]	ε'_c [x10^{-3}]	E_{cs} [MPa]
1	55.7	2.974	31296
2	52.7	3.015	27856
Average	54.2	2.994	29895

A.1.7 Test Set DC-P4

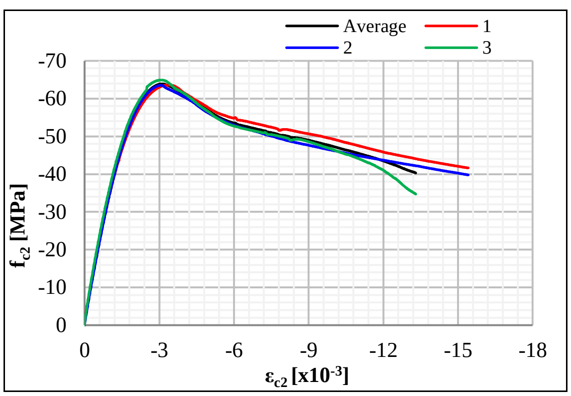

DC-P4 – 28-Day Cylinder Tests

Cylinder	7-Day f'_c [MPa]	28-Day f'_c [MPa]	ε'_c [x10^{-3}]	E_{cs} [MPa]
1	56.1	63.6	2.974	31296
2	54.0	63.5	3.015	27856
3	57.6	64.9	2.993	30533
Average	55.9	64.0	2.994	29895

A.1.8 Test Set DC-P4

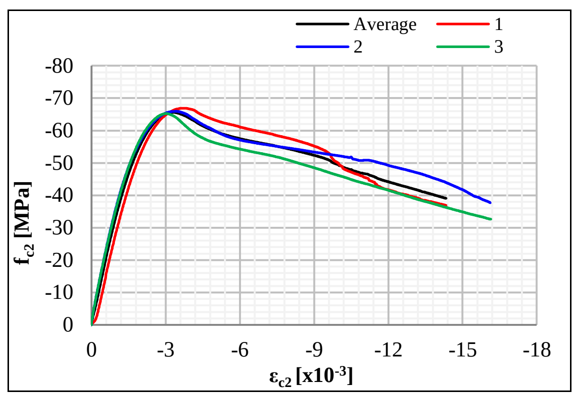

DC-P4 – Test Day Cylinder Tests

Cylinder	Test Day f'_c [MPa]	ε'_c [x10^{-3}]	E_{cs} [MPa]
1	66.9	2.974	31296
2	66.0	3.015	27856
3	65.3		
Average	66.0	2.994	29895

A.1.9 Test Set DC-P5

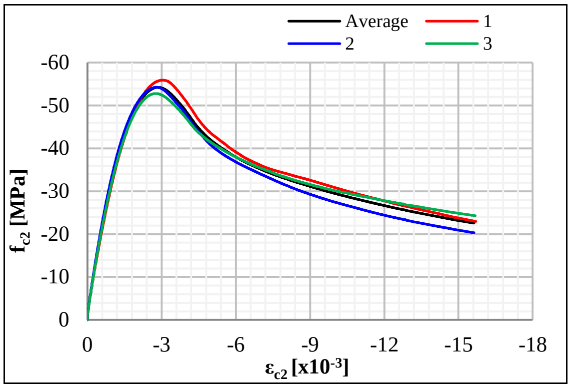

DC-P5 – 28-Day Cylinder Tests

	18 Day	28-Day		
Cylinder	f'_c [MPa]	f'_c [MPa]	ε'_c [x10^{-3}]	E_{cs} [MPa]
1	52.0	55.9	2.974	31296
2	53.7	54.3	3.015	27856
3	50.2	52.8	2.993	30533
Average	52.0	54.3	2.994	29895

A.1.10 Test Set DC-P5

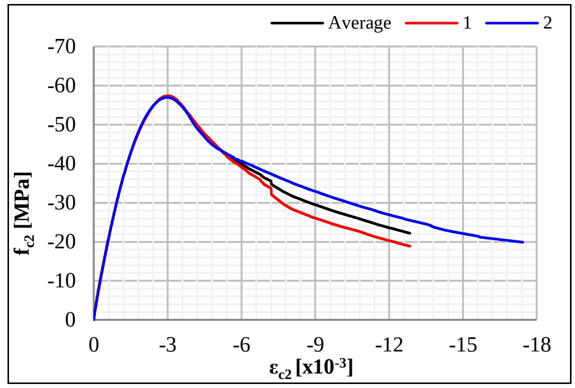

DC-P5 – Test Day Cylinder Tests

	Test Day		
Cylinder	f'_c [MPa]	ε'_c [x10^{-3}]	E_{cs} [MPa]
1	57.4	2.974	31296
2	57.0	3.015	27856
3	-		
Average	57.2	2.994	29895

A.2 Uniaxial Direct Tension Test Data

A.2.1 Test Set DC-DB1

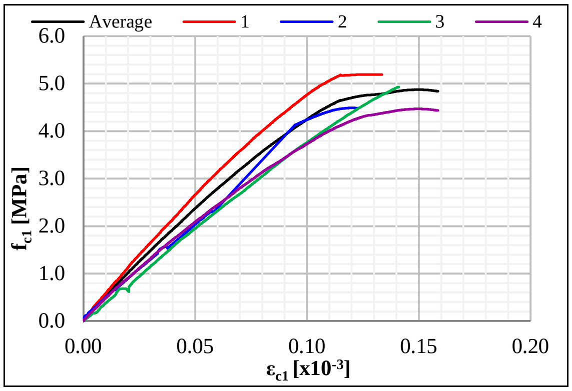

DC-DB1 – Pre-cracked response

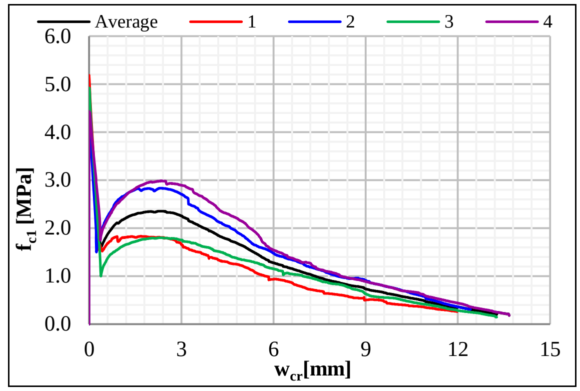

DC-DB1 – Post-cracked response

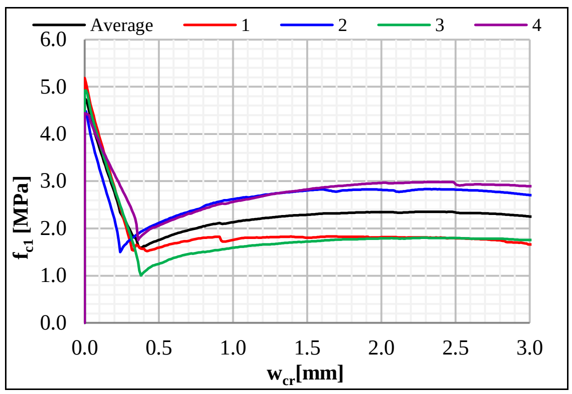

DC-DB1 – Post-cracked response magnified

Dogbone	f_t' [MPa]	ε_t' [x10^{-3}]	E_{ct} [MPa]	f_{c1} [MPa] at a w_{cr} of				
				0.5 mm	1.5 mm	3.0 mm	6.0 mm	12.0 mm
1	5.19	0.1497	43177	1.590	1.805	1.659	0.936	-
2	4.48	0.1706	34473	2.118	2.805	2.708	1.477	0.360
3	4.92	0.1524	43757	1.249	1.722	1.756	1.153	0.283
4	4.47	0.2103	36161	2.060	2.828	2.893	1.542	0.438
Average	4.77	0.1708	39392	1.754	2.290	2.254	1.277	0.360

A.2.2 Test Set DC-DB2

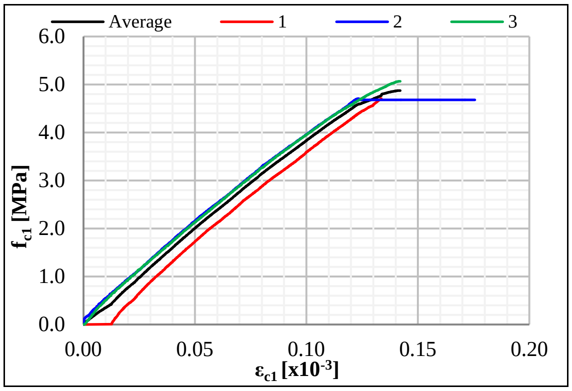

DC-DB2 – Pre-cracked response

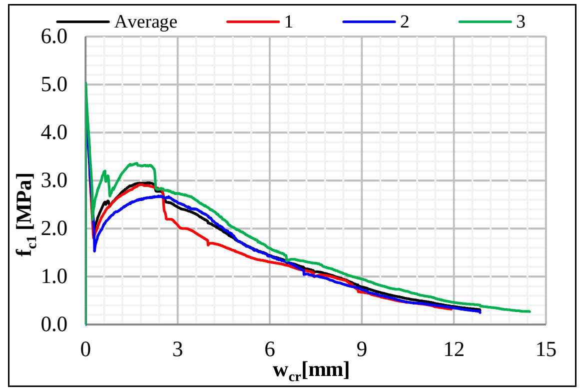

DC-DB2 – Post-cracked response

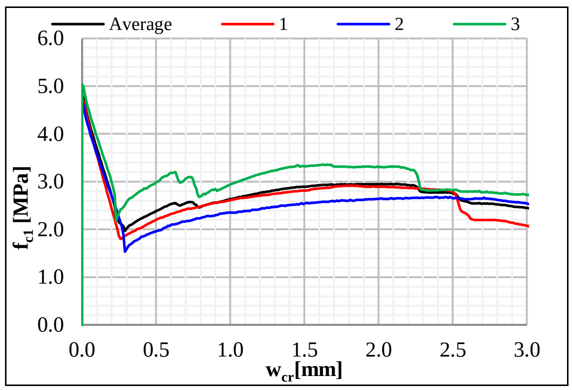

DC-DB2 – Post-cracked response magnified

Dogbone	f'_t **[MPa]**	ε'_t **[x10^{-3}]**	E_{ct} **[MPa]**	f_{c1} **[MPa] at a** w_{cr} **of**				
				0.5 mm	**1.5 mm**	**3.0 mm**	**6.0 mm**	**12.0 mm**
1	4.71	0.1583	38824	2.202	1.805	1.659	0.936	-
2	4.67	0.1465	41624	1.965	2.805	2.708	1.477	0.360
3	5.03	0.1154	43084	2.984	1.722	1.756	1.153	0.283
Average	4.80	0.1401	41177	2.384	2.290	2.254	1.277	0.360

A.2.3 Test Set DC-P1

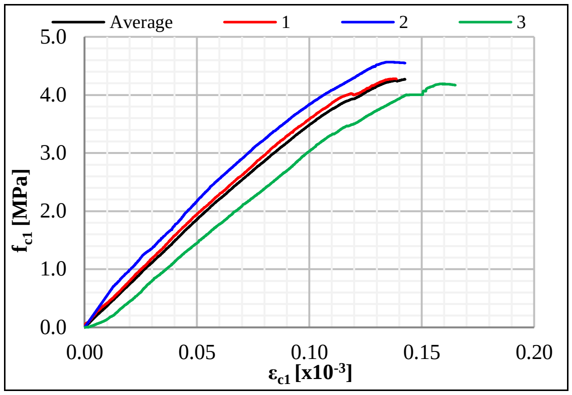

DC-P1 – Pre-cracked response

Dogbone	f'_t **[MPa]**	ε'_t **[x10^{-3}]**	E_{ct} **[MPa]**
1	4.28	0.1377	40748
2	4.57	0.1418	40513
3	4.19	0.1644	34417
Average	4.35	0.1480	38559

A.2.4 Test Set DC-P2

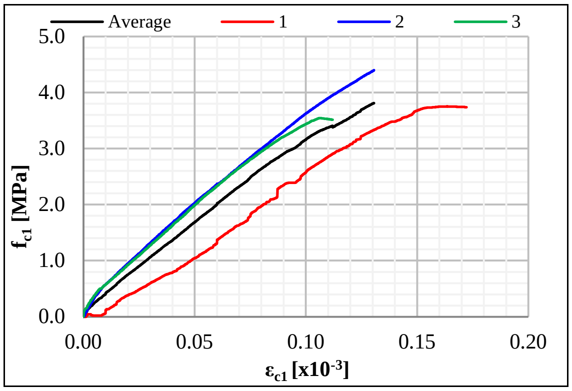

DC-P2 – Pre-cracked response

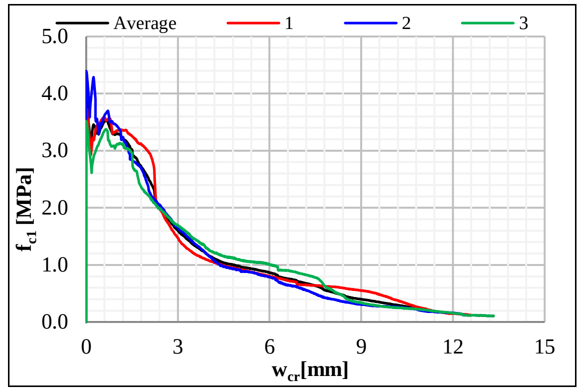

DC-P2 – Post-cracked response

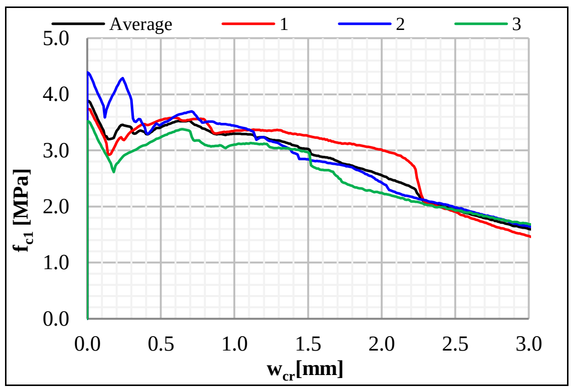

DC-P2 – Post-cracked response magnified

Dogbone	f'_t **[MPa]**	ε'_t **[x10^{-3}]**	E_{ct} **[MPa]**	f_{c1} **[MPa] at a** w_{cr} **of**				
				0.5 mm	**1.5 mm**	**3.0 mm**	**6.0 mm**	**12.0 mm**
1	3.75	0.2385	24062	3.542	1.805	1.659	0.936	-
2	4.41	0.1601	32517	3.457	2.805	2.708	1.477	0.360
3	3.54	0.1520	30412	3.234	1.722	1.756	1.153	0.283
Average	3.90	0.1836	28997	3.411	2.290	2.254	1.277	0.360

A.2.5 Test Set DC-P3

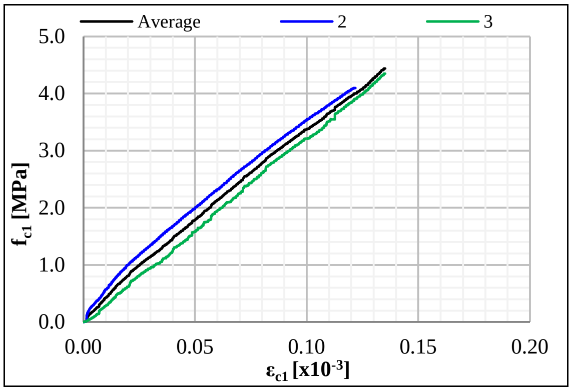

DC-P3 – Pre-cracked response

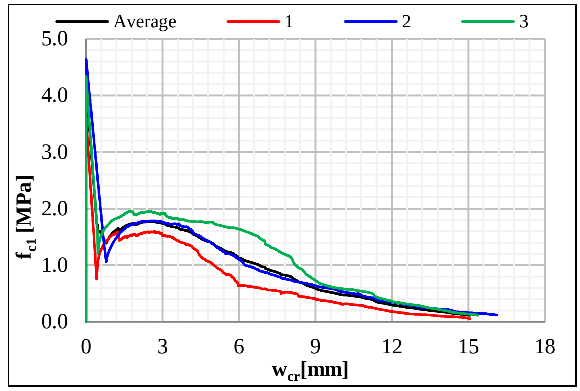

DC-P3 – Post-cracked response

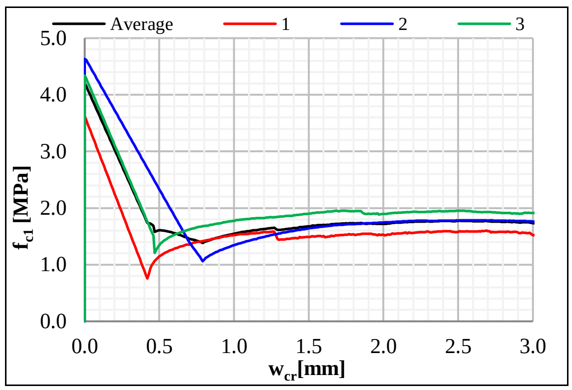

DC-P3 – Post-cracked response magnified

Dogbone	**f'_t [MPa]**	**ε'_t [x10^{-3}]**	**E_{ct} [MPa]**	**f_{c1} [MPa] at a w_{cr} of**				
				0.5 mm	**1.5 mm**	**3.0 mm**	**6.0 mm**	**12.0 mm**
1	-	-	-	1.145	1.805	1.659	0.936	-
2	4.64	0.1237	41002	2.332	2.805	2.708	1.477	0.360
3	4.35	0.1405	30491	1.344	1.722	1.756	1.153	0.283
Average	4.49	0.1321	35746	1.607	2.290	2.254	1.277	0.360

A.2.6 Test Set DC-P4

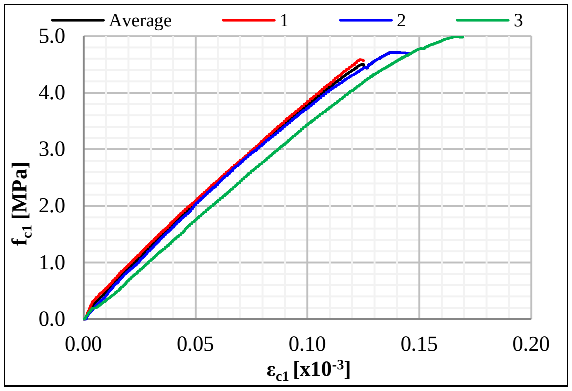

DC-P4 – Pre-cracked response

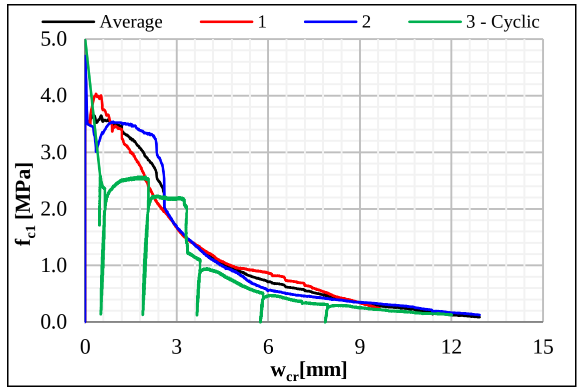

DC-P4 – Post-cracked response

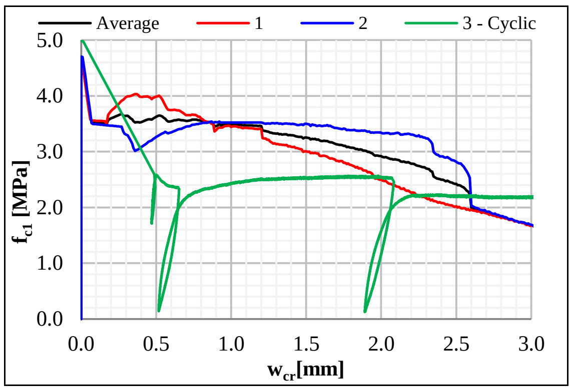

DC-P4 – Post-cracked response magnified

Dogbone	f'_t [MPa]	ε'_t [x10^{-3}]	E_{ct} [MPa]	f_{c1} [MPa] at a w_{cr} of				
				0.5 mm	1.5 mm	3.0 mm	6.0 mm	12.0 mm
1	4.59	0.1412	34576	3.988	3.006	1.670	0.871	-
2	4.72	0.1443	41945	3.263	3.497	1.690	0.555	0.167
3	4.99	0.1685	37144	-	-	-	-	-
Average	4.76	0.1513	37888	3.626	3.252	1.680	0.713	0.167
3 - Cyclic*	-	-	-	2.576	2.525	2.176	0.465	0.129

* Not included in average of monotonic dogbones

A.2.7 Test Set DC-P5

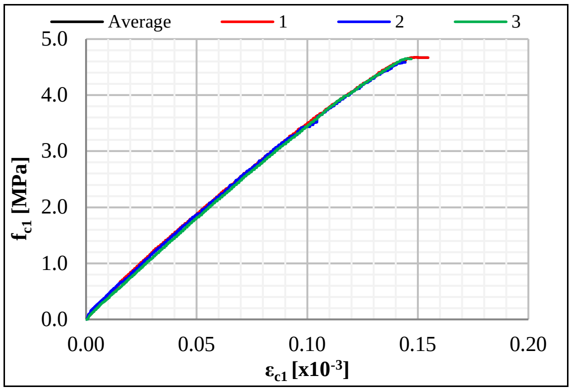

DC-P5 – Pre-cracked response

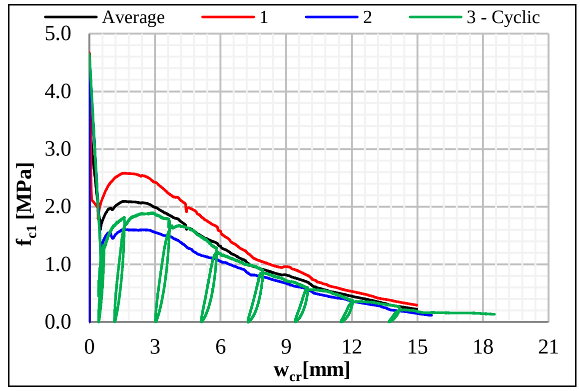

DC-P5 – Post-cracked response

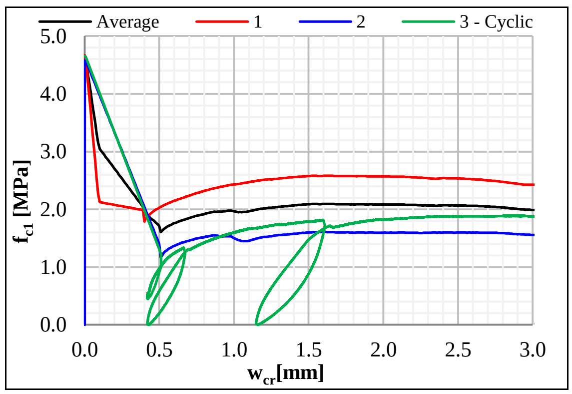

DC-P5 – Post-cracked response magnified

Dogbone	f'_t [MPa]	ε'_t [x10^{-3}]	E_{ct} [MPa]	f_{c1} [MPa] at a w_{cr} of 0.5 mm	1.5 mm	3.0 mm	6.0 mm	12.0 mm
1	4.68	0.1521	40003	2.028	3.006	1.670	0.871	-
2	4.67	0.1448	36384	1.396	3.497	1.690	0.555	0.167
3	4.65	0.1454	37785	-	-	-	-	-
Average	4.67	0.1474	38057	1.712	3.252	1.680	0.713	0.167
3 - Cyclic*	-	-	-	1.306	2.525	2.176	0.465	0.129

* Not included in average of monotonic dogbones

A.3 Modulus of Rupture Test Data

A.3.1 Test Set DC-P1

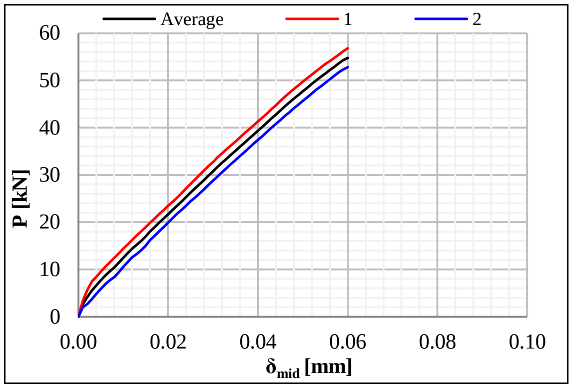

MOR	f_1 [MPa]	f_p [MPa]	f^D_{600} [MPa]	f^D_{150} [MPa]	T^D_{150} [J]	$R^D_{T,150}$ [%]	P [kN] at a displacement of 1.0 mm	2.0 mm	4.0 mm	8.0 mm
1	7.46	7.46	-	-	-	-	-	-	-	-
2	6.97	6.97	-	-	-	-	-	-	-	-
Average	7.22	7.22	-	-	-	-	-	-	-	-

A.3.2 Test Set DC-P3

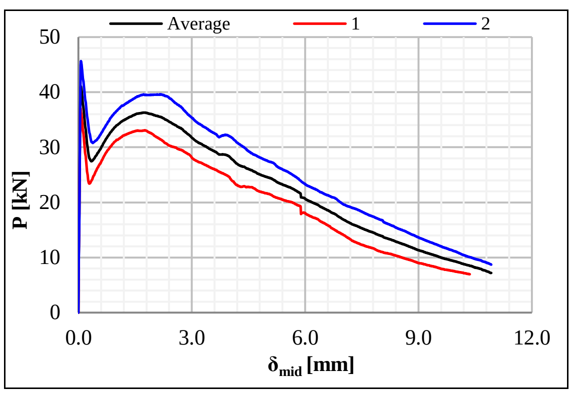

MOR	f_1 [MPa]	f_p [MPa]	f^D_{600} [MPa]	f^D_{150} [MPa]	T^D_{150} [J]	$R^D_{T,150}$ [%]	P [kN] at a displacement of 1.0 mm	2.0 mm	4.0 mm	8.0 mm
1	4.78	4.78	3.75	3.56	92.0	80.7	31.3	32.2	24.6	11.1
2	5.84	5.84	4.35	4.46	112.7	80.4	36.5	39.5	32.0	16.8
Average	5.31	5.31	4.05	4.01	102.4	80.6	33.9	35.9	28.3	13.9

A.3.3 Test Set DC-P4

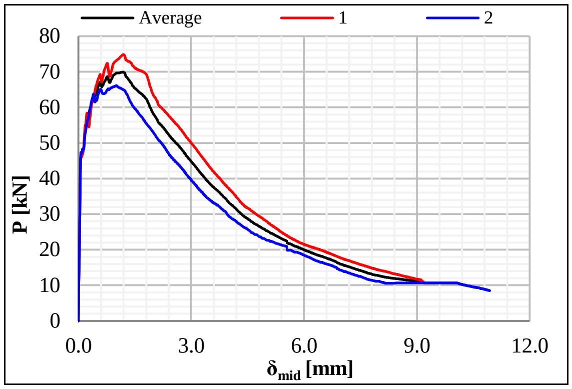

MOR	f_1 [MPa]	f_p [MPa]	f^D_{600} [MPa]	f^D_{150} [MPa]	T^D_{150} [J]	$R^D_{T,150}$ [%]	P [kN] at a displacement of 1.0 mm	2.0 mm	4.0 mm	8.0 mm
1	7.32	9.39	9.07	6.19	191.8	107.8	73.1	63.6	37.2	14.3
2	6.22	8.51	8.34	5.03	166.8	113.2	66.1	52.8	29.3	11.1
Average	6.77	8.95	8.71	5.61	179.3	110.5	69.6	58.1	33.3	12.7

A.3.4 Test Set DC-P5

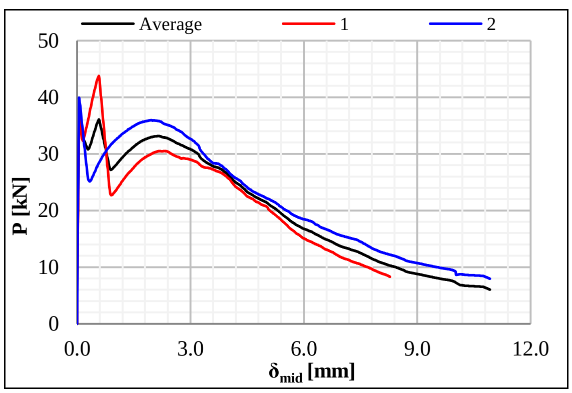

MOR	f_1 [MPa]	f_p [MPa]	f^D_{600} [MPa]	f^D_{150} [MPa]	T^D_{150} [J]	$R^D_{T,150}$ [%]	P [kN] at a displacement of 1.0 mm	2.0 mm	4.0 mm	8.0 mm
1	4.60	5.45	2.90	3.60	92.1	81.6	23.3	30.1	25.7	9.0
2	5.16	5.16	3.92	4.17	100.4	82.2	32.4	35.9	26.9	12.8
Average	4.88	5.31	3.41	3.89	96.3	81.9	27.9	33.0	26.3	10.9

A.4 Reinforcing Steel Data

A.4.1 D4 Reinforcing Steel

A_s = 25.81 mm^2

d_b = 5.72 mm

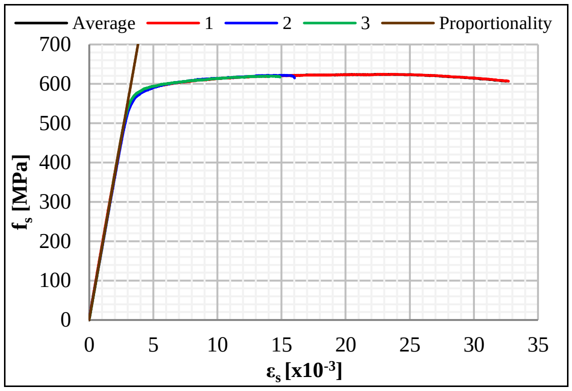

Coupon	E_s [MPa]	f_y [MPa]	ε_y [x10^{-3}]	f_u [MPa]	ε_u [x10^{-3}]
1	185508	469.3	2.530	624.4	22.71
2	179704	469.0	2.610	621.9	15.02
3	183991	491.3	2.670	620.0	13.89
Average*	183850	484.3	2.670	624.4	22.71

* Calculated from line of best fit of the 3 coupons

A.4.2 D8 Reinforcing Steel

A_s = 51.61 mm^2

d_b = 8.10 mm

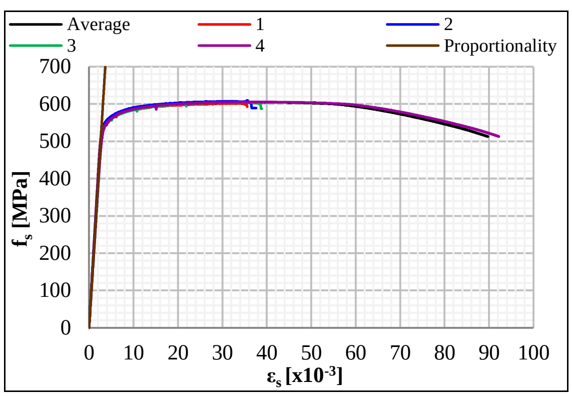

Coupon	E_s [MPa]	f_y [MPa]	ε_y [x10^{-3}]	f_u [MPa]	ε_u [x10^{-3}]
1	200167	488.4	2.440	601.8	32.85
2	197272	467.5	2.370	610.1	35.52
3	187161	454.8	2.430	604.3	34.67
4	183142	461.5	2.520	605.5	37.13
Average*	192515	466.4	2.430	605.4	37.13

* Calculated from line of best fit of the 4 coupons

A.4.3 5/16”x18 High Strength Threaded Rod

A_s = 49.48 mm^2

d_b = 7.93 mm

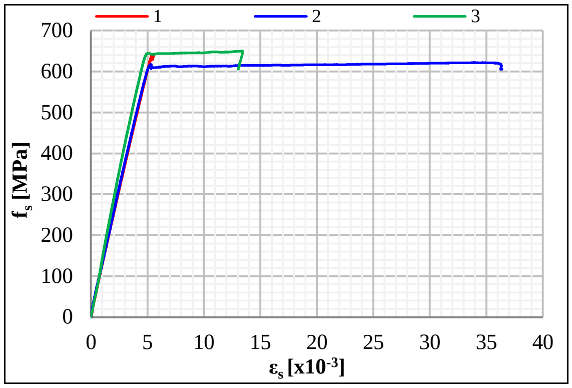

Coupon	E_s [MPa]	f_y [MPa]	ε_y [x10^{-3}]	f_u [MPa]	ε_u [x10^{-3}]
1	118225	623.2	5.206	641.6	5.51
2	115201	616.0	5.240	621.7	34.70
3	131000	641.0	4.870	649.9	13.38
Average	121475	626.8	5.105	637.7	34.70

A.4.4 5/16”x18 Normal Strength Threaded Rod

A_s = 49.48 mm^2

d_b = 7.93 mm

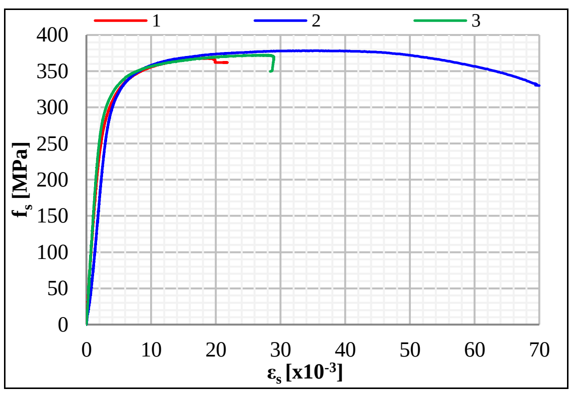

Coupon	E_s [MPa]	f_y [MPa]	ε_y [x10^{-3}]	f_u [MPa]	ε_u [x10^{-3}]
1	95900	262.3	2.450	368.1	18.22
2	84700	279.6	3.420	378.3	35.61
3	101000	285.6	2.590	372.2	27.33
Average	93867	275.8	2.820	372.9	35.613

A.5 Fibre Data

A.5.1 RC80/30-BP Product Data Sheet

PRODUCT DATA SHEET BEKAERT

NEW

Dramix®

R | C | -80/30- | B | P
45 65 80 l/d | Bright | High Carbon

- **Description:** Dramix® fibres are filaments of wire, deformed and cut to lengths, for reinforcement of concrete, mortar and other composite materials. Dramix® RC-80/30-BP is a high carbon wire fibre, with hooked ends, and glued in bundles.

- **Applications:**
recommended in applications with concrete strength > C50/60
  - segmental linings
  - prestressed beams
  - military structures
  - vaults
  - self levelling high strenght concrete
  - high strength shotcrete

- **Geometry:**
Length (l): **30** mm
Diameter (d): **0.38** mm
80 Performance class: **80**
Aspect ratio (= l/d): 79
34 000 fibres/kg
Min. dosage = 10 kg/m³
(According to spacing theory McKee)

- **Tensile strength:**
  - on the wire: minimum 2300 N/mm²

- **Coating:** None

- **Approvals:**

Product	Conforms to	Quality System in Belgian Plants
ATG 1857	ASTM A 820	ISO 9001 Dramix

Recommendations - mixing

1. General

✓ preferably add fibres in the mixer at batching plant
✓ recommended maximum dosage:

Dosage (kg/m³)	Aggregate size		
	2/8	4/16	4/32
pour	70	60	45
pump	55	45	35

✓ a continuous grading is preferred
✓ mix until all glued fibres are separated into individual fibres. Fibres don't increase mixing time significantly.
✓ if special cements or admixtures are used, a preliminary test is recommended

2. Fibre addition

2.1. In batching plant mixer

✓ never add fibres as first component in the mixer
✓ fibres can be introduced together with sand and aggregates, or can be added in freshly mixed concrete
✓ **only for drummixer:** unopened degradable bags can be thrown directly in the mixer

2.2. Truckmixer

✓ put mixer on maximum drum speed: 12-18 rpm
✓ adjust slump to a min. of 12 cm (preferably with water reducing agents or high water reducing agents)
✓ add fibres with maximum speed of 40 kg/min
✓ unopened degradable bags can be added provided that drum speed is min. 12 rpm
✓ optional equipment: belt-hoist elevator
✓ after adding the fibres, continue mixing at highest speed for 4-5 min. (± 70 rotations)

2.3. Automatic dosing

✓ Fibres in bulk can be dosed at rates up to 3,5 kg/sec with a specially developed dosing equipment

Recommendations - storage

Protect the pallets against rain

Do not stack the pallets on top of each other

Delivered in
degradable bags of 20 kg on pallet 1200 kg
big bag 1100 kg

N.V. Bekaert S.A. - Bekaertstraat 2 - 8550 Zwevegem - Belgium
Tel. +32 (0) 56 / 76 69 86 Fax +32 (0) 56 / 76 79 47

Resp. editor: Ann Lambrechts, Kortrijk www.doise.be - 03/2003

A.5.2 MasterFiber MAC Matrix Product Data Sheet

BASF
The Chemical Company

3		Product Data
	03 30 00	Cast-in-Place Concrete
	03 37 13	Shotcrete
	03 40 00	Precast Concrete
	03 70 00	Mass Concrete

MasterFiber™ MAC Matrix

Macrosynthetic Fiber

Description

MasterFiber MAC Matrix is a macrosynthetic fiber that is manufactured from a proprietary blend of polypropylene resins. MasterFiber MAC Matrix product meets the requirements of ASTM C 1116/C 1116M "Standard Specification for Fiber-Reinforced Concrete."

MasterFiber MAC Matrix product is specifically designed to provide excellent finishability in shotcrete and slab-on-ground applications, relative to other fibers in the marketplace.

MasterFiber MAC Matrix product is engineered for use as secondary reinforcement to control shrinkage and temperature cracking, and settlement cracking.

MasterFiber MAC Matrix product provides excellent flexural performance in concrete and is a true replacement for welded-wire reinforcement (WWR), conventional light gauge steel reinforcement and steel fiber, depending on the application.

MasterFiber MAC Matrix product also provides increased flexural toughness and increased impact and shatter resistance to help improve the long-term durability and integrity of concrete.

Applications

Recommended for use in:

- Shotcrete
- Composite metal decks
- Industrial and warehouse floors
- Pavements
- Precast concrete
- Residential and commercial slabs-on-ground
- Thin-wall precast
- Tunnel linings
- Wall systems
- Whitetopping/overlays

Features

- Excellent flexural performance
- Excellent finishability

Benefits

- Eliminates the need for welded-wire reinforcement (WWR) and conventional steel bars as secondary reinforcement, depending on the application
- Effective tight crack control
- Provides excellent control of settlement cracking
- Reduces production time and overall labor and material costs
- Improves green strengths and permits earlier stripping of forms with less rejection
- Reduces the effects of handling and transportation stresses

Performance Characteristics

Physical Properties

Configuration	Stick-like fiber
Fiber Type	Embossed
Material	100% virgin polypropylene
Specific Gravity	0.91
Melting Point	320 °F (160 °C)
Ignition Point	1094 °F (590 °C)
Available Lengths	1.9 in. and 2.1 in. (48 mm and 54 mm)
Water Absorption	Nil
Tensile Strength	85 ksi (585 MPa) min
Alkali Resistance	Excellent
Chemical Resistance	Excellent
Color	White, translucent
Electrical Conductivity	Low

Master Builders

Product Data: MasterFiber™ MAC Matrix

Guidelines for Use

Dosage: The dosage range of MasterFiber MAC Matrix product is 3 to 12 lb/yd^3 (1.8 to 7.2 kg/m^3). The recommended dosage range for slab-on-ground applications is typically 3 to 5 lb/yd^3 (1.8 to 3 kg/m^3). For shotcrete, the typical dosage range of MasterFiber MAC Matrix product is 11 to 12 lb/yd^3 (6.6 to 7.2 kg/m^3).

Mixing: MasterFiber MAC Matrix product should be introduced at the beginning of the mixing cycle, but not at the same time as the cement. For slab-on-ground applications, the entire bag should be dispensed into the mixer to allow for easy handling, while leaving no waste on site. For shotcrete, the bag should be opened so that the fibers can be dispensed directly into the mixer. Three to five minutes of additional mixing will be required to disperse the fibers depending on when the product is added to the mixer. BASF recommends utilizing good concrete mixing practices as outlined in ASTM C 1116/C 1116M.

Packaging

MasterFiber MAC Matrix product is packaged in a 5-lb (2.3-kg) degradable bag that can be added directly to the mixing system. For shotcrete, the fibers are packaged in 11-lb (5-kg) and 15.4-lb (7-kg) bags which should be opened prior to dispensing the fibers into the mixer.

Engineering Specifications

MasterFiber MAC Matrix product is an option for the replacement of WWR and is an easy-to-use secondary reinforcing system that is rust proof, alkali resistant, and compliant with industry codes when mixed in accordance with ASTM C 1116/C 1116M. MasterFiber MAC Matrix product enhances safety and should be specified for use in applications for:

- Increased flexural toughness
- Reduced rebound
- Increased cohesion
- Increased impact and shatter resistance
- Extended pump life
- Replacement of WWR and other secondary reinforcement
- Improved residual strength
- Improved durability
- Use in areas requiring no metal

Storage and Handling

MasterFiber MAC Matrix product should be stored in a clean, dry area protected from the weather and at temperatures below 140 °F (60 °C). Avoid storing near strong oxidizers and avoid sources of ignition. Use caution when stacking to avoid unstable conditions. Store in a sprinkled warehouse.

Product Notes

MasterFiber MAC Matrix product is not a replacement for primary/structural steel reinforcement and should not be used to replace reinforcing steel where the area of the steel is used in the calculation of the load-carrying capacity of the concrete member.

Placement and Finishing: BASF recommends that the standard practices detailed in ACI 302.1R, ACI 506.1R and ACI 544.3R for placing, finishing and curing concrete be followed when using MasterFiber MAC Matrix product.

Related Documents

Material Safety Data Sheets: MasterFiber MAC Matrix

Additional Information

For additional information on MasterFiber MAC Matrix product, contact your local sales representative.

The Admixture Systems business of BASF's Construction Chemicals division is a leading provider of innovative admixtures for specialty concrete used in the ready-mixed, precast, manufactured concrete products, underground construction and paving markets throughout the North American region. The Company's respected Master Builders brand products are used to improve the placing, pumping, finishing, appearance and performance characteristics of concrete.

LIMITED WARRANTY NOTICE. We warrant our products to be of good quality and will

BASF Corporation
Admixture Systems
www.masterbuilders.com
United States 23700 Chagrin Boulevard, Cleveland, Ohio 44122-5544 ● Tel: 800 628-9990 ● Fax: 216 839-8821
Canada 1800 Clark Boulevard, Brampton, Ontario L6T 4M7 ● Tel: 800 387-5862 ● Fax: 905 792-0651

Master Builders

APPENDIX B

Panel Test Observations and Data Analysis

B.1 Comparison of LED and LVDT Responses

As mentioned in Chapter 4, two data acquisition systems were used in the panel tests. The LVDTs recorded data continuously without any pauses for crack width measurements at load stages. The data acquisition system used to acquire the LVDT readings was also used to acquire the pressure transducer data. Thus, the stress versus strain relationship could be directly found without the need to perform time synchronization. The other data acquisition system, for the LED targets, was paused during the performance of crack width measurements due to problems with the software observed during past experimental programs. Separate data files were saved for each loading phase that had to be stitched together. In addition, this system was not directly linked to the pressure transducers, so the pressure recordings had to be synchronized with the LED data based on the real time of the recordings. Unfortunately, it was discovered after the experimental program that the two computers used to run the respective data acquisition systems did not keep time at the same rate; the clock of the LVDT data acquisition computer was approximately 0.64 s per hour faster than that of the LED computer. Since the LED system acquired data at 1 to 2 Hz this represented a substantial error. Using this best guess of the computer clock discrepancy, the data points were shifted. A program called Timeline.exe (Ruggerio, 2011), developed by a Ph.D. Candidate from the University of Toronto, was used to stitch together the LED data and convert the recorded position data to linear strains within the LED grid. Then, the data were output to a spreadsheet where the pressure readings could be synchronized using linear interpolation based on the adjusted time of the recordings. This process was time consuming and possibly inaccurate due to the uncertainty surrounding the computer clocks.

Figure B.22 to Figure B.26 present the averaged measured strains for the x-, y-, 45° and 135° directions (sub-figures (a), (b), (c) and (d) respectively) and the calculated shear strain (sub-figure (e)). The measured responses from both systems are plotted so that a comparison can be made. It is worth noting that since the LED targets were placed on the back face of the panel only, then it is plotted against the data recorded by the back face LVDTs. From this comparison, it can be seen that the measured responses are similar in shape, but there is a great deal of disagreement in the values. In general, for most of the strain directions, the LED system recorded a higher strain for a given stress level. This may be attributable to the gauge length of the LED system. The LED system consisted of 200x200 mm subgrids, making up a larger 600x600 mm area of interest. The LVDT system covered a larger area of the panel, as the gauge length for the 45° and 135° instruments was 1000 mm (compared to the roughly 850 mm diagonal for the LED grid) and the gauge length for the x-direction and y-direction instruments was 740 mm (compared to the 600 mm grid for the LEDs). From the execution of the tests, it was observed that most of the cracking occurred within this inner area of interest, suggesting that both systems read roughly the same value of elongation, but the LVDT reading was divided by the larger gauge length to yield a lower strain value. However, even though this experimental program was one of the first to utilize the LED target system for panel tests, many programs in the past have used Zurich gauges. This Zurich gauge system consisted of an identical 200x200 mm subgrid of targets. The displacement between targets was accurately measured at each load stage and strain data was calculated. Susetyo (2009) used this system and the LVDTs and saw good agreement between the measured and calculated responses in general. In addition, any disagreement observed by Susetyo (2009) was much more systematic than the LED and LVDT comparison depicted herein. From Figure B.22 to Figure B.26, it is clear that there is significant noise and high standard deviations at low strains. In some cases (DC-P2, DC-P3 and DC-P5), the relatively low x-direction strains do not match at all. In addition, if the above hypothesis relating to the gauge length was the only concern, then the LED system should provide a higher strain on the negative half-cycles of the reversed cyclic tests as well. However, this is not the case, as the shear strains measured by the LEDs on the negative half-cycles were less than those of the LVDT system in general. Also, the responses from the LED system contain significant jumps in stress and strain. This was due to that fact that certain LED targets would register as invisible for a few seconds and did not record position data. It has subsequently been discovered that the LED camera is extremely sensitive to lighting conditions, including the difference in ambient light from morning to afternoon. This high sensitivity to light leads to these seemingly random invisibilities.

Overall, the LVDT system provided a rational and reliable set of data, so the numerous issues, labour intensive post-processing, and overall unreliability of the LED system led to the decision to not proceed with further calculations using the data acquired from the LED system. In all subsequent graphs and discussion, both in the body of this document and in the rest of this Appendix, only the LVDT measurements were utilized.

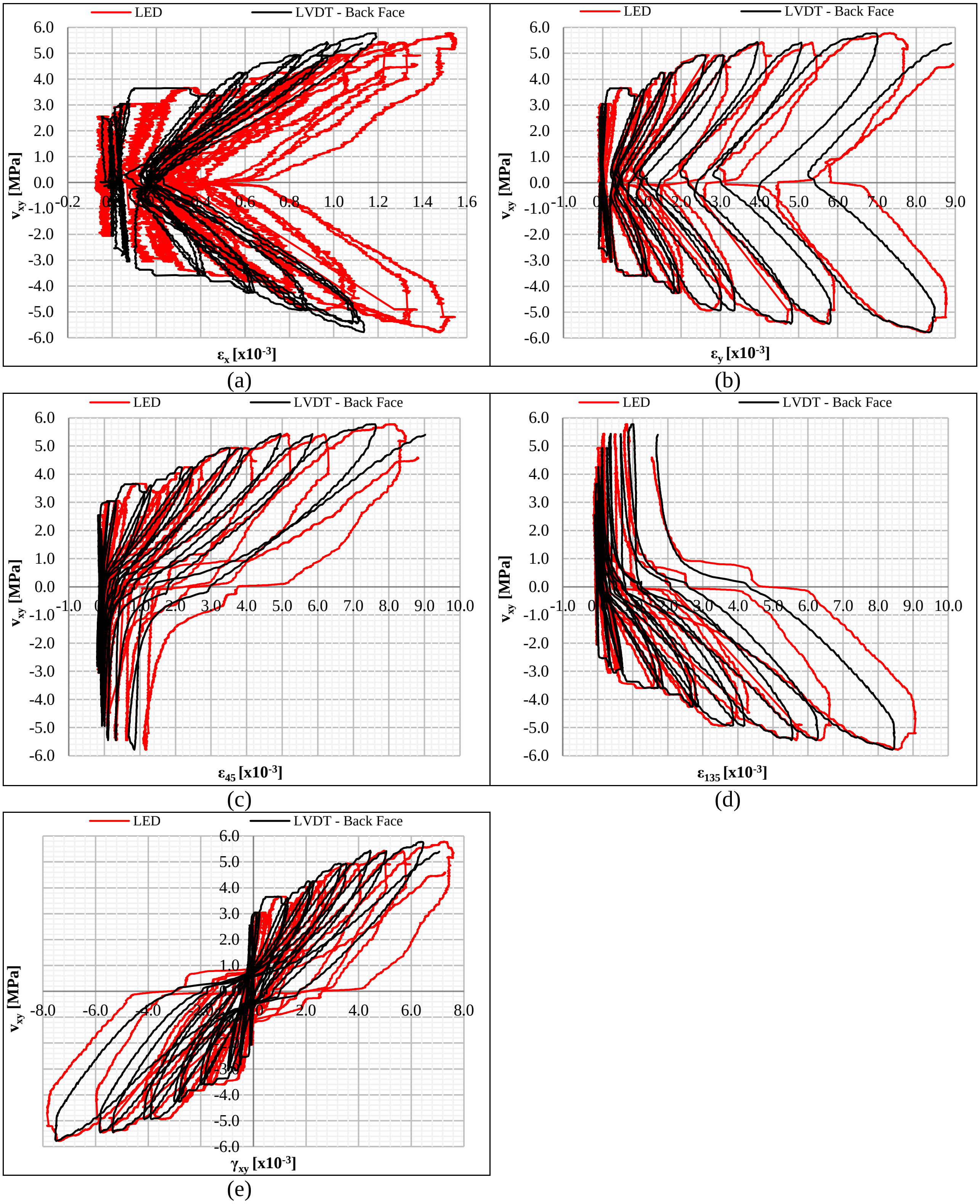

Figure B.22: Panel DC-P1 - LED and LVDT measured responses for the back face

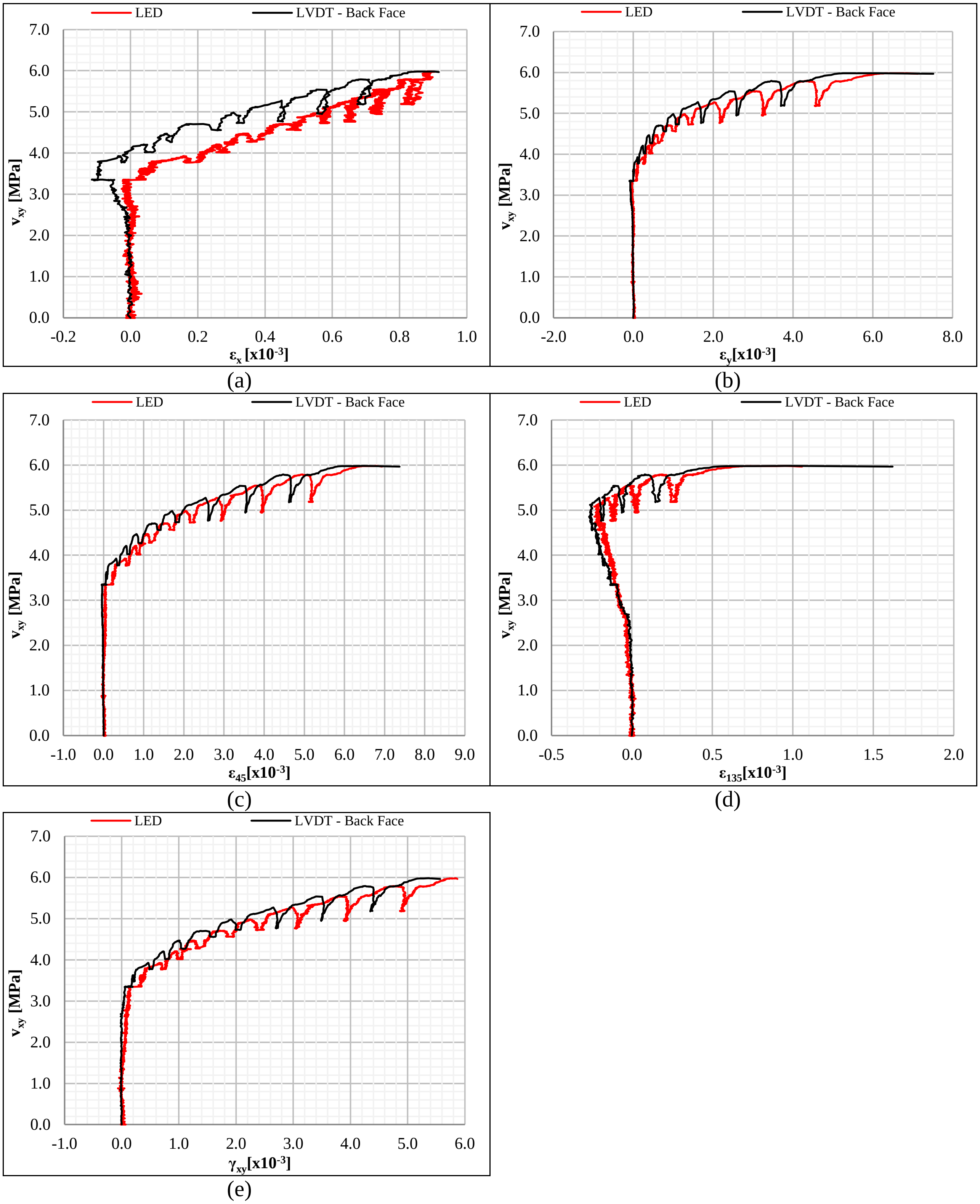

Figure B.111: Panel DC-P2 - LED and LVDT measured responses for the back face

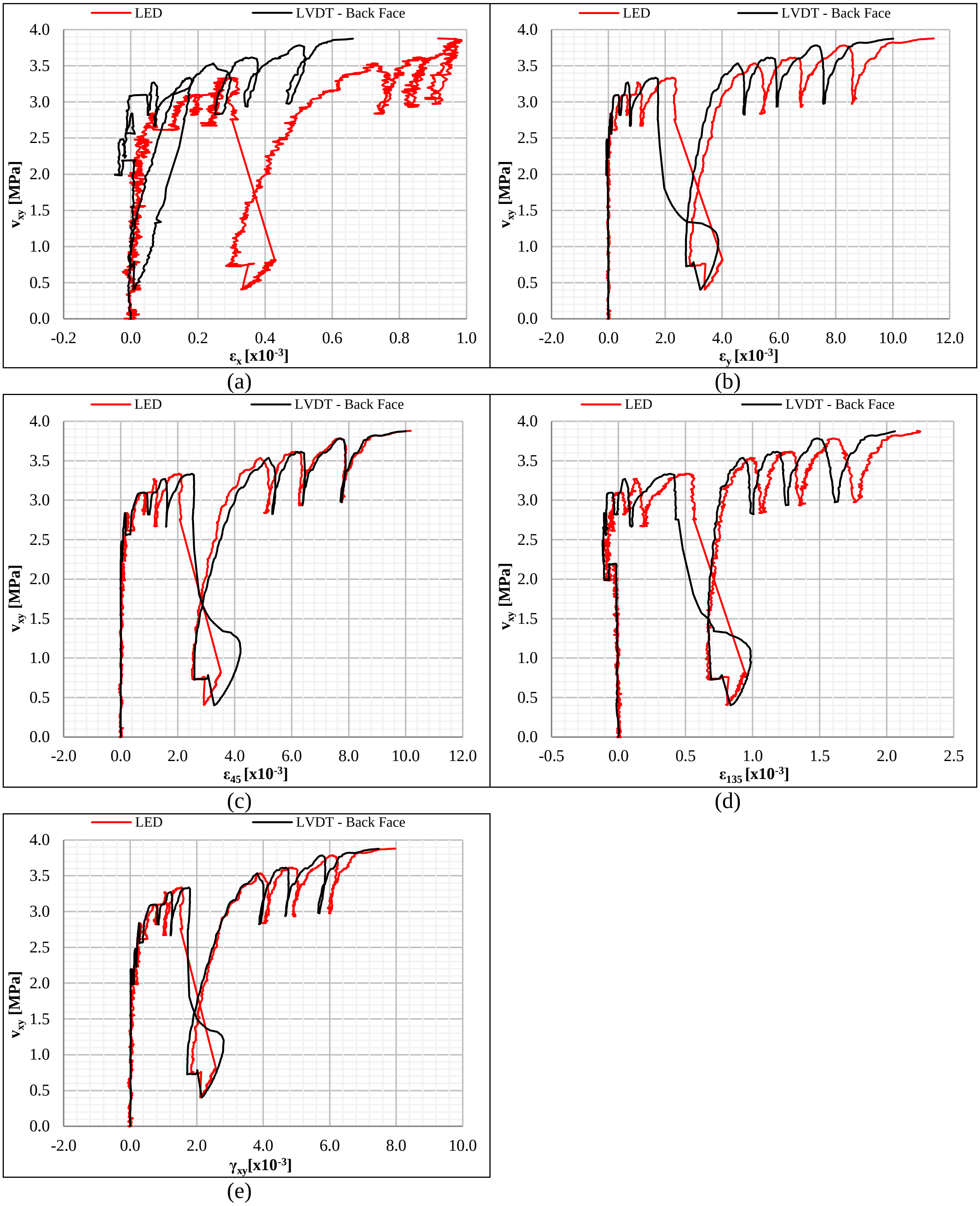

Figure B.112: Panel DC-P3 - LED and LVDT measured responses for the back face

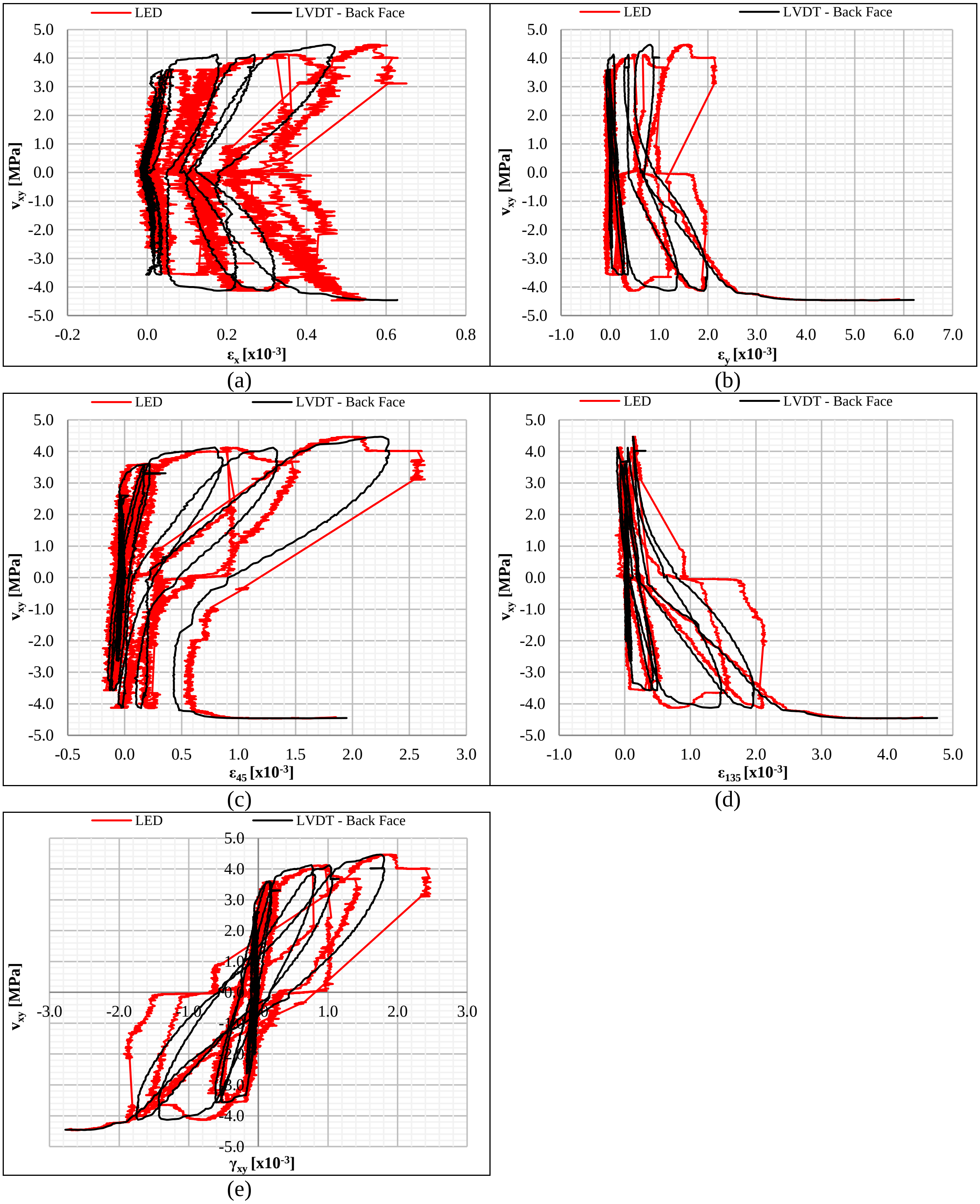

Figure B.113: Panel DC-P4 - LED and LVDT measured responses for the back face

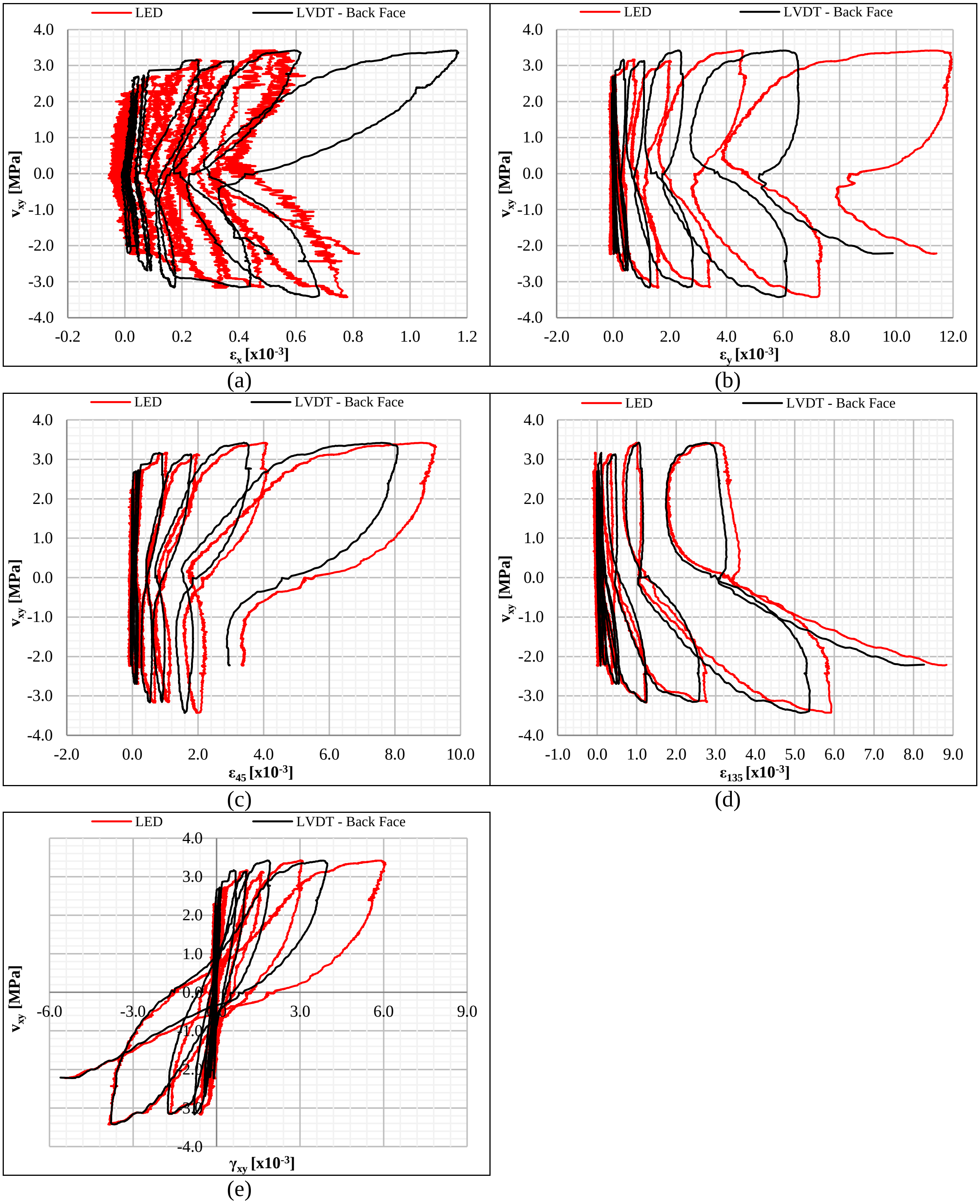

Figure B.26: Panel DC-P5 - LED and LVDT measured responses for the back face

B.2 Panel DC-P1

Panel DC-P1 was constructed as the plain reinforced concrete control panel for the reversed cyclic test specimens. This panel was reinforced with 40 D8 bars in the x-direction for a reinforcement ratio of ρ_x = 3.31%, and 10 D4 bars in the y-direction for a reinforcement ratio of ρ_y = 0.42%. The compressive and uniaxial tensile strengths of the concrete were 71.7 MPa and 4.35 MPa.

B.2.1 Test Observations

Select crack patterns for Panel DC-P1 are depicted in Figure B.6. The first crack occurred on the front face of the panel during Cycle 3, Load Stage 7 at a shear stress of 1.43 MPa; the crack width was 0.05 mm. This crack was premature and likely due to undesired out-of-plane restraint. Additional cracks did not developed until Cycle 5, Load Stage 11 was reached at a shear stress of 2.50 MPa; the first cracking on the back face occurred during Cycle 5, Load Stage 12 at -2.50 MPa. At this point, crack widths steadily increased and crack spacings steadily decreased as cycles progressed. The crack widths and spacings under positive and negative shear matched closely as shown in Figure B.116. At the final load stage, the average crack width and average crack spacing were 0.57 mm and 55.6 mm, respectively.

This panel failed at a shear stress of 5.79 MPa during Cycle 18. The failure occurred at the east edge of the panel, as the y-direction reinforcement ruptured at the connection between the panel and the shear keys. The shear keys then separated from the concrete. This is typically not indicative of a full failure of the concrete panel but the response showed significant softening in the final cycles up until this eventual failure. Thus, the failure point was deemed reasonable.

B.2.2 Data Analysis

Figure B.117 depicts various responses of the panel after completion of the data analysis. A linear behaviour in the shear stress-shear strain response, the principal tensile stress-principal tensile strain response, and the principal compressive stress-principal compressive strain response was observed up to the first premature crack at a shear stress of 1.43 MPa and a corresponding shear strain of 0.116×10^{-3}. As a result of this premature cracking (which is attributable to unwanted out-of-plane restraint effects due to either the overtightening of the bolts connecting the shear keys to the test machine or incorrect adjustment of the out-of-plane tension links), subsequent cycles of the shear stress versus shear strain response were shifted from the origin and became centred on a positive shear strain value of roughly 0.275×10^{-3}. This is visible in the isolated cycles presented in Figure B.118.

The panel continued to exhibit a highly linear but softened response, with little to no stress in the reinforcement, until subsequent cracking occurred at a shear stress of 2.48 MPa and a shear strain of 0.528×10^{-3} on Cycle 5. On the corresponding negative half-cycle, cracks developed on the back face of the panel at a shear stress of -2.50 MPa and a shear strain of -0.164×10^{-3}. From here, more significant softening was observed as further cracking developed. In addition, the out-of-plane issues ceased, as the cycles continued to centre on a shear strain of approximately 0.275×10^{-3}. During Cycle 13, the y-direction reinforcement yielded. At this point, the elastic-plastic tensile response shown in Figure B.119 was employed to calculate the stress in the steel with consideration for plastic offsets. This yielding was accompanied by further substantial softening. Finally, during the 18th cycle the panel failed at a shear stress of 5.79 MPa and corresponding shear strain of 7.98×10^{-3}.

The principal tensile stress and the principal tensile strain at first-cracking were 1.43 MPa and 0.048×10^{-3}, respectively. Tension stiffening was exhibited until the maximum principal tensile stress of 2.82 MPa was attained at a principal tensile strain of 0.967×10^{-3}. Negative principal tensile stresses were observed, attributable to slip along the crack surfaces and cracks remaining open at low stresses. The response softened significantly to a plateau near 1.00 MPa. The failure occurred at a principal tensile stress of 0.65 MPa, with a strain of 10.60×10^{-3}.

The principal compressive stress and principal compressive strain at first-cracking were -1.43 MPa and -0.068×10^{-3}, respectively. The response is somewhat erratic, yet appears to follow two mostly linear paths (one for positive applied shears and one for negative applied shears), with little softening. The principal compressive stress at failure was -11.63 MPa at a strain of -0.445×10^{-3}.

The orientations of the principal directions were mostly the same for both stress and strain until first cracking, as would be expected. At the point of substantial cracking (at a shear stress of around 2.50 MPa), rotation of the stress and strain fields began. The rotation of the principal strain direction lagged behind the principal stress direction, but both steadily increased to an inclination at failure of 59.2° for the stress field and 66.9° for the strain field.

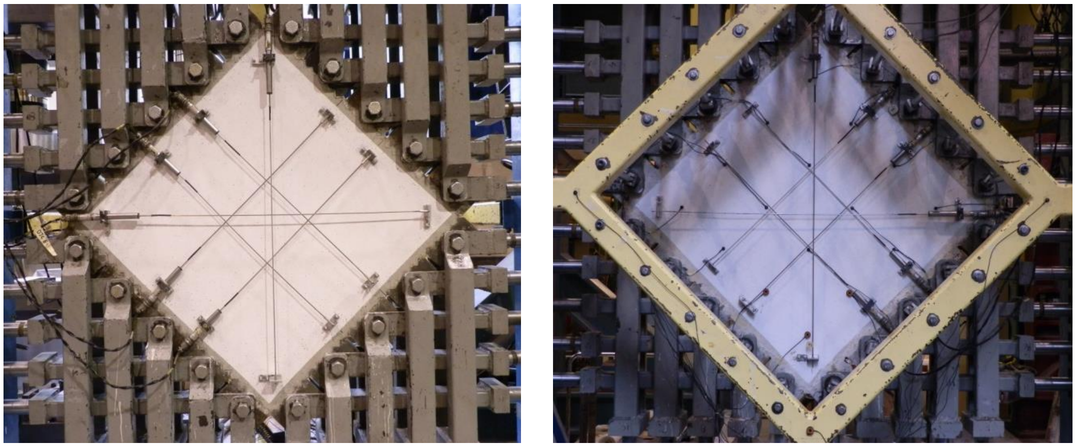

Cycle 0, Stage 0: v_{xy} = 0 MPa; γ_{xy} = 0x10^{-3}; w_m = 0 mm; s_m = ∞ mm.

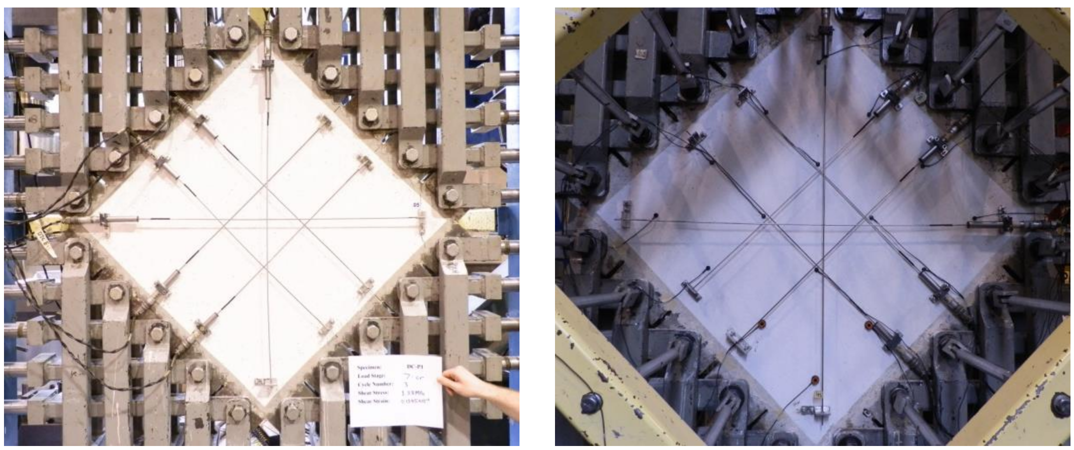

Cycle 3, Stage 7: v_{xy} = 1.43 MPa; γ_{xy} = 0.116x10^{-3}; w_m = 0.05 mm; s_m = 750 mm.

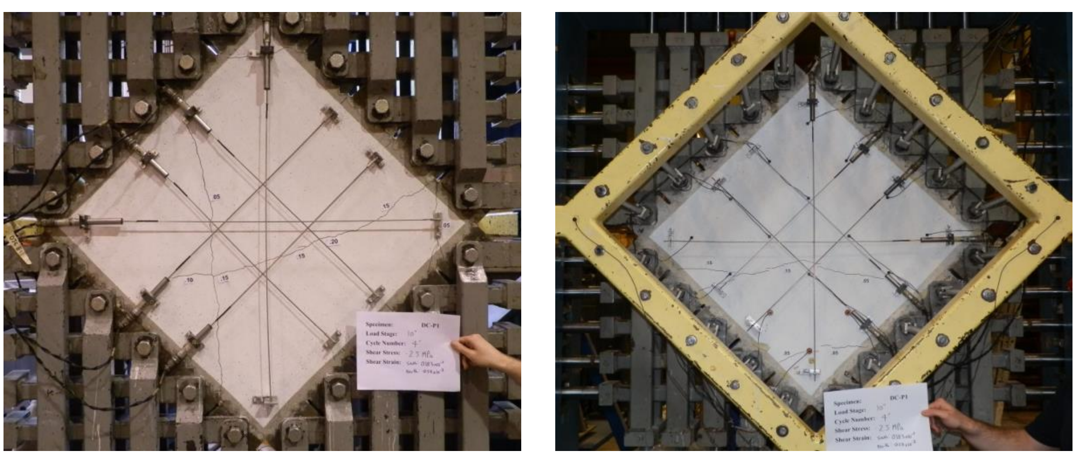

Cycle 5, Stage 12: v_{xy} = -2.50 MPa; γ_{xy} = -0.164x10^{-3}; w_m = 0.12 mm; s_m = 500 mm.

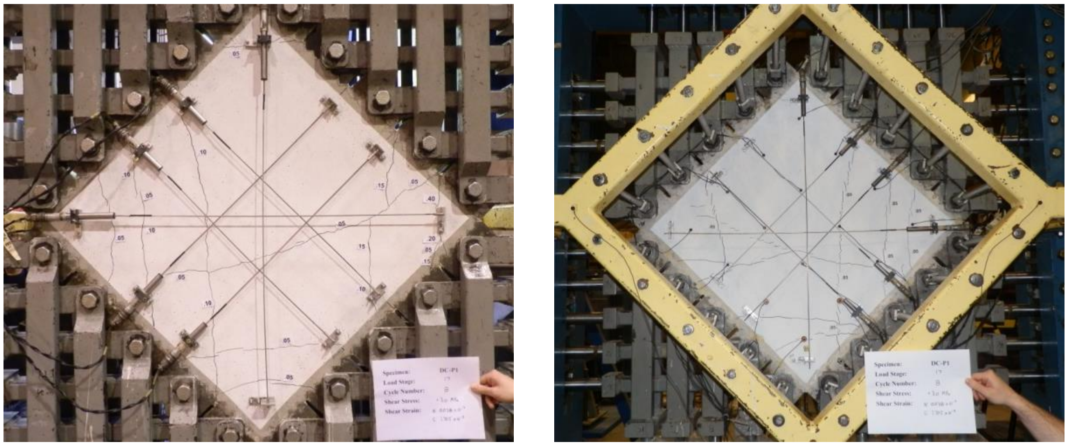

Cycle 8, Stage 17: v_{xy} = 3.00 MPa; γ_{xy} = 0.822x10^{-3}; w_m = 0.083 mm; s_m = 222 mm.

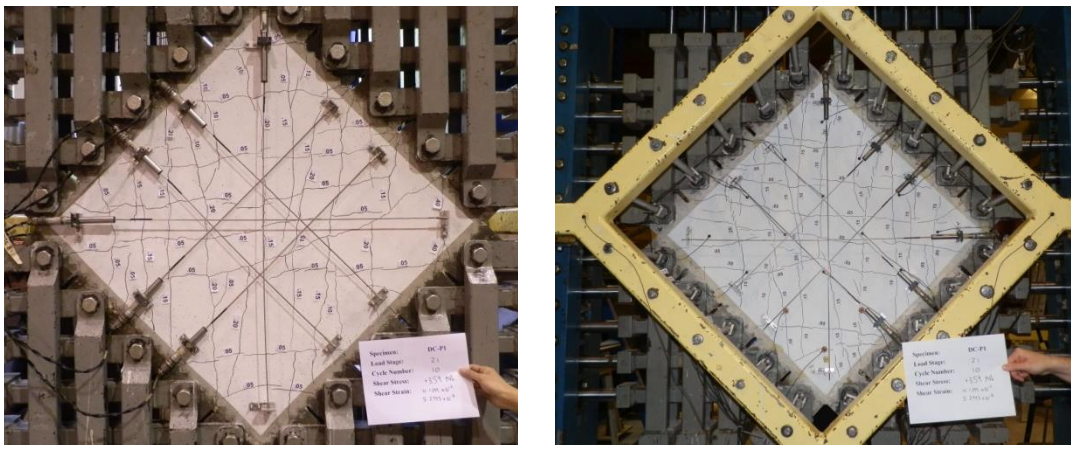

Cycle 10, Stage 21: v_{xy} = 3.59 MPa; γ_{xy} = 2.12x10^{-3}; w_m = 0.13 mm; s_m = 103 mm.

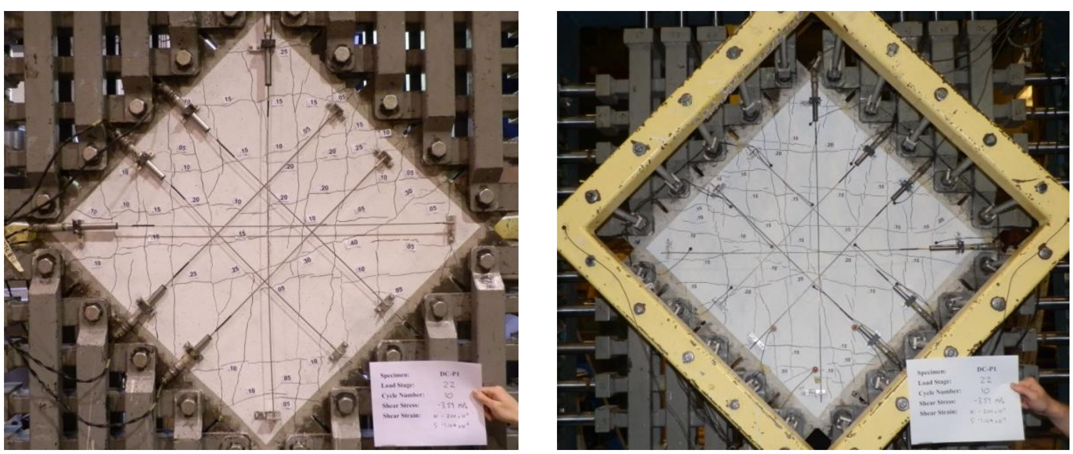

Cycle 10, Stage 22: v_{xy} = -3.59 MPa; γ_{xy} = -1.558x10^{-3}; w_m = 0.14 mm; s_m = 105 mm.

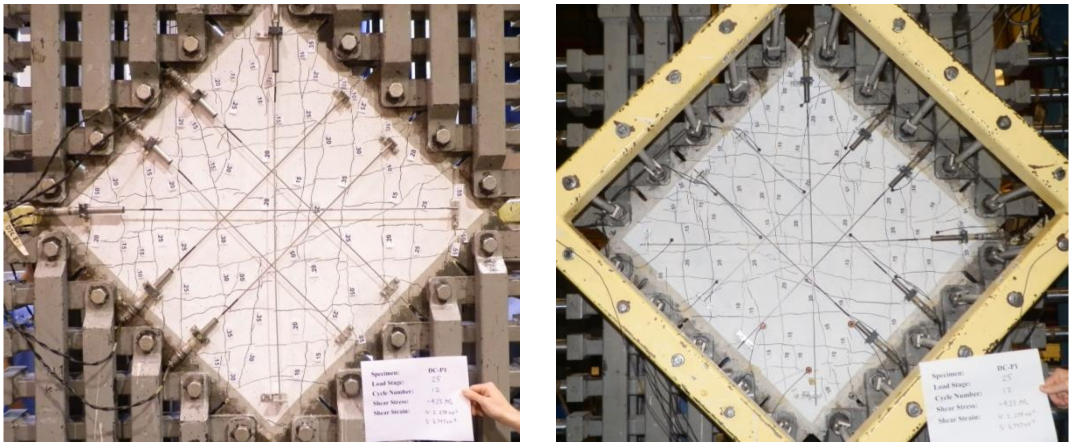

Cycle 12, Stage 25: v_{xy} = 4.23 MPa; γ_{xy} = 3.04x10^{-3}; w_m = 0.17 mm; s_m = 83 mm.

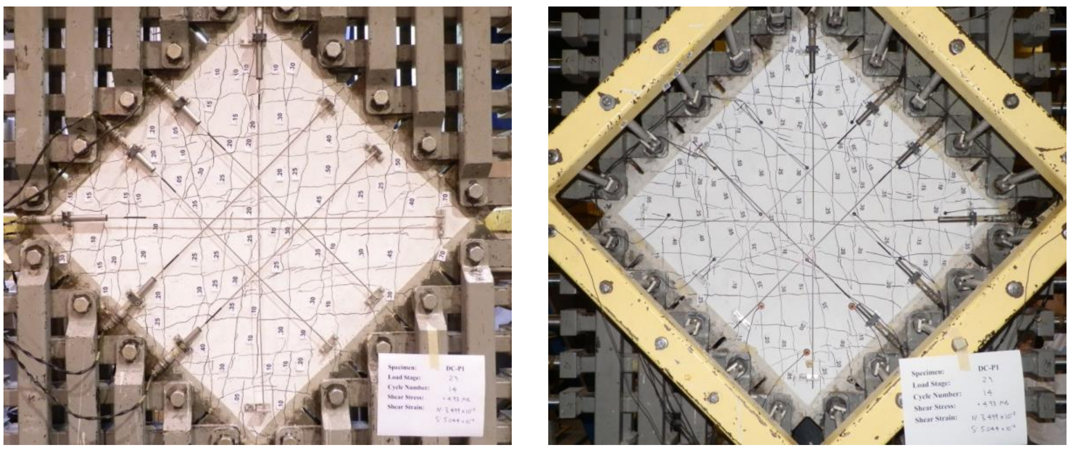

Cycle 14, Stage 29: v_{xy} = 4.93 MPa; γ_{xy} = 4.27x10^{-3}; w_m = 0.22 mm; s_m = 77 mm.

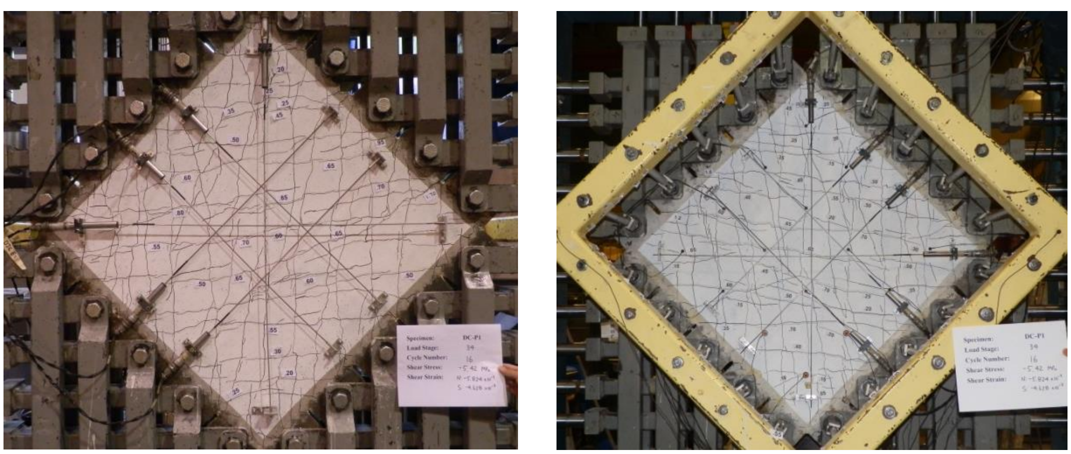

Cycle 16, Stage 34: v_{xy} = -5.42 MPa; γ_{xy} = -5.23x10^{-3}; w_m = 0.43 mm; s_m = 68 mm.

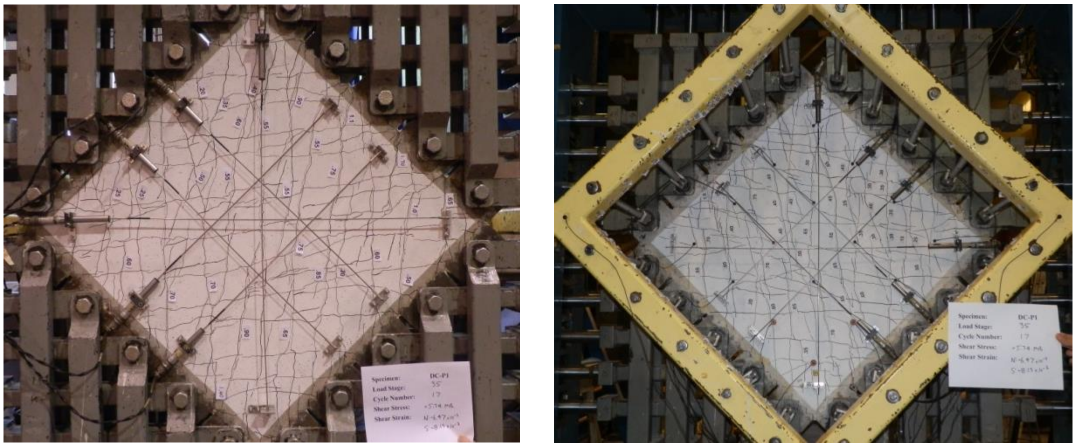

Cycle 17, Stage 35: v_{xy} = -5.74 MPa; γ_{xy} = 7.30x10^{-3}; w_m = 0.52 mm; s_m = 57 mm.

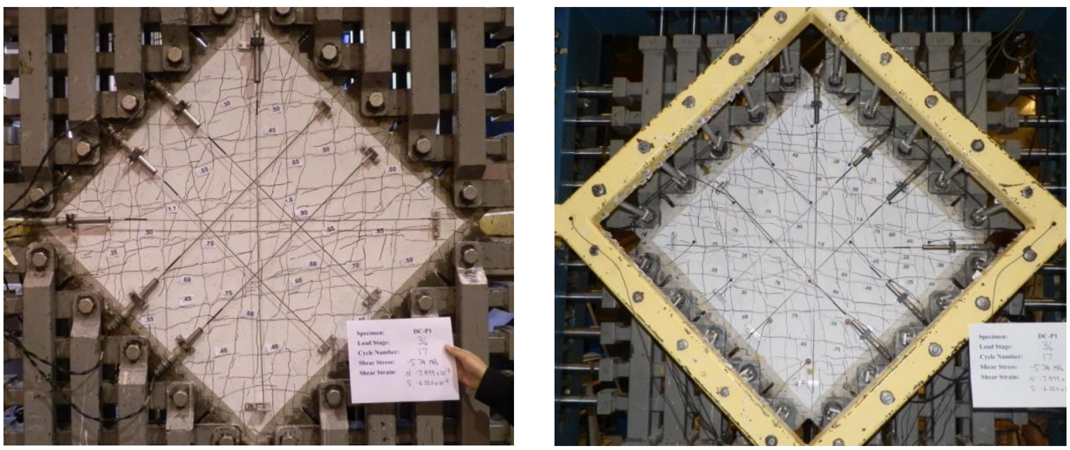

Cycle 17, Stage 36: v_{xy} = -5.74 MPa; γ_{xy} = -6.86x10^{-3}; w_m = 0.57 mm; s_m = 55.6 mm.

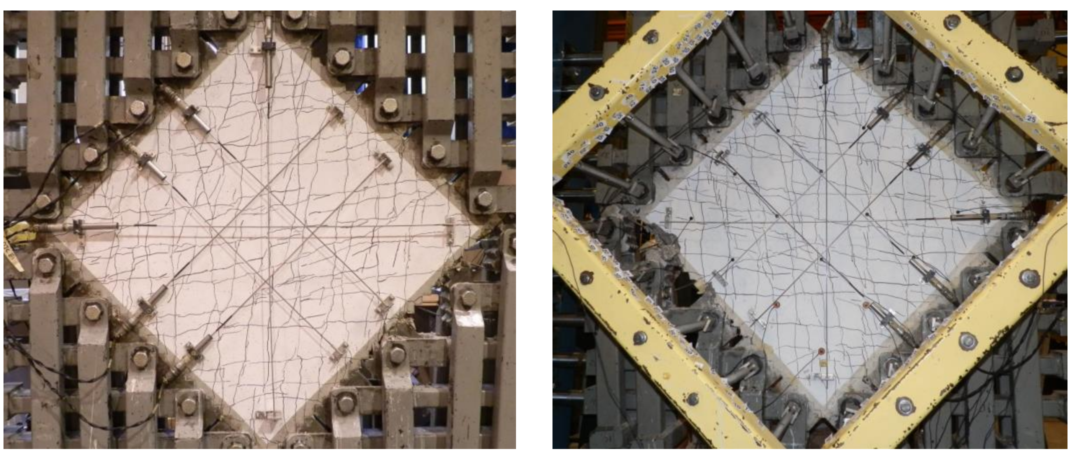

Failure: v_u = 5.79 MPa; γ_u = 7.98x10^{-3}.

Figure B.115: Panel DC-P1 – Selected crack patterns

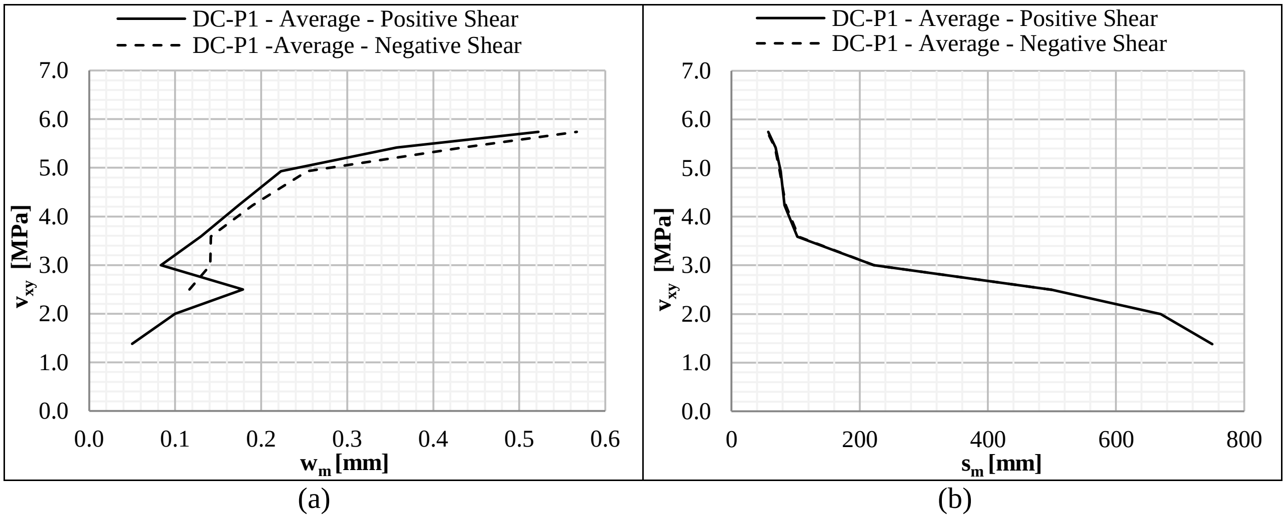

Figure B.116: Panel DC-P1 – Cracking of the panel

No significant stress was developed in the longitudinal or transverse reinforcement until a shear stress of 2.48 MPa. The subsequent response showed a linear increase in the longitudinal reinforcement stresses as the shear stress was increased. The longitudinal bars did not experience yielding as, at panel failure, the stress in the steel was 267 MPa. As mentioned before, the y-direction reinforcement yielded on the 13th cycle. It subsequently ruptured at the panel edge at an average reinforcement stress of 611 MPa.

B.2.3 Comparison of the Responses of the Front and Back Face

Figure B.120 shows the comparison between the LVDT responses of the front face and the back face of the panel. The shear stress versus shear strain response shows a constant offset between the two faces. Thus, after the initial out-of-plane issues were overcome, further out-of-plane issues were not evident. This is consistent with the other responses depicted in the figure, as the other responses also exhibit a similar consistent offset. However, the cracking stress on the back face occurred at a higher stress than on the front face. The back face exhibited a stiffer response in terms of principal compressive stress and stress in the steel. The principal compressive stress-strain response displays a large amount of scatter, yet the general trend is towards smaller strains on the back face. All of this is likely attributable to the initial out-of-plane bending caused by either improper out-of-plane alignment of the panel or overtightening of the bolts that connected the jacks to the shear keys, leading to unwanted frictional restraint.

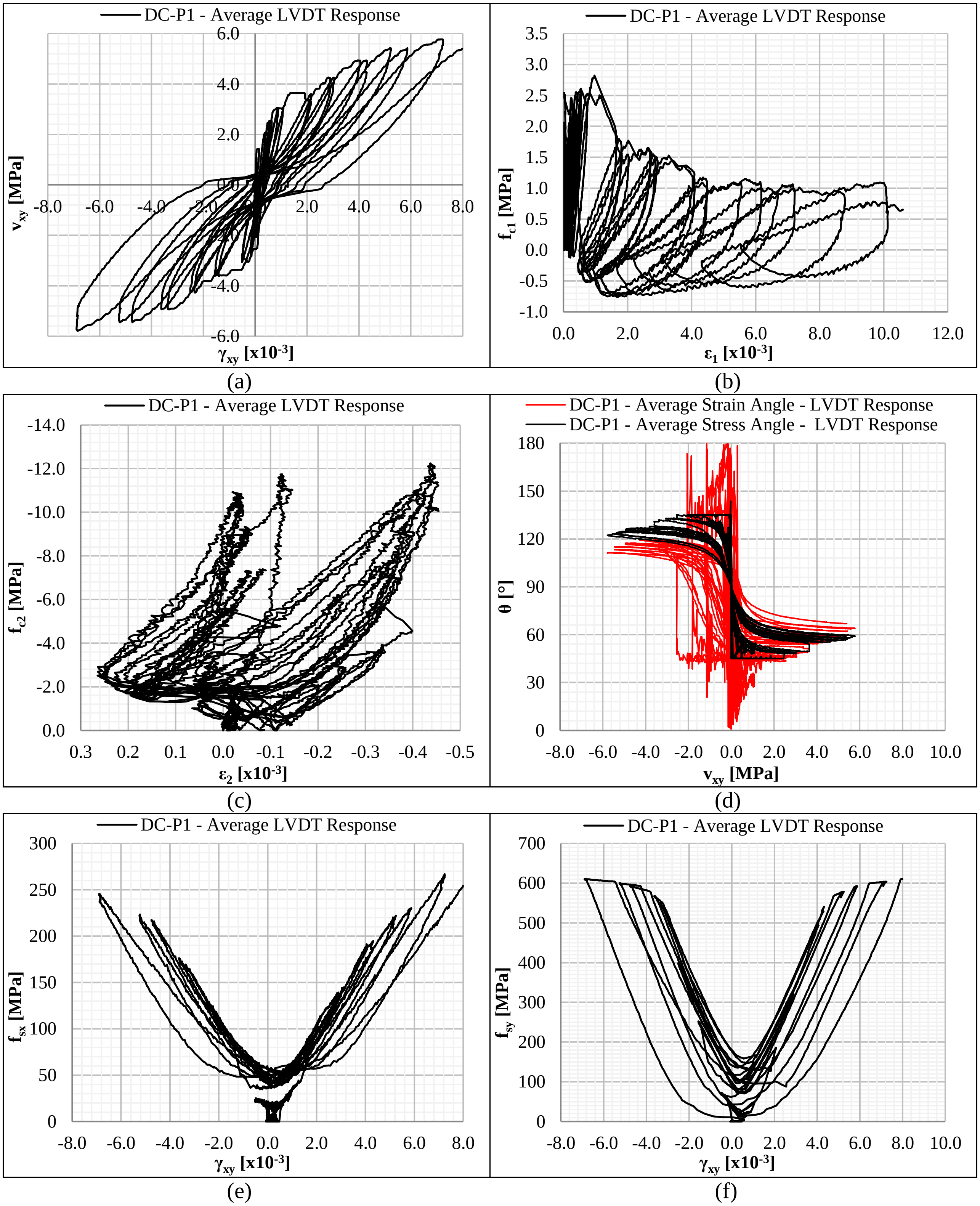

Figure B.117: Panel DC-P1 – Responses of the panel

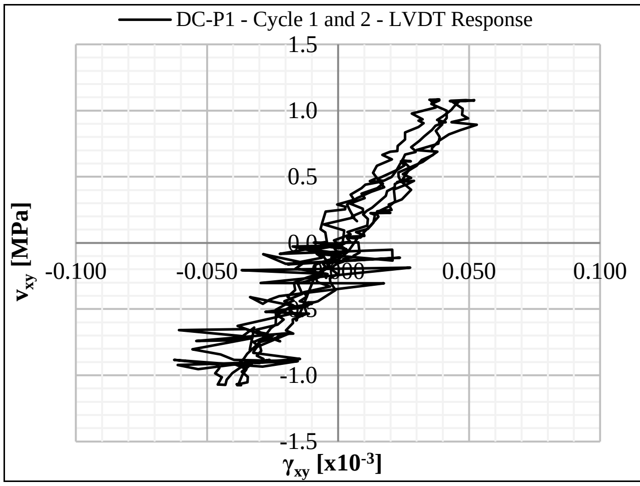
DC-P1 - Cycle 1 and 2 - LVDT Response
v_{xy} [MPa]
γ_{xy} [x10^{-3}]

(a)

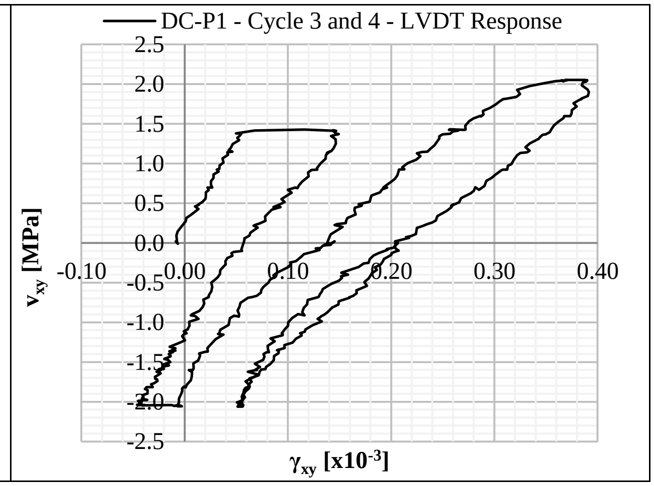
DC-P1 - Cycle 3 and 4 - LVDT Response
v_{xy} [MPa]
γ_{xy} [x10^{-3}]

(b)

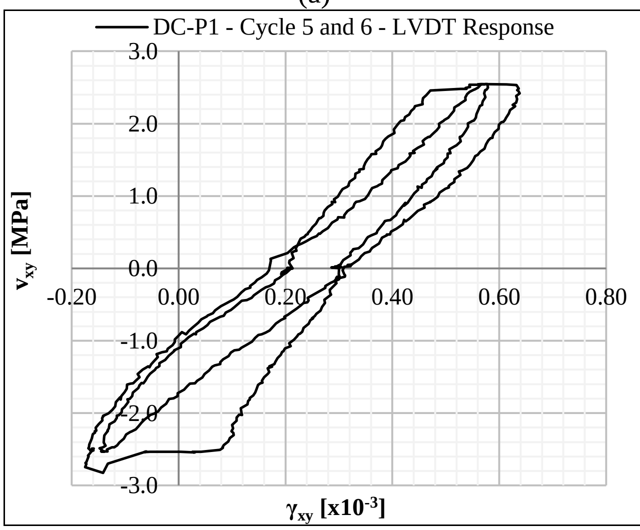
DC-P1 - Cycle 5 and 6 - LVDT Response
v_{xy} [MPa]
γ_{xy} [x10^{-3}]

(c)

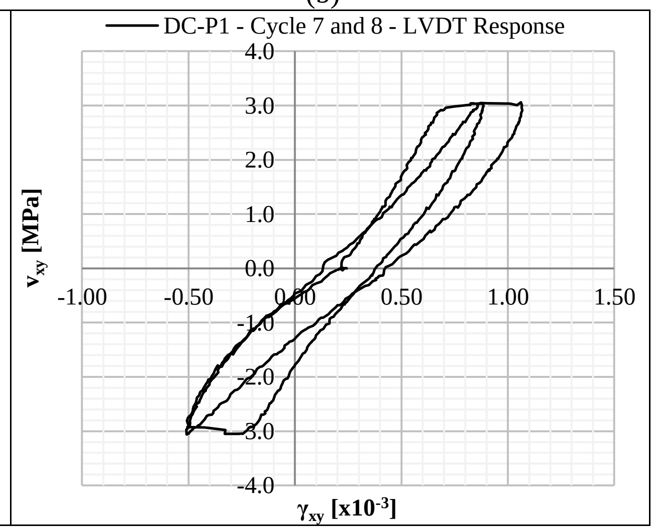
DC-P1 - Cycle 7 and 8 - LVDT Response
v_{xy} [MPa]
γ_{xy} [x10^{-3}]

(d)

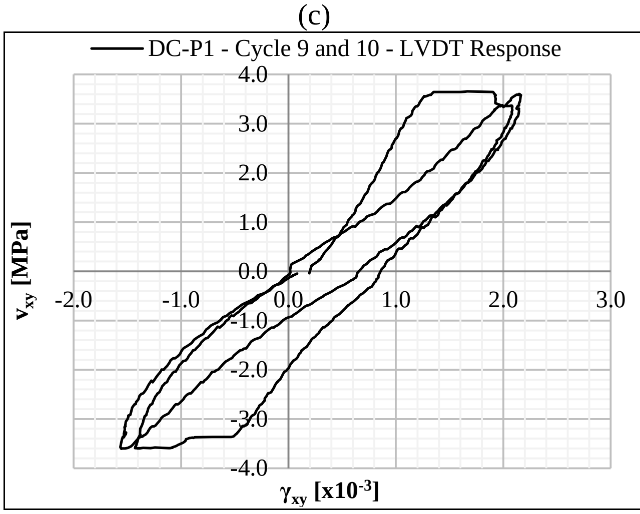
DC-P1 - Cycle 9 and 10 - LVDT Response
v_{xy} [MPa]
γ_{xy} [x10^{-3}]

(e)

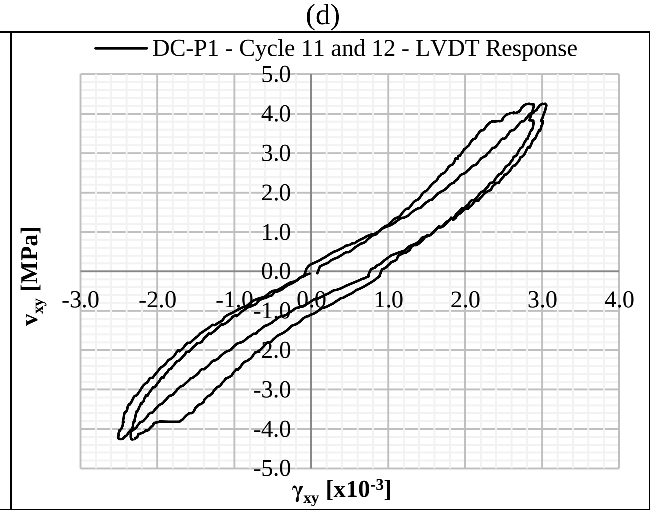
DC-P1 - Cycle 11 and 12 - LVDT Response
v_{xy} [MPa]
γ_{xy} [x10^{-3}]

(f)

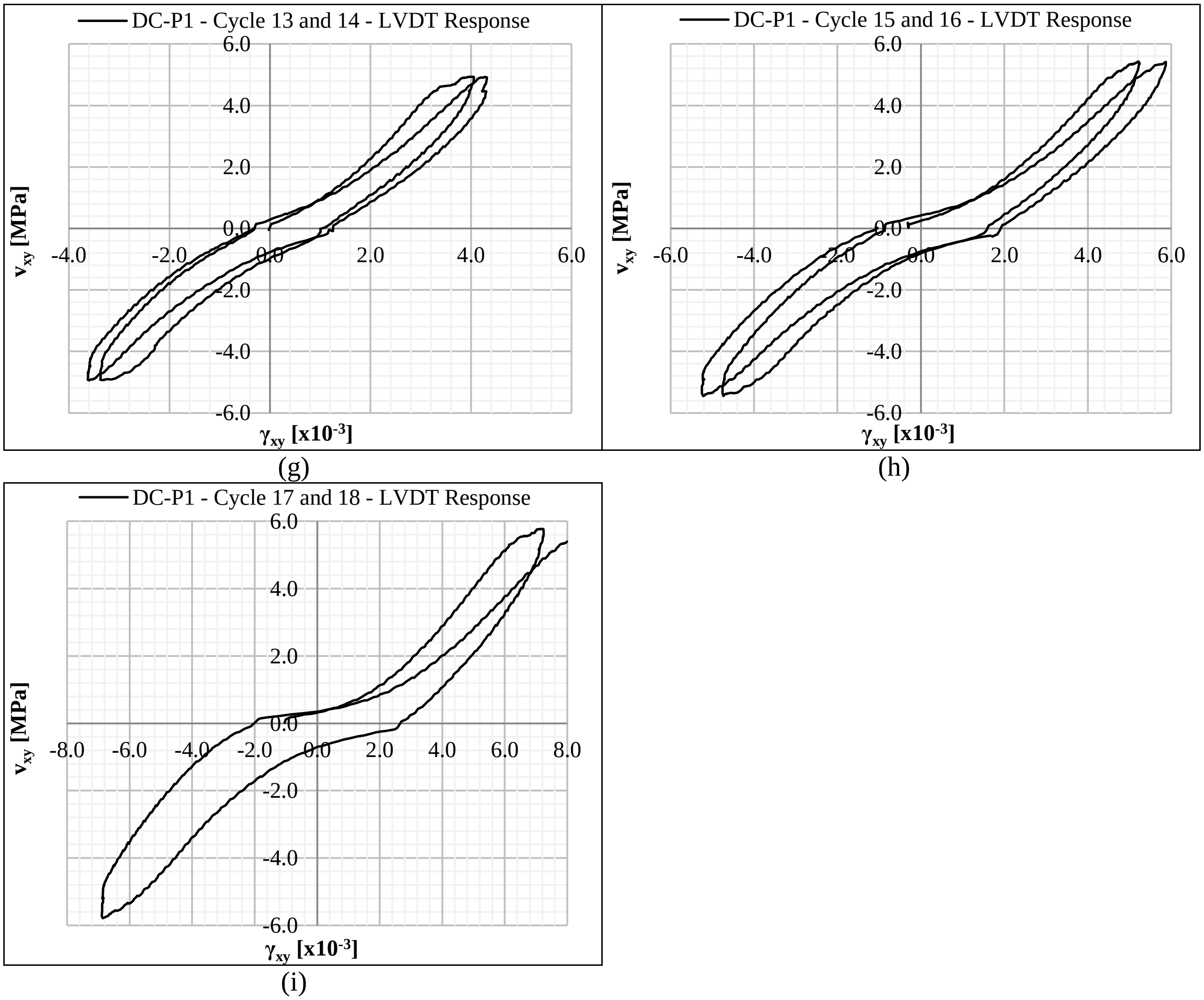

Figure B.118: Panel DC-P1 – Shear stress versus shear strain; isolated cycles

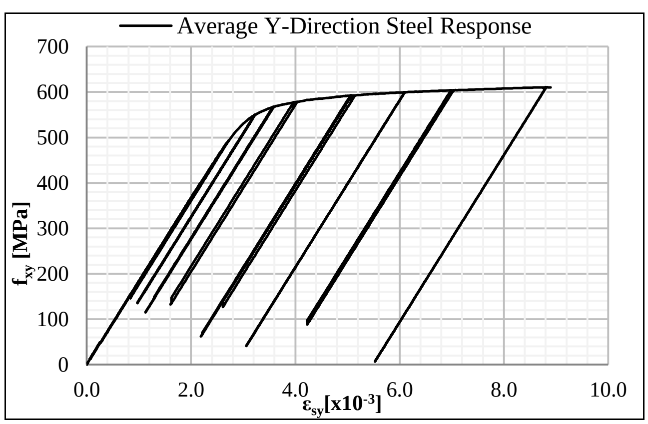

Figure B.119: Panel DC-P1 – Elastic-plastic relationship employed for the yielding of y-direction steel

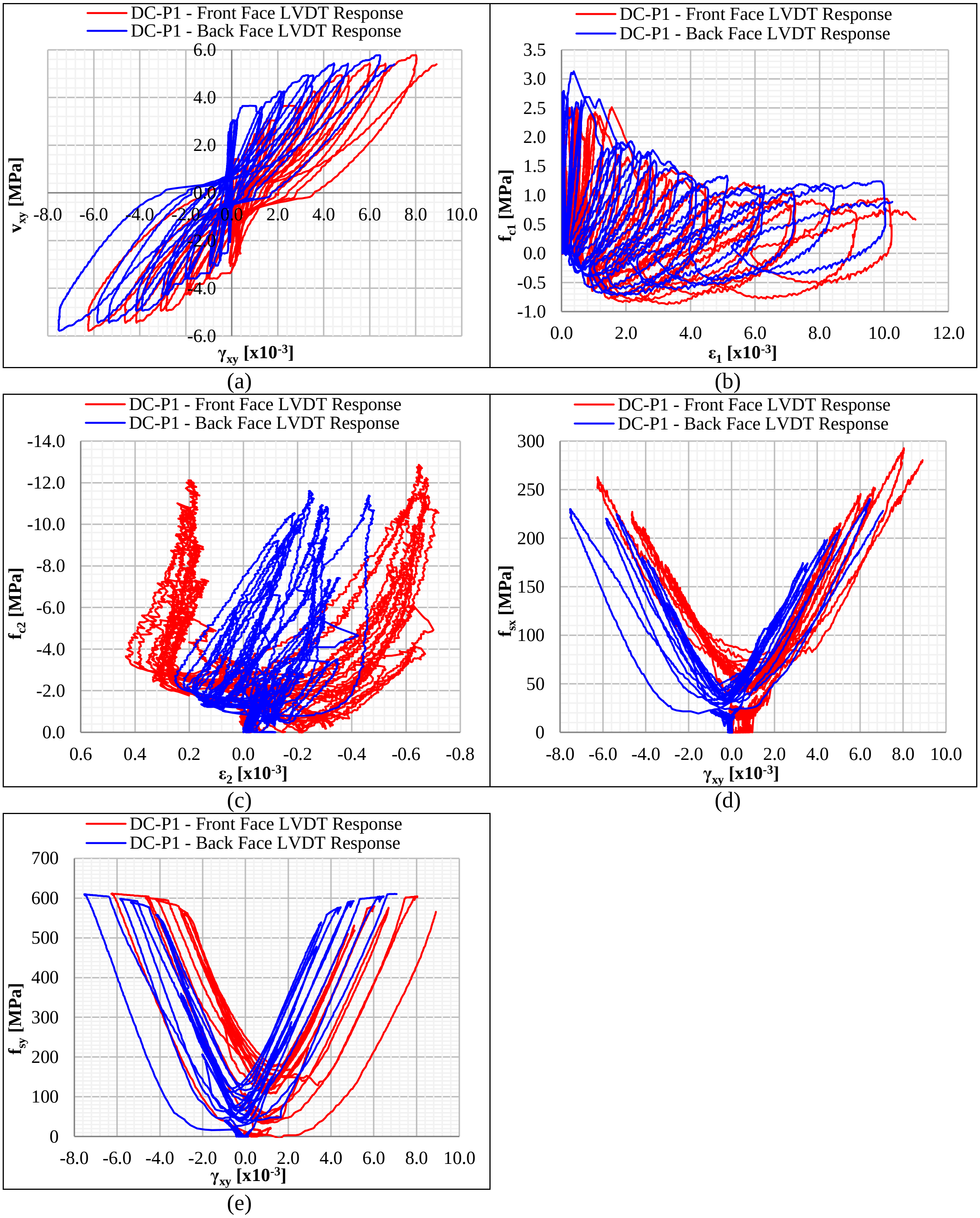

Figure B.120: Panel DC-P1 – Comparison of the front face and back face responses

B.3 Panel DC-P2

Panel DC-P2 was constructed of steel fibre reinforced concrete with 1.0% by volume RC80/30BP fibres. This specimen was tested under monotonic pure shear loading conditions. This panel was reinforced with 40 D8 bars in the x-direction for a reinforcement ratio of ρ_x = 3.31%, and no y-direction reinforcement. The compressive and uniaxial tensile strengths of the concrete were 62.1 MPa and 3.90 MPa.

B.3.1 Test Observations

Select crack patterns of Panel DC-P2 are depicted in Figure B.121. The first crack occurred on the front face of the panel at a shear stress of 2.60 MPa. The crack width was approximately 0.05 mm. Loading continued under the monotonic condition with only slight softening until, at Load Stage 4, cracking occurred on the back face of the panel at a shear stress of 3.36 MPa. After this, more significant softening of the response was observed. Many additional cracks developed at very small crack widths, as the average crack width stayed below 0.10 mm until an applied shear stress of 4.98 MPa. Thus, many small, tightly spaced cracks were evident. This is consistent with the rapid decrease in crack spacing but slow increase in crack width shown in Figure B.122. As the test neared failure, strains and crack widths began to increase rapidly. Lastly, at the final load stage, the average crack width and average crack spacing were 0.21 mm and 43.0 mm, respectively.

This panel failed at a shear stress of 5.94 MPa at the 14th load stage. The main failure plane was inclined at roughly 15° to the x-axis of the panel, with an additional steeply inclined large crack meeting the main crack near the centre of the panel. As the test was progressing towards the end, some popping sounds could be heard indicative of fibre pull-out across the main cracks. Finally, at failure, significant popping occurred rapidly and subsequent sliding occurred in a slow and controlled manner. Thus, the nature of the failure was fibre pull-out followed by aggregate interlock failure along the main crack.

B.3.2 Data Analysis

Figure B.123 shows some of the various panel responses after completion of the data analysis. The behaviour was highly linear until the first crack for the shear stress-shear strain response, the principal tensile stress-principal tensile strain response, and the principal compressive stress-principal compressive strain response. The first crack occurred at a shear stress of 2.60 MPa and a corresponding shear strain of 0.136×10^{-3}.

The panel did not show much softening in the response until cracking occurred on the back face of the panel. At this point, a significant strain increase was observed, followed by a softening response as loading progressed. This higher cracking stress on the back face was either due to a high percentage of coarse aggregate near the top face of the panel or due to out-of-plane bending causing compression on the back face as a result of improper panel installation. The development of cracking on the panel back face improved this out-of-plane effect, yet the response of the back face was still stiffer than the front face. This is also attributable to a higher percentage of fibres near the back face of the panel. Finally, the panel failed at a shear stress of 5.97 MPa and corresponding shear strain of 5.94×10^{-3}.

The principal tensile stress and the principal tensile strain at first-cracking were 2.49 MPa and 0.075×10^{-3}, respectively. Tension stiffening was exhibited until a relatively high maximum principal tensile stress of 3.37 MPa was attained at a principal tensile strain of $1.466\text{x}10^{-3}$. This represented a significant amount of tension stiffening. Slight softening in the principal tensile response was observed until the failure at a principal tensile stress of 2.95 MPa and a relatively low strain of $8.58\text{x}10^{-3}$.

The principal compressive stress and principal compressive strain at first-cracking were -2.71 MPa and -0.062×10^{-3}, respectively. As the test progressed, the principal compressive stress and strain increased linearly for most of the test. At the end of the test, the principal compressive strain became tensile, supporting the observed crack slip at failure. The principal compressive stress at failure was –12.05 MPa at a strain of 0.141×10^{-3}.

The orientations of the principal directions were nearly the same for both stress and strain until first cracking. After cracking, the rotation of the principal strain direction lagged behind the principal stress direction. The inclination at failure was 63.7° for the stress field and 67.6° for the strain field, consistent with the inclination of the failure plane.

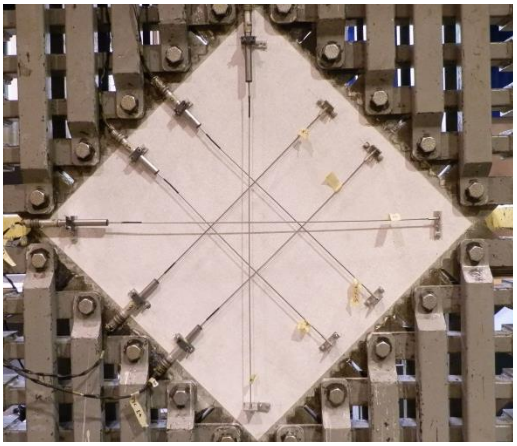 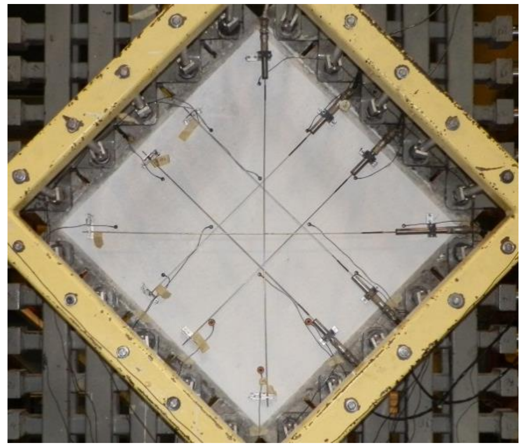

Stage 0: v_{xy} = 0 MPa; γ_{xy} = 0x10^{-3}; w_m = 0 mm; s_m = ∞ mm.

Stage 2: v_{xy} = 2.60 MPa; γ_{xy} = 0.136x10^{-3}; w_m = 0.05 mm; s_m = 500 mm.

 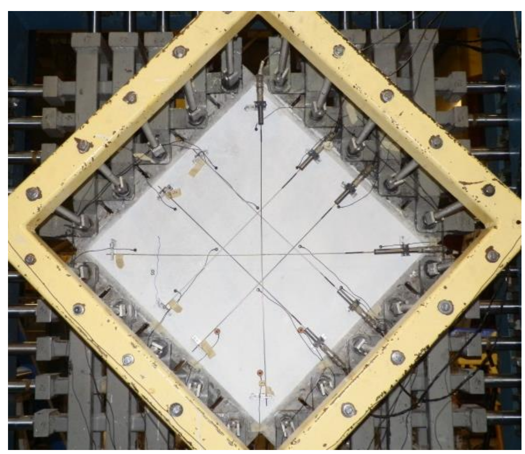

Stage 4: v_{xy} = 3.36 MPa; γ_{xy} = 0.443x10^{-3}; w_m = 0.055 mm; s_m = 330 mm.

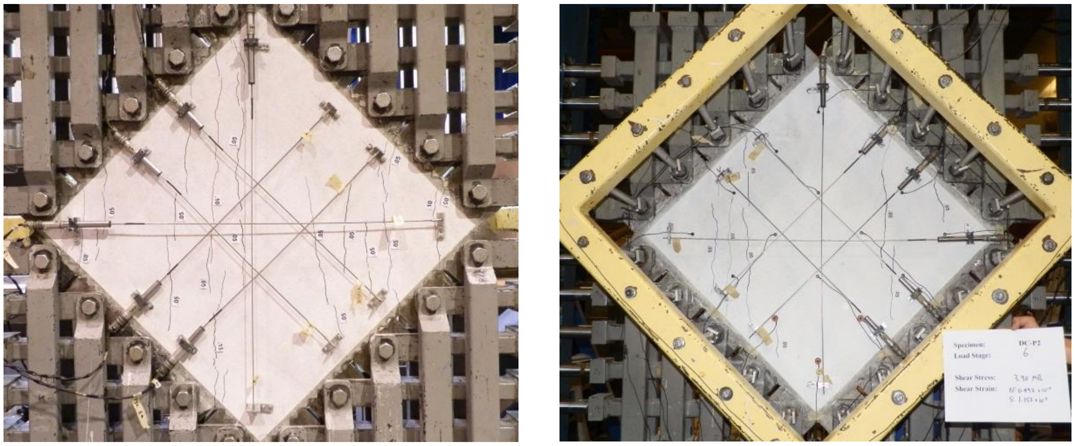

Stage 6: v_{xy} = 3.90 MPa; γ_{xy} = 0.823x10^{-3}; w_m = 0.059 mm; s_m = 150 mm.

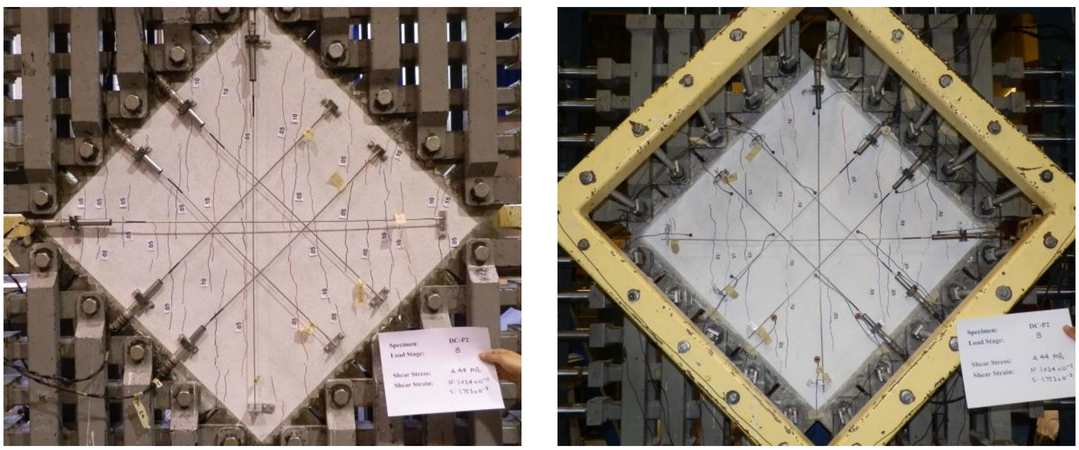

Stage 8: v_{xy} = 4.44 MPa; γ_{xy} = 1.389x10^{-3}; w_m = 0.088 mm; s_m = 74 mm.

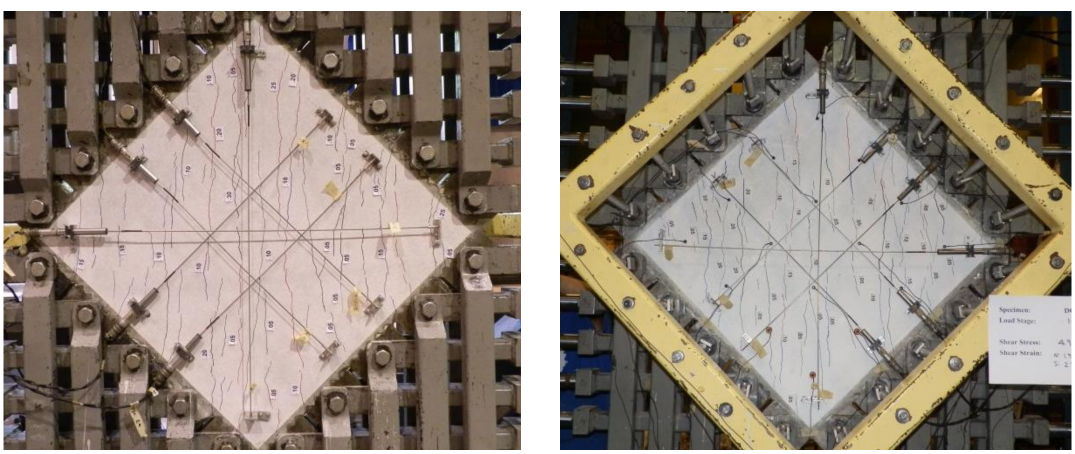

Stage 10: v_{xy} = 4.98 MPa; γ_{xy} = 2.33x10^{-3}; w_m = 0.11 mm; s_m = 69 mm.

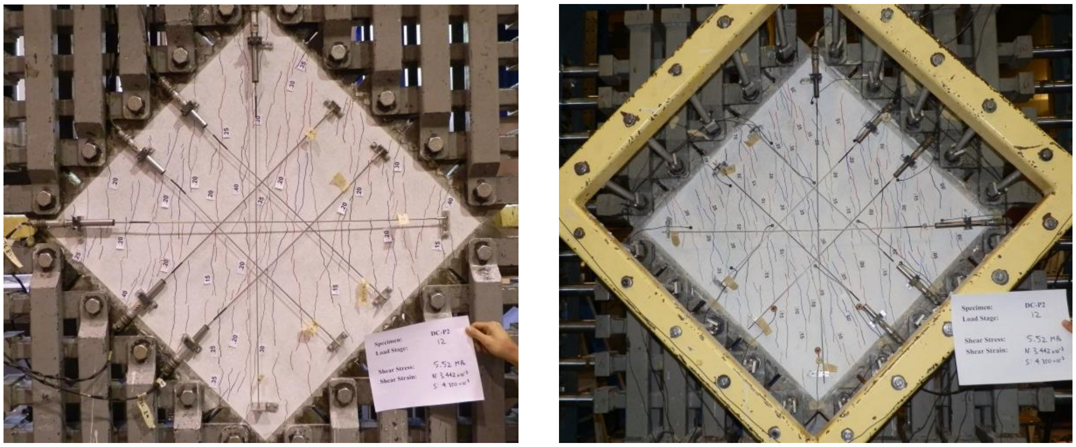

Stage 12: v_{xy} = 5.52 MPa; γ_{xy} = 3.90x10^{-3}; w_m = 0.18 mm; s_m = 51 mm.

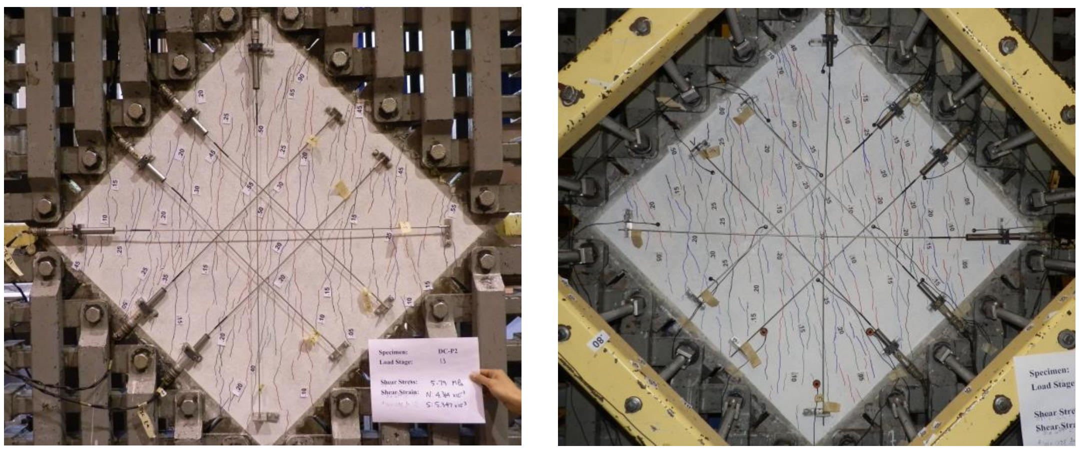

Stage 13: v_{xy} = 5.79 MPa; γ_{xy} = 4.86x10^{-3}; w_m = 0.21 mm; s_m = 43 mm.

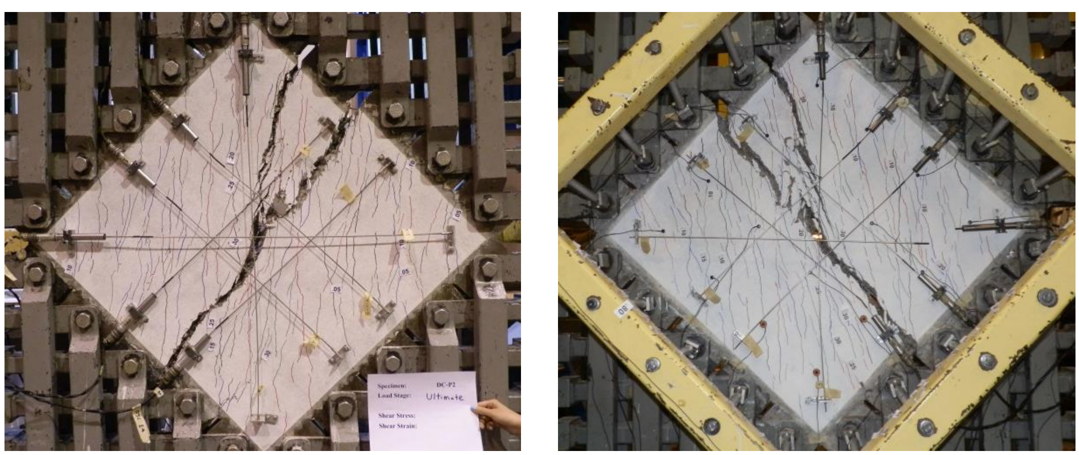

Failure: v_u = 5.97 MPa; γ_u = 5.94x10^{-3}.

Figure B.121: Panel DC-P2 – Selected crack patterns

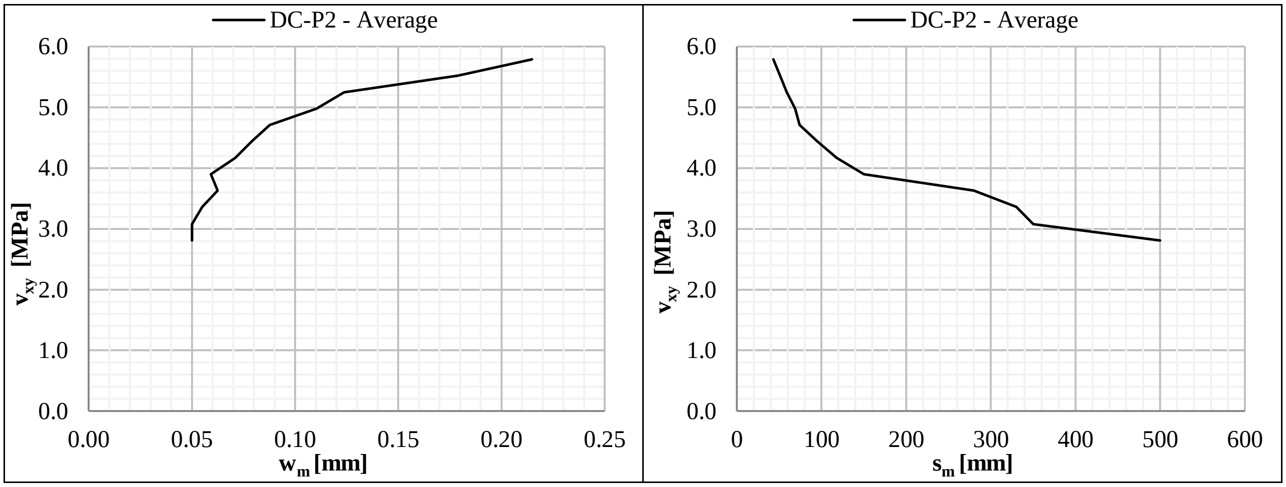

(a) (b)

Figure B.122: Panel DC-P2 – Cracking of the panel

No significant stress was developed in the longitudinal reinforcement until cracking. The stresses in the longitudinal reinforcement increased linearly as the shear stress was increased. The steel did not experience yielding as, at panel failure, the stress in the steel was 275 MPa. This stress at failure was the highest of the experimental program, however, suggesting that the steel fibres prevent overrotation of the principal directions. This allowed the reinforcing steel to carry significant amounts of stress.

B.3.3 Comparison of the Responses of the Front and Back Face

Figure B.124 shows the comparison between the LVDT responses of the front face and the back face of the panel. From the principal tensile response, it was evident that the back face of the panel experienced cracking at a much higher load. This remained true throughout the test, as the back face carried much higher principal tensile stresses at all strains. This was due to a higher concentration of aggregate and fibres on the finished face of the panel, as a result of the tight reinforcement spacing. The shear stress versus shear strain response shows a strain offset between the two faces that remains roughly the same as the test progressed. In general, the back face exhibited a stiffer response in terms of shear stress. The Mohr’s circle of stress for the back face was shifted to higher principal tensile stresses relative to the front face, leading to a reduction in principal compressive stress and x-direction reinforcement stress.

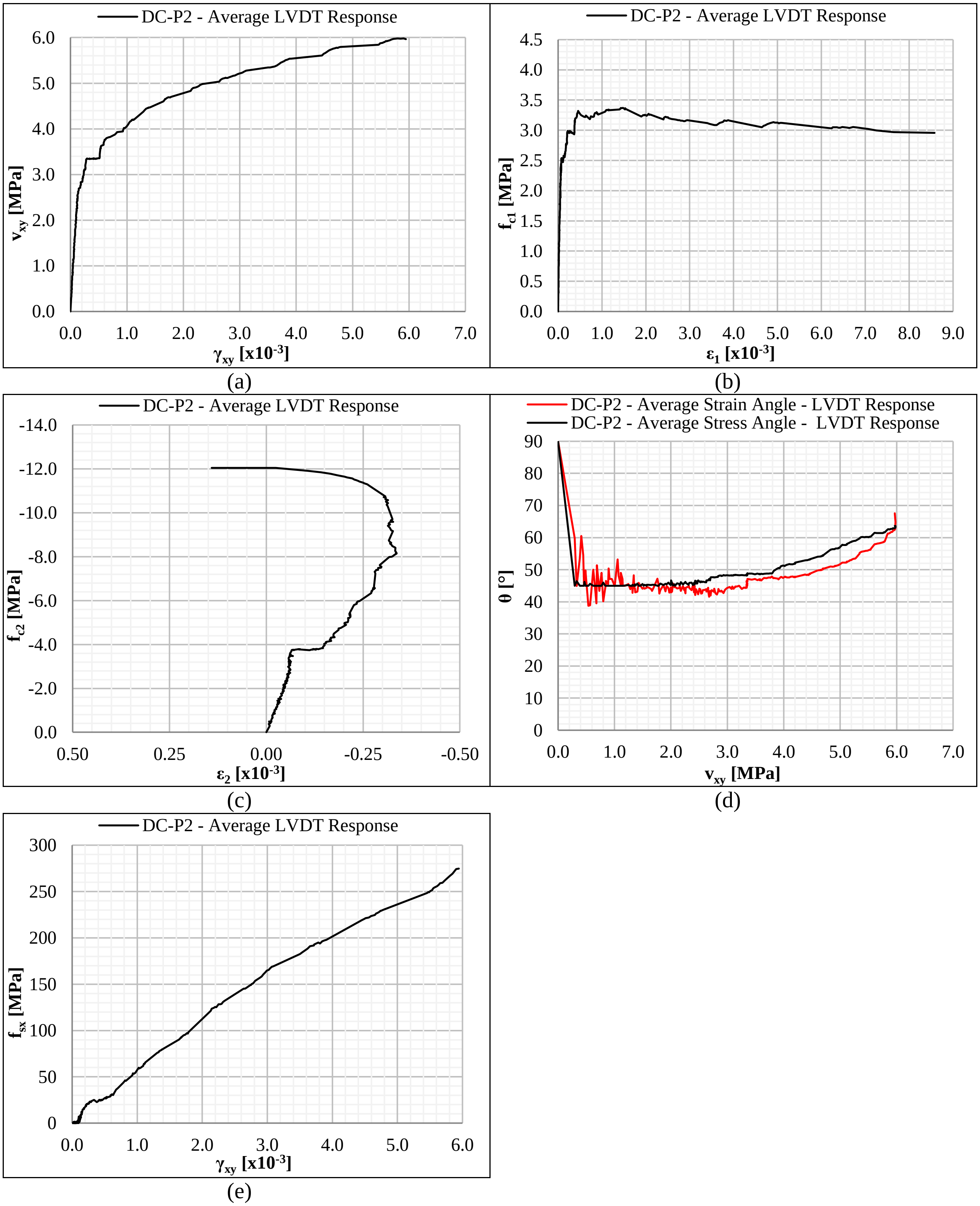

Figure B.123: Panel DC-P2 – Responses of the panel

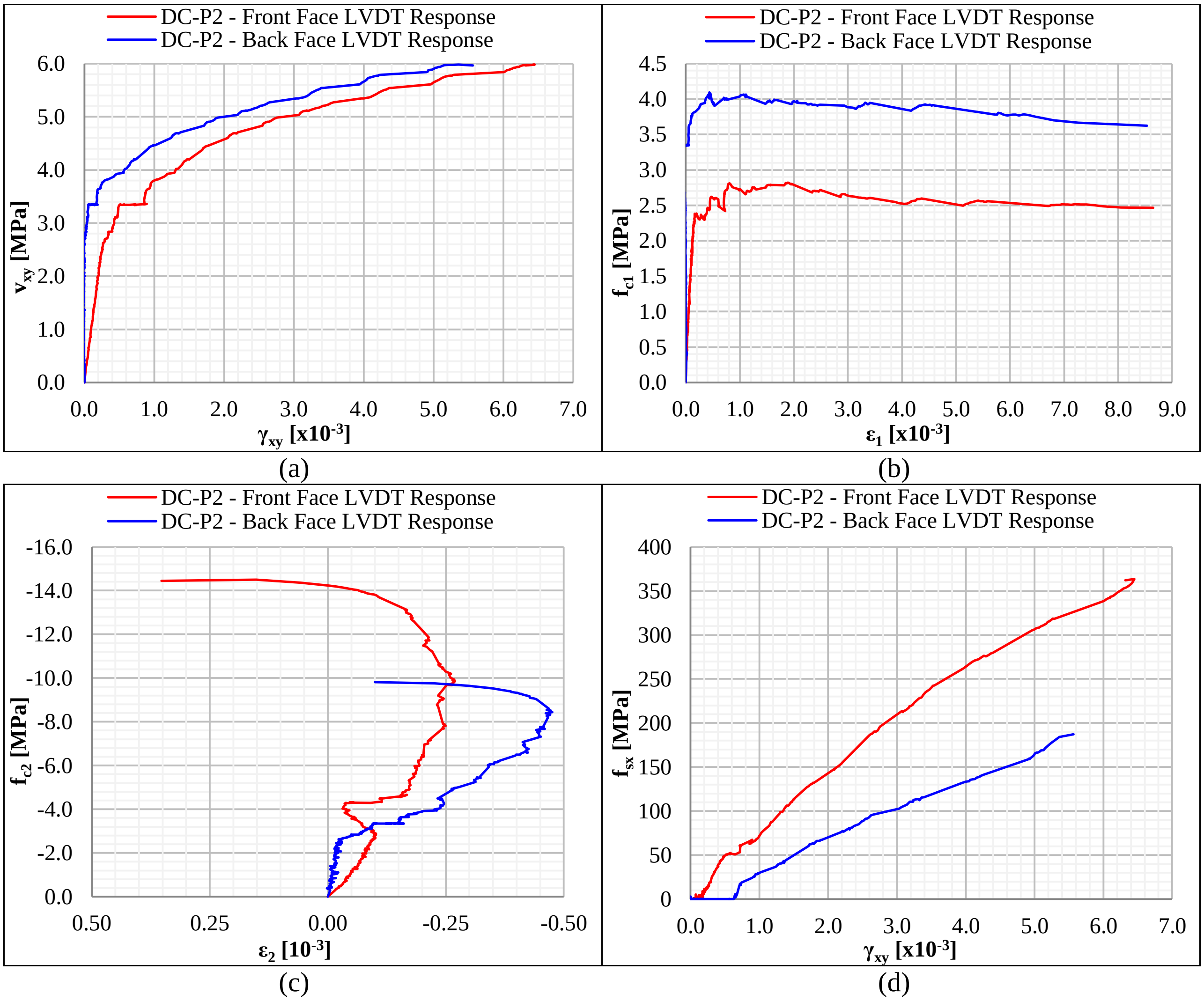

Figure B.124: Panel DC-P2 – Comparison of the front face and back face responses

B.4 Panel DC-P3

Panel DC-P3 was constructed of macro-synthetic fibre reinforced concrete with 2.0% by volume MAC Matrix fibres. This specimen was tested under a monotonic shear loading condition. Like DC-P2, this panel was reinforced with 40 D8 bars in the x-direction for a reinforcement ratio of ρ_x = 3.31%, and no y-direction reinforcement ratio. The compressive and uniaxial tensile strengths of the concrete were 50.9 MPa and 4.49 MPa.

B.4.1 Test Observations

Some of the load stage crack patterns of Panel DC-P3 are depicted in Figure B.125. The first crack occurred on the front face of the panel at 1.50 MPa however, no softening was observed. Thus, this crack was deemed to be due to a local surface imperfection and did not represent first cracking of the panel. Cracking and significant softening occurred at a shear stress of 2.17 MPa. The first crack was relatively large at 0.11 mm, consistent with the experimental findings using PPFRC. Subsequent cracking was at first characterized by development of new cracks of similar size, until Load Stage 7 when crack widths began to increase drastically. This is shown in Figure B.126. At Load Stage 8, the hydraulic pump overheated and shut off. As a result of this, hydraulic pressure in line 1 jumped to near zero, whereas the pressure in line 2 slowly decreased. This pressure condition (line 2 on with line 1 at zero) represents biaxial tension plus shear applied stress. This caused the opening of a significant crack between the fourth and fifth shear keys aligned with the x-axis. After a few minutes, the pump was cooled and the test resumed. Upon increasing to the previously attained pure shear applied stress, the strain in the panel was seen to have substantially increased. However, the panel did not fail and continued to take increased applied stresses, suggesting that the stress and strain at failure were not affected by this pump shut down. The test continued until the final load stage at an average crack width and average crack spacing of 0.57 mm and 72.0 mm, respectively.

This panel failed at a shear stress of 3.87 MPa. The failure plane was aligned with the x-axis, at the location of the crack that opened during the pump shut down. The failure occurred with significant warning, as the response had substantially softened. The failure was through fibre pull-out followed by aggregate interlock failure and crack sliding.

B.4.2 Data Analysis

Figure B.127 shows the various panel responses after completion of the data analysis. As with other panels, linear behaviour in the shear stress-shear strain response, the principal tensile stress-principal tensile strain response, and the principal compressive stress-principal compressive strain response was observed up to the first crack at a shear stress of 2.17 MPa and a corresponding shear strain of 0.148×10^{-3}. This was true, despite the occurrence of the premature crack observed at 1.50 MPa.

This panel had a drastically softened response, as the shear stress increased by only 1.70 MPa between cracking and failure; the shear strain increased by $7.81\text{x}10^{-3}$ from cracking to failure. Similar to DC-P2, cracking on the back face occurred at a higher shear stress (2.50 MPa). The back face exhibited a stiffer response after cracking due to a higher percentage of fibres and aggregate near the back face of the panel. Finally, the panel failed at a shear stress of 3.87 MPa and corresponding shear strain of 7.96×10^{-3}.

The principal tensile stress and the principal tensile strain at first-cracking were 2.13 MPa and 0.075×10^{-3}, respectively. Slight tension stiffening was exhibited, with a maximum principal tensile stress of 2.42 MPa at a principal tensile strain of $0.717\text{x}10^{-3}$. From here, roughly linear softening occurred until a tensile stress at failure of 1.73 MPa and a strain of $11.82\text{x}10^{-3}$. This strain capacity was much greater than that of the plain concrete and steel fibre reinforced concrete panels.

The principal compressive stress and principal compressive strain at first-cracking were -2.22 MPa and -0.073×10^{-3}, respectively. The principal compressive stress at failure was –8.69 MPa at a strain of -0.434×10^{-3}.

As with other panels, the orientations of the principal directions were nearly the same for both stress and strain until first cracking. After cracking, the rotation of the principal strain direction lagged behind the principal stress direction, until cracking occurred on the back face of the panel. At this point, the strain angle became more steeply inclined than the stress angle. At the pump shut down, a significant jump in inclination occurred, consistent with the eventual failure plane. The inclination at failure was 66.0° for the stress field and 69.7° for the strain field.

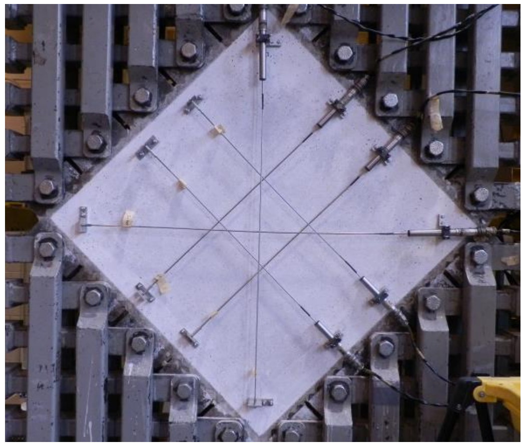

Stage 0: v_{xy} = 0 MPa; γ_{xy} = 0x10^{-3}; w_m = 0 mm; s_m = ∞ mm.

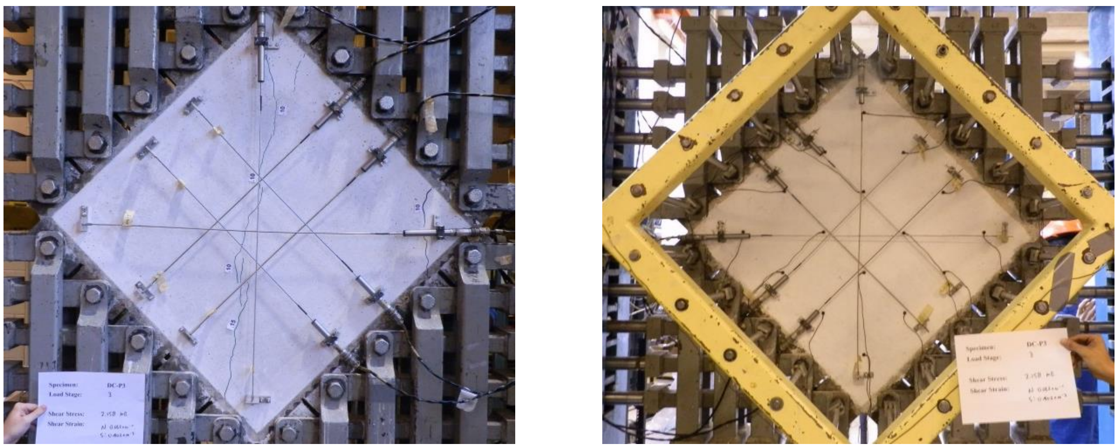

Stage 3: v_{xy} = 2.17 MPa; γ_{xy} = 0.148x10^{-3}; w_m = 0.11 mm; s_m = 670 mm.

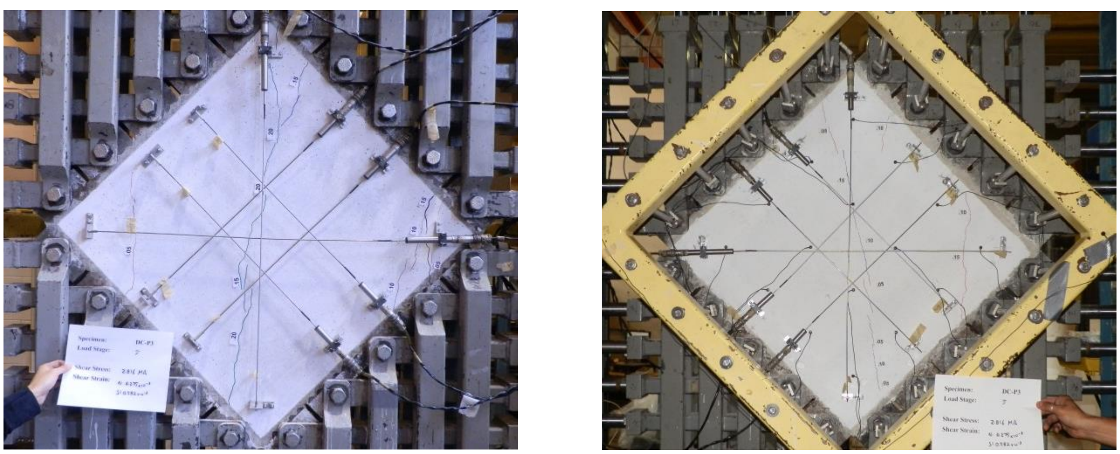

Stage 5: v_{xy} = 2.82 MPa; γ_{xy} = 0.429x10^{-3}; w_m = 0.113 mm; s_m = 310 mm.


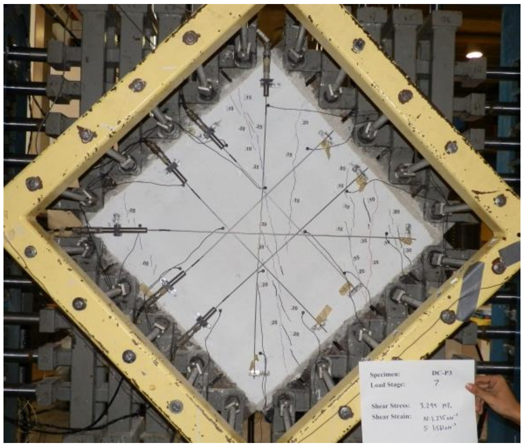

Stage 7: v_{xy} = 3.25 MPa; γ_{xy} = 1.398x10^{-3}; w_m = 0.20 mm; s_m = 140 mm.


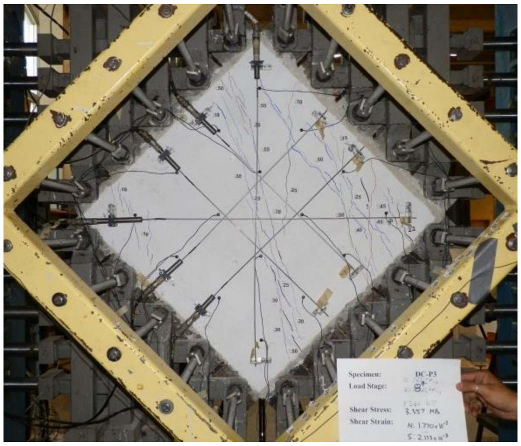

Stage 8 (after pump malfunction): v_{xy} = 3.36 MPa; γ_{xy} = 1.952x10^{-3}; w_m = 0.34 mm; s_m = 99 mm.

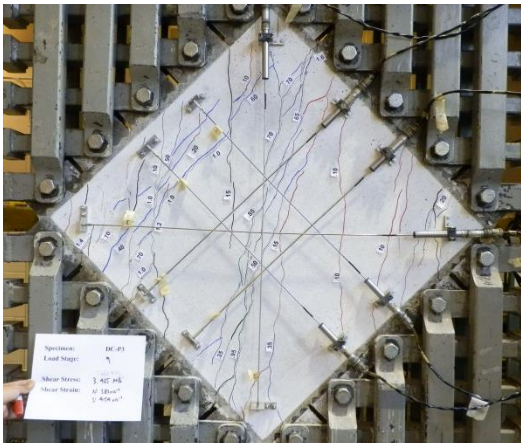
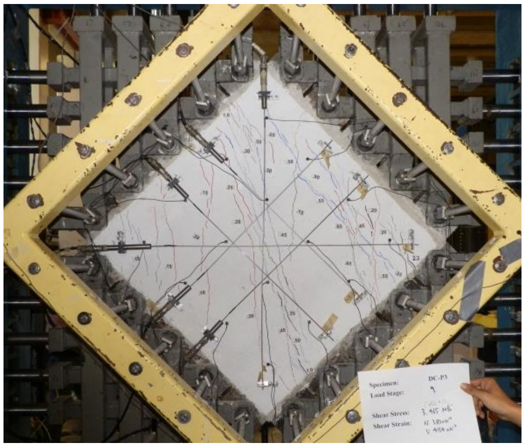

Stage 9: v_{xy} = 3.47 MPa; γ_{xy} = 4.19x10^{-3}; w_m = 0.39 mm; s_m = 83 mm.

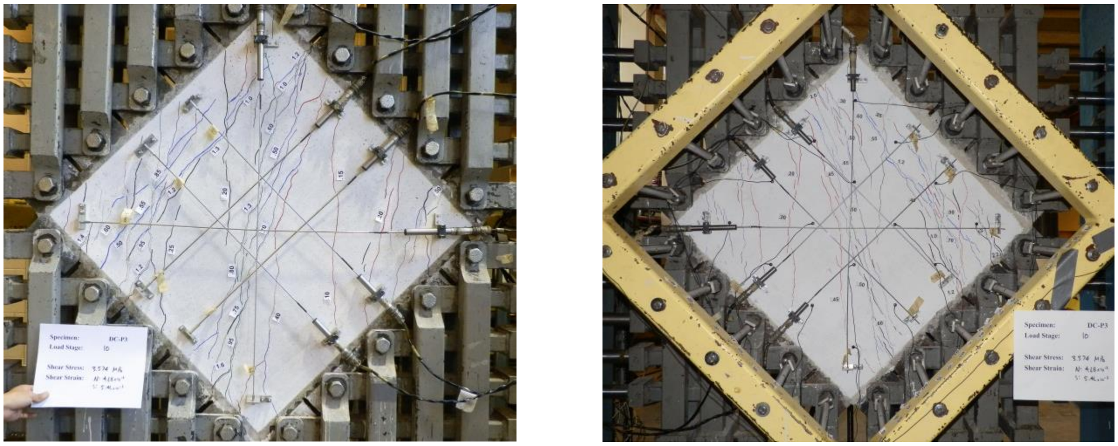

Stage 10: v_{xy} = 3.57 MPa; γ_{xy} = 5.05x10^{-3}; w_m = 0.53 mm; s_m = 83 mm.

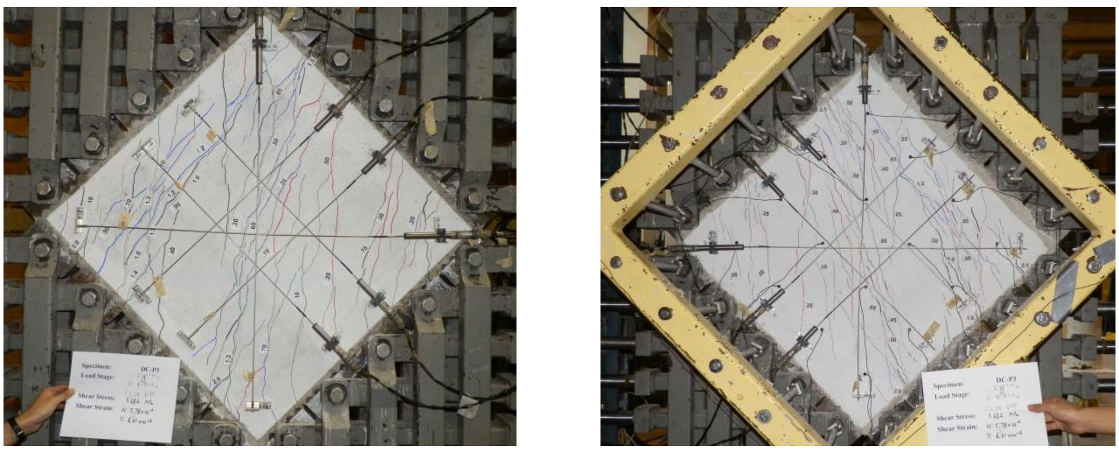

Stage 11: v_{xy} = 3.68 MPa; γ_{xy} = 6.20x10^{-3}; w_m = 0.57 mm; s_m = 72 mm.

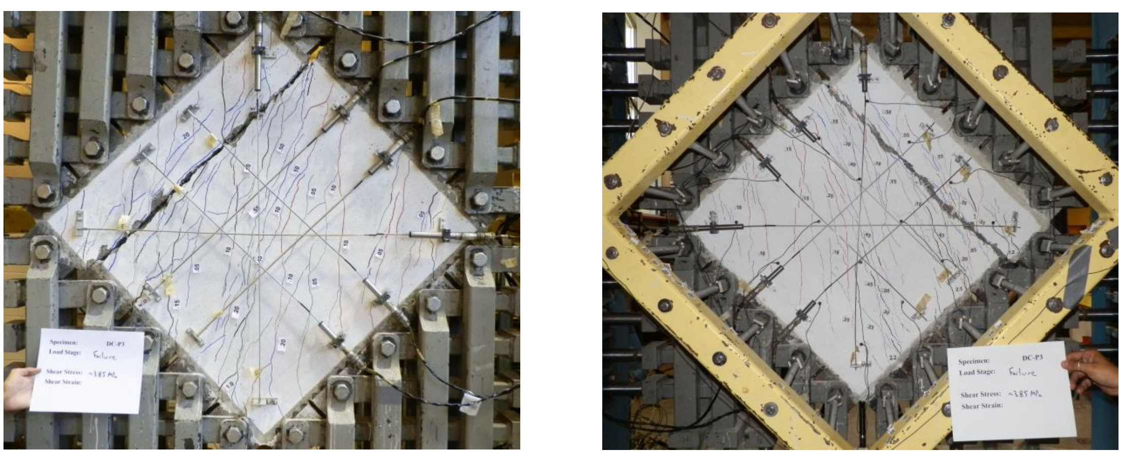

Failure: v_u = 3.87 MPa; γ_u = 7.96x10^{-3}.

Figure B.125: Panel DC-P3 – Selected crack patterns

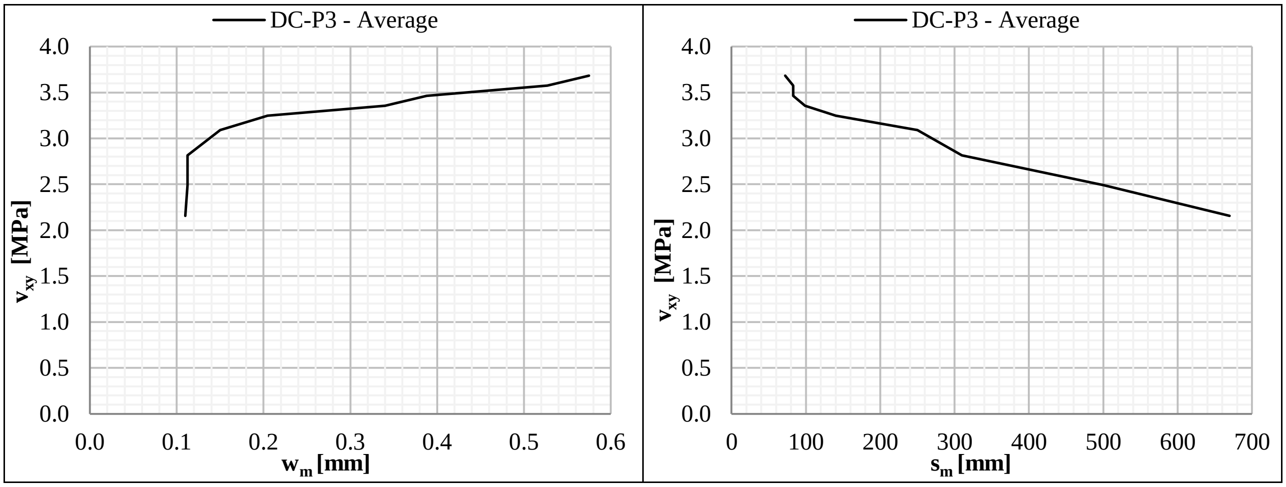

(a) (b)

Figure B.126: Panel DC-P3 – Cracking of the panel

No significant stress was developed in the longitudinal bars until a shear stress of 2.17 MPa. The stresses in the longitudinal reinforcement increased linearly as the shear stress increased. As with all other panels, the longitudinal bars did not experience yielding as, at panel failure, the stress in the steel was merely 210 MPa.

B.4.3 Comparison of the Responses of the Front and Back Face

Figure B.128 shows the comparison between the LVDT responses of the front face and the back face of the panel. The shear stress versus shear strain response showed an offset between the two faces that became gradually more pronounced as the test progressed. Also, the principal tensile stress on the back face was larger throughout the test. This is the similar to DC-P2 and is due to the higher percentage of fibres and aggregate near the back surface of the panel. In general, the back face exhibited a stiffer response in terms of shear stress and carried less principal compressive stress and x-direction reinforcement stress. Other installation issues may have caused some out-of-plane bending, creating the premature crack observed on the front face of the panel.

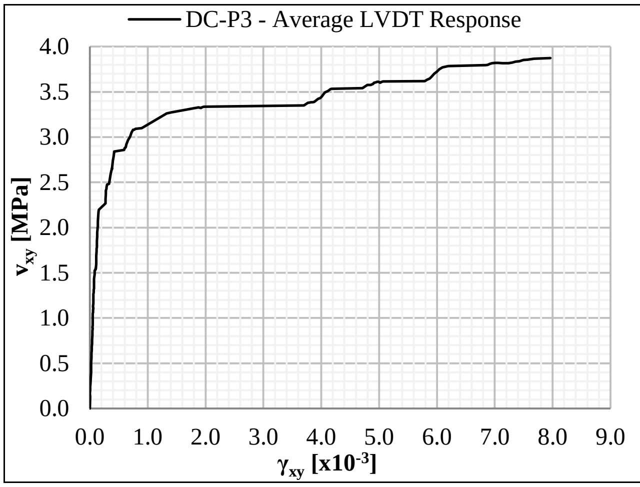

(a)

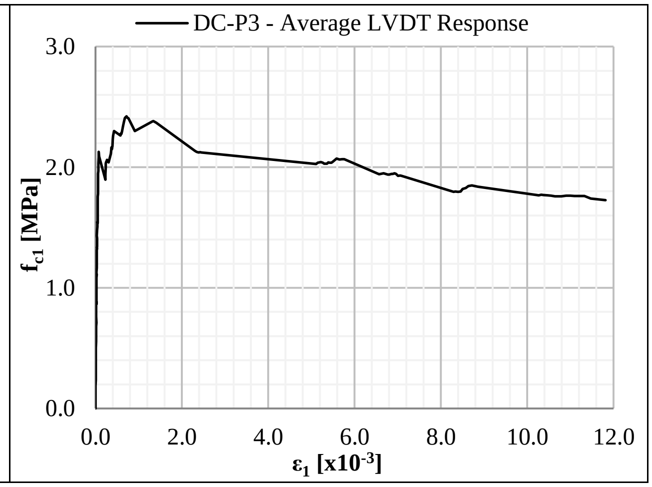

(b)

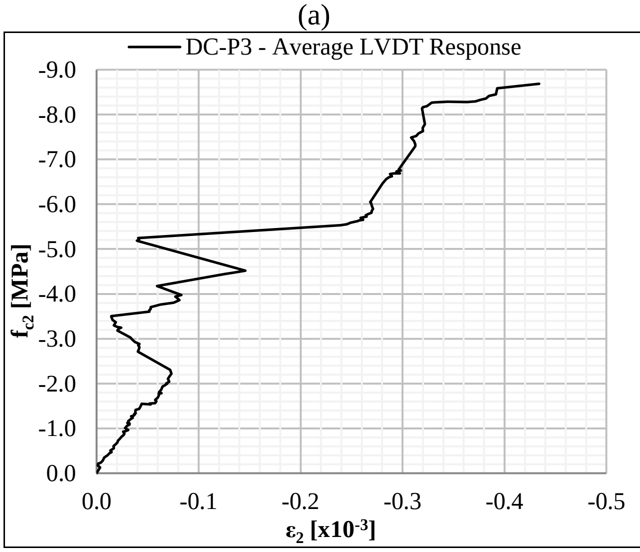

(c)

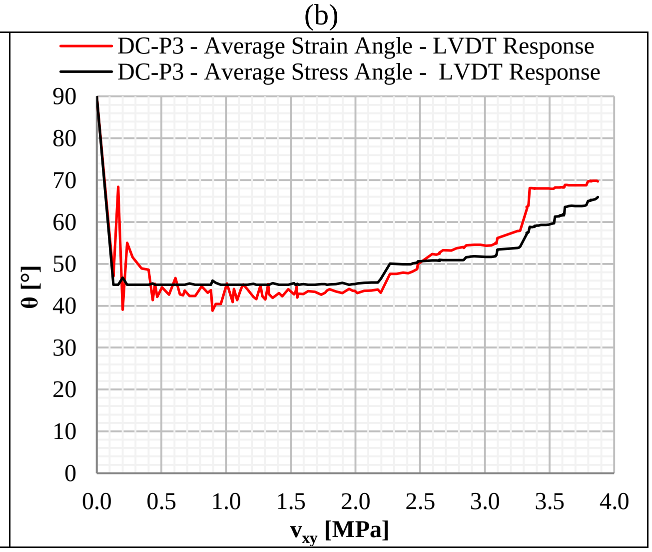

(d)

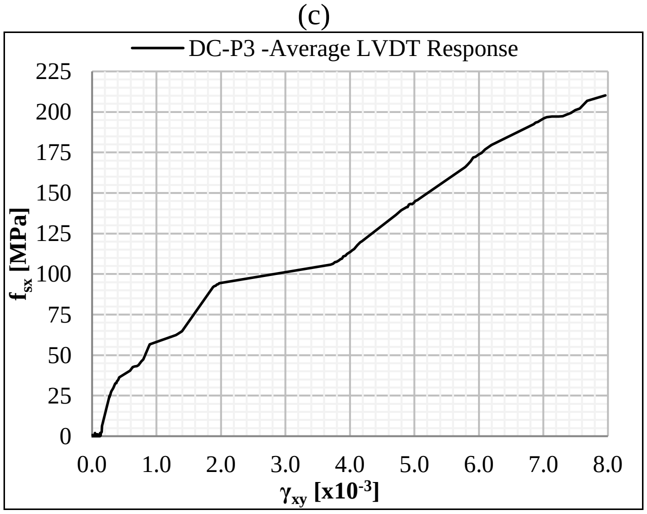

(e)

Figure B.127: Panel DC-P3 – Responses of the panel

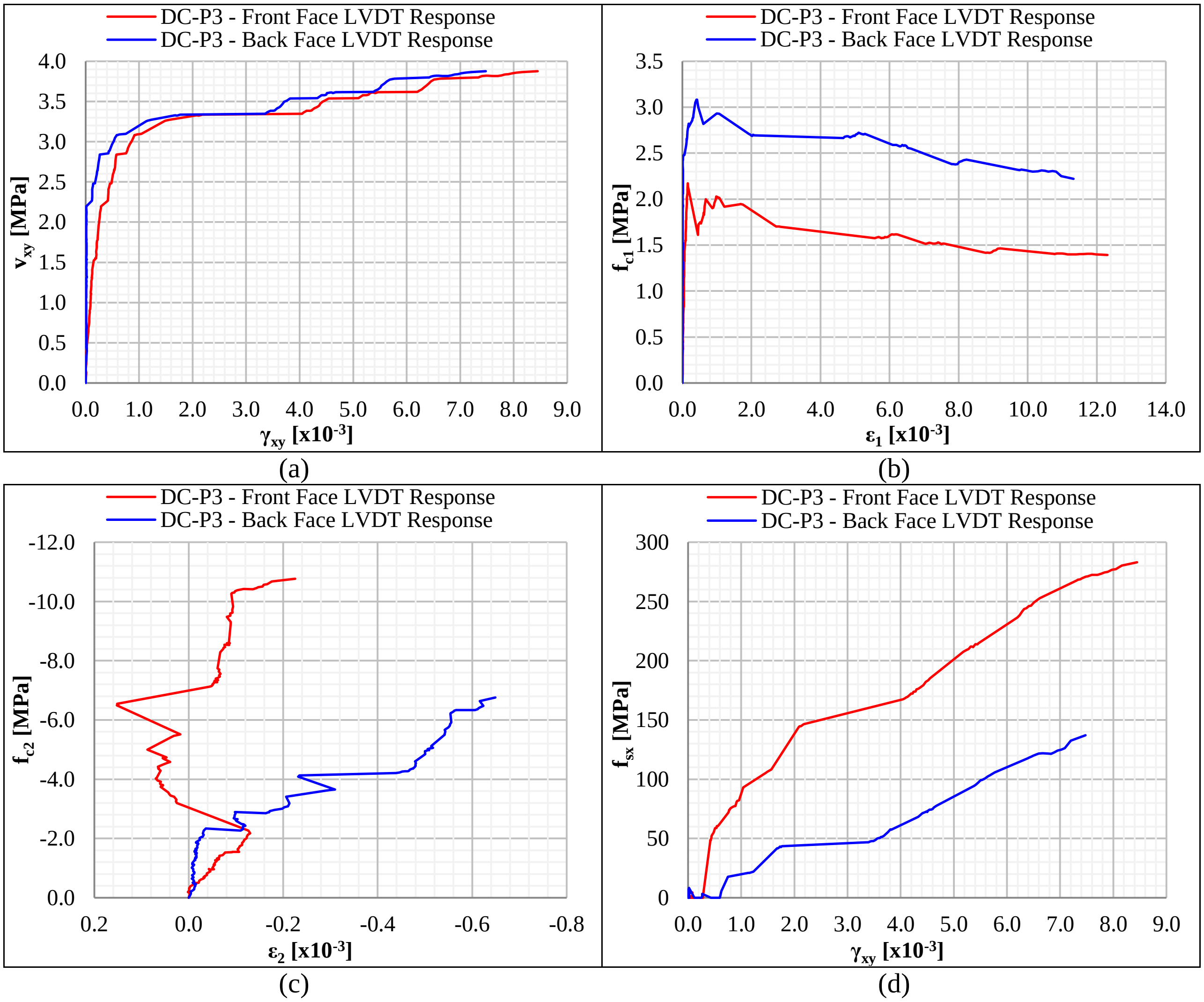

Figure B.128: Panel DC-P3 – Comparison of the front face and back face responses

B.5 Panel DC-P4

Panel DC-P4 was constructed of steel fibre reinforced concrete with 1.0% by volume RC80/30BP fibres. This specimen was tested under a reversed cyclic shear loading condition. Like the other panels, this panel was reinforced with 40 D8 bars in the x-direction for a reinforcement ratio of ρ_x = 3.31%, and no y-direction reinforcement ratio. The compressive and uniaxial tensile strengths of the concrete were 64.0 MPa and 4.76 MPa.

B.5.1 Test Observations

Select crack patterns of Panel DC-P4 are depicted in Figure B.129. The first crack occurred on the front face of the panel during Cycle 5, Load Stage 9 at a shear stress of 2.60 MPa. The crack width was small, likely less than 0.05 mm, as it was not visually observed until completion of the 10th load stage. Many additional cracks developed during subsequent cycles at relatively small crack widths. The number of cracks formed under positive and negative shear matched closely, evident by the similar crack spacings for both sets of cracks shown in Figure B.130. The crack widths were larger under negative shear, consistent with the eventual failure of the panel during a negative half cycle. During the loading of the negative half of the 8th cycle, it was discovered that the two lines of hydraulic pressure being applied to the panel through the load maintainer were not increasing in the correct ratios. It was determined that the hydraulic seals in one of the jacks had failed, and oil was passing through the system without applying the correct load. Thus, the test was stopped and repairs were undertaken. The repair was performed without affecting the specimen or instrumentation. The test resumed six days later, when the final cycles were performed. At the final load stage, the average crack width and average crack spacing were 0.22 mm and 71.0 mm, respectively.

This panel failed at a shear stress of 4.47 MPa during Cycle 11. The failure plane was aligned with the x-axis of the panel and passed through the panel between the fourth and fifth shear key, similar to Panel DC-P3 and DC-P5. As the test was progressing, popping could be heard, indicative of fibre pull-out across the main cracks. Finally, at failure, significant popping occurred rapidly, suggesting that the fibres were rapidly pulled out and could no longer transmit the applied stresses across the main crack. After fibre bridging was overcome, the panel experienced aggregate interlock failure and crack sliding.

B.5.2 Data Analysis

Figure B.131 shows the various panel responses after completion of the data analysis. As with other panels, linear behaviour in the shear stress-shear strain response, the principal tensile stress-principal tensile strain response, and the principal compressive stress-principal compressive strain response was observed up to the first crack at a shear stress of 2.60 MPa and a corresponding shear strain of 0.136×10^{-3}.

The panel exhibited a softened response, with linearly increasing stresses in the x-direction reinforcement. Although out-of-plane issues were not exhibited in the linear elastic range, the back face exhibited a stiffer response after cracking due to a higher percentage of fibres and aggregate near the back face of the panel. Finally, during the 11th cycle, the panel failed at a shear stress of 4.47 MPa and corresponding shear strain of 2.87×10^{-3}. The isolated cycles are shown separately in Figure B.132.

The principal tensile stress and the principal tensile strain at first-cracking were 2.60 MPa and 0.071×10^{-3}, respectively. Tension stiffening was exhibited until a relatively high maximum principal tensile stress of 3.54 MPa was attained at a principal tensile strain of $0.402x10^{-3}$. This strain at peak was much lower than the monotonic DC-P2. From here, the response softened slightly until the failure at a principal tensile stress of 2.59 MPa and a low strain of $6.75x10^{-3}$.

The principal compressive stress and principal compressive strain at first-cracking were -2.60 MPa and -0.065×10^{-3}, respectively. As the test progressed, the principal compressive strain became tensile, suggesting deterioration of the concrete. The principal compressive stress at failure was –7.66 MPa at a strain of 0.399×10^{-3}.

As with all other panels, the orientations of the principal directions were nearly the same for both stress and strain until first cracking. After cracking, the rotation of the principal strain direction lagged behind the principal stress direction, yet matched closely under positive shear. In negative shear, the strain field was much more steeply inclined than the stress field, consistent with the failure plane. The inclination at failure was 120.2° for the stress field and 103.4° for the strain field.

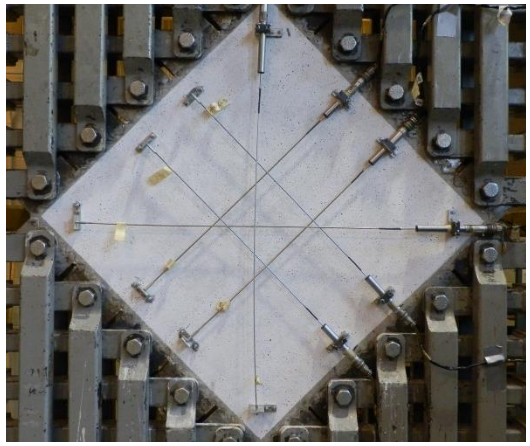

Cycle 0, Stage 0: v_{xy} = 0 MPa; γ_{xy} = 0x10^{-3}; w_m = 0 mm; s_m = ∞ mm.

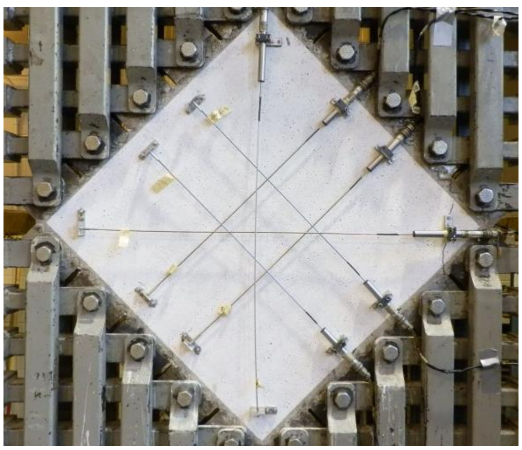

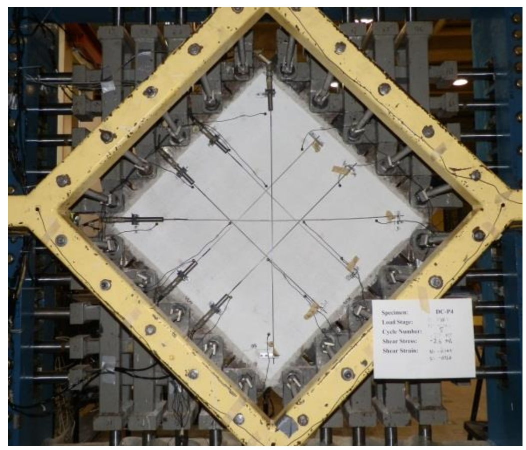

Cycle 5, Stage 9: v_{xy} = 2.60 MPa; γ_{xy} = 0.136x10^{-3}; w_m = 0.05 mm; s_m = 500 mm.

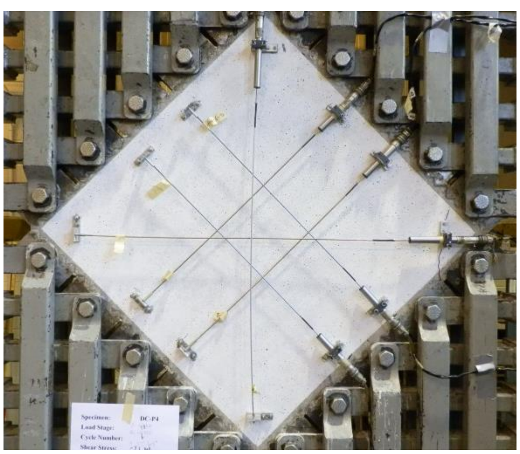

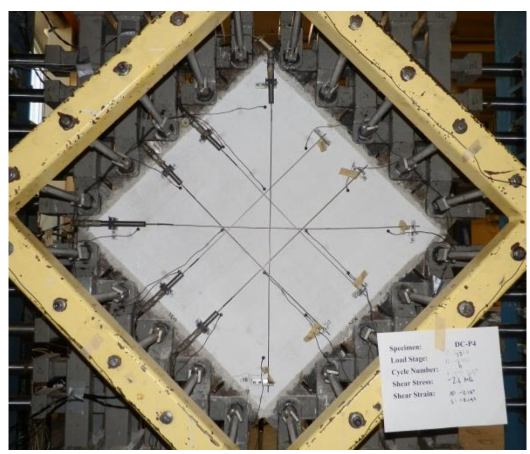

Cycle 6, Stage 12: v_{xy} = -2.60 MPa; γ_{xy} = -0.165x10^{-3}; w_m = 0.10 mm; s_m = 500 mm.

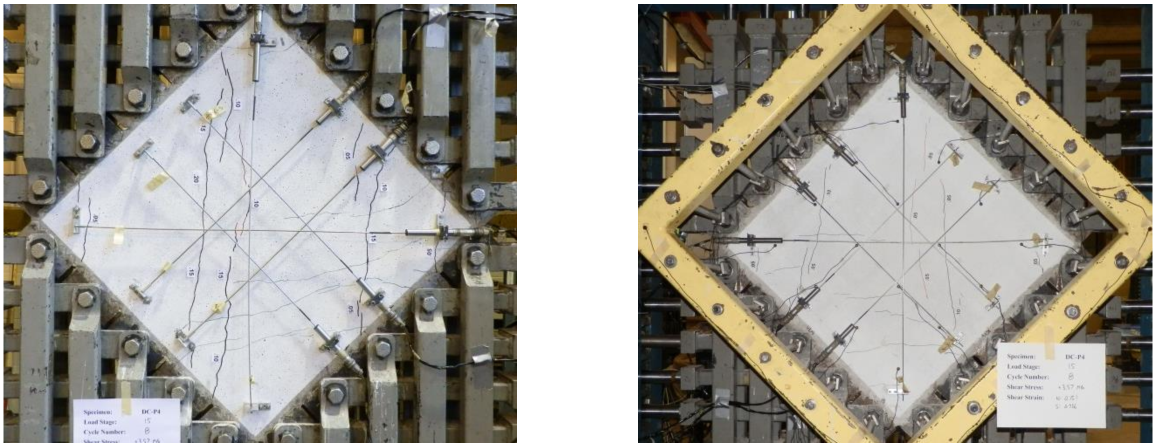

Cycle 8, Stage 15: v_{xy} = 3.57 MPa; γ_{xy} = 0.444x10^{-3}; w_m = 0.087 mm; s_m = 200 mm.

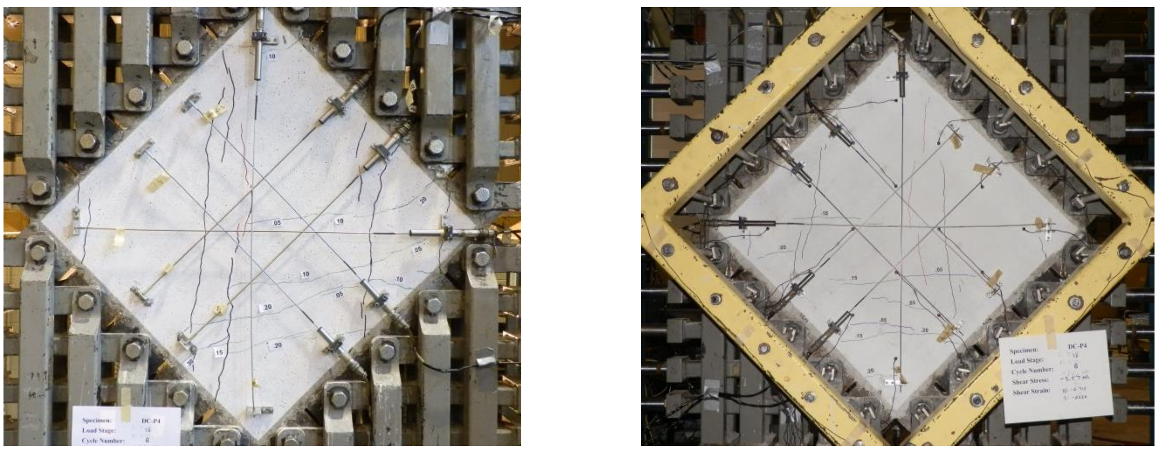

Cycle 8, Stage 16 (after jack repairs): v_{xy} = -3.57 MPa; γ_{xy} = -0.670x10^{-3}; w_m = 0.12 mm; s_m = 222 mm.

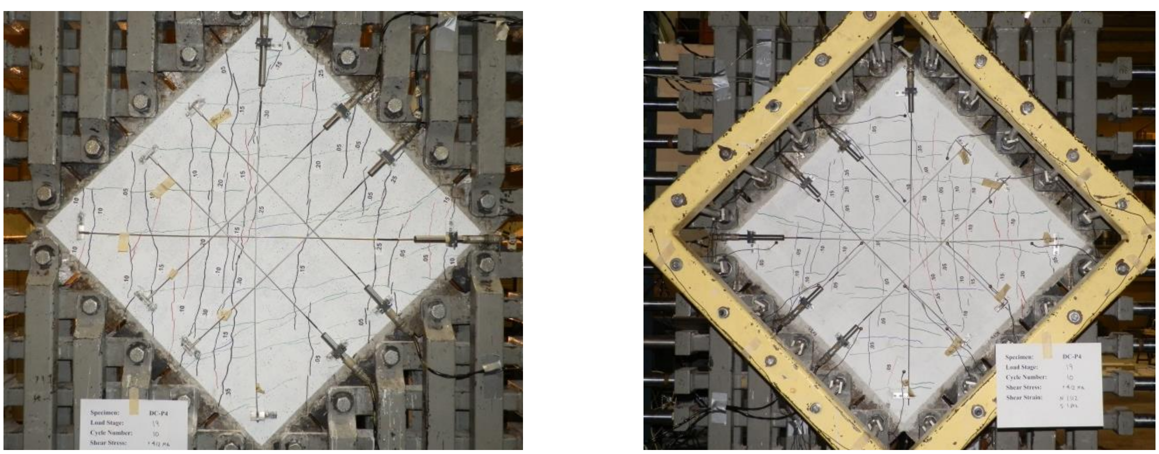

Cycle 10, Stage 19: v_{xy} = 4.12 MPa; γ_{xy} = 1.402x10^{-3}; w_m = 0.14 mm; s_m = 91 mm.

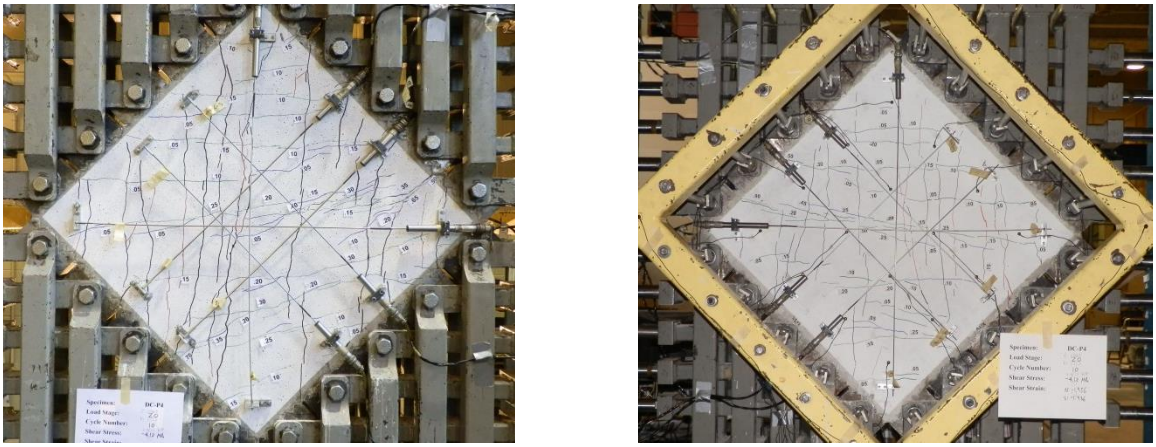

Cycle 10, Stage 20: v_{xy} = -4.12 MPa; γ_{xy} = -1.946x10^{-3}; w_m = 0.19 mm; s_m = 95 mm.

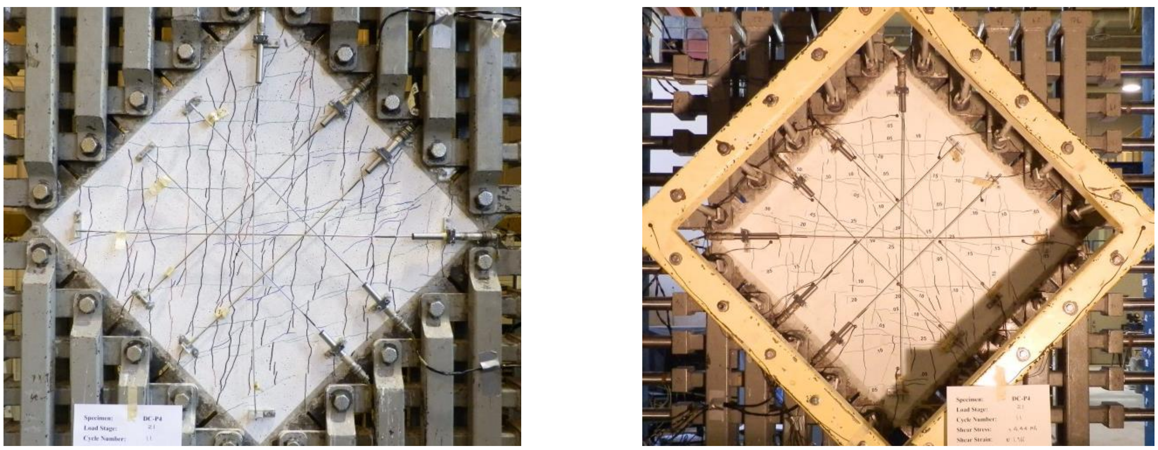

Cycle 11, Stage 21: v_{xy} = 4.47 MPa; γ_{xy} = 2.25x10^{-3}; w_m = 0.22 mm; s_m = 71 mm.

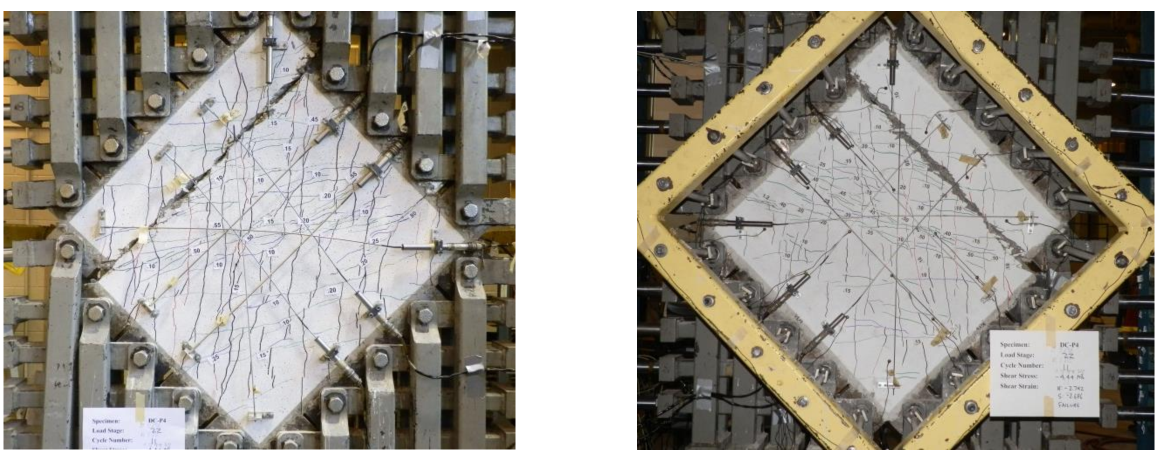

Failure: v_u = 4.47 MPa; γ_u = 2.87x10^{-3}.

Figure B.129: Panel DC-P4 – Selected crack patterns

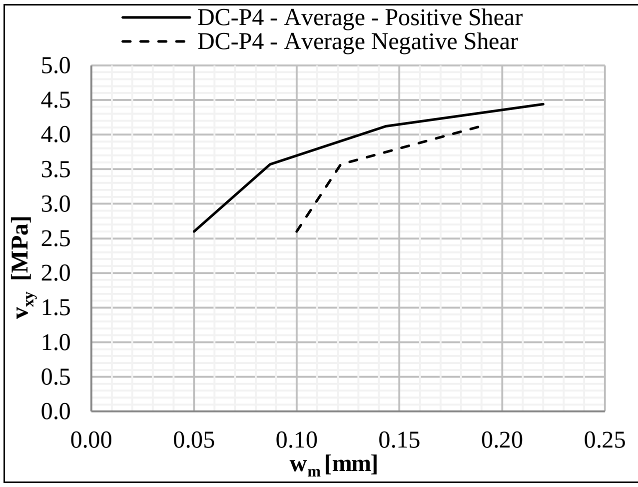

(a)

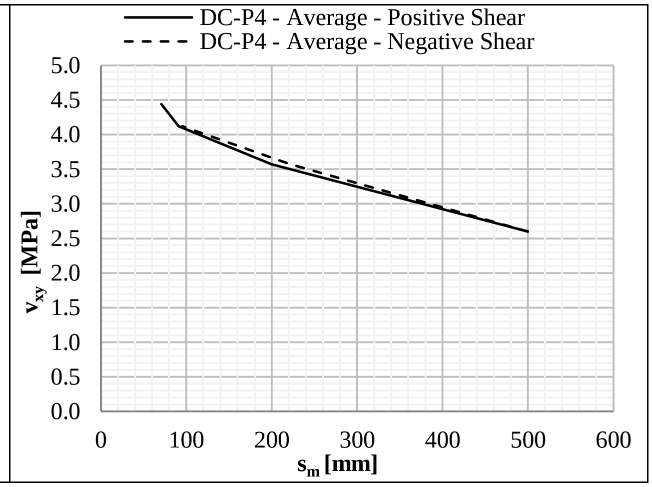

(b)

Figure B.130: Panel DC-P4 – Cracking of the panel

No significant stress was developed in the x-direction steel until a shear stress of 2.60 MPa. The stresses in the longitudinal reinforcement increased linearly as the applied shear stress was increased. As with all other panels, the longitudinal bars did not experience yielding as, at panel failure, the stress in the steel was merely 153 MPa. This was significantly lower than the monotonic panel DC-P2 at failure. Significant degradation of the response was observed for steel FRC under reversed cyclic loads.

B.5.3 Comparison of the Responses of the Front and Back Face

Figure B.133 shows the comparison between the LVDT responses of the front face and the back face of the panel. The shear stress versus shear strain response shows an offset between the two faces that gets gradually worse as the test continues. In general, the back face exhibited a stiffer response in terms of shear stress. As with most other panels, the back face Mohr's circle was shifted to the tension side, yielding low principal compressive stresses and x-direction reinforcement stresses, in addition to higher residual principal tensile stresses. As with other panels, this was due to a higher concentration of aggregate and fibres on the finished face of the panel, due to the tight reinforcement spacing.

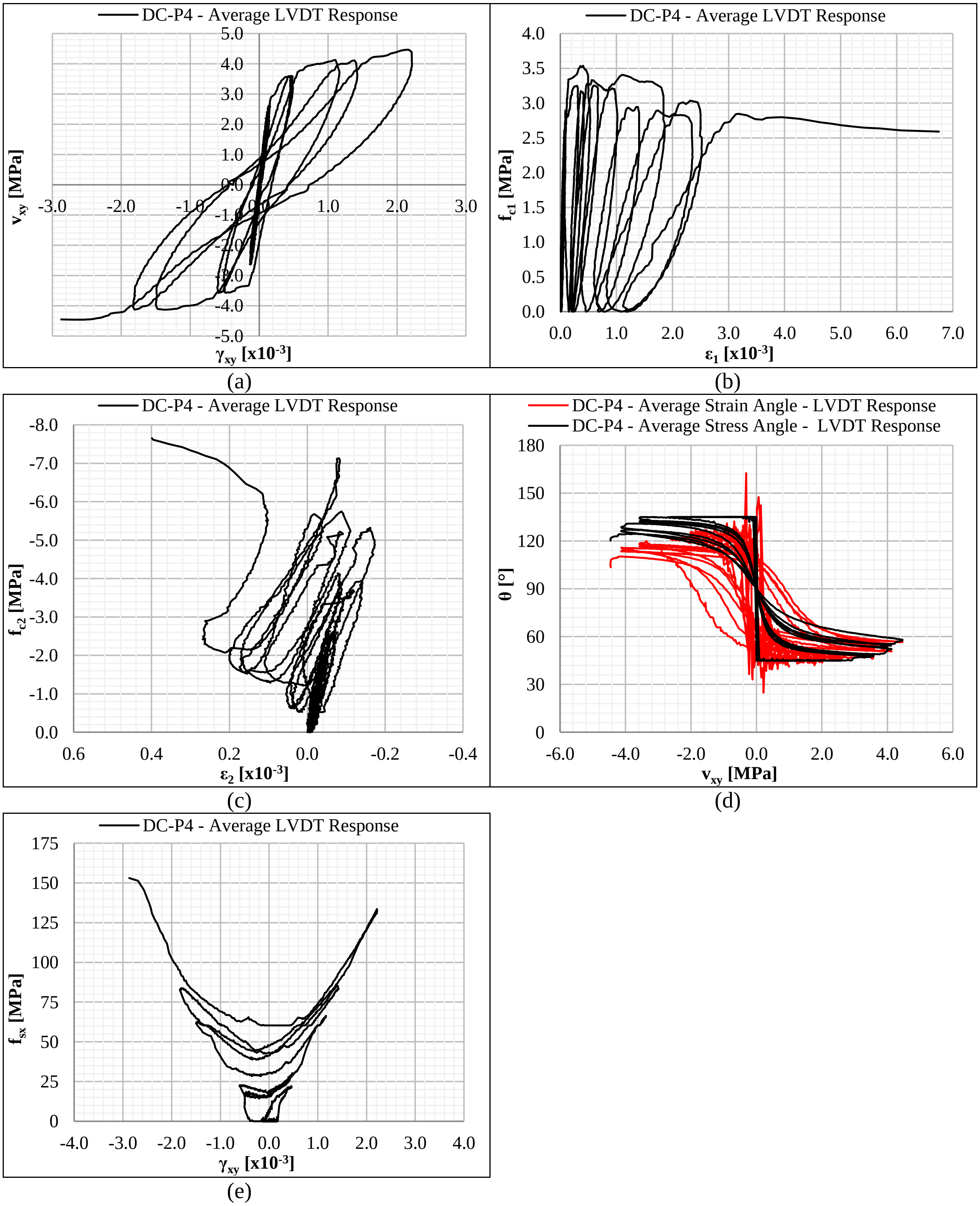

Figure B.131: Panel DC-P4 – Responses of the panel

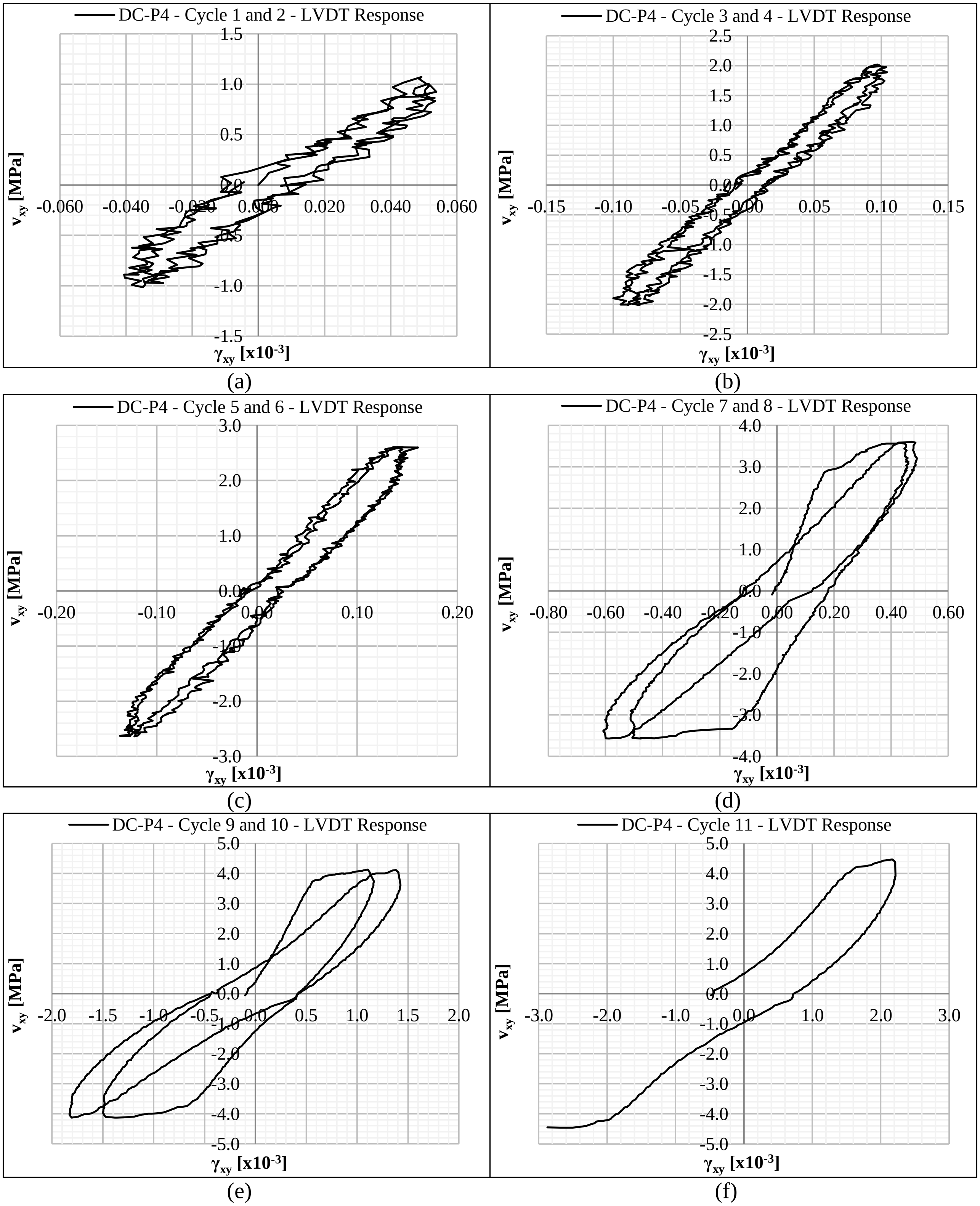

Figure B.132: Panel DC-P4 – Shear stress versus shear strain; isolated cycles

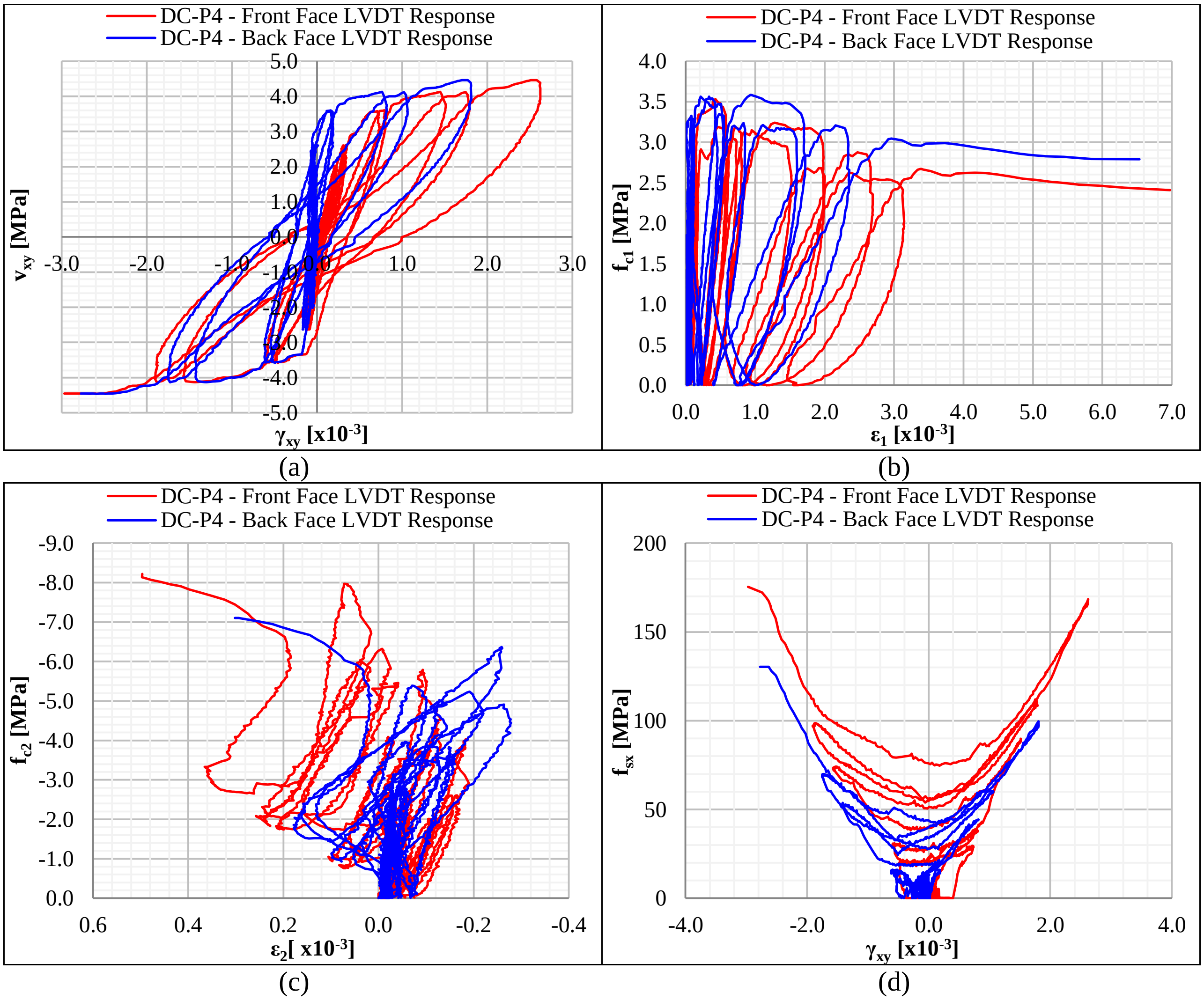

Figure B.133: Panel DC-P4 – Comparison of the front face and back face responses

B.6 Panel DC-P5

Panel DC-P5 was constructed of macro-synthetic fibre reinforced concrete with 2.0% by volume MAC Matrix fibres. This specimen was tested under a reversed cyclic shear loading condition. Like all the other panels, this panel was reinforced with 40 D8 bars in the x-direction for a reinforcement ratio of ρ_x = 3.31%, and no y-direction reinforcement ratio. The compressive and uniaxial tensile strengths of the concrete were 54.3 MPa and 4.67 MPa.

B.6.1 Test Observations

A number of the load stage crack patterns for Panel DC-P5 are depicted in Figure B.134. For this panel, the first crack occurred on both the front and back face of the panel during Cycle 5, Load Stage 9 at a shear stress of 2.23 MPa. The crack width was relatively large (0.1 mm), in agreement with other experimental findings for PPFRC. Unlike the steel fibre and plain reinforced concrete reversed cyclic tests, the first few cracks experienced significant opening before subsequent cracks developed. This was also inconsistent with the monotonic PPFRC test, which saw steady development of new cracks with some increased crack openings at early stages. Overall, the number of cracks formed under positive and negative shear matched closely, evident by the similar crack spacings at all stress levels shown in Figure B.135. Similar to DC-P4, the crack widths were larger under negative shear. During the 10th cycle, significant multiple cracking was exhibited, accompanied by a considerable softening of the response. At the final load stage, the average crack width and average crack spacing were 0.59 mm and 59.0 mm, respectively.

Panel DC-P5 reached an ultimate shear stress of 3.43 MPa during the positive half of Cycle 12. On the following negative half cycle, the panel failed through fibre pull-out and aggregate interlock failure along the main crack surface. The failure plane was aligned with the x-axis of the panel and passed through the panel between the fourth and fifth shear key. Little to no audible popping could be heard near failure, yet the instrument readings showed significant softening. This provided some forewarning of the failure. This lack of popping sounds was inconsistent with the SFRC panel specimens.

B.6.2 Data Analysis

Figure B.136 shows the various panel responses after completion of the data analysis. As with all other panels, linear and nearly elastic behaviour was observed in the shear stress-shear strain response during Cycles 1 through 4. This can be seen through the isolated cycles plotted in Figure B.137. The same linearity was observed in the principal tensile stress-principal tensile strain response and the principal compressive stress-principal compressive strain response until the first crack at a shear stress of 2.23 MPa and a corresponding shear strain of 0.104×10^{-3}.

After this cracking point, the panel exhibited a softened response, and the x-direction reinforcement began taking some stress. The stress in the reinforcement increased linearly as substantial cracks opened and the response softened further. During the 12th cycle the panel failed, achieving an ultimate shear stress of 3.43 MPa. The shear strain at failure was 5.15×10^{-3}.

The principal tensile stress and the principal tensile strain at first-cracking were 2.12 MPa and 0.071×10^{-3}, respectively. Some slight tension stiffening was exhibited to a maximum principal tensile stress of 2.56 MPa at a principal tensile strain of $1.615\text{x}10^{-3}$. This was similar to the degree of stiffening experienced by the monotonically loaded DC-P3; however this strain at peak tensile stress was larger. From here, the response softened significantly until the failure at a principal tensile stress of 1.27 MPa and a relatively high strain of $10.94\text{x}10^{-3}$.

The principal compressive stress and principal compressive strain at first-cracking were -2.35 MPa and -0.034×10^{-3}, respectively. Thus, this panel showed a significantly stiffer response in compression before cracking than the other panel tests. As the test progressed, the principal compressive straining became tensile. However, during the final excursion of the 12th cycle, the strain switched back to compression. Thus, the principal compressive stress at the point of failure was –3.83 MPa at a strain of -0.399×10^{-3}. The maximum principal compressive stress attained throughout the course of the test was -8.18, close to DC-P3.

In terms of the inclination of the principal directions, the rotation of the principal strain direction lagged behind the principal stress direction, yet matched closely under positive shear. In negative shear, the strain field was more steeply inclined than the stress field, consistent with the failure. The inclination at failure was 120.0° for the stress field and 105.0° for the strain field.

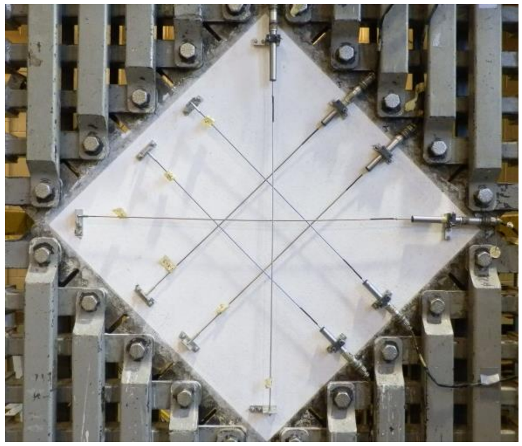

Cycle 0, Stage 0: v_{xy} = 0 MPa; γ_{xy} = 0x10^{-3}; w_m = 0 mm; s_m = ∞ mm.

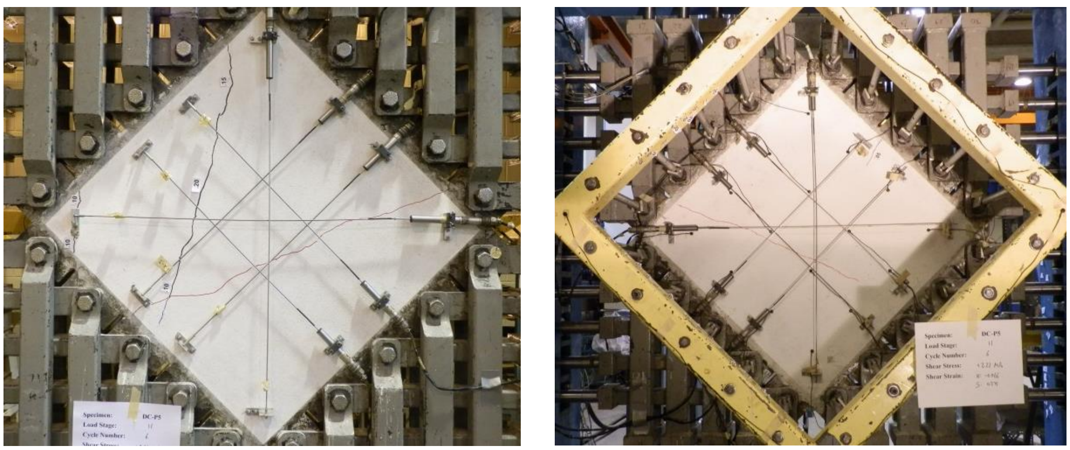

Cycle 6, Stage 11: v_{xy} = 2.23 MPa; γ_{xy} = 0.104x10^{-3}; w_m = 0.12 mm; s_m = 500 mm.

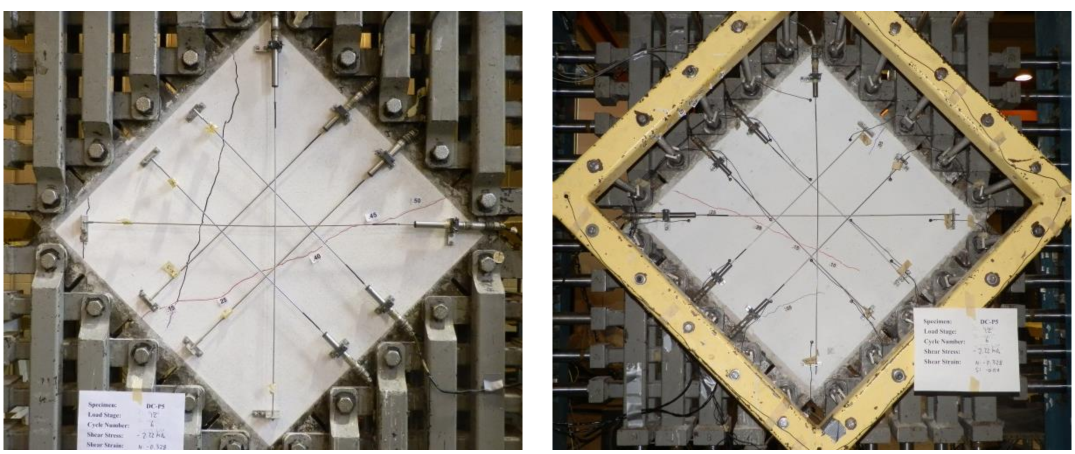

Cycle 6, Stage 12: v_{xy} = -2.23 MPa; γ_{xy} = -0.241x10^{-3}; w_m = 0.25 mm; s_m = 500 mm.

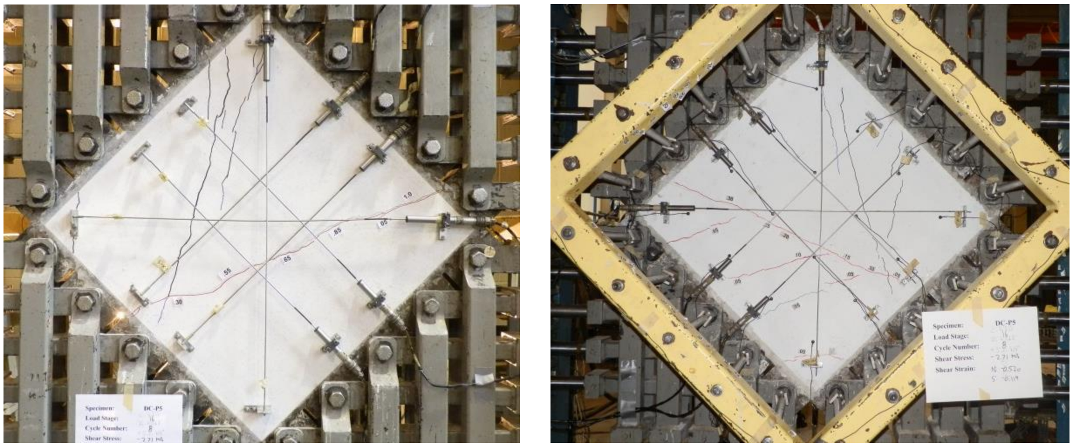

Cycle 8, Stage 16: v_{xy} = -2.71 MPa; γ_{xy} = -0.319x10^{-3}; w_m = 0.28 mm; s_m = 330 mm.

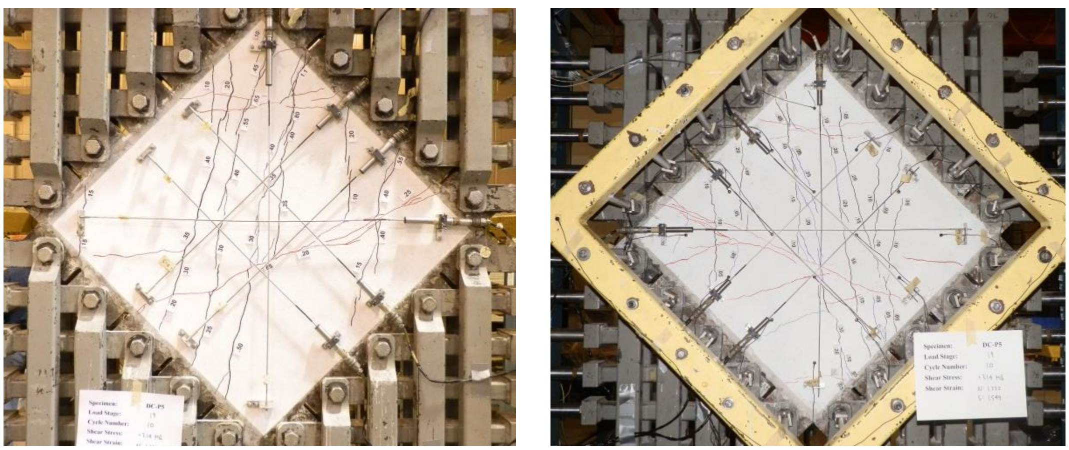

Cycle 10, Stage 19: v_{xy} = 3.14 MPa; γ_{xy} = 1.386x10^{-3}; w_m = 0.25 mm; s_m = 129 mm.

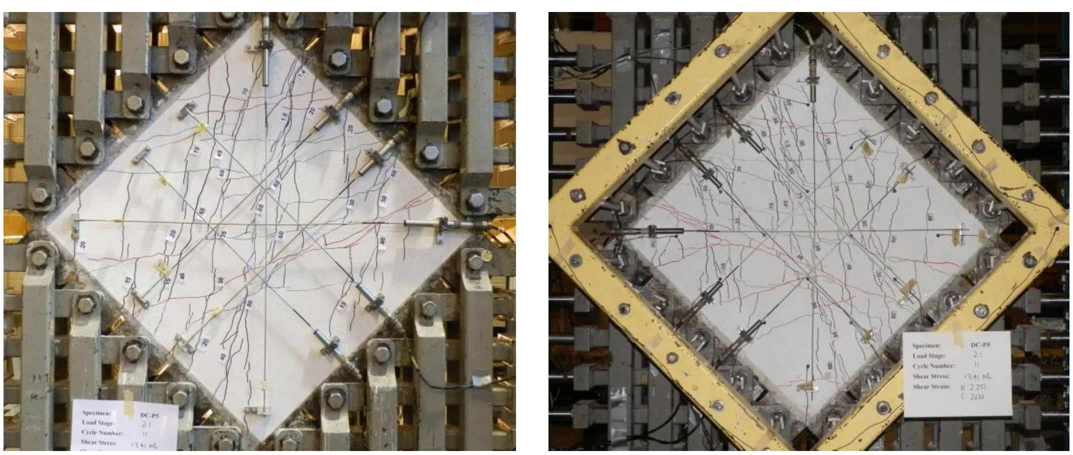

Cycle 11, Stage 21: v_{xy} = 3.41 MPa; γ_{xy} = 2.44x10^{-3}; w_m = 0.33 mm; s_m = 82 mm.

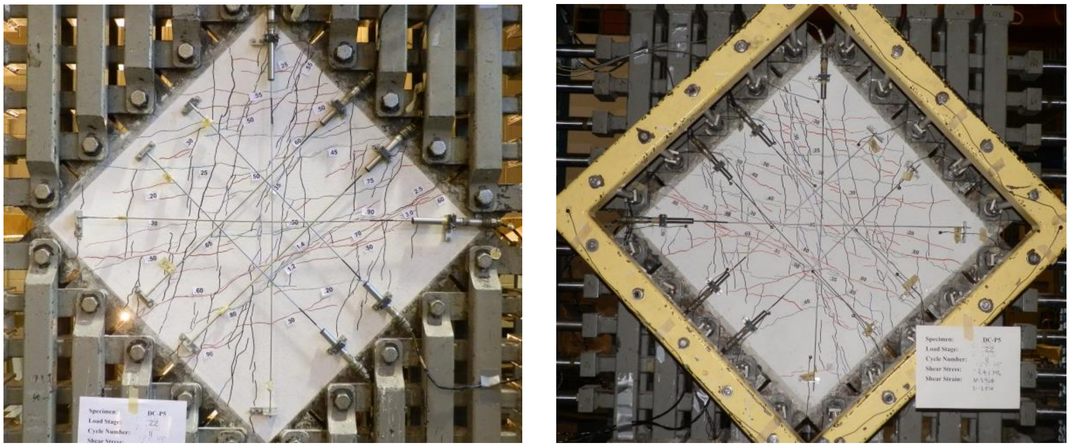

Cycle 11, Stage 22: v_{xy} = -3.41 MPa; γ_{xy} = -3.71x10^{-3}; w_m = 0.47 mm; s_m = 71 mm.

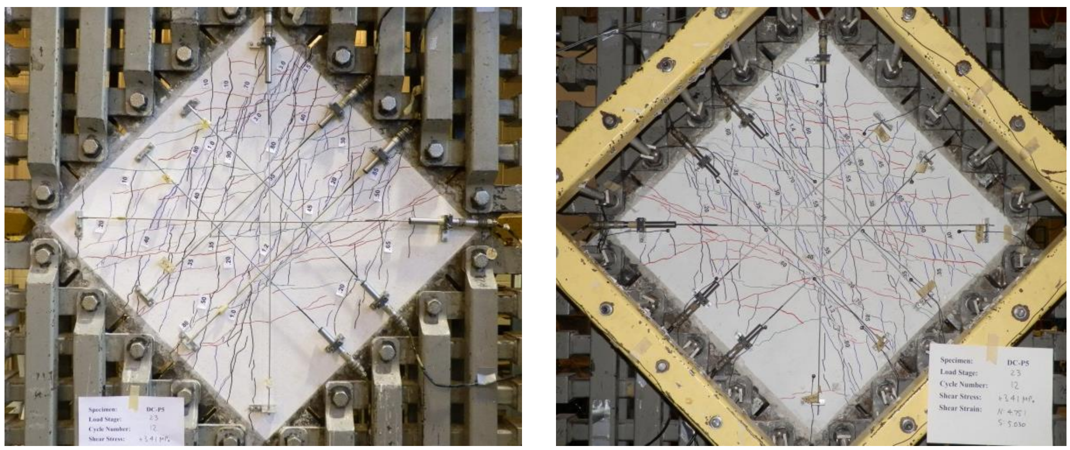

Cycle 12, Stage 23: v_{xy} = 3.43 MPa; γ_{xy} = 4.82x10^{-3}; w_m = 0.59 mm; s_m = 59 mm.

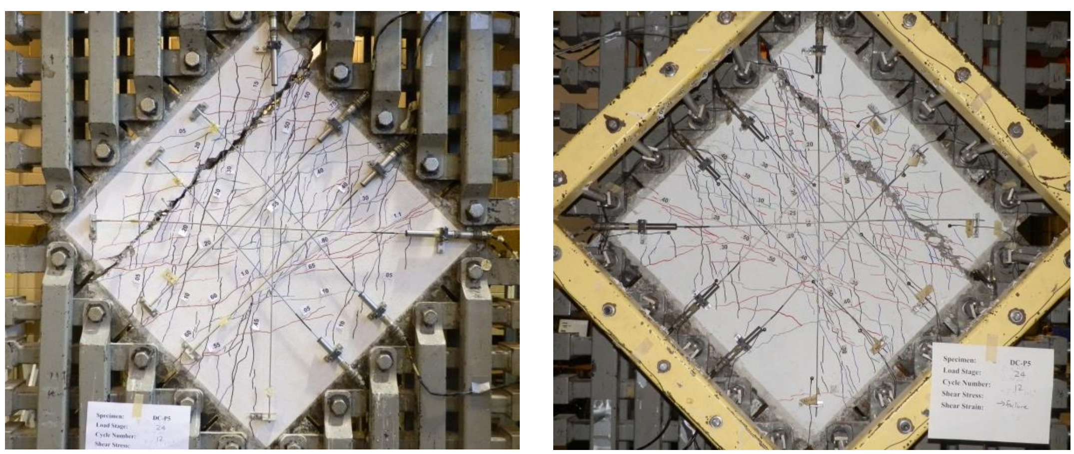

Failure: v_u = 3.43 MPa; γ_u = 5.15x10^{-3}.

Figure B.134: Panel DC-P5 – Selected crack patterns

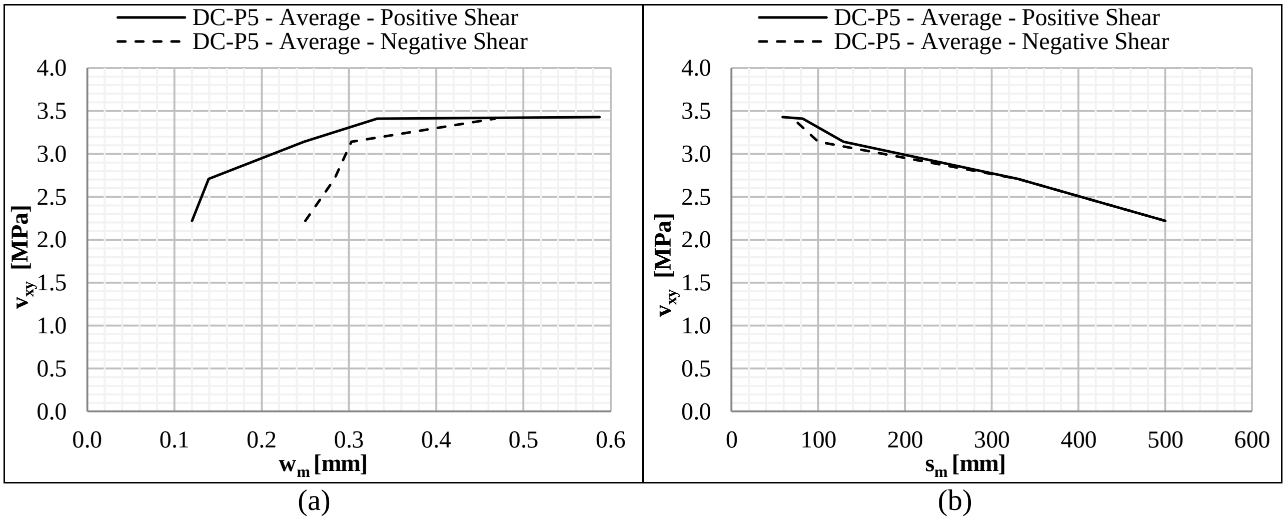

Figure B.135: Panel DC-P5 – Cracking of the panel

No significant stress was developed in the longitudinal reinforcement until cracking. The stresses in the longitudinal reinforcement increased linearly as the shear stress was increased, suggesting that the bars did not yield. The maximum stress in the steel was 204 MPa, similar to DC-P3 but much greater than the SFRC reversed cyclic panel DC-P4.

B.6.3 Comparison of the Responses of the Front and Back Face

Figure B.138 shows the comparison between the LVDT responses of the front face and the back face of the panel. As with other panels, the shear stress versus shear strain response showed a strain offset between the two faces that gradually became more pronounced as the test continued, particularly in positive shear. However, inconsistent with the findings from the other panel tests, the back face of the panel experienced lower principal tensile stresses and greater principal compressive stresses. In addition, the reinforcement stresses as calculated using the back face measurements were greater than the front face. This perhaps suggests a more uniform dispersion of coarse aggregate and fibres when compared to the other panel tests. However, it was apparent from the shear stress versus shear strain behaviour that other out-of-plane issues affected the response. This may be attributable to improper alignment of the panel in the test machine, or overtightening of the bolts used to attach the panel shear keys to the hydraulic jacks.

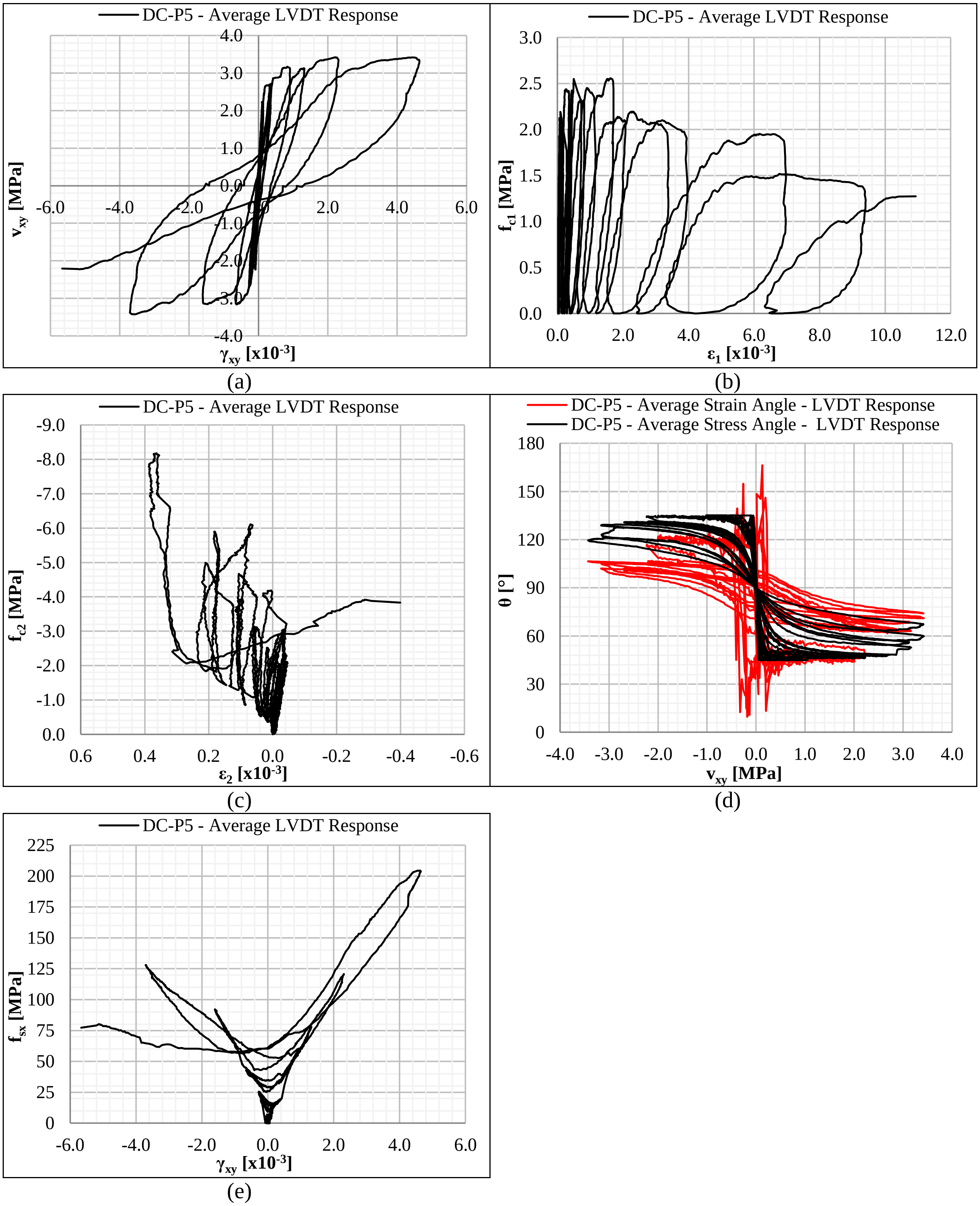

Figure B.136: Panel DC-P5 – Responses of the panel

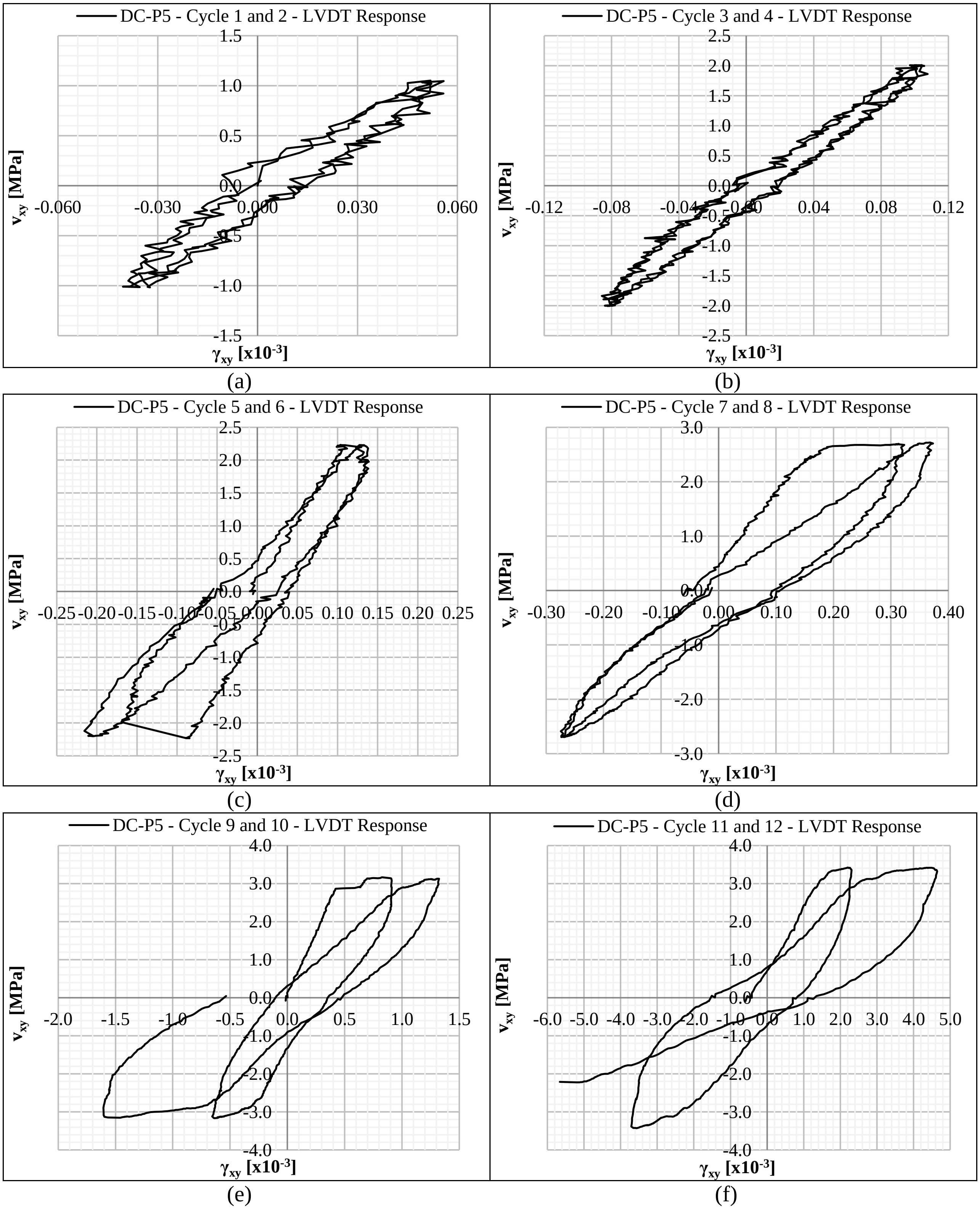

Figure B.137: Panel DC-P5 – Shear stress versus shear strain; isolated cycles

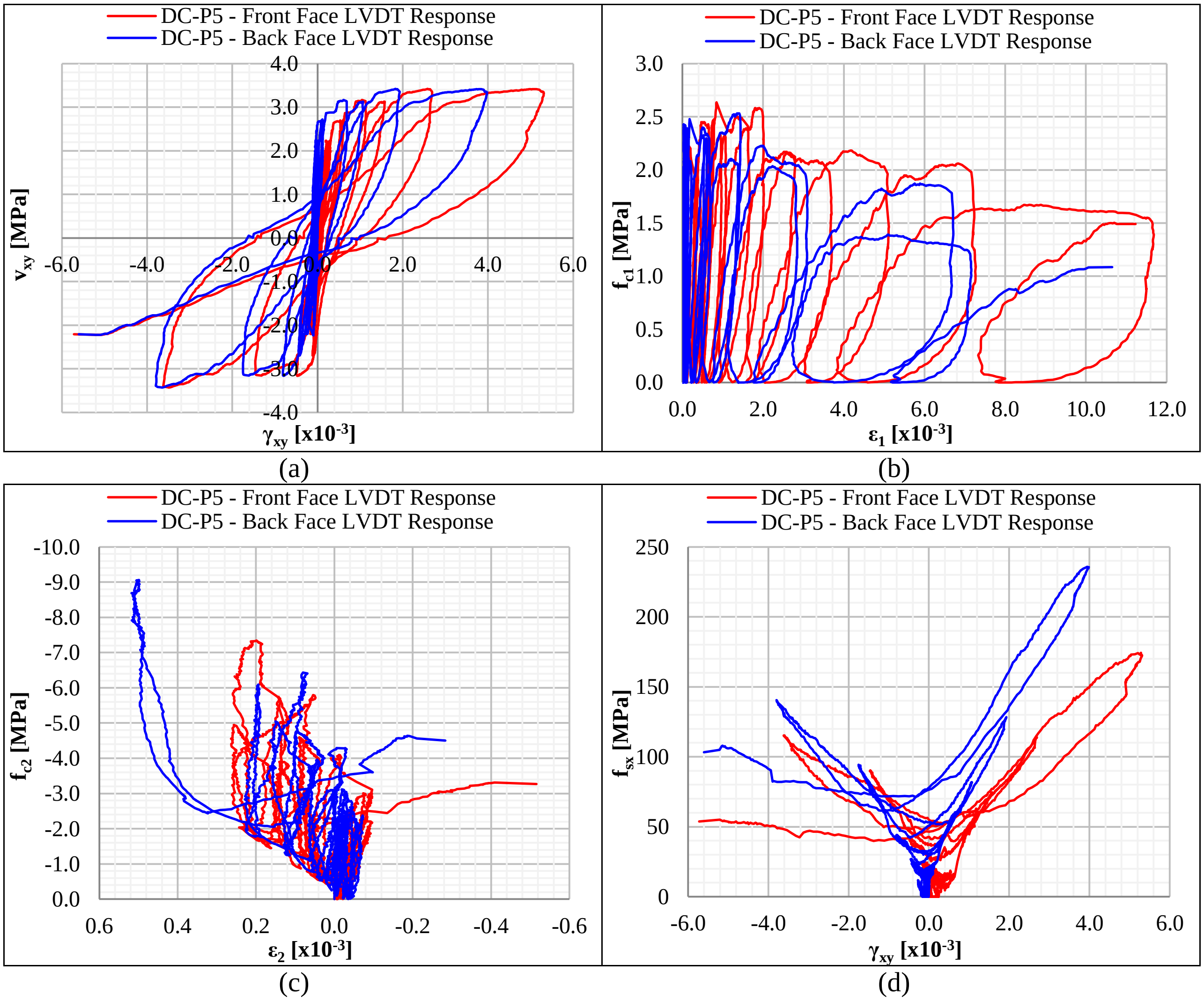

Figure B.138: Panel DC-P5 – Comparison of the front face and back face responses